Transactions of the ASME®

Journal of Fluids Engineering

Published Quarterly by The American Society of Mechanical Engineers

VOLUME 124 • NUMBER 3 • SEPTEMBER 2002

Transactions of the ASME, Journal of Fluids Engineering (ISSN 0098-2202) is published quarterly (Mar., June, Sept., Dec.) by The American Society of Mechanical Engineers, Three Park Avenue, New York, NY 10016. Periodicals postage paid at New York, NY and additional mailing offices.
POSTMASTER: Send address changes to Transactions of the ASME, Journal of Fluids Engineering, c/o THE AMERICAN SOCIETY OF MECHANICAL ENGINEERS, 22 Law Drive, Box 2300, Fairfield, NJ 07007-2300.
CHANGES OF ADDRESS must be received at Society headquarters seven weeks before they are to be effective. Please send old label and new address.
STATEMENT from By-Laws. The Society shall not be responsible for statements or opinions advanced in papers or ... printed in its publications (B7.1, Par. 3).

INDEXED by Applied Mechanics Reviews and Engineering Information, Inc. Canadian Goods & Services Tax Registration #126148048.

TECHNICAL PAPERS

(**Contents continued on inside back cover**)

This journal is printed on acid-free paper, which exceeds the ANSI Z39.48-1992 specification for permanence of paper and library materials. ♾™
♻ 85% recycled content, including 10% post-consumer fibers.

TECHNICAL BRIEFS

DISCUSSION

ANNOUNCEMENTS

Liquid Film Atomization on Wall Edges—Separation Criterion and Droplets Formation Model

F. Maroteaux
Université Paris VI - LMP,
2 place de la gare de ceinture,
78210 St Cyr L'Ecole, France
e-mail: maroteau@ccr.jussieu.fr

D. Llory

J-F. Le Coz

C. Habchi

IFP, 1&4 avenue du bois préau,
92852 Rueil-Malmaison, France

In order to predict the fuel mixture preparation inside the cylinder of port fuel injection engines, a model for the aerodynamic stripping of the fuel film deposited on the manifold walls is discussed, and a model for the fuel film separation and atomization near the sharp edges is developed. A separation criterion is set up using an analogy with Rayleigh-Taylor instabilities driven by the inertial forces of the liquid film. To determine the physical parameters of the resulting droplets, a liquid sheet atomization scheme is used. The critical value for the separation criterion is adjusted using experimental data obtained in 2D wind tunnel equipped with different steps shaped as a valve seat, and reproducing the main characteristics of the intake of spark ignition engine. CFD simulations are performed using the KMB code, a modified version of KIVA-2 already including a stochastic Lagrangian description of the spray, and an Eulerian liquid film model. Computations results for different operating conditions are in good agreement with the images of film separation and measured droplet size distributions. [DOI: 10.1115/1.1493811]

Introduction

Hydrocarbon (HC) emissions for spark ignition SI engines are mainly due to poor air-fuel mixing. In port fuel injection engines, the major part of the injected fuel impacts the intake valve and pipe walls [1–4] and forms a film which flows slowly and vaporizes partially. Hence the liquid quantity stored in the film represents three to nine times the mass amount of one injection, depending on the intake pipes and valves temperature [5–7].

This film is drawn by the air flow during the intake process. Packets of droplets were observed by many authors [8–11] flowing into the cylinder. At the present time, it is not clear if those droplets are the results of the liquid film aerodynamic stripping or separation and atomization on the sharp edge of the valve and the seat. Valve liquid film separation was acknowledged by Shin et al. [12] to be one of the major contributors of liquid fuel atomization in the engine cylinder and was determined to provide poor atomization, which leads to large droplets and ligaments.

Generally, break-up occurs when strong disturbances develop in a liquid-gas interface. We can distinguish two types of instabilities which can produce a liquid film atomization: aerodynamic instabilities (i.e., Kelvin-Helmoltz instabilities) and gravitational or inertial instabilities (i.e., Rayleigh-Taylor instabilities). The former involves the shearing effect of coflowing air at high velocity which induces an interface stripping and the latter can occur when two fluids of different densities are submitted to a body force.

In their experimental study on break-up at cold start conditions, Koederitz and Drallmeier [13] have observed that inertial atomization and aerodynamic stripping occur at different valve lifts. Furthermore, their experimental observations have shown that the break-up mode appears to be extremely sensitive to air flow changes at low valve lifts (lower than 5 mm). For this case inertial atomization is dominant. The authors confirm that this break-up mode produces large droplets and that aerodynamic stripping produces much smaller ones.

For the different operating conditions of port fuel injected engines, the two types of instabilities can develop, during the intake stroke and especially for the cold start operations when the fuel film is thicker. In fact, during the intake stroke, the film deposited on the manifold walls and the intake valves is pulled by the air flow toward the cylinder. For the fuel deposited on the intake valve, inertial instabilities may develop when the film reaches the sharp valve corner (or seat). In the case of the manifold wall film, the aerodynamic instabilities can occur at the film surface.

The objective of this study is to understand the atomization process of liquid fuel film from intake valve and port walls in conditions similar to those found in the intake manifold of spark ignition engines, in order to study the mixture formation with a 3D CFD code. A model of film separation on wall edges together with a droplet diameter prediction model that uses a liquid sheet atomization scheme are described.

In the first part of this paper, the potential of aerodynamic instabilities to atomize a liquid film from intake valve and port walls, in typical engines conditions, is discussed. In the second part, a theory of inertial instabilities based on an analogy of Rayleigh-Taylor instabilities is presented and is used to build a numerical model for film separation and sheet atomization. The evaluation of the model is done by considering experimental data [14] obtained on a film drawn on a step by the air flow in a wind tunnel. The separation criterion is confronted to the atomization process shown by photographs taken just downstream of the step.

The diameter prediction model is described and the model is evaluated by comparison to diameter distributions measured downstream of the step by Phase-Doppler Anemometry.

1 Atomization Potential of Aerodynamic Instabilities

Model. During the intake stroke, a part of the liquid film is drawn by air flow into the cylinder due to the gas shear on the film surface. In order to build a model to describe the aerodynamic instabilities which can develop on the film surface and lead to the droplets production, we have used the assumption of small disturbances to obtain the dispersion equation, which allows to calculate the most unstable wavelength and its maximum growth rate, which are assumed to be responsible for liquid film stripping.

According to Rayleigh-Taylor theory about instabilities of small sinuous disturbances, the variables are separated in an average term and a fluctuating term to linearize the Navier-Stokes equations as following:

$$P = \overline{P}(y) + p(y)e^{i\kappa x + \omega t}$$

$$U = \overline{U}(y) + u(y)e^{i\kappa x + \omega t}$$

Contributed by the Fluids Engineering Division for publication in the JOURNAL OF FLUIDS ENGINEERING. Manuscript received by the Fluid Engineering Division July 11, 2001; revised manuscript received March 21, 2002. Associate Editor: J. Katz.

$$V=\overline{V}(y)+v(y)e^{i\kappa x+\omega t} \tag{1}$$

where P is the pressure. U and V are the velocity components parallel and perpendicular to the main flow direction. The upper bar denotes the average term. p,u,v represent the amplitude of the fluctuating term for the pressure and the velocity components. κ is the wave number in the x direction, and the real part of ω is the growth rate of the perturbation.

The introduction of the system (1) in the Navier-Stokes equations, with boundary conditions, allows to link ω and κ by a dispersion equation of general expression $f(\omega,\kappa)=0$. In this way, an analytical relation between ω and κ cannot be derived from direct resolution of the equations. Consequently, we have used an approach proposed by Taylor [15,16], based on small disturbances $\delta(x,t)$ and which describes the liquid motion by a potential of velocity (irrotational part) and by a stream function (rotational or viscous part). The schematic configuration of the liquid film is shown on Fig. 1. The model assumes that a two-dimensional (x,y), viscous incompressible liquid film of thickness h moves through an inviscid incompressible gas medium. In the coordinate system used in the present work, the liquid film moves with a velocity U_l and the gas phase flows with a velocity U_g. Using Eq. (1), the Navier-Stokes equations can be written as follow for the gas and liquid phases:

Gas Phase.

$$\frac{\partial u_g}{\partial x}+\frac{\partial v_g}{\partial y}=0$$

$$\frac{\partial u_g}{\partial t}+\overline{U}_g\frac{\partial u_g}{\partial x}=-\frac{1}{\rho_g}\frac{\partial p_g}{\partial x}$$

$$\frac{\partial v_g}{\partial t}+\overline{U}_g\frac{\partial v_g}{\partial x}=-\frac{1}{\rho_g}\frac{\partial p_g}{\partial y} \tag{2}$$

Liquid Phase.

$$\frac{\partial u_l}{\partial x}+\frac{\partial v_l}{\partial y}=0$$

$$\frac{\partial u_l}{\partial t}+\overline{U}_l\frac{\partial u_l}{\partial x}=-\frac{1}{\rho_l}\frac{\partial p_l}{\partial x}+\nu_l\left(\frac{\partial^2 u_l}{\partial x^2}+\frac{\partial^2 u_l}{\partial y^2}\right)$$

$$\frac{\partial v_l}{\partial t}+\overline{U}_l\frac{\partial v_l}{\partial x}=-\frac{1}{\rho_l}\frac{\partial p_l}{\partial y}+\nu_l\left(\frac{\partial^2 v_l}{\partial x^2}+\frac{\partial^2 v_l}{\partial y^2}\right) \tag{3}$$

Boundary Conditions. The boundary conditions for the gas phase are:

$$u_g(y=+\infty)=0;\ v_g(y=+\infty)=0 \text{ and } p_g(y=+\infty)=0$$

The boundary conditions for the liquid phase are:

$$u_l(y=0)=0 \text{ and } v_l(y=0)=0$$

Adherence conditions: $u_l(y=0)=0;\ v_l(y=0)=0$

Tangential stress equal to zero:

$$\frac{\partial u_l}{\partial y}+\frac{\partial v_l}{\partial x}=0$$

Mass flux is equal to zero at the free surface:

$$v_l=\frac{\partial \delta}{\partial t}+\overline{U}_l\frac{\partial \delta}{\partial x}$$

$$v_g=\frac{\partial \delta}{\partial t}+\overline{U}_g\frac{\partial \delta}{\partial x}$$

Normal stress continuity at $y=h$:

$$-p_l+2\mu_l\frac{\partial v_l}{\partial y}=-p_g+\sigma\frac{\partial^2 \delta}{\partial x^2}$$

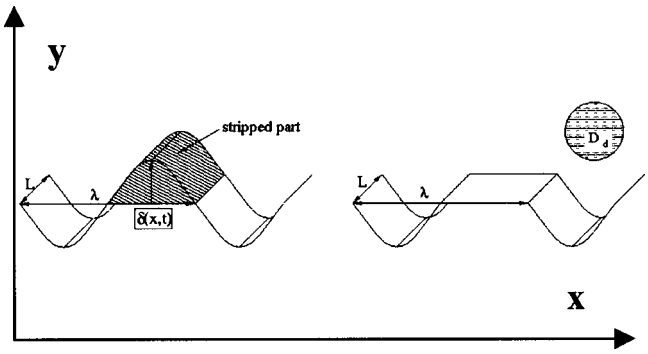

Fig. 1 Configuration of film disturbance and stripping

Writing the velocity components with a potential of velocity $\psi=\Psi e^{ikx+\omega t}$ and a stream function $\phi=\Phi e^{ikx+\omega t}$ following Taylor method [15]:

$$u=\frac{\partial \psi}{\partial x}-\frac{\partial \phi}{\partial y}$$

$$v=\frac{\partial \psi}{\partial y}+\frac{\partial \phi}{\partial x}$$

the following dispersion equation is obtained:

$$\omega^2+2\nu_l\omega k^2(1-F)=\frac{k^2}{\rho_l}\left[\rho_g\left(U_g-\frac{i\omega}{k}\right)^2-\sigma\kappa\right]G \tag{4}$$

where F and G are two functions of film thickness h, defined as follows:

$$F=\frac{2kl[k\cosh(lh)\cosh(kh)-l\sinh(lh)\sinh(kh)]-l(k^2+l^2)}{(k^2+l^2)[k\sinh(lh)\sinh(kh)-l\cosh(lh)\cosh(kh)]+2k^2l}$$

$$G=\frac{(l^2-k^2)[k\sinh(lh)\cosh(kh)-l\cosh(lh)\sinh(kh)]}{(k^2+l^2)[k\sinh(lh)\sinh(kh)-l\cosh(lh)\cosh(kh)]+2k^2l}$$

$$l=\sqrt{k^2+\omega/\nu}$$

Equation (4) is used to calculate the most unstable disturbance which is function of the film thickness h and of the aerodynamic velocity U_g.

To establish the conditions in which the development of aerodynamics instabilities produces drops, we wrote an energy balance during the droplet expulsion. This energy balance allowed us to calculate the droplet diameter, the amplitude and the normal velocity of the disturbance.

If we assume that to obtain a drop, the increase of the free surface of the film due to the drop formation is compensated by the kinetic energy of the instability, then the total energies (kinetic and surface tension) before and after the droplet expulsion are equal. The schematic states of a drop formation are plotted on Fig. 1 and the energy balance can be written as following:

$$E_{\text{film1}}=E_{\text{film2}}+E_{\text{drop}} \tag{5}$$

where: E is the total energy and subscripts 1 and 2 correspond to the state before and after stripping. If we assume that the kinetic energy of the drop is equal to zero, then Eq. (5) gives the minimum energy required for the formation of a drop:

$$(E_{\text{kin}}+E_{\text{ten}})_{\text{film1}}=(E_{\text{ten}})_{\text{film2}}+(E_{\text{ten}})_{\text{drop}} \tag{6}$$

where E_{kin} is the kinetic energy and E_{ten} is the surface tension energy.

The disturbance is described by a sinuous function with an amplitude $\delta(t)$ and a wavelength $\lambda(=2\pi/k)$:

$$\delta(x,t)=\delta(t)\sin(\kappa x) \tag{7}$$

Our interest here is in the most unstable mode which is defined by a maximum growth rate ω of the disturbance given by Eq. (4). Then the disturbance velocity can be written if we assume that the velocity remains constant in the y axis direction as:

$$v(x)=\omega\delta(x,t) \tag{8}$$

Equation (7) allows to calculate the stripped mass corresponding to the half of the wavelength. If this mass forms a drop with a radius r_d, then:

$$r_d=\frac{3}{4}\frac{\delta(t)\lambda L}{\pi^2} \tag{9}$$

From Eqs. (7), (8), (9) the different energies introduced in Eq. (6), can be written as following:

$$\frac{\rho\lambda\omega^2\delta(t)^3}{3\pi}+\frac{\sigma}{2}\int_0^{\lambda/2}\sqrt{1+(\kappa\delta(t)\cos(\kappa x))^2}dx=\frac{\sigma\lambda}{2}+\frac{\sigma 4\pi r_d^2}{L} \tag{10}$$

To solve this equation the wave width L has to be fixed and we have tested two assumptions:

1. The wave width is equal to the amplitude of the disturbance: $(L=\delta(t))$.
2. The wave width is equal to the wavelength: $(L=\lambda)$.

Equation (10) can then be written as a function of ω, λ, δ, and r_d and allows to calculate the stripping amplitude and the disturbance normal velocity, Eq. (4) giving the characteristics of the unstable disturbance.

Results. The model above gives the characteristics of the disturbance required to obtain film stripping and has been written with the assumption of small disturbances which implies that:

The amplitude of the disturbance is negligible against the film thickness and the wave width;

The velocity of the disturbance is negligible against the mean motion.

Thus, we have compared the amplitude and the velocity of the disturbance with a reference length and velocity defined as following:

The reference amplitude, is fixed to the tenth of the film thickness.

The reference disturbance normal velocity is fixed to the tenth of the gas velocity and the reference tangential film velocity to the spray velocity at the nozzle of the injector (about 20 m/s).
This choice has been guided by the fact that the increase of the film momentum is due to the impingement of droplets on the walls [17]. Furthermore, the injection velocity gives an idea of the maximum velocity which can be reached by the film (as a reminder the film velocity in the intake manifold is lower than 1 m/s).

The model has been applied to a thin film (thickness $<200\ \mu$m) of gasoline fuel, similar to those present on the intake valve or on the wall of the intake manifold of spark ignition engines, and for different aerodynamic velocities (gas velocities) from 0 m/s up to 300 m/s. As a reminder in these applications, the gas velocity is adjusted around a maximum value of 100 m/s for the optimization of the volumetric efficiency.

Figures 2–7, show the results obtained (amplitude and normal velocity of the disturbance) for different film thickness (25, 50, 100 μm) and for the two assumptions concerning the length scale L chosen above, when the gas velocity increases from 0 m/s to 300 m/s.

A first analysis of these figures leads to identify the main idea of the stripping mechanism behavior:

When the gas velocity is low (<80 m/s), the amplitude required for stripping is high (greater than the film thickness).

When the gas velocity is high, more energy is transferred to the film and stripping occurs for small amplitudes, but high normal velocity waves.

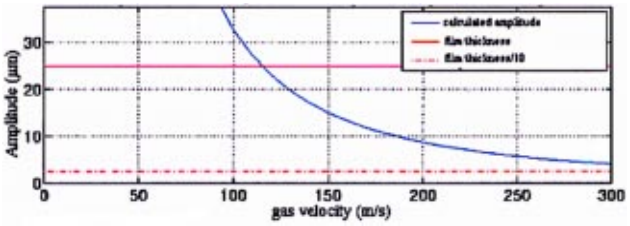

Fig. 2 Amplitude of disturbance for film thickness of 25 μm

For the two assumptions adopted here, the amplitudes obtained are in the same range, which is due to the fact that δ and λ are close (the rate δ/λ is around 1.5 for the assumption $L=\delta$ and about 2 for the assumption $L=\lambda$).

We can observe from these figures that for a gas velocity lower than 150 m/s, the stripping amplitude is greater than the reference length and the normal velocity is approximately twice as high as the reference normal velocity. Furthermore, above 100 m/s the stripping velocity exceeds the reference tangential film velocity, which corresponds to its maximum.

The results show that for film thickness and velocities similar to those found in the spark ignition engines:

The amplitude or the disturbance velocity is not negligible against the mean motion.

The amplitude is larger than the disturbance wavelength.
Consequently, a high level of disturbance energy is required to obtain a film stripping. The resulting amplitudes and velocities of the disturbance do not fit in with the assumption of small disturbances. This shows that it is difficult to reach aerodynamic stripping in the conditions studied here.

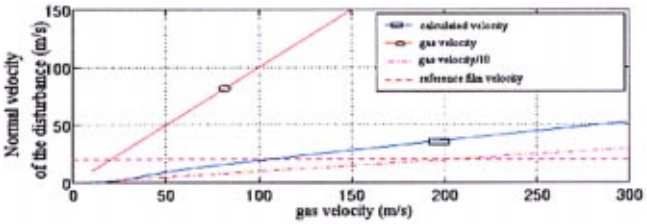

Fig. 3 Normal velocity of disturbance for film thickness of 25 μm

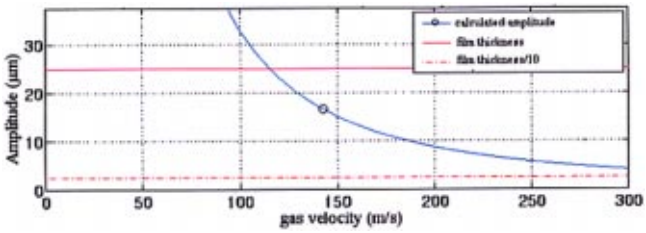

Fig. 4 Amplitude of disturbance for film thickness of 50 μm

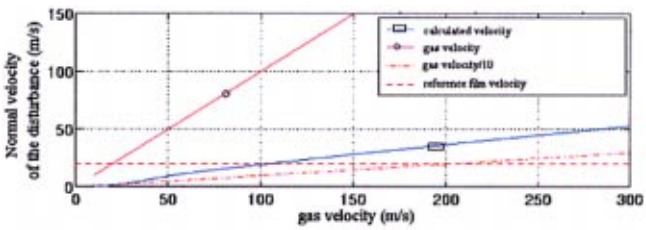

Fig. 5 Normal velocity of disturbance for film thickness of 50 μm

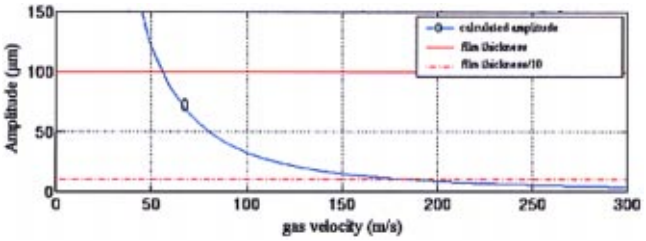

Fig. 6 Amplitude of disturbance for film thickness of 100 μm

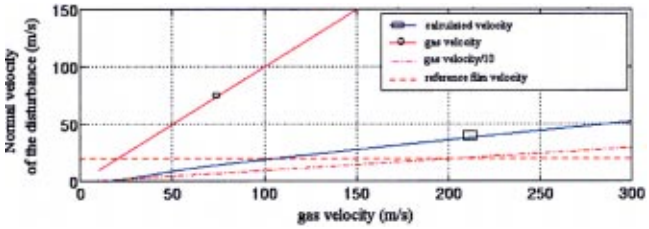

Fig. 7 Normal velocity of disturbance for film thickness of 100 μm

This conclusion was also drawn by Pullin [18] for nonlinear instabilities. He shows that above a given amplitude (smaller than the wavelength), the disturbance unfurls and the amplitude stops increasing. Moreover, results obtained by Li et al. [19] using 3D DNS show the same trend of disturbance vanishing. Thus the nonlinearity of disturbances does not lead to a high level of disturbance energy. Finally, we can conclude that aerodynamic stripping is not likely to happen for typical operating conditions of port injected spark ignition engines.

2 Atomization Potential of Inertial Instabilities

In the second part of this study, we have focused our investigation on the film deposited on the intake valve, where inertial instabilities can develop when the film reaches the sharp valve corner. In this first step the exact geometry of an intake valve was not taken into account. Our model considers only a simple geometry: two planes joining at one edge with a given angle. This geometry was chosen to validate 3D models with experimental data obtained on a film drawn on a step by air flow of a wind tunnel.

Model Description. The model is based on an analogy with Rayleigh-Taylor instabilities. These inertial instabilities develop when two fluids of different densities are submitted to a body force like acceleration (Fig. 8).

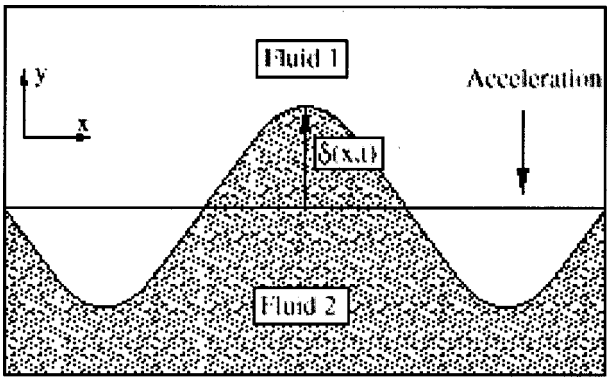

Fig. 8 Perturbation resulting from a difference of density

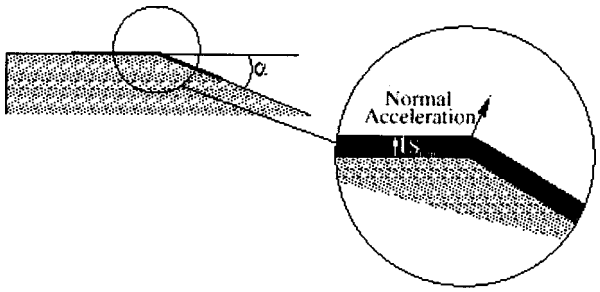

Fig. 9 Analogy with Rayleigh-Taylor instabilities

In the study of liquid film atomization on sharp edges, we consider the passage of the liquid from one side to another (Fig. 9). During this phase, the film is submitted to its inertial force. It is considered as a normal acceleration toward the gas. In this condition, Rayleigh-Taylor instabilities could develop at the liquid interface leading to droplet separation.

The Separation Model. To build the separation criterion, the theory of Rayleigh-Taylor instabilities is used. A spectrum of infinitesimal disturbances of the form $\delta(x,t)=\delta_0 e^{(ikx+\omega t)}$ is imposed on the initial steady motion producing fluctuating velocities and pressures for both the liquid and the gas. δ_0 is the initial perturbation, ω is the growth rate and κ is the wave number defined by $\kappa=2\pi/\lambda$. The proposed separation criterion is based on the ratio between the final amplitude of the disturbance and the initial one, which is written as:

$$\frac{\delta}{\delta_0}=\exp(\omega_m t_{pas}) \tag{11}$$

t_{pas} is the time required by the film to flow over the edge and it is also the time during which the film is subject to the normal acceleration. t_{pas} is calculated assuming a purely liquid film rotating block motion of α_{edge} degrees around the edge as following (see Fig. 10):

$$t_{pas}=\frac{\alpha_{edge} h_{film}}{U_{film}} \tag{12}$$

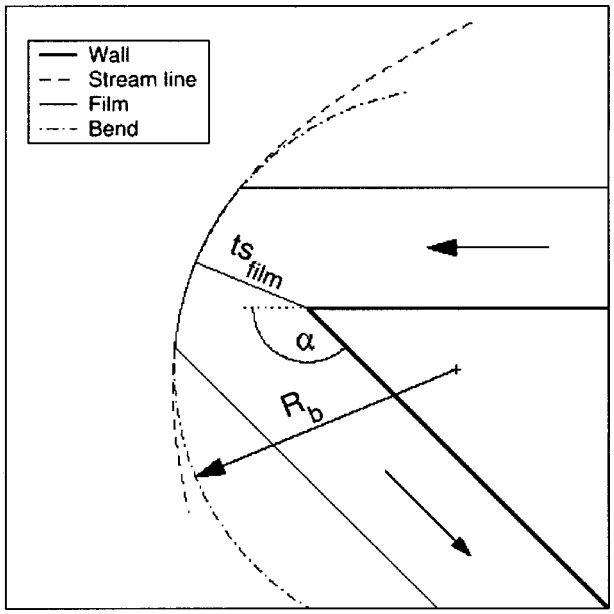

Fig. 10 Film configuration for a step angle of 135 deg (ts_{film}: film thickness)

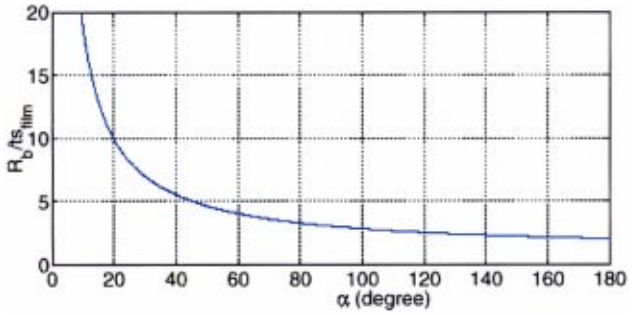

Fig. 11 Ratio between the bend radius and the film thickness versus step angle

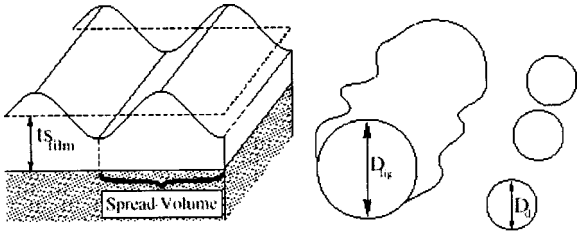

Fig. 12 Atomization scheme (ts_{film}: film thickness)

where h_{film} is the film thickness and U_{film} is the film velocity at the edge location. ω_{m} is the most unstable growth rate assumed to be responsible for droplets separation on sharp edges. Thus, it is desired to obtain a dispersion relation $\omega=\omega(\kappa)$ from which ω_{m} can be deduced.

Calculation of the Maximum Wave Growth ω_m. The wave growth rate is evaluated following the method of Jain and Ruckenstein [20], where the assumption of small disturbances has been adopted and the equations have been resolved using a stream function. The dispersion equation obtained is written as following:

$$\omega=-\left(\frac{\sigma-(\Delta\rho a/\kappa^2)}{2\mu_l h}\right)\left[\frac{(kh)\sinh(kh)\cosh(kh)-k^2h^2}{\cosh^2(kh)+k^2h^2}\right] \tag{13}$$

where $\Delta\rho=\rho_l-\rho_g$ is the difference of density between liquid and gas, μ_l is the viscosity of the liquid and "a" is the acceleration applied to the liquid film.

Calculation of the Acceleration "a": To evaluate the acceleration, it is important to define an approach where the result depends of the edge angle α cleared by the film. This consideration excludes the assumption of the block motion to calculate the acceleration, since in this case the acceleration remains constant (independent of the edge angle α_{edge}).

Then to obtain the acceleration "a," the bend radius R_b of a corner flow stream line is used. It is written as:

$$a=\frac{U_{film}^2}{R_b} \tag{14}$$

The corner flow is defined by a potential flow of complex function: $f(Z)=KZ^n$; with K a constant and $n=\pi/\pi+\alpha_{edge}$ (see Fig. 10). The streamline is found from $\psi=C$ with ψ such as $f(Z)=\phi+i\psi$ and C a constant.

Constants C and K are eliminated by evaluating the ratio between the bend radius and the film thickness leading to:

$$\frac{R_b}{h}=\frac{\pi}{\alpha_{edge}}+1 \tag{15}$$

In this way, the acceleration is related to the edge angle α_{edge}: for small angles, R_b becomes infinite (Fig. 11) leading to a near zero acceleration as expected. In the present model, film separation is assumed to occur when:

$$\frac{\delta}{\delta_0}>\left(\frac{\delta}{\delta_0}\right)_{critic} \tag{16}$$

where $(\delta/\delta_0)_{critic}$ is a fixed value which could be evaluated using available experimental data (see next section). To make the comparison with experimental data easier and more convenient, the separation criterion (16) is expressed as function of the geometrical edge angle α_{edge} as following:

$$\alpha_{edge}\leqslant\alpha_{critical}$$

The critical angle α_{critical} is defined as the angle above which a film of given thickness and velocity is stripped. It may be obtained using Eqs. (11) and (12).

$$\alpha_{critical}=\frac{U_{film}}{\omega_m h_{film}}Log\left(\frac{\delta}{\delta_0}\right)_{critic}$$

This value has been set up from the experimental observations.

Using Eq. (13), different values (10, 15, 20) of the critical ratio $(\delta/\delta_0)_{\text{critic}}$ have been tested. The value of 20 leads to a good agreement with experimental observations, as shown in the next section, and has been adopted.

The Droplet Size Model. The first part of the model gives the behavior of the film. In the case of film separation, droplets are created. In order to evaluate the droplet size, an atomization scheme (Fig. 12) is used. It is assumed that each wave produces a ligament. This ligament becomes cylindrical and breaks up into droplets according to the classical theory described by Rayleigh [21].

The ligament volume is obtained by the mass conservation leading to:

$$D_{lig}=2\sqrt{\frac{\lambda_m h}{\pi}} \tag{17}$$

The Rayleigh theory of the disintegration of a liquid column gives:

$$D_d=3.78\sqrt{\frac{\lambda_m h}{\pi}} \tag{18}$$

To evaluate the droplet size, the characteristics of the most unstable surface wave are used. λ_m is found from the wave number κ_{m} corresponding to ω_{m}.

The parent droplet diameter (D_d) is the result of Eq. (18). Since the atomization is not a deterministic process, the parent droplet diameter (D_d) is used in a Rosin-Rammler droplet diameter distribution written as:

$$F(D)=1\text{-}\exp\left(-\left(\frac{D}{X}\right)^q\right) \tag{19}$$

where X and q are the parameters of the distribution.

X is defined so that $F(D_{\max})=0.999$ (calculated from Eq. (18)):

$$X=\frac{D_{\max}}{(3\ln(10))^{1/q}} \tag{20}$$

The q parameter has been fitted from the numerical simulations and the experimental measurements, this part will be discussed in the experimental approach.

Experimental Validation. In order to have a better understanding of the film separation phenomenon due to sharp edges and to validate the model, an experimental study of the liquid film flowing on a step and droplet production is conducted.

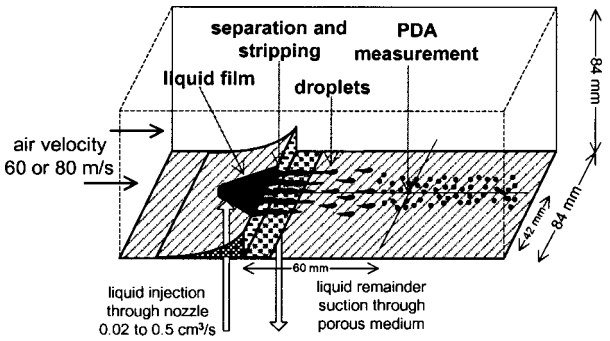

Fig. 13 Wind-tunnel configuration

Experimental Apparatus. The experiments are done in a square section stationary wind tunnel, with 3 transparent sides. An opaque step made of anodized aluminum is fitted on the bottom wall of the tunnel. The configuration is described in Fig. 13. Two different steps (both 1 cm high and 45 degree step angle) are tested (Table 1).

The tunnel has a square section of 84 mm per 84 mm. The liquid comes from a vertical nozzle with a diameter of 1.2 mm. This apparatus generates stable film flow nearly 10 mm wide.

The fuel is dodecane (for security reason), which has a surface tension close to that of gasoline but a twice higher viscosity. A volumetric pump supplies the fuel with accurate flow rate.

The air flow is induced by a high volumetric fan. It provides a mean velocity up to 80 m/s in the upstream square section.

The separation phenomenon is qualitatively observed to validate the criterion. Visualizations are made using a video camera and a stroboscopic flash lamp. The stripping or separation quality is obtained from the pictures by observing the qualitative density of ejected droplets. Figure 14 shows a typical view of stripping phenomenon on the edge, the visualization area is 60 mm long in the direction of flow (see Fig. 13).

The film thickness is measured just upstream of the edge using a laser induced fluorescence (LIF) technique that is somewhat different from that found in previous work done on unsteady liquid films on transparent walls [22]. The film is illuminated by a 2 cm wide laser spot (20 mW, 442 nm He-Cd laser), and a video camera with standard sensitivity collects the fluorescence across the top window of the tunnel, with an integration time of 20 seconds (Fig. 15). A small concentration of commercial green dye used to mark unleaded gasoline is introduced in the liquid. The fluorescence intensity is proportional to film thickness, as proven by calibrating the system on a liquid wedge confined between a quartz window and a black plate, where the thickness is varied between 0 and 400 μm. The accuracy is about ± 3 μm over thickness of 20 to 100 μm. The film velocity is estimated from the mean flowing section and the fuel rate injected.

The droplet size measurements are made using the Phase Doppler Anemometry technique (called PDA hereafter). The arrangement is the following : Ar laser at 488 nm, laser separation 35 mm, focal length 350 mm, collection off-axis angle 30 degrees, 3 detectors with solid angles leading to 0-350 μm diameter range,

Table 1 Side view of the tested steps

	
15°straight step	15° "springboard" step

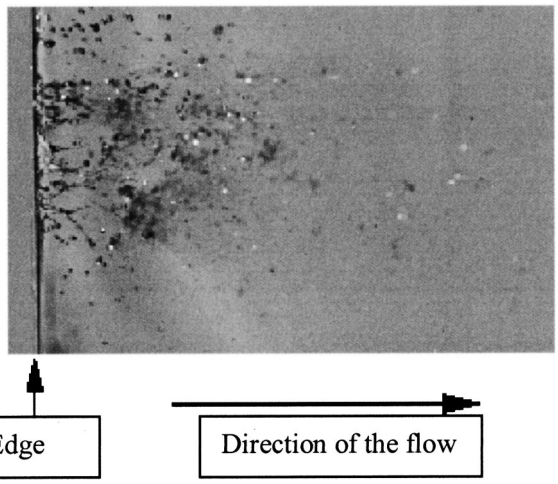

Fig. 14 Typical image, condition with established stripping

Aerometrics RSA signal processor. Drop size measurements are accumulated until a sufficient number of validated data is accumulated (10,000). The droplet volume distribution is calculated by multiplying the diameter probability density function by the diameter raised to the power of 3. No droplet spatial density is calculated here and the validation rate remained all the time over 90%. The measurement point is located 60 mm downstream of the step (Fig. 13).

Boundary Conditions.

Liquid flow: The experimental film thickness profile (Fig. 16) is considered as a boundary condition at the edge for the calculation. The film thickness was never symmetrical around the center. It should be noted that in an experiment the air flow and the step geometry cannot be totally even in the transverse direction, and that free-surface phenomena are very sensitive to that. At this location the liquid film velocity is evaluated using the film thickness profile and the flow rate.

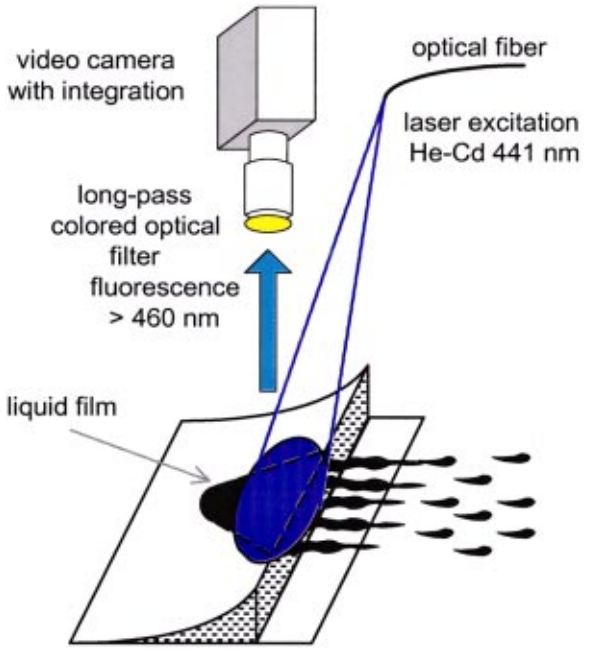

Fig. 15 Optical arrangement for film thickness measurement on the step

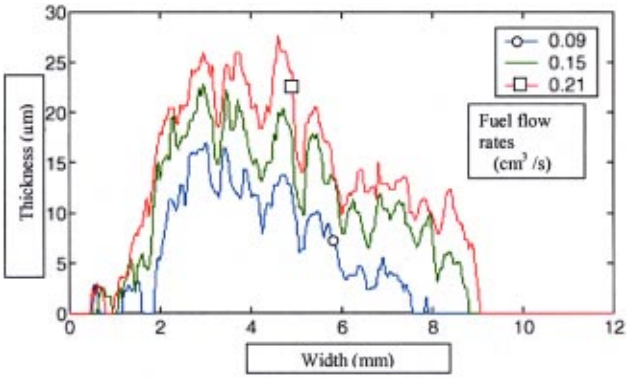

Fig. 16 Measured film thickness for 80 m/s air velocity (springboard step case)

The two steps provide slightly different conditions of film thickness and velocity : the ⟪springboard⟫ step provides slightly higher velocity and smaller thickness.

For the spray study, high liquid flow rates are used (0.5 cm^3/s), for which good film separation occurs.

Gas flow: Only two cases are tested : 60 m/s and 80 m/s leading to film thickness of the order of magnitude of those found in SI engines (10 to 30 μm).

Numerical Results and Discussion About the Separation Criterion. The operating conditions are summarized in Table 2 with the calculated critical angle results and the qualitative experimental observations. The terms used do not correspond to precisely measured drop densities, but to drop number in the images; rare: 0-3 droplets, some: 5-20 droplets, established stripping more than 20.

When the total liquid flow rate is gradually increased, a limit value is found, below which stripping is never or sporadically observed. The limit liquid flow rate diminishes strongly when the air flow rate is increased and depends on the step geometry, as indicated by Table 3. The transition is rather smooth, which explains why only orders of magnitude are given. It must be noted that in all conditions above the threshold, a certain part of the liquid film still moves around the step, and does not atomize (Fig. 17). The flow rate that does not separate from the step is difficult to determine, and was not measured here.

The comparison between experiments and calculations shows that in most cases no separation is observed when the calculated critical angle exceeds 135 degrees, and vice versa. The agreement

Table 2 Numerical results and observations

Step	Air velocity (m/s)	Fuel Flow Rate (cm^3/s)	Maximum Film Thickness (μm)	Estimated Fuel Velocity (m/s)	Calculated critical Angle with $(\delta/\delta_0)_{critic}$=20	Experimental Observation
Springboard	80	0.04	17	2.3	No Stripping	No Droplet
Springboard	80	0.10	23	3.2	128°	Some Droplets
Springboard	80	0.16	28	3.8	94°	Established Stripping
Springboard	60	0.09	21	2.5	174°	Rare Droplets
Springboard	60	0.13	29	2.9	118°	Some Droplets
Springboard	60	0.22	38	2.6	87°	Established Stripping
Straight	80	0.09	26	2.05	No Stripping	No Droplet
Straight	80	0.15	26	2.4	158°	Rate Droplets
Straight	80	0.21	32	3.2	99°	Established Stripping
Straight	60	0.15	34	1.8	165°	No Droplet
Straight	60	0.20	37	1.8	160°	No Droplet
Straight	60	0.27	41	2.25	115°	Established Stripping

Table 3 Limit liquid flow rate for the two steps

Step	Straight		springboard	
air velocity (m/s)	60	80	60	80
limit liquid flow rate (cm^3/s)	0.4	0.2	0.1	<0.1

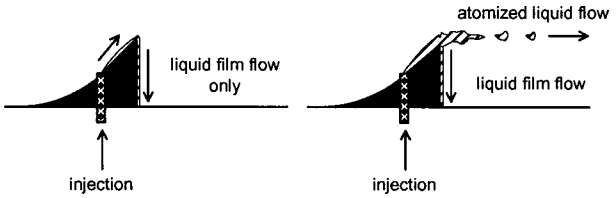

Fig. 17 Film behavior versus liquid flow rate. Left: below the limit flow rate, no film separation. Right: above the limit flow rate, part of the film is converted into droplets.

is not satisfactory in cases 4 and 8 (in gray in Table 2), for which some rare droplets are observed although the calculated critical angle is over 135 deg. However we have to consider that the film thickness data are time averages over 20 seconds. Furthermore, during the experiments, surface instabilities of the film were observed. These perturbations increase the instantaneous thickness and velocity leading to the intermittent generation of random droplets.

Figures 18–21 present the calculated critical angle in a direction orthogonal to the flow for different flow rates. When established stripping is observed (Table 2), critical angles are less than 135 deg for a broad range of the width. For limit cases (⟪some or rare droplets⟫), when only a few droplets are observed, the criterion is satisfied in few locations.

For the springboard step and a velocity of 80 m/s, the limit flow rate is between 0.04 cm^3/s and 0.1 cm^3/s. In the case of 0.04 cm^3/s, the critical angle is about 180 deg, which implies that there is no stripping as observed experimentally. When the flow rate is equal to 0.1 cm^3/s, some droplets are produced (Fig. 22). In this case, Fig. 18 shows three points under the geometrical angle; the ratio between the stripping length and the total length is about

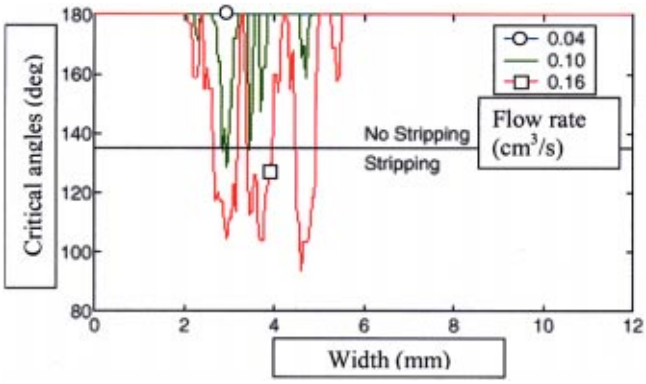

Fig. 18 Critical angle for 80 m/s air velocity (springboard step)

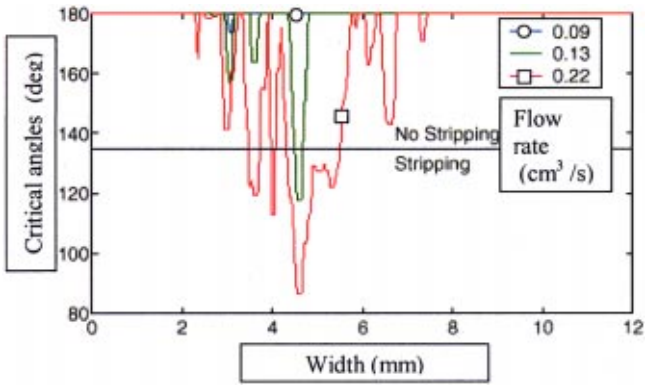

Fig. 19 Critical angle for 60 m/s air velocity (springboard step)

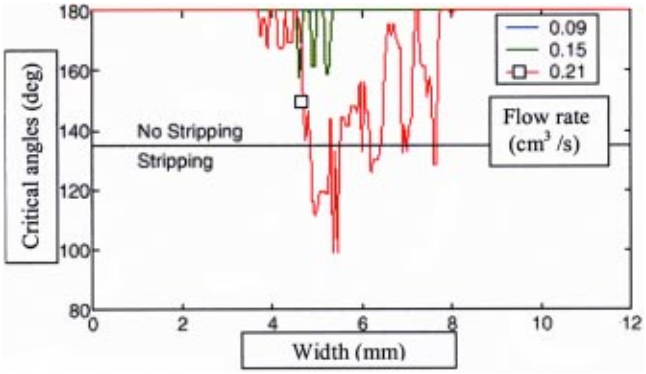

Fig. 20 Critical angle for 80 m/s air velocity (straight step)

2%, in agreement with Fig. 22. When the flow increases above this level, the stripping is established (all the calculated angles are smaller than 135 deg, Fig. 18) and the ratio between the stripping length and the total length increases. Figure 23 shows the observations for a high flow rate, here the ratio is close to 70%.

For the air velocity of 60 m/s, thicker and slower films are observed. In this case the limit flow rate is around 0.1 cm^3/s. Figure 24 (flow rate equal to 0.09 cm^3/s) shows a few droplets. The model predicts a minimum angle of stripping of 169 deg; during the experiment a local unsteady phenomenon (similar to aerodynamic instabilities) is observed. The established stripping occurs for flow rates higher than 0.21 cm^3/s and, as for 80 m/s, the ratio between the stripping length and the total length increases from 20% (for 0.21 cm^3/s) to 72% (for 0.5 cm^3/s, Fig. 25).

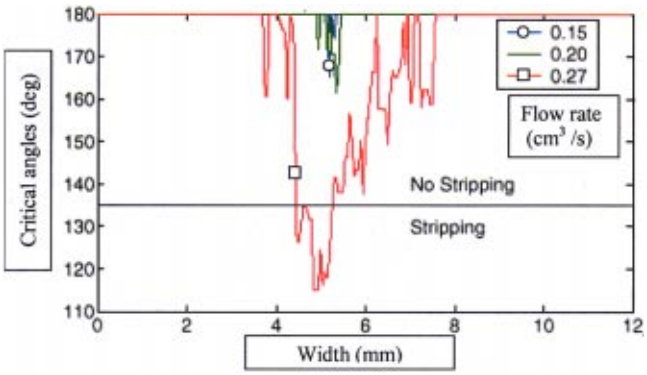

Fig. 21 Critical angle for 60 m/s air velocity (straight step)

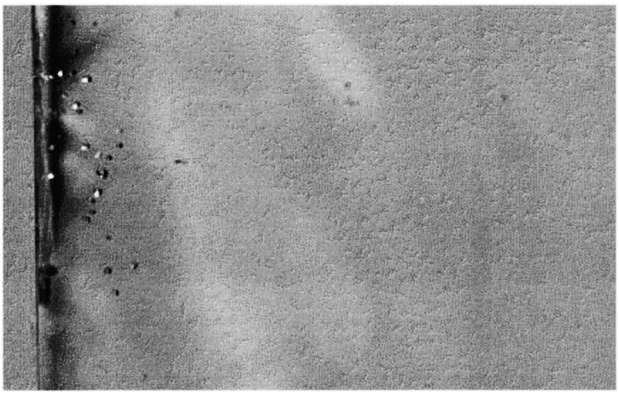

Fig. 22 Experimental view (springboard step), air velocity 80 m/s, fuel flow rate 0.1 cm^3/s: some droplets

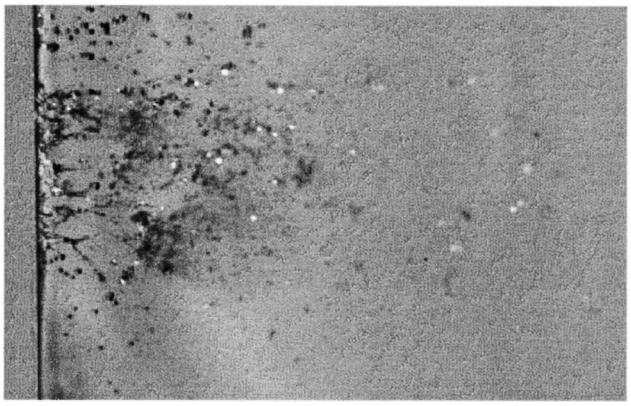

Fig. 23 Experimental view (springboard step), air velocity 80 m/s, fuel flow rate 0.5 cm^3/s: established stripping

The straight step allows larger films (i.e., reduced velocities and thickness for given flow rates). The limit flow rates for stripping in this case are higher than for the springboard (Table 3). When the air velocity is equal to 80 m/s the limit flow rate is around 0.2 cm^3/s and for a slightly lower (0.15 cm^3/s) flow rate, a few droplets are observed (Fig. 26). In Fig. 20, a few points are close to an angle of 140 deg, this production of droplets is due to the instabilities which reached the edge (see Fig. 26). Figure 27 shows a picture for an established stripping (flow rate equal to 0.24 cm^3/s).

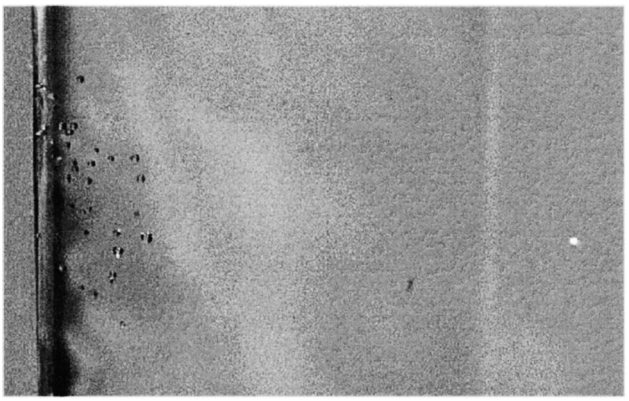

Fig. 24 Experimental view (springboard step), air velocity 60 m/s, fuel flow rate 0.09 cm^3/s: rare droplets

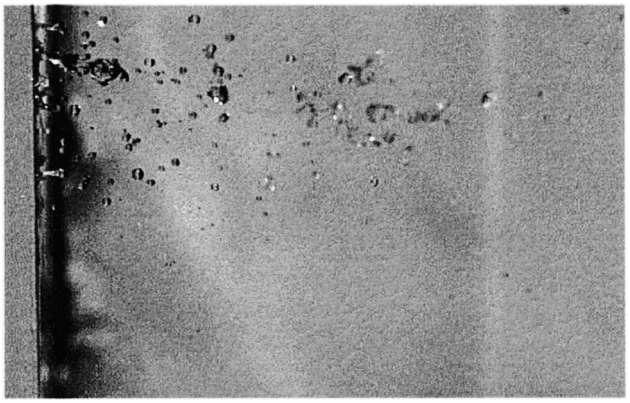

Fig. 25 Experimental view (springboard step), air velocity 60 m/s, fuel flow rate 0.5 cm^3/s: established stripping

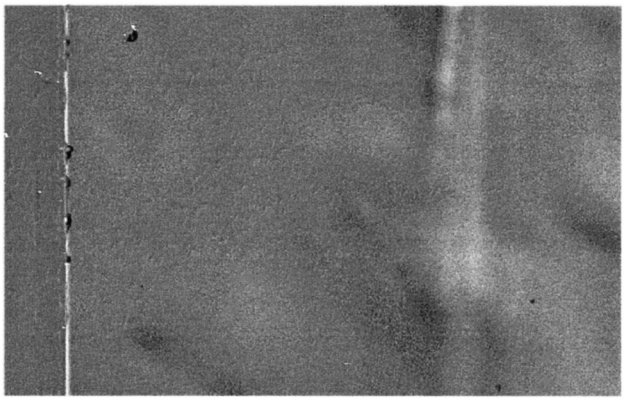

Fig. 26 Experimental view (straight step), air velocity 80 m/s, fuel flow rate 0.16 cm^3/s: rare droplets

From the experimental observations and the model developed here, we can propose a general scheme of film stripping based on the geometrical step angle ($\alpha_{\text{geometrical}}$) and the calculated critical angle (α_{critical}) as following:

$$\text{When: } (\alpha_{\text{geometrical}})-(\alpha_{\text{critical}})<0 \Rightarrow \text{rare droplets}$$

$$\text{When: } 0<(\alpha_{\text{geometrical}})-(\alpha_{\text{critical}})<15 \Rightarrow \text{some droplets}$$

$$\text{When: } (\alpha_{\text{geometrical}})-(\alpha_{\text{critical}})>15 \Rightarrow \text{established stripping}$$

Validation of the Atomization Model. Visualization provides estimated values of maximum parent droplet diameters, by detecting in the images the maximum drop size close to the edge. These are rather rough values (Table 4).

Droplet size distributions are measured by PDA 60 mm downstream from the step, after break-up has happened (Fig. 13).

In this study, we chose to plot volume distributions because our interest is in the spatial distribution of fuel mass. Hence, a small number of large particles have an important weight in the distribution shape, which leads to large fluctuations of the volume distribution in the large diameter range, because of very few but unavoidable wrong diameter values. A practical consequence is that the maximum droplet diameter is very unlikely detectable by PDA. The drop diameter distribution in the calculation is described by Rosen-Rammler distribution. The width parameter (q) of the distribution was fixed with the help of numerical simulations. Therefore, we reproduced numerically the experimental wind tunnel plotted on Fig. 13, and the KIVA-MB code [23] has been used to calculate the air flow in the tunnel ($\kappa-\varepsilon$ model), which code uses the Wave-FIFA droplet break-up model [24].

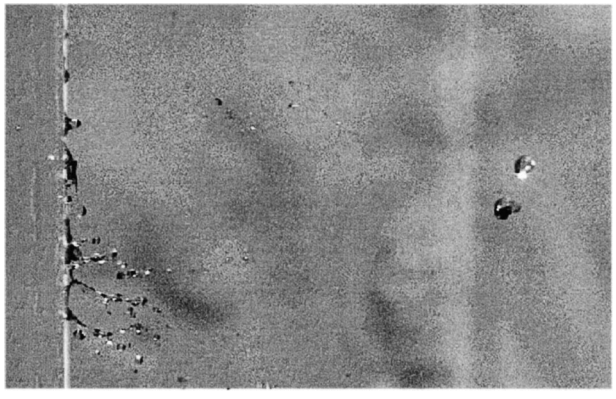

Fig. 27 Experimental view (straight step), air velocity 80 m/s, fuel flow rate 0.24 cm^3/s: established stripping

Table 4 Maximum parent droplet diameters

Step	Straight		Springboard	
Air velocity (m/s)	60	80	60	80
Droplet parent diameter (mm)	0.3 to 1	$<$0.2 to 0.5	$<$0.1 to 0.4	$<$0.1 to 0.2

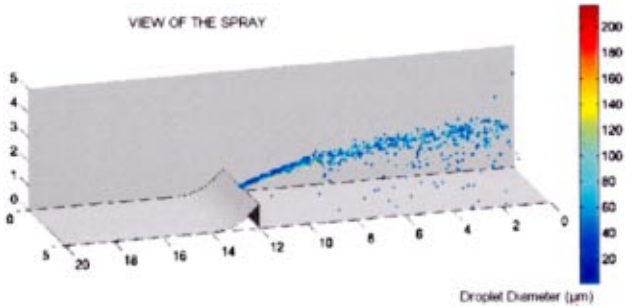

Fig. 28 Computation example: air velocity=80 m/s, fuel rate =0.5 cm^3/s (numerical tunnel configuration: 20 cm long, section 5 cm per 5 cm; computation of droplets distribution are made at 6 cm along the tunnel axis)

We considered two types of atomization:

The primary atomization which occurs at the edge.

The secondary atomization which occurs in the tunnel due to break-up.

To calibrate the atomization model, we have chosen the experimental case which corresponds to the fuel flow rate of 0.5 cm^3/s and the air velocity equal to 80 m/s with the springboard step, for which established stripping is found. Figure 28 shows the numerical visualization of stripping in the tunnel and Figs. 29 and 30 show, respectively, the initial (or parent) volume distribution at the edge for two width parameters ($q=2$ and $q=5$) and the distribution calculated 60 mm downstream. Generally, a small value of the q parameter yields higher density of small droplets, and a high value of q higher density of large droplets in the distribution. These figures show that in both cases, the maximum diameter in the downstream distribution is below 100 μm. Furthermore, in the downstream distribution the density of droplets smaller than 40 μm depends almost only on the initial distribution.

In order to study the influence of the time constant of the secondary atomization model, we have fixed the width parameter equal to 5 and we have simulated two break-up modes. One mode with a short break-up time constant and the other with a long time

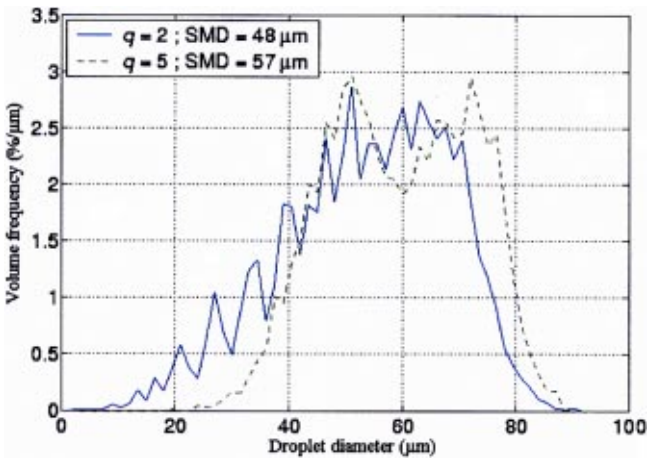

Fig. 29 Initial distribution at the edge for two width parameters (q)

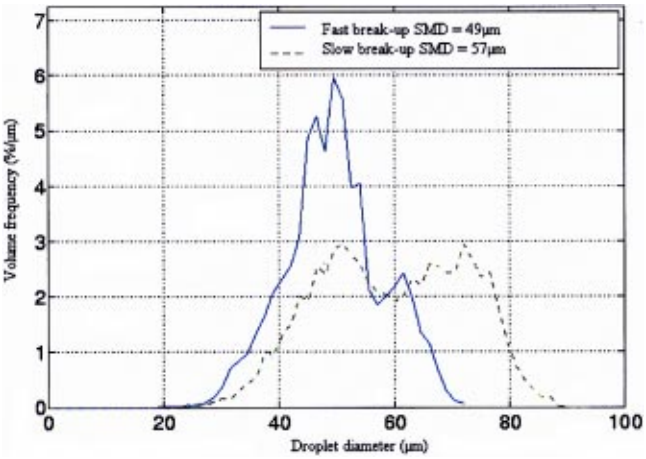

Fig. 30 Calculated distribution 60 mm downstream

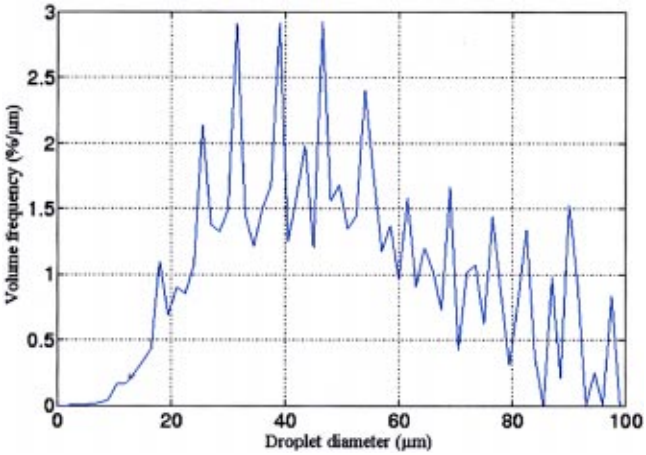

Fig. 31 Measured distribution 60 mm downstream (air velocity of 80 m/s and fuel flow rate of 0.5 cm^3/s)

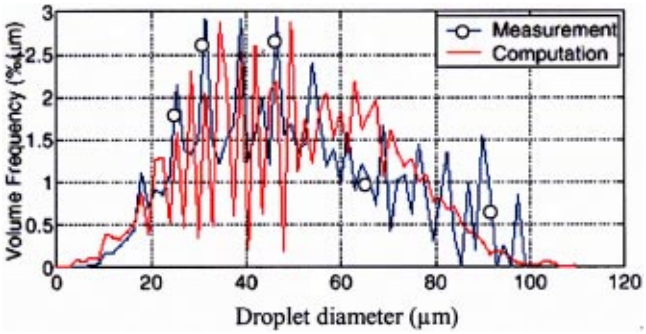

Fig. 32 Droplet size distribution (springboard step), air velocity 80 m/s, fuel rate 0.5 cm^3/s

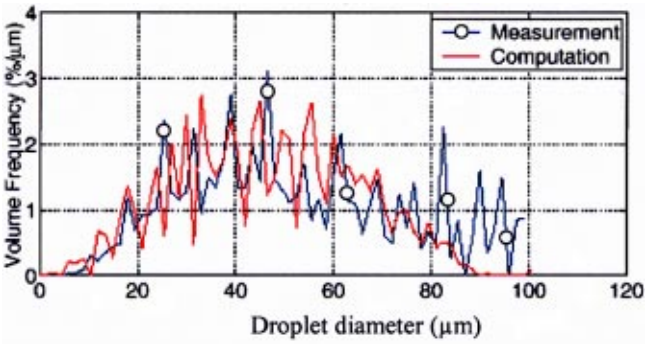

Fig. 33 Droplet size distribution (springboard step), air velocity 80 m/s, fuel rate 0.29 cm^3/s

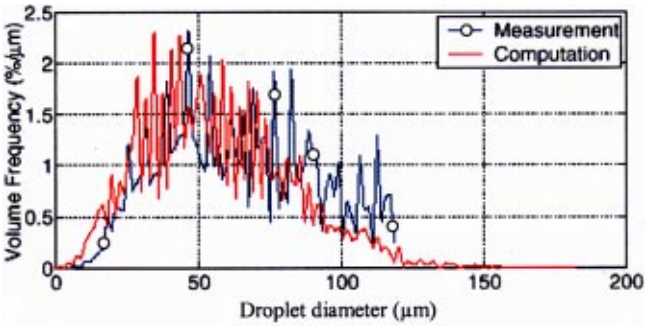

Fig. 34 Droplet size distribution (springboard step), air velocity 60 m/s, fuel rate 0.5 cm^3/s

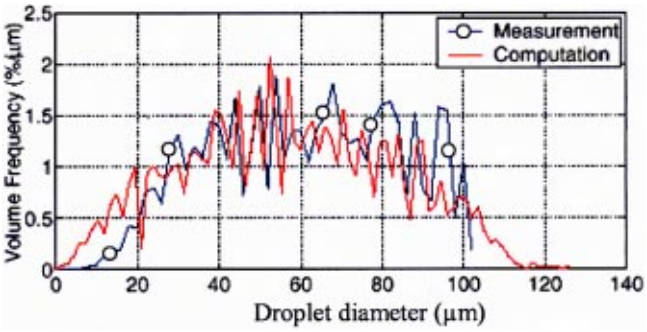

Fig. 35 Droplet size distribution (straight step), air velocity 80 m/s, fuel rate 0.5 cm^3/s

constant. Figure 30 reproduces the results obtained: with fast break up, droplets are concentrated between 40 μm and 60 μm and the lowest droplet diameter obtained is around 20 μm (low limit of the initial distribution). With slow break-up, two peaks are observed: a first one at 50 μm similar to that with fast break-up, and a second one around 70 μm. The latter peak is more likely produced by break-up of droplets larger than 100 μm, while droplets smaller than 30 μm originate directly from the initial distribution, generated at the edge. Figure 31 shows the distribution measured 60 mm downstream; we can see from this figure that the experimental distribution contains more drops around 40 μm and some drops around 100 μm.

From the results above, we have then fixed the width parameter equal to 1.5 to represent the high population of small droplets, and the short break-up time constant was selected to reproduce the big droplets observed experimentally. Figures 32–35, present the comparison between the experimental and computed distributions for different cases. In all four cases, predictions are in good agreement with the experimental measurements for medium and small droplets. The prediction for large droplet size appears less accurate because of the chosen distribution representation. Some discrepancies appear in the large diameter range (>80 μm) because the PDA technique cannot catch the tail of a volume distribution.

Computations show that the small droplets found downstream are generated at the edge. But it could be assumed that small droplets are quickly accelerated up by air velocity. Hence droplets reach a stable diameter of order of magnitude 50 μm. Conse-

quently, we could expect that the small diameter range in the distribution comes directly from the atomization of the liquid film on the edge and the large diameter range comes from the break up of large parent droplets in the shearing air flow.

Conclusion

In order to improve the prediction of fuel mixing in SI engines, a model for the aerodynamic stripping of the fuel film deposited on the manifolds walls is discussed and a model for fuel film separation and atomization near the sharp edges is developed.

The results of the aerodynamic model based on the assumption of small disturbances, have shown that to obtain atomization of the liquid film from the intake valve and port walls, a high level of disturbance energy is required, in typical engine conditions. The resulting amplitudes and velocities of disturbance do not fit in with the assumption of small disturbances. Furthermore, it is difficult to reach aerodynamic stripping for typical operating conditions of port injected spark ignition engines. This conclusion was also drawn by other authors for nonlinear instabilities.

The theory of inertial instabilities based on an analogy of Rayleigh-Taylor instabilities has been used to develop a model for film separation and sheet atomization on the sharp edges, for the film deposited on the intake valve. The model is able to predict if the film separates or sticks to the wall and to estimate the size of the ejected droplets. The proposed separation criterion has been set up using experimental data. By evaluating the critical angle in the width of the film for separation limit cases, the separation criterion has been validated for a set of operating conditions including different steps shapes, air velocities and liquid flow rates. From the experimental observations, we have observed that, when the total liquid flow rate is gradually increased, a limit value is found, below which stripping is never or sporadically observed. The limit liquid flow rate decreases strongly when the air flow rate is increased and depends on the step geometry. It has been also observed, that in all conditions above the threshold, a certain part of the liquid film still moves around the step, and does not atomize.

From the experimental observations and the model developed in this study, a general scheme of film stripping based on the geometrical step angle and the calculated critical angle is proposed.

Acknowledgments

This research was funded in part by the GSM (Groupement Scientifique Moteur - PSA, Renault and IFP). The authors wish to thank the GSM.

Nomenclature

a = acceleration
D = droplet diameter
E = energy
f = complex potential function
F = Rosin-Rammler equation
h = film thickness
p = pressure
q = distribution parameter of Rosin-Rammler equation
R_b = bend radius
R = radius
r_d = drop radius
t_{pas} = time required by the film to pass over the edge
U = velocity
U_{film} = film velocity
X = size parameter of Rosin-Rammler equation
z = complex coordinate
α = the angle of the edge
$\delta(t,x)$ = amplitude of the perturbation
δ_0 = initial amplitude
μ = dynamic viscosity
ν = kinematics viscosity
λ = wavelength
ω = growth rate of perturbation
Φ = stream function
ψ = potential function
ρ = density
σ = surface tension

Subscript

critic = condition for film separation
d = relevant to the droplet
film = relevant to the film
g = relevant to gas phase
kin = relevant to the kinetic energy
l = relevant to liquid phase
lig = relevant to the ligament
m = relevant to the maximum growth rate
ten = relevant to the surface tension energy

References

[1] Maroteaux, F., and L. Le Moyne, 1995, ''Modeling of Fuel Deposition Rate in Port Fuel Injected Spark Ignition Engine,'' SAE paper 952484.
[2] Guntz, C., S. Guilain, and F. Maroteaux, 1997, ''Modeling of Fuel Behavior in The Intake Manifold of Port Fuel Injected Spark Ignition Engine,'' SAE paper 972992.
[3] Fox, J., W. Cheng, J. B. Heywood, and K. Min, 1992, ''Mixture Preparation in A SI Engine With Port Fuel Injection During Starting and Warm-Up,'' SAE paper 922170.
[4] Bourke, M. C., and L. W. Evers, 1994, ''Fuel Film Dynamics in The Intake Port of a Fuel Injected Engine,'' SAE paper 940446.
[5] Imatake, N., K. Saito, S. Morishima, S. Kudo, and A. Ohhata, 1997, ''Quantitative Analysis of Fuel Behavior in Port-Injection Gasoline Engine,'' SAE paper 971639.
[6] Le Moyne, L., and F. Maroteaux, 1997, ''Air-Fuel Modeling Applied to The Reduction of Air-Fuel Ratio Excursions During Transients in Port Injected Spark Ignition Engines,'' SAE paper 970513.
[7] Shin, Y., W. K. Cheng, and J. B. Heywood, ''Liquid Gasoline Behavior in the Engine Cylinder of SI Engine
[8] Meyer, R., and J. B. Heywood, 1997, ''Liquid Fuel Transport Mechanisms into the Cylinder of Firing Port-Injected SI Engine During Start Up,'' SAE paper 970865.
[9] Meyer, R., and J. B. Heywood, 1999, ''Effect of Engine and Fuel Variables on Liquid Fuel Transport into the Cylinder in Port Injected SI Engines,'' SAE paper 1999-01-0563.
[10] Koederitz, K. R., and J. A. Drallmeier, 1999, ''Film Atomization from Valve Surfaces During Cold Start,'' SAE paper 1999-01-0566.
[11] Yilmaz, E., R. Meyer, and J. B. Heywood, 1998, ''Liquid Fuel Flow in the Vicinity of the Intake Valve of a Port Injected SI Engines,'' SAE paper 982471.
[12] Shin, Y., W. K. Cheng, and J. B. Heywood, 1994, ''Liquid Gasoline Behavior in the Engine Cylinder of a SI Engine.'' SAE paper 941872.
[13] Koederitz, K. R., and J. A. Drallmeier, 1999, ''Film Atomization from Valve Surfaces During Cold Start,'' SAE paper 1999-01-0566.
[14] Le Coz, J-F., P. Lossard, and V. Ricordeau, ''Visualisation du Mélange Air-Carburant Sur Moteur Transparent Arrachement de Film Stationnaire en Soufflerie,'' Internal IFP report.
[15] Taylor, G. I., 1959, ''The Dynamics of Thin Sheets of Fluid II. Waves on Fluid Sheets,'' Proc. R. Soc. London, Ser. A, **253**, pp. 296–312.
[16] Taylor, G. I., 1959, ''The Dynamics of Thin Sheets of Fluid III. Disintegration of Fluid Sheets,'' Proc. R. Soc. London, Ser. A, **253**, pp. 313–321.
[17] Habchi, C., and H. Foucart, 2000, ''Multidimensional Modeling of Gasoline Spay Impingement and Liquid Film Heat Transfer and Boiling on Heated Surfaces,'' Eighth International Conference on Liquid and Spray Systems, CA, USA, July.
[18] Pullin, D. I., 1982, ''Numerical Studies of Surface Tension Effects in Nonlinear Kelvin-Helmholtz and Rayleigh-Taylor Instabilities,'' J. Fluid Mech., **119**, pp. 507–532.
[19] Li, J., Zaleski, S., and Scardovelli, R., ''Similutaion Numerique 3D de l'Arrachement de Gouttes sur une Couche Liquide,'' Technical report, Laboratoire de Modélisation en Mécanique, Université Pierre et Marie Curie.
[20] Jain, R. K., and Ruckenstein, E., 1976, ''Stability of Stagnant Viscous Films on a Solid Surface,'' J. Colloid Interface Sci., **54**(1), Jan.
[21] Lefebvre, A. H., 1989, *Atomization and Sprays*. Hemisphere Publishing.
[22] Le Coz, J-F., and T. Baritaud, 1996, ''Application of Laser Induced Fluorescence for Measuring the Thickness of Evaporating Gasoline Liquid Films,'' In 7th INT.SYMP., Developments in Laser Techniques and Applications to Fluid Mechanics, Proceedings of the 7th Intl.Symp. ISBN: 3-540-60236-4.
[23] Habchi, C., and A. Torros, 1992, ''A 3-D Multi-Block Structured Version of the Kiva-2 Code,'' First European CFD Conference Proceedings, Vol. 1.
[24] Habchi, C., D. Verhoeven, C. Huynh Huu, L. Lambert, J. T. Vanhemelryck, and T. Baritaud, 1997, ''Modeling Atomization and Break Up in High-Pressure Diesel Sprays,'' SAE paper 970881.

T. Watanabe
Research Engineer
e-mail: watanabe@sugar.tokai.jaeri.go.jp

K. Ebihara
Research Engineer
e-mail: ebihara@sugar.tokai.jaeri.go.jp

Center for Promotion of Computational Science and Engineering,
Japan Atomic Energy Research Institute,
Tokai-mura, Naka-gun,
Ibaraki, 319-1195, Japan

Numerical Simulation of Droplet Flows and Evaluation of Interfacial Area

Droplet flows with coalescence and breakup are simulated numerically using the lattice Boltzmann method. It is shown that the rising velocities are in good agreement with those obtained by the force balance and the empirical correlation. The breakup of droplets after coalescence is simulated well in terms of the critical Weber number. A numerical method to evaluate the interfacial area and the volume fraction in two-phase flows is proposed. It is shown that the interfacial area corresponds to the shape, the number and the size of droplets, and the proposed method is effective for numerical evaluation of interfacial area even if the interface changes dynamically. [DOI: 10.1115/1.1490128]

1 Introduction

It is important for safety analyses of nuclear reactors to predict two-phase flow phenomena under abnormal or accidental conditions. Reactor safety analysis codes based on the two-fluid model [1,2] are most commonly used for best-estimate safety analyses, since these codes are capable of predicting two-phase flow phenomena with reasonable accuracy and computational efficiency. In the two-fluid model, the conservation of mass, momentum, and energy is calculated for each phase separately, and the interactions between two phases are represented by the interfacial transfer terms in the conservation equations. Interfacial area is one of the most important parameters for modeling the interfacial transfer terms since the mass, momentum, and energy exchanges occur through the interface. In addition, prediction of interfacial phenomena in two-phase flows has become more important for environmental engineering [3], where the interfacial transfer plays an important role in droplet flows of liquid CO_2 injected into the deep ocean for the mitigation of greenhouse effects.

The interfacial area has been extensively measured and several empirical correlations and models have been proposed. These correlations were reviewed briefly by Lee [4], Delhaye and Bricard [5], Kocamustafaogullari et al. [6], and Zeitoun et al. [7]. Various flow parameters and fluid properties are involved in the correlations according to the experimental conditions. The exponents of the parameters are, however, different even though the same parameters are used, since the interfacial phenomena are complicated and an accurate measurement is difficult.

In order to simulate two-phase flows with interfaces, numerical techniques based on a discrete particle approach have recently progressed a great deal. Instead of solving continuous fluid equations, motions of fluid particles or molecules are calculated, and macroscopic flow variables are obtained from the particle motion. The interface or surface is calculated to be the edge or the boundary of the particle region. Among particle simulation methods, the lattice gas automata (LGA) is one of the simple techniques for simulating phase separation and free surface phenomena, as well as macroscopic flow fields. In the LGA introduced by Frisch et al. [8], space and time are discrete, and identical particles of equal mass populate a triangular lattice. The particles travel to neighboring sites at each time step, and obey simple collision rules that conserve mass and momentum. Macroscopic flow fields are obtained by coarse-grain averaging in space and time. Since the algorithm and programming are simple, and complex boundary geometries are easy to represent, the LGA has been applied to numerical simulations of hydrodynamic flows, including multiphase flows [9]. The LGA has, however, some inherent drawbacks such as velocity dependence of the equation of state, the lack of Galilean invariance, and statistical noise in the results. These drawbacks are overcome by using the Boltzmann equation [10].

The main feature of the lattice Boltzmann method (LBM) is to neglect individual particle motion and to replace the particle occupation variables, which are Boolean variables in the LGA, with single-particle distribution functions[11]. These functions are the ensemble average of particle occupation and real variables. In the LBM, which is used widely, the collision process of particles is simplified to become a relaxation process of the distribution function toward the local equilibrium [12], and the local equilibrium distribution is chosen to recover the Navier-Stokes equations [13]. Previous research recounted by Chen and Doolen [10] and Benzi et al. [14] showed that various kinds of fluid flows involving interfacial dynamics and complex boundaries were simulated using the LBM. Recently, rising bubbles and their interaction [15], a rising bubble in a viscoelastic fluid [16], the Rayleigh-Tayler instability [17–19], and the breakup of a droplet in a simple flow field [20,21] were simulated, and the dynamics of the interface was discussed. Although the fundamental phenomena of interfacial dynamics were discussed using the LBM in these studies, droplet or bubbly flows with coalescence and breakup and the variation of interfacial area were not studied.

In this study, the two-component two-phase LBM is used to simulate two-phase flow fields, and a numerical method to evaluate the interfacial area and the volume fraction is proposed. Measured values of the interfacial area and the volume fraction are compared to analytical values for basic geometries such as spherical and sinusoidal interfaces. The variation of interfacial area is measured and discussed for droplet flows with coalescence and breakup. The applicability of numerical simulations and evaluation methods to obtain detailed information on two-phase flows is shown.

2 Two-Component Two-Phase Lattice Boltzmann Method

The two-component two-phase LBM has been developed by Gunstensen and Rothman [22] based on the two-species variant of the LGA [23]. This model was extended by Grunau et al. [24] to include two-phase fluid flows that have variable densities and viscosities. In this model, red and blue particle distribution functions $f_i^r(x,t)$ and $f_i^b(x,t)$ at space x and time t are introduced to represent two different fluids. The subscript i indicates the direction of

Contributed by the Fluids Engineering Division for publication in the JOURNAL OF FLUIDS ENGINEERING. Manuscript received by the Fluids Engineering Division May 18, 2001; revised manuscript received April 17, 2002. Associate Editor: Q. Celik.

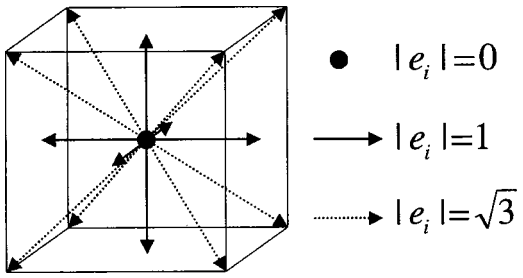

Fig. 1 Lattice configuration for 3-D 15-direction model

a moving particle on a lattice. The 3-D 15-direction model shown in Fig. 1 is used in this study, while the 2-D hexagonal lattice was used originally [24].

The total particle distribution function is defined as

$$f_i = f_i^r + f_i^b . \tag{1}$$

The lattice Boltzmann equation for both red and blue fluids is written as

$$f_i^k(x+e_i,t+1) = f_i^k(x,t) + \Omega_i^k(x,t), \tag{2}$$

where k denotes either the red or blue fluid, and

$$\Omega_i^k = (\Omega_i^k)^1 + (\Omega_i^k)^2 \tag{3}$$

is the collision operator. The first term of the collision operator represents the process of relaxation to local equilibrium. The linearized collision operator with a single time relaxation parameter is written as

$$(\Omega_i^k)^1 = \frac{-1}{\tau_k}(f_i^k - f_i^{k(eq)}). \tag{4}$$

Here $f_i^{k(eq)}$ is the local equilibrium state depending on the local density and velocity, and τ_k is a spatially dependent characteristic relaxation time for species k. Conservation of mass and momentum must be satisfied:

$$\rho_r = \sum f_i^r = \sum f_i^{r(eq)}$$

$$\rho_b = \sum f_i^b = \sum f_i^{b(eq)} \tag{5}$$

$$\rho u = \sum f_i^k e_i = \sum f_i^{k(eq)} e_i$$

where ρ_r and ρ_b are densities of the red and blue fluids, respectively,

$$\rho = \rho_r + \rho_b \tag{6}$$

is the total density, and u is the local velocity. Using the Chapman-Enskog multiscale expansion, the second part of the collision operator for the 3-D 15-direction model is obtained as

$$(\Omega_i^k)^2 = a_k|F|\left[\frac{(e_i\cdot F)^2}{|e_i|^2|F|^2} - \frac{1}{3}\right], \tag{7}$$

where a_k is a parameter controlling the surface tension, and F is the local color gradient, defined as

$$F(x) = \sum e_i[\rho_r(x+e_i) - \rho_b(x+e_i)]. \tag{8}$$

Note that $F=0$ in a single-phase region, and the second term of the collision operator only has a contribution at two-phase interfaces. To maintain interfaces, the method of Rothman and Keller [23] is applied to force the local color momentum,

$$j = \sum_i (f_i^r - f_i^b)e_i , \tag{9}$$

to align with the direction of the local color gradient. In other words, the colored distribution functions at interfaces are redistributed to maximize $-j\cdot F$. The equilibrium distribution of the species k is obtained as

$$f_i^k = \rho_k\left(\frac{n_k}{7+n_k} - \frac{1}{3}u^2\right) \quad \text{for } |e_i|=0,$$

$$f_i^k = \rho_k\left[\frac{1}{7+n_k} + \frac{1}{3}(e_i\cdot u) + \frac{1}{2}(e_i\cdot u)^2 - \frac{1}{6}u^2\right) \quad \text{for } |e_i|=1, \tag{10}$$

$$f_i^k = \frac{\rho_k}{8}\left[\frac{1}{7+n_k} + \frac{1}{3}(e_i\cdot u) + \frac{1}{2}(e_i\cdot u)^2 - \frac{1}{6}u^2\right) \quad \text{for } |e_i|=\sqrt{3},$$

so that the macroscopic mass and momentum conservation equations for continuous fluid are recovered. In the above equations, n is a parameter representing the ratio of the particles at rest to the $|e_i|=1$ particles when velocity is zero. Coefficients in the equilibrium distribution functions obtained here are slightly different from those calculated for 2-D hexagonal lattice [24]. The viscosity is obtained as

$$\mu_k = -\left(\frac{1}{2} - \tau_k\right)\frac{3}{7+n_k}\rho_k . \tag{11}$$

The surface tension is parameter calculated *a posteriori* from Laplace's formula [25,26]

$$\Delta p = \frac{2\sigma}{R}, \tag{12}$$

where Δp is the pressure difference between the inside and outside of a droplet, σ is the surface tension, and R is the radius of a droplet.

The gravitational effect is taken into account to simulate rising droplets. An external force field denoted by $m_i G\cdot e_i$ is introduced in the right-hand side of Eq. (2) [17],

$$f_i^k(x+e_i,t+1) = f_i^k(x,t) + \Omega_i^k(x,t) - m_i G\cdot e_i , \tag{13}$$

where m_i is a constant in the lattice direction i and G is the external force. The constant m_i is determined so that the Navier-Stokes equation has an appropriate gravitational term, $-\rho g$ in the vertical direction, where g is the gravitational acceleration. The external force in the LB equation is given by $G=-\rho g$. Using the Chapman-Enskog multiscale expansion again, m_i is calculated to be 1/2 for $|e_i|=1$ and 1/8 for $|e_i|=3^{1/2}$. These values are different from those calculated for the 2-D square lattice by Nie et al. [17].

The numerical accuracy of the LBM for the interior mesh points is second order [10]. The outflow and periodic boundary conditions are applied at the top and the side boundaries of the simulation region, respectively. The bounce-back condition is used as the half-way shifted wall so that the no-slip boundary is assumed to be in the middle of the bottom wall and the lowest fluid node. It was shown by Kandhai et al. [27] that second order accuracy was achieved by this boundary condition. The simulation program is parallelized using the message passing interface (MPI) libraries, and the numerical simulations are performed on a workstation cluster [28].

3 Simulation of Rising Droplets

3.1 Rising Velocity. The simulation region is filled with blue fluid initially and a red droplet of radius R is placed near the bottom wall. The parameters a, τ, n and the density are 0.001, 1.0, 3.0, and 2.34, respectively, for the red phase and 0.001, 1.0, 2.0, and 2.6, respectively, for the blue phase. These parameters are almost the same as those used by Hou et al. [25] in their paramet-

Table 1 Parameters and nondimensional numbers

Parameters	Minimum value	Maximum value
Number of lattice nodes in horizontal direction (L)	80	160
Droplet radius (R)	6	14
Gravitational acceleration (g)	0.0005	0.0015
Weber number (We)	0.84	7.30
Reynolds number (Re)	5.63	23.5
Eotvos number (Eo)	1.83	10.95
Morton number (M)	6.37×10^{-4}	1.91×10^{-3}

ric studies for two-phase LB models. It was reported that stable and thin interfaces were obtained by these parameters. The gravitational acceleration is set equal to 0.001. The variables and parameters used in the LBM are nondimensional, and their values in the numerical simulations are computed to obtain the appropriate range of nondimensional numbers that characterize droplet flows. The minimum and maximum values of parameters and nondimensional numbers used in our numerical simulations are listed in Table 1, where We, Re, Eo, and Mo are the Weber, Reynolds, Eotvos, and Morton numbers defined by $\mathrm{We}=\rho(2R)u^2/\sigma$, $\mathrm{Re}=\rho u(2R)/\mu$, $\mathrm{Eo}=g\Delta\rho(2R)^2/\sigma$, and $\mathrm{M}=g\Delta\rho\mu^4/(\rho^2\sigma^3)$, respectively.

The effect of the region size on the simulation results is examined in Fig. 2, where the trajectories of rising droplets in simulated regions of different sizes are shown. The height of the simulation region is 200 lattice nodes, and the number of the lattice nodes in the horizontal direction, L, is varied from 80 to 160. The top and bottom positions of the droplet on the center axis are shown for two cases with different Eo: Eo=7.30 for a large droplet and Eo=1.83 for a small droplet. It is found that the magnitude of the effect caused by region size is larger for the large droplet. The effect of the region size on the rising velocity, Ut, is shown in Fig. 3. The rising velocities for Eo=7.30 after the initial transient are about 0.119, 0.127 and 0.129 for the cases with 80×80, 120×120 and 160×160 lattice nodes, respectively. In the horizontal directions, 120×120 lattice nodes are thus used in the following simulations. The calculation time and the memory size for one case with 120×120×200 lattice nodes in Fig. 2 are about 24 hours and 1.5 GB, respectively, in our computer system.

The trajectory of a droplet is shown in Fig. 4, where the Weber number is varied by changing the gravitational acceleration. It is

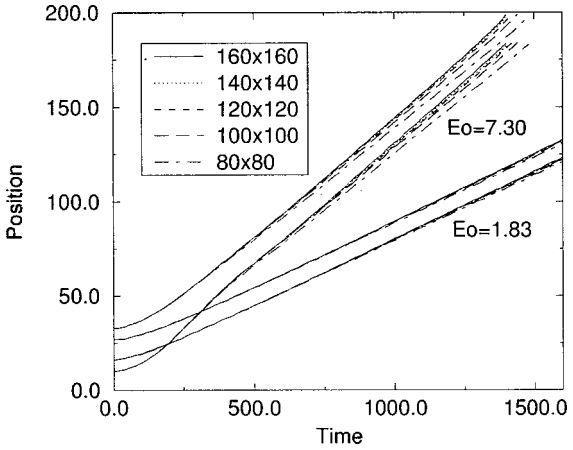

Fig. 2 Effect of region size on trajectories of rising droplets

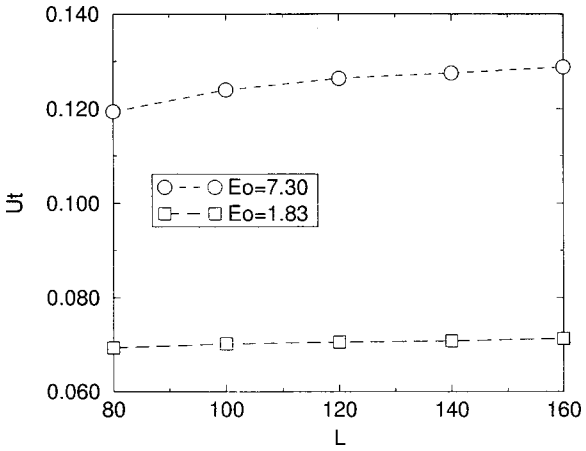

Fig. 3 Effect of region size on rising velocity

seen in Fig. 4 that after the initial transient the rising velocity is almost constant and increases according to the Weber number as the gravitational acceleration increases. The terminal velocity of a droplet moving in a dense medium is given by

$$Ut=\left(\frac{2}{3}\frac{\Delta\rho gR}{K\rho}\right)^{1/2} \tag{14}$$

from the force balance, where the drag coefficient K is assumed to be 0.5 for a body of spherical shape [29]. In Fig. 5, the rising velocity obtained by the LB simulation, Ut_{LB}, is compared to the terminal velocity given by the force balance, Ut_{FB}. The data shown in Fig. 5 are obtained by varying both the radius of the droplet and the gravitational acceleration. It is found that the agreement between the simulation and the force balance is reasonable.

The rising velocity is compared to the empirical correlation for the terminal velocity of bubbles and drops [30]. The empirical correlation is expressed in terms of nondimensional parameters as

$$J=0.94H^{0.757}, \tag{15}$$

where

$$H=\frac{4}{3}\mathrm{Eo}\,M^{-0.149}c(\mu),$$
$$J=\mathrm{Re}\,M^{0.149}+0.857. \tag{16}$$

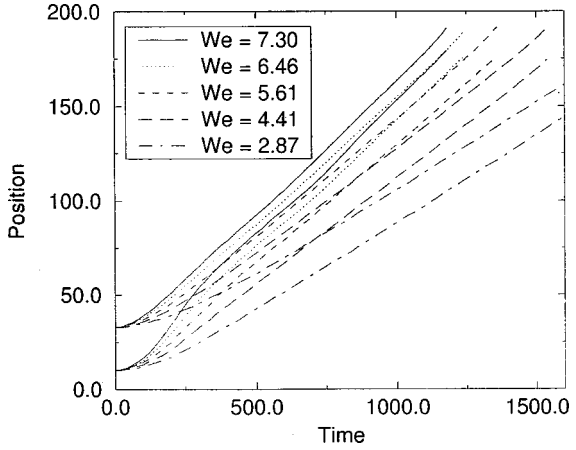

Fig. 4 Effect of Weber number on trajectories of rising droplets

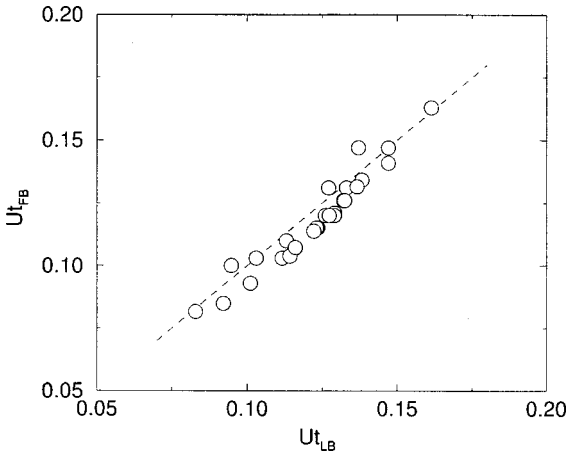

Fig. 5 Comparison of rising velocity between simulations and force balance

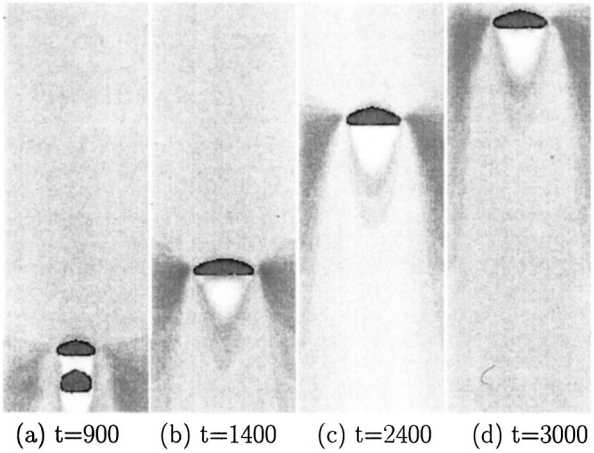

Fig. 7 Coalescence of two rising droplets for Eo=7.30

In the above equations, $c(\mu)$ is the coefficient depending on the viscosity. The parameters J and H obtained by the simulation are shown in Fig. 6 along with the empirical correlation having $c(\mu)=0.69$. The agreement between the simulation and the correlation is satisfactory in Fig. 6. It is found from Figs. 5 and 6 that the rising droplets are simulated well in our numerical simulations.

3.2 Coalescence and Breakup. The rising droplets and their coalescence are shown in Fig. 7. The shape of the droplet is depicted and the flow velocity in the vertical direction is indicated: dark regions at the side of the droplet are downward flow regions and light regions at the bottom are upward flow regions. The simulation region consists of $120\times120\times512$ in this case. The boundary conditions and the parameters are the same as those used in the single droplet case. Two droplets of Eo=7.30 are initially placed at the vertical positions $z=20$ and $z=70$. The trajectories of the top and bottom positions of the droplets on the center axis are shown in Fig. 8. The trajectories of single droplets, which are obtained by the simulation of a droplet placed at $z=20$ or 70 under the same condition, are also shown in Fig. 8. The Weber number for the single droplet is about 5.55. When two droplets are rising, the lower droplet goes up faster since the upward flow is established in the wake of the upper droplet. It is clearly seen in Figs. 7 and 8 that the lower droplet is attracted to the upper droplet, and the trajectory of the lower droplet deviates from that of the single droplet. The trajectory of the droplet after coalescence is almost the same as that of the single droplet. These phenomena are observed in the similar experiment for two bubbles [31].

The breakup of the droplet is observed after coalescence in Fig. 9 for Eo=8.57. Two droplets coalesced as was the case with Eo =7.30 in Fig. 7, but then break up into small droplets. The average Weber number of the droplet after coalescence is calculated to

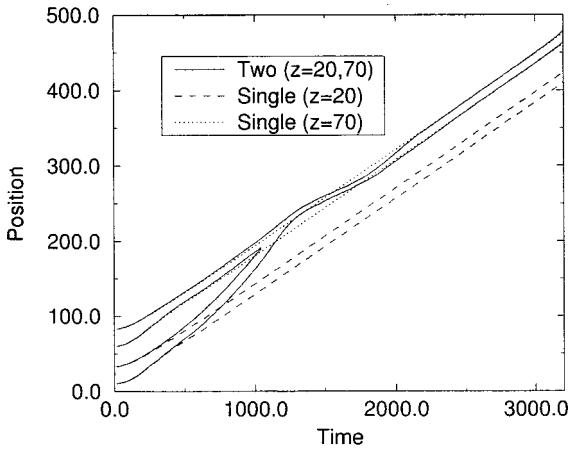

Fig. 8 Trajectory of two rising droplets for Eo=7.30

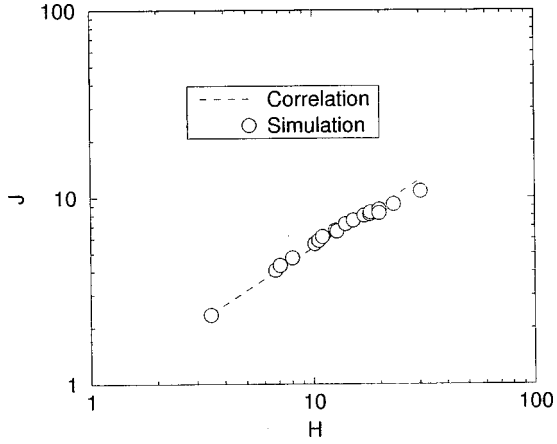

Fig. 6 Comparison of rising velocity between simulations and empirical correlation

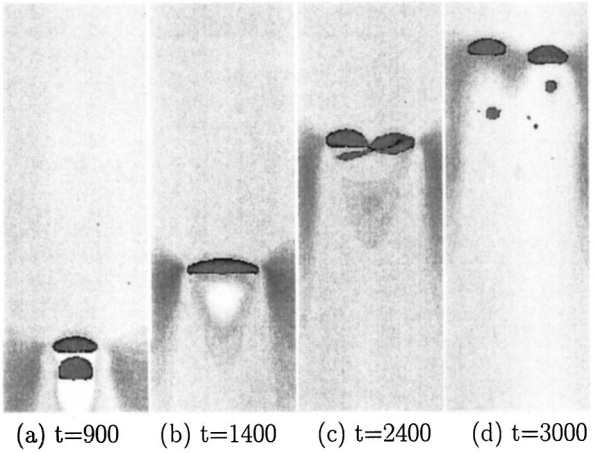

Fig. 9 Coalescence and breakup of two rising droplets for Eo =8.57

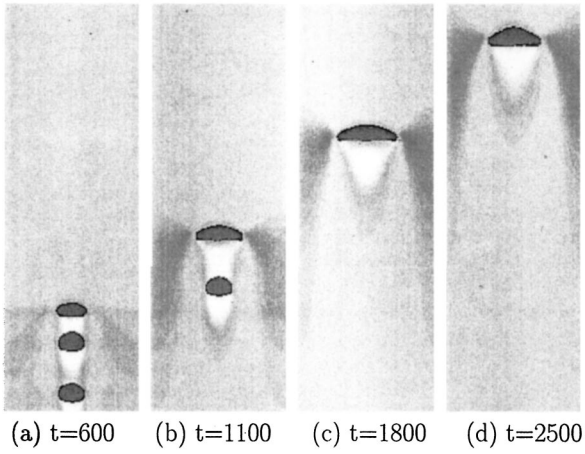

Fig. 10 Coalescence of three rising droplets for Eo=6.14

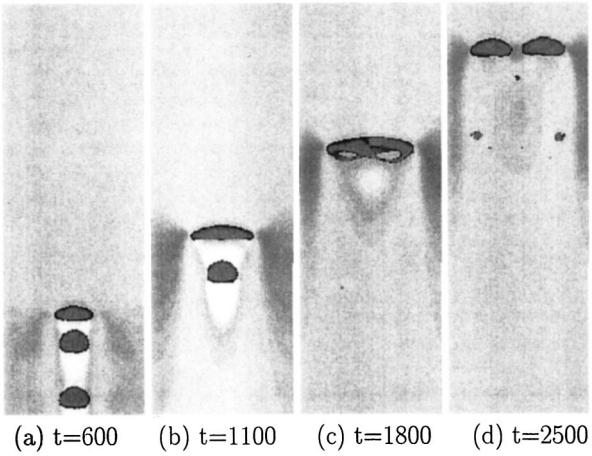

Fig. 12 Coalescence and breakup of three rising droplet for Eo=7.30

be about 13.3 for Eo=7.30 and 15.5 for Eo=8.57, by using the average momentum at the coalescence. The breakup of droplet occurs when the Weber number exceeds the critical value [32]. The critical Weber number is given by

$$\mathrm{We}=12\left[1+\left(\frac{\mu_d^2}{2\rho_d R\sigma}\right)^{0.36}\right], \tag{17}$$

where μ_d and ρ_d are the viscosity and the density of the droplet, respectively. The critical Weber number for the coalesced droplet obtained by Eq. (17) is about 14.3 for Eo=7.30 and 14.2 for Eo=8.57, and thus the occurrence of breakup is to be expected.

Three rising droplets and their coalescence are shown in Fig. 10 for Eo=6.14, and the trajectories of droplets, which are initially placed at $z=20$, 60, and 100, are shown in Fig. 11. The trajectories of a single droplet under the same condition are also shown. These figures demonstrate that the lower droplets are attracted to the upper droplet and the trajectories of lower droplets deviate from those of the single droplet, as seen in Fig. 8. The trajectory of the droplet after coalescence is slightly different from that of the single droplet in this case. The average Weber number of the droplet is about 12.5 for the first coalescence and 12.7 for the second coalescence, while the critical Weber number is calculated to be 14.4 and 14.3 for the first and second coalescences, respectively. The average Weber number is smaller than the critical value, thus the breakup does not occur. The breakup of the droplet after coalescence for three rising droplets is observed in Fig. 12 for Eo=7.30, where the average Weber number of the droplet is 15.5 and 14.6 for the first and second coalescences, respectively. The critical Weber number is 14.2 for both coalescences, and thus the occurrence of breakup is simulated well. It is confirmed through these results that droplet flows are simulated reasonably well in our numerical simulations.

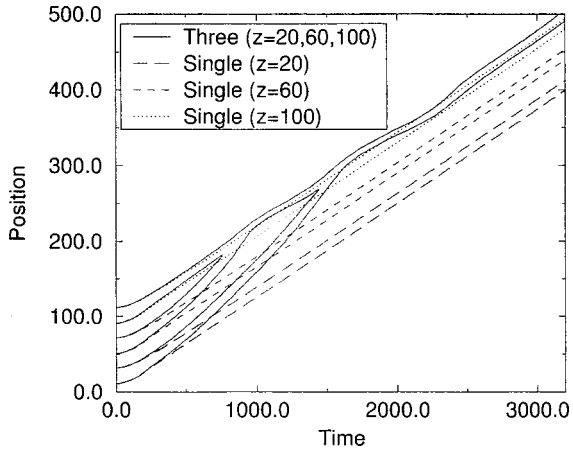

Fig. 11 Trajectory of three rising droplets for Eo=6.14

4 Evaluation of Interfacial Area

4.1 Definition of Interface. In order to define the interface in our simulations, the Atwood number, $\mathrm{At}=(\rho_r-\rho_b)/(\rho_r+\rho_b)$, is calculated at the lattice node. The red and blue phases are defined as the region where At>0 and At<0, respectively. The lattice node is classified into red or blue according to the Atwood number. The interface is located somewhere in between red and blue nodes. In the 3-D 15-direction lattice shown in Fig. 1, the lattice node is at the center of a unit cube. It is assumed that each node has a unit volume and may have an interfacial area. If the sign of the Atwood number at the node (x,y,z) is the same as that at neighboring nodes, the interface does not exist around the node and the unit volume is purely red or blue. The volume at the node is divided into red and blue portions if the interface exists around the node. In this case, a plane interface is simply assumed to divide the volume as shown in Fig. 13, where the interface is indicated as dark planes. When At>0 at the node (x,y,z) and At<0 at $(x+1,y,z)$, for instance, the interface exists in the x direction of the node (x,y,z) as shown in Fig. 13(a). If the interface exists in the x direction alone, the red and blue portions of the volume at the node (x,y,z) are 1.0 and 0.0, respectively. The interface of unit area shown in Fig. 13(a) belongs to this node in this case. If At>0 at the node (x,y,z) and At<0 at $(x+1,y,z)$ and $(x,y+1,z)$, the interface exists in the x and y directions as shown in Fig. 13(b). A half of a unit area is assumed to be seen in the x and y directions. If At>0 at the node (x,y,z) and At<0 at $(x+1,y,z)$, $(x,y+1,z)$ and $(x,y,z+1)$, the interface exists in x, y,

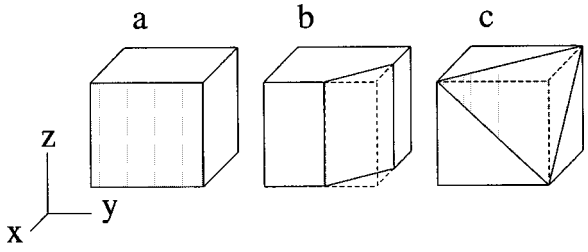

Fig. 13 Definition of interface and volume fraction at a node

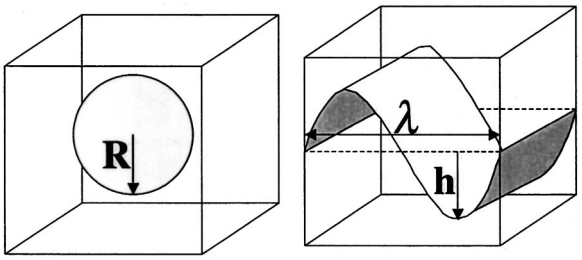

Fig. 14 Geometries of sphere and sinusoidal wave

and z directions as shown in Fig. 13(c). A half of a unit area is assumed to be seen in the x, y, and z directions in this case. After applying this method in the positive directions from the first node to the last node in the simulation region, the volume fraction and the interfacial area at every lattice node are obtained. This method is simple and numerically efficient, since only three neighboring nodes in the positive directions are used.

In order to test the validity of the above definition, the volume fraction and the interfacial area are measured for basic geometries in two-phase flows: a sphere and a sinusoidal wave shown in Fig. 14. For a sphere, the spherical interface with radius R is placed in the center of a cubic region, and the inside and outside of the sphere are filled with red and blue phases, respectively. For a wave, the sinusoidal interface with height h and wavelength λ is placed at the mid-elevation of a cubic region, and the lower and upper sides of the wave are filled with red and blue phases, respectively. The cubic region is $80\times80\times80$ in both cases. Measured and analytical values of the volume fraction of the red phase and the interfacial area are normalized in the simulation region and shown in Fig. 15 for the sphere and in Fig. 16 for the wave. The analytical values are indicated by broken lines. The measured values are in good agreement with the analytical values even for small spheres and for large and short waves, though the definition of interfacial area and volume fraction is quite simple. It is thus confirmed that the proposed method of measurement is reasonably accurate for numerical evaluation of interfacial area and volume fraction.

4.2 Interfacial Area of Droplet Flow. The volume fraction and the interfacial area of a rising droplet normalized in the simulation region are shown in Fig. 17. The interfacial area increases initially due to the deformation. It is seen in the case with a larger Weber number that the deformation is large and the interfacial area oscillates according to the oscillation of the droplet shape.

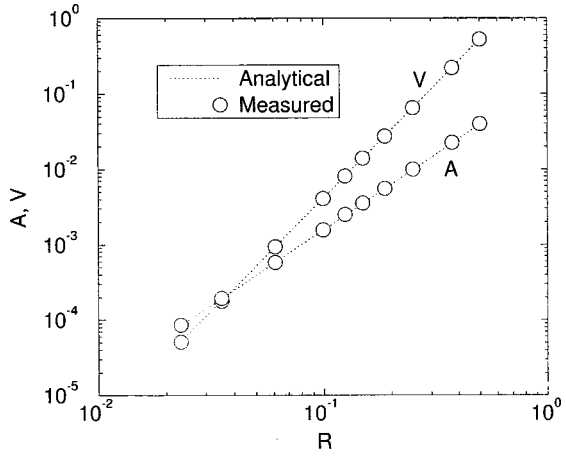

Fig. 15 Measured and analytical interfacial area and volume fraction for sphere

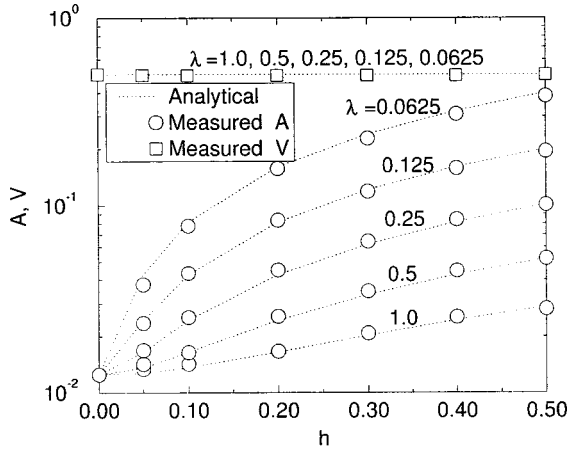

Fig. 16 Measured and analytical interfacial area and volume fraction for wave

These are also indicated in Fig. 4, where the top and bottom positions of the droplet are shown. The volume fraction of the droplet is slightly affected by the change in Weber number since the density distribution in the droplet is affected by the flow field.

The interfacial area of two rising droplets are shown in Fig. 18. The Weber number in Fig. 18 is obtained for single droplet which rises individually under the same condition. It is shown at about

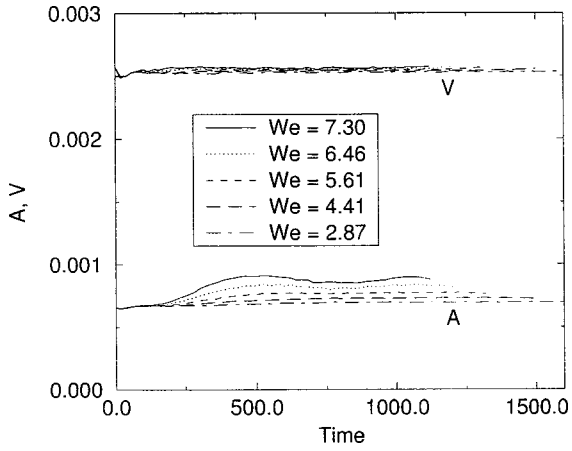

Fig. 17 Variation of interfacial area and volume fraction for a rising droplet

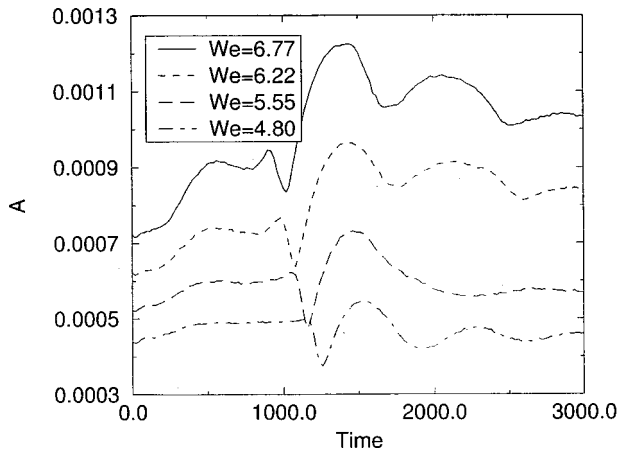

Fig. 18 Variation of interfacial area for two rising droplets

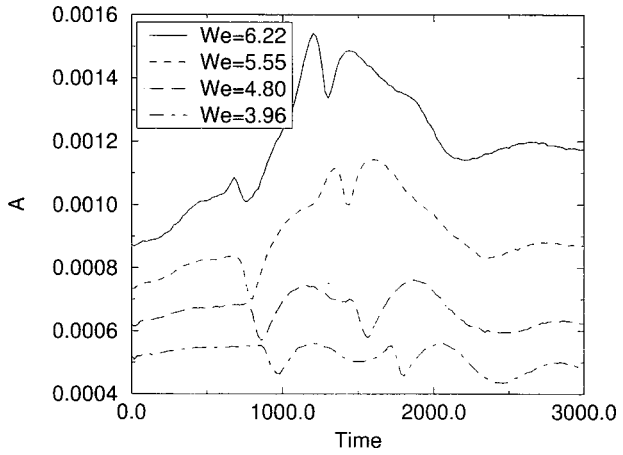

Fig. 19 Variation of interfacial area for three rising droplets

900-1200 time steps that the interfacial area decreases largely during coalescence, since the interfaces at the bottom of the upper droplet and at the top of the lower droplet are merged. The interfacial area then increases due to the deformation, and oscillates according to the oscillation of the droplet shape. For the four cases in Fig. 18, it is apparent that the case with the largest Weber number shows the largest increase in interfacial area. The breakup of the droplet after coalescence occurs in the case with We=6.77 and 6.22 in Fig. 18, and the interfacial area becomes larger than before coalescence. The droplet is disrupted into small droplets. The size and the number of small droplets are not always the same and vary with the simulation conditions. It is found that, when the breakup of coalesced droplet does not occur, the interfacial area becomes smaller than before coalescence. The interfacial area of a droplet is always smaller than the total area of small droplets as far as the total volume is the same, and thus the variation of interfacial area shown in Fig. 18 is expected.

The change in the interfacial area for three rising droplets is shown in Fig. 19. The Weber number in Fig. 19 is obtained for a single droplet which rises individually under the same condition. The interfacial area decreases two times in Fig. 19: at about 700-1000 time steps due to the coalescence of the upper and middle droplets, and at about 1200-1800 time steps due to the coalescence of the lower droplet as shown in Figs. 10 and 11. The breakup of droplet after coalescence occurs in the case with We =6.22 and 5.55 in Fig. 19, and the interfacial area becomes larger than before coalescence. Two or three large fragments and smaller ones are often formed after breakup in our simulations. As seen in Fig. 18, the interfacial area becomes smaller when the breakup does not occur. The variation of interfacial area in droplet flows corresponds to the change in the number and the size of droplets as well as the droplet deformation. It is found that the proposed method is effective for measurement of the interfacial area even if the interface changes dynamically including coalescence and breakup.

5 Conclusions

In this study, droplet flows with coalescence and breakup were simulated using the two-component two-phase LBM. The rising velocity of a droplet was in good agreement with that obtained by the force balance and the empirical correlation. The breakup of droplets after coalescence was simulated reasonably well in terms of the critical Weber number. A simple and efficient numerical method to evaluate the interfacial area and the volume fraction in two-phase flows has been proposed. It was shown for basic geometries such as spherical and sinusoidal interfaces that the measured and analytical interfacial area and the volume fraction were in good agreement. It was found that the interfacial area decreased during coalescence, and then increased and oscillated due to the deformation of the droplet. The variation of interfacial area was shown to correspond to the change in the number and the size of droplets as well as the droplet deformation, and the proposed method was effective for numerical evaluation of interfacial area in droplet flows even if the shape of the interface changed dynamically including coalescence and breakup.

Droplet flows with two or three droplets were simulated numerically and the variation of interfacial area during coalescence and breakup was evaluated here. In future research, we plan to simulate flows with a large number of droplets under various flow conditions and evaluate the interfacial area. The cost of numerical simulations depends not on the number of droplets but on the size of the simulation region, since no special treatment is necessary for the interface. This is an advantageous feature of the LBM and the proposed evaluation method. Numerical correlations for the interfacial area in droplet flows might be proposed in the future.

Nomenclature

a = parameter for surface tension
A = interfacial area
At = $(\rho_r-\rho_b)/(\rho_r+\rho_b)$ Atwood number
$c(\mu)$ = coefficient depending on viscosity
e = velocity vector
Eo = $g\Delta\rho(2R)^2/\sigma$ Eotvos number
f = particle distribution function
F = local color gradient
g = gravitational acceleration
G = external force
h = wave height
H, J = parameter in velocity correlation
j = local color momentum
K = drag coefficient
L = number of lattice nodes in horizontal direction
m = constant in external force term
n = ratio of rest particle
M = $g\Delta\rho\mu^4/(\rho^2\sigma^3)$ Morton number
p = pressure
R = droplet radius
Re = $\rho u(2R)/\mu$ Reynolds number
t = time
u = local velocity
Ut = terminal velocity
We = $\rho(2R)u^2/\sigma$ Weber number
x,y,z = spatial coordinate
V = volume fraction
λ = wavelength
μ = viscosity
Ω = collision operator
ρ = density
σ = surface tension
τ = relaxation time

Sub- and Superscript

b = blue phase
d = droplet
eq = equilibrium state
i = direction
k = red or blue phase
r = red phase

References

[1] The RELAP5 Development Team, 1995, "RELAP5/MOD3 Code Manual," NUREG/CR-5535.
[2] Safety Code Development Group, 1986, "TRAC-PF1/MOD1: An Advanced Best Estimate Computer Program for Pressurized Water Reactor Thermal-Hydraulic Analysis," NUREG/CR-3858.
[3] Sato, T., Jung, R.-T., and Abe, S., 2000, "Direct Simulation of Droplet Flow With Mass Transfer at Interface," ASME J. Fluids Eng., **122**, pp. 510–516.

[4] Lee, W. J., 1998, ''State-of-the-Art Report on the Theoretical Modeling of Interfacial Area Concentration,'' KAERI/AR-497/98.
[5] Delhaye, J. M., and Bricard, P., 1994, ''Interfacial Area in Bubbly Flow: Experimental Data and Correlations,'' Nucl. Eng. Des., **151**, pp. 65–77.
[6] Kocamustafaogullari, G., Huang, W. D., and Razi, J., 1994, ''Measurement and Modeling of Average Void Fraction, Bubble Size and Interfacial Area,'' Nucl. Eng. Des., **148**, pp. 437–453.
[7] Zeitoun, O., Shoukri, M., and Chatoorgoon, V., 1994, ''Measurement of Interfacial Area Concentration in Subcooled Liquid-Vapor Flow,'' Nucl. Eng. Des., **152**, pp. 243–255.
[8] Frisch, U., Hasslacher, B., and Pomeau, Y., 1986, ''Lattice-Gas Automata for the Navier-Stokes Equation,'' Phys. Rev. Lett., **56**, pp. 1505–1508.
[9] Rothman, D. H., and Zaleski, S., 1994, ''Lattice-Gas Models of Phase Separation: Interfaces, Phase Transitions, and Multiphase Flow,'' Rev. Mod. Phys., **66**, pp. 1417–1479.
[10] Chen, H., and Doolen, G. D., 1998, ''Lattice Boltzmann Method for Fluid Flows,'' Annu. Rev. Fluid Mech., **30**, pp. 329–364.
[11] McNamara, G. G., and Zanetti, G., 1988, ''Use of the Boltzmann Equation to Simulate Lattice-Gas Automata,'' Phys. Rev. Lett., **61**, pp. 2332–2335.
[12] Bhatnagar, P. L., Gross, E. P., and Krook, M., 1954, ''A Model for Collision Processes in Gases. I: Small Amplitude Processes in Charged and Neutral One-Component System,'' Phys. Rev., **94**, pp. 511–525.
[13] Chen, H., Chen, S., and Matthaeus, W. H., 1992, ''Recovery of the Navier-Stokes Equations using a Lattice-Gas Boltzmann Method,'' Phys. Rev. A, **45**, pp. R5339–R5342.
[14] Benzi, R., Succi, S., and Vergassola, M., 1992, ''The Lattice Boltzmann-Equation—Theory and Applications,'' Phys. Rep., **222**, pp. 145–197.
[15] Takada, N., Misawa, M., Tomiyama, A., and Fujiwara, S., 2000, ''Numerical Simulation of Two- and Three-Dimensional Two-Phase Fluid Motion by Lattice Boltzmann Method,'' Comput. Phys. Commun., **129**, pp. 233–246.
[16] Wagner, A. J., Giraud, L., and Scott, C. E., 2000, ''Simulation of a Cusped Bubble Rising in a Viscoelastic Fluid with a New Numerical Method,'' Comput. Phys. Commun., **129**, pp. 227–232.
[17] Nie, X., Qian, Y.-H., Doolen, G. D., and Chen, S., 1998, ''Lattice Boltzmann Simulation of the Two-Dimensional Rayleigh-Taylor Instability,'' Phys. Rev. E, **58**, pp. 6861–6864.
[18] He, X., Zhang, R., Chen, S, and Doolen, G. D., 1999, ''On the Three-Dimensional Rayleigh-Taylor Instability,'' Phys. Fluids, **11**, pp. 1143–1152.
[19] He, X., Chen, S., and Zhang, R., 1999, ''A Lattice Boltzmann Scheme for Incompressible Multiphase Flow and Its Application in Simulation of Rayleigh-Taylor Instability,'' J. Comput. Phys., **152**, pp. 642–663.
[20] Sehgal, B. R., Nourgaliev, R. R., and Dinh, T. N., 1999, ''Numerical Simulation of Droplet Deformation and Bread-Up by Lattice-Boltzmann Method,'' Prog. Nucl. Energy, **34**, pp. 471–488.
[21] Xi, H., and Duncan, C., 1999, ''Lattice Boltzmann Simulations of Three-Dimensional Single Droplet Deformation and Breakup Under Simple Shear Flow,'' Phys. Rev., **59**, pp. 3022–3026.
[22] Gunstensen, A. K., and Rothman, D. H., 1991, ''Lattice Boltzmann Model of Immiscible Fluids,'' Phys. Rev. A, **43**, pp. 4320–4327.
[23] Rothman, D. H., and Keller, J. M., 1988, ''Immiscible Cellular-Automaton Fluids,'' J. Stat. Phys., **52**, pp. 1119–1127.
[24] Grunau, D., Chen, S., and Eggert, K., 1993, ''A Lattice Boltzmann Model for Multiphase Fluid Flows,'' Phys. Rev. A, **5**, pp. 2557–2562.
[25] Hou, S., Shan, X., Zou, Q., Doolen, G. D., and Soll, W. E., 1997, ''Evaluation of Two Lattice Boltzmann Models for Multiphase Flows,'' J. Comput. Phys., **138**, pp. 695–713.
[26] Landau, L. D., and Lifshitz, E. M., 1959, *Fluid Mechanics*, Pergamon, New York.
[27] Kandhai, D., Koponen, A., Hoekstra, A., Kataja, M., Timonen, J., and Sloot, P. M. A., 1999, ''Implementation Aspects of 3D Lattice-BGK: Boundaries, Accuracy, and a New Fast Relaxation Method,'' J. Comput. Phys., **150**, pp. 482–501.
[28] Watanabe, T., Ebihara, K., Ito, G., and Kohno, K., 2000, ''Development of a Two-Phase Flow Simulation Code using the Lattice Boltzmann Method and Its Parallelization,'' JAERI-Data/Code 2000-029.
[29] Levich, V. G., 1962, *Physicochemical Hydrodynamics*, Prentice Hall, N.J.
[30] Clift, R., Grace, J. R., and Weber, M. E., 1978, *Bubbles, Drops, and Particles*, Academic Press, New York.
[31] Crabtree, J. R., and Bridgwater, J., 1971, ''Bubble Coalescence in Viscous Liquids,'' Chem. Eng. Sci., **26**, pp. 839–851.
[32] Wallis, G. B., 1969, *One-Dimensional Two-Phase Flow*, McGraw-Hill, New York.

Finite Element Simulations of Free Surface Flows With Surface Tension in Complex Geometries

Gang Wang
Senior Development Engineer,
Multiphysics Group, ANSYS, Inc.,
275 Technology Drive, Canonsburg,
PA 15317-9565

The finite-element program, ANSYS/FLOTRAN, has been enhanced at Release 5.7 to predict free surface flows with surface tension in complex geometries. The two-dimensional incompressible Navier-Stokes and energy equations are solved in both Cartesian and axisymmetric coordinate systems. At Release 5.6, the free surface capabilities have been incorporated into ANSYS/FLOTRAN using the CLEAR-VOF algorithm. The main contribution of this work is to implement a surface tension model into ANSYS/FLOTRAN to study free surface flows with surface tension in complex geometries. Both normal and tangential components of surface tension forces are modeled at the interface through a continuum surface force (CSF) model. This new algorithm is first validated with two model problems: a droplet in equilibrium and an oscillating droplet. For the first problem, the computed pressure value is compared with the theoretical value, whereas for the second problem, the oscillation frequency is compared with both the analytical solution and experimental data. The computer program is then applied to thermocapillary flows in two types of trapezoidal cavities to investigate the interesting flow and heat transfer characteristics. Systematic calculations are performed to study the influence of Marangoni number, capillary number and static contact angle on Marangoni convection.
[DOI: 10.1115/1.1466458]

Introduction

The interfacial physics of free surface flows is a topic of continued interest to engineers. In such flows, the liquid and the gas are clearly separated with large-scale interfaces, and the density ratio between the two is quite large. For example, this ratio is approximately 1000 between water and air. Due to the low density and negligible viscosity, both the inertia and the viscous force of the gas are insignificant, and the only influence of the gas is the pressure that acts on the interface. Hence, the gas phase can be treated as vacuum without loss of accuracy, and only the motion of the liquid has to be modeled. The issue that remains is how to locate and track the interface on which a proper pressure boundary condition can be applied. One popular technique for tracking the interface is the volume-of-fluid (VOF) method [1–3]. The VOF method determines the shape and location of the interface based on the concept of a fractional volume of fluid, and describes the evolution of the interface through an advection algorithm for volume fraction. Recently, Barbat and co-workers [4] proposed an original VOF algorithm and then implemented it in a finite element computer program, ANSYS/FLOTRAN 5.6. In contrast to the traditional purely Eulerian VOF methods, this algorithm is based on the concept of Computational Lagrangian-Eulerian Advection Remap (CLEAR). The basic idea behind the CLEAR-VOF algorithm is to move the fluid portion of an element in a Lagrangian sense, and redistribute it locally in the Eulerian fixed mesh. In this algorithm, there is no limitation on mesh topology, aspect ratio, or mesh orientation, and it is thus possible to implement it into a finite-element method to handle free surface flows in complex geometries.

In free surface flows, surface tension is a key factor for a number of industrial applications such as ink-jet printers, the mold-filling process, and the microfluid handling in MEMS devices. Surface tension is an inherent characteristic of material interfaces acting as a localized surface force on the fluid elements at the interface. One method of modeling the surface tension is the continuum surface force (CSF) model [5]. Rather than as a boundary condition, the CSF model reformulates the surface force into an equivalent volumetric force in the momentum equation. There are two main components in the surface force. The first one is normal to the interface due to the local curvature, and the second one is due to the tangential variation of the surface tension coefficient.

The objective of the present work is to develop an accurate and robust computational tool to predict the interfacial dynamics in complex geometries. Rather than a finite volume method [6], a finite element method [7,8] is used here for its ease of handling complex geometry. The two-dimensional incompressible Navier-Stokes equations are discretized in both Cartesian and axisymmetric coordinate systems. Here, the free surface is tracked with the CLEAR-VOF algorithm, and the surface tension effect is modeled with the CSF method. In the following sections, this paper will describe the mathematical formulation, modeling of surface tension, validation of the computer program, and finally, some computational results for Marangoni convection in trapezoidal cavities.

Numerical Methodology

Mathematical Formulation. The partial differential equations governing two-dimensional transient motion of an incompressible fluid are the Navier-Stokes equations. To calculate the flow and thermal fields, the Navier-Stokes and energy equations are integrated with a weighted residual method:

$$\int_\Omega \nabla w^p \cdot (\rho \vec{v}) d\Omega = \int_\Gamma w^p \rho \vec{v} \cdot \hat{n} d\Gamma, \tag{1}$$

$$\int_\Omega \left\{ \vec{w}^v \cdot \rho \left(\frac{\partial \vec{v}}{\partial t} + \vec{v} \cdot \nabla \vec{v} \right) + \mu \nabla \vec{w}^v : \nabla \vec{v} \right\} d\Omega = -\int_\Omega \vec{w}^v \cdot \nabla p d\Omega + \int_\Omega \vec{w}^v \cdot \vec{F} d\Omega + \int_\Gamma \vec{w}^v \cdot (\mu \hat{n} \cdot \nabla \vec{v}) d\Gamma, \tag{2}$$

Contributed by the Fluids Engineering Division for publication in the JOURNAL OF FLUIDS ENGINEERING. Manuscript received by the Fluids Engineering Division March 8, 2001; revised manuscript received January 11, 2002. Associate Editor: G. Karniadakis.

$$\int_\Omega \left\{ w^T \rho C_p \left(\frac{\partial T}{\partial t} + \vec{v} \cdot \nabla T \right) + k \nabla w^T \cdot \nabla T \right\} d\Omega = \int_\Omega w^T S d\Omega + \int_\Gamma w^T k \hat{n} \cdot \nabla T d\Gamma. \quad (3)$$

Here, $\vec{v}$, p, T, $\vec{F}$, S, μ and k are the velocity, pressure, temperature, body force, heat generation, dynamic viscosity and thermal conductivity, respectively. At the free surface, the pressure is prescribed to be zero, and natural conditions are used for the velocity and temperature degrees of freedom. The surface tension effect is included in the body force term through the continuum method [5]. Details of the surface tension modeling will be presented in a later section. Here, w^p, $\vec{w}^v$, and w^T are the weighting functions for the pressure, velocity and the temperature degrees of freedom, Ω is the finite element domain, and Γ is the domain boundary with $\hat{n}$ as its unit normal vector.

In the present method, equal-order interpolation functions are used for the pressure, velocity and temperature degrees of freedom. Bilinear shape functions are used on quadrilateral elements to approximate Eqs. (1)–(3). To warrant numerical stability, the convection terms are treated with the Streamline Upwind/Petrov-Galerkin (SUPG) method [9]. The transient terms are treated in a lumped mass fashion by a first order backward implicit formulation. Finally, the discretized equations are solved in a segregate manner with a SIMPLE-like algorithm [10,11].

Mathematical Modeling of Free Surface. The free surface is modeled through the volume of fluid (VOF) method. The shape and the location of the free surface are determined by a unique distribution of the volume fraction field. The evolution of the free surface is computed through an advection scheme. In this paper, the CLEAR-VOF algorithm [4] is used due to its accuracy, robustness and ease of handling arbitrary mesh topology. This algorithm consists of two main components. One is the advection step and the other is the reconstruction step.

In the advection step, the polygon of fluid is advected in a Lagrangian sense. The local velocity is used to calculate the displacements and new locations of the polygon vertices. This new polygon is then redistributed into the immediate neighbors of the corresponding home element using a computational algorithm for intersection of polygons. After all the advected polygons of fluids have been redistributed locally in the Eulerian fixed mesh, a sweep through all elements is performed to update the fluid volume/area in each home element. The new volume fraction is just the fluid volume/area divided by the element volume/area.

In the reconstruction step, the surface normal vector is first computed from the local volume fraction distribution,

$$\vec{n} = \nabla F, \quad (4)$$

where $\vec{n}$ is the normal vector, and F is the volume fraction. A computational geometry algorithm is then used for the intersection of a line with a polygon (i.e., element) and an additional equation is formed to enforce the local conservation of the fluid volume. This reconstruction process establishes the shape and location of the free surface.

At the end of the VOF algorithm, both local and global adjustments are performed for the volume fraction field if necessary. Local adjustment is performed to remove unphysical partial elements, and the global adjustment is performed to enforce the global mass/volume conservation. The details of the CLEAR-VOF algorithm and volume fraction adjustment are given in Barbat et al. [4].

Mathematical Modeling of Surface Tension. The basic concept of the continuum surface force (CSF) method is to model the surface tension localized at the fluid interface by a continuous process on fluid elements everywhere within a thin transition region near the interface. Therefore, the surface process is replaced with an equivalent volume process. The CSF method removes all topological restrictions without losing accuracy [5], and it has thus been used widely and successfully in a variety of studies [12–14].

The surface tension is a force per unit area given by

$$\vec{f}_s = \sigma \kappa \hat{n} + \nabla_t \sigma, \quad (5)$$

where $\vec{f}_s$ is the surface force, σ is the surface tension coefficient, κ is the surface curvature, $\hat{n}$ is the unit normal vector, and ∇_t is the surface gradient. Here, the curvature and unit normal vector are respectively given by

$$\kappa = -\nabla \cdot \hat{n} = \frac{1}{|\vec{n}|} \left[\left(\frac{\vec{n}}{|\vec{n}|} \cdot \nabla \right) |\vec{n}| - (\nabla \cdot \vec{n}) \right] \quad (6)$$

and

$$\hat{n} = \frac{\vec{n}}{|\vec{n}|} = \frac{\nabla F}{|\nabla F|}. \quad (7)$$

The surface gradient is given by

$$\nabla_t = \hat{t}(\hat{t} \cdot \nabla) = \nabla - \hat{n}(\hat{n} \cdot \nabla), \quad (8)$$

where $\hat{t}$ is the tangential unit surface vector. In Eq. (5), the first term is acting normal to the interface, and is directed toward the center of the local curvature of the interface. The second term is acting tangential to the interface, and is directed toward the region of higher surface tension coefficient σ.

In the CSF model, the surface force is reformulated into a volumetric force $\vec{F}_s$ as follows:

$$\vec{F}_s = \vec{f}_s \delta_s \frac{F}{\langle F \rangle}, \quad (9)$$

where $\langle F \rangle$ is the averaged volume fraction across the interface, and δ_s is the surface delta function given by

$$\delta_s = |\vec{n}| = |\nabla F|. \quad (10)$$

The δ_s function is only non-zero within a finite thickness transition region near the interface, and the corresponding volumetric force $\vec{F}_s$ will only act within this transition region.

At the solid boundary, the effect of wall adhesion is modeled through the use of a static contact angle θ between the interface and the wall [5]. The wall adhesion force is calculated in the same manner as the surface tension volume force using Eq. (9) except that the unit normal vector at the wall is modified as follows:

$$\hat{n} = \hat{n}_w \cos\theta + \hat{n}_t \sin\theta, \quad (11)$$

where $\hat{n}_w$ is the unit wall normal vector directed into the wall, and $\hat{n}_t$ is the unit vector normal to the interface near the wall. Here, $\hat{n}_t$ is calculated from Eq. (7) with the smoothed value of volume fraction. In the case of a moving contact line, this treatment of wall adhesion is a physical approximation because the contact angle is assumed to be constant independent of wall and fluid conditions. In the case where the wall does not align with the coordinate axis, the present implementation interprets the contact angle as the exact angle between the contact line and the wall rather than a numerical approximation between the contact line and the coordinate axis used in previous implementations [12].

Numerical Evaluation of Surface Tension. The present implementation does not rely on special mesh topology or mesh orientation, and it is capable to handle arbitrary interfacial flows in complex geometries partially due to the CLEAR-VOF algorithm. In this algorithm, however, there is no value of the volume fraction available at any individual node, and the volume fraction is defined as a constant over each element. In order to evaluate surface forces that depend on the derivatives of the volume fraction, information on elements surrounding the reference element must be taken into account. In the present implementation of the CSF model, the surface curvature, the surface delta function and the unit normal vector are also stored as constants over each element within the transition region. The representative point for

these element-based quantities at each element is here chosen as the centroid of the corresponding element: (x_i^c, y_i^c). For the surface normal vector $(\vec{n} = n_x \vec{i} + n_y \vec{j})$, on the other hand, two sets of values are calculated and stored. The first set is the element-based normal vectors located at the element centers, whereas the second set is the nodal normal vectors located at the element vertices. The evaluation of the element-based normal vectors is essentially the same with that used in the reconstruction step of the CLEAR-VOF algorithm. First, Taylor series expansions are formed from the volume fraction (F_i) at each reference element to the volume fraction values (F_k) of its neighboring elements. The method of Least Squares Gradient is then used to calculate the element-based surface normal (n_x^e, n_y^e) or the gradients of the volume fraction [15]:

$$\begin{bmatrix} \sum_{k=1}^{N_i} \frac{\delta x_{ik}^2}{d_{ik}} & \sum_{k=1}^{N_i} \frac{\delta x_{ik}\delta y_{ik}}{d_{ik}} \\ \sum_{k=1}^{N_i} \frac{\delta x_{ik}\delta y_{ik}}{d_{ik}} & \sum_{k=1}^{N_i} \frac{\delta y_{ik}^2}{d_{ik}} \end{bmatrix} \begin{bmatrix} (n_x^e)_i \\ (n_y^e)_i \end{bmatrix} = \begin{bmatrix} \sum_{k=1}^{N_i} \frac{\delta x_{ik}\delta F_{ik}}{d_{ik}} \\ \sum_{k=1}^{N_i} \frac{\delta y_{ik}\delta F_{ik}}{d_{ik}} \end{bmatrix}. \tag{12}$$

Here, N_i is the number of neighboring elements for the corresponding element i, and other quantities in the above equation are given as:

$$\begin{aligned} \delta x_{ik} &= x_k^c - x_i^c \\ \delta y_{ik} &= y_k^c - y_i^c \\ d_{ik} &= \sqrt{\delta x_{ik}^2 + \delta y_{ik}^2} \\ \delta F_{ik} &= F_k^c - F_i^c . \end{aligned} \tag{13}$$

For the nodal normal vectors, Taylor series expansions are formed from the value $(\vec{n}_j^d)$ at each vertex of the reference element to the element-based values $(\vec{n}_k^e)$ connected to the corresponding node j. To handle the arbitrary mesh connectivity, the method of Least Squares is then used to approximate the nodal surface normal $(\vec{n}_j^d = n_x^d \vec{i} + n_y^d \vec{j})$:

$$\begin{bmatrix} N_j & \sum_{k=1}^{N_j} \frac{\delta x_{jk}}{d_{\max}} & \sum_{k=1}^{N_j} \frac{\delta y_{jk}}{d_{\max}} \\ \sum_{k=1}^{N_j} \frac{\delta x_{jk}}{d_{\max}} & \sum_{k=1}^{N_j} \frac{\delta x_{jk}^2}{d_{\max}^2} & \sum_{k=1}^{N_j} \frac{\delta x_{jk}\delta y_{jk}}{d_{\max}^2} \\ \sum_{k=1}^{N_j} \frac{\delta y_{jk}}{d_{\max}} & \sum_{k=1}^{N_i} \frac{\delta x_{jk}\delta y_{jk}}{d_{\max}^2} & \sum_{k=1}^{N_j} \frac{\delta y_{jk}^2}{d_{\max}^2} \end{bmatrix} \begin{bmatrix} \vec{n}_j^d \\ d_{\max}\left(\frac{\partial \vec{n}}{\partial x}\right)_j^d \\ d_{\max}\left(\frac{\partial \vec{n}}{\partial y}\right)_j^d \end{bmatrix} = \begin{bmatrix} \sum_{k=1}^{N_j} \vec{n}_k^e \\ \sum_{k=1}^{N_j} \frac{\delta x_{jk}\vec{n}_k^e}{d_{\max}} \\ \sum_{k=1}^{N_j} \frac{\delta y_{jk}\vec{n}_k^e}{d_{\max}} \end{bmatrix}. \tag{14}$$

Here, N_j is the number of surrounding elements that have the corresponding node j as one of its vertices. In the above equation, the values are normalized by the maximum distance $(d_{\max})$ between the centers of the surrounding elements and the node j, and the maximum distance $(d_{\max})$ is defined by the following quantities:

$$\begin{aligned} \delta x_{jk} &= x_k^c - x_j \\ \delta y_{jk} &= y_k^c - y_j \\ d_{\max} &= \max\{\sqrt{\delta x_{jk}^2 + \delta y_{jk}^2}; j = 1, N_j\}. \end{aligned} \tag{15}$$

Finally, the surface curvature is calculated from Eq. (6) using the nodal values of the surface normal vector, and the surface delta function and the unit normal vector are directly evaluated from the element-based surface normal vector. The surface gradient operator is evaluated based on Eq. (8) using the unit normal vector, and the volumetric force is calculated with Eq. (9).

Mathematically, the surface curvature depends on the second derivatives of the volume fraction. On the other hand, the volume fraction from the CLEAR-VOF algorithm is discontinuous near the free surface, and it will usually vary from zero to one within a single layer of partial elements. As a result, there may exist large variations in the distribution of the surface curvature near the interface, and this in turn may introduce artificial noises in the pressure distribution near the surface. To alleviate this problem, the present implementation introduces a spatial smoothing operation using the Least Squares method. Consequently, the evaluation of the surface tension force will be derived from a weighted volume fraction field, and the transition region will be increased to a couple layers of elements near the free surface. In order to minimize any unphysical smearing of the interface shape, only one sweep of the smoothing operation is performed for the values of the volume fraction, the element based normal vector and the surface curvature. An under-relaxation procedure is also used for those variables, and the relaxation factor is set to one half. Further, this smoothing operation is only performed during the evaluation of the surface tension forces, and the original unsmoothed volume fraction is used in the CLEAR-VOF advection algorithm and the flow solution procedure.

Validation of Computer Program

The computer program is validated for two model problems: (1) a droplet in equilibrium, and (2) an oscillating droplet. Systematic grid refinements have been conducted in both problems to ensure numerical accuracy of the results.

Droplet in Equilibrium. In this section, both the cylindrical and the spherical static drop problems are investigated. The cylindrical drop problem is simulated in a two-dimensional Cartesian coordinate system, and the spherical one is simulated in a two-dimensional axisymmetric coordinate system. Computations have been performed with grids containing 30×30, 60×60 and 120×120 elements for the planar geometry, and 15×30, 30×60 and 60×120 elements for the axisymmetric geometry. Assuming the ambient gas pressure is zero, the theoretical drop pressure (P_{theory}), induced by surface tension, is σ/R for the cylindrical drop and $2\sigma/R$ for the spherical drop. Here, R is the radius of the two drops. On the other hand, the numerical drop pressure is defined by averaging the nodal drop pressure:

$$P_{\text{num}} = \frac{1}{N} \sum_{n=1}^{N} p_n , \tag{16}$$

where N is the number of nodes inside the drop, and P_n is the nodal pressure. Here, an interior node is defined as a node that is connected to only full elements. The relative error between the numerical and theoretical drop pressure is given by the root mean square (rms) value:

$$L_2 = \left[\frac{1}{N P_{\text{theory}}^2} \sum_{n=1}^{N} (P_n - P_{\text{theory}})^2 \right]^{1/2}. \tag{17}$$

Table 1 shows the numerical mean pressures compared with the theoretical value in addition to the root mean square values. Also listed in Table 1 are the numerical results by Brackbill and coworkers [5] obtained with a finite-difference method. In their con-

Table 1 Numerical mean pressure and rms error for the cylindrical drop problem

	Brackbill et al.		Present method	
$R/\Delta x$	P_{num}/P_{theory}	L_2 error	P_{num}/P_{theory}	L_2 error
10	1.034	5.56×10^{-2}	1.022	1.13×10^{-1}
20	1.016	2.82×10^{-2}	1.019	7.75×10^{-2}
40	N/A	N/A	1.006	5.74×10^{-2}

tinuum surface force model, Brackbill and co-workers have presented numerical results using four different schemes, and Table 1 only list the best set in their results using indirect differentiation of the unit normal with smoothing operations. On the two coarse grids, both numerical methods are able to predict the mean pressure quite accurately. For the root mean square error, the present method tends to give higher value than the method by Brackbill et al. [5]. This is because the present method adopts a one-fluid model whereas they have used a two-fluid model with a moderate density ratio of 0.5. As pointed out by Lafaurie et al. [16], gas-liquid flows are subject to the so-called parasitic currents due to a large ratio of density, and those spurious currents scale with surface tension and viscosity. Further, one-fluid model implementation of the present CLEAR-VOF algorithm is capable to resolve the sharp interface within a single layer of partial element and does not lead to any artificial smearing of the interface as the two-fluid model does in the gas-liquid flows. Therefore, the present model is expected to be more prone to the spurious currents than the numerical results of liquid-liquid flows, and this in turn yields higher rms values in the present predictions. The best prediction of the mean pressure is obtained on the finest grid by the present method, and the difference is observed to be less than 1%. For the spherical drop, shown in Table 2, the error for the mean pressure is smallest on the finest grid with the deviation less than 1%, and the difference on the other two grids is found to be approximately 2%. Further, as expected, the rms error reduces when the mesh is progressively refined.

Oscillating Droplet. In this example, a system of a liquid droplet oscillating in a dynamically inactive gas is considered. Assuming an infinitesimal amplitude oscillation of an ellipsoid of inviscid fluid, the angular frequency ω of the oscillation can be easily obtained following a balance between the kinetic energy and the potential energy due to surface tension:

$$\omega^2=\frac{8\sigma}{\rho R_F^3} \tag{18}$$

where R_F is the radius of the nonperturbed spherical drop. When considering viscous effects, the angular frequency is modified by

$$\omega_v^2=[8-(5/\mathrm{Re})^2]\frac{\sigma}{\rho R_F^3} \tag{19}$$

where Re is the Reynolds number, defined by

$$\mathrm{Re}=\frac{\sqrt{\rho\sigma R_F}}{\mu} \tag{20}$$

Table 2 Numerical mean pressure and rms error for the spherical drop problem

$R/\Delta x$	P_{num}/P_{theory}	L_2 error
10	1.020	1.23×10^{-1}
20	1.019	7.91×10^{-2}
40	0.998	5.77×10^{-2}

Table 3 Computed oscillation frequencies (KHz) Compared with the theory and experiment

		Numerical prediction	
Theory	Experiment	$R_F/\Delta r=10$	$R_F/\Delta r=20$
43.0	44.0	42.2	43.5

For higher degree of the spherical harmonic mode, the oscillation frequency is given in Rayleigh [17] and Prosperetti [18]. Basaran [19] and Mashayek and Ashgriz [20,21] have further investigated nonlinear oscillations of drops with moderate and large amplitudes.

In this paper, we consider a water ellipsoid with Re=38.2 according to the experiment by corresponding to Söderkvist [22]. The initial semiaxes are 18 μm in the r- direction (or x- and z-direction), and 24.69 μm in the y-direction. This corresponds to a non-perturbed radius of $R_F=20$ μm. The material properties for water are $\rho=10^3$ kg/m^3, $\mu=10^{-3}$ kg/(m·s), and $\sigma=0.073$ N/m. Two computational grids, (1) $R_F/\Delta r=10$ and (2) $R_F/\Delta r=20$, have been selected in this study with uniform spacing in both r- and y-directions. The time increments are set to 2×10^{-7} s for grid (1) and 1×10^{-7} s for grid (2). The temporal signatures are collected every 3 and 5 time steps, respectively. The total times for two oscillation cycles are 4.74×10^{-5} s and 4.6×10^{-5} s, corresponding to oscillation frequencies of $f=42.2$ kHz and $f=43.5$ kHz, as shown in Table 3. Both values agree well with the analytical solution of $f=43.0$ kHz according to Eq. (19).

Table 3 also shows the oscillation frequency from the experiment by Söderkvist [22]. The experiment was conducted on water droplets emerging from an ink jet printer head. The electric drive cycle was adjusted such that only a single droplet was formed and there was no satellite droplets created behind the main droplet. Measurements were done using a microscope and a stroboscope whose trigger delay could be varied. The oscillation frequency was observed to be 44 kHz for a droplet diameter of 40 μm traveling 0.9 mm in 10 oscillation cycles (corresponding to a velocity of 4 m/s). This frequency agrees well with both the numerical predictions and the analytical solutions, and the slight difference may be due to the inaccuracy in the measurement of the droplet diameter (1-2 μm).

Numerical Results

This section presents results for several free surface problems with surface tension in complex geometries to demonstrate the capability and flexibility of the current computer program. As a first step, calculations were performed to investigate surface tension phenomenon for a number of problems in simple geometries. The first problem investigates a droplet impacting on a rigid surface, and the second problem studies the collision of two identical droplets moving toward each other. The effects of wall adhesion are also illustrated through a shallow pool of water in a tank with two extreme contact angles. Detailed flow pattern and free surface characteristics are presented in Wang [23], and thus they will not be presented here. Good agreement with previous numerical results was obtained, indicating the accuracy of the present computer program.

In this section, the computer program is applied to thermocapillary flows in complex cavities to investigate the interesting phenomenon of Marangoni convection. In such flows, the surface tension coefficient varies with the temperature distribution, and the fluid along the free surface moves from a low to a high surface tension region. In the past, there have been a number of studies on Marangoni convection in rectangular cavities to study the fluid and heat transfer characteristics at the free surface [14,24,25]. This is partially due to the geometric simplicity that makes it possible to investigate the interesting interfacial dynamics due to a

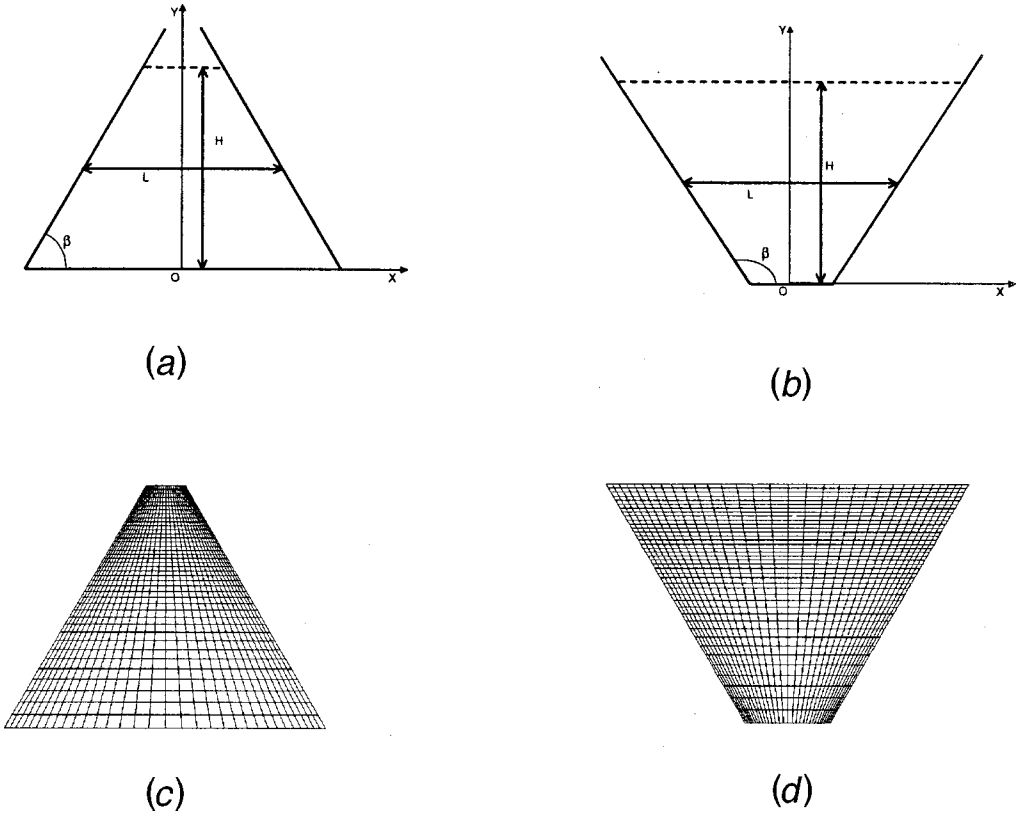

Fig. 1 Coordinate system and geometrical configurations for the trapezoidal cavities: (*a*) β=60 deg, (*b*) β=120 deg. Representative meshes of 32×40 elements: (*c*) β=60 deg, (*d*) β=120 deg.

variable sufficient tension coefficient. Marangoni convection in a rectangular cavity is also studied using the present computer program [23], and the computational results agree with previous numerical simulations [14].

Figure 1 shows the coordinate system, geometrical configurations and representative meshes of two trapezoidal cavities. The domain under consideration contains a Newtonian fluid with average height of H and average width of $L=H$. To allow for deformation of the free surface, the computational domain extends slightly to $1.2H$ in the y-direction for most cases. The inclination (β) between the left wall and the bottom wall is set to 60 degrees and 120 degrees, respectively. Unless otherwise stated, nonuniform meshes are generated in both directions consisting of 64×80 elements. In the x-direction, the mesh points are clustered close to the sidewalls, and the ratio of mesh size between the center and the end elements are set to 3.0. In the y-directions, a finer mesh is first generated uniformly close to the free surface, and the mesh is then stretched out toward the bottom wall. The ratio of mesh sizes between the end elements is set to 3.0 in the y-direction.

In this paper, effects of gravity are not considered, and there are no other external forces. Hence, the fluid motion is purely induced by differences in the surface tension force at the free surface due to a non uniform temperature distribution. Similar to Sasmal and Hochstein [14], the Prandtl number is set to unity for all calculations. As for boundary conditions, no-slip conditions are specified on all walls with the velocity set to zero. At the free surface, the pressure is prescribed to be zero, and a natural condition is imposed for velocity degrees of freedom. Hence, the fluid is allowed to slip along the interface, and this is consistent with the fact that the air is treated as vacuum in this study. For temperature degree of freedom, a natural or adiabatic condition is used at both the free surface and the bottom wall, whereas constant values of T_{hot} and T_{cold} are specified at the left and right wall, respectively. The surface tension coefficient is set to vary linearly with temperature:

$$\sigma=\sigma_{\text{ref}}+\frac{\partial\sigma}{\partial T}(T-T_{\text{ref}}), \tag{21}$$

where $\partial\sigma/\partial T$ is a negative constant for a given fluid, and σ_{ref} is the reference surface tension coefficient at the reference temperature T_{ref}. Calculations are performed over a range of capillary numbers and Marangoni numbers, with the two numbers respectively defined as

$$\begin{aligned}\text{Ca}&=|\partial\sigma/\partial T|(T_{\text{hot}}-T_{\text{cold}})/\sigma_{\text{ref}}\\ \text{Ma}&=\rho C_p|\partial\sigma/\partial T|(T_{\text{hot}}-T_{\text{cold}})H/\mu k.\end{aligned} \tag{22}$$

Here, ρ, μ, k, and C_p are the density, dynamic viscosity, thermal conductivity, and specific heat, respectively.

First, computations are performed for Marangoni convection in a rectangular cavity at an extreme static contact angle of θ=10 deg. This case can also be viewed as a special case of Marangoni convection in a trapezoidal cavity with an inclination of 90 degrees. The computational domain in the y-direction is increased to $1.4H$ in order to account for large deformation of the free surface, and calculations are performed on two grids, consisting of 32×50 and 64×100 elements, respectively. Figure 2 shows the variation of local Nusselt number along the left hot wall of this cavity. Here, the local Nusselt number is defined as the ratio of the local heat flux to the heat flux for pure conduction between the left hot wall and the right cold wall:

$$\text{Nu}=\frac{k|\partial T/\partial n|}{k(T_{\text{hot}}-T_{\text{cold}})/L}. \tag{23}$$

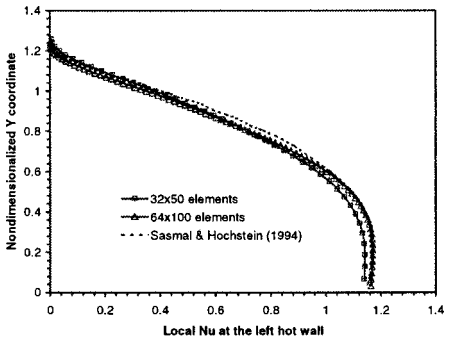

Fig. 2 Nusselt number variation along the left hot wall of a rectangular cavity for a contact angle of 10 degrees.

As seen in Fig. 2, the coarse grid gives a slightly lower Nusselt number than the fine grid near the bottom wall, and a slightly higher Nusselt number close to the free surface. Figure 2 also presents the computational results by Sasmal and Hochstein [14] using a finite difference method with a 34×55 mesh. Good agreement with Sasmal and Hochstein [14] was obtained on both meshes, providing additional confidence of the present finite-element model in studying Marangoni convection with large deformation of the free surface.

Figure 3 shows steady-state streamlines and isotherms of the thermocapillary flows in a trapezoidal cavity with an inclination of 60 degrees for a neutral static contact angle of 90 degrees. At the free surface, the flow is observed to move toward the cold wall, driven by the tangential component of the surface tension force. As a result, a clear vortex is formed underneath the free surface due to this thermocapillary convection, and such a vortical motion is responsible for the distortion in the temperature profile. It is observed that the free surface profiles are perpendicular to the sidewalls, indicating the adequacy of the present implementation of the static contact angles. As expected, the fluid height is the lowest at the center of the free surface for this neutral contact angle. At the higher Marangoni number of 500, the streamlines show a stronger asymmetric pattern, and the fluids are drawn further into the junction region between the free surface and the sidewalls. An increased distortion of the isotherms is also observed at this higher Ma number, and the isotherms are shifting toward the cold wall. Figure 4 shows the streamlines and isotherms at two different static contact angles of 60 and 120 degrees for a Marangoni number of 100 and a capillary number of 0.1. At the contact angle of 60 degrees, the free surface deforms considerably due to wall adhesion effects. The fluid is drawn upward along the sidewalls, and the fluid height is much lower at the center. On the other hand, at the contact angle of 120 degrees, there is little deformation of the free surface, and the fluid height remains nearly constant as expected.

Figures 5 and 6 reveal the influence of the Marangoni number, capillary number, and static contact angle on local Nusselt number at the sidewalls. Similar to the rectangular case, the local Nusselt number is defined as the ratio of local heat flux to the pure conduction between the left hot wall and the right cold wall at their averaged distance. At $Ma=0$, the surface tension is constant independent of temperature, and the heat transfer is characterized by pure conduction with the presence of a deformed free surface. At $Ma=10$, the local Nusselt number is almost indistinguishable from that at $Ma=0$, indicating the dominance of heat conduction for this Marangoni number. For the case of $Ma=100$, the heat transfer is still dominated by conduction away from the free surface, and the influence of Marangoni convection on the Nusselt number distribution becomes important only in regions close to

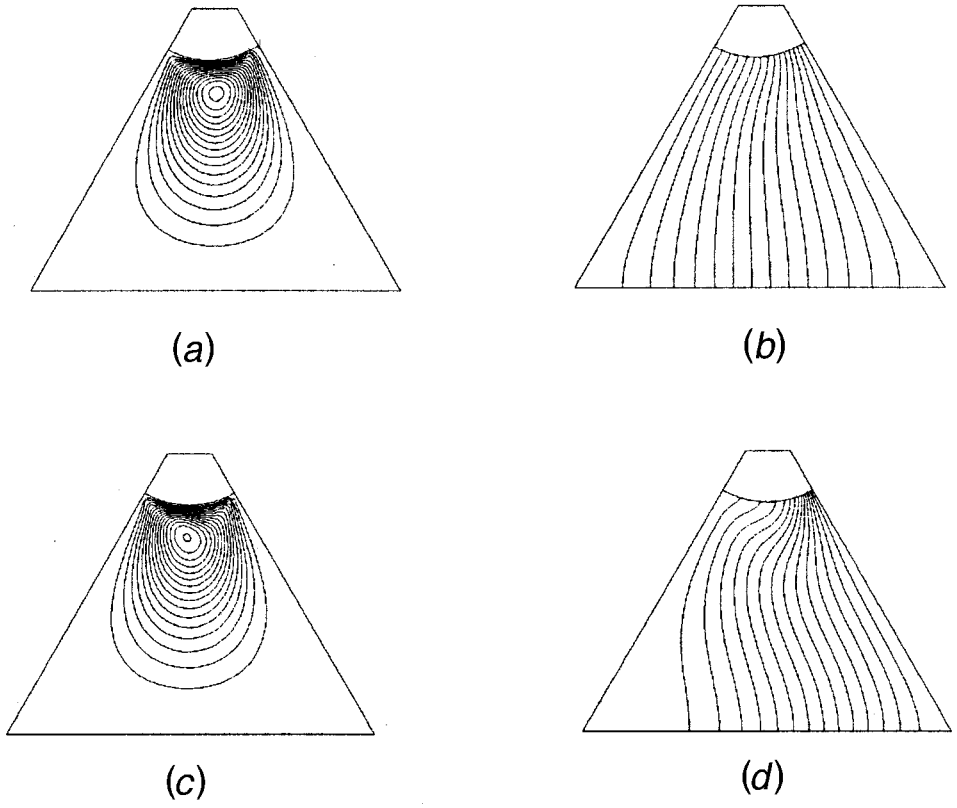

Fig. 3 Marangoni convection in a trapezoidal cavity with an inclination of 60 degrees for a static contact angle of 90 degrees. Streamlines: (*a*) Ma=100, Ca=0.1 and (*c*) Ma=500, Ca =0.05. Isotherms: (*b*) Ma=100, Ca=0.1 and (*d*) Ma=500, Ca=0.05.

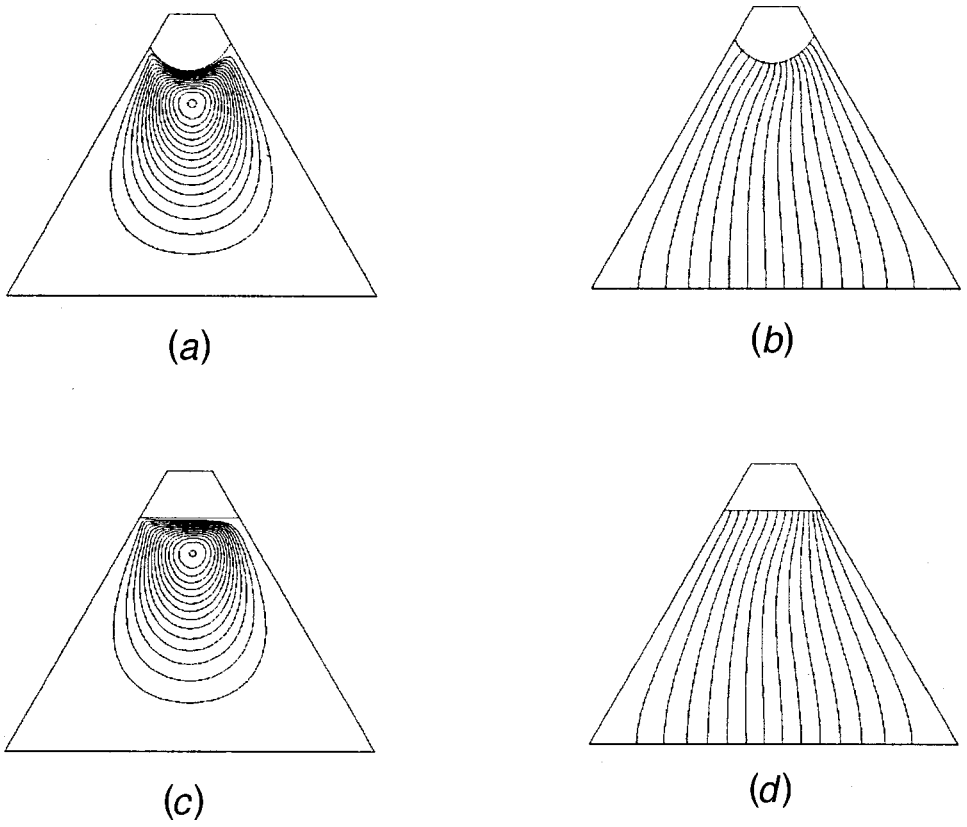

Fig. 4 Marangoni convection in a trapezoidal cavity with an inclination of 60 degrees for a Marangoni number of 100 and a capillary number of 0.1. Streamlines: (*a*) θ=60 deg and (*c*) θ=120 deg. Isotherms: (*b*) θ=60 deg and (*d*) θ=120 deg.

the free surface. Figure 5 also shows a greater variation in the local Nusselt number along the sidewalls for the case of Ma=500. This is consistent with the flow pattern, temperature variations and interface shapes previous depicted in Fig. 3. As the intensity of the vortical motion increases, advective transport enhances heat transfer and the shifting of the isotherms lead to a maximum Nusselt number near the free surface at the cold wall. The lower Nusselt number along the hot wall is also because of this increased vortical motion that brings higher temperature fluid from the bottom upward toward the free surface. At the contact angle of 60 degrees, shown in Fig. 6, the Nusselt number is relatively small near the free surfaces because the streamline does not penetrate the free surface and the advective transport is not significant. As the contact angle increases, the fluid starts to move into the contact region, and contributions from the advective transport will thus become more important. Therefore, the Nusselt number near the free surface increases as the static contact angle increases, and the maximum Nusselt number occurs at the contact line for the cases of higher contact angles.

Figure 7 shows streamlines and isotherms for a trapezoidal cav-

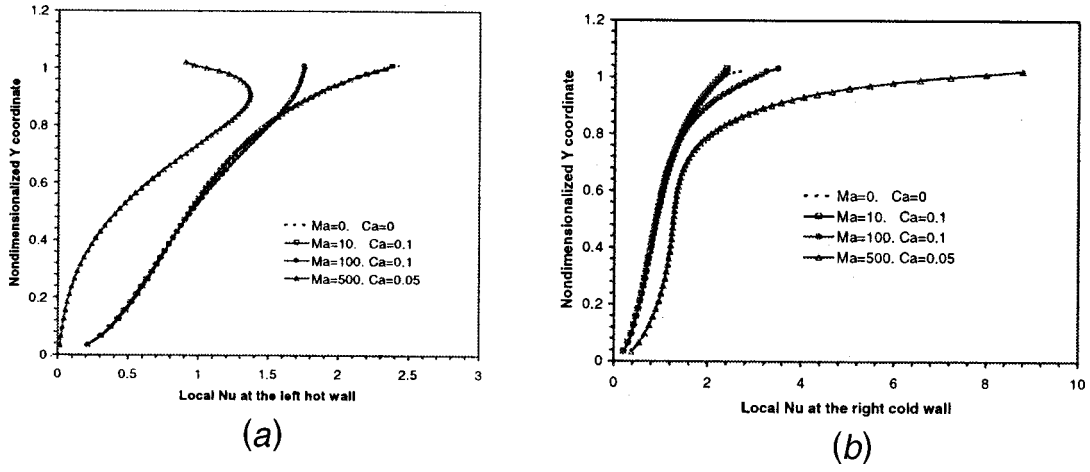

Fig. 5 Variations of local Nusselt number along the cavity walls at various Marangoni numbers and capillary numbers for an inclination of 60 degrees and a static contact angle of 90 degrees. (*a*) Left hot wall, (*b*) right cold wall.

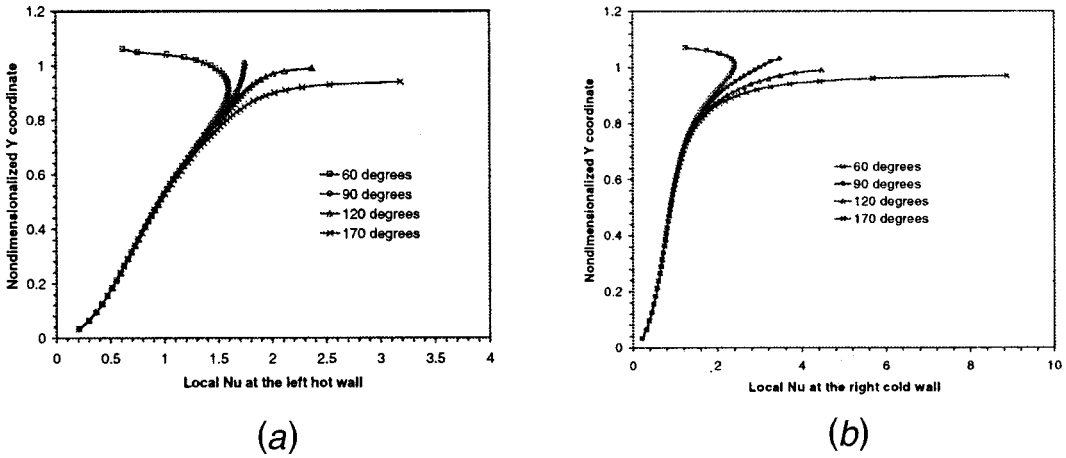

Fig. 6 Variations of local Nusselt number along the cavity walls at various static contact angle for an inclination of 60 degrees, Ma=100, Ca=0.1. (*a*) Left hot wall, (*b*) right cold wall.

ity with an inclination of 120 degrees and a neutral static contact angle of 90 degrees. For this geometry, the size of the vortex formed underneath the free surface is much larger than that for an inclination of 60 degrees, and such a vortical motion further results in larger distortion of the temperature distributions. Due to the neutral contact angle of 90 degrees, the fluid height is observed to be the highest at the center of the free surface. At Ma =500, the temperature profiles are considerably distorted due to the vortical motion, and the isotherms are shifting toward the hot wall contrary to the cavity with an inclination of 60 degrees. Figure 8 shows the streamlines and isotherms at two different static contact angles of 60 and 120 degrees for Ma=100 and Ca=0.1. At the contact angle of 60 degrees, there is only a slight deformation of the free surface, and the fluid height is slightly higher at the right wall than that at the left wall. At the contact angle of 120 degrees, on the other hand, the free surface deforms considerably, and the fluid height is much higher at the center than that at the sidewalls.

Figure 9 shows the influence of the Marangoni number and the capillary number on local Nusselt number at both the hot and cold walls for a static contact angle of 90 degrees. Similar to the cavity with an inclination of 60 degrees, there is little difference in the local Nusselt number distributions between Ma=10 and Ma=0, indicating the dominance of conduction. The influence of Marangoni convection is observed to become stronger at Ma=100, and a noticeable difference is observed for the local Nusselt number even near the bottom regions. At Ma=500, a greater variation of the local Nusselt number is observed along the sidewalls. The

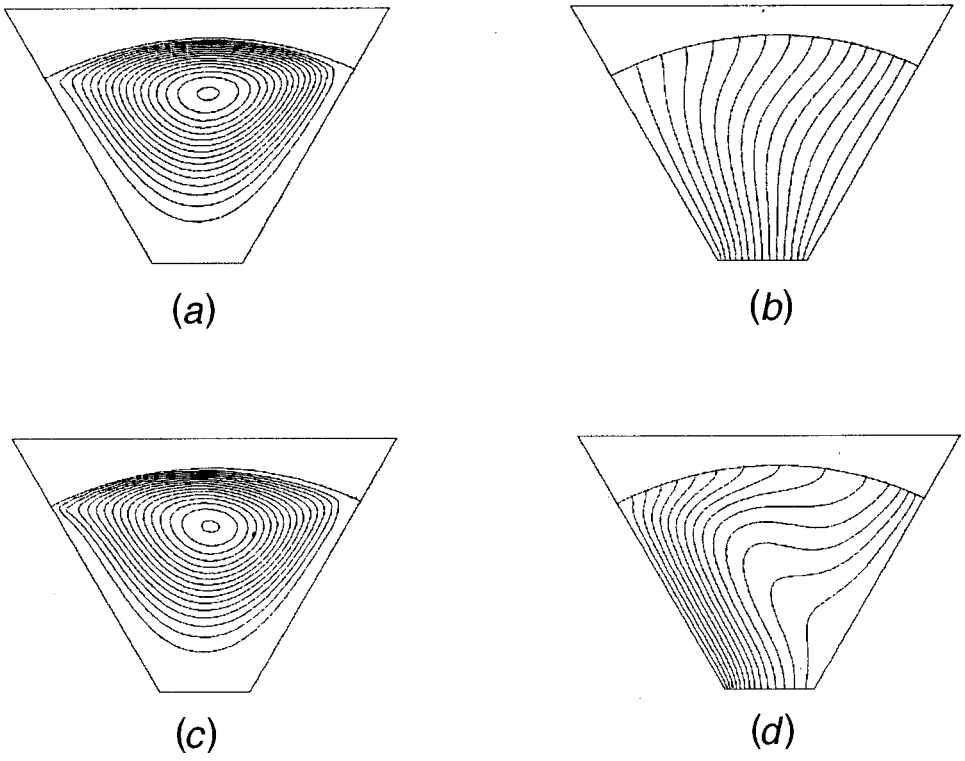

Fig. 7 Marangoni convection in a trapezoidal cavity with an inclination of 120 degrees for a static contact angle of 90 degrees. Streamlines: (*a*) Ma=100, Ca=0.1 and (*c*) Ma=500, Ca =0.05. Isotherms: (*b*) Ma=100, Ca=0.1 and (*d*) Ma=500, Ca=0.05.

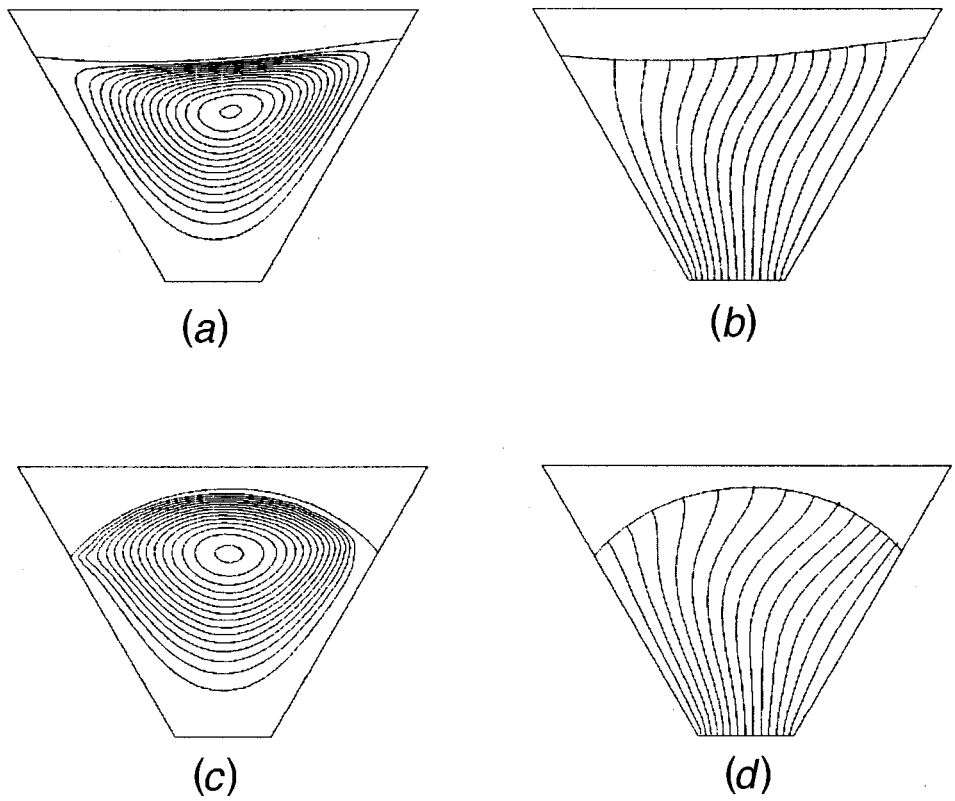

Fig. 8 Marangoni convection in a trapezoidal cavity with an inclination of 120 degrees for a Marangoni number of 100 and a capillary number of 0.1. Streamlines: (*a*) θ=60 deg and (*c*) θ=120 deg. Isotherms: (*b*) θ=60 deg and (*d*) θ=120 deg.

Nusselt number along the left hot wall is much higher than the other two cases of lower Marangoni numbers, and this is due to the increased intensity of the vortical motion and the shifting of the isotherms toward the left wall. Further, the motion of the vortex underneath the free surface brings cooler fluid from the top downward along the right wall, and thus results in a lower Nusselt number in the bottom region of the cavity. Figure 10 shows the influence of various static contact angles on the Nusselt number distributions for Ma=100 and Ca=0.1. Simulation of the small contact angle (10 degrees) flows was performed using a nonuniform grid of 64×110 elements, and the computational domain in the y-direction was increased to 1.5H in order to capture large deformation of the free surface. The Nusselt number is observed to decrease rapidly with height at both walls, and approaches zero at the free surface. This is also consistent with the observations of Sasmal and Hochstein [14] in the case of a rectangular cavity. Because the streamline does not penetrate this narrow region between the free surface and left wall, Sasmal and Hochstein [14] suggest that the fluid is nearly stagnant in this region, and thus the fluid temperature will approach the wall temperature when steady state is reached. As the contact angle is increased, flow into the

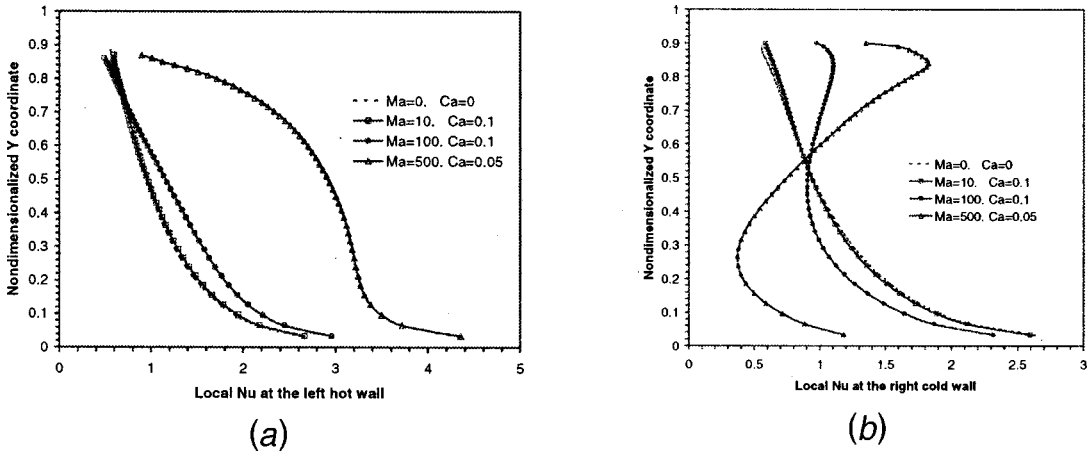

Fig. 9 Variations of local Nusselt number along the cavity walls at various Marangoni numbers and capillary numbers for an inclination of 120 degrees and a static contact angle of 90 degrees. (*a*) Left hot wall, (*b*) right cold wall.

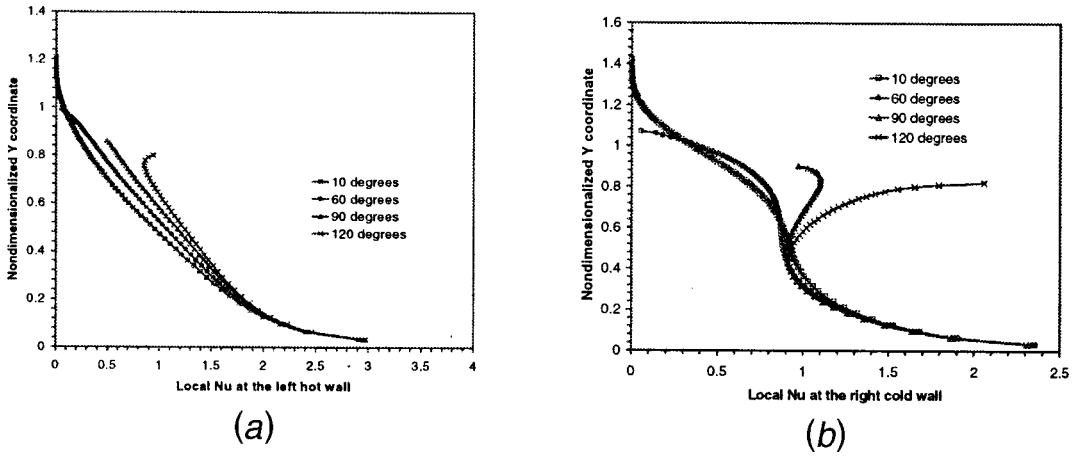

Fig. 10 Variations of local Nusselt number along the cavity walls at various static contact angle for an inclination of 120 degrees, Ma=100, Ca=0.1. (*a*) Left hot wall, (*b*) right cold wall.

contact region will thus enhance the heat transfer near the free surface resulting in higher Nusselt numbers at large contact angles.

Summary and Conclusion

ANSYS/FLOTRAN at Release 5.7 has been enhanced to predict free flows with surface tension in complex geometries. The CLEAR-VOF algorithm is used to track the time evolution of the free surface, and the CSF model is used to evaluate the normal and tangential components of the surface tension forces. Computational predictions by this computer program have shown good agreement with both analytical and experimental results for two model problems: a droplet in equilibrium and an oscillating droplet. The computer program is then applied to Marangoni convection in a rectangular cavity at an extreme contact angle of 10 degrees, and the computed local Nusselt numbers agree well with previous numerical studies. Finally, Marangoni convection in two types of trapezoidal cavities is studied to investigate the interesting flow and heat transfer characteristics in complex geometries. Systematic calculations have been performed over a range of Marangoni numbers, capillary numbers and static contact angles. For the trapezoidal cavity with an inclination of 60 degrees, the vortex formed underneath the free surface is of a smaller size, and the influence of Marangoni convection on the local Nusselt number is reflected mainly in regions close to the free surface. The vortical motion tends to bring hotter temperature fluid upward from the bottom along the left wall, and this in turn results in the shifting of isotherms close to the free surface toward the right wall. For the trapezoidal cavity with an inclination of 120 degrees, on the other hand, the vortex is of a much larger size, and the influence on heat transfer is significant throughout the flow domains. Contrary to the other cavity, the vortical motion here brings the cooler fluid downward from the top along the right wall, and this results in the shifting of isotherms toward the left wall in the bottom region.

Acknowledgments

The author would like to thank Dale Ostergaard, Director of Multiphysics at ANSYS, Inc., for his constant support and encouragement throughout this development. Many thanks are owed to Jan Söderkvist, Associate Professor at Colibri Pro Development AB in Sweden, for helpful discussions on the oscillating droplet problem. The author would also like to thank Dr. T. Barbat and Prof. N. Ashgriz at the State University of New York, University at Buffalo for providing some numerical results from the RIPPLE code.

Nomenclature

Ca = capillary number
C_p = specific heat
f = surface tension force; oscillation frequency
F = volume fraction; body force
k = thermal conductivity
Ma = Marangoni number
n = coordinate normal to the interface
Nu = Nusselt number
p = pressure
R = radius of the spherical drop
Re = Reynolds number
S = source term
t = vector tangential to the interface
T = temperature
x, y = coordinates
v = velocity
w = weighting function
Γ = boundary of finite element domain
Ω = finite element domain
β = inclination of the trapezoidal cavity
δ = surface delta function
κ = curvature
μ = dynamic viscosity
θ = contact angle
σ = surface tension coefficient
ω = angular frequency of oscillation

Superscripts

c = related to element center
d = related to node
e = related to element
p = related to pressure
T = related to temperature
v = related to velocity
$\wedge$ = unit vector

Subscripts

cold = related to cold walls
hot = related to hot walls
i = related to element i
j = related to node j
k = related to element k
ref = reference value
s = related to interface

References

[1] Hirt, C. W., and Nichols, B. D., 1981, ''Volume of Fluid (VOF) Method for the Dynamics of Free Boundaries,'' J. Comput. Phys., **39**, pp. 201–225.

[2] Ashgriz, N., and Poo, J. Y., 1991, ''FLAIR: Flux Line-Segment Model for Advection and Interface Reconstruction,'' J. Comput. Phys., **93**, pp. 449–468.

[3] Kim, S.-O., and No, H. C., 1998, ''Second-Order Model for Free Surface Convection and Interface Reconstruction,'' Int. J. Numer. Methods Fluids, **26**, pp. 79–100.

[4] Barbat, T., Ashgriz, N., and Wang, G., 2002, ''CLEAR-VOF and Its Application to Free Surface Flows,'' to be submitted.

[5] Brackbill, J. U., Kothe, D. B., and Zemach, C., 1992, ''A Continuum Method for Modeling Surface Tension,'' J. Comput. Phys., **100**, pp. 335–354.

[6] Patankar, S. V., 1980, *Numerical Heat Transfer and Fluid Flow*, Hemisphere Publishing Corporation, New York.

[7] Zienkiewicz, O. C., and Taylor R. L., 1989, *The Finite Element Method, Vol. 1*, 4th Edition, McGraw-Hill, London.

[8] Heinrich, J. C., and Pepper, D. W., 1998, *Intermediate Finite Element Method: Fluid Flow and Heat Transfer Applications*, Taylor & Francis, Washington, DC.

[9] Brooks, A. N., and Hughes, J. T. R., 1982, ''Streamline Upwind/Petrov-Galerkin Formulations for Convective Dominated Flows with Particular Emphasis of the Incompressible Navier-Stokes Equations,'' Computer Methods for Applied Mechanics and Engineering, **32**, pp. 199–219.

[10] Rice, J. G., and Schnipk, R. J., 1986, ''An Equal-Order Velocity-Pressure Formulation that does not exhibit spurious pressure modes,'' Computer Methods in Applied Mechanics and Engineering, **58**, pp. 135–149.

[11] Wang, G., 2001, ''A Fast and Robust Variant of the SIMPLE Algorithm for Finite-Element Simulations of Incompressible Flows,'' *Computational Fluid and Solid Mechanics*, K. J. Bathe ed., Elsevier Science Ltd, Kidlington, UK, 2, pp. 1014–1016.

[12] Kothe, D. B., and Mjolsness, R. C., 1992, ''RIPPLE: A New Model for Incompressible Flows with Free Surfaces.'' AIAA J., **30**, pp. 2694–2700.

[13] Richards, J. R., Lenhoff, A. M., and Beris, A. N., 1994, ''Dynamic breakup of liquid-liquid jets,'' Phys. Fluids, **8**, pp. 2640–2655.

[14] Sasmal, G. P., and Hochstei, J. I., 1994, ''Marangoni Convection with a Curved and Deforming Free Surface in a Cavity,'' ASME J. Fluids Eng., **116**, pp. 577–582.

[15] Kothe, D. B., Rider, W. J., Mosso, S. J., Brock, J. S., and Hochstein, J. I., 1996, ''Volume Tracking of Interfaces Having Surface Tension in Two and Three Dimensions,'' *AIAA Paper 96-0859*, presented at the 34rd Aerospace Sciences Meeting and Exhibit.

[16] Lafaurie, B., Nardone, C., Scardovelli, R., Zaleski, S., and Zanetti, G., 1994, ''Modelling Merging and Fragmentation in Multiphase Flows with SURFER,'' J. Comput. Phys., **113**, pp. 134–147.

[17] Rayleigh, J. W. S., 1879, ''On the Capillary Phenomena of Jets,'' Proc. R. Soc. London, **29**, p. 71.

[18] Prosperetti, A., 1980, ''Free Oscillations of Drops and Bubbles: The Initial-Value Problem,'' J. Fluid Mech., **100**, p. 333.

[19] Basaran, O. A., 1992, ''Nonlinear Oscillations of Viscous Liquid Drops,'' J. Fluid Mech., **241**, pp. 169–198.

[20] Mashayek, F., and Ashgriz, N., 1995, ''A Spline-Flux Method for Simulating Free Surface Flows,'' J. Comput. Phys., **122**, pp. 367–379.

[21] Mashayek, F., and Ashgriz, N., 1998, ''Nonlinear Oscillations of Drops with Internal Circulation,'' Phys. Fluids, **10**, pp. 1071–1082.

[22] Söderkvist, J., 1986, private communication.

[23] Wang, G., 2000, ''Finite Element Simulations of Gas-Liquid Flows with Surface Tension,'' *Proc. the ASME Fluids Engineering Division-2000*, T. J. O'Hern, ed., FED **253**, pp. 161-167.

[24] Zebib, A., Homsy, G. M., and Meiburg, E., 1985, ''High Marangoni Number Convection in a Square Cavity,'' Phys. Fluids, **12**, pp. 3467–3476.

[25] Chen, J. C., Sheu, J. C., and Jwu, S. S., 1990, ''Numerical Computation of Thermocapillary Convection in a Rectangular Cavity,'' Numer. Heat Transfer, **17**, pp. 287–308.

Does the Minimum Fluidization Exist?

Arnaud Delebarre
e-mail: Arnaud.Delebarre@emn.fr
Ecole des Mines de Nantes,
La Chantrerie, BP 20722,
44307 Nantes Cedex 3, France

This work proposes an equation giving the pressure drop of a gas flowing through a porous medium or a granular bed. The consequences for the onset of the fluidization are then discussed. It appears that the notion of minimum gas mass-flow rate would improve the description of the transition between fixed and fluidized bed regimes. An equation is then proposed to calculate the minimum fluidization gas mass-flow rate. It is then proved that the minimum fluidization is not only a function of the medium and fluid characteristics but also that it increases with bed inventory. It is then shown that a batch of particles has a minimum fluidization depending on its arrangement in a column and that in some cases, this minimum does not exist at all. As a consequence, the minimum of fluidization, whether it is a velocity or a mass flow rate, cannot be considered as a criterion to characterize a powder. [DOI: 10.1115/1.1490377]

Introduction

Rereading Ergun Equation. One of the most employed correlations giving the pressure drop of a fluid flowing through a granular bed is the one proposed by Ergun [1] [Eq. (1)] after Forchheimer [2]. It should be noticed that Ergun originally wrote Eq. (1) with the mass-flow rate of fluid G and a fluid velocity named U_m defined by Ergun as a ''superficial fluid velocity measured at average pressure.'' Following the Forchheimer's form, Ergun then proposed the analytical form of the two coefficients that balance the U_m term and the GU_m term. These two coefficients are expressed as a function of the porosity and of the equivalent particle size. Finally, Ergun has fitted his correlation with the help of 640 experiments carried out with various gases and particles introducing two constants whose values are 150 and 1,75.

$$\frac{\Delta P}{H}=150\left[\frac{(1-\varepsilon)^2}{\varepsilon^3}\frac{\mu U_m}{d_p^2}\right]+1{,}75\left[\frac{(1-\varepsilon)}{\varepsilon^3}\frac{GU_m}{d_p}\right] \tag{1}$$

Most often works which quote Eq. (1) have written it *de facto* with U and U^2 and have rarely specified which superficial velocity U should be used. In contrast, Geldart [3] has effectively used a ''superficial fluid velocity at average pressure'' by using the superficial velocity at inlet conditions and by multiplying the right-hand side of Eq. (1) by a ratio of the pressure at inlet to the average pressure in the bed without giving the way the average is calculated.

Numerous works have used Eq. (1) for specific porous or granular media. Some have only modified the 150 and 1,75 constants to improve their predictions, *e.g.*, Bitaud et al. [4] with 650 and 5,89, respectively, for a bed of coke particles. Other studies have both statistically adjusted the constants and improved the analytical form of the terms that balance U_m and GU_m [5]. Some other have modelled these terms for specific cases such as parallelepipedal particles [6]. In addition, Laguérie [7], Kunii and Levenspiel [8] and others reminded that Ergun equation (Eq. (1)) must be used with the driving or piezometric pressure $\mathcal{P}=P+g\rho z$ instead of the pressure P.

Thus an Ergun-like equation may be written as Eq. (2) where a and b depend on medium and fluid characteristics:

$$\frac{\Delta\mathcal{P}}{H}=(a+bG)U_m \tag{2}$$

Using Ergun-Like Equations With a Constant (Average) Gas Velocity. It must be pointed out that U_m which appears in the right-hand side of Eq. (1) and Eq. (2) depends on the mass-flow rate G and on the fluid density ρ. In the case of a compressible fluid, the right-hand side depends on the pressures intervening in the left-hand side of these equations. Hence the calculation of one of the variables knowing the others is not straightforward.

Sutherland [9] followed by Mathur and Epstein [10] has proposed a method to evaluate the pressure drop of a gas fluidized bed or of the gas distributor accounting for an average gas superficial velocity U_m in the bed or through the grid. These authors have calculated U_m using Eq. (3) and an average gas density ρ_m through Eq. (4) as a function of the upstream and downstream pressures (of the bed or the fluidization grid) and of the gas density ρ_N at given reference pressure P_N:

$$U_m=\frac{G}{\rho_m} \tag{3}$$

$$\rho_m=\rho_N\left(\frac{P(\text{upstream})+P(\text{downstream})}{2P_N}\right) \tag{4}$$

Then Sutherland and Mathur and Epstein replaced U_m and ρ_m in Eq. (1) with ΔP being equal to $P(\text{upstream})-P(\text{downstream})$, they concluded that it is the difference of the square of the inlet and outlet pressures and not the difference of the pressures that remain constant for a given mass-flow rate. In the case of a gas flowing vertically through a packed bed or a porous media extending from 0 (upstream) to H (downstream) and if the reference pressure P_N is chosen at $z=H$ ($P_N=P(H)$), $P(0)$ can thus be calculated with Eq. (5):

$$P(0)=P(H)\left[1+2\frac{(a+bG)G}{\rho(H)^2 g}\frac{H}{H_0}\right]^{1/2} \tag{5}$$

where H_0 is the measurement of the pressure $P(H)$ at the free surface of the bed ($z=H$) using Eq. (6). Equation (6) means that $P(H)$ is expressed by the mean of a gas height, the gas being considered as a fluid with a constant density equal to the one it has in downstream conditions at $z=H$:

$$P(H)=\rho(H)gH_0 \tag{6}$$

Results

If the mean gas density as calculated in Eq. (4) is replaced in the Ergun equation, Eq. (2), the relationship between $P(0)$ and $P(H)$ is then given by Eq. (7):

Contributed by the Fluids Engineering Division for publication in the JOURNAL OF FLUIDS ENGINEERING. Manuscript received by the Fluids Engineering Division December 8, 2000; revised manuscript received April 17, 2002. Associate Editor: L. Mondy.

$$\frac{[P(0)+\rho(0)g0]-[P(H)+\rho(H)gH]}{H} = (a+bG)\frac{G}{\rho(H)\dfrac{P(0)+P(H)}{2P(H)}} \quad (7)$$

Equation (7) can then be solved noticing it has only one positive solution for $P(0)$ and thus the upstream $P(0)$ pressure can be deduced from $P(H)$ by Eq. (8):

$$P(0)=P(H)\left\{\frac{H}{2H_0}+\left[\left(\frac{H}{2H_0}+1\right)^2+2\frac{(a+bG)G}{\rho(H)^2 g}\frac{H}{H_0}\right]^{1/2}\right\} \quad (8)$$

The upstream pressure $P(0)$ calculated with Eq. (8) that accounts for the piezometric pressure is always greater than the same pressure $P(0)$ calculated after Eq. (5) which omits the ρgh terms. Nevertheless, the difference between the two pressure drops is significant only when the height of the medium becomes large compared to the "gas height" H_0 which corresponds to the pressure $P(H)$ at the downstream conditions.

In contrast, when the height H of the medium is sufficiently low compared to the gas height H_0, Eq. (8) might be developed in MacLaurin series neglecting the terms of order greater than or equal to the second (Eq. (9)). Notice that H_0 is lower in the case of a fluid with a high density or in the case of a low pressure at the outlet.

$$P(0)-P(H)=\rho(H)gH+(a+bG)\frac{G}{\rho(H)}H \quad (9)$$

Accounting that U_m is given by Eq. (3), and that if $H \ll H_0$, then ρ_m is nearly equal to $\rho(H)$, Eq. (9) is thus identical to Eq. (2). In other words, Eq. (8) is the Ergun equation Eq. (1) when it is solved with the correct parameters it requires: an average (and constant) velocity U_m through the porous layer and the driving pressure $\mathcal{P}=P+g\rho z$ instead of the pressure P.

The method proposed by Sutherland and others remains unsatisfactory especially when the dimensions of the medium are large. On the one hand, it assumes an average pressure and on the other hand it imposes an arithmetic average. This study proposes to avoid these two disadvantages by generalyzing Ergun-like equations.

Integrating Ergun-Like Equations Through a Medium. Let us apply Ergun equation (Eq. (2)) to the gas flowing through a layer having an infinitely small thickness dz allowing to assume that gas velocity is constant (Eq. (10)):

$$-\left(\frac{dP(z)}{dz}+g\rho(z)+zg\frac{d\rho(z)}{dz}\right)=(a+bG)U_m(z) \quad (10)$$

The local average superficial velocity $U_m(z)$ and the gas density $\rho(z)$ are, respectively, given by Eq. (11) and Eq. (12) as a function of the average pressure $P(z)$ in the layer of thickness dz and $P(H)$ as reference conditions:

$$U_m(z)=\frac{G}{\rho(z)} \quad (11)$$

$$\rho(z)=\rho(H)\frac{P(z)}{P(H)} \quad (12)$$

Substituting $U_m(z)$, $\rho(z)$, $P(H)$, and $\rho(H)$ in Eq. (10) by their expression given by Eq. (11), Eq. (12), and Eq. (8), it yields Eq. (13):

$$-\frac{dP(z)}{dz}P(z)\left(1+\frac{z}{H_0}\right)-\frac{1}{H_0}P^2(z)=gH_0(a+bG)G \quad (13)$$

Equation (13) can then be integrated with the hypothesis that the coefficients a and b are independent of z. In the case of Ergun equation coefficients, this condition corresponds to a constant gas viscosity and constant medium characteristics. The gas pressure $P(z)$ at any location z in the medium comprised between $z=0$ and $z=H$ is thus given by Eq. (14):

$$P(z)=P(H)\left[\left((a+bG)\frac{G}{\rho(H)^2 g}+1\right)\times\left(\left(\frac{H+H_0}{z+H_0}\right)^2-1\right)+1\right]^{1/2} \quad (14)$$

For $z=0$, Eq. (14) gives $P(0)$; hence the pressure drop for the complete flow across the medium can be calculated knowing the pressure at $z=H$ by Eq. (15):

$$P(0)^2-P(H)^2=P(H)^2\left((a+bG)\frac{G}{\rho(H)^2 g}+1\right)\times\left(\left(\frac{H}{H_0}+1\right)^2-1\right) \quad (15)$$

As for the preceding equations, Eq. (5) and Eq. (8), Eq. (15) also shows that for a given mass-flow rate G, it is the difference of the square of the pressures which remains constant and not the difference of the pressures as might have been deduced from the Ergun equations, Eq. (1) or Eq. (2). Moreover, in contrast with the Ergun equation with its two sides depending on pressure, Eq. (14) and Eq. (15) allow calculating directly a pressure at any height in the medium or its whole pressure drop knowing the gas mass-flow rate, the downstream pressure, and the set of parameters a and b.

When the height H of the medium is sufficiently low compared to the height H_0 which corresponds to the pressure $P(H)$ at the downstream conditions, Eq. (15) might be developed in MacLaurin series neglecting the terms of order greater than the second (Eq. (16)). Notice that H_0 is lower in the case of a fluid with a high density or in the case of a low pressure at the outlet.

$$P(0)^2-P(H)^2=2P(H)H\left[(a+bG)-\frac{G}{\rho(H)}+g\rho(H)\right] \quad (16)$$

By writing the left-hand side of Eq. (16) as the product of the difference of the pressures and of their sum and by accounting that U_m is given by Eq. (3), Eq. (16) yields Eq. (17). Moreover, if $H \ll H_0$, then ρ_m is nearly equal to $\rho(H)$; Eq. (17) is thus identical to Eq. (2). Hence Eq. (2), *id est* Ergun equation written with $\mathcal{P}$ and a gas velocity at average pressure, is an approximation of Eq. (15) for the cases of thin porous or granular media.

$$\frac{P(0)-P(H)}{H}=(a+bG)\frac{G}{\rho_m}+g\frac{\rho(H)^2}{\rho_m} \quad (17)$$

Table 1 Conditions used in calculations

	Symbol	Value	Units
Porosity	ϵ	0,45	(-)
Gas viscosity	μ	$20\ 10^{-6}$	(Pa.s)
Gas density	$\rho(H)$	1,293	kg/m^3
Solid density	ρ_p	2000	kg/m^3
Acceleration of gravity	g	9,81	m/s^2
Mean particle diameter	d_p	0,0001	m
Outlet pressure	P(H)	101325	Pa
Medium thickness	H	0,1; 1; 10; 100; 1000	m
Gas mass-flow rate	G	$1,293\ 10^{-3}$; $1,293\ 10^{-4}$	$kg/m^2.s$

Application of the Generalized Ergun-Like Equation to Flow Through Porous Media. Table 2 gives the pressure drop of a gas flowing in the conditions given in Table 1, calculated according to three methods. The first one consists in using Eq. (5)

Table 2 Gas pressure drop ΔP across the medium calculated as a function of the medium thickness H and the outlet gas velocity after Eq. (5) (Mathur and Epstein [10]), Eq. (8) and Eq. (14) of this work.

ΔP(Pa)	Eq. (5) [Mathur-Epstein, 1974]		This work: Eq. (8)		This work: Eq. (14) with z=0	
H (m)	1mm/s	0,1mm/s	1mm/s	0,1mm/s	1mm/s	0,1mm/s
0,1	99,55	9,960	100,8	11,23	100,8	11,23
1	991,2	99,54	1004	112,2	1004	112,2
10	9513	991,1	9635	1117	9635	1117
100	73180	9512	74180	10730	74280	10730
1000	359200	73170	367000	83270	375600	84260

which comes from the Ergun law with an average gas velocity according to Mathur and Epstein [10]. The second way of calculations uses Eq. (8) of this work, thus the whole Ergun law and nothing else but the Ergun law. In other words, the second method involves the driving pressures and an average gas velocity. The third method corresponds to Eq. (14) of this work which was obtained by integration of Ergun equation along the medium height. The chosen values of G correspond to a fixed bed regime gas flow. As a matter of fact, the two values of gas superficial velocity at outlet are 0,1 mm/s and 1 mm/s, sufficiently smaller than 6 mm/s, the minimum fluidization velocity according to Wen and Yu [11] for solids having a density ρ_p of 2000 kg/m^3.

As previously deduced from the mathematical forms, Table 2 shows that the Ergun equation applied to the whole medium with an average velocity U_m based on an arithmetic mean of the inlet and outlet pressures (Eq. (5)) underestimates the gas pressure drop when compared to the same calculations where P has been replaced by $\mathcal{P}$ (Eq. (8)). Equation (8) gives smaller pressure drops than those calculated through Eq. (14) of this work. The relative deviation between pressure drops calculated after Eq. (14) and Eq. (5) increases with medium height but decreases when the gas flow rate is increased. In contrast, relative deviation between pressure drops calculated after Eq. (14) and Eq. (8) are smaller than the preceding ones, and increases both with bed height and the mass-flow rate. The deviation between Eq. (8) and Eq. (14) is so limited that it can only be observed for very large height of the porous media which fall out of common fields of applications. The 100 m and 1000 m calculations have only been presented to illustrate the difference between the two above-cited equations.

Application of the Generalized Ergun-Like Equation to the Minimum Fluidization. The fluidization theoretically corresponds to a gas P-pressure drop equal to the total weight of the granular bed per unit of bed cross-section W_{total} [12,13], as long as the friction at the wall and the gas phase inertial terms remain negligible [14]. The onset of fluidization occurs for the smallest gas flow rate with the gas P-pressure drop being equal to the weight of solids W_p and that of the gas W_g present in the bed per unit of cross-section (Eq. (18)) or, in other words, the smallest flow rate giving the $\mathcal{P}$-pressure difference being equal to the apparent weight of the solids by unit area of bed cross-section [14].

$$P(0)-P(H)=W_{\text{total}}=W_p+W_g \tag{18}$$

The elimination of $P(0)$ between Eq. (15) and Eq. (18) gives a second degree polynomial for the gas mass-flow rate G. This polynomial has only one real positive solution because the gas flow imposes that the pressure downstream $P(H)$ is always at least equal to the weight W_g of the gas involved in the flow. The real positive solution is obviously the gas mass-flow rate corresponding to the fluidization of the whole bed and may be called the minimum gas mass-flow rate of fluidization G_{mf}. It is given by Eq. (19):

$$G_{mf}=\frac{a}{2b}\left[-1+\left[1+\frac{2b\rho(H)}{a^2HP(H)}\left(W_{\text{total}}^2-2W_{\text{total}}P(H)\left(\frac{H}{2H_0}-1\right)-2P^2(H)\frac{H}{H_0}\right)\right]^{1/2}\right] \tag{19}$$

where the two coefficients a and b can be the ones proposed by Ergun as given by Eq. (20) and Eq. (21):

$$a=150\frac{(1-\varepsilon_{mf})^2}{\varepsilon_{mf}^3}\frac{\mu}{d_p^2} \tag{20}$$

$$b=1{,}75\frac{(1-\varepsilon_{mf})}{\varepsilon_{mf}^3 d_p} \tag{21}$$

Most often, W_g is relatively small compared to the weight of solid W_p (if the gas weight cannot be neglected, the minimum gas mass-flow rate G_{mf} can be found numerically by the equations given in Appendix). Moreover, W_p can be expressed as a function of the bed height H_{mf}, such as Eq. (22):

$$W_p=g(1-\varepsilon_{mf})\rho_p H_{mf} \tag{22}$$

Thus, replacing W_{total} by W_p in Eq. (19) and then substituting W_p by its expression Eq. (22), the minimum gas mass-flow rate G_{mf} is then given by Eq. (23) and appears to depend on the bed height H_{mf}:

$$G_{mf}=\frac{a}{2b}\left[-1+\left[1+\frac{4b}{a^2}(\rho_p(1-\varepsilon_{mf})-\rho(H_{mf}))\times g\left(\frac{H_{mf}}{2H_0}\rho_p(1-\varepsilon_{mf})+\rho(H_{mf})\right)\right]^{1/2}\right] \tag{23}$$

Equation (19) and Eq. (23) show that the minimum fluidization gas mass-flow rate G_{mf} is a function of the solid inventory as well as the solid of the fluid characteristics. The minimum fluidization gas mass-flow rate G_{mf} increases with the mass of solids present in the bed. However, it must be remembered that Eq. (15) has been obtained with the two major assumptions that the gas viscosity and the constant medium characteristics are constant. In the case of the onset of fluidization of the whole bed expressed by Eq. (18), this last hypothesis means that the voidage ε_{mf} is the same at any position in the bed and thus that one neglects a greater expansion in the upper part of the bed (due to a greater gas velocity [3]) compared to the one near the gas distributor.

In contrast Eq. (24) gives the minimum fluidization velocity calculated by usual methods, *cf.* for instance [8], that use the following conditions: (1) the Ergun equation is used with the pressure P instead of the driving pressure $\mathcal{P}$; (2) the gas mass-flow rate G appearing in the Ergun equation is replaced by its expression as a function of the superficial gas velocity and its density such as Eq. (3); (3) the pressure conditions, at which the superficial gas velocity U_{mf} and the gas density ρ must be considered, are not specified; (4) the onset of fluidization is said to occur when the pressure drop given by the Ergun equation is equal to the apparent weight of solids W_p^a per unit area of bed cross-section:

$$G_{mf}=\rho U_{mf}=\frac{a}{2b}\left[-1+\left[1+\frac{4b}{a^2}\frac{\rho W_p^a}{H_{mf}}\right]^{1/2}\right] \tag{24}$$

with the apparent specific weight of solid W_p^a/H_{mf} present in Eq. (24) expressed as a function of the gas and solid density and of the bed voidage such as Eq. (25):

$$\frac{W_p^a}{H_{mf}}=g(1-\varepsilon_{mf})(\rho_p-\rho) \tag{25}$$

If it is replaced in Eq. (24), the minimum fluidization mass-flow rate (and the minimum fluidization velocity) are given by Eq. (26) and appears to be independent on bed height H_{mf}, in contrast with Eq. (19) and Eq. (23) of this study:

$$G_{mf}=\rho U_{mf}=\frac{a}{2b}\left[-1+\left[1+\frac{4b}{a^2}\rho g(1-\varepsilon_{mf})(\rho_p-\rho)\right]^{1/2}\right] \quad (26)$$

Another way to predict the effect of the inventory on the minimum fluidization consists in assuming that upper part of the bed is fluidized before the lower one because of a higher gas velocity in the upper part. There is a beginning and a complete fluidization velocity: the minimum fluidization is reached when the fluidization is completed at the bottom of the bed. This progressive onset of the fluidization has been more particularly observed for processes working at reduced pressure. Some authors have given equations to calculate the height of the fixed and the fluidized bed parts accounting for a Knudsen and a viscous flow regime contribution on the pressure drop [15]. An identical reasoning can be applied to a relationship between the Reynolds and the Archimedes numbers used to estimate the minimum fluidization velocity as given by [16]. However, to account for a progressive onset of fluidization and to calculate the minimum velocity as the complete fluidization velocity, the relationship should be used with values of their variables calculated in pressure and temperature conditions existing at of $z=0$, *i.e.*, with local gas characteristics at the bottom of the solid bed, instead of average or other values:

$$\mathrm{Re}_{mf}(0)=\frac{\rho(0)d_p U_{mf}(0)}{\mu}=[C_1^2+C_2\mathrm{Ar}(0)]^{1/2}-C_1 \quad (27)$$

with:

$$\mathrm{Ar}(0)=\frac{\rho(0)d_p^3(\rho_p-\rho(0))g}{\mu^2} \quad (28)$$

and where C_1 and C_2 are constant, for instance, respectively equal to 27,2 and 0,0408 after [16]. If the gas density $\rho(0)$ present in the Reynolds and Archimedes numbers for bottom conditions is replaced by its value at the free surface using Eq. (12), then using Eq. (18) with a negligible weight of gas, Eq. (27) gives Eq. (29):

$$G_{mf}=\frac{\mu}{d_p}\left\{\left[C_1^2+C_2\left(1+\frac{W_p}{P(H_{mf})}\right)\times\left(\frac{\rho_p-\rho(H_{mf})\left(1+\frac{W_p}{P(H_{mf})}\right)}{\rho_p-\rho(H_{mf})}\right)\mathrm{Ar}(H_{mf})\right]^{1/2}-C_1\right\} \quad (29)$$

with:

$$\mathrm{Ar}(H_{mf})=\frac{\rho(H_{mf})d_p^3(\rho_p-\rho(H_{mf}))g}{\mu^2} \quad (30)$$

Equation (29) demonstrates that the minimum fluidization depends on the bed inventory. Equation (29) also shows that the solid class given by $\mathrm{Ar}(H_{mf})$ influences the relation between the minimum fluidization and the inventory (this will be discussed in the next section).

Table 3 compares the results of the calculations of the minimum fluidization gas mass-flow rate G_{mf} with the minimum fluidization velocity U_{mf} at surface and bottom part conditions as given, on the one hand, by usual application (Eq. (26)) and on the other hand by Eq. (23) developed in this study. It can be seen that, in the first case the minimum fluidization gas mass-flow rate G_{mf} is obviously independent of the bed height, while it is the opposite when G_{mf} is given by Eq. (23). G_{mf} is always higher in this case and the relative deviation with the "usual" G_{mf} increases with bed height.

Table 3 Minimum gas mass-flow rate G_{mf} as a function of the bed height after Eq. (26) (usual) and after Eq. (23) of this work (new). The minimum fluidization velocity U_{mf} is also calculated at the free surface and at bottom part of the layer with P(0) after Eq. (5) and Eq. (8). Gas and solid characteristics are given at Table 1.

	G_{mf} (kg/m2.s)		U_{mf} (cm/s) bottom/top		Relative deviation (%) Inew-usuall / usual	
H_{mf} (m)	Usual Eq.(26)	New Eq.(23)	Eq.(5)	Eq.(8)	G_{mf}	U_{mf} (z=0)
0,1	0,01399	0,01405	1,07 / 1,08	1,07 / 1,09	0,41	0,41
1	0,01399	0,01472	0,98 / 1,08	1,03 / 1,14	5,19	4,7
10	0,01399	0,02139	0,61 / 1,08	0,80 / 1,65	52,9	31,0

Discussion

Influence of the Bed Inventory on the Minimum Fluidization. The literature gives some experimental results dealing with the influence of the bed inventory on minimum fluidization velocities. The published data do not unfortunately allow to calculate precisely the minimum gas mass-flow rate according to Eq. (23) or Eq. (29).

Cranfield and Geldart [17] have measured the minimum fluidization velocity for alumina beads of 1520 μm diameter and different bed inventory in a 2-D model. The minimum velocity regularly increased from 0,51 m/s to 0,64 m/s when the bed height varied from 0,05 to 0,3 m. However, other experiments carried out by the same authors on a 3-D model with nearly similar particles do not confirm this trend. Denloye [18] mentioned that the minimum fluidization velocity of a 1020 μm sand increases from 0,4 to 0,45 (11%) when the static bed height increases from 5 to 30 centimeters. The author explained that it is probably due to the increase from 94% to 99% of the ratio of bed pressure drop to weight of the particles per unit area of bed cross-section [18].

Thonglimp et al. [19] studied the influence of particle diameter and density, the bed inventory and the column diameter on the minimum fluidization velocity and the bed expansion. The experiments carried out by these authors with glass beads from B and D Geldart classes cover a relatively broad range of the parameters: particle diameter from 112,5 μm to 2125 μm; column diameters of 5 cm, 9,5 cm, 19,4 cm and 43,4 cm; bed inventory varying from 50 kg/m2 to 500 kg/m2.

Their results for the glass beads of class D, expressed as the measured minimum fluidization velocity as a function of the inventory and the particle diameter, are shown in Fig. 1. The minimum fluidization velocity increases with the bed inventory. The measured minimum fluidization gas mass-flow rate G_{mf} of these

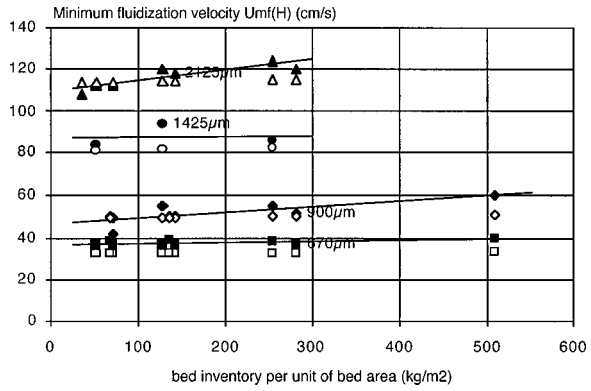

Fig. 1 Calculated U_{mf}(H) by Eq. (29) (open symbols) and measured U_{mf} (black symbols and lines) for glass beads as a function of the weight of solids per unit area of bed cross-section (after [19] and [20])

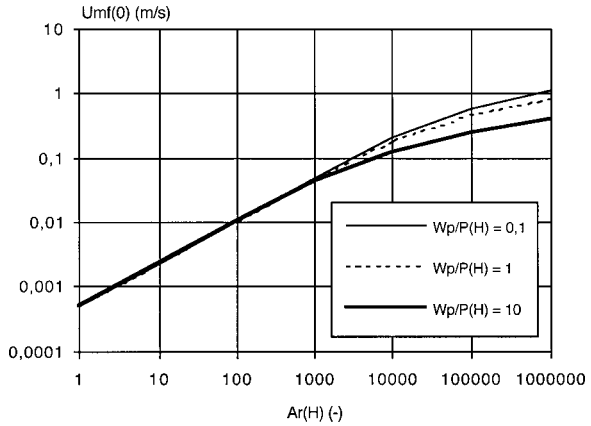

Fig. 2 Minimum fluidization velocity $U_{mf}(0)$ as a function of the Archimede number reported to gas pressure at the bed surface and the bed inventory per unit area of bed cross-section (after Eq. (29)).

solids can also be considered as increasing with the bed inventory if it is assumed that the velocity has been given by the authors on the basis of a nearly constant gas pressure $P(H)$. For the class B particles used by Thonglimp et al., the minimum fluidization velocity remains nearly constant. Figure 1 also shows the calculated values with Eq. (29) and the same hypothesis on the pressure $P(H)$ (the velocity has been given by the authors on the basis of a nearly constant gas pressure). The values of the coefficients C_1 and C_2 of Eq. (29) are those proposed by Thonglimp et al.: $C_1 = 31{,}6$ and $C_2 = 0{,}0425$. Figure 1 shows that Eq. (29) underestimate the increasement of $U_{mf}(H)$ with bed inventory. In a more recent paper, Tannous et al. [20] have given complementary results of experiments carried out on the same rigs as Thonglimp et al. with glass beads of class D. Tannous et al. have used three methods to measure the minimum fluidization velocity and have confirmed the preceeding conclusions concerning class D solids.

Figure 2 gives an illustration of Eq. (29) with C_1 and C_2 chosen after [16] and for gas and solid characteristics given in Table 1. It can be seen that the greater is the Archimede number (*e.g.*, the greater is the solid size), the greater the effect of the bed inventory on the (complete) minimum fluidization velocity $U_{mf}(0)$. The transition is at $\mathrm{Ar}(H)$ equal to 1000, *i.e.*, a gas-solid system having the following characteristics: diameter of 250 μm, density of 2000 kg/m3, gas is air at normal conditions. In contrast, the same equation Eq. (29) shows that the inventory influences $U_{mf}(H)$ and G_{mf} whatever $\mathrm{Ar}(H)$ is. Figure 2 may explain that the influence of the bed inventory on the minimum fluidization velocity has been observed more frequently for large particles, particularly if the published minimum fluidization velocities are given on the basis of the conditions at the bottom part of the bed.

Does the Minimum Fluidization Velocity Exist? Rodriguez et al. wrote that the notion of minimum fluidization velocity has no precise meaning in the case of wide particle size distribution or of fluidization at reduced pressure because of the progressive transition between the fixed and the fluidized bed [21]: (i) Gauthier et al. recently correlated the spread of the transition between quiescent and fluidized bed regime with the type of the particle size distribution around the mean size [22]; (ii) Kusakabe et al. have proposed some correlations to calculate the location of the boundary between the fixed part of the bed and the fluidized one for Knudsen, viscous and intermediate regimes [15].

There is, nevertheless, an obvious weak point in the minimum fluidization velocity notion for gas-solid systems. As a matter of fact, whatever the solid-gas regime is (fixed bed, beginning, intermediate or complete fluidization), the superficial gas velocity is not constant along the flow direction in the bed in the case of a compressible fluid. For that reason and the former one, the minimum fluidization velocity might be replaced favorably by the complete or minimum fluidization gas mass-flow rate, the smallest gas throughput giving the so-called complete fluidization, which is obviously constant at any cross-section of the bed.

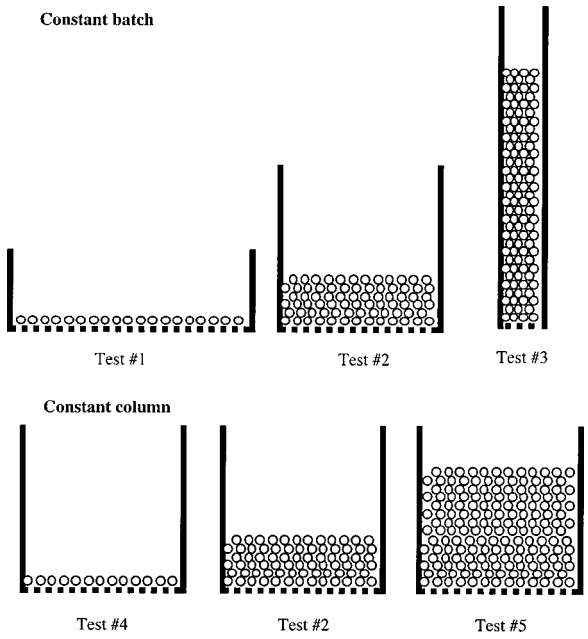

Fig. 3 Two series of three thought experiments for the determination of the minimum fluidization

Does a Batch of Solids Have a Minimum Fluidization? The influence of the mass of the bed inventory on the minimum fluidization conditions can also be transposed to three experiments carried out on a given batch of particles fluidized in three different columns or to three other experiments devoted to the fluidization of three batches of a given powder in a given column (Fig. 3).

The common objective of these two series of three experiments is to measure the minimum fluidization (velocity). In the first three tests, the given batch of particles is fluidized in three columns having three different areas in such a way that the mass of solids per unit area of bed cross-section and the height of the layer are very different from one test to the other. Test no. 1 would correspond to the fluidization of a very thin layer of solids having a height of one to few times the particle diameter. Test no. 2 would be the case of an ordinary operation. Finally, test no. 3 would address a very thick layer of solid particles. In the second set of three tests, the column is constant but the three batches of the given powder change from very small for test no. 4, to relatively large for test no. 5.

As a result, test no. 1 will provide a minimum fluidization velocity that will be nearly the terminal velocity of a single particle because the fluidization corresponds to the drag force by the moving gas that equals the weight of particles, which is also the condition of the free fall velocity of a single particle. Experiments carried out in the operating conditions of test no. 2 will give a minimum fluidization velocity as predicted by usual correlations. If the bed inventory is great enough, test no. 3 will not give any minimum fluidization velocity for the complete batch of solids. As a matter of fact, some particles may be elutriated above the free surface before the bottom layers begin to fluidize because of the difference on gas velocity at free surface compared to the one in the bottom part. As far as the onset of elutriation or entrainment may be considered as roughly characterized by the terminal settling velocity or the transport velocity of the particles, a comparison of the three characteristic velocities of solids (minimum fluidization velocity, terminal settling velocity, transport velocity)

shows that the difference between them is larger for fine particles than for large ones [23]. For instance, it can be calculated that for large particles their three characteristic velocities given in the same order worth, respectively, 1, 9, and 9 [24].

For the same reasons, the second series of three experiments carried out in a given column but with three different quantities of a powder, may yield three different minimum fluidization to the tested powder. The comparison of these results proves that (i) the minimum fluidization does not always exist; (ii) a batch of particles has a fluidization behavior depending on its arrangement in the column; (iii) a batch of particles may fluidize (or not) differently from another batch of similar particles; (iv) the minimum fluidization can not be rigorously considered as a characteristic of a powder. To summarize, a given batch of a powder has no intrinsic minimum fluidization; a given powder has no intrinsic minimum fluidization whatever is the nature of this minimum, velocity or flow-rate.

Conclusions

The conclusions that may be drawn from the present study are the following:

1 A new reading and a further analyze of relationships describing the gas flow through a porous medium yields a new equation to calculate its pressure drop.

2 It is then proved that the onset of fluidization is better characterized by a minimum fluidization gas mass-flow rate G_{mf} rather than a minimum fluidization velocity U_{mf}. This minimum flow rate is a function of the medium and fluid characteristics as for the velocity U_{mf} but, as a consequence of the new equation, it also increases with the bed height. In the case of extremely high beds, the minimum fluidization of a given batch of particles does not exist at all.

3 The minimum fluidization of one batch of particles depends on its arrangement or on the number of particles. As a consequence, when it exists, the onset of fluidization can not be considered as a criterion to characterize a powder.

Acknowledgments

The author would like to thank Professor N. Midoux for the useful discussions and Professor R. Ocone for the encouragment toward the realization of this work. Professor D. Geldart and Professor M. Rhodes have helped to overcome some difficult reviewing by an in-depth reading and their open minded comments in spite of the attack on the sacred cow named ''minimum fluidization velocity.''

Appendix

The gas weight present in the bed per unit of bed area, W_g, can be expressed according to Eq. (*A*1)

$$W_g = \int_0^H g\varepsilon\rho(z)dz \tag{A1}$$

If the bed voidage $\varepsilon(z)$ is constant in the whole bed, thus:

$$W_g = \rho(H)\frac{\varepsilon}{P(H)}\int_0^H P(z)dz \tag{A2}$$

Equation (*A*1) can be integrated using Eq. (14) that yields Eq. (*A*3):

$$W_g = P(H)\frac{H+H_0}{H_0}\varepsilon\lambda^{1/2}\left[z - \arctan h(z)\right]_{(1-\lambda-1/\lambda(H_0/H+H_0)^2)^{1/2}}^{(1/\lambda)^{1/2}} \tag{A3}$$

where λ is defined by Eq. (*A*4):

$$\lambda = (a+bG)\frac{G}{\rho(H)^2 g} + 1 \tag{A4}$$

If the gas weight cannot be neglected in comparison with the solid one, G_{mf} can numerically be found by using Eq. (15) and Eq. (18) together with Eq. (*A*3).

References

[1] Ergun, S., 1952, ''Fluid Flow Through Packed Columns,'' Chem. Eng. Prog., **48**(2), p. 89.
[2] Forchheimer, P. H., 1901, ''Wasserbewegung Durch Boden,'' Z. Ver. Deutsch. Ing., **45**, p. 1781.
[3] Geldart, D., 1986, *Gas Fluidization Technology*, D. Geldart, ed., Wiley, NY.
[4] Bitaud, B., Regnier, M.-C., Picard, M., Delebarre, A., Leclerc, D., Dodds, J., and Thomas, D., 1995, ''Etude du Transport et de la Capture de Fines Particules Dans un Milieu Granulaire: Application à l'injection de Charbon Dans le Haut Fourneau,'' Le Génie des Procédés Complexes, Groupe Français de Génie des Procédés, *Technique et Documentation-Lavoisier, Cachan, France*, **9**(42), p. 177.
[5] MacDonald, I. F., El Sayed, M. S., Mow, K., and Dullien, F. A. L., 1979, ''Flow Through Porous Media-the Ergun Equation Revisited,'' Ind. Engng Chem. Fundam., **18**, p. 199.
[6] Comiti, J., and Renaud, M., 1989, ''A New Model for Determining Mean Structure Parameters of Fixed Beds From Pressure Drop Measurements: Application to Beds Packed With Parallelepipedal Particles,'' Chem. Eng. Sci., **44**, p. 1539.
[7] Laguérie, C., 1988, ''Techniques de Mise en Contact Entre Phases Solides et Gazeuses,'' Traité Génie des Procédés, ed. Techniques de l'Ingénieur, J2 III, A 5850.
[8] Kunii, D., and Levenspiel, O., 1991, *Fluidization Engineering*, Butterworth-Heinemann, eds., Boston.
[9] Sutherland, J. P., 1964, ''The Measurement of Pressure Drop Across a Gas Fluidized Bed,'' Chem. Eng. Sci., **19**, p. 839.
[10] Mathur, K. B., and Epstein, N., 1974, *Spouted Beds*, Academic Press, New York.
[11] Wen, C. Y., and Yu, Y.-H., 1966, ''A Generalized Method for Predicting the Minimum Fluidization Velocity,'' AIChE J., **16**, p. 610.
[12] Jean, R.-H., and Fan, L.-S., 1992, ''On the Model Equations of Gibilaro and Foscolo With Corrected Buoyancy Force,'' Powder Technol., **72**, p. 201.
[13] Molodtsof, Y., 1992, ''Hydrodynamics and Heat Transfer to Vertically Flowing Gas-Solids Suspensions,'' Kona, **10**, p. 41.
[14] Couderc, J.-P., 1985, *Fluidization*, J.-F. Davidson, R. Clift, and D. Harrison, ed., Academic Press, London.
[15] Kusakabe, K., Kuriyama, T., and Morooka, S., 1989, ''Fluidization of Fine Particles at Reduced Pressure,'' Powder Technol., **58**, p. 201.
[16] Grade, J. R., 1982, ''*Fluidized Beds Hydrodynamics*,'' *Handbook of Multiphase Systems*, G. Hestroni, ed, McGraw-Hill, New York.
[17] Cranfield, R. R., and Geldart, D., 1974, Chem. Eng. Sci., **29**, p. 935.
[18] Denloye, A. O., 1982, ''Bed Expansion in a Fluidized Bed of Large Particles,'' J. of Powder and Bulk Tech., **6**(3), p. 11.
[19] Thonglimp, V., Hiquily, N., and Laguérie, C., 1984, ''Vitesse Minimale de Fluidisation et Expansion Des Couches Fluidisées par un gaz,'' Powder Technol., **38**, p. 233.
[20] Tannous, K., Hemati, M., and Laguérie, C., 1994, ''Caractéristiques de Fluidisation et Expansion des Couches Fluidisées de Particules de la Catégorie D de Geldart,'' Powder Technol., **80**, p. 55.
[21] Rodriguez, R., Caussat, B., Hémati, M., and Couderc, J.-P., 1997, ''Etude Hydrodynamique des Lits Fluidisés Sous vide et Sous Haute Température en vue de Réaliser des Dépôts CVD,'' Proceedings du 2d Congrès Européen sur la Fluidisation, M. Olazar et M. J. San José, eds., Universidad del Pais Vasco, Bilbao, Espagne, p. 445.
[22] Gauthier, D., Zerguerras, S., and Flamant, G., 1999, ''Influence of the Particle Size Distribution of Powders on the Velocities of Minimum and Complete Fluidization,'' Chem. Eng. J., **74**(3), p. 181.
[23] Delebarre A., 1997, ''Acquis et Lacunes d'une Innovation: le cas des Lits Fluidisés,'' Mémoire d'Habilitation à Diriger des Recherches, Institut National Polytechnique de Lorraine.
[24] Delebarre, A., 1997, ''De la Particule à la Poudre,'' Première Rencontre Autour des états Dispersés.

N. Berchiche
Department of Naval Architecture
and Ocean Engineering,
SE-412 96 Göteborg, Sweden
e-mail: bena@na.chalmers.se

J. P. Franc
e-mail: Jean-Pierre.Franc@hmg.inpg.fr

J. M. Michel
e-mail: Jean-Marie.Michel@hmg.inpg.fr

Laboratoire des Ecoulements
Géophysiques et Industriels,
BP 53, 38041 GRENBOLE Cedex 9, France

A Cavitation Erosion Model for Ductile Materials

An analytical model is proposed for the prediction of cavitation erosion of ductile materials. It is based upon a physical analysis of the work-hardening process due to the successive bubble collapses. The material is characterized by its classical stress-strain relationship and its metallurgical behavior is analyzed from microhardness measurements on cross sections of eroded samples. The flow aggressiveness is determined from pitting tests, using the material properties to go back to the impact loads. The histogram of impact loads is applied numerically a large number of times on the material surface and the evolution of the mass loss with the exposure time is computed. The approach is supported by experimental tests. [DOI: 10.1115/1.1486474]

1 Introduction

A lot of work has been done in the field of cavitation erosion. Roughly speaking, the techniques of prediction of cavitation erosion can be classified into three main categories:

- empirical correlations with material properties or with electrochemical or noise measurements
- simulation techniques using special test devices to reproduce a given aggressiveness in an accelerated way
- analytical methods.

Detailed information on the two first categories of techniques can be found in review papers such as Hammitt [1] Karimi and Martin [2], Franc and Michel [3]. The present paper is especially devoted to analytical techniques whose objective is to predict cavitation erosion without model tests or at least with a limited request to experiments as firstly imagined by Kato et al. [4]. Such techniques are still in development and represent a real challenge to research workers in cavitation erosion for the next years. They require extensive research efforts and, therefore, it is not surprising that the first attempts, including the present work, do not lead to models fully operational and satisfactory. However, such a new research direction is worthwhile being explored, in our opinion, as it might open a new field of techniques of prediction of cavitation erosion.

The present paper is a contribution to this subject. It presents a model of prediction of the erosion damage applicable to ductile materials only. Other limitations of the model will be pointed out along the presentation. The originality of this work lies in the fact that the proposed model is fully predictive and involves no parameters to be adjusted on the basis of experimental data. It is based upon the original work of Karimi and Leo [5]. Contrary to Karimi and Leo in which each pit is treated as a whole, the present approach is much more local. A regular mesh, with a characteristic size of the order of a few micrometers only, is defined on the material surface, so that each pit is described by a significant number of cells. This technique allows to compute, with a space resolution which can be refined as much as required, the strain field on the material surface and inside, from which the erosion rate is deduced. The main input is the surface distribution of impact loads which is determined from pitting tests.

The characteristic of a ductile material exposed to cavitation is to be progressively hardened by the successive collapses. The work-hardening process is here characterized by the thickness of the hardened layers together with the shape of the strain profile inside the material.

The first step of the proposed model consists in the quantification of the hydrodynamic aggressiveness of the cavitating flow. This is done from classical pitting tests, each pit being characterized by its diameter and its depth. The surface distribution of the impact load responsible for each pit is deduced from this couple of data, using the strain profile and the stress-strain relationship of the material. The flow aggressiveness is finally characterized by a distribution of impact loads.

In a second step, this distribution derived from short duration tests is numerically applied a large number of times on the material surface. The present model computes the mass-loss as a function of the exposure time. To support this approach, a few pitting and mass loss tests were conducted on an experimental device which produces cavitation erosion from the collapse of a cavitating vortex (Dominguez-Cortazar et al. [6] Filali and Michel [7], Filali et al. [8]).

2 Presentation of the Model

The principle of the model is presented in the simplified case of a perfectly reproducible impact (Fig. 1). Let us consider a given point of the material surface on which a stress σ_1 is applied due to a bubble collapse. The material is initially supposed to be virgin, i.e., the strain is zero everywhere, on the surface and inside the material. If σ_1 is lower than the elastic limit σ_e, the material is supposed to return to its original state after unloading. Hence the impact loads below the elastic limit have no effect. In particular, fatigue mechanisms are not taken into account. Thus, the present model is applicable to sufficiently aggressive flows, which present a substantial number of impacts beyond the elastic limit.

After the first impact, the strain on the surface of the material has become ε_1, which is deduced from the stress-strain relationship of the material (Eq. (6)). The distribution of strain inside the material is supposed to be given, for $x \leqslant l$, by the following empirical relation (Fig. 1):

$$\varepsilon(x) = \varepsilon_s \left(1 - \frac{x}{l}\right)^{\theta} \tag{1}$$

where ε_s is the surface strain at the point of impact, l the depth of the hardened layer, θ the shape factor of the strain profile and $\varepsilon(x)$ the strain at the distance x from the surface. After the first impact, we have $\varepsilon_s = \varepsilon_1$ and $l = l_1$. The energy absorbed by the material is the shaded area.

A second collapse of exactly the same amplitude σ_1 is supposed to occur at exactly the same point. The surface strain will be increased up to a certain value ε_2, which is determined from the

Contributed by the Fluids Engineering Division for publication in the JOURNAL OF FLUIDS ENGINEERING. Manuscript received by the Fluids Engineering Division June 12, 2001; revised manuscript received February 18, 2002. Associate Editor: J. Katz.

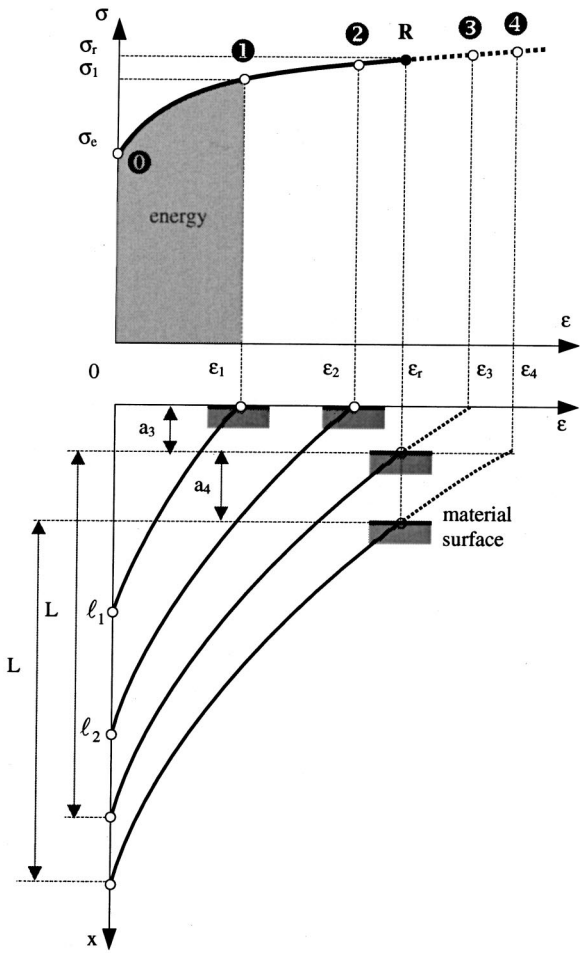

Fig. 1 Principle of the model. The stress-strain relationship, together with the strain profiles inside the material are presented as a function of the exposure time.

conservation of the impact energy. We suppose that the same energy (indicated by the shaded area on Fig. 1) is absorbed by the material, but this time, the material is no longer virgin. The conservation of the impact energy consists in writing that the area under the $\sigma(\varepsilon)$ curve between points ❶ and ❷ is the same as the one between points ❼ and ❶. This condition determines the surface strain ε_2. The strain profile is still given by Eq. (1) with $\varepsilon_s = \varepsilon_2$ and a greater depth $l = l_2$ of the hardened layer which will be determined later, from Eq. (4)

Suppose that a third, still identical, impact is applied. In the particular case of Fig. 1, the conservation of energy leads to a surface strain beyond rupture denoted by *R*. In this case, the $\sigma(\varepsilon)$ curve is extrapolated to get the virtual surface strain ε_3. The strain profile is still given by Eq. (1). As the material cannot withstand a strain greater than its rupture strain, it is supposed that the thickness a_3 is removed, which corresponds to the domain in which ε is greater than ε_r. It can easily be shown that the thickness of the eroded layer is given by:

$$a = L\left[\left(\frac{\varepsilon_s}{\varepsilon_r}\right)^{1/\theta} - 1\right] \tag{2}$$

ε_s is the virtual surface strain (greater than ε_r) and L the maximum thickness of the hardened layer, corresponding to the rupture strain ε_r.

If a fourth identical impact is applied, the surface strain is increased from ε_r to ε_4. The virtual strain ε_4 is still determined by the conservation of energy, the area below the $\sigma(\varepsilon)$ curve between points R and ❹ being equal to the original impact energy (shaded area). The thickness of the eroded layer is still given by Eq. (2).

As soon as the surface strain has reached the rupture strain ε_r, hardening is maximum. The strain profile inside the material remains unchanged and given by:

$$\varepsilon(x) = \varepsilon_r\left(1 - \frac{x}{L}\right)^{\theta} \tag{3}$$

L appears as the maximum thickness of the hardened layer. For partial hardening, leading to a surface strain $\varepsilon_s < \varepsilon_r$, it can easily be shown that the thickness *l* of the hardened layer is smaller than *L* and given by:

$$l = L\left(\frac{\varepsilon_s}{\varepsilon_r}\right)^{1/\theta} \tag{4}$$

This equation results from the assumption that the strain profile for partial hardening (Eq. (1)) corresponds to a truncated part of the complete profile described by Eq. (3).

Above, we have examined in detail the simplified case of a perfectly reproducible impact. The principle of the method remains applicable to the more general case of variable loading occurring in the real process of cavitation erosion. The main difference is that the energy absorbed by the material does not remain constant and has to be evaluated for each impact. However, the method is still based upon the principle of energy conservation.

Another difference with respect to the above simplified presentation lies in the evaluation of the energy. In the computation, the energy is not limited to the one absorbed by the surface of the material (as we could believe from Fig. 1), but it corresponds to the total energy actually absorbed by all the hardened layers inside the material. The energy absorbed by the material per unit surface area between an initial virgin state and a state characterized by the strain profile given by Eq. (1) can be calculated as follows:

$$W = \int_0^{l_1}\left[\int_0^{\varepsilon}\sigma d\varepsilon\right]dx = \frac{\sigma_e \varepsilon_1 l_1}{\theta+1} + \frac{K\varepsilon_1^{n+1} l_1}{(n+1)(n\theta+\theta+1)} \tag{5}$$

The quantities σ_e, *K*, and *n* are characteristics of the stress-strain relationship and are defined in Eq. (6).

The model is purely one-dimensional. It is supposed that there is no interaction between two neighboring points situated on the material surface or at the same distance from it. The limitations of this assumption are not yet fully understood. In the following computations, a regular surface mesh of 440×440 points is defined on the material surface. The distance between two consecutive points was chosen equal to 5 μm. This value appeared to be a good compromise between the accuracy of the computation and the CPU time. In particular, the mesh size must be small enough to allow a good description of the smallest pits. In the present case, the pits with a diameter smaller than 20μm where not considered. Hence, the smallest pits are defined by a mesh of about 5×5 points.

In conclusion, the present model consists in computing, at each time step, the distribution of strain limited to the material surface, from which all other data can be deduced, including mass-loss and strain field inside the material.

3 Material Characteristics

Two series of tests are used to characterize the material. The first one is the classical tensile test which allows to determine the stress-strain relationship. For ductile materials, it is correctly represented by a Ludwig type equation:

$$\sigma = \sigma_e + K\varepsilon^n \tag{6}$$

Because of the high value of the rupture strain for ductile materials, the elastic part of the curve can be considered as almost vertical and the elastic energy can be neglected. In the case of stain-

less steel 316L considered here, we obtained: $\sigma_e = 400$ MPa, $\sigma_r = 1020$ MPa, $n = 0.5$ and K = 900 MPa. The rupture strain is $\varepsilon_r \equiv 47\%$.

It has to be emphasized that these data were obtained from classical quasi-steady tests, with a very small strain rate of the order of 10^{-4} s^{-1}. They are used here without any modification for the analysis of cavitation erosion which is known to be characterized by an incomparable higher strain rate of the order of $10^4 - 10^5$ s^{-1}. The influence of the strain rate is difficult to take into account. A possible approach could consist in artificially increasing the elastic and rupture limits of the material, but this was not done in the present work due to the lack of data.

The two main metallurgical parameters introduced in the model, the maximum depth of the hardened layer L and the shape factor of the strain profile θ are determined from micro-hardness measurements on cross-sections of an eroded target. We obtained the following values $L = 200$ μm and $\theta = 5.0$.

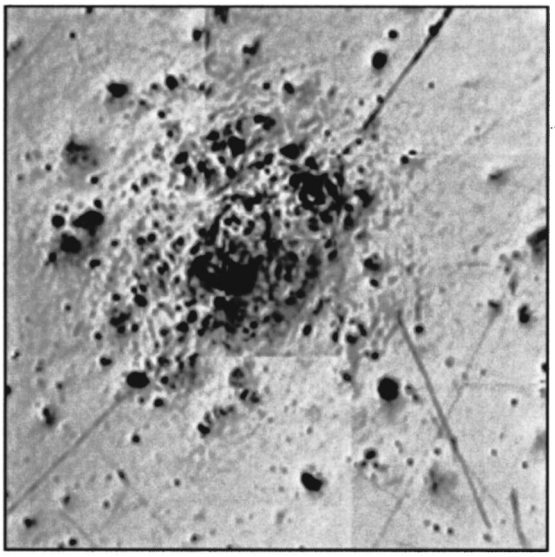

(*a*)

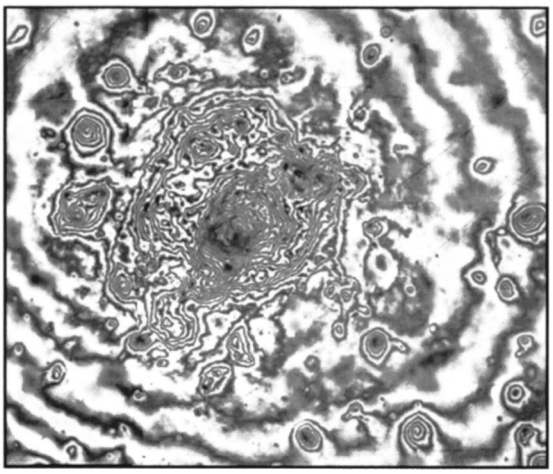

(*b*)

Fig. 2 Photograph of the impacted zone on Stainless Steel 316 after a pitting test of 30 shots on the Cavermod. (*a*) Nomarski interferometric technique; (*b*) Mirau interferometric technique (100 μm corresponds to 0.8 cm and 0.6 cm, respectively).

4 Pitting Tests

Two pitting tests have been carried out on stainless steel 316L after 30 shots of the experimental device. The number of shots was selected to get a large enough number of pits without significant overlapping. Figure 2 presents two photographs of the same eroded surface with two different observation techniques. Figure 2(*b*) is obtained on a metallurgical microscope using a Mirau interferometric technique (Belahadji et al. [9]). The main advantage

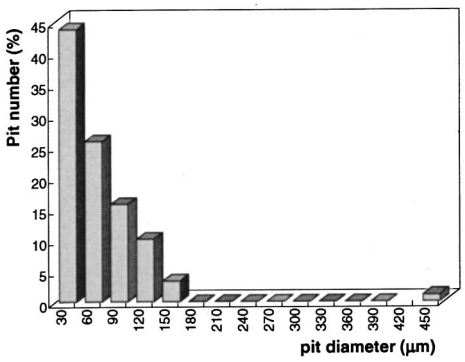

(*a*)

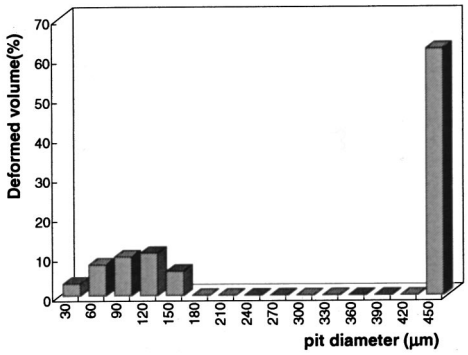

(*b*)

Fig. 3 Histograms of pit number (*a*) and deformed volume (*b*) corresponding to the pitting test presented in Fig. 2. The deformed volume is defined as the volume of the pits below the original surface.

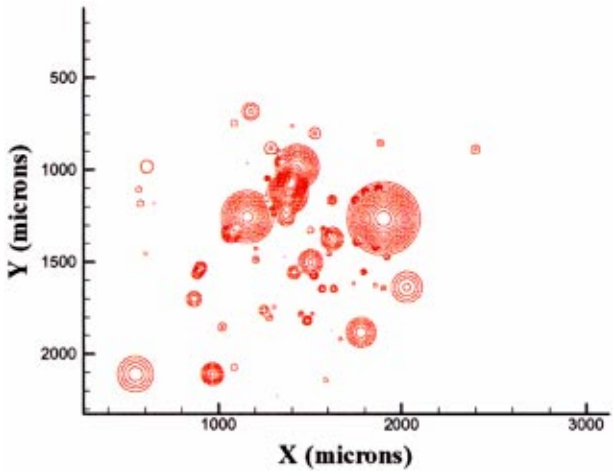

Fig. 4 Pitting test reproduced by the model. The difference in height between two consecutive curves is .46 μm

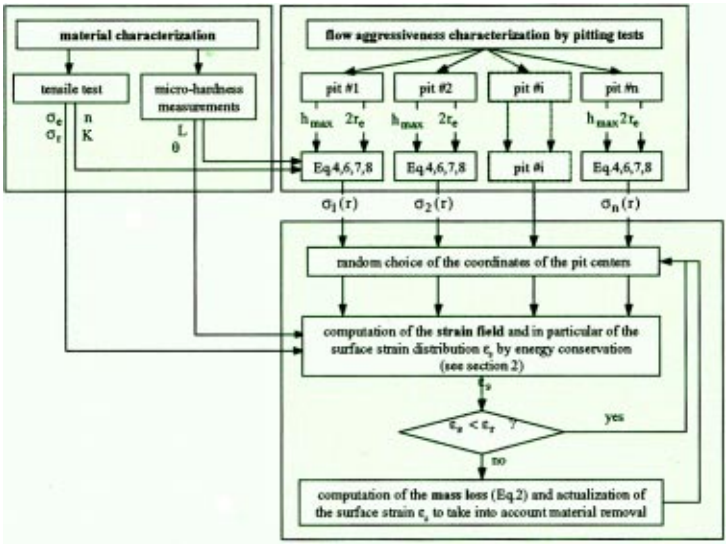

Fig. 5 Step-by-step description of the entire predicting process

of this technique is to allow the estimation of the depth of each pit as the distance between two black fringes corresponds to half a wavelength (0.273 μm).

A large pit is observed in the center, surrounded by smaller pits distributed randomly on the impacted zone. The diameter of this zone is approximately 1000 μm. It depends on the size of the cavitating vortex and the resistance of the material (Filali and Michel [7]).

The analysis of a pitting test consists in determining, for each pit, the coordinates of its center, its maximum depth and its diameter ($2r_e$). The deformed volume is here estimated assuming a simplified conical shape for each pit. This assumption, which consists in supposing that the fringes in Fig. 2(*b*) are circular and equidistant, proved to be a reasonable approximation. More accurate techniques for the determination of the complete 3D-shape of the pits have been developed (see e.g., Belahadji et al. [9]) but were not available for this work.

Figure 3(*a*) shows the histogram of pits number versus the pit diameter, resulting from the analysis of the photograph of Fig. 2. Although the number of small pits is very large, they have a relatively small contribution to the deformed volume, which results mainly from the larger pit as shown on Fig. 3(*b*).

The aggressiveness of the cavitating flow in terms of applied stresses is deduced from the analysis of the pits produced on the material surface during the early stage of erosion. Let us consider a pit of maximum depth $h_{\max}$. By integration of the strain profile (Eq. (1)), we obtain the following relation between pit depth and surface strain ε_s:

$$h_{\max} = \int_0^l \varepsilon(x).dx = \frac{l\varepsilon_s}{\theta+1} \tag{7}$$

The measurement of pit depth allows to determine the surface strain, and as a result, the original stress $\sigma_{\max}$ by the use of the stress-strain relationship (Eq. (6)).

Once the maximum load at the center of the pit is known, the radial distribution is determined by assuming that it follows a gaussian law:

$$\sigma = \sigma_{\max}\left[\frac{\sigma_{\max}}{\sigma_e}\right]^{-r^2/r_e^2} \tag{8}$$

where r_e is the measured pit radius. This assumption would not be necessary in case of a complete 3D measurement of the pit shape. The Mirau interferometric technique is considered to give a good estimate of the size of the plastic zone. This equation takes into account that the stress is equal to the elastic limit σ_e at the limit $r=r_e$ of the plastic zone.

By considering all the pits which were identified on Fig. 2(*b*) it is possible to go back to the distribution of stresses. The reproduction of this distribution by the numerical model allows to reconstruct the image of the surface after the pitting test. Figure 4 presents the results of the "numerical" pitting test. Each pit in Figs. 2(*a*) and 2(*b*) can be identified in Fig. 4. The main difference is the perfectly circular shape of each pit in the model.

5 Computation of the Erosion Rate and Comparison With Experiment

Once the distribution of impact loads resulting from a reference pitting test is determined, it is applied randomly over the exposed area a large number of times until mass loss occurs. For each pit, only the coordinates of its center are chosen randomly, whereas the impact load and the pit diameter are kept unchanged. A step-by-step description of the entire prediction process is given in Fig. 5. Results of the prediction are presented in Figs. 6, 7, and 8. Let us notice that the number of shots is here equivalent to a classical exposure time as encountered in the case of continuous cavitation.

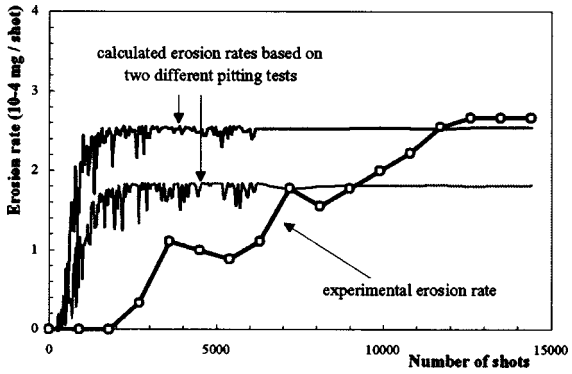

Fig. 6 Calculated and measured erosion rates versus the number of shots (stainless steel 316L). The two calculated erosion rates are based upon two different pitting tests used to characterize the flow aggressiveness.

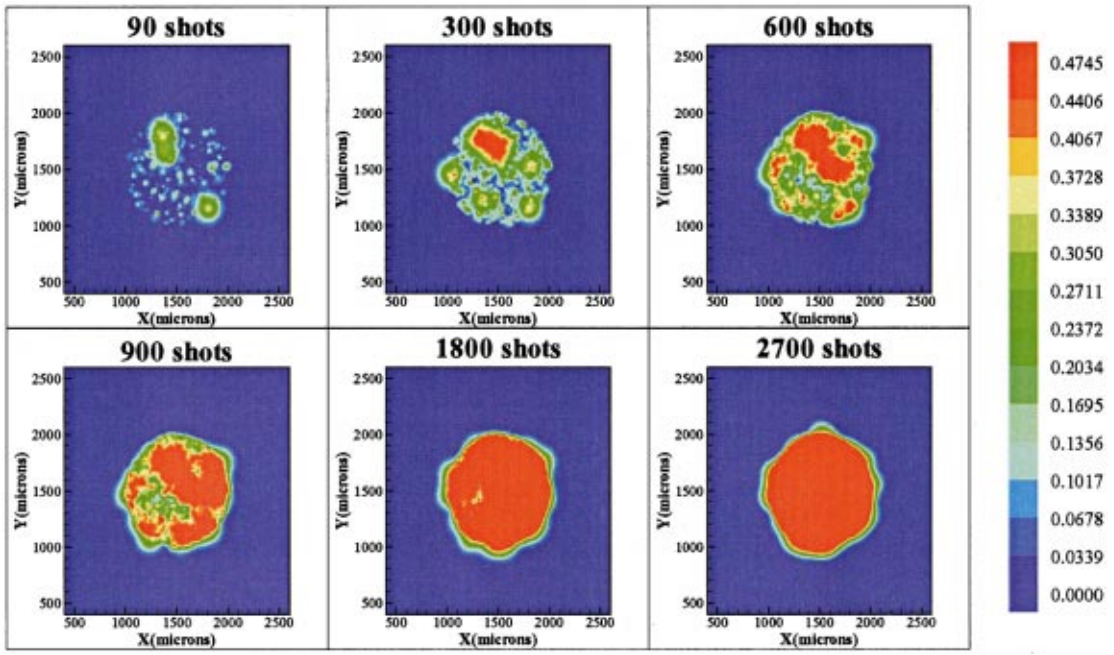

Fig. 7 Computed evolution of the strain on the surface of the material (stainless steel 316L). The blue color corresponds to zero strain, whereas the red color corresponds to the rupture strain in %.

Figure 6 presents the two calculated erosion rates obtained from two different pitting tests. Three main stages are predicted in the erosion process: incubation, acceleration and steady state erosion. The mass-loss fluctuations are important during the period of acceleration and vanish in the steady state. This effect is typical of a random distribution of impacts loads. In the case of a repetitive single impact, these fluctuations do not exist (Berchiche [10]). They are due to the fact that the same impact can lead to a very different mass loss according to the degree of hardening. Mass loss is minimum if the impact falls on a virgin surface and maximum if hardening is completed.

Although the pitting tests were carried out under the same experimental conditions, we observe a variation of 30% between the two calculated erosion rates (Fig. 6). Hence, the accuracy of the long-term prediction depends strongly upon the pitting test from which the flow aggressiveness is characterized. In order to limit the sensitivity of the prediction to the pitting test, we suggest to use several pitting tests for the determination of the cavitating flow aggressiveness. This observation is not surprising in so far as pit size and pit load were kept constant throughout the modeling procedure. It could be envisaged to use a more complicated model, by considering statistical laws for the distribution of size

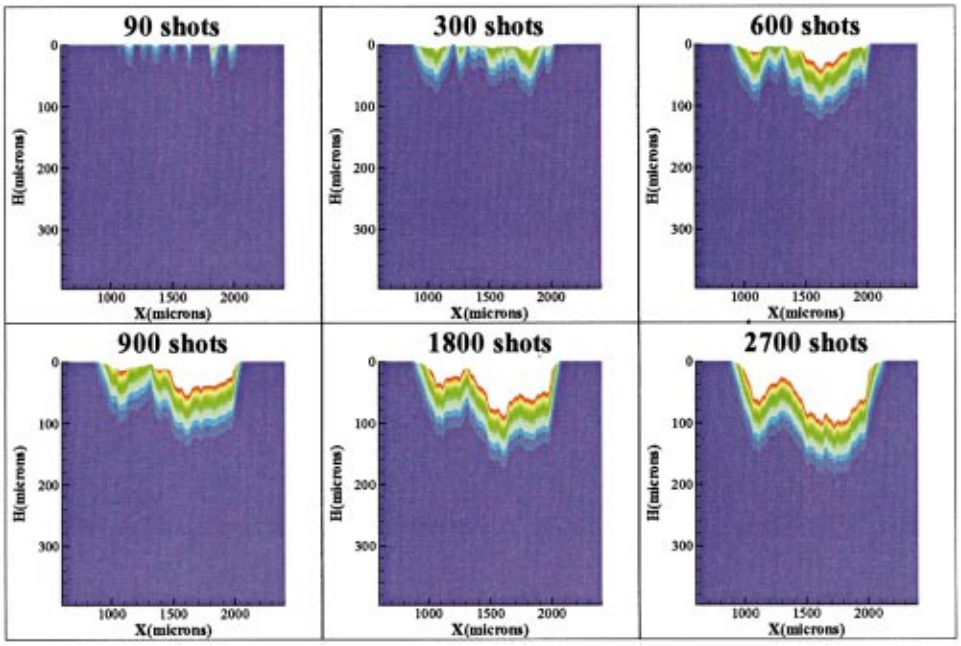

Fig. 8 Computed evolution of the strain field on a cross section of the material and of the shape of the eroded surface

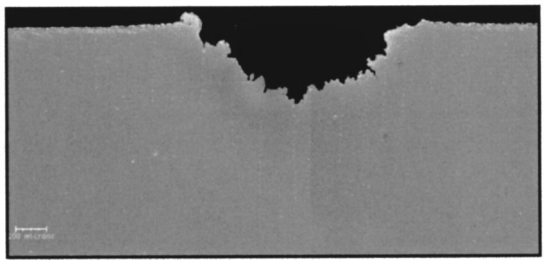

Fig. 9 Cross-section of an eroded sample after 14400 shots (SS316L). The marks for microhardness measurements are hardly visible.

and amplitude of the impact loads. However, such an approach would require a further analysis to determine precisely these laws and know if they can be considered as independent ones or not.

The evolution of the surface strain as a function of the number of shots is given in Fig. 7. During the acceleration period, the fraction of the surface which is fully hardened (in red) progressively increases. When the whole exposed area is hardened, the erosion rate becomes constant: it is the steady state period.

Figure 8 presents the predicted evolution of strain on a cross section, together with the evolution of the shape of the material surface. During the incubation period, the pit depth results only of plastic deformation. Once the rupture strain is reached on the surface, mass loss occurs.

In order to validate the proposed model, mass loss tests have been carried out on stainless steel 316L in the same experimental conditions than those which were chosen for the determination of hydrodynamic solicitations (Fig. 9). The sample was weighted after each series of 900 shots. The calculated and experimental erosion rates are compared in Fig. 6.

The order of magnitude of the predicted erosion rate in the final steady stage of erosion appears to be in reasonable agreement with the experiment, whereas the duration of the incubation period is significantly underestimated. Concerning the total mass loss after 14400 shots, the experimental value is 2.2 mg whereas the two cumulative mass losses predicted by the model using the two different pitting tests are 2.4 and 3.4 mg. Once more, the order of magnitude of the computed mass loss is consistent with experiments. It is clear that further comparisons to experiments are required for the improvement and the validation of the model. However, the present results are considered as satisfactory in so far as the whole model is fully predictive. It does not involve any adjustable parameter. All the data required for the prediction are determined in a unique way from the material parameters which, in their turn, are determined from classical mechanical or metallurgical tests.

Finally, let us mention that the sensitivity of the prediction to the metallurgical and mechanical parameters of the material was studied. A material characterized by a large value of the shape factor and a small thickness of the hardened layer is more resistant to cavitation erosion. In addition, the duration of the incubation period is independent of the thickness of the hardened layer, but decreases when the shape factor increases.

6 Perspectives

Although the present model is fully predictive, we must be aware that several assumptions or shortcuts were necessary to complete the modelling. Among the most critical ones, we can mention the influence of the strain rate which was ignored. In addition, the material was characterized from tensile tests whereas the actual solicitation in cavitation erosion is a compression. The consequences of the one-dimensional nature of the model are also difficult to estimate.

In the future, it would be interesting to link this kind of model to a classical computation of the cavitating flow. Such a tool would allow a prediction of cavitation erosion based only on the flow geometry, the operating hydrodynamic conditions (pressure and flow velocity) and the mechanical and metallurgical properties of the material. The main steps would be the following.

1 The cavitating flow is computed using a Navier-Stokes solver completed by a cavitation model. Bubble models (see e.g., Kubota et al. [11]) are probably the most suitable for a further prediction of cavitation erosion.

2 The hydrodynamic aggressiveness is deduced from the former computation. In the cavitation model of Kubota et al. for example, the evolution of the bubble radius is determined from the resolution of a Rayleigh-Plesset equation. As a consequence, for each bubble, the interface velocity during the phase of collapse is computed. It can be considered as the key parameter for the estimation of the aggressiveness of the collapsing bubble. Although this procedure has still to be cleared up, it seems physically realistic.

3 The last step consists in modelling the material response and computing the erosion rate using a model as the one presented in this work.

Nomenclature

a = thickness of the eroded layer
K = constant in the stress-strain relationship (Eq. (6))
l, L = depth of hardened layers
n = exponent in the stress-strain relationship (Eq. (6))
r = radius
x = distance from the surface
ε = strain
σ = stress
θ = metallurgical shape factor (Eq. (1))

Subscripts

e = elastic
r = rupture
s = surface

References

[1] Hammitt, F. G., 1979, ''Cavitation Erosion: The State of The Art And Predicting Capability,'' Appl. Mech. Rev., **32**(6), pp. 665–675.
[2] Karimi, A., and Martin, J. L., 1986, ''Cavitation Erosion of Materials,'' Int. Met. Rev., **31**(1), pp. 1–26.
[3] Franc, J. P., and Michel, J. M., 1997, ''Cavitation Erosion Research in France: The State of The Art,'' Journal of Marine Science and Technology, **2**, pp. 233–244.
[4] Kato, H., Konno, A., Maeda, M., and Yamaguchi, H., 1995, ''Possibility of Quantitative Prediction of Cavitation Erosion Without Model Test,'' ASME J. Fluids Eng., **118**, pp. 582–588.
[5] Karimi, A., and Leo, W. R., 1987, ''Phenomenological Model for Cavitation Rate Computation,'' Mater. Sci. Eng., **95**, pp. 1–14.
[6] Dominguez-Cortazar, M., Franc, J. P., and Michel, J. M., 1997, ''The Erosive Axial Collapse of a Cavitating Vortex: An Experimental Study,'' ASME J. Fluids Eng., **119**(3), pp. 686–691.
[7] Filali, E. G., and Michel, J. M., 1999, ''The Cavermod Device: Hydrodynamic Aspects And Erosion Tests,'' ASME J. Fluids Eng., **121**, pp. 305–311.
[8] Filali, E. G., Michel, J. M., Hattori, S., and Fujikawa, S., 1999, ''The Cavermod Device: Force Measurements,'' ASME J. Fluids Eng., **121**, pp. 312–317.
[9] Belahadji, B., Franc, J. P., and Michel, J. M., 1991, ''A Statistical Analysis of Cavitation Erosion Pits,'' ASME J. Fluids Eng., **113**, pp. 700–706.
[10] Berchiche, N., 2000, ''Erosion De Cavitation d'un Métal Ductile: Étude Expérimentale Et Modélisation,'' PhD thesis Institut National Polytechnique de Grenoble (in French).
[11] Kubota, A., Kato, H., and Yamaguchi, H., 1992, ''A New Modelling of Cavitating Flows: A Numerical Study of Unsteady Cavitation on a Hydrofoil Section,'' J. Fluid Mech., **240**, pp. 59–96.

Jules W. Lindau
Robert F. Kunz
David A. Boger
David R. Stinebring
Howard J. Gibeling

Penn State Applied Research Laboratory,
University Park,
PA 16802

High Reynolds Number, Unsteady, Multiphase CFD Modeling of Cavitating Flows

A preconditioned, homogeneous, multiphase, Reynolds Averaged Navier-Stokes model with mass transfer is presented. The model is preconditioned in order to obtain good convergence and accuracy regardless of phasic density ratio or flow velocity. Engineering relevant validative unsteady two and three-dimensional results are given. A demonstrative three-dimensional, three-field (liquid, vapor, noncondensable gas) transient is also presented. In modeling axisymmetric cavitators at zero angle-of-attack with 3-D unsteady RANS, significant asymmetric flow features are obtained. In comparison with axisymmetric unsteady RANS, capture of these features leads to improved agreement with experimental data. [DOI: 10.1115/1.1487360]

Introduction

The ability to properly model multiphase flows has significant potential engineering benefit. In particular, sheet cavitation may occur in flow over submerged high speed vehicles as well as pumps, propellers, nozzles, and numerous other venues. Traditionally, cavitation has had negative implications associated with damage and/or noise. However, for high speed submerged vehicles, the reduction in drag associated with a natural or ventilated supercavity has great potential benefit. Cavitation modeling remains a difficult task, and only recently have full three-dimensional, multi-phase, Reynolds-Averaged, Navier-Stokes (RANS) tools reached the level of utility that they might be applied for engineering purposes.

The computational tool applied here, UNCLE-M, represents the state-of-the-art in CFD analysis of cavitation. UNCLE-M contains appropriate physics to properly model flow fields dominated by attached cavities. These cavities are presumed to be amenable to a homogeneous approach, are generally unsteady, and contain regions of phase separated flow. In flows modeled here, interface curvatures are small, and pressure and velocity are approximately continuous across the interface. Thus, it is presumed that nonequilibrium interface dynamics are of negligible magnitude, and the effect of surface tension is not incorporated.

Previously, Kunz et al. [1] have developed and demonstrated the capabilities of UNCLE-M. Here, UNCLE-M is applied to several engineering relevant configurations. These configurations represent experimentally documented test cases. Model results are presented, and both steady (averaged) and unsteady behavior of the flow is compared with experiments. In addition, interesting unsteady numerical results are presented in a field form for comparison with photographic data. Some intriguing results due to the fundamentally three-dimensional nature of turbulent multiphase flow will be discussed. This will serve to further demonstrate and validate the capabilities of the multiphase RANS model.

Physical Model

The physical model equations solved here have been described previously [1]. The basis of the model is the incompressible multiphase Reynolds Averaged Navier Stokes Equations in a homogeneous form. Each field is treated as a separate species and requires the inclusion of a new continuity equation. A liquid, a vapor, and a noncondensable gas phase are modeled. Mass transfer between the liquid and vapor phases is achieved through a finite-rate model. Other researchers have applied similar models with a single species approach. However, with the ability to easily include more than one or two fields in a single control volume and discretely model mass transfer, the multiple species model of multiphase flow is presented as a more flexible physical approach. A high Reynolds number form of two-equation models with standard wall functions provides turbulence closure.

The governing differential equations, cast in Cartesian tensor form are given as Eq. (1):

$$\left(\frac{1}{\rho_m\beta^2}\right)\frac{\partial p}{\partial \tau}+\frac{\partial u_j}{\partial x_j}=(\dot{m}^+ +\dot{m}^-)$$

$$\left(\frac{1}{\rho_l}-\frac{1}{\rho_v}\right)\frac{\partial(\rho_m u_i)}{\partial \tau}+\frac{\partial(\rho_m u_i)}{\partial t}+\frac{\partial(\rho_m u_i u_j)}{\partial x_j}$$

$$=-\frac{\partial p}{\partial x_i}+\frac{\partial((\mu_{m,t}+\mu_m)t_{ij})}{\partial x_j}$$

$$\left(\frac{\alpha_l}{\rho_m\beta^2}\right)\frac{\partial p}{\partial \tau}+\frac{\partial \alpha_l}{\partial \tau}+\frac{\partial \alpha_l}{\partial t}+\frac{\partial(\alpha_l u_j)}{\partial x_j}=\left(\frac{\dot{m}^+}{\rho_1}+\frac{\dot{m}^-}{\rho_v}\right)$$

$$\left(\frac{\alpha_{ng}}{\rho_m\beta^2}\right)\frac{\partial p}{\partial \tau}+\frac{\partial \alpha_{ng}}{\partial \tau}+\frac{\partial \alpha_{ng}}{\partial t}+\frac{\partial(\alpha_{ng} u_j)}{\partial x_j}=0$$

$$t_{ij}=\frac{\partial u_i}{\partial x_j}+\frac{\partial u_j}{\partial x_i} \tag{1}$$

where mixture density and viscosity have been defined in Eq. (2).

$$\rho_m=\rho_1\alpha_l+\rho_v\alpha_v+\rho_{ng}\alpha_{ng}$$

$$\mu_m=\mu_l\alpha_l+\mu_v\alpha_v+\mu_{ng}\alpha_{ng}$$

$$\mu_{m,l}=\frac{\rho_m C_\mu k^2}{\varepsilon} \tag{2}$$

In the present work, the density and molecular viscosity of each constituent is taken as constant. Equation (1) represents the conservation of mixture volume, mixture momentum, liquid phase volume fraction and non-condensable gas volume fraction, respectively. Physical time derivatives are included for unsteady computations. The formulation incorporates preconditioned *pseudo*-time-derivatives ($\partial/\partial\tau$ terms), scaled by parameter β, which provide favorable convergence characteristics for steady-state and unsteady computations, as discussed in the following.

Two separate models are used to describe the transformation of liquid to vapor and the transformation of vapor back to liquid.

Contributed by the Fluids Engineering Division for publication in the JOURNAL OF FLUIDS ENGINEERING. Manuscript received by the Fluids Engineering Division August 11, 2000; revised manuscript received March 4, 2002. Associate Editor: J. Katz.

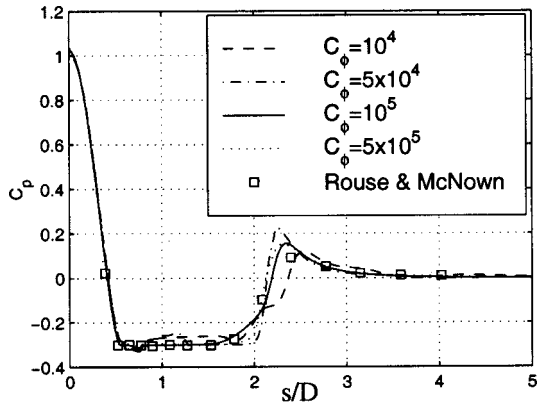

Fig. 1 Comparison of effect of rate constants (Eq. 3) and experimental data [6] for naturally cavitating flow over a hemispherical head and cylindrical afterbody. Steady-state results.

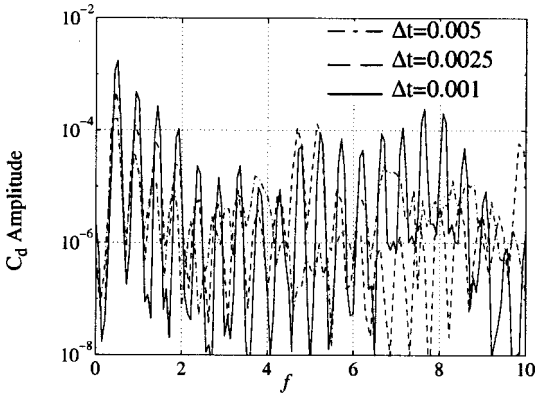

Fig. 2 Spectral comparison of effect of physical integration time step size on C_d history. UNCLE-M result. Flow over a hemispherical forebody with cylindrical afterbody. $Re_D=1.36\times10^5$. $\sigma=0.3$.

These are given in Eq. (3). For transformation of liquid to vapor, $\dot{m}^-$ is modeled as being proportional to the product of the liquid volume fraction and the difference between the computational cell pressure and the vapor pressure. This model is similar to the one used by Merkle et al. [2] for both evaporation and condensation. For transformation of vapor to liquid, a simplified form of the Ginzburg-Landau potential [3] is used for the mass transfer rate, $\dot{m}^+$.

$$\dot{m}^- = \frac{C_\phi \rho_v \alpha_l MIN[0, p-p_v]}{\frac{1}{2} p_l U_\infty^2 t_\infty}$$

$$\dot{m}^+ = \frac{C_\phi \rho_v (\alpha_l - \alpha_{ng})^2 (1-\alpha_l)}{(500) t_\infty} \tag{3}$$

C_ϕ is an empirical constant. Both mass transfer rates are nondimensionalized with respect to a mean flow time scale. For all work presented here, $t_\infty=1$ and $C_\phi=10^5$. These values were arrived at by an investigation of average attached cavity lengths over ogives and comparison with experimental results of Rouse and McNown [4]. A demonstration of the comparison and sensitivity to the values of the constants are given in Fig. 1.

A two-equation turbulence model with standard wall functions has been implemented to provide closure. The k-ε model is represented in Eq. (4). As with velocity, the turbulence scalars are interpreted as being mixture quantities.

$$\frac{\partial(\rho_m k)}{\partial t} + \frac{\partial(\rho_m k u_j)}{\partial x_j} = \frac{\partial}{\partial x_j}\left(\frac{\mu_{m,t}}{\mathrm{Pr}_{tk}} \frac{\partial k}{\partial x_j}\right) + P - \rho_m \varepsilon$$

$$\frac{\partial(\rho_m \varepsilon)}{\partial t} + \frac{\partial(\rho_m \varepsilon u_j)}{\partial x_j} = \frac{\partial}{\partial x_j}\left(\frac{\mu_{m,t}}{\mathrm{Pr}_{l\varepsilon}} \frac{\partial \varepsilon}{\partial x_j}\right) + [C_1 P - C_2 \rho_m \varepsilon]\left(\frac{\varepsilon}{k}\right) \tag{4}$$

Numerical Method

The described model equations are solved in the UNCLE-M code. This code has its origins as the UNCLE code, developed for incompressible flows at Mississippi State University (Taylor et al. [5]). Later this code was extended to multiphase mixtures, substantially revised, and named UNCLE-M [1]. The code is structured, multiblock, implicit and parallel with upwind flux-difference splitting for the spatial discretization and Gauss-Seidel relaxation for the inversion of the implicit operator. Primitive variable (MUSCL) interpolation with limiting was applied to retain higher order accuracy in flow fields containing physical discontinuities. In keeping with the finding of Kunz [1], only those source terms associated with vapor production were linearized for inclusion in the implicit linear system left-hand-side. Terms associated with liquid production were treated explicitly and under-relaxed with a factor of 0.1. At each pseudo-time step, the turbulence transport equations were solved subsequent to solution of the mean flow equations. During this investigation, attention was given to the necessity of temporal and spatial discretization independence. As a requirement, to accommodate the use of wall functions, for regions of attached liquid flow, fine-grid near-wall points were established at locations yielding $10<y^+<100$. Further details regarding the numerical method are available in Kunz [1].

Care was taken to establish independence of integration refinement. Figure 2 contains a comparison of the spectral content of results for flow over a hemispherical forebody and cylindrical afterbody, with $Re_D=1.36\times10^5$ and $\sigma=0.3$, for three, successively smaller, integration step sizes. Here, with a physical time step, $\Delta t=0.005$ seconds, the computation resulted in a dimensionless cavity cycling frequency, Str=0.0680, with a time step, $\Delta t=0.0025$ seconds, Str=0.0622, and with $\Delta t=0.001$ seconds, Str=0.0680. More significantly, as demonstrated in the figure, for the smaller two integration step sizes, over the range of relevant (shown) harmonic content, there was very similar modal behavior. Only the fine-grid models tended to provide unsteady results.

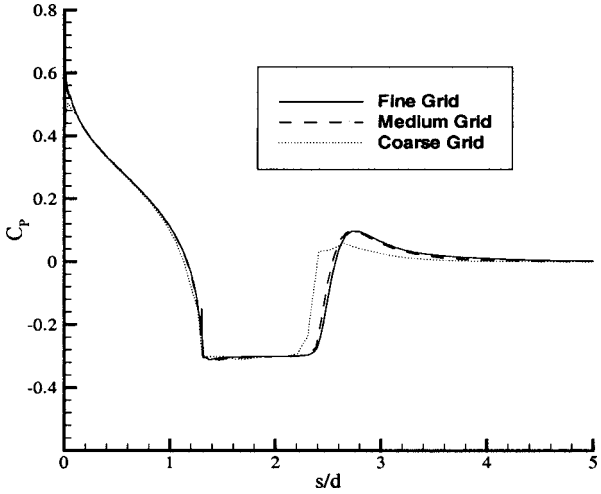

Fig. 3 Comparison of predicted surface pressure distributions for naturally cavitating axisymmetric flow over a conical cavitator with cylindrical afterbody, $\sigma=0.3$. Coarse (65×17), medium (129×33) and fine (257×65) mesh solutions are plotted.

Thus time and spatial fidelity were judged independently. A demonstration of the steady-state spatial convergence of the modeled conical forebody and cylindrical afterbody is given in Fig. 3.

Results

Several cavitating flow-fields have been modeled. In particular, an attempt to validate the method for unsteady two-phase flows has been made. Reboud et al. [6,7] have documented detailed flow features during the vaporous cavity flow in a Venturi section. Stinebring et al. [8] documented the unsteady cycling behavior and average cavity parameters for flow over several axisymmetric cavitators. Steady, average, measurements of cavity parameters for flow over axisymmetric cavitators have been documented by Rouse and McNown [4] and May [9]. In addition to zero angle-of-attack axisymmetric cavitator flows, a demonstrative three-phase result of a transient supercavitating vehicle maneuver is included here. Based on the findings of Stinebring et al. [8], it is expected that the dominant unsteady cavity behavior and many relevant time-averaged and integrated cavity parameters will be independent of whether the cavity formation occurs due to vaporization or ventilation. It should be noted that the results of Rouse and McNown [4] indicated that for the cavitator types and flows at or above the range of experimental Reynolds numbers reported and investigated here, the flow should be turbulent over a significant portion of the forebody. Therefore, for single phase flow, particularly for geometrically smooth shapes, the well-known chaotic, critical laminar separation and transition regime should have been avoided. The numerical results employ a fully turbulent model.

Cavitating Flow in a Venturi. Reboud et al. [5,6] have performed detailed unsteady, flowfield measurements of vaporous cavitating flow in the two-dimensional Venturi section of a water tunnel. The test section captures significant physics found on the suction side in a blade passage. Thus their experiment and the current model results represent partially cavitating flow in a turbomachinery-like environment. In Fig. 4, the average and RMS fluctuating portions of the liquid volume fraction is presented based on the modeled flow. This figure serves to illustrate the geometry of the modeled test section as well as the results obtained during modeling. The test section had a height at the throat equal to 43.7 mm and a constant width equal to 44 mm. The nominal cavity length for comparison here was 80 mm in the horizontal direction. The nominal angle of the lower surface of the Venturi downstream of the throat, with respect to a horizontal line, was 4 deg. The experiments were conducted at Reynolds numbers based on cavity length from 4.3×10^5 to 2.1×10^6 and at a range of cavitation numbers, based on the upstream pressure and velocity, from 0.6 to 0.75. It may be seen from the figure that although there is a high degree of unsteadiness in the region of the cavitating flow, this unsteadiness is confined to the test section area. This is consistent with the commentary [5].

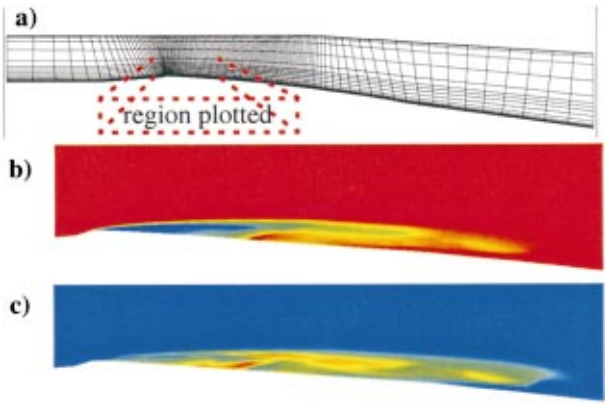

Fig. 4 Computational result. Unsteady, naturally cavitating, two-dimensional flow. $Re_L=7.1\times10^5$ (based on cavity length). Modeling of a two-dimensional cavitation tunnel [6,7], (a) Grid with every 4th point shown; (b) mean liquid volume fraction; red, $\alpha_l>0.995$; blue, $\alpha_l<0.005$; (c) RMS fluctuating component of liquid volume fraction; red indicates a value of 0.5 or greater; blue indicates negligible fluctuating component.

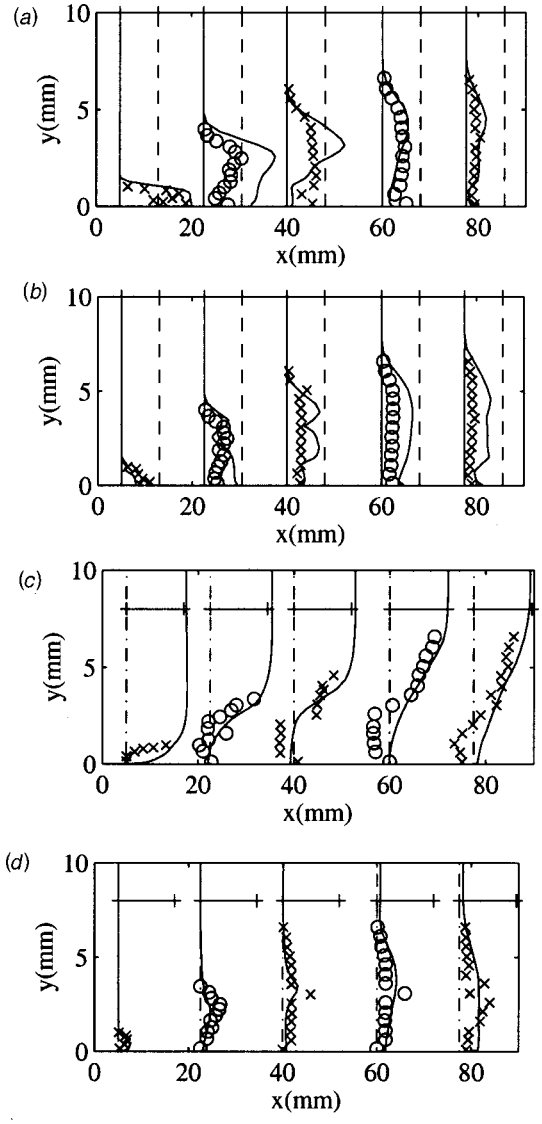

Fig. 5 Comparison of modeled, unsteady cavitating flow to measurements at five horizontal stations [6]. y, vertical distance from wall. x, horizontal distance downstream of throat. (a) Mean vapor volume fraction (α_v); (b) fluctuating RMS vapor volume fraction; (At each station, solid line indicates 0 and dashed line indicates 0.5.) (c) mean horizontal velocity; (d) fluctuating RMS horizontal velocity. (Horizontal bars at stations indicate 12 m/s, the approximate free stream velocity).

In Fig. 5, the current computational results are presented with the experimental data [6]. In the figure, results have been plotted at the five measurement stations used in the experiments. Each of these stations is given at a horizontal position. The experimental cavity was initiated due to the suction peak on the lower surface of the throat of the test section, a reference position of $x=0$. In part (a) of the figure, the mean vapor volume fraction is plotted at the five axial stations. Clearly the model tends to over estimate the void fraction, particularly at the forward region of the cavity, at $x=22.5$ mm. However, the average quantities are in excellent

agreement at the tail end. Similar agreement is demonstrated with the unsteady portion of the RMS void fraction, part (b). Here, the error is greater in the closure region, at $x=60$ mm and $x=80$ mm. Considering the difficulty of modeling in the closure region, this level of agreement is also pleasing. In part (c), the average axial velocity is given, and, in part (d), the RMS fluctuating component is given at the five measurement stations. Here the agreement is generally good, except at the tail end for the average velocity, where the reverse flow is missed. It should be noted that, by application of a two-phase Navier-Stokes model based on a barotropic state law, Reboud et al. [5] were able to obtain similarly good agreement with the experimental data.

Axisymmetric Vaporous Cavitation. Figure 6 contains a series of snapshots of the volume fraction field from an unsteady model computation of flow over a blunt cavitator. Here the Reynolds number, Re_D, was 1.46×10^5 and the cavitation number was 0.3. The time history for this case is given in model seconds, and at $t=0$, unsteady integration was initiated after obtaining a steady-state, $\Delta t=\infty$, initial condition. Thus it is expected that there was some start-up transient associated with initialization from an artificially maintained set of conditions. For the volume fraction contours, dark blue indicates vapor, a liquid volume fraction of less than 0.005, and bright red indicates liquid, a volume fraction of one.

This result is presented over an approximate model cycle. The figure also includes the corresponding time history of drag coefficient. Note that the spikes in drag near $t=37.725$ and $t=38.925$ seconds correspond to reductions in the relative amount of vapor near the sharp leading edge. This marks the progress of a bulk volume of liquid from the closure region to the forward end of the cavity as part of the reentrant jet process. Although far from regular, these spikes also delineate the approximate model cycle. This picture serves to illustrate the basic phenomenon of natural sheet cavitation captured by UNCLE-M. This result is notable for the spatial and temporally irregular nature of the computed flow field. Even after significant integration effort, a clearly periodic result had not emerged. Thus, to deduce the dominant frequency with some confidence, it was necessary to apply ensemble averaging.

An examination of the flow pattern captured suggests qualitative validity. Note, in Fig. 6 that over a significant portion of the sequence, the leading, or formative, edge of the cavity sits slightly downstream from and not attached to the sharp corner. In their experiments, Rouse and McNown [4] observed this phenomenon. They suggested that this delay in cavity formation was due to the tight separation eddy which forms immediately downstream of the corner and, due to interaction with a reentrant jet, locally increases the pressure. The corresponding evolution of cavitation further downstream, at the separation interface, was proposed to be due to tiny vortices. These vortices, after some time, subsequently initiate the cavity. Figure 7 shows a single frame at $t=37.8$ seconds from the same model calculation shown in Fig. 6. Here, to clarify what is captured, the volume fraction contours have been enhanced with illustrative streamlines. Note that these are streamlines drawn from a frozen time slice. Nonetheless, if all of the details envisioned by Rouse and McNown were present, the streamlines should indicate smaller/tighter vortical flows. The current level of modeling was unable to capture this. However, the overall computation was apparently able to capture the gross effects of these phenomena and reproduce a delayed cavity. In fact, from examination of the cavity cycle evolution shown in Fig. 6, and the streamlines shown in the snapshot, it appears that gross unsteadiness is driven by a combination of a reentrant jet and some type of cavity pinching [9,10]. The pinching process is particularly well demonstrated in Fig. 6 from $t=38.125$ to 38.325 seconds.

The low frequency mode apparent in most of the experimental 0-caliber results appears to have been captured at the lowest cavitation number ($\sigma=0.3$), as shown in Fig. 6. In Fig. 8, the drag

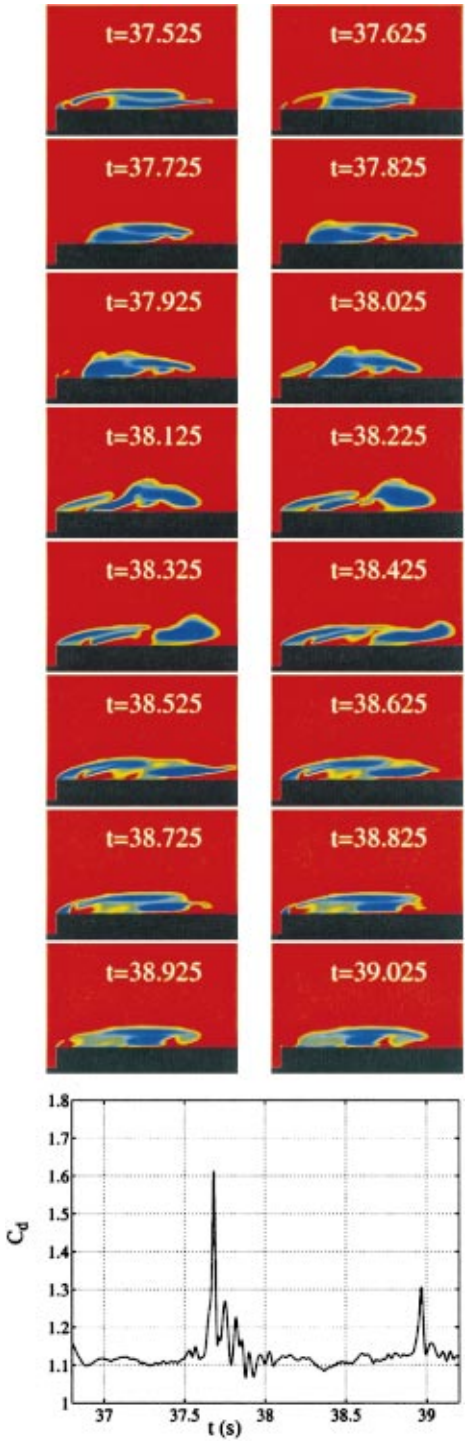

Fig. 6 Modeled flow over a 0-caliber ogive. Liquid volume fraction contours (red, $\alpha_l>0.995$; blue, $\alpha_l<0.005$) and corresponding drag history. UNCLE-M result. $\sigma=0.3$. $\mathrm{Re}_D=1.46\times10^5$. $D/U_\infty=0.146$(s), physical time step, $\Delta t=0.001$(s).

coefficient history for a 40 model second interval from the same computation as in Fig. 6 is shown. Here, a clear picture of the persistence, over a long integration time, of the irregular flow behavior is documented. At higher cavitation numbers, the current set of 0-caliber cavitator results indicates a more regular periodic motion. This is contrary to the experimental data [8]. However, as Fig. 7 indicates, the ability to capture this motion at any cavitation number may not necessarily require the explicit capture of the finer flow details of the vortical flow structure.

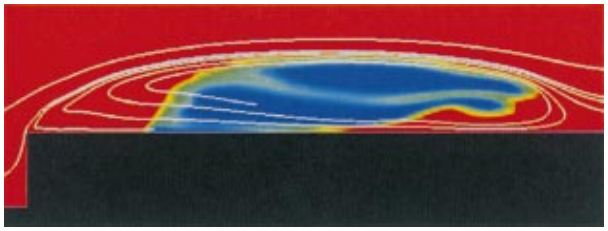

Fig. 7 Snapshot of modeled flow over a 0-caliber ogive. Liquid volume fraction contours (red, $\alpha_l > 0.995$; blue, $\alpha_l < 0.005$) and selected streamlines. UNCLE-M result. $\sigma = 0.3$. $Re_D = 1.46 \times 10^5$.

Figure 9 presents the spectral content of the result given in Fig. 8. As is typical of highly nonlinear sequences, the experience of this unsteady time integration demonstrated that, additional time records merely enrich the power spectral density function. However, the additional records do serve to improve the confidence intervals, and, therefore, add reliability to the numerical convergence process. The model result used, was, as indicated by the confidence intervals, sufficient for a comparison to experimental, unsteady results.

Figure 10 contains a series of snapshots from the unsteady model computation of a hemispherical cavitator at $Re_D = 1.36 \times 10^5$ and $\sigma = 0.2$. This result is presented over a period slightly longer than the approximate model cycle. In this case the model Strouhal frequency is 0.0326. There are ten frames presented, and

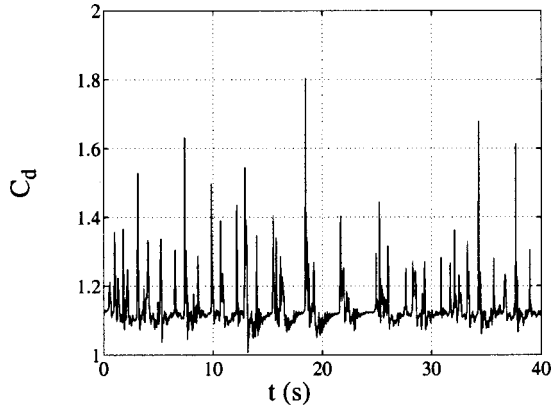

Fig. 8 Model time record of drag coefficient for flow over a 0-caliber ogive at $Re_D = 1.46 \times 10^5$ and $\sigma = 0.3$. In model units, $D/U_\infty = 0.146$(s), physical time step, $\Delta t = 0.001$(s).

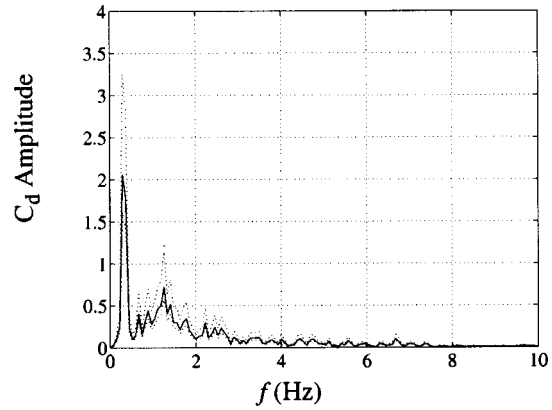

Fig. 9 UNCLE-M result. 0-caliber ogive at $Re_D = 1.46 \times 10^5$ and $\sigma = 0.3$. Power spectral density function with 50% confidence intervals shown.

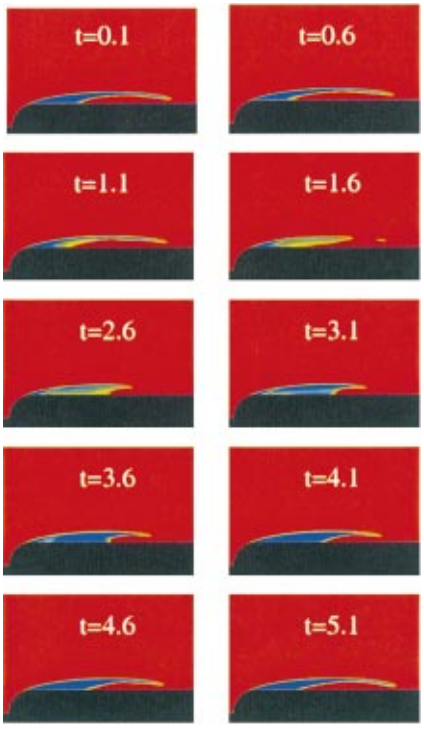

Fig. 10 Liquid volume fraction contours (red, $\alpha_l > 0.995$; blue, $\alpha_l < 0.005$). Modeled flow over a hemispherical forebody and cylinder. UNCLE-M result. $\sigma = 0.2$, $Re_D = 1.36 \times 10^5$.

the first (or last) nine of those ten constitute an approximate model cycle. The drag history trace in Fig. 11 demonstrates how, relative to the modeled flow over the blunt forebody, the pattern of flow over the hemispherical forebody is regular and periodic. This is consistent with experimental observations made (for example) by Rouse and Mcnown [4]. Note the evolution of flow shown in Fig. 10 as it compares to the drag history shown in Fig. 11. As would be expected, the large spike in drag corresponds to the minimum in vapor shown near the modeled $t = 1.6$ seconds.

Figure 12 contains a survey of modeled, unsteady, axisymmetric, computational results and experimentally obtained data [7]. Here, cycling frequency is shown over a range of cavitation numbers. It is clear that (for a given cavitation number) the computational results are bounded by the experimental data, and the proper trends (rate of change of cycling frequency with cavitation

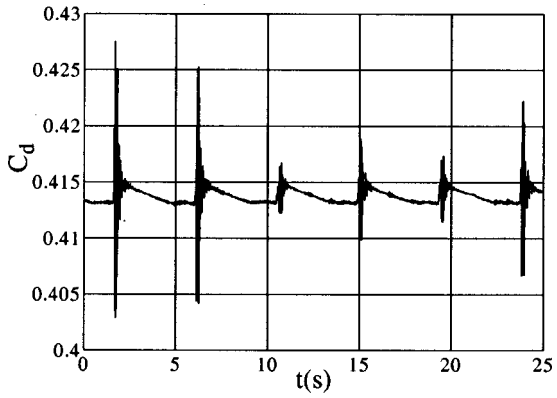

Fig. 11 Unsteady drag coefficient. Flow over a hemispherical forebody and cylinder. UNCLE-M result. $\sigma = 0.2$, $Re_D = 1.36 \times 10^5$. In model units, $D/U_\infty = 0.136$(s), physical time step, $\Delta t = 0.001$(s).

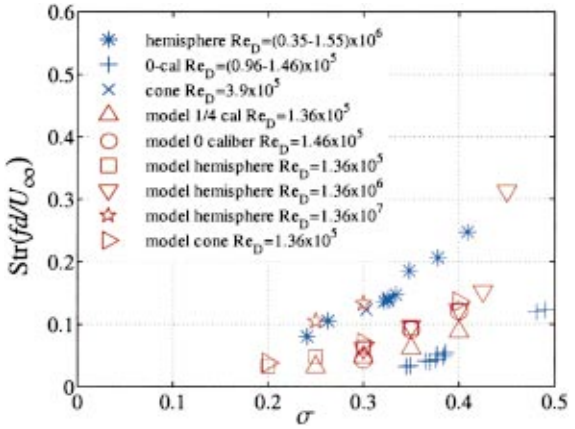

Fig. 12 Axisymmetric vaporous cavitators. Strouhal frequency and cavitation number. UNCLE-M axisymmetric results (open symbols) and data [8].

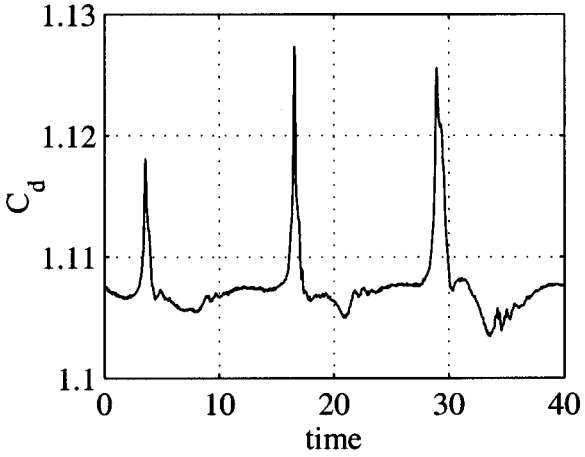

Fig. 14 Profile drag, C_d, history spanning an approximate model cycle. Dimensionless time [tU_∞/D]. Modeled vaporous cavity flow over a blunt cylinder, $\sigma=0.275$.

number) are well captured. More insight into the physical relevance of the data requires examination of specific results.

For axisymmetric modeling results particular to the hemispherical forebody, there is a significant but almost constant offset between the measured unsteady data and the modeled results. Both model and experiments follow a nearly linear trend over the range presented. An interesting result occurs in the model data for the hemispherical forebody with $Re_D=1.36\times10^7$ (pentagrams in Fig. 12). Here the numerical results appear to agree quite well with the experimental data for hemispherical forebodies. The experiments were taken at an order of magnitude lower Reynolds number, but the agreement is apparent in both cases where model results have been obtained.

Another result found is the tendency of the axisymmetric modeled flows to become steady at higher cavitation numbers. For the modeled hemisphere, the upper limit of cavitation number to yield unsteady model results was found to be Reynolds number dependent. This type of trend indicates agreement with the known transition in mode of unsteadiness. Experimentally, a transition does occur from cavity driven to separated, turbulent, but single phase driven flow. The cavity driven regime exists at moderate cavitation numbers and is indicated by a low Strouhal frequency where the value of Str will have an apparent linear dependence on *s*. The second regime tends toward much higher cycling frequencies. Here the dependent Strouhal frequency appears to asymptotically approach a vertical line with higher cavitation number, just prior to the complete elimination of the cavity. This is documented in Stinebring [7] and demonstrated in Fig. 12 for the modeled hemisphere at $Re_D=1.36\times10^6$. Based on the model results, it appears that this is characteristic of a change from a flow mode dominated by a large unsteady cavity to one dominated by other, single-phase, turbulent, sources of unsteadiness.

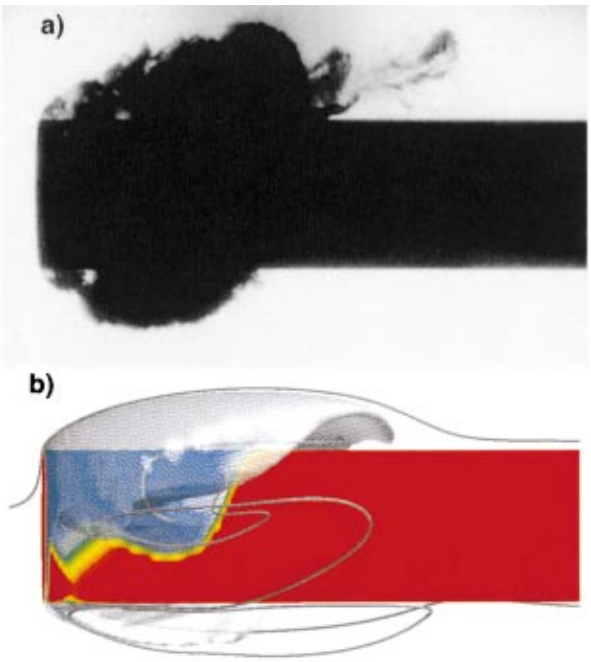

Fig. 13 Blunt cavitator at zero angle-of-attack: (a) In water tunnel at $\sigma=0.35$ [11]; (b) model result from UNCLE-M at $\sigma=0.4$. Isosurface (translucent) at $\alpha_l=0.5$. Selected (instantaneous) streamlines. Surface of cylinder colored by α_l (red, $\alpha_l>0.995$; blue, $\alpha_l<0.005$).

Fully Three-Dimensional Naturally Cavitating Flow. Turbulent, naturally cavitating flow over axisymmetric bodies is known to be a highly nonlinear and three-dimensional event. This is clearly illustrated in Fig. 13. Here, a photograph during water tunnel testing of a blunt cavitator at zero angle-of-attack, $\sigma\approx0.35$, and $Re_D\approx1.5\times10^5$ is shown in part (a) to be compared and contrasted to the model result in part (b). To obtain the model result, turbulent vaporous cavitating flow over a blunt cavitator was modeled. σ was set to 0.4 and Re_D was 1.46×10^5. An appropriate high Reynolds number grid with approximately 1.2 million nodes was used. The snapshot of part (b) represents a physical time slice taken after a clear model cavity cycle had been established. In the figure, an isosurface at $\alpha_l=0.5$ has been presented with selected streamlines, and the surface of the cylinder has been colored by volume fraction. The streamlines are merely suggestive (but helpful), as they have been generated based on instantaneous velocity vectors. Clearly in neither the model result nor the photograph is the flowfield in and around the cavity axisymmetric. It is suspected that physical, chaotic, dynamic interdependencies are responsible. For instance, there is little likelihood of obtaining purely axisymmetric conditions in even the most well controlled environments. Even the identification of all factors necessary to be controlled is a difficult task. This is compounded by the influence of highly nonlinear turbulent flow dominated by phase transition, etc. It is not suggested that, in obtaining the result of Fig. 13(*b*), the exact causal mechanism of the three-dimensional and unsteady flow has been reproduced. Rather it is

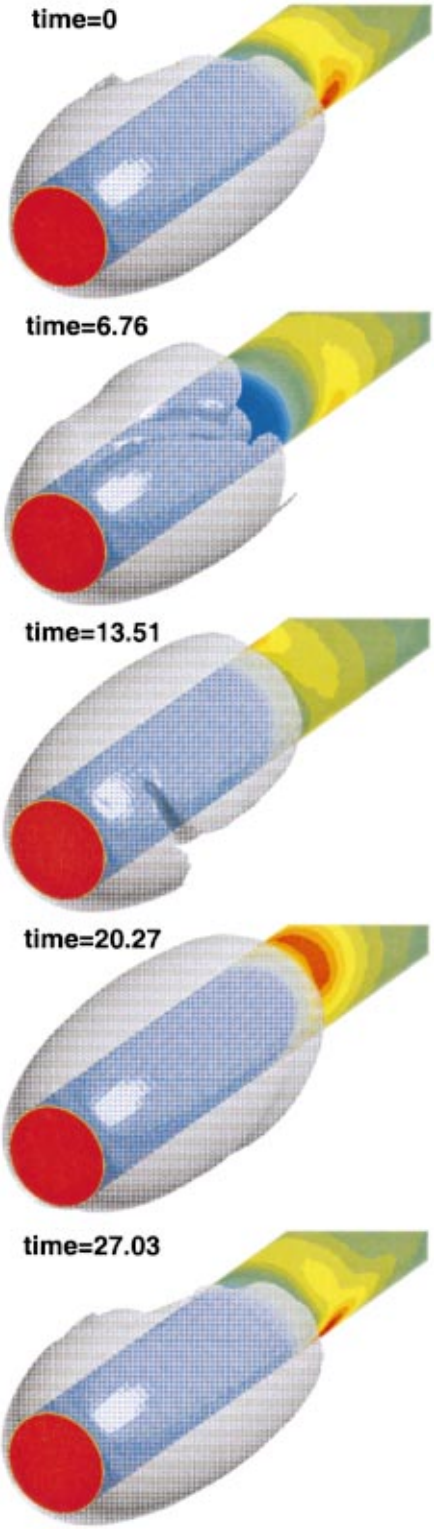

Fig. 15 Snapshots of modeled vaporous cavitation. $\sigma=0.275$. Translucent isosurface at $\alpha_l=0.5$. Surface of cylinder colored by pressure.

suggested that via an adequate level of modeling, the real flow has been well captured. Positive understanding of the causal mechanisms is a subject for further research.

Here a striking example of the divergence of three-dimensional and axisymmetric modeling is given. A sample of the results obtained by three-dimensional modeling of vaporous cavitation over a blunt ogive at zero angle of attack is presented in Fig. 13(*b*) and Fig. 15. These results appear to agree with both significant qualitative and quantitative experimental observations. As in the experiment, the modeled reentrant flow has been observed to follow a helical pattern. This helical flow revolves around the circumference of the cylinder. The flow emanates from the high pressure region downstream of the cavity. This high pressure region is situated at the aft end of the azimuthal section of the cavity of greatest axial extent. This area of the surface of the cylinder contains the stagnation point of an imaginary streampath. This streampath follows the outer edge of the cavity along that azimuthal sector. It is recalled that the cavitation number of flow over axisymmetric bodies is highly correlated with mean cavity length. Thus, at that instant in time, this streampath traces a cavity profile representing an instantaneous minimum cavitation number. A maximum instantaneous cavitation number is similarly related to the axial streampath outlining the cavity of minimum axial extent. The correct cavitation number lies between this minimum and maximum. The reentrant flow tends to move away from this stagnation region. During its initial formation, due perhaps to turbulent fluctuations, the reentrant flow was initially driven and then moved permanently in a helical path. At the same time the helical path was established, other aspects of the flow tended to cause a cavity cycle that is largely axial. This axial cycle fits the typical observations of reentrant flow [7,8]. This axial motion is observable in the snapshots and is also well captured by the profile drag coefficient history given in Fig. 14. Here the drag history has been given over a model cycle as defined by the three-dimensional flow. Clearly the zero-dimensional drag coefficient is insufficient, by itself, to provide the true model cycle. However by examination of Fig. 14 in conjunction with Fig. 15, snapshots of the three-dimensional flowfield, it is possible to deduce the model cycle. The axial cycle may be nearly modeled, in a linearized simplification, as superimposed on the previously discussed circumferential motion. The circumferential motion is not divisible precisely by an integer number of axial periods. In fact the axial cycle is not regular and has poorly defined amplitude. Therefore, this cavity cycle is appropriately described as nonlinear and quasi-periodic.

Due to the observed helical (not symmetric) nature of the reentrant region, it was necessary, experimentally, to use high speed movies to determine the period of cavity cycling (Stinebring [7,11]). Generally two consecutive observed cycles were required to determine the reported cycle. This would then coincide with the

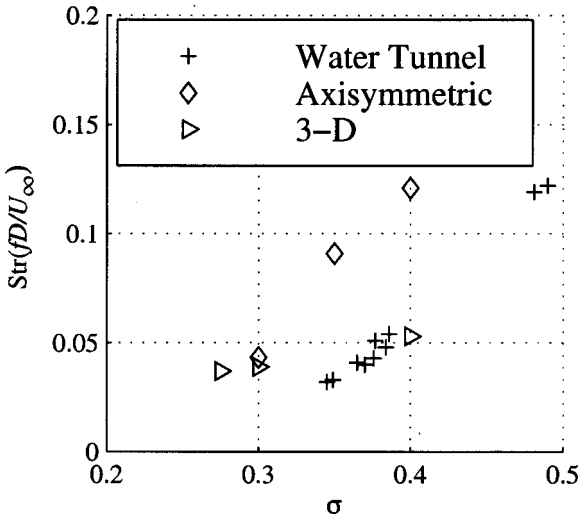

Fig. 16 Cavity cycling frequency versus cavitation number. Vaporous cavitation over blunt cylinder. Comparison of experimental [8], model axisymmetric, and model three-dimensional results.

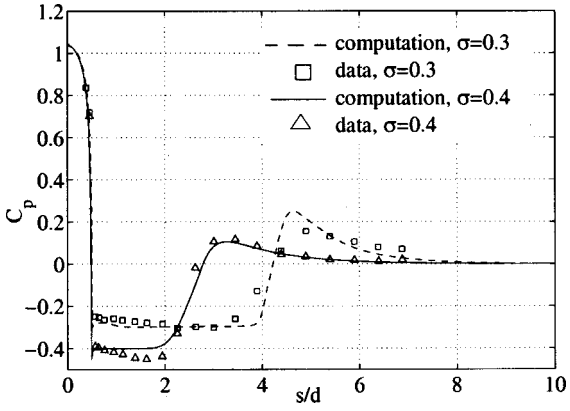

Fig. 17 Flow over a 0-caliber cavitator (s/D=arc length over diameter). Averaged unsteady pressure computations and measured data [4].

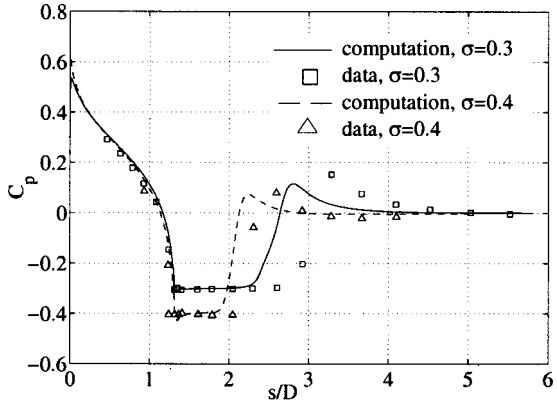

Fig. 19 Flow over a conical cavitator (s/D=arc length over diameter). Averaged unsteady pressure computations and measured data [4].

cycle determined by a complete revolution of the reentrant jet. This is the cycle reported in three-dimensional model results of Fig. 16. Here the model results from the current three-dimensional modeling are compared with the previous axisymmetric results and experimental observations [8].

Axisymmetric Averaged and Integrated Results. Although the dynamics of cavity flow over axisymmetric bodies are three-dimensional, the arithmetically averaged axisymmetric modeled results have been compared to the experiments of Rouse and McNown [4]. Figure 17 contains a comparison for flow over the 0-caliber cavitator, Fig. 18 contains a similar comparison for flow over a hemispherical cavitator, and Fig. 19 contains a similar comparison for flow over a conical cavitator. In each of these figures, the overall computed results generally agree with the measured data. For both the numerical and experimental results, the average initiation and termination point of the cavity may be deduced from this figure. Accordingly, the ability of the numerical model to properly capture the average cavity is presented in these figures. The averaged numerical results for flow over the 0-caliber cavitator are in better agreement with the data than for either of the other shapes. The numerical results for flow over the conical cavitator compare least favorably. It is thought that the formation point of the average cavity should be well defined in the axisymmetric shapes with discontinuous profile slopes. Thus it is not clear why the prediction of termination of the cavity should, on average, be worst for the modeled flow over the conical shape.

Several parameters of relevance in the characterization of cavitation bubbles include body diameter, D, bubble length, L, bubble diameter, d_m, and form drag coefficient associated with the cavitator, C_d. For convenience, bubble length has been defined as twice the axial distance from cavity leading edge to the location of maximum bubble diameter. The form drag coefficient is taken as the pressure drag on an isolated cavitator shape. The pressure contribution to C_d associated with the back of the cavitator is assumed equal to the cavity pressure ($\approx p_v$). For the model computations, d_m is determined by examining the $\alpha_l = 0.5$ contour and determining its maximum radial location.

Figures 20 and 21 compare time-averaged model results from UNCLE-M with the voluminous experimental data assembled by May for cavity running vehicles [9]. In Fig. 20, the quantity $L/(DC_d^{1/2})$ is plotted against cavitation number. UNCLE-M results are included for ten unsteady computations made with three cavitator shapes. The experimental data and model results do correlate well, close to independently of cavitator shape. Another parameter, tabulated by May, that has been established to correlate well with cavitation number is the fineness ratio, L/d_m. Figure 21 contains a summary of the data from May and a series of unsteady UNCLE-M results for fineness ratio, plotted against cavitation number.

Three-Dimensional Supercavitating Transient. The authors are also interested in the hydrodynamic performance of supercavitating vehicles in maneuvers. Of particular interest are predicted

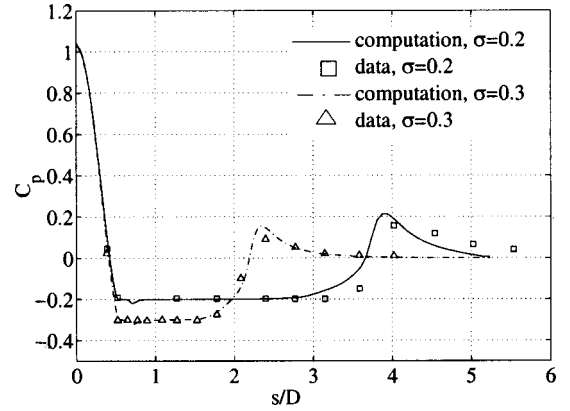

Fig. 18 Flow over a hemispherical cavitator (s/D=arc length over diameter). Averaged unsteady pressure computations and measured data [4].

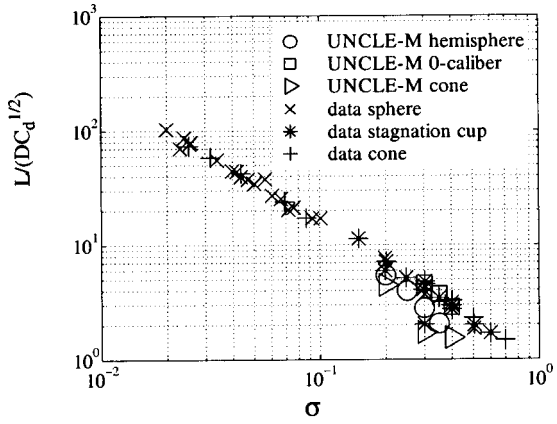

Fig. 20 Dimensionless drag to bubble length parameter and cavitation number. Flow over axisymmetric cavitators. Arithmetically averaged, unsteady UNCLE-M results and data [9].

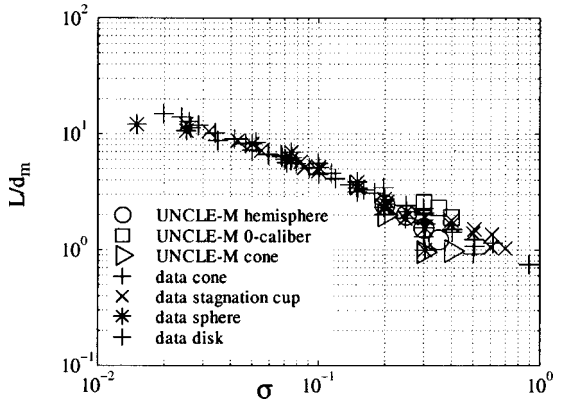

Fig. 21 Cavity fineness ratio and cavitation index. Flow over axisymmetric cavitators. Arithmetically averaged, unsteady, UNCLE-M results and data [9].

transient forces and moments, as well as transient cavity behavior, which are important in the design of vehicle control systems and gas ventilation schemes.

In Fig. 22, a set of preliminary proscribed motion results for a notional supercavitating vehicle is presented. Figure 22(*a*) illustrates a view of the geometry, which has a relatively blunt cavitator and three annular ventilation ports with aft oriented gas deflectors. A cavity gas ventilation rate is proscribed that is sufficient to enshroud the entire vehicle during steady flight. A gas propellant flow rate is also specified at the exhaust nozzle. For this analysis, the gas flow is assumed incompressible. A proscribed pitch-up-pitch-down maneuver is specified (see Fig. 22(*i*). A nondimensional timestep of $\Delta t/t_{ref}=0.09473$ was specified, where $t_{ref}=L_{vehicle}/U_{\infty}$. A 1,218,536 vertex grid was used. Figure 22(*b*) through (*h*) shows several snapshots of the evolving cavity during the maneuver, as designated by isosurfaces of liquid volume fraction, $\alpha_l=0.5$. A three-field simulation was carried out. Vaporous cavitation occurs upstream of the first gas deflector. Clearly evident is the significant perturbation in the cavity for this maneuver. Indeed, the cavity intersects the body at $t/t_{ref}=47.4$. Also, natural cavitation near the leading edge is not sufficient to keep the first injection port dry. Figure 22(*i*) shows the predicted lift history for the vehicle during the maneuver, as well as the proscribed angle-of-attack.

Summary and Conclusions

It should be noted that during this investigation, steady-state, axisymmetric results (time integrations based on $\Delta t=\infty$) using UNCLE-M have been found to be quite consistent with arithmetically averaged time-dependent results produced with axisymmetric geometries and boundary conditions. This result is expected to be useful in expediting the future interpretation of complex three-dimensional flows.

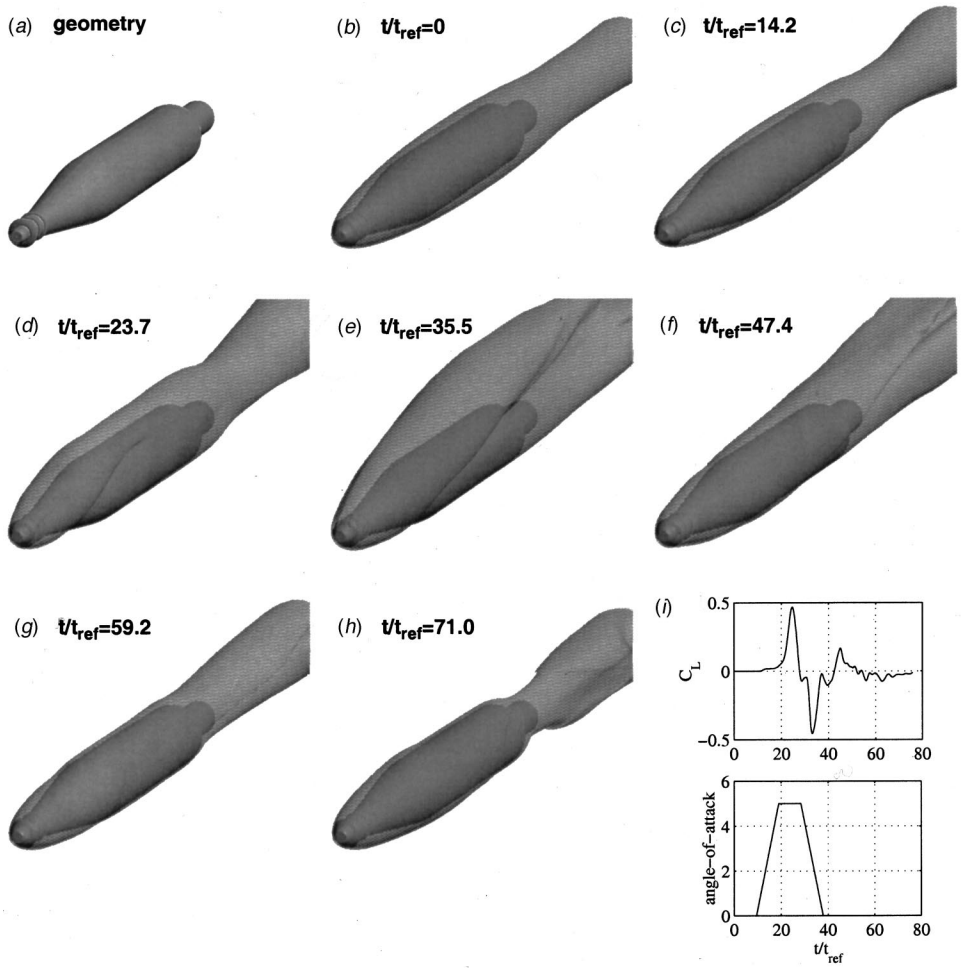

Fig. 22 Elements of 3-D unsteady simulation of proscribed maneuver of a notional high speed supercavitating vehicle (a) View of geometry; (b–h) cavity surface shape vs. time as indicated by isosurface of $\alpha_l=0.5$; (i) proscribed angle-of-attack and lift history vs. time.

Results have been given demonstrating capabilities of the computational model. Complex two-dimensional, three-dimensional, and unsteady representative and validative flows have been examined. Supportive experimental results have been included, and detailed discussion of the modeled flow features has been given. The differential and computational form as well as the solution of the fully three-dimensional, three-phase model with mass transfer has been presented.

The validative results include modeled vaporous cavity flow in a Venturi section compared to experiments reported by Reboud et al. [6,7], and modeled vaporous cavity flow over various axisymmetric forebodies experimentally reported by Stinebring et al. [11], Rouse and McNown [4], and May [9]. In each of these cases the flow was unsteady, complex, and almost certainly three-dimensional. In the case of the Venturi, two-dimensional model results appear good considering the complex unsteady nature of the flow and the high level of detail provided by the experimental results. However, the transverse (not modeled) dimension of the test section was 44 mm while the height was 43.7 mm. Based on other modeling and experimental evidence offered here, it is suspected that three-dimensional modeling of such a Venturi section would be useful.

In the case of the flow over axisymmetric bodies at zero angle of attack, it is apparent that model and experimental results for vaporous cavitation may not be symmetric. This is shown in Fig. 13 and experimentally reported in various sources [4,11]. However, much of the notable physics and the general trends of cavity cycling behavior are well captured by axisymmetric modeling. This is demonstrated in Fig. 6 and 16.

Success with geometrically simple validative results suggests that the modeling method may be applied to more complicated design level tasks with confidence. This has been demonstrated here in the case of a three-phase model of a supercavitating vehicle undergoing a transient maneuver.

Acknowledgments

This work was supported by the Office of Naval Research, contract #N00014-98-0143 and #N00014-01-1-0325, with Dr. Kam Ng as contract monitor, and a grant of DoD 2001 Challenge Project HPC resources from the Army Research Laboratory Major Shared Resource Center and the Army High Performance Computing Research Center. The provision of information by Drs. Benoit Stutz and Jean-Luc Reboud is also appreciated.

Nomenclature

C_1, C_2 = turbulence model constants
C_ϕ = mass transfer model constants
C_P = pressure coefficient
C_d = drag coefficient
D = body diameter
d_m = bubble diameter
f = cycling frequency (Hz)
k = turbulent kinetic energy
L = bubble length
$\dot{m}^-$, $\dot{m}^+$ = mass transfer rates
P = turbulent kinetic energy production
$\mathrm{Pr_{tk}}$, $\mathrm{Pr_{t\varepsilon}}$ = turbulent Prandtl numbers for $\mathbf{k}$ and $\boldsymbol{\varepsilon}$
p = pressure
Re_D = Reynolds number based on body diameter ($\rho_l U_\infty D/\mu_l$)
Str = Strouhal frequency (fD/U_∞)
s = arc length along configuration (also seconds)
t, t_∞, Δt = physical time, mean flow time scale, time step
U = velocity magnitude
u_i = Cartesian velocity components
x_i = Cartesian coordinates
y^+ = dimensionless wall distance
α = volume fraction, angle of attack
β = preconditioning parameter
τ = pseudo-time
ε = turbulence dissipation rate
μ = molecular viscosity
ρ = density
σ = cavitation number ($\equiv p_\infty - p_\nu)/(\frac{1}{2}\rho U_\infty^2$)

Subscripts, Superscripts

D = body diameter
L = cavity length
l = liquid
m = mixture
ng = noncondensable gas
t = turbulent
ν = condensable vapor
∞ = free stream value

References

[1] Kunz, R. F., Boger, D. A., Stinebring, D. R., Chyczewski, T. S., Lindau, J. W., Gibeling, H. J., Venkateswaran, S., and Govindan, T. R., 2000, "A Preconditioned Navier-Stokes Method for Two-Phase Flows with Application to Cavitation Prediction," Comput. Fluids, **29**, pp. 849–875.
[2] Merkle, C. L., Feng, J., and Buelow, P. E. O., 1998, "Computational Modeling of the Dynamics of Sheet Cavitation," Third International Symposium on Cavitation, Grenoble, France.
[3] Hohenberg, P. C., and Halperin, B. I., 1977, "Theory of Dynamic Critical Phenomena," Rev. Mod. Phys., **49**(3), pp. 435–479.
[4] Rouse, H. and McNown, J. S., 1948, "Cavitation and Pressure Distribution, Head Forms at Zero Angle of Yaw," *Studies in Engineering Bulletin 32*, State University of Iowa.
[5] Taylor, L. K., Arabshahi, A., and Whitfield, D. L., 1995, "Unsteady Three-Dimensional Incompressible Navier-Stokes Computations for a Prolate Spheroid Undergoing Time-Dependent Maneuvers," AIAA Paper 95-0313.
[6] Reboud, J., Stutz, B. and Coutier, O., 1998, "Two-Phase Flow Structure of Cavitation: Experiment and Modelling of Unsteady Effects," Third International Symposium on Cavitation, Grenoble, France.
[7] Stutz, B. and Reboud, J., 1997, "Two-Phase Flow Structure of Sheet Cavitation," Physics of Fluids, **9**(12).
[8] Stinebring, D. R., Billet, M. L., and Holl, J. W., 1983 "An Investigation of Cavity Cycling for Ventilated and Natural Cavities," Technical Memorandum, TM 83-13, The Pennsylvania State University Applied Research Laboratory.
[9] May, A., 1975 "Water Entry and the Cavity-Running Behavior of Missles," Naval Sea Systems Command Hydroballistics Advisory Committee, Technical Report No. 75-2.
[10] Brennen, C. E., 1995, *Cavitation and Bubble Dynamics*, Oxford University Press, New York.
[11] Stinebring, D. R., 1976, "Scaling of Cavitation Damage," M. S. thesis, The Pennsylvania State University, University Park, Pennsylvania.

Mathematical Basis and Validation of the Full Cavitation Model

Ashok K. Singhal
e-mail: aks@cfdrc.com

Mahesh M. Athavale

Huiying Li

Yu Jiang

CFD Research Corporation,
Huntsville, AL 35805

Cavitating flows entail phase change and hence very large and steep density variations in the low pressure regions. These are also very sensitive to: (a) the formation and transport of vapor bubbles, (b) the turbulent fluctuations of pressure and velocity, and (c) the magnitude of noncondensible gases, which are dissolved or ingested in the operating liquid. The presented cavitation model accounts for all these first-order effects, and thus is named as the "full cavitation model." The phase-change rate expressions are derived from a reduced form of Rayleigh-Plesset equation for bubble dynamics. These rates depend upon local flow conditions (pressure, velocities, turbulence) as well as fluid properties (saturation pressure, densities, and surface tension). The rate expressions employ two empirical constants, which have been calibrated with experimental data covering a very wide range of flow conditions, and do not require adjustments for different problems. The model has been implemented in an advanced, commercial, general-purpose CFD code, CFD-ACE+. Final validation results are presented for flows over hydrofoils, submerged cylindrical bodies, and sharp-edged orifices. Suggestions for possible extensions of the model implementation, e.g., to nonisothermal flows, for ingestion and mixing of noncondensible gases, and for predictions of noise and surface damage are outlined.
[DOI: 10.1115/1.1486223]

Introduction

The capability for multidimensional simulation of cavitating flows is of critical importance for efficient design and performance of many engineering devices. Some examples are: industrial turbomachinery, turbopumps in rocket propulsion systems, hydrofoils, marine propellers, fuel injectors, hydrostatic bearings, and mechanical heart valves. In most cases, cavitation is an undesirable phenomenon, causing significant degradation in the performance, e.g., reduced flow rates, lower pressure increases in pumps, load asymmetry and vibrations and noise. Multidimensional simulations can enable a designer to eliminate, reduce or shift the cavitation regions. The objective of the present study is to develop a practical cavitation model capable of predicting major performance parameters. Its extensions to prediction of cavitation related surface damage, which affects the life of the equipment, may be considered in future.

Numerical simulation of cavitating flows poses unique challenges, both in modeling of the physics and in developing robust numerical methodology. The major difficulty arises due to the large density changes associated with phase change. For example, the ratio of liquid to vapor density for water at room temperature is over 40,000. Furthermore, the location, extent and type of cavitation are strongly dependent on the pressure field, which in turn is influenced by the flow geometry and conditions. Therefore, in a practical modeling approach, *a priori* prescription (or assumption) of the location and/or size of cavitation region should not be required. Likewise, the phase change correlations should have minimum essential empiricism so that diverse applications can be simulated without adjusting any constants or functions.

Over the last several decades, considerable effort from both experimental and analytical fronts has been devoted to understanding cavitation. For example, References [1–12] include some recent reviews as well as attempts on modeling and application of cavitation. Unfortunately, all past models, including the two developed by the principal author and his colleagues [10,11], have had limited success, primarily due to: (a) the lack of robustness of numerical algorithms, and (b) lack of generality of the correlations or approach used. As a result, no cavitation model was routinely used for practical CFD-based design optimization studies.

The Full Cavitation Model described here meets all the above-mentioned requirements and is already beginning to get routinely used in industry for water and oil pumps, inducers, impellers, and fuel injection systems.

Contributed by the Fluids Engineering Division for publication in the JOURNAL OF FLUIDS ENGINEERING. Manuscript received by the Fluids Engineering Division April 20, 2001; revised manuscript received February 28, 2002. Associate Editor: J. Katz.

Description of the Full Cavitation Model

The basic approach consists of using the standard viscous flow (Navier-Stokes) equations for variable fluid density and a conventional turbulence model (e.g., k-ε model). The fluid density is a function of vapor mass fraction f, which is computed by solving a transport equation coupled with the mass and momentum conservation equations. The ρ-f relationship is:

$$\frac{1}{\rho}=\frac{f}{\rho_v}+\frac{1-f}{\rho_l} \tag{1}$$

and the vapor volume fraction α is deduced from f as:

$$\alpha\equiv f\frac{\rho}{\rho_v} \tag{2}$$

The vapor mass fraction, f, is governed by a transport equation:

$$\frac{\partial}{\partial t}(\rho f)+\nabla\cdot(\rho\vec{V}f)=\nabla\cdot(\Gamma\nabla f)+R_e-R_c \tag{3}$$

The source terms R_e and R_c denote vapor generation (evaporation) and condensation rates, and can be functions of: flow parameters (pressure, flow characteristic velocity) and fluid properties (liquid and vapor phase densities, saturation pressure, and liquid-vapor surface tension).

The above formulation employs a homogenous flow approach, also known as Equal-Velocity-Equal-Temperature (EVET) ap-

proach. For the objective of a practical and general model of cavitating flows, this is a fairly good simplification because of the following reasons:

1 In most engineering devices, the low-pressure regions, where cavitation occurs, are also the regions of relatively high velocities. In such high-velocity regions, the velocity slips between the liquid and vapor phases are rather small.

2 Most often, the generated vapor takes the form of small bubbles. While such flows can be characterized by a more rigorous two-fluid approach, which allows for velocity slip between the liquid and vapor phases, the computed flow fields strongly depend upon the physical models used for the computation of local bubble sizes and interface drag forces. Unfortunately, there are no general or reliable physical models for these parameters, and therefore the extra computational effort in the two-fluid approach is of little practical value.

The present model focuses on the use of simple rational formulations for phase change rates (R_e and R_c).

Bubble Dynamics Consideration. We assume that, in most engineering situations, there are plenty of nuclei for the inception of cavitation. Thus, our primary focus is on proper account of bubble growth and collapse. In a flowing liquid with zero velocity slip between the fluid and bubbles, the bubble dynamics equation can be derived from the generalized Rayleigh-Plesset equation as [1,12]:

$$\Re_B\frac{D^2\Re_B}{Dt^2}+\frac{3}{2}\left(\frac{D\Re_B}{Dt}\right)^2=\left(\frac{P_B-P}{\rho_l}\right)-\frac{4\nu_l}{\Re_B}\dot{\Re}_B-\frac{2S}{\rho_l\Re_B} \quad (4)$$

This equation provides a physical approach to introduce the effects of bubble dynamics into the cavitation model. In fact, it can be considered to be an equation for void propagation and, hence, mixture density.

To obtain an expression of the net phase change rate, the two-phase continuity equations are written as follows: Liquid phase:

$$\frac{\partial}{\partial t}[(1-\alpha)\rho_l]+\nabla\cdot[(1-\alpha)\rho_l\vec{V}]=-R \quad (5)$$

Vapor phase:

$$\frac{\partial}{\partial t}(\alpha\rho_v)+\nabla\cdot(\alpha\rho_v\vec{V})=R \quad (6)$$

Mixture:

$$\frac{\partial}{\partial t}(\rho)+\nabla\cdot(\rho\vec{V})=0 \quad (7)$$

where R is the net phase change rate $=(R_e-R_c)$, and ρ is the mixture density. Combining Eqs. (5)–(7) yields a relation between the mixture density and void fraction α:

$$\frac{D\rho}{Dt}=-(\rho_l-\rho_v)\frac{D\alpha}{Dt} \quad (8)$$

The vapor volume fraction α can be related to the bubble number density, "n" and radius of bubble $\Re_B$ as

$$\alpha=n\frac{4}{3}\pi\Re_B^3 \quad (9)$$

substituting Eq. (9) into Eq. (8) we obtain

$$\frac{D\rho}{Dt}=-(\rho_l-\rho_v)(n4\pi)^{1/3}(3\alpha)^{2/3}\frac{D\Re_B}{Dt} \quad (10)$$

Using the Rayleigh-Plesset Equation, Eq. (4), without the viscous damping and surface tension terms (the 2nd and 3rd term on r.h.s.), and combining Eqs. (5), (6), (8), and (10), the expression for the net phase change rate R is finally obtained as:

$$R=(n4\pi)^{1/3}(3\alpha)^{2/3}\frac{\rho_v\rho_l}{\rho}\left[\frac{2}{3}\left(\frac{P_B-P}{\rho_l}\right)-\frac{2}{3}\Re_B\frac{D^2\Re_B}{Dt^2}\right]^{1/2} \quad (11)$$

Using Eqs. (3) and (11), and ignoring the second-order derivative of $\Re_B$ (important mainly during initial bubble acceleration), we get the following simplified equation for vapor transport:

$$\frac{\partial}{\partial t}(\rho f)+\nabla\cdot(\rho fV)=(n4\pi)^{1/3}(3\alpha)^{2/3}\frac{\rho_v\rho_l}{\rho}\left[\frac{2}{3}\left(\frac{P_B-P}{\rho_l}\right)\right]^{1/2} \quad (12)$$

where the right side of the equation represents the vapor generation or "evaporation" rate. Though we expect the bubble collapse process to be different from that of the bubble growth, as a first approximation, Eq. (12) is also used to model the collapse (condensation), when $P>P_B$, by using the absolute value of the pressure difference and treating the right side as a sink term. The local far-field pressure P is taken to be the same as the cell center pressure. The bubble pressure P_B is equal to the saturation vapor pressure in the absence of dissolved gas, mass transport and viscous damping, i.e., $P_B=P_v$.

Equation (12) is referred to here as the *Reduced Bubble Dynamics Formulation*.

Phase Change Rates. In Eq. (12), all terms except "n" are either known constants or dependent variables. In the absence of a general model for estimation of the number density, the Phase Change Rate expression is rewritten in terms of bubble radius, $\Re_B$, as follows:

$$R_e=\frac{3\alpha}{\Re_B}\cdot\frac{\rho_v\rho_l}{\rho}\left[\frac{2}{3}\frac{P_v-P}{\rho_l}\right]^{1/2} \quad (13)$$

For simplicity, the typical bubble size $\Re_B$ is taken to be the same as the limiting (maximum possible) bubble size. Then, $\Re_B$ is determined by the balance between aerodynamic drag and surface tension forces. A commonly used correlation in the nuclear industry is [13]:

$$\Re_B=\frac{0.061\mathrm{We}\,\sigma}{2\rho_l v_{\mathrm{rel}}^2} \quad (14)$$

For bubbly flow regime, V_{rel} is generally fairly small, e.g., 5–10% of liquid velocity. By using various limiting arguments, e.g., $\Re_B\rightarrow 0$ as $\alpha\rightarrow 0$, and the fact that the per unit volume phase change rates should be proportional to the volume fractions of the donor phase, the following expressions for vapor generation/condensation rates are obtained in terms of the vapor mass fraction f:

$$R_e=C_e\frac{V_{ch}}{\sigma}\rho_l\rho_v\left[\frac{2}{3}\frac{P_v-P}{\rho_l}\right]^{1/2}(1-f) \quad (15)$$

$$R_c=C_c\frac{V_{ch}}{\sigma}\rho_l\rho_l\left[\frac{2}{3}\frac{P-P_v}{\rho_l}\right]^{1/2}f \quad (16)$$

Here C_e and C_c are two empirical coefficients and V_{ch} is a characteristic velocity, which reflects the effect of the local relative velocity between liquid and vapor. These relations are based on the following assumptions:

1. In the bubble flow regime, the phase change rate is proportional to V_{rel}^2; however, in most practical two-phase flow conditions, the dependence on velocity is found/assumed to be linear.
2. The relative velocity between the liquid and vapor phase is of the order of 1 to 10% of the mean velocity. In most turbulent flows, the local turbulent velocity fluctuations are also of this order. Therefore, as a first pragmatic approximation, V_{ch} in Eqs. (15) and (16) can be expressed as the square root of local turbulent kinetic energy $\sqrt{k}$.

The Effect of Turbulence. Several experimental investigations have shown significant effect of turbulence on cavitating flows (e.g., references [3,14]). Also, Singhal et al. [11] reported a numerical model, using a probability density function (PDF) approach for accounting the effects of turbulent pressure fluctuations. This approach required: (a) estimation of the local values of the turbulent pressure fluctuations as [15]:

$$P'_{\text{turb}} = 0.39\rho k \tag{17}$$

and (b) computations of time-averaged phase-change rates by integration of instantaneous rates in conjunction with assumed PDF for pressure variation with time. In the present model, this treatment has been simplified by simply raising the phase-change threshold pressure value as:

$$P_v = (P_{\text{sat}} + P'_{\text{turb}}/2) \tag{18}$$

This practice has been found to be much simpler, robust and almost as good as the more rigorous practice of ref. [11].

Effect of Noncondensable Gases (NCG). In most engineering equipment, the operating liquid contains a finite amount of non-condensable gas (NCG) in dissolved state, or due to leakage or by aeration. Even a small amount (e.g., 10 ppm) of NCG can have significant effects on the performance of the machinery [16,17]. The primary effect is due to the expansion of gas at low pressures which can lead to significant values of local gas volume fraction, and thus have considerable impact on density, velocity and pressure distributions. The secondary effect can be via increases in the phase-change threshold pressure. This has been neglected due to lack of a general correlation.

Final Form of Full Cavitation Model. The working fluid is assumed to be a mixture of liquid, liquid vapor and NCG. The calculation of the mixture density (Eq. (1)) is modified as:

$$\frac{1}{\rho} = \frac{f_v}{\rho_v} + \frac{f_g}{\rho_g} + \frac{1 - f_v - f_g}{\rho_l} \tag{19}$$

Non-condensable gas density ρ_g is calculated as:

$$\rho_g = \frac{WP}{RT} \tag{20}$$

Volume fractions of NCG and liquid are modified as:

$$\alpha_g = f_g \frac{\rho}{\rho_g}; \tag{21}$$

$$\alpha_l = 1 - \alpha_v - \alpha_g \tag{22}$$

Finally, with the consideration of the NCG effect, and also using $\sqrt{k}$ to replace V_{ch}, Eqs. (15) and (16) are rewritten as:

$$R_e = C_e \frac{\sqrt{k}}{\sigma} \rho_l \rho_v \left[\frac{2}{3} \frac{P_v - P}{\rho_l} \right]^{1/2} (1 - f_v - f_g) \tag{23}$$

$$R_c = C_e \frac{\sqrt{k}}{\sigma} \rho_l \rho_l \left[\frac{2}{3} \frac{P - P_v}{\rho} \right]^{1/2} f_v \tag{24}$$

where the phase-change threshold pressure P_v is estimated from Eqs. (17) and (18). The recommended values of the empirical constants C_e and C_c are 0.02 and 0.01, respectively. The basis for these values is described below.

Model Implementation

The full cavitation model has been implemented into an advanced, general purpose, commercial CFD code, CFD-ACE+ [18]. The relevant features of CFD-ACE+ include: unstructured/adaptive/hybrid grids, a finite volume, pressure-based formulation for incompressible and compressible flows, a variety of turbulence models, multi-media heat transfer, steady-state and time-accurate solution, arbitrary sliding interface treatment, and moving grids for deforming/sliding domains.

Some points to be noted about the current cavitation model are:

1. The cavitation model can be applied to any geometric system (3D, 2D planar, or 2D axisymmetric); all grid cell types (quad, tri, hex, tet, prism, poly) and arbitrary interfaces are supported;
2. Concurrent use of the turbulence, grid deformation and/or structures solution modules are fully supported;
3. Flow is assumed isothermal and fluid properties are taken as constant at a given temperature for the entire flow domain. Due to this assumption, the cavitation module currently is decoupled from heat transfer and radiation modules.
4. Noncondensible gas mass fraction f_g is assumed to be constant in the flow field. An appropriate value of f_g, estimated based on the operating liquid and conditions, is prescribed as a part of the model input.

The simplifications listed in items 3 and 4 above can be removed in future as outlined at the end of the paper.

Determination of Empirical Constants C_e and C_c. The two constants, C_e and C_c, have been determined by performing several series of computations for sharp-edged orifice and hydrofoil flows. Both of these flows have excellent data, covering a wide range of operating conditions. Numerical computations were initially performed assuming $C_e = C_c$, and nominal values were found to be in the range 0.01–0.1. The assessment criteria included:

(a) Comparison of computed mass flow rates, discharge coefficients, and flow pattern (location and extent of cavitation zone); and
(b) Special attention to the calculated minimum pressures, and their sensitivity to the assumed values of coefficients.

The primary objectives of this exercise were to: completely eliminate negative pressure regions, obtain minimum pressures close to saturation pressures and obtain minimal sensitivity to pressure variations. It was found that to reproduce experimental trends, $C_c < C_e$. Several other postulations for slowing down the condensation (vapor destruction) process were also tried. None of these were found to be very general or robust. Therefore, C_c values were varied in the range of C_e to $0.1C_e$. A large number of combinations of C_e and C_c values were tried for several orifice flow conditions (upstream total pressure = 2, 3, 5, 50, and 500 bar) and for selected hydrofoil flow cases (representative low and high flow rates for two angles of attack, i.e., for leading and mid-chord cavitation). After many hundreds of permutations and combinations, the most satisfactory values were found to be

$$C_e = 0.02 \quad \text{and} \quad C_c = 0.01 \tag{25}$$

These values were then used for many other problems, including flows past submerged cylindrical bodies, inducers, impellers and axial pumps. All these simulations produced satisfactory results, i.e., good convergence rates, no negative pressures, and reasonable comparison with available data and/or flow patterns. Therefore, the present set of values, $C_e = 0.02$ and $C_c = 0.01$ seems quite satisfactory for general use.

Validation of Full Cavitation Model

This section presents some of the validation results for flow over a hydrofoil, over a submerged cylindrical body, and flow in a sharp-edged orifice. In each case experimental data is available for wide range of conditions. Good agreement has been obtained in all cases without adjusting any coefficient values.

In all the simulations presented below, the working fluid was water at 300 K, with liquid and vapor densities of 1000 and 0.02558 kg/m^3, saturation pressure of 3540 Pa and surface tension

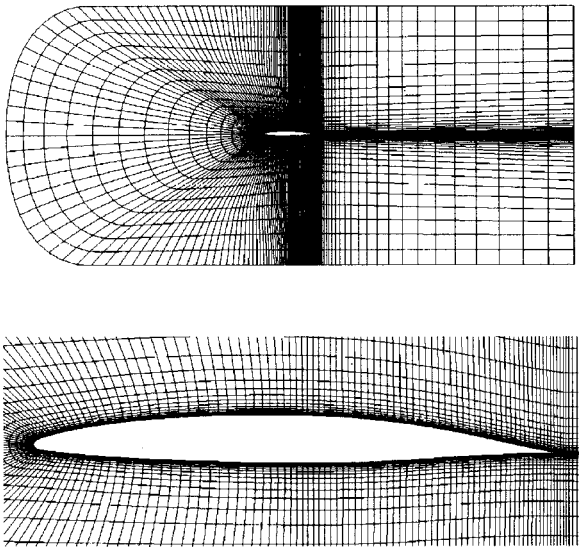

Fig. 1 Computational domain and grid, and grid distribution near the hydrofoil for $\alpha = 4$ deg

$\sigma = 0.0717$ N/m. A second-order upwind scheme was used to discretize the convective fluxes, and turbulence was treated using the standard k-ε model

1 Cavitating Flow Over a Hydrofoil. Effects of leading edge and mid-chord cavitation on the hydrodynamic forces on a hydrofoil were experimentally investigated by Shen and Dimotakis [19]. A NACA66 (MOD) airfoil section with camber ratio of 0.02, mean line of 0.8 and thickness ratio of 0.09 was used. A 2-D working section of the hydrofoil was mounted in a water tunnel. Static pressures on hydrofoil surface were measured at different angles of attack and Reynolds numbers. The non-dimensional parameters of interest were:

$$\mathrm{Re} = \frac{\rho_l U_\infty C}{\mu_1}, \quad \Sigma = \frac{P_\infty - P_v}{\frac{1}{2}\rho_l U_\infty^2}, \quad C_p = \frac{P - P_\infty}{\frac{1}{2}\rho_l U_\infty^2} \tag{26}$$

A two-block grid consisting of 30×130 cells/block (7800 cells) is shown in Fig. 1. Two other grids consisting of 4250 and 14,700 cells were also used to check grid sensitivity of solutions. Calculated C_p values for the two higher cell count grids were found to differ less than 1%. Velocities, turbulence quantities and NCG mass fraction were specified at the left (inlet) boundary and an exit pressure was specified at the right (exit) boundary. The flow rate was varied to change the flow Reynolds number and the angle of attack was changed by airfoil section rotation. The NCG level was set to $f_g = 1$ ppm.

1.1 Leading Edge Cavitation. Simulations were performed at $\mathrm{Re} = 2 \times 10^6$ and an angle of attack of 4 deg; under these conditions, the cavitation is confined to the front of the hydrofoil. The exit pressure was varied to yield Σ values of 1.76, 1.0, 0.91 and 0.84. Calculated *Cp* values on hydrofoil top surface for two of the four cases are shown in Figs. 2 and 3 together with experimental data, and good correlation is seen. A typical vapor mass fraction distribution is shown in Fig. 4, which shows the cavitation zone on the hydrofoil surface.

1.2 Mid-Chord Cavitation. Simulations were performed at $\mathrm{Re} = 3 \times 10^6$ and an angle of attack of 1 deg. Cavitation inception was seen at $\Sigma = 0.415$; simulations were performed at $\Sigma = 0.43$, 0.38 and 0.34. Calculated and experimental plots of *Cp* on the hydrofoil top surface for two of the three cases are shown in Figs. 5 and 6. A cavitation zone exists in the mid-chord region and

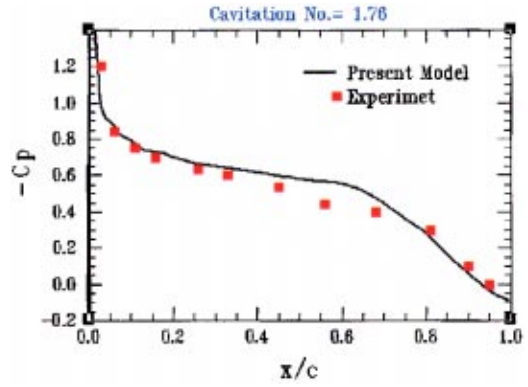

Fig. 2 Pressure variation on the suction side of a hydrofoil; $\Sigma = 1.76$

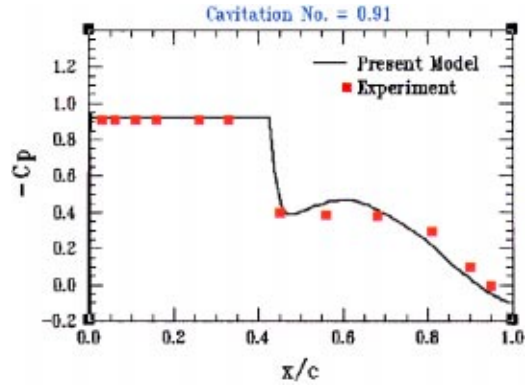

Fig. 3 Pressure variation on the suction side of a hydrofoil; $\Sigma = 0.91$

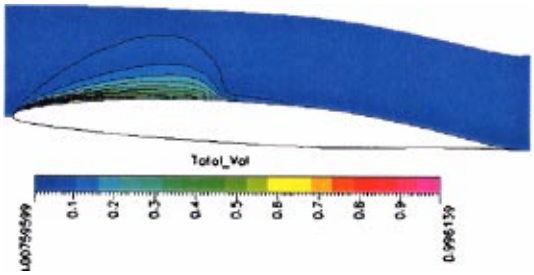

Fig. 4 Computed total volume fraction distributions at cavitation number = 0.91

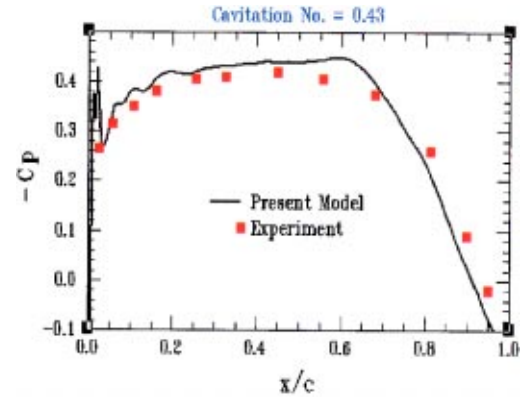

Fig. 5 Pressure variation on the suction side of a hydrofoil; $\Sigma = 0.43$

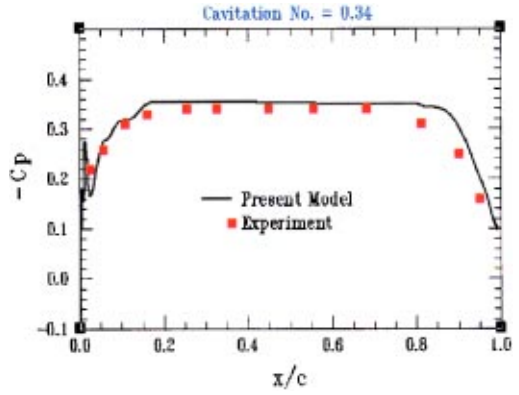

Fig. 6 Pressure variation on the suction side of a hydrofoil; $\Sigma = 0.34$

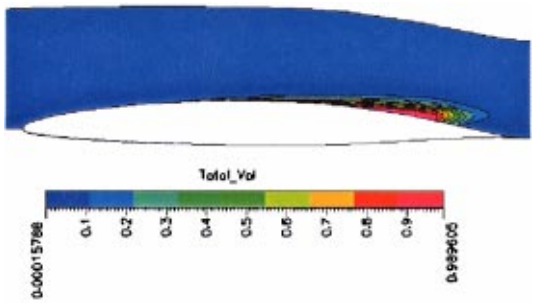

Fig. 7 Volume fractions for $\Sigma = 0.34$, showing mid-chord cavitation

extends towards the trailing edge with decreasing Σ. A view of the cavitation zone for $\Sigma = 0.34$ is shown in Fig. 7.

2 Front Cavitation Over Submerged Cylindrical Bodies The present cavitation model was applied and assessed for cavitating flows over cylindrical submerged bodies with different types of head shapes. Extensive experimental data are reported by Rouse and McNown [20]. The experiments were conducted in a water tunnel with cylindrical test objects 0.025 m in diameter and 0.3048 m in length (1.0 in. and 12 in.). The flow was characterized using the parameters defined as:

$$\mathrm{Re} = \frac{\rho_1 U_\infty d}{\mu_1}, \quad \Sigma = \frac{P_\infty - P_v}{0.5\rho_1 U_\infty^2}, \quad C_p = \frac{P - P_\infty}{0.5\rho_1 U_\infty^2} \tag{27}$$

2-D axisymmetric computational grids were built for these problems. All simulations were performed at a fixed inlet $U_\infty = 10$ m/s and exit pressure levels were varied to achieve the proper inlet pressure P_∞. The NCG level was set to $f_g = 1$ ppm for the deaerated water used in the experiments. Computations were performed on bodies with hemispherical, 45 deg conical, and blunt heads. Details of the body with a 45 deg conical head are shown here.

The computational grid shown in Fig. 8 has two blocks with 61×39 and 124×39 cells (total of 7200 cells). Two other grids with 3375 and 12,700 cells were also used to check grid-independence of the solutions, and the C_p results for the two larger grids again differed by less than 1%. Results were obtained at $\Sigma = 0.3$, 0.4, 0.5, 0.7, 1.0 and 1.3. Calculated and experimental distributions of *Cp* for four of the Σ values are shown in Fig. 9. Computed results match well with the experimental data. Pressure coefficients along the conical head, inside the cavitation zone and the recovery zone show very good agreement. Results for the other two cases (hemispherical and blunt heads) also showed similar agreements.

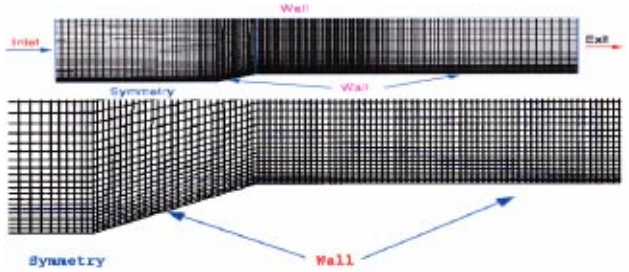

Fig. 8 Computational domain and grid, and grid distribution near a 45-degree conical fore-body

3 Cavitating Flow in a Sharp-Edged Orifice. Pressure-driven flow in a sharp-edged orifice is typically encountered in fuel-injectors, and has received a lot of attention. This is a very challenging flow computation, because the pressure differentials involved can be very high (up to 2500 bar), which drive a flow through a very small orifice, and the problem tests the robustness of the numerical and physical models.

Nurick [21] has published extensive experimental data for cavitation in a sharp-edged circular orifice. Geometrical parameters of the orifice are $D/d = 2.88$ and $L/d = 5$, where D, d, and L are inlet diameter, orifice diameter, and orifice length, respectively. Experiments were done with a fixed exit pressure, $P_b = 0.95$ bar, and the upstream total pressure, P_0, was varied to generate different flow rates. High flow velocities near the orifice entrance generate a zone of very low pressure right after the constriction, where the flow cavitates. This reduces the flow rate (choking type phenomenon) and can lead to surface damage downstream of the orifice.

The discharge coefficient for the orifice, C_d, is of interest and the cavitation number Σ characterizes the flow:

$$\Sigma = \frac{P_o - P_v}{P_o - P_b}, \quad C_d = \frac{\dot{m}_{\text{actual}}}{\dot{m}_{\text{ideal}}} = \frac{\dot{m}_{\text{actual}}}{A_o\sqrt{2\rho_1(P_o - P_b)}} \tag{28}$$

$$C_d = C_c\sqrt{\Sigma} \tag{29}$$

where C_c, the contraction coefficient, was evaluated at 0.62.

The flow is 2-D axisymmetric, and a 2-block structured grid with 2800 cells (20×20 cells in the first block and 20×120 cells in the second) was employed to discretize the geometry with grid clustering around the sharp-edged corner (Fig. 10). The other grids used for grid sensitivity check had 1300 and 5400 cells. The predicted mass flow rates from the 2800 and 5400 cell grids varied by less than 1%. A large number of cases were computed, with the inlet total pressure ranging from 1.9 to 2500 bars; the inlet pressures and the corresponding cavitation numbers are listed in Table 1. NCG level f_g was set to 15 ppm.

Figure 11 shows the comparison between the predicted discharge coefficients C_d with Nurick's correlation, Eq. (29). The calculated values are in very close agreement with the experimental data. The model correctly predicts the inception of cavitation at $\Sigma = 1.7$. The discharge coefficient *Cd* is constant in the non-cavitating flow ($\Sigma > 1.7$), while it clearly shows a square-root dependence on Σ in the cavitation regime. The cavitation easily handles the flows at very low Σ values, where the upstream pressures are very high, over 2000 bar. Simulation of flows with such high pressure-ratios is a difficult task even for single-phase flow; but there were no difficulties in treating this flow with the full cavitation model, indicating the robustness of the numerical procedure.

Solution and Convergence Characteristics. In all the validation cases presented above, the computed minimum pressures are fairly close to the saturation pressures, and all error residuals drop by at least 4 orders of magnitude. Figures 12(*a*) and 12(*b*) show typical convergence plots for the hydrofoil and orifice cases

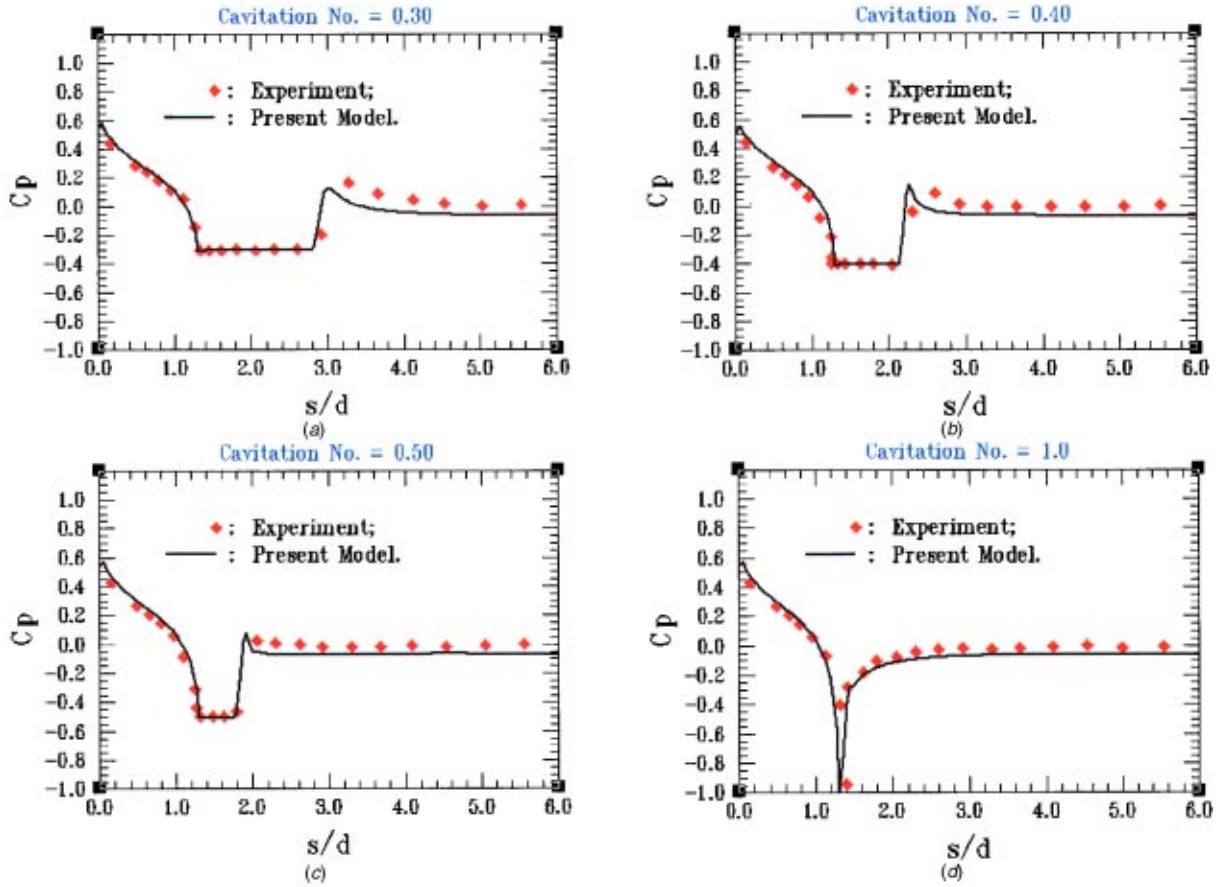

Fig. 9 Comparison between computed and measured Cp over a fore-body with a 45-degree conical head

Fig. 10 Computational grid used for the sharp-edged orifice

respectively. Convergence for the orifice case shows a plateau initially while the initial condition errors in the flow are convected out after which the solution converges rapidly.

Applications of the Full Cavitation Model

While the results presented here focused on the validation aspects of the cavitation model, this model has also been used successfully on a variety of different problems for research as well as commercial applications. These include:

1. Cavitation in diesel fuel injectors with complex multi-port geometries and time-varying geometries and pressure loading

Table 1 Total inlet pressure and cavitation number

$P_o \times 10^5$(Pa)	1.9	2.0	2.5	3.0	3.75	5.0
Σ	1.0004	1.001	1.009	1.019	1.101	1.226
$P_o \times 10^5$(Pa)	10	50	100	500	1000	2500
Σ	1.327	1.446	1.590	1.704	1.871	1.963

2. Cavitation in rocket turbomachinery, e.g., cavitation in rocket inducers and impellers has been analyzed, and results validated against experiments. This work is being published separately [22,23].
3. Automotive Vane and Gear pump oil pump design optimization.
4. Cavitation in automotive thermostatic valves.

In all of these applications, the basic set of equations and constants described in previous sections have been found to generate accurate solutions with robust convergence characteristics.

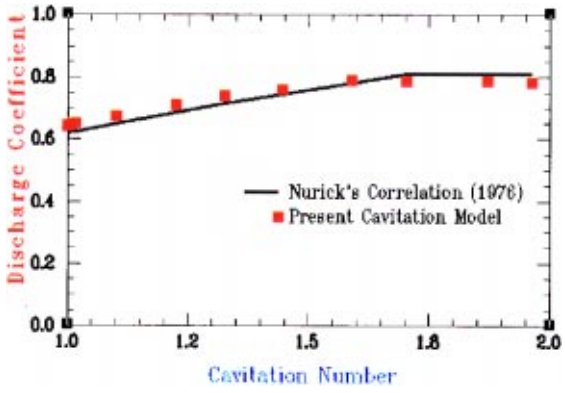

Fig. 11 Orifice cavitation: comparison of cavitation model predictions with Nurick's correlation

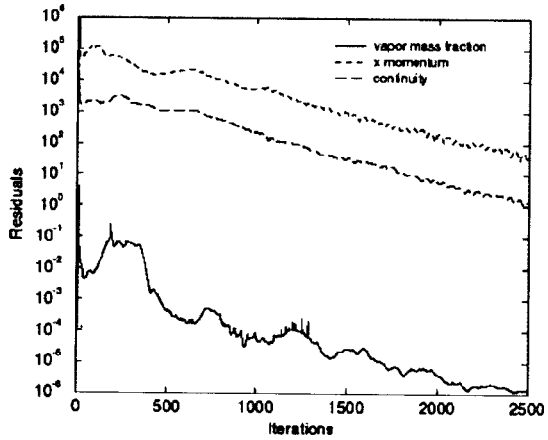

(*a*) ***Hydrofoil, Σ=0.34***

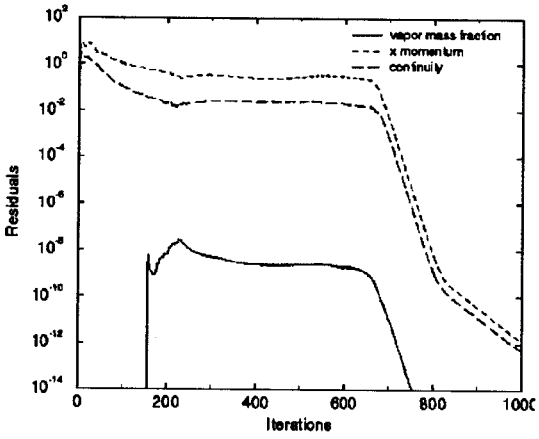

(*b*) ***Orifice, Upstream pressure=500 Bar***

Fig. 12 Convergence characteristics for two of the validation cases presented above; (*a*) hydrofoil, (*b*) orifice

Potential Extensions and Collaborations

The current limitations in the implementation of Full Cavitation Model in CFD-ACE+ include isothermal flow assumption, and a fixed, uniform mass concentration of NCG. Both of these assumptions can be easily relaxed by solving appropriate additional transport equation, and modifying corresponding parameters like P_{sat} and f_g. The present model provides many useful flow characteristics such as local gradients of pressure, density and volume fractions, general location and approximate extents of vapor regions, and approximate values of turbulence intensity. Approximate bubble size variations can also be deduced if desired. Since the model seems to be reasonably accurate for predictions of performance parameters over a wide range of conditions, it is very likely that the detailed flow characteristics are also in the realistic ranges. Such details can provide a sound foundation for the development of correlations for cavitation induced noise levels. A preliminary module based on integration of Lighthill equation using a Kirchoff-Ffowacs-Williams-Hawking (KWFH) solver has already been developed and used on vane pump noise predictions. Likewise, appropriate additional equations and modules can be incorporated for the predictions of approximate location and magnitude of cavitation induced surface damage.

Because of the intricate inter-coupling of various physical models and numerical solution procedures and computer software data structures, the model extensions mentioned above will be best performed by universities and/or interested R&D groups working in close collaboration with the authors of the present paper.

Summary and Conclusions

A comprehensive model for cavitating flows has been developed and incorporated into an advanced CFD code for performance predictions of engineering equipment. This CFD code and cavitation model was applied to a number of validation and demonstration problems to verify the accuracy of the model and to assess the convergence performance on difficult engineering problems. Presented here were validation results for high-speed flow cavitation on hydrofoil and submerged cylindrical bodies, and in both cases the predictions from the cavitation model were in very good agreement with the experimental data. The model was also applied to cavitating flow through an orifice and computed results compared well with experimental data, even for very severe flow conditions involving very high pressure differentials across the orifice. The full cavitation model, coupled with CFD-ACE+ code, can be applied to a wide range of problems, and be a valuable prediction tool for design verification and optimization. Collaborative efforts are encouraged to extend this model, e.g., to include thermal effects and the prediction of cavitation damage.

Acknowledgments

This work was funded in part under NSF SBIR Grant No. DMI-9801239; this support is gratefully acknowledged. The authors would like to thank:

1. Dr. N. Vaidya and Ram Avva for their contributions in the development of two earlier models, which laid the basis for the current model; and
2. Mr. Dennis Gibson of Caterpillar, Inc., for his introduction and initial support for the development of cavitation model (even though it has taken over eight years to meet the challenge of developing a practical capability).

Nomenclature

C = hydrofoil chord length
C_e, C_c = constants in vapor generation condensation rate expression
D, d = diameter
f_v, f_g = vapor, gas mass fraction
k = turbulence kinetic energy
m_{actual} = actual orifice mass flow
m_{ideal} = ideal orifice mass flow
n = bubble number density
P = pressure
P_v = vapor pressure
P'_{turb} = turbulence pressure fluctuation
Q = flow rate
R = universal gas constant
R_e, R_c = vapor generation, condensation rates
Re = Reynolds number
$\Re_B$ = bubble radius
S = surface tension
T = temperature
U_∞ = freestream velocity
V = fluid velocity vector
V_{ch} = flow characteristic velocity
W = molecular weight of non-condensible gas
We = Weber number

Greek

α = angle of attack
α_e, α_v, α_g = liquid, vapor, gas volume fraction
ρ, ρ_e, ρ_v = density of mixture, liquid, vapor
σ = surface tension
μ, ν = dynamic, kinematic viscosities
Σ = cavitation number

References

[1] Kubota, A., Kato, H., and Yamaguchi, H., 1992, ''A New Modeling of Cavitating Flows: A Numerical Study of Unsteady Cavitation on a Hydrofoil Section,'' J. Fluid Mech., **240**, pp. 59–96.

[2] Wang, Y-C. and Brennen, C. E., 1994, ''Shock Wave Development in the Collapse of a Cloud of Bubbles,'' ASME FED, Vol. 194, Cavitation and Multiphase Flow, pp. 15–19.

[3] Keller, A. P., and Rott, H. K., 1997, ''The Effect of Flow Turbulence on Cavitation Inception,'' ASME FED Meeting, Vancouver, Canada.

[4] Janssens, M. E., Hulshoff, S. J., and Hoejijmakers, H. W. M., ''Calculation of Unsteady Attached Cavitation,'' 28th AIAA Fluid Dynamics Conference, AIAA-97-1936.

[5] Hsiao, C.-T., and Pauley, L. L., 1997, ''Numerical Study of Tip Vortex Cavitation Inception Using a Bubble Dynamics Model,'' ASME FED Meeting, Vancouver, Canada.

[6] Choi, J. K., and Kinnas, S. A., 1997, ''Cavitating Propeller Analysis Inside of a Tunnel,'' ASME FED Meeting, Vancouver, Canada.

[7] Fortes-Patella, R., and Reboud, J. L., 1998, ''A New Approach to Evaluate the Cavitation Erosion Power,'' ASME J. Fluids Eng., **120**, pp. 335–388.

[8] Kunz, R. F., Boger, D. A., Chyczewski, T. S., Stinebring, D. R., Gibeling, H. J., and Govindan, T. R., 1999, ''Multi-Phase CFD Analysis of Natural and Ventilated Cavitation about Submerged Bodies,'' FEDSM99-3764, ASME Fluids Eng. Conf., San Francisco, CA.

[9] Roth, K. W., and Massah, H., 1999, ''Prediction of Caviation Damage: A Comparison of Computational Fluid Dynamics and Experimental Results,'' FEDSM99-6760, ASME Fluids Eng. Conf., San Francisco, CA.

[10] Avva, R. K., Singhal, A. K., and Gibson, D. H., 1995, ''An Enthalpy Based Model of Cavitation,'' ASME FED Summer Meeting, Hilton Head Island.

[11] Singhal, A. K., Vaidya, N., and Leonard, A. D., 1997, ''Multi-Dimensional Simulation of Cavitating Flows Using a PDF Model for Phase Change,'' ASME FED Meeting, Paper No. FEDSM'97-3272, Vancouver, Canada.

[12] Brennen, C. E., 1995, *Cavitation and Bubble Dynamics*, Oxford University Press, Oxford.

[13] Markatos, N. C., and Singhal, A. K., 1982, ''Numerical Analysis of One-Dimensional, Two-Phase Flow a Vertical Cylindrical Pump,'' Adv. Eng. Software, **4**(**3**), pp. 99–106.

[14] Stoffel, B., and Schuller, W., 1995, ''Investigations Concerning the Influence of Pressure Distribution and Cavity Length on Hydrodynamic Cavitation Intensity,'' ASME Fluids Eng. Conf., Hilton Head, SC.

[15] Hinze, J. O., 1975, *Turbulence*, 2nd Ed. McGraw Hill, New York.

[16] Watanabe, M., and Prosperetti, A., 1994, ''The Effect of Gas Diffusion on the Nuclei Population Downstream of a Cavitation Zone,'' ASME FED Vol. 190, Cavitation and Gas Liquid Flow in Fluid Machinery and Devices.

[17] Reisman, G., Duttweiler, and Brennen, C., 1997, ''Effect of Air Injection on the Cloud Cavitation of a Hydrofoil,'' ASME FED Meeting, Vancouver, Canada.

[18] CFDRC, 2001, ''CFD-ACE+ Theory and Users' Manuals and Tutorials.''

[19] Shen, Y. J., and Dimotakis, P. E., 1989, ''The Influence of Surface Cavitation on Hydrodynamic Forces,'' Proc. 22nd ATTC, St. Johns.

[20] Rouse, H., and McNown, J. S., 1948, ''Cavitation and Pressure Distribution, Head Forms at Zero Angle of Yaw,'' Iowa Institute of Hydraulic Research, Iowa City.

[21] Nurick, W. H., 1976, ''Orifice Cavitation and its Effect on Spray Mixing,'' ASME J. Fluids Eng., **98**, pp. 681–687.

[22] Athavale, M. M., Li, H. Y., Jiang, Y, and Singhal, A. K., 2000, ''Application of the Full Cavitation Model to Pumps and Inducers,'' ISROMAC-8, Honolulu, HI.

[23] Athavale, M. M., Li, H. Y., and Singhal, A. K., 2001, ''Numerical Analysis of Cavitating Flows in Rocket Turbopump Elements,'' Paper No. AIAA-2001-3400.

Continuous Wavelet Transforms of Instantaneous Wall Pressure in Slug and Churn Upward Gas-Liquid Flow

Heather L. McClusky

Mary V. Holloway

Donald E. Beasley
Fellow ASME

Jay M. Ochterbeck

Department of Mechanical Engineering,
Clemson University,
Clemson, SC 29634

Continuous wavelet transforms are employed to determine the time-localized frequency content (scalogram) of instantaneous wall pressure signals in upward gas-liquid flow. The flow conditions correspond to well-defined slug flow, well-defined churn flow, and flows near the transition from slug-to-churn flow. Scalograms demonstrate that the frequency content of the pressure signals is time-dependent, and visual observations of the flow conditions suggest that the time-dependent frequencies are related to identifiable physical behaviors of the flow. In well-defined slug flow, the scalograms are characterized by the presence of a dominant frequency throughout the duration of the signal and by frequency shifting events. Scalograms representing well-defined churn flow contain intermittent frequencies, and the energy density in churn flow is spread over a wider range of frequencies than in slug flow. The present results provide evidence that flows near transition alternately display characteristics of both well-defined slug and well-defined churn flows. [DOI: 10.1115/1.1490376]

Introduction

Upward gas-liquid flow is characterized by distinct patterns of the phases in the pipe. The phases are distributed across the flow cross-section and along the flow direction. For a given liquid flow rate, a dominant characteristic of the phase distribution remains constant over a range of gas flow rates; such identifiable physical behaviors are used to classify upward gas-liquid flow conditions in terms of flow regimes. The primary flow regimes in upward gas-liquid flow are bubbly, slug, churn, and annular. These flow regimes are traditionally identified through visual observation. The focus of the present study is on flow conditions corresponding to slug and churn flows. Slug flow is characterized by alternating regions of clearly defined gas slugs and liquid slugs. The liquid slugs may or may not contain small gas bubbles, and the large-scale gas slugs, or Taylor bubbles, fill the cross section except for a thin liquid film at the wall. Churn flow is characterized by oscillatory liquid motion, with both upward and downward motion of the liquid occurring in each cycle. The transition from slug-to-churn flow is progressive, and visual characteristics of the phase distributions near the transition point may be difficult to interpret.

For a steady-state flow condition, characteristic features of the flow are not spatially or temporally homogeneous. Characteristic features include the physical size of the flow structures and the frequency of the occurrence of events; such features vary in time. For slug flow conditions, the dominant feature of the flow is the alternate passage of the Taylor bubbles and the liquid slugs; however, variations in the Taylor bubble length and the liquid slug length are observed in the flow. The density and distribution of small bubbles in the liquid slug also may vary. A typical event that occurs in slug flow is the coalescence of consecutive Taylor bubbles. The coalescence events are observed to occur over non-uniform intervals of time. In churn flows, the frequency of bursting appears highly non-uniform in time where a sequence of bursts each with a short time duration may be followed by a sequence of bursts with each burst having a longer time duration. For flows near the slug-to-churn flow transition, the characteristic features of both slug flow and churn flow are present.

As described in the following Upward Gas-Liquid Flow section, previous investigations of upward gas-liquid flow analyzed local, instantaneous measurements to gain insight into the averaged frequency content. Fourier energy spectra were calculated using Fourier transform methods to analyze the signals from these local, instantaneous measurements: the analysis yielded the averaged frequency content for the entire time series. Upward gas-liquid slug and churn flows contain similar averaged frequency characteristics, as both regimes exhibit dominant frequencies in a narrow bandwidth of low frequency energy. Slug flow displays repeating variations in local instantaneous variables that are associated with the alternate passage of liquid slugs and Taylor bubbles. Local instantaneous measurements in churn flow exhibit dominant frequencies that are associated with oscillatory liquid motion. However, in the absence of windowing or other localization methods, Fourier transforms provide no information concerning the time variation of frequency content in the time series. The time-frequency content of instantaneous data may be realized through numerous mathematical alternatives including windowed Fourier transforms, Wigner-Ville functions and wavelet transforms. Wavelet transforms illuminate two important properties of time series: the time variation of frequency content and the localization in time of transient phenomena.

In the present study, continuous wavelet transforms of time-resolved pressure signals of well-defined slug flow and well-defined churn flow, and flows near the transition between the two regimes are implemented to quantify time-frequency characteristics of the flow conditions. Changes in the physical size of flow structures and in the occurrence of events present in the flow are quantified by examining the time-varying frequency characteristics. Flow conditions at two liquid superficial velocities are studied over a range of gas superficial velocities. Each of the present flow conditions is steady in time, and the corresponding pressure signals are statistically stationary over long time scales.

Contributed by the Fluids Engineering Division for publication in the JOURNAL OF FLUIDS ENGINEERING. Manuscript received by the Fluids Engineering Division September 7, 2000; revised manuscript received March 4, 2002. Associate Editor: J. Katz.

Upward Gas-Liquid Flow: Transition Models and Experiments

The information presented in this section is restricted to the physics of upward gas-liquid flow. The following section, Wavelet Transform Analysis and Applications, addresses the wavelet transform method used in the present study and previous applied studies using time-frequency localization techniques.

The purpose of this section is to provide the fundamental physics of the slug and churn flow regimes to allow interpretation of the continuous wavelet transforms. This section is divided into two subsections: Flow Regime Transition Models and Experiments. Proposed mechanisms for the underlying physics of the slug-to-churn transition, and the mechanistic models for this flow transition are presented in the Flow Regime Transition Model subsection. The Experiments subsection reviews previous investigations that address instantaneous measurements in gas-liquid flows. Both models and experiments are presented to allow comparison of the classification of present flow conditions with previous works.

Flow Regime Transition Models. In upward gas-liquid flows, the parameters that influence flow regime transition include fluid properties, pipe geometry, pressure, and gas and liquid flow rates. Flow regimes may be identified using a flow regime map, which is a two-dimensional plot of parameters such as the gas superficial velocity and the liquid superficial velocity. Flow regime maps have been proposed with dimensional and non-dimensional coordinates. However, there is no theoretical basis to generalize the results; therefore, the non-dimensional coordinates do not have a distinct advantage over the dimensional coordinates (Jayanti and Hewitt [1]), and the resulting flow regime maps are limited to a particular application. The pipe geometry, fluid properties, and pressure are specified for a given flow regime map, whether the coordinates are dimensional or non-dimensional. The transition boundaries on the flow regime map are obtained from experimental measurements and from mechanistic models of proposed transition mechanisms.

For a fixed pipe geometry, given fluid properties, and pressure, the slug-to-churn flow regime transition depends on gas and liquid flow rates. In general, as the liquid flow rate is increased, experimental data show that the critical gas flow rate associated with flow regime transition increases. The slug-to-churn flow transition boundary is challenging to predict for various reasons, including inconsistencies in the description of the observed flow patterns, difficulties in interpretation of the visual data, and a lack of a clear understanding of the underlying mechanism(s). For example, McQuillan and Whalley [2] developed transition models and compared their models with existing experimental data. Their model correctly predicted churn flow for only nine out of 341 experimentally observed churn flow conditions. For slug flow, half of the experimental measurements were predicted correctly. Higher success rates were obtained for the bubbly and annular regimes.

Following Jayanti and Hewitt [1], the proposed slug-to-churn flow transition mechanisms are categorized as:

1 entry length mechanism,
2 wake effect mechanism,
3 bubble coalescence mechanism, and
4 flooding mechanism.

For each of the four mechanisms, numerous mechanistic models have been proposed. Recent models in each of the four categories are briefly reviewed here.

The entry length mechanism of Taitel et al. [3] presented churn flow as an entry phenomenon that develops into stable slug flow further downstream in the pipe. As the flow develops in the pipe, the length of a liquid slug increases until sufficient liquid is present to form a stable slug. At this point in the pipe slug flow is observed. The model predicts the length over which the flow regime is churn flow.

The second mechanism is the wake effect mechanism. Consider a slug flow condition just prior to the transition to churn flow. This condition corresponds to a train of consecutive Taylor bubbles in the pipe, and the average liquid slug length is small compared to the average Taylor bubble length. A wake region behind the bubble forms and the liquid slug becomes unstable. The liquid slug is destroyed, Taylor bubbles coalesce, and the flow transitions to churn flow. Two mechanistic models of this proposed mechanism are reviewed here. Mishima and Ishii [4] modeled the wake effect mechanism based on void fraction. In this model as the flow transitions to churn flow, the effect of the wake is modeled by equating the void fraction of the entire Taylor bubble and liquid slug region to that of the Taylor bubble region. Jayanti and Hewitt [1] stated that the predicted gas flow rate for the model of Mishima and Ishii [4] agreed well with experimental data at small to moderate gas flow rates. The second wake effect model reviewed here is that of Chen and Brill [5]. The model of Chen and Brill [5] is based on a maximum void fraction of the gas in the liquid slug and a minimum dimensionless liquid slug length. At the transition from slug-to-churn flow, Chen and Brill [5] assumed that the maximum possible void fraction was 0.52, and the minimum dimensionless slug length was 0.15. Chen and Brill [5] showed that the predicted flow regime transition agreed well with experimental observations from previous studies.

The bubble coalescence mechanism is based on the appearance of aerated slugs just prior to transition to churn flow. Brauner and Barnea [6] attributed the slug-to-churn transition to bubble coalescence. The bubble coalescence model was based on the gas hold-up in the liquid slug. Coalescence was proposed to occur when the turbulent dispersion forces are greater than the surface tension forces. It was assumed that the maximum void fraction in the slug is independent of the amount of turbulent energy and the maximum void fraction was 0.52. Jayanti and Hewitt [1] showed that results from the transition model of Brauner and Barnea [6] predict the flow regime transition quite well at high gas flow rates.

Flooding is a phenomenon that occurs in countercurrent flows, such as for the Taylor bubble region of slug flow. In this region, the liquid film flows downward and the bubbles flow upward. For a fixed liquid flow rate, as the gas flow rate is increased interfacial waves are formed. For a sufficiently large gas flow rate, the waves form a liquid region that bridges the cross section of the pipe. Transition boundaries based on the physics of flooding are supported by pressure gradient measurements near the slug-to-churn transition (Jayanti and Hewitt [1]). McQuillan and Whalley [2] modeled flooding using the Nusselt relation for film velocity and a semi-empirical model for flooding velocities to predict the flow regime transition. The transition criteria of McQuillan and Whalley [2] predicted the experimental data quite well for small gas flow rates (Jayanti and Hewitt [1]). Jayanti and Hewitt [1] incorporated the effect of the falling film length and employed a more comprehensive film velocity relationship valid over a wider range of Reynolds numbers. Jayanti and Hewitt [1] showed that their flooding model predicted the transition boundary more accurately than the flooding model of McQuillan and Whalley [2].

Experiments. Together, visualization of the flow condition and analysis of time-resolved measurements such as wall pressure or void fraction provide insight into upward gas-liquid flow. Wall pressure measurements contain both global and local hydrodynamics, while void fraction represents a purely local, area-averaged variable. Analysis techniques for extraction of flow characteristics from such measured variables include energy spectral density functions, probability density functions, classical statistical measures, and fractal and chaos techniques.

In the work of Hubbard and Dukler [7], wall pressure fluctuations of a horizontal gas-liquid flow were analyzed using Fourier transforms to obtain the averaged frequency content presented as energy spectra. Further, several studies have examined Fourier energy spectra of instantaneous void fraction measured in upward gas-liquid systems (see for example, Jones and Zuber [8]; Vince

and Lahey [9]). These investigations, as well as those employing wall pressure (Langford [10]), reveal that slug and churn upward gas-liquid flow contain similar Fourier energy spectra characteristics, as both regimes exhibit dominant frequencies in a narrow bandwidth of low frequency energy.

Statistical methods for characterization of gas-liquid flows include analysis of instantaneous measured variables using higher-order moments and probability density functions. Jones and Zuber [8], Vince and Lahey [9], and Costigan and Whalley [11] analyzed instantaneous measurements of void fraction, and Matsui [12,13] and Langford et al. [14] measured wall pressure or differential pressure in vertical two-phase flows. Bubbly and annular flows were consistently described by unimodal probability density distributions, but both bimodal and unimodal distributions resulted from slug and churn flows. Jones and Zuber [8], Vince and Lahey [9], Matsui [12,13], and Langford et al. [14] visually identified the flow regimes according to traditional classification and these investigations revealed a gradual change in the shape of the probability density function within a flow regime. Rather than visually identifying the flow regime, Costigan and Whalley [11] identified six flow regimes in upward gas-liquid flow by analyzing time traces of instantaneous void fraction measurements and corresponding probability density distributions. Variance, skewness, and kurtosis of the measured variable were examined by Vince and Lahey [9] and by Langford et al. [14] for possible flow regime identification.

Recent investigations suggest that gas-liquid flow is consistent with deterministic chaos under certain operating conditions, and that chaos measures show promise as flow regime identification techniques. Franca et al. [15] used correlation dimension estimates and phase space trajectories from pressure data to identify the presence of chaos in a horizontal air-water flow. The authors suggested that the number of slopes in the correlation integral and the shape of the trajectory in phase space can identify the flow regime. Drahos et al. [16] identified chaotic behavior in pressure measurements of a horizontal air-water flow. Phase space trajectories, Lyapunov exponents, and correlation dimension estimates were used to characterize pressure measurement from a horizontal flow in a rectangular tube as consistent with chaos by Cai et al. [17]. The correlation dimension was identified by Cai et al. [17] as a possible flow regime identifier, but is not independent of mass flux. Langford et al. [14] and Langford [10] demonstrated a correlation between chaos measurements, such as Kolmogorov entropy, and flow parameters in upward gas-liquid flows. Biage et al. [18] studied the flooding transition using correlation dimensions calculated from film thickness measurements at five axial locations in a vertical test section. Their results showed that the flooding transition point was associated with a dramatic decrease in the correlation dimension of the film thickness measurements.

Wavelet Transform Analysis and Applications

The purposes of this section are to present the continuous wavelet transform method employed in the present investigation, and to review previous studies in the area of fluid mechanics that extracted time-dependent frequency information from instantaneous data; emphasis is placed on multiphase flow systems. In this investigation, continuous wavelet transforms are employed to obtain the wavelet energy density of wall pressure measurements.

Wavelet Transform Analysis. The development of the nascent research area of continuous wavelet transforms began two decades ago, where this research area continues to evolve at a rapid pace in diverse fields such as mathematics, physics, science, engineering, and medicine. A historical account of the development and formalization of the continuous wavelet transform is provided by Farge [19] and Daubechies [20]. The origin of the continuous wavelet transform stems from diverse research areas, which has led to a wealth of papers, and continual progress toward standardization of this data analysis method. The literature on continuous wavelet transforms is mathematically intense. Farge [19] offers a mathematically rigorous, yet accessible, presentation of wavelet transforms. A detailed description of the implementation of the continuous wavelet transform to obtain the wavelet coefficients is provided by Jordan et al. [21]. Lewalle [22] presents both the theoretical and the applied aspects of the continuous wavelet transform with particular emphasis on post-transform algorithms implemented to obtain energy and related features from the wavelet coefficients. In the present paper, the key elements of the wavelet transform are presented.

A wavelet is a mathematical function that meets the following conditions: admissibility, similarity, invertibility, regularity, and cancellations (Farge [19]). Numerous wavelet families exist; therefore, careful selection of the wavelet allows accurate extraction of the signal characteristics of interest. The three wavelets most commonly employed in the area of fluid mechanics are the Mexican hat, the slope detector, and the Morlet wavelet. Two real-valued wavelets that are employed to detect sharp transitions in the signal are (1) the negative of the second derivative of the Gaussian (Mexican hat or Marr wavelet) and (2) the negative of the first derivative of the Gaussian (slope detector wavelet). The Mexican hat wavelet is used to detect peaks in the signal whereas the slope detector wavelet is useful for distinguishing changes in the slope of the signal. The Morlet wavelet is a locally periodic, complex-valued wavelet that may be used to separate amplitude and phase information contained in a signal. The pressure signals in the present study are quasi-periodic; therefore, the complex-valued Morlet wavelet was selected as the analyzing wavelet. The complex-valued Morlet wavelet, also referred to as the Gabor wavelet (Morlet et al. [23] and [24], Mallat [25]), is mathematically defined as

$$\varphi(t)=\pi^{-1/4}e^{ik_{\varphi}t}e^{-t^2/2} \tag{1}$$

or the modulation of a plane wave with a Gaussian envelope. The Morlet wavelet used in the present investigation had a center frequency k_{φ} of 5 rad/s, which satisfies the condition of admissibility. In general, scaled and translated wavelets are generated from the wavelet as

$$\varphi_{lt'}=l^{-1/2}\varphi\left[\frac{t-t'}{l}\right] \tag{2}$$

where l is the scaling parameter and t' is the translation parameter. A continuous wavelet transform produces wavelet coefficients by performing the inner product or convolution integral of the signal with the complex conjugate of the scaled and translated wavelets. The wavelet transform in physical space is

$$W[l,t']=\int P_f(t)\varphi^*_{lt}dt \tag{3}$$

where $W[l,t']$ represents the wavelet coefficients and $\varphi^*_{lt'}$ indicates the complex conjugate of the scaled and translated wavelet. This convolution integral also may be computed in Fourier space. For a complex-valued wavelet, such as the Morlet wavelet, the wavelet coefficients contain both amplitude and phase information. In the present study, the complex-valued wavelet coefficients are used to obtain the time-localized frequency content of the pressure signals. The phase information alone is unimportant; therefore, the modulus of the wavelet coefficients is used for further calculations. The energy level of a given signal is obtained by squaring the modulus of the wavelet coefficients (Farge [19]), and the space-scale energy density (Farge [19]), or wavelet energy density, is defined as

$$E[l,t']=l^{-1}|W[l,t']|^2. \tag{4}$$

In this definition, the wavelet energy density is a function of time and scale.

In the present study, the continuous wavelet transforms of the pressure signals were performed using the Wavelab software package (Mallat [25]). The wavelet transform was performed in Fourier space. The wavelet energy densities of the pressure mea-

surements are calculated as defined in Eq. (4). To relate each scale of the wavelet to a frequency, possibly a more meaningful parameter, a functional relationship was established (Jordan et al. [21], Lewalle [22]). The relationship between a given wavelet scale l and the frequency f is

$$f = l^{-1} f_s \frac{k_\varphi}{2\pi}. \tag{5}$$

The present experimental time series were sampled at $f_s = 300$ Hz, and the center frequency of the wavelet was $k_\varphi = 5$ rad/s. Using the relationship in Eq. (5), wavelet energy density is expressed as a function of time and frequency. The wavelet energy density is plotted using a linear scale in time and a logarithmic scale for frequency, and the resulting plot of the wavelet energy density is referred to as a scalogram.

Wavelet Transform Applications. Kovačević and Daubechies [26] provided an overview of the use of wavelets through examples from quite diverse research fields. In the research area of fluid mechanics, Farge pioneered the use of wavelet transforms with application in turbulence. Farge [19] in 1992 provided a historical account and review of the application of wavelet transforms to turbulent flows, and in 1996 Farge et al. [27] updated the review of papers in this subject area. The fluid mechanics literature is rich with papers employing wavelet techniques, and a comprehensive review here is not possible. A selection of recent papers is provided instead. In the area of signal analysis, recent papers include Higuchi et al. [28], Poggie and Smits [29], Buresti et al. [30], Li [31], and Lewalle et al. [32]. Wavelet transforms are well suited to providing insight into the large-small scale interactions in turbulent flows as described by Yeung et al. [33]. Lewalle [34] and Moridis et al. [35] explored wavelets in the context of numerical computations of turbulent flows and discretization schemes for numerical solution of equations.

The localized frequency information provided by wavelet transforms has been realized in a variety of multiphase flow systems. A multi-resolution method was implemented by Bakshi et al. [36] on local gas holdup measurements in a bubble column. The authors suggest that this discrete wavelet transform based technique efficiently extracts flow features in a time-frequency basis. Hervieu and Seleghim [37] presented an instantaneous flow pattern transition detection method that exploits the non-stationary characteristic of flow pattern transition using the time-frequency covariance of conductivity signals. Li and Tomita [38] examined the time-frequency characteristics of pressure measurements in a solid-gas, horizontal pipe flow. Continuous wavelet transforms were used to obtain the time-localized frequency information. Li and Tomita [38] showed that both high frequencies and low frequencies are simultaneously present in the flow.

Experimental Facility and Measurements

The air-water experimental facility used to obtain the data for the current study is shown in Fig. 1. The vertical test section was constructed from alternating sections of aluminum and quartz tubing having the same internal diameter (0.022 m). The aluminum sections allowed flush mounting of a strain-gauge type pressure transducer for local instantaneous pressure measurements. The two 1.2 m sections of quartz tubing allowed visual determination of the flow regimes; multiple digital images of each flow condition were recorded using a digital camera.

Two-phase flow was generated by injecting filtered oil-free compressed air through a porous disk (40 μm average pore size) into the upward flowing water stream at a tee junction in the piping. From this mixing point, the test section extended 6 m in the vertical direction and the two sections of quartz tubing were placed 1.8 m and 4 m above the mixing point. The air-water mixture discharged from the vertical flow section into a gas-liquid separator vented to atmosphere and the water returned to a constant head tank providing a closed loop system. Precise control of

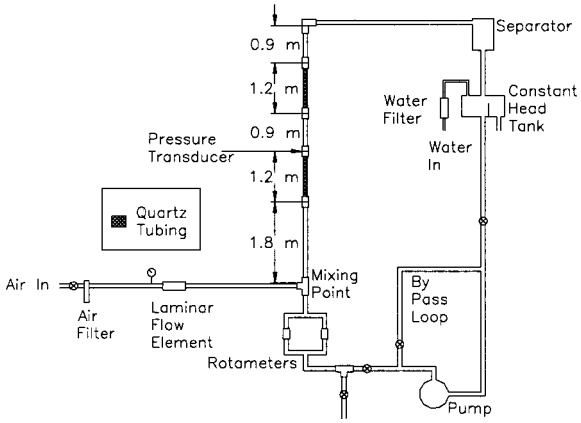

Fig. 1 Drawing of the experimental facility

the water flow rate was accomplished by employing a large volume constant head tank, a pump by-pass loop, and several control valves. Two water rotameters were arranged in parallel and used individually to measure the water flow rate. The absolute uncertainties in the two liquid superficial velocities for this study were less than ± 0.0013 m/s. The surface tension of the water used in the present investigation was measured using a balance having a resolution of one milligram and a platinum-iridium ring (ASTM D 1590-60). The average surface tension of water samples collected after a wide range of residence times in the flow loop was 71.1 $\pm 0.1 \times 10^{-3}$ N/m (95%) at 22°C. A laminar flow element was used to measure the air flow rate in the horizontal pipeline prior to injection into the test section. Additionally, a Heise gauge measured the pressure at the laminar flow element and was used in conjunction with the average pressure at the pressure transducer to determine the gas superficial velocity at the measurement location. The gas superficial velocities at the pressure transducer ranged from 0.74 to 2.6 m/s, and the corresponding relative uncertainty was determined to range from $\pm 1\%$ to $\pm 7\%$, with a typical relative uncertainty of $\pm 3\%$.

The Cooper pressure transducer (Model # PSG 112) located 3 m above the mixing point at the junction between the quartz and aluminum tubing provided time-resolved pressure measurements. Placement of the pressure transducer downstream of the quartz tubing section allowed visual identification of the flow pattern to coincide with the measured pressure. Before installation, the pressure transducer was calibrated using a reference Heise gauge. The calibration identified the slope for the transducer as constant within $\pm 0.2\%$ at all times. Initial calibrations also revealed that the zero pressure reading had a drift of up to ± 400 Pa. Therefore, zero pressure readings were collected before and after each data set. The relative uncertainties in the mean pressure and pressure fluctuations were $\pm 2\%$ and $\pm 0.2\%$, respectively.

The design of the facility provided the ability to maintain steady flow rates of air and water, and all data were acquired for steady-state operating conditions. Instantaneous pressure data were acquired using an Analog Devices 12 bit A/D board (Model # STB-50). The sampling rate for all data acquired in these experiments was 300 Hz with a sample time of 57 s. Of the 57 s of data collected for each operating condition, 2^{14} (16,384) data points were used for analysis. Fourier energy spectra showed that no significant frequency content was present above 20 Hz thereby, confirming that the selected sample rate was appropriate for this investigation.

Results

Results are presented for two liquid superficial velocities, $U_l = 0.0055$ and 0.055 m/s. For these two liquid flow rates, the flow regime transitions from slug to churn flow with increasing gas

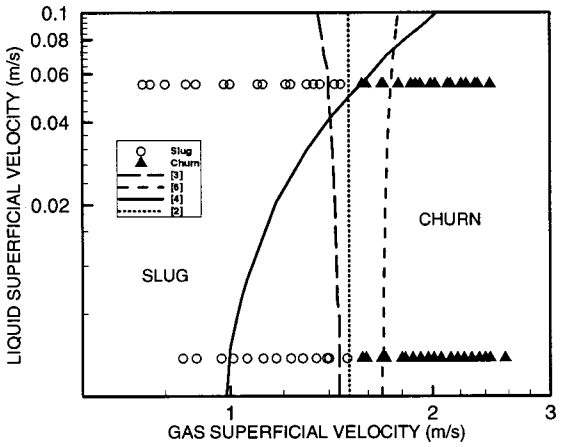

Fig. 2 Flow regime map showing the experimental data from the present study and flow regime transition boundaries (D_p =22 mm, Fluids: Air and Water, Temperature=20°C, Pressure =101 kPa). Transition boundaries were predicted from the entry length model of Taitel et al. [3], the bubble coalescence model of Braunner and Barnea [6], the wake effect model of Mishima and Ishii [4], and the flooding model of McQuillan and Whalley [2].

flow rate. Gas superficial velocities ranging from 0.7 to 2.6 m/s were examined. Wall pressure measurements were obtained for well-defined slug flow, well-defined churn flow, and flows near transition for each superficial liquid velocity. Before detailed discussion of wavelet energy density, the present data are compared to existing flow regime maps, and representative energy spectra are discussed.

An underlying assumption of this analysis is that the long-term behavior of the system is steady, and that the instantaneous pressure measurements are statistically stationary. To confirm that these conditions were achieved in the experiments, gas and liquid flow rates were carefully monitored and remained constant during the experiments, and extensive statistical analysis of the signals was performed. These analyses included comparison of the mean, standard deviation, histogram, and energy spectrum of the entire signal (16,384 data points) with smaller portions of the same signal. As determined by these measures, the present signals are statistically stationary over time scales that are long compared to single events within the flow, such as the passage of bubbles in slug flow, or the bursting phenomena in churn flow.

The flow regime map in Fig. 2 shows the 65 experimental data sets examined in the present investigation and the predicted flow regime transitions as determined using mechanistic models. Flow regime identification was accomplished through visual observation according to the major flow regimes as identified by Hetstroni [39] and Tong and Tang [40]. In the present investigation, the onset of churn flow was identified when destruction of water slugs occurred, producing the characteristic oscillatory liquid motion associated with churn flow. Under some flow conditions classified as churn flow, a few Taylor bubbles having a highly turbulent wake region persisted. Four slug-to-churn transition predictions are shown in Fig. 2. The basis for each of these predictions was discussed in the Upward Gas-Liquid Flow section. At both liquid superficial velocities, the flow regimes identified for the present data agree well with the transition models of Taitel et al. [3] and McQuillan and Whalley [2]. The model of Taitel et al. [3] requires an entry length parameter, which in the present case was taken to be the vertical distance from the mixing location to the pressure measurement location; the model is quite sensitive to this parameter. The prediction of Mishima and Ishii [4] does not correlate well with the present data at the smaller liquid superficial velocity. By careful examination of the flow regimes identified for the present experimental data, we may conclude that the present flow

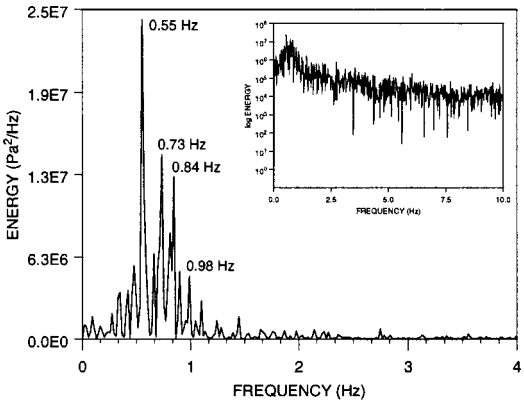

Fig. 3 Fourier energy spectra representing well-defined slug flow with U_l=0.0055 m/s and U_g=1.01 m/s

loop, including the method of mixing the gas and liquid, results in flow regime behavior that is consistent with experimental observations in previous studies.

Figures 3 and 4 show Fourier energy spectra of the fluctuating component of the wall pressure signals in well-defined slug and churn flows, at a water superficial velocity of 0.0055 m/s. These are representative of energy spectra for slug and churn flows at the two liquid superficial velocities examined in this study. Energy spectra for all of the flow conditions represented in Fig. 2 were examined in detail. Frequency content in both slug and churn flows is contained in a narrow bandwidth, with dominant frequencies typically between 0.25 and 1 Hz. For the flow conditions presented in Figs. 3 and 4, the dominant frequencies are provided in the figures. In general, the magnitude of the dominant peak in slug flow is larger than that in churn flow, and energy spectra in churn flow display a wider range of frequencies. However, these differences would not allow flow regime transition identification (Jones and Zuber [8], Vince and Lahey [9]). The energy spectra presented in Figs. 3 and 4 provide the averaged frequency content of the entire signal, and thereby provide no time-resolved frequency information.

The representative signals presented in this paper were selected based on the information gained from analyzing all of the experimental data shown in Fig. 2. Figures 5–12 illustrate time-frequency characteristics of the fluctuating component of the measured wall pressure; each of these figures presents a plot of the fluctuating component of the wall pressure as a function of time, and wavelet energy density as a function of time and frequency (scalogram). All 16,384 data points in each pressure signal were used in the analysis and 12 seconds (3600 data points) of data are

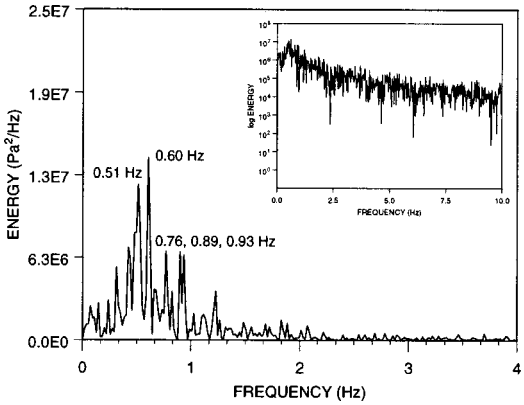

Fig. 4 Fourier energy spectra representing well-defined churn flow with U_l=0.0055 m/s and U_g=2.57 m/s

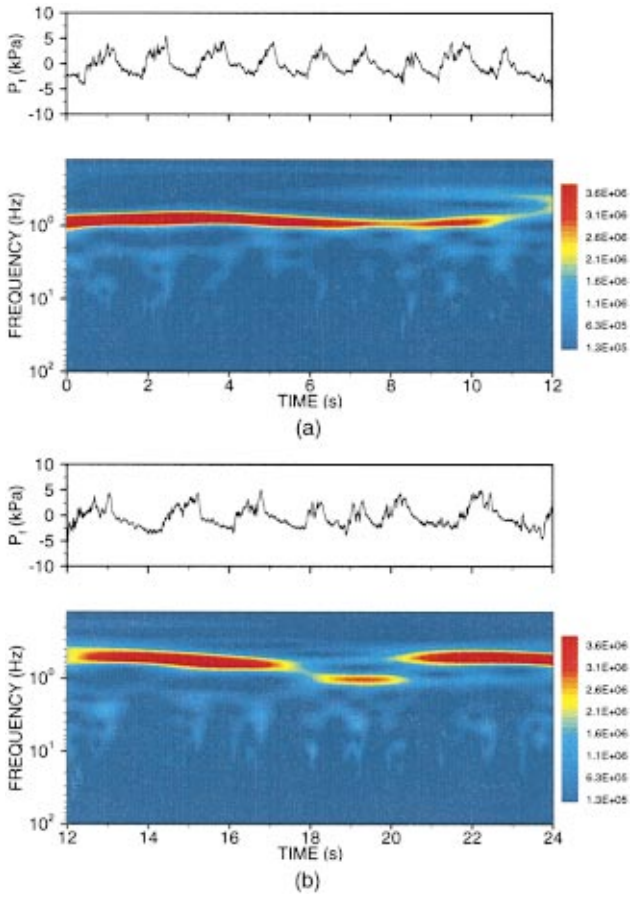

Fig. 5 Wall pressure (fluctuating component) and scalogram for slug flow with U_l=0.0055 m/s and U_g=1.01 m/s (*a*) 0–12 seconds, (*b*) 12–24 seconds

presented in each scalogram to illuminate the characteristic features of the flow. Each scalogram presents time on the abscissa using a linear scale, frequency on the ordinate using a base 10 logarithmic scale, and the coloration represents the wavelet energy density as defined in Eq. (4). The red coloration in the scalogram indicates a large magnitude of the wavelet energy density. The magnitude of the wavelet energy density is associated with the oscillations of the signal at a certain frequency and at a given point in time. A wavelet energy density of zero corresponds to no oscillations in the signal whereas a large magnitude of wavelet

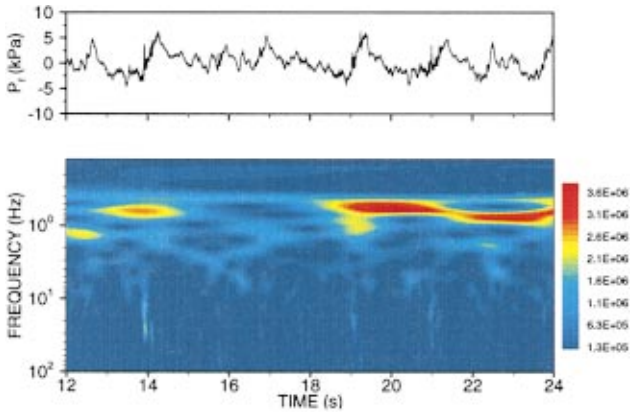

Fig. 6 Wall pressure (fluctuating component) and scalogram for churn flow with U_l=0.0055 m/s and U_g=2.57 m/s

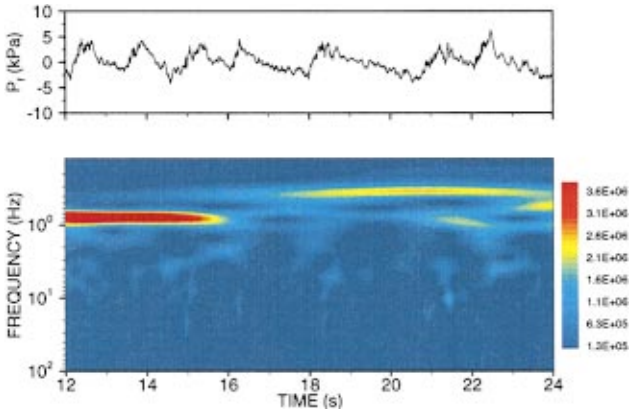

Fig. 7 Wall pressure (fluctuating component) and scalogram for flow near the slug to churn transition with U_l=0.0055 m/s and U_g=1.49 m/s

energy density shows that the signal contains significant oscillations at the current wavelet frequency, or scale (Farge [19]).

Scalograms of the pressure signals at the liquid superficial velocity of 0.0055 m/s are presented prior to the results at a liquid superficial velocity of 0.055 m/s. The well-defined slug flow in Figs. 5(*a*) and 5(*b*) corresponds to 24 seconds of pressure data at U_g=1.01 m/s and U_l=0.0055 m/s. This flow contained long Taylor bubbles followed by liquid slugs containing many small

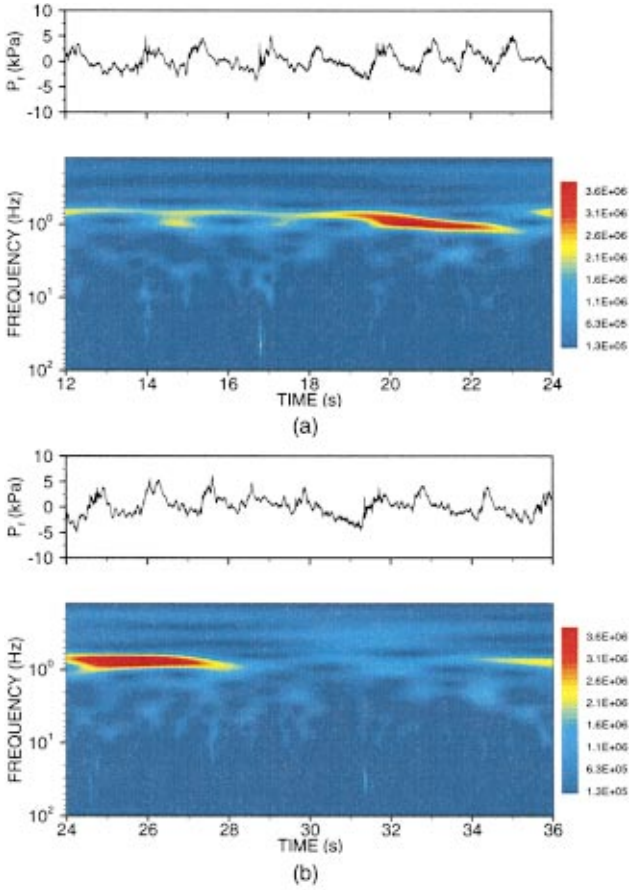

Fig. 8 Wall pressure (fluctuating component) and scalogram for flow near the slug to churn transition with U_l=0.0055 m/s and U_g=1.57 m/s (*a*) 12–24 seconds, (*b*) 24–36 seconds

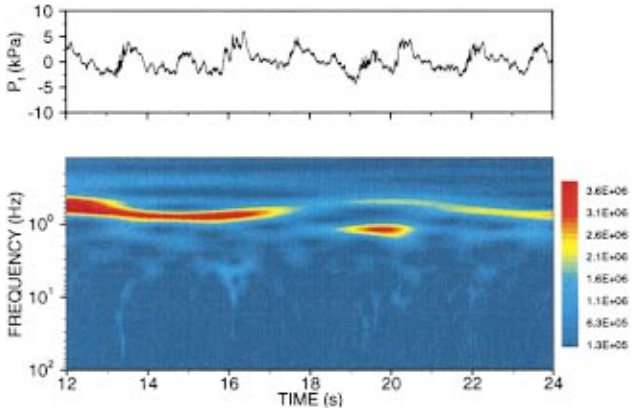

Fig. 9 Wall pressure (fluctuating component) and scalogram for flow near the slug to churn transition with $U_l = 0.0055$ m/s and $U_g = 1.68$ m/s

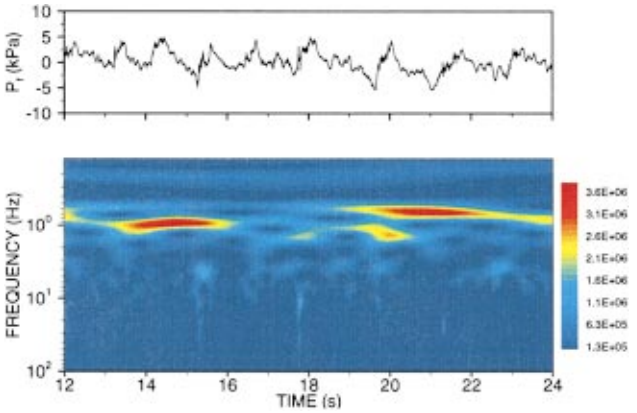

Fig. 12 Wall pressure (fluctuating component) and scalogram for churn flow with $U_l = 0.055$ m/s and $U_g = 1.86$ m/s

bubbles. The scalogram in Fig. 5(*a*) displays a dominant frequency near 0.83 Hz from 0 to 10 s. This dominant frequency can be attributed to the passage of Taylor bubbles in the flow. A change in the physics of the flow as measured by the wall pressure occurred near a time of 11 s. A dominant frequency of 0.50 Hz appears at a time of 12 s as shown in Fig. 5(*b*). At a time of 18 s a frequency of 1.0 Hz is present in the signal. This higher frequency is attributed to the passage of several smaller Taylor bubbles that had not coalesced prior to the pressure measurement location. At the pressure measurement location, such smaller Taylor bubbles rarely appeared in the flow for this well-defined slug flow conditions. After the passage of these smaller bubbles, a dominant frequency of 0.50 Hz is present. The dominant frequencies that range from 0.50 to 0.80 Hz, as identified from the scalograms of this flow, are consistent with the time-averaged frequency content shown in Fig. 3. The event at a time of 11 s as shown in Fig. 5(*a*) is the sole occurrence of such an event for the entire duration of this pressure signal. The entire data set is well characterized by dominant frequencies of less than 0.83 Hz. Therefore, the existence of a dominant frequency for a majority of the signal as well as frequency shifting events that can be clearly associated with the passage of bubbles in the flow, as observed in Figs. 5(*a*) and 5(*b*) are characteristic of well-defined slug flow.

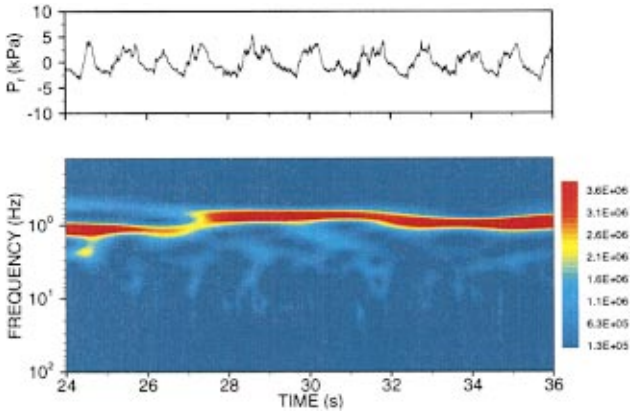

Fig. 10 Wall pressure (fluctuating component) and scalogram for slug flow with $U_l = 0.055$ m/s and $U_g = 0.89$ m/s

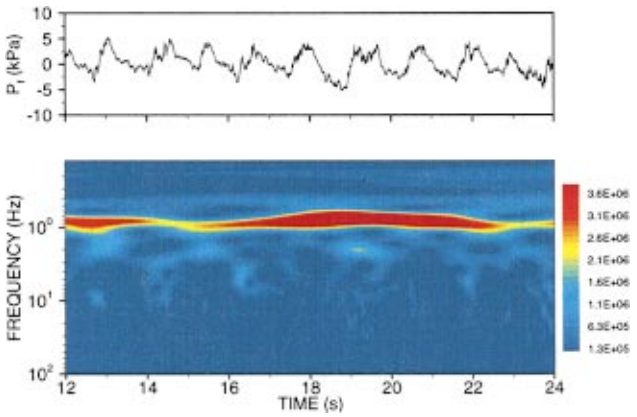

Fig. 11 Wall pressure (fluctuating component) and scalogram for flow near the slug to churn transition with $U_l = 0.055$ m/s and $U_g = 1.46$ m/s

The fluctuating pressure signal and scalogram in Fig. 6 represent well-defined churn flow having $U_g = 2.57$ m/s, and $U_l = 0.0055$ m/s. The larger air superficial velocity of this flow condition created a highly turbulent, quasi-periodic bursting motion. This complex temporal behavior of the flow results in the time-varying nature of the frequency content shown in Fig. 6. Multiple intermittent frequencies exist for the entire time series. In the present context, the term intermittent frequency, or intermittency, is used to describe a single frequency having an energy density magnitude that alternates between a small and a large value. This indicates that at a particular instant in time the frequency is either present or absent in the signal. These intermittent frequencies are spread over range of frequencies from 0.55 to 1.24 Hz, and are present in the averaged frequency content for this pressure signal (Fig. 4). However, the scalogram demonstrates that the frequencies are not present for the entire duration of the signal. The energy density in well-defined churn flow is spread over a range of frequencies, whereas for well-defined slug flow the energy density is concentrated over a narrower range of frequencies (Figs. 5(*a*) and 5(*b*)). In the churn flow condition shown in Fig. 6, between 19 and 24 s in the signal, the scalogram indicates a clear shift in frequency between 0.55 and 0.74 Hz. Complexity in the scalogram in the form of intermittent frequencies over a range of frequencies is characteristic of well-defined churn flow. This is in contrast with the well-defined slug flow shown in Figs. 5(*a*) and 5(*b*), which has dominant frequency content spread over a smaller range of frequencies.

Figures 7 and 9 present flow conditions very near the slug-to-churn transition at a liquid superficial velocity of 0.0055 m/s for gas superficial velocities of 1.49, 1.57, and 1.68, m/s, respectively. The flow conditions in Figs. 7, 8, and 9 are very near the transition between slug and churn flows; however, the flows were classified

as slug flow, churn flow, and churn flow, respectively. This set of figures represents a progression of small increases in the gas superficial velocity for a fixed liquid flow rate.

Figure 7 represents flow conditions very near the transition from slug to churn flow ($U_g = 1.49$ m/s, and $U_l = 0.0055$ m/s). This flow was classified as slug flow, and contained highly turbulent bubble wakes, but without the oscillatory liquid motion resulting from complete destruction of liquid slugs that bridged the cross-section of the pipe. The scalogram in Fig. 7 shows a dominant frequency of 0.74 Hz from 12 to 14 s. At a time near 17 s, there is a clear frequency shift from 0.74 to 0.33 Hz that represents bubble coalescence. Such bubble coalescence events were visually observed in this flow and are evident in the pressure signal. Further, the flow contained a thin, wavy, falling film surrounding each Taylor bubble; the wakes of the bubbles were highly turbulent. The wavy interface may support flooding as the transition mechanism at these flow conditions (Hewitt [41]). Figure 7 suggests that this near-transition flow is characterized in time-frequency space by significant variations in frequency with time caused by increased bubble coalescence at the measurement location and can be contrasted with well-defined slug flow having a dominant frequency present throughout a majority of the signal.

Figures 8(*a*) and 8*(b)* represent 24 s of churn flow data near the transition boundary ($U_g = 1.57$ m/s, and $U_l = 0.0055$ m/s). These data correspond to flow having oscillatory liquid motion usually associated with churn flow, coupled with large-scale bullet shaped air-water interfaces. The 24 s of data are shown here to highlight the intermittent frequency of approximately 0.74 Hz that is present throughout the signal. The increase in air flow rate from the conditions in Fig. 7 to the conditions in Figs. 8(*a*) and 8*(b)* results in a higher degree of intermittency in the dominant frequency of the flow and is characteristic of this flow condition.

The low frequency oscillatory liquid motion characteristic of churn flow near transition results in the scalogram shown in Fig. 9 ($U_g = 1.68$ m/s and $U_l = 0.0055$ m/s). This flow lacked bullet-shaped gas-liquid interfaces, and the gas-liquid interface in the falling liquid film remained wavy until the upward flowing air destroyed the film and entrained the water. The fundamental oscillatory flow of the liquid phase occurs at a frequency range of 0.055 to 0.74 Hz. This frequency range is intermittent throughout the entire signal. Higher frequency intermittent bursts around 1.17 Hz, shown at about 20 seconds in Fig. 9, are present throughout the signal. Figure 9, in contrast with Fig. 8, has a more complex scalogram with significant frequency content spread over a wider range of frequencies.

All results presented thus far have been for the smaller liquid superficial velocity of 0.0055 m/s. Scalograms for a larger liquid superficial velocity of 0.055 m/s were also investigated to compare the localized frequency characteristics and slug-to-churn flow transitions of the two liquid flow rates. Figures 10, 11, and 12 provide scalograms for a liquid superficial velocity of 0.055 m/s, with few conditions corresponding to well-defined slug flow, slug flow near the transition to churn flow, and well-defined churn flow, respectively. The scalogram for the slug flow condition in Fig. 10 indicates a frequency shift from 1.11 to about 0.70 Hz at a time of about 27 s. A dominant frequency is present throughout a majority of the signal. Comparison of the wavelet coefficients in Figs. 5(*a*) and 5*(b)* with Fig. 10 indicate that the characteristics of the localized frequency content in well-defined slug flow at these liquid superficial velocities are nearly identical, with a larger magnitude dominant frequency at the larger liquid superficial velocity. Figure 11 represents slug flow very near transition to churn flow. Dominant frequencies and intermittent frequencies are characteristic of the time-varying frequency for the flow condition in Fig. 11. The 12 s of data shown in Fig. 11 is characterized by dominant frequencies. There is a dominant frequency of 0.78 Hz present from 12 to 14 s, and a dominant frequency of about 0.83 Hz present from 16 to 22 s. These frequencies are intermittent throughout other portions of the signal, and the time variation of the intermittent frequencies is similar to that shown in Fig. 8. Figure 12 represents well-defined churn flow with intermittent frequencies ranging from 0.62 Hz to 1.32 Hz. The intermittency over a wide range of frequencies as shown in both Figs. 6 and 12 is consistent with well-defined churn flow. It seems evident that the characteristics of the flows revealed in the scalograms are consistent across these two liquid superficial velocities.

Summary

The time-frequency content of wall pressure measurements of slug and churn upward gas-liquid flows was examined in the present investigation. Continuous wavelet transforms using the complex-valued Morlet wavelet were used to determine the time variation of frequency content of the wall pressure measurements. Results were presented as wavelet energy densities (scalograms). This technique provides detailed information that may not be obtained from time-averaged statistical measures and spectra.

Data of the present study represent flow conditions in well-defined slug flow, well-defined churn flow, and flow near the slug-to-churn transition. Pressure signals were measured for two liquid superficial velocities (0.0055 and 0.055 m/s) over a range of gas superficial velocities (0.7 to 2.6 m/s) in a 22 mm circular tube. Fourier energy spectra presented the averaged frequency content in the pressure signals, and scalograms showed the time variation of the frequencies. Both liquid superficial velocities showed similar time variations in frequency for a particular flow regime. Pressure signals in slug flow had a dominant frequency present throughout the duration of the signal. However, churn flow pressure signals were characterized by intermittent frequencies. Dominant frequencies and intermittent frequencies were present during different portions of the scalograms for flow near the slug-to-churn transition. Higher frequencies were present at the larger liquid superficial velocity.

Scalograms showed that the frequency content in wall pressure measurements in slug and churn flow regimes varies in time in a manner consistent with the observed physics of the flow. This provides quantitative insight into the physics of the flow that is indistinguishable using statistical measures or averaged spectral techniques. Future work includes detailed investigation of the behavior of flows near the slug-to-churn transition as well as examination of using time-varying frequency content for flow regime identification.

Nomenclature

$E[l,t'] =$ wavelet energy density (Pa^2)
$f =$ frequency (Hz)
$f_s =$ sample rate (Hz)
$k_\varphi =$ wavevector or center frequency (rad/s)
$l =$ scale
$P_f =$ fluctuating component of the pressure signal (kPa)
$t =$ time (s)
$t' =$ translation parameter
$U_g =$ gas superficial velocity (m/s)
$U_l =$ liquid superficial velocity (m/s)
$W[l,t'] =$ wavelet coefficient (Pa)
$\varphi(t) =$ wavelet
$\varphi_{lt'}(t) =$ scaled and translated wavelet

References

[1] Jayanti, S., and Hewitt, G. F., 1992, "Prediction of the Slug-to-Churn Flow Transition in Vertical Two-Phase Flow," Int. J. Multiphase Flow, **18**, pp. 847–860.
[2] McQuillan, K. W., and Whalley, P. B., 1985, "Flow Patterns in Vertical Two-Phase Flow," Int. J. Multiphase Flow, **11**, pp. 161–175.
[3] Taitel, Y., Bornea, D., and Dukler, A. E., 1980, "Modeling Flow Pattern Transitions for Steady Upward Gas-Liquid Flow in Vertical Tubes," Journal of the American Institute of Chemical Engineers, **26**, pp. 345–354.
[4] Mishima, K., and Ishii, M., 1984, "Flow Regime Transition Criteria for Upward Two-Phase Flow in Vertical Tubes," Int. J. Heat Mass Transf., **27**, pp. 723–737.

[5] Chen, X. T., and Brill, J. P., 1997, ''Slug to Churn Transition in Upward Vertical Two-Phase Flow,'' Chem. Eng. Sci., **52**, pp. 4269–4272.
[6] Brauner, N., and Barnea, D., 1986, ''Slug/Churn Transition in Upward Gas-Liquid Flow,'' Chem. Eng. Sci., **41**, pp. 159–163.
[7] Hubbard, M. G., and Dukler, A. E., 1966, ''The Characterization of Flow Regimes for Horizontal Two-Phase Flow: I. Statistical Analysis of Wall Pressure Fluctuations,'' *Proceedings of the Heat Transfer and Fluid Mechanics Institute*, Santa Clara, CA, June, pp. 100–121.
[8] Jones, O. C., and Zuber, N., 1975, ''The Interrelation Between Void Fraction Fluctuations and Flow Patterns in Two-Phase Flow,'' Int. J. Multiphase Flow, **2**, pp. 273–306.
[9] Vince, M. A., and Lahey, R. T., 1982, ''On the Development of an Objective Flow Regime Indicator,'' Int. J. Multiphase Flow, **8**, pp. 93–124.
[10] H. M. Langford, 1998, ''Analysis of Chaos Measures and Statistical Characteristic of Gas-Liquid, Vertical, Upward Flow,'' MS thesis, Clemson University, Clemson, SC.
[11] Costigan, G., and Whalley, P. B., 1997, ''Slug Flow Regime Identification from Dynamic Void Fraction Measurements in Vertical Air-Water Flows,'' Int. J. Multiphase Flow, **23**, pp. 263–282.
[12] Matsui, G., 1984, ''Identification of Flow Regimes in Vertical Gas-Liquid Two-Phase Flow Using Differential Pressure Fluctuations,'' Int. J. Multiphase Flow, **10**, pp. 711–720.
[13] Matsui, G., 1986, ''Automatic Identification of Flow Regimes in Vertical Two-Phase Flow Using Differential Pressure Fluctuations,'' Nucl. Eng. Des., **95**, pp. 221–231.
[14] Langford, H. M., Beasley, D. E., and Ochterbeck, J. M., 1998, ''Observations on Chaos in Upward Gas-Liquid Flow,'' *Proceedings of the ASME International Mechanical Engineering Conference and Exposition*, HTD **361-5**, pp. 247–254.
[15] Franca, F., Acikgoz, M., Lahey, R. T., and Clausse, A., 1991, ''The Use of Fractal Techniques for Flow Regime Identification,'' Int. J. Multiphase Flow, **17**, pp. 545–552.
[16] Drahos, J., Tihon, J., Serio, C., and Lubbert, A., 1996, ''Deterministic Chaos Analysis of Pressure Fluctuations in a Horizontal Pipe at Intermittent Flow Regime,'' Chem. Eng. J., **64**, pp. 149–156.
[17] Cai, Y., Wambsganss, M. W., and Jendrejczyk, J. A., 1996, ''Application of Chaos Theory and Identification of Two-Phase Flow Patterns and Transitions in a Small, Horizontal, Rectangular Channel,'' ASME J. Fluids Eng., **118**, pp. 383–390.
[18] Biage, M., Delhaye, J. M., and Nakach, R., 1989, ''The Flooding Transition: An Experimental Appraisal of the Chaotic Aspect of Liquid Film Flow Before the Flooding Point,'' *AlChE Symposium Series*, 269, **85**, Philadelphia, Pennsylvania, pp. 274–279.
[19] Farge, M., 1992, ''Wavelet Transforms and Their Applications to Turbulence,'' Annu. Rev. Fluid Mech., **24**, pp. 395–457.
[20] Daubechies, I., 1996, ''Where Do Wavelets Come From? A Personal Point of View,'' Proc. IEEE, **84**, pp. 510–513.
[21] Jordan, D., Miksad, R. W., and Powers, E. J., 1997, ''Implementation of the Continuous Wavelet Transform for Digital Time Series Analysis,'' Rev. Sci. Instrum., **68**, pp. 1484–1494.
[22] Lewalle, J., 1998, *Applications of Continuous Wavelets to Data Analysis Parts I, II, and III*, von Karman Institute Lecture Series.
[23] Morlet, J., Arens, G., Fourgeau, E., and Giard, D., 1982, ''Wave Propagation and Sampling Theory—Part I: Complex Signal and Scattering in Multilayered Media,'' Geophysics, **47**, pp. 203–221.
[24] Morlet, J., Arens, G., Fourgeau, E., and Giard, D., 1982, ''Wave Propagation and Sampling Theory—Part II: Sampling Theory and Complex Waves,'' Geophysics, **47**, pp. 222–236.
[25] Mallat, S., 1999, *A Wavelet Tour of Signal Processing*, 2nd Edition, Academic Press, Chestnut Hill, MA.
[26] Kovačević, J., and Daubechies, I., Ed., 1996, *Special Issue on Wavelets*, Proc. IEEE, **84**, pp. 507–686.
[27] Farge, M., Kevlahan, N., Perrier, V., and Goirand, E., 1996, ''Wavelets and Turbulence,'' Proc. IEEE, **84**, pp. 639–669.
[28] Higuchi, H., Lewalle, J., and Crane, P., 1994, ''On the Structure of a Two-Dimensional Wake Behind a Pair of Flat Plates,'' Phys. Fluids, **6**, pp. 297–305.
[29] Poggie, J., and Smits, A., 1997, ''Wavelet Analysis of Wall-Pressure Fluctuations in a Supersonic Blunt-Fin Flow,'' AIAA J., **35**, pp. 1597–1603.
[30] Buresti, G., Petagna, P., and Talamelli, A., 1998, ''Experimental Investigation on the Turbulent Near-Field of Coaxial Jets,'' Exp. Therm. Fluid Sci., **17**, pp. 18–36.
[31] Li, H., 1998, ''Identification of Coherent Structure in Turbulent Shear Flow with Wavelet Correlation analysis,'' ASME J. Fluids Eng., **120**, pp. 778–785.
[32] Lewalle, J., Delville, J., and Bonnet, J., 2000, ''Decomposition of Mixing Layer Turbulent into Coherent Structures and Background Fluctuations,'' Flow, Turbul. Combust., **64**, pp. 301–328.
[33] Yeung, P. K., Basseur, J. G., and Wang, Q., 1995, ''Dynamics of Direct Large-Small Scale Couplings in Coherently Forced Turbulence: Concurrent Physical- and Fourier-Space Views,'' J. Fluid Mech., **283**, pp. 43–95.
[34] Lewalle, J., 1994, ''Wavelet Transforms on Some Equations of Fluid Mechanics,'' Acta Mech., **104**, pp. 1–25.
[35] Moridis, G. J., Nikolaou, M., and You, Y., 1996, ''The Use of Wavelet Transforms in the Solution of Two-Phase Flow Problems,'' Soc. Pet. Eng. J., **29144**, pp. 169–177.
[36] Bakshi, B. R., Zhong, H., and Fan, L. S., 1995, ''Analysis of Flow in Gas-Liquid Bubble Columns Using Multi-Resolution Methods,'' Trans. Inst. Chem. Eng., **73**, pp. 608–614.
[37] Hervieu, E., and Seleghim, Jr., P., 1998, ''An Objective Flow Regime Indicator for Two-Phase Flow Pattern Transition,'' Nucl. Eng. Sci., **184**, pp. 421–435.
[38] Li, H., and Tomita, Y., 1998, ''Wavelet Analysis of Gas-Solid Two-Phase Flow in a Horizontal Pipe,'' *Proceedings of the Third International Conference on Multiphase Flow*, Lyon, France, June, Paper Number 122.
[39] Hetstroni, G., 1982, *Handbook of Multiphase Systems*, Hemisphere, Washington, D.C.
[40] Tong, L. S., and Tang, Y. S., 1997, *Boiling Heat Transfer and Two-Phase Flow*, Taylor and Francis, Washington, D.C.
[41] Hewitt, G. F., 1996, ''In Search of Two-Phase Flow,'' ASME J. Heat Transfer, **118**, pp. 518–527.

Film Thickness and Wave Velocity Measurements in a Vertical Duct

Ranganathan Kumar
Lockheed Martin Corporation,
Schenectady, NY 12301

Matthias Gottmann

K. R. Sridhar

The University of Arizona,
Tucson, AZ 85721

This paper describes the experimental investigation of an upward annular air-water flow in a duct with a 6.35 mm by 63.5 mm rectangular cross section. The test section was instrumented to measure the film thickness and the interfacial wave velocity. Flush-wire electrical conductivity probes were used to obtain local film thickness measurement with a spatial resolution of 200 μm or better and a temporal resolution greater than 2 kHz. Measurements of the base films range from 50 μm to ~325 μm (2% to 10% of half-channel thickness). Statistical analysis shows that the standard deviation of the film thickness is a good measure of the film roughness. The relative roughness and the nondimensional film thickness are correlated as functions of the phasic Reynolds number ratio, $R = Re_l^{0.15}/Re_g^{0.3}$. It is found that at $R = 0.15$, the relative roughness is a maximum. A simple model developed by matching the interfacial shear in the two fluids, predicts the wave velocity data very well. [DOI: 10.1115/1.1493808]

Introduction

Within the field of two-phase flows, the annular flow regime enjoys special attention due to its prevalence and complexity. Annular flow is important because it persists over a wide range of flow rates, most of the heat exchange occurs in this regime; and also because it is the last stage before dryout, which is a critical failure mode in two-phase heat transfer equipment. In this flow regime, the interface between the liquid film and gas core is characterized by interfacial waves which play a dominant role in governing system parameters. The characteristics and the topology of the waves have been a subject of research interest for a number of years. The two types of waves that have been reported in the literature are the disturbance and the ripple waves [1,2]. The disturbance waves are the large amplitude waves, and are caused by the disturbances on the liquid film. These waves are a necessary condition for droplet entrainment in the core. The ripple waves are the low amplitude high frequency waves that contribute primarily to the interfacial shear. These interfacial waves travel at a much higher velocity than the base liquid film on the wall. These wave parameters affect the interfacial shear between two continuous fluids. Earlier models [3,4] made great contributions in the development of a two-phase friction factor analogous to the pipe friction factor in single-phase flows. However, they did not include the wave motion. It has been shown that the interfacial shear depends on the wave amplitude or the relative roughness of the film, the wave frequency and the wave propagation velocity [5,6]. Both papers discussed the importance of the wave velocity and the high frequency content in their measurements. However, the focus was either to provide interfacial shear models for only the ripple wave region [5] or for a falling film flow [6]. The pressure rise across the interface is another important quantity which can be expressed in terms of the interfacial velocity [7]. Such a model was used by Gersey and Mudawar [8] who obtained the critical heat flux in terms of the pressure difference evaluated at twice the critical Kelvin-Helmholtz wavelength.

A thorough review of the papers in annular flow is provided by Azzopardi [9] who discusses different types of measurements made on the wavy interface. The current paper adds valuable information to the existing literature by providing a complete set of measurements of mean film thickness (50 to 325 μm), wave amplitude and wave velocity at a high temporal and spatial resolution for high and low liquid and vapor Reynolds numbers. High temporal resolution is required to measure the root mean square film thickness fluctuations accurately.

The second aspect of this research is to make the above measurements in a very thin vertical rectangular duct, and therefore, it is important to have high spatial resolution of film thickness measurements. The need for more compact heat exchangers and cooling channels in microelectronics has created an interest in flows in rectangular ducts. The flow in rectangular geometries is more complex and less understood than in circular geometries. The open literature documents a number of investigations of two-phase flows in rectangular channels [2,10–13]. These papers concentrated more on global behavior of pressure drop and flow regime maps and less on high-accuracy local measurements. The current paper compares the churn-turbulent to annular flow transition regime with those in other rectangular geometries.

In summary, the objectives of this paper are to provide local measurements of film thickness, its standard deviation, and wave velocity using flush-wire conductivity probes in an upward annular flow. These measurements are made in a 6.35 mm vertical rectangular duct with high spatial and temporal resolution, covering the entire spectrum of annular flow where both disturbance waves and ripple waves dominate. The wave velocity measurements which are important for annular flow model development are compared with a model based on a simple force balance.

Experimental Method

Test Facility. The experimental apparatus was designed to create fully developed, vertical, upward annular air-water flows in a duct with a 63.5 mm×6.35 mm rectangular cross section. Water and air flow sources and controls provided constant flow rates for test runs of over three hours in duration. Figure 1 presents the schematic of the experimental apparatus which includes a 1.83 m long test section. A maximum air flow rate of 0.02 m^3/s (42 cfm) can be generated. Air flow rate is calibrated using a laminar flow element in the air supply line. A large 1.2 m^3 (310 gal) water tank provides a constant head water source. Two turbine flowmeters measure the water flow rates between 3.1×10^{-5} m^3/s (0.5 gpm) and 3.75×10^{-3} m^3/s (60 gpm). A gate valve is used to control the water flow rate. The injector inserts water at the bottom of the test section along the side walls while guiding the air flow in the center of the channel. Figure 2 shows a photograph and a cross-sectional view of the injector. The injector is crucial for obtaining a high quality flow and minimizing the length of the test section where the flow is developing. The test section is built from Plexiglas side walls and T-shaped aluminum spacers to facilitate visual

Contributed by the Fluids Engineering Division for publication in the JOURNAL OF FLUIDS ENGINEERING. Manuscript received by the Fluids Engineering Division February 14, 2001; revised manuscript received April 10, 2002. Associate Editor: J. Katz.

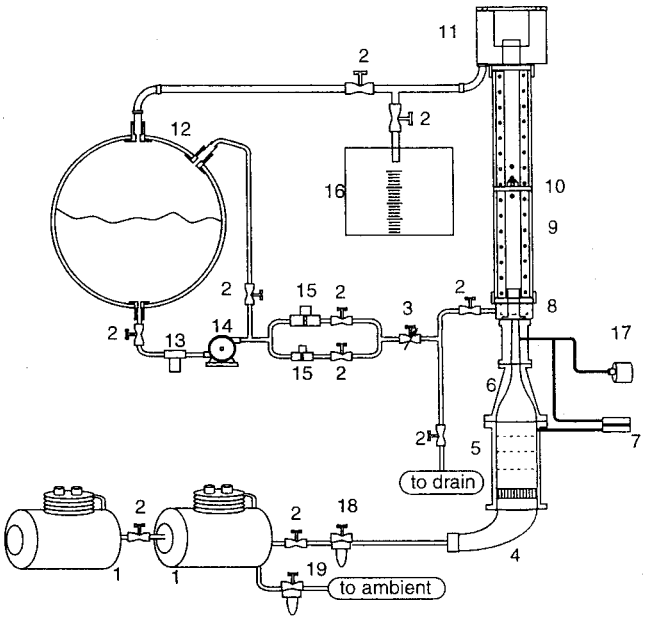

1	compressor
2	shut off valve
3	control valve
4	elbow
5	flow straightener
6	contraction
7	differential pressure transducer
8	water injector
9	test section
10	measurement port
11	separator
12	water tank
13	water filter
14	centrifugal water pump
15	flow meter
16	metering container
17	absolute pressure transducer
18	pressure regulator
19	back pressure regulator

Fig. 1 Schematic of the experimental apparatus

observation of the flow and provide structural rigidity. The instrumentation ports are located at 1.04 m from the injector inlet, a distance of approximately 90 hydraulic diameters.

Flush-Wire Conductivity Probe. Various measurement methods have been utilized to determine the thickness of the liquid film. Most experimental approaches have used either optical or electrical properties of the liquid to detect the phase boundary. Measurements with capacitance sensors can be realized non-intrusively, but spatial measurement resolution is low. In order to obtain local film thickness measurement with a high spatial and temporal resolution, flush-wire electrical conductivity probes are used in this study. The flush-wire probe is a combination of the flush-flush probe [14] where both electrodes are mounted flush on the wall and the wire-wire probe [15] where two wire probes are inserted in the film. This flush-wire probe was first studied by Kang and Kim [16] who showed that it could be designed such that the flow disturbances caused by the intrusion were minimal. Their study on falling films also showed that the flush-wire probe detected the interface shape without losing the small high frequency waves which are important to our study.

The details of the two flush-wire probes used in the current experiment are shown in Fig. 3. The flush electrodes are 2 mm platinum pads mounted in a Plexiglas plug. The wire probes are 50 μm diameter platinum wire with 1 mm exposed length. Each platinum wire is supported and insulated by a 150 μm outer diameter glass tube. Outside the flow field, the glass encased platinum probe is mounted in a 1 mm outer diameter steel sheath which provides a rigid interface to the traversing mechanism and electrical shielding. Both wire probes are inserted through the test section side wall opposing the flush wire electrode. The separation distance between the tip of the wire probe and the flush electrode can be individually adjusted with two micro-stages. The streamwise separation between the electrodes is 2 mm.

Conductivity is measured by the application of a 100 kHz carrier frequency signal to the electrodes. This frequency was chosen in order to avoid ionic reactions at the electrodes [14]. Two transformers provided galvanic separation of the conductivity probe from the environment. The circuit also consisted of an amplifier, a full wave rectifier and a 10 kHz low pass filter. The output signal is proportional to the conductivity between the electrodes. The signal is then fed into a measurement amplifier and an A/D converter.

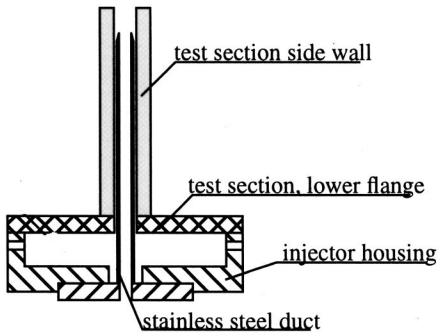

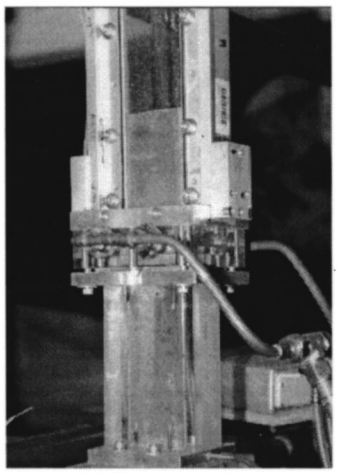

Fig. 2 Cross-section and photograph of injector

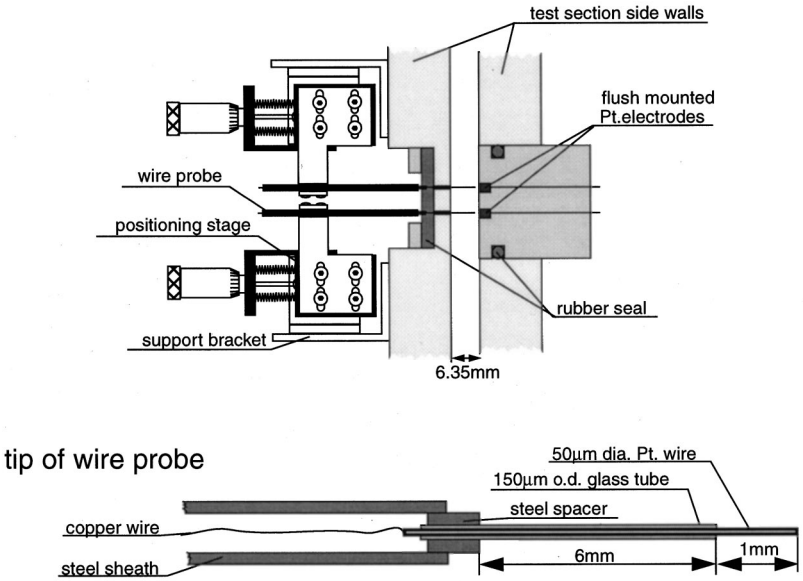

Fig. 3 Details of the flush-wire probe

Statistical Calibration of the Flush-Wire Probe. The calibration of the conductivity probe follows the procedure outlined by Kang and Kim [16]. For a constant water and air flow rate, the statistical properties of a series of conductivity measurements will be constant, and the film thickness would have a certain probability. Since every film thickness corresponds uniquely to one value of conductivity, this conductivity value would have the same probability. The basic idea of statistical calibration is to use the conductivity probe in two different ways, i.e., first in a ''contact mode'' as explained in the next paragraph and then in a ''conductivity mode.'' Representative conductivity signals of wave scans are shown in Fig. 4 for four different insertion depths of the probe tip.

In the contact mode, the probe is positioned at a distance away from the wall, where the needle is not in permanent contact with the liquid film. The only information needed from this measurement is whether the probe touches the liquid film. The horizontal portions of the wave scans below the dashed line mark the intervals where the probe tip is not touching the film. Summing up these intervals and dividing by the overall time of the scan yields the probability, P, of the probe not contacting the film (Fig. 5). Since the wall is always wetted, contact probability approaches unity as the probe moves closer to the wall, and zero as it is retracted away from the wall. This contact probability is plotted against the distance from the wall in Fig. 5(b).

Next, the probe is put in conductivity mode and inserted into the film. A histogram of the conductivity signal is obtained, smoothed, and normalized to provide the cumulative probability versus the voltage level, as shown in Fig. 5(a). The similarity between the cumulative probability in Fig. 5(a) and the contact probability in Fig. 5(b) suggests that there exists a one-to-one correspondence between conductivity and film thickness. Therefore, the two probability functions can be combined to yield the calibration chart of voltage versus film height as shown in Fig.

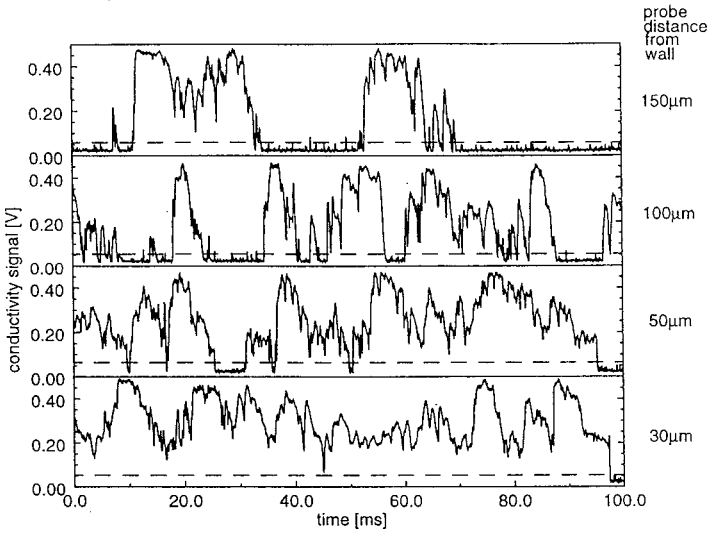

Fig. 4 Conductivity probe signal for different separation distances between the wire tip and the flush electrode at 9.4×10^{-3} m^3/s (20 cfm) air and 1.25×10^{-4} m^3/s (2 gpm) water flow rate

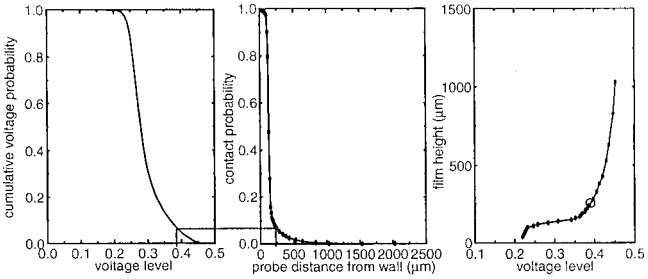

Fig. 5 Calibration chart for film thickness based on conductivity probe data

5(*c*). Conductivity depends only on the phase distribution around the wire probe and not on any other flow field properties such as velocity or pressure. Therefore, the conductivity to film thickness relation is valid regardless of the flow rates. After calibration, the wire probe remained fixed in the fully submerged position within the film.

The probability argument is valid only if the probability does not change during calibration. Constant probability conditions can be assumed if all flow properties, such as flow rates, temperatures, and pressures remain constant and the sampling occurs over sufficiently long time intervals. Changes in water conductivity and electrode properties can occur due to temperature variations or changing water impurity levels, which would impact measurements. The relationship between the conductivity and the film thickness is nonlinear as seen in Fig. 5(*c*) and highly sensitive to the exact probe geometry and water conductivity, and therefore, an *in situ* calibration was performed.

Accuracy and Resolution of the Flush-Wire Probe. In order to determine the film thickness the resistance between the flush probe and the needle tip is measured and then converted to film thickness. The conductivity probes provide a weighted average measurement over a column of liquid in the vicinity of the sensor. For the flush-wire probe, this area spans approximately four diameters, i.e., 200 μm, which is much better than the spatial resolution of the flush-flush probe or the wire-wire probe [16]. The temporal resolution is only limited by the electronic implementation of the conductivity measurement. The process of removing the 100 kHz carrier signal from the measurements limits temporal resolution to about 10 kHz. Frequency spectra of the film thickness will show later that this frequency resolution is sufficient.

Inaccuracies in the film thickness measurement can be traced to three sources: (i) the accuracy of the probe adjustment, (ii) electrical noise, and (iii) uncertainty in the statistically determined calibration curve. The accuracy of the probe adjustment determined by the system is about 5 μm. Over the entire range of measurement the relative error due to noise is less than 4% of the measured film thickness. The average error due to calibration accuracy is less than 6% of the measured film thickness. However, in the central region of the voltage level (Fig. 5(*c*)), the error is small and at steeper slopes, the error may be larger than 6%. At low film thickness, the maximum error is dominated by probe adjustment, and at large film thicknesses by noise and calibration uncertainty.

Measurement accuracy can also be affected by the shape and size of the probe. Since the wire is very thin, deflections caused by the forces exerted by the flow can change the conductivity measurement. This is so because the conductivity signal depends on the distance between the probe tip and the flush electrode. The worst case deflection of the probe tip is estimated to be 2 μm from theoretical analysis for static loads. In addition, a meniscus can be formed on the probe, caused by the difference in surface tension between air-water and water-platinum. A hysteresis effect, which increases the meniscus when the film is retreating and diminishes the meniscus when the film is rising, is to be expected. Koskie et al. [15] observed that the distortion caused by the meniscus is typically a fraction of the wire diameter and is on the order of a few μm.

Results and Discussion

Test for Quasi-Equilibrium State. The annular flow regime presents a complicated distribution of the liquid phase classified into the base film, the wavy surface and the droplets. The droplets are entrained at the tips of the disturbance waves, and are redeposited on the film surface. This simultaneous occurrence of entrainment and deposition makes the interface convoluted and it takes time for the disturbance waves to reach its developed state in the entrance region. However, far downstream from the inlet, the relative roles of the entrainment and deposition mechanisms are somewhat decoupled and a quasi-equilibrium state could be reached. In order to check for this quasi-equilibrium and self-similarity of the film thickness and any deviation, conductivity probes were placed at 70, 80, and 90 hydraulic diameters downstream from the inlet. Seven combinations of air and liquid flow rates were run, spanning the entire range of the annular flow regime. ($3000 < \mathrm{Re}_g < 30{,}000; 160 < \mathrm{Re}_l < 12{,}000$).

The average film thickness and standard deviation were computed using nearly 2×10^6 instantaneous film thicknesses at each location for each case. The average film thickness did not vary significantly between 80 and 90 hydraulic diameters. Some variations in measurements were seen between 70 and 80 hydraulic diameters, especially for low water flow and high air flow combination. The average film thickness and standard deviation plotted against Re_l and Re_g (not shown here) did not show any statistical trend. Even the lowest water flow rate and the highest air flow combination which represented a very thin film and an occasional dryout appeared to have reached a quasi-steady state. Next, the power spectra for all the cases were plotted at all axial locations. The signal was preconditioned with a low pass filter, Fast Fourier transformed after removing the linear trend and using Hanning filter. The sampling rate and filtering assured that no aliasing effects occurred in the domain of interest. In general, no statistical variation of significance was seen. However, the lowest water flow and highest air flow combination, which did not display a large scatter in the average thickness and deviation, showed variations in the spectra due to intermittent dryout. Thus, except for some flow conditions outside the domain of annular flow, the flow appears to have reached a quasi-equilibrium condition about 90 hydraulic diameters from the injector inlet. This downstream location is somewhat closer to the inlet compared to the literature. However, it should be noted that most researchers have used a porous tube to generate annular flows starting from bubbly flow. In this work, the two wall injectors have stabilized the flow, and brought it to a quasi-equilibrium state much earlier for majority of the annular flow conditions of interest.

Flow Regime Map. The flow regime map is expected to be different for thin rectangular geometries compared to circular tubes. There has been a number of flow regime investigations in vertical rectangular ducts of thickness 1 mm to 5 mm [13,17–19]. In Fig. 6, flow regime maps are constructed both in terms of superficial momentum fluxes as well as superficial velocities. The annular flow regime is limited by lower air flow rates where the churn-turbulent regime exists, and by dryout at a combination of high air flow and low water flow rates. The 35 runs that were tested spanned the entire annular flow regime at the low and high ends of both air and water flows. These cases are labeled according to their flow rates in Fig. 6(*a*) (for example, air flow of 21 cfm and water flow of 0.6 gpm is labeled as 21-06). Selected visualized data points for rectangular ducts [13,19] and for a circular tube [20] are overlaid for comparison with the data in the current study in Fig. 6(*b*) Wilmarth and Ishii [19] showed that the transi-

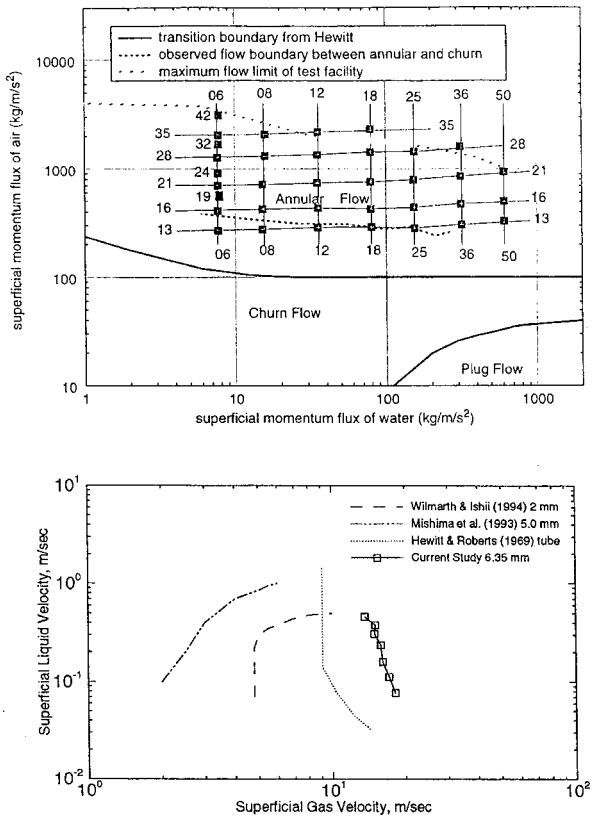

Fig. 6 Flow regime map: (a) current study in rectangular test section with test matrix; (b) comparison of transition from churn-turbulent to annular flow regime with available data in rectangular and circular ducts

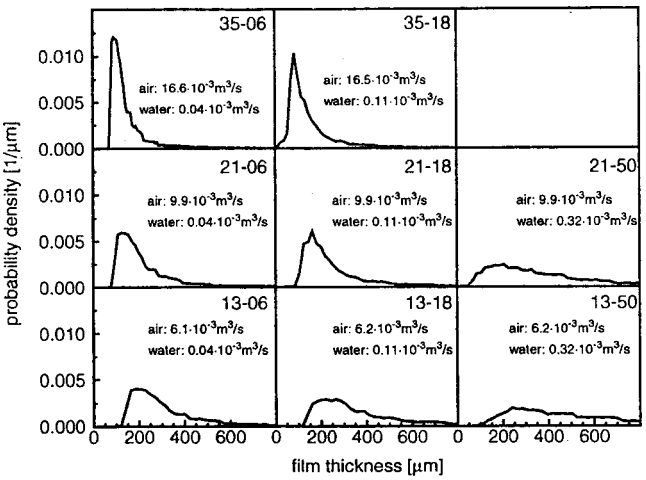

Fig. 7 Probability density plots of film thickness for various combinations of air and water flow rates

tion lines across all the flow regimes corresponded reasonably well with Ali and Kawaji's [18] results for the 1 mm duct; however, the data of Mishima et al. [13] showed that the flow reached the annular regime at much lower gas velocities. Comparison with the current study also shows that their 5 mm data reach the annular regime again at much lower gas velocities. It must be noted that the evaluation of the transition lines is subjective even with fast photography. The liquid plugs breaking away from the edges may be large enough that the flow regime can be categorized as churn-turbulent. Second, the method of injection of air is different in the three comparative studies. Mishima et al. [13] used 14 capillary tubes to inject air. Wilmarth and Ishii [19] used a porous plug to inject air. The current study used two wall injectors to inject water in an airflow. In all three tests, the width/thickness aspect ratio is between 7.5 and 10. Thus, the method of injection may explain the large variation, i.e., almost a factor of 10 in the superficial gas velocity between two similar ducts, in the transition between the churn-turbulent and the annular flow regimes, and this research needs to be pursued.

Film Thickness Measurements. Probability density distributions of film thickness are given for various air and water flow rates in Fig. 7. Probability density for a given film thickness times the width of the interval yields the probability that the film thickness is within this interval. As can be seen from these plots, at high air flow rates, the probability density is narrow and sharp, i.e., the interface is almost smooth and the deviations from the average thickness are small and occur infrequently. At high water flow rates, especially at low air flow rates, the profiles exhibit the opposite phenomenon. The probability density displays a broad maximum and extends to large film thicknesses. This indicates a spectrum of large amplitude waves at the interface, as seen from the raw data. For almost all the cases, a thin liquid film is always present on the wall. This film, also called the substrate, has been previously identified in annular flow in circular pipes by Telles and Dukler [21] and Chien and Ibele [22]. In Fig. 7, at very high liquid and gas flow rates, the substrate or the base film is very thin. The thickest substrate is found for the lowest air flow rates. Comparing these structures with time traces (not shown) of the two probes, it has been identified that the small surface waves have small amplitudes that are typically of the order of 20 μm over 3 ms. The larger disturbance waves have amplitudes that are typically 500 μm over 5 ms. However, these amplitudes include the substrate thickness which appear to be substantial as shown in Fig. 7.

Based on the experimental observations in the literature [21,22] and the above discussion of Fig. 7, the liquid film in the annular flow can be divided into a continuous layer adjacent to the wall called the ''base film'' and a wavy layer close to the liquid-gas interface. The conductivity probe measures both the continuous and the wavy part of the film thickness. If the root-mean-square fluctuation is subtracted from the measured average film thickness (which includes the continuous and the wavy part), the mean base film thickness can be obtained. The disturbed wavy layer has a locally varying thickness which can be approximated as the sum of several sine waves at different frequencies. A perfect sine wave with an amplitude of ''a,'' has a root-square-mean of $(1/\sqrt{2})a$. The r.m.s. of a perfect square wave with an amplitude of a is a. If the film thickness signal is assumed to be in between a series of sine waves and a square wave, its r.m.s. can be approximated to be the wave amplitude. Then, the ratio of the root mean square fluctuation to the base film thickness can be taken to be a good measure of the relative roughness in the film.

The standard deviation in film thickness is plotted against the nondimensional base film thickness in Fig. 8. The standard deviation increases steadily with increase in film thickness but stays constant after the film reaches a thickness about 6% of half the duct thickness. These deductions are made based on the experimental data for a range of liquid Reynolds numbers from 1150 to 10,900. These statistics show that σ_δ is a reasonably good measure of the film roughness.

In Fig. 9, the base film thickness and its standard deviation are plotted against Re_g for a wide range of Re_l. It is seen that the base film thickness increases if either Re_g is decreased or Re_l is increased. This fact is also corroborated by the probability density plot in Fig. 7. The standard deviation or the wave amplitude also decreases with increasing Re_g. At low Re_l, the film thickness reaches a constant value of approximately 50 μm for $\mathrm{Re}_g > 30{,}000$. For a given Re_g, the standard deviation increases with Re_l, but reaches a constant value as seen in Fig. 8 especially for

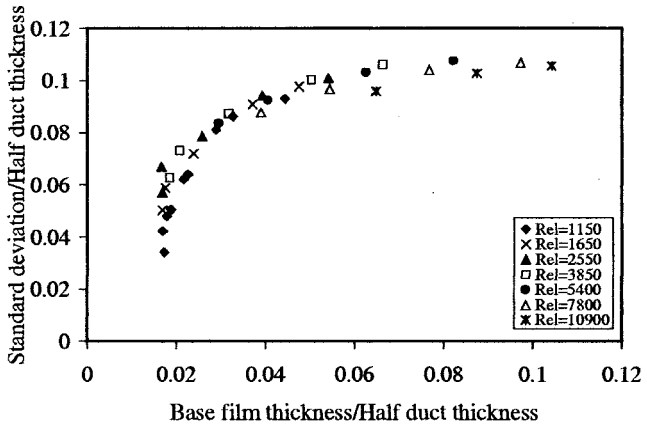

Fig. 8 Nondimensional standard deviation versus nondimensional base film thickness

low Re_g. From these observations in the data trend, an attempt will be made to replot the data to gain better understanding of the wave characteristics. The basis for replotting the data with a combination of dimensionless parameters is explained next.

Hewitt and Whalley [23] suggest that at high gas velocities, the disturbance waves tend to occur at a fixed liquid flow rate. Although this is true for a limited gas and liquid flow range, a general correlation at which the transition to disturbance wave-

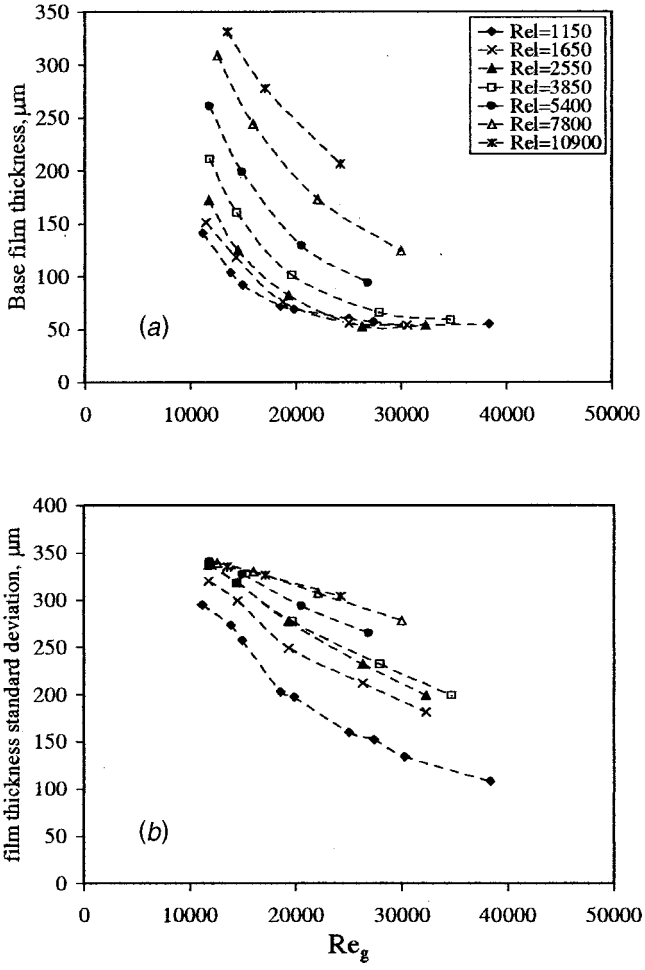

Fig. 9 (a) Base film thickness versus Re_g; (b) standard deviation of film thickness versus Re_g

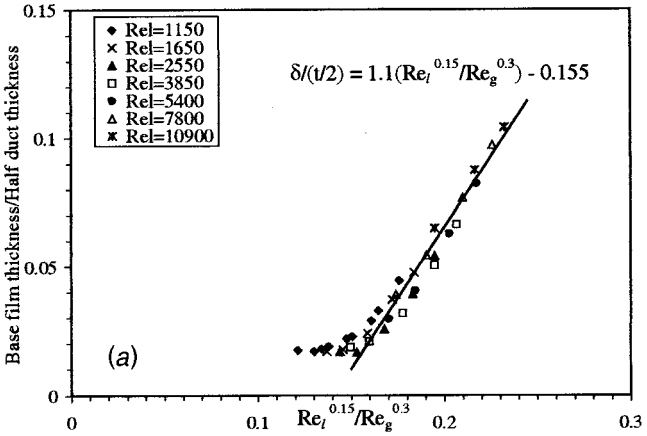

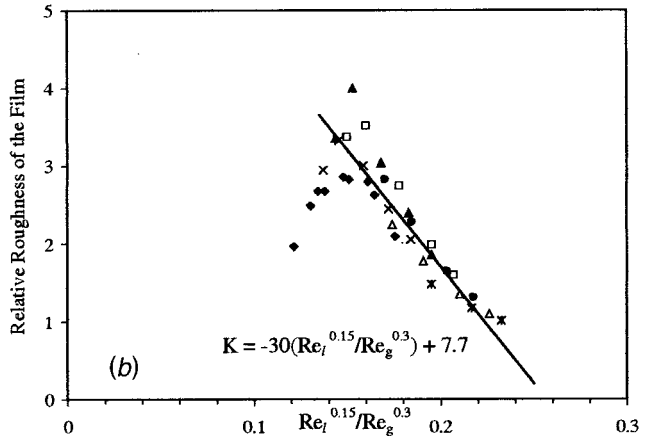

Fig. 10 (a) Nondimensional base film thickness versus Reynolds number ratio; (b) relative roughness of the film versus Reynolds number ratio

dominant flow takes place can be developed. The liquid film is considered to be a rough surface to the gas core. The friction factor correlations in the literature are based on the premise that the interface structure for a given ratio of film thickness to diameter is approximately the same independent of the phasic flow rates. However, the local phasic flow rates determine the base film thickness as shown in Fig. 9. In turn, the relative roughness of the film also should depend on the flow rates. Therefore, correlations for base film thickness and relative roughness should be functions of Re_g and Re_l. This also suggests that the liquid film should not be treated purely as a roughened surface. If we treat the interface to provide roughness both to the liquid film as well as the gas core, the interfacial friction in each phase would be dependent on the Reynolds number of that phase. Thus, it is conceivable that the film thickness and the wave roughness depend on the ratio of phasic Reynolds numbers. Alternatively, a less heuristic and more physical reasoning can be obtained if the shear and velocity at the interface can be equated from each phase. Since the friction factor would depend on the phasic Reynolds number raised to different exponents, it motivates us to correlate the film thickness and roughness as a function of Re_l^m/Re_g^n as shown in Fig. 10. The data are well-contained when the film thickness and relative roughness are plotted against $Re_l^{0.15}/Re_g^{0.3}$. Denoting this ratio as R, it is interesting to note that a clear demarcation develops at $R=0.15$. Above this value, it appears that the base film thickness increases linearly and the relative roughness decreases linearly upto the highest liquid flow rates. For $R<0.15$, the film is at a constant 50 μm thick but the wave amplitude as seen from the standard de-

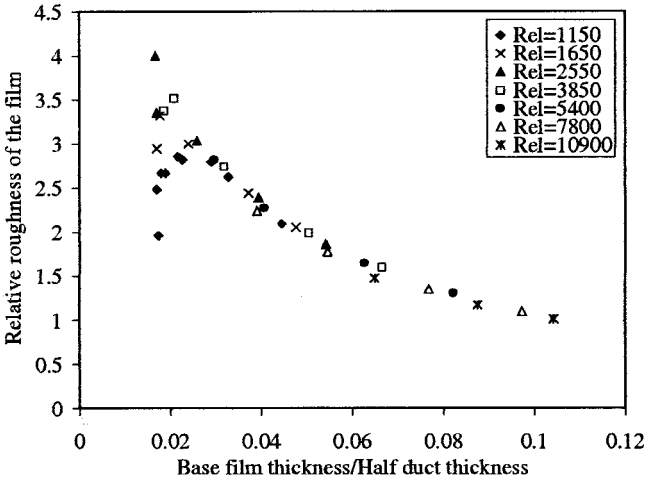

Fig. 11 Relative roughness or wave roughness of the film versus nondimensional base film thickness

viation plot diminishes as Re_g increases. This decreases the relative roughness, K, as R is decreased below 0.15. The thin liquid film is periodically washed by the disturbance waves having amplitudes as high as four times the base film thickness. At $R=0.15$, the relative roughness is maximum for different combinations of air and water flow rates. It appears that the transition to disturbance wave-dominant regime occurs at approximately $R \geqslant 0.15$. This will be investigated further from the power spectra. Although the relative roughness has been correlated with film thickness in the literature, the film thickness itself is not known a priori in annular flow. Therefore, based on the plots in Fig. 10, the following correlations are provided in terms of phasic Reynolds numbers:

$$\frac{\delta}{(t/2)} = 1.1(\mathrm{Re}_l^{0.15}/\mathrm{Re}_g^{0.3}) - 0.155 \tag{1}$$

$$K = -30(\mathrm{Re}_l^{0.15}/\mathrm{Re}_g^{0.3}) + 7.7 \tag{2}$$

In Fig. 11, the relative roughness of the film is given in terms of the nondimensional base film thickness. At $\delta/(t/2)=0.02$, the relative roughness peaks to nearly 4.0 and steadily drops to a value of 1.0 for thicker base films. This maximum ratio of the disturbance wave amplitude to mean film thickness is close to the value of 5.0 reported by Hewitt [24]. However, contrary to what he reported based on the fluorescence studies, Fig. 11 shows that the wave amplitude to mean film thickness ratio is a strong function of the film thickness. For a combination of $Re_l \leqslant 3850$ and $Re_g > 30{,}000$, $\delta/(t/2)$ slightly less than 0.02, where the film thickness is nearly a constant, the relative roughness increases with very slight increase in the liquid flow rate of Re_l. In this region where R is less than 0.15, a slight increase in the liquid flow rate in a high gas annular flow regime renders a spiky signal. This means that the waves are predominantly ripples with pulses of disturbance waves. These pulses, which increase the film roughness, have also been identified by Hall-Taylor et al. [1]. For these flow conditions, the flow regime is near the churn flow boundary. The waves are associated with a process similar to the flooding process described by Hewitt and Walley [23] based on a standing wave experiment performed by Shearer and Davison [25].

Power Spectra. The power spectra for a representative liquid flow and different vapor flows are shown in Fig. 12. This set of cases is picked so that the Reynolds number ratio, R, falls on either side of $R=0.15$ where the relative roughness is a maximum for the chosen liquid flow. At the lowest vapor flow, the spectral density is maximum at nearly 2 Hz. As the vapor flow increases, energy shifts to higher frequencies. Energy also was seen to shift to higher frequencies when the liquid flow was increased for a given vapor flow. At higher liquid flow rates not shown here, the dominant frequency was seen to be as high as 50 Hz. At these low frequencies, disturbance waves exist and are primarily responsible for increasing the roughness of the liquid film. In general, the maximum frequency was seen to increase with an increase in gas Reynolds number, or conversely, with a decrease in base film thickness. This observation is also supported by Sekoguchi et al. [5] for vertical tubes. The high frequency components which are

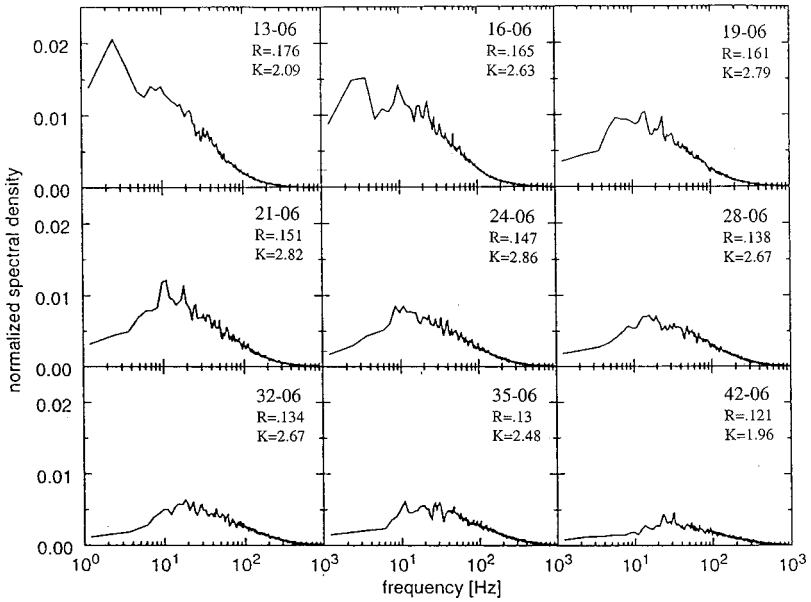

Fig. 12 Spectral density plots for increasing air flow rates (from top left to bottom right) and for the same water flow rate of 0.6 gpm (indicated by xx-06 in each plot). The Reynolds number ratio, R, and the relative roughness, K, are also given for each flow combination.

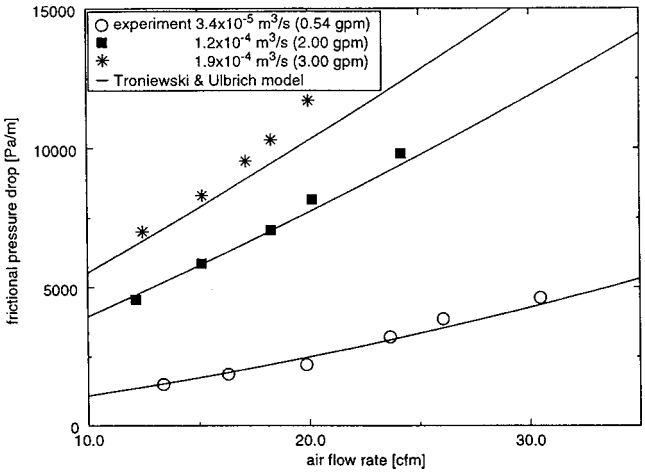

Fig. 13 Frictional pressure drop in the test section

characteristic of ripple waves always exist for all vapor Reynolds numbers, and the spectral density decays at approximately the same rate. It is primarily the pulses in the ripples that cause the roughness even in smooth films.

Estimation of Film Thickness at the Edges. The film thickness on the flat side of the test section can be different from that near the short side. Since direct measurements of film thickness were not made near the test section edges using the flush-wire probe, the local edge film thickness on the short side can only be estimated through visual observation and the pressure drop measurement. Pressure drop was measured over a distance of 19 mm (0.75 in.) in the fully developed region of the channel using a magnetic reluctance type pressure transducer. This differential pressure transducer was a Validyne DP103 with an accuracy of 0.5% of full scale. The differential pressure sensor was set up for a maximum pressure difference of 350 Pa. It was calibrated using two columns of water with known difference in surface level. The calibrated pressure transducer provided a measurement accuracy better than 1.5% of the measured value over the full range. The percentage error is expected to be high when the pressure drop is low for a given combination of air and water flow rates. Friction head was determined by subtracting the gravity head from the measured overall pressure drop. The film thickness in the narrow dimension is measured as discussed in the previous sections, and is assumed to be constant across the width. Visual observations showed that the edge film thickness is nearly the product of the cross-section aspect ratio ($W/t=10$) and the measured narrow dimension film thickness. Treating the ratio of the width-to-narrow dimension film thicknesses as an unknown constant of proportionality, Troniewski and Ulbrich's [26] pressure drop model for annular flows in a rectangular cross section was used to fit the data. Figure 13 shows that using a constant of proportionality of 7.0, the frictional pressure drop collapses well with the predictions especially for low flow rates. For higher liquid flow rates the pressure drop is not predicted well for a constant of 7.0. The agreement improves if a larger constant of proportionality is chosen, suggesting that the edge film thickness is dependent on the ratio of phasic Reynolds numbers as seen before in the narrow dimension. More detailed measurements of edge films for various channel aspect ratios are needed to improve available models and to develop new models.

Interfacial or Wave Velocity Measurements. The exact average time delay between the upstream and the downstream probe signals can be determined from the maximum of the cross-correlation of the two signals. The wave velocity is then calculated from the time delay and the known probe separation distance of 2 mm. The accuracy of the wave velocity is limited by the temporal resolution of the data acquisition and the uncertainty in streamwise probe separation distance. The uncertainty is typically 8% for wave velocities of about 2 m/s. The uncertainty increases with increasing wave velocity to about 20% for a wave velocity of 7 m/s.

As discussed previously, the liquid film is not considered merely as added roughness to the wall, but rather as a flow field separated from the gas flow by an interface. Then conceptually, an appropriate shear model at the interface between the gas and the liquid phase should account for the interfacial waves as follows:

$$\tau_i|_g=\frac{1}{2}C_{f_i}|_g\rho_g(u_g-u_i)^2 \tag{3}$$

$$\tau_i|_l=\frac{1}{2}C_{f_i}|_l\rho_l(u_i-u_l)^2. \tag{4}$$

Since the shear is the same at the interface, combinings Eqs. (3) and (4), an expression for the interfacial velocity can be obtained as

$$u_i=\frac{Cu_g+u_l}{1+C} \tag{5}$$

where

$$C=\sqrt{\frac{\rho_g}{\rho_l}\frac{C_{f_i}|_g}{C_{f_i}|_l}}. \tag{6}$$

For fully rough interfaces as in the case of the disturbance waves, C_{f_i} is a function of wave roughness in each phase, and the ratio $\sqrt{C_{f_i}|_g/C_{f_i}|_l}$ can be written in terms of the Reynolds number ratio as seen in the earlier section. The measured wave (interfacial) velocity (Fig. 14(*a*)) shows an increasing trend with both Re_g and Re_l as expected. The model as postulated above in Eq. (5) predicts the data very well if C is correlated by

$$C=5.5\left(\frac{\rho_g}{\rho_l}\right)^{1/2}\left(\frac{\mathrm{Re}_l}{\mathrm{Re}_g}\right)^{1/4}. \tag{7}$$

As in the case of film thickness and roughness, now the wave velocity can also be determined a priori purely in terms of the phasic superficial velocities and Reynolds numbers.

Summary and Conclusions

Measurements of average and fluctuating film thickness and wave velocity have been made using flush-wire conductivity probes in a high aspect ratio vertical duct for a wide range of air and water flow rates in the annular flow regime. The following general conclusions can be made:

- The transition line from churn-turbulent to the annular flow regime is compared with the available rectangular channel data in the literature. Since the method of air injection is different for each study and the evaluation of the transition line from photography is subjective, it is difficult to plot a conclusive flow regime transition map for thin, high aspect ratio, rectangular channels without further study.
- The base film thickness measurements made in this paper are believed to be among the thinnest films measured in the literature. Measurements of the base films range from 50 μm to $\sim$325 μm (2% to 10% of half-channel thickness).
- Statistical analysis shows that the standard deviation of the film thickness is a good measure of the film roughness. In the literature, the relative roughness has been correlated in terms of the film thickness, which is a measured quantity. In this study, the liquid film is treated as a separate flow field and not merely as a roughened surface to the gas core. This has allowed us to correlate the relative roughness and the non-dimensional film thickness as functions of the phasic Reynolds number ratio, which is known a priori.

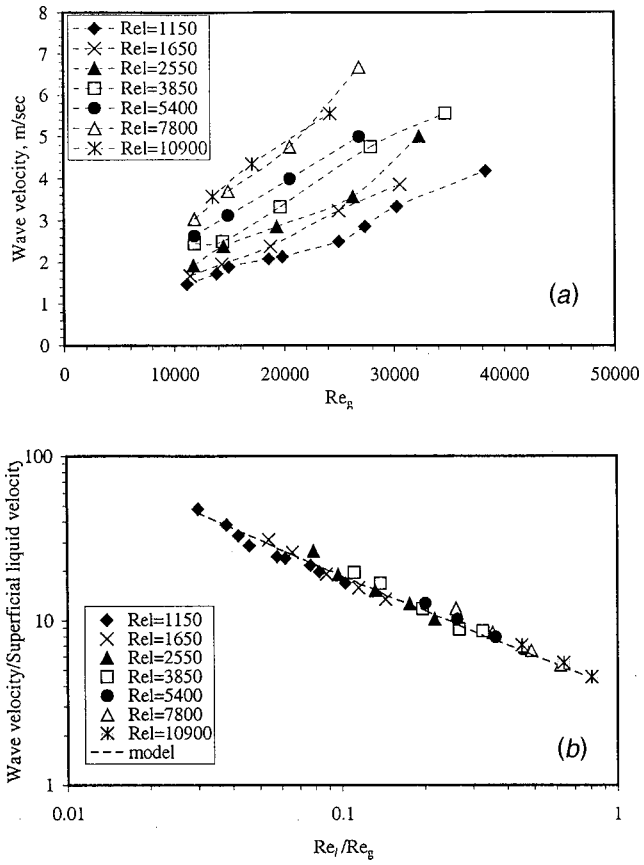

Fig. 14 (a) Dimensional wave velocity versus Re_g; (b) Nondimensional wave velocity versus Re_l/Re_g

• As reported in the literature [23,24], the maximum ratio of the disturbance wave amplitude to mean film thickness is close to a value of 4.0. This value was found to occur at a Reynolds number ratio, $R=\mathrm{Re}_l^{0.15}/\mathrm{Re}_g^{0.3}=0.15$ for a wide range of liquid and air flow rates, with the roughness decreasing on either side of R.

• Contrary to what is reported in the literature [24], the wave amplitude to mean film thickness ratio is a strong function of the film thickness. For $R<0.15$, the film thickness is at a constant of about 50 μm, and the waves that appear on the base film are ripples with pulses of disturbance waves, increasing the relative roughness with slight increases in the liquid flow rate. For $R>0.15$, with the increase in the liquid flow, the energy in the spectrum is seen to shift to higher frequencies with diminishing amplitude. Therefore, the relative roughness reduces from a maximum of 4.0 to nearly 1.0.

• A simple model for the wave velocity, obtained by matching the interfacial shear in the two fluids, predicts the data very well.

Nomenclature

C = coefficient used in the wave velocity correlation
C_{f_i} = friction coefficient
d_h = hydraulic diameter
K = relative roughness, σ_δ/δ
Re = Reynolds number, $\mathrm{Re}=\rho u d_h/\mu$
R = Reynolds number ratio, $R=\mathrm{Re}_l^{0.15}/\mathrm{Re}_g^{0.3}$
t = duct thickness, mm
u_g = superficial vapor velocity, m/s
u_l = superficial liquid velocity, m/s
u_i = interfacial or wave velocity, m/s
W = duct width, mm

Symbols:

δ = base film thickness; μm
ρ = density, kg/m^3
σ_δ = standard deviation of film thickness
τ_i = interfacial shear, N/m^2

Subscripts:

g = vapor
l = liquid

References

[1] Hall-Taylor, N., Hewitt, G. F., and Lacey, P. M. C., 1963, "The Motion and Frequency of Large Disturbance Waves in Annular Two-Phase Flow of Air-Water Mixtures," Chem. Eng. Sci., **18**, pp. 532–552.
[2] Hewitt, G. F., and Govan, A. H., 1990, "Phenomena and Prediction in Annular Two-Phase Flow," ASME FED-Vol. 99, *Advances in Gas-Liquid Flows*, Kim, J. H., et al., eds., pp. 41–56.
[3] Lilleleht, L. U., and Hanratty, T. J., 1961, "Relation of Interfacial Shear Stress to the Wave Height for Cocurrent Air-Water Flow," AIChE J., **7**, pp. 548–550.
[4] Wallis, G. B., 1969, *One-Dimensional Two-Phase Flow*, McGraw-Hill, New York, pp. 320–321.
[5] Sekoguchi, K., Hori, K., Nakazatomi, M., and Nishikawa, K., 1978, "On Ripple of Annular Two-Phase Flow - 2. Characteristics of Wave and Interfacial Friction Factor," Bull. JSME, **21**, No. 152.
[6] Kang, H. C., and Kim, M. H., 1993, "The Relation Between the Interfacial Shear Stress and the Wave Motion in a Stratifield Flow," Int. J. Multiphase Flow, **19**(1), pp. 35–49.
[7] Lamb, H., 1945, *Hydrodynamics*, Dover, New York.
[8] Gersey, C. O., and Mudawar, I., 1995, "Effects of Heater Length and Orientation on the Trigger Mechanism for Near-Saturated Flow Boiling Critical Heat Flux--II. Critical Heat Flux Model," Int. J. Heat Mass Transf., **38**(4), pp. 643–654.
[9] Azzopardi, B. J., 1997, "Drops in Annular Two-Phase Flow," Int. J. Multiphase Flow, **23**, pp. 1–53.
[10] Martin, R., 1972, "Measurement of the Local Void Fraction at High Pressure in a Heating Channel," Nucl. Sci. Eng., **48**, pp. 125–138.
[11] Sadatomi, M., Sato, Y., and Saruwatari, S., 1982, "Two-phase Flow in Vertical Non-circular Channels," Int. J. Multiphase Flow, **8**, pp. 641–655.
[12] Moriyama, K., and Inoue, A., 1992, "The Thermal Hydraulic Characteristics of Two-Phase Flow in Extremely Narrow Channels," Heat Transfer-Jpn. Res., **21**, pp. 823–837.
[13] Mishima, K., Hibiki, T., and Nishihara, H., 1991, "Some Characteristics of Gas-Liquid Flow in Narrow Rectangular Ducts," *Proc. International Conference on Multiphase Flows*, pp. 485–488.
[14] Coney, M. W. E., 1973, "The Theory and Application of Conductance Probes for the Measurement of Liquid Film Thickness in Two-Phase Flow," Journal of Physics and Engineering: Scientific Instrumentation, **6**, pp. 903–910.
[15] Koskie, J. E., Mudawar, I., and Tiederman, W. G., 1989, "Parallel-Wire Probes for Measurement of Thick Liquid Films," Int. J. Multiphase Flow, **15**(4), pp. 521–530.
[16] Kang, H. C., and Kim, M. H., 1992, "The Development of a Flush-Wire Probe and Calibration Methods for Measuring Liquid Film Thickness," Int. J. Multiphase Flow, **18**(3), pp. 423–437.
[17] Wambsganss, M. W., Jendrzejczyk, J. A., France, D. M., 1991, "Two-Phase Flow Patterns and Transitions in a Small, Horizontal, Rectangular Channel," Int. J. Multiphase Flow, **17**, pp. 327–342.
[18] Ali, M., and Kawaji, M., 1991, The Effect of Flow Channel Orientation on Two-Phase Flow in a Narrow Passage Between Flat Plates, ASME/JSME Thermal Engineering Proc., **2**, pp. 183–190.
[19] Wilmarth, T., and Ishii, M., 1994, "Two-Phase Flow Regimes in Narrow Rectangular Vertical and Horizontal Channels," Int. J. Heat Mass Transf., **37**(12), pp. 1749–1758.
[20] Hewitt, G. F., and Roberts, D. N., 1969, "Studies of Two Phase Flow Patterns by Simultaneous X-Ray and Flash Photography," Report, AERE-M2159, UKAEA, Harwell.
[21] Telles, A. S., and Dukler, A. E., 1970, "Statistical Characteristics of Thin, Vertical, Wavy Liquid Films," Ind. Eng. Chem. Fundam., **9**(3), pp. 412–421.
[22] Chien, S., and Ibele, W., 1964, "Pressure Drop and Liquid Film Thickness of Two-Phase Annular and Annular-Mist Flows," ASME J. Heat Transfer, **86**, pp. 80–86.
[23] Hewitt, G. F., and Whalley, P. B., 1989, "Vertical Annular Two Phase Flow," Multiphase Science and Technology, **4**, Hemisphere Publishing, New York.
[24] Hewitt, G. F., 1969, "Disturbance Waves in Annular Two-Phase Flow," Proc. Inst. Mech. Eng., Vol. **184**, pp. 142–150.
[25] Shearer, C. J., and Davidson, J. F., 1965, "The Investigation of a Standing Wave Due to Gas Blowing Upwards Over a Liquid Film: Its Relation to Flooding in Wetted Wall Columns," J. Fluid Mech., **22**, pp. 321–335.
[26] Troniewski, L., and Ulbrich, R., 1983, "Two-Phase Gas-Liquid Flow in Rectangular Channels," Chem. Eng. Sci., **39**, No. 4, pp. 751–765.

M. J. A. M. van Putten
C. R. Kleijn[1]
H. E. A. van den Akker

Kramers Laboratorium voor Fysische Technologie,
Faculty of Applied Sciences,
Delft University of Technology,
Prins Bernardlaan 6,
2628 BW Delft,
The Netherlands

Multi-Parameter Sensing With a Thermal Silicon Flow Sensor

We present a method for multi-parameter sensing in the application of thermal vector flow sensors. The method is based on the property that two independent signals can be obtained from a single sensing element, viz. a thermal vector flow sensor. For particular applications, this reduces the number of sensors in the measurement process. It may also allow redundant measurement of physical parameters, such as temperature; these redundant measurements are important for self-diagnostics of proper operation of a measurement system. The method is applied to a bidirectional silicon flow sensor, that generates two independent signals, both being a function of the Re number and the fluid temperature. This allows both temperature and mass flow measurement by use of a single sensor. Temperature estimates are accurate within 0.64 K and mass flow estimates within 5.6%. [DOI: 10.1115/1.1486471]

1 Introduction

In many technical applications, the measurement of flow in terms of its mass units is of increasing interest. In process control of chemical reactions, for example, mass flow rates are often needed to determine energy balances in process plants. Accurate mass flow rate measurements are also clearly required when a product is sold on a weight basis.

Several approaches to direct mass flow measurement are known to which different physical principles may apply, for instance; (i) moment of inertia of the fluid; (ii) differential pressure measurement; or (iii) heat transfer from a heated body to the fluid. Coriolis meters [1] are representatives of the first principle. They find applications particularly in the measurement of liquids and slurries. An example of the second principle is the standard Venturi tube [2], where the pressure difference is determined using tappings at the inlet and throat of the device. Heat flux thermal flow sensors are representatives of the third measurement principle [3]. Various devices are known, ranging from hot-wires and hot-films to silicon integrated sensors [4–8]. Applications of silicon flow sensors have recently been advanced by a new method for drift elimination [9,10]. It applies to sensors with directional sensitivity (*vector* sensors), successfully tested on silicon flow sensors [9], demonstrating enhanced stability, accuracy and dynamic range [11].

In this paper, we present a silicon thermal mass flow sensor that provides two independent signals: (i) a total heat flow signal and (ii) a signal that contains a measure for the flow induced thermal gradient across its surface. The second characteristic makes it suitable for bidirectional flow measurement [9] and zero-drift elimination [10]. In addition, combination of the signals (i) and (ii), allows multi-parameter sensing, i.e., estimation of both mass flow and fluid temperature, which is the topic of the present paper.

2 Operation of the Device

The sensor consists of a silicon chip, on which two Wheatstone bridges are integrated, as illustrated in Fig. 1.

This design was originally proposed and realized by A.F.P. van Putten in 1980 [12]. The outer bridge, *M*, is the actual measurement bridge, that is fed by a current I_M from a constant current source; the inner bridge is the heater bridge, *H*. The voltage, V_M, that is generated over the measurement bridge, is kept constant and equal to a reference voltage, V_{ref}, by application of thermal feedback. This is realized by driving the heater bridge, where the feedback loop is created by thermal conduction in the sensor substrate. This principle of thermal feedback assures a constant reference voltage across the constant current driven measurement bridge, thereby realizing a constant-current-constant-voltage biasing [13,5]. By this construction, a *constant mean surface temperature*, T_w, of the sensor is realized. A flow across the surface will (i) increase the current in the heater bridge, in order to realize a constant mean temperature, and (ii) induce a small temperature gradient in the sensor surface. This streamwise gradient is detected by the measurement bridge and contains the flow signal, V_{grad}. In summarizing, two processes occur when a forced flow component is present: First, there is an increase in the total amount of heat transferred from the sensor to the fluid. This increase in heat loss is ''compensated'' by an increase in heat production by the heater bridge to ensure a constant dissipation in the measurement bridge (*global variations, process I*). Second, a small temperature gradient is induced across the surface, that contains information about both the direction and strength of the flow (*local variations, process II*). Under operating conditions, therefore, two different sensor signals can be obtained: the voltage across the heater bridge, V_H, that serves as measure for changes in the total heat loss (Process I), and the gradient voltage, generated over the measurement bridge, V_{grad}, Process II (cf. Fig. 1).

In practice, the sensor is positioned in the center of a tube with cross-sectional area *A*, where it measures the *local* velocity across its surface. For a given medium, Reynolds number and tube geometry, which is in fact part of our measurement device, there is a fixed relation between the local velocity and the total mass flow, ϕ_m. This relationship is determined experimentally for the Reynolds range of interest, using a computer controlled measurement setup, including a rotary piston meter that acts as an accurate reference for the total mass flow. In this setup, the flow is fully developed. Obviously, the relation between the point measurement of the velocity and the total mass flow will be different if the flow in an actual measuring situation differs from the profile in a fully developed flow, which may be the case directly after bends or contractions.

We will now further discuss the processes I and II in more detail and show how their combined measurement can be used to determine both the mass flow and the fluid temperature.

2.1 Process I: Total Heat Flow Measurement. The total electrical dissipation, P_{tot}, of the sensor is given by the sum of the dissipation in the measurement bridge, P_M, and that in the heater

[1]Corresponding author. e-mail: crkleijn@klft.tn.tudelft.nl

Contributed by the Fluids Engineering Division for publication in the JOURNAL OF FLUIDS ENGINEERING. Manuscript received by the Fluids Engineering Division June 19, 2000; revised manuscript received January 29, 2002. Associate Editor: J. Bridges

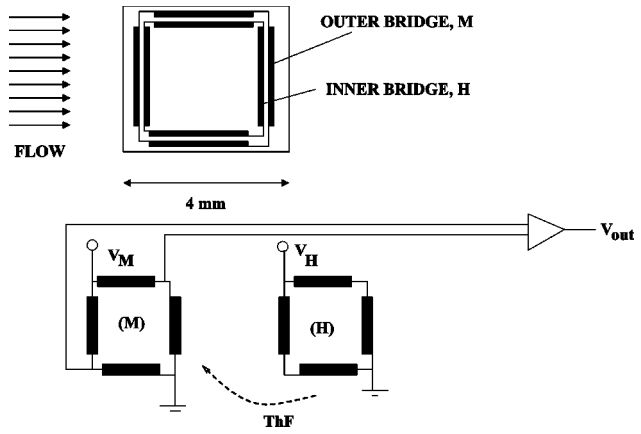

Fig. 1 Top: Schematic drawing of the sensor; both bridges are indicated. Bottom: principle of the double bridge configuration. The measurement bridge is denoted by (M), the heater bridge by (H); ThF denotes thermal feedback, realized by thermal conduction in the silicon substrate. The gradient signal is measured by the operational amplifier, and yields the signal $V_{out}=V_{grad}$.

bridge, P_H, i.e.,

$$P_{tot}=P_M+P_H=\underbrace{V_M I_M}_{\text{constant}}+V_H^2/R_H. \quad (1)$$

where V_H is the heater bridge voltage and R_H is the heater bridge resistance. Since by construction, as discussed in the previous section, the measurement bridge is operated at both a constant voltage and a constant current [14], the dissipation, P_M, in the measurement bridge is constant. Since the (mean) temperature of the sensor is constant as well, $R_H=$constant, too. Therefore, changes in the total electrical dissipation of the device are reflected in changes in the *heater* bridge voltage, V_H, only.

The total heat flow, Φ_H, from the plate equals the sum of the radiated heat, ϕ_{rad}, free and forced convected heat, ϕ_{conv}, and the conductive heat losses, ϕ_{cond}, to the substrate onto which the plate is mounted by four small glass piles ($\approx 0.2\times 0.2\times 0.2$ mm), respectively, i.e.,

$$\Phi_H=\phi_{conv}+\phi_{cond}+\phi_{rad}. \quad (2)$$

Due to conservation of energy, the total electrical dissipation, P_{tot}, will equal the total heat loss, Φ_H, which yields

$$P_{tot}=\Phi_H=V_M I_M+V_H^2/R_H. \quad (3)$$

Since the operating temperature, T_w, of the flat plate is constant, and as long as changes in radiation losses due to changes in the tube wall temperature may be ignored, we may set $\phi_{rad}=$constant$=c_2$. For the heat loss to the carrier on which the sensor is mounted, we write $\phi_{cond}=c_1\Delta T=c_1(T_w-T_f)$, according to Newton's heat flux law and assuming the carrier is at the fluid temperature T_f. This reduces Eq. (2) to

$$\Phi_H=\phi_{conv}+c_1\cdot\Delta T+c_2=(h_{conv}A_w+c_1)\cdot\Delta T+c_2 \quad (4)$$

with h_{conv} denoting the convective heat transfer coefficient and A_w the contact area of the sensor to the fluid. Introducing the Nu number, $\mathrm{Nu}=h_{conv}L/\lambda$ (for a definition of symbols used, see the Nomenclature), results in

$$\Phi_H=\left(\frac{\mathrm{Nu}\cdot\lambda\cdot A_w}{L}+c_1\right)\cdot\Delta T+c_2. \quad (5)$$

Since the flow sensor may operate in both mixed and forced convective flows, it is important to distinguish between those situations where the flow can be regarded as essentially forced, the forced-flow domain, and those where free convection cannot be neglected: the mixed-flow domain. In the mixed flow domain, the free and the forced convective forces are of comparable magnitude, and the flow field is defined by both contributions. Here, the Nu number is not only a function of the Reynolds number Re and the Prandtl number Pr, but also of the Grashof number Gr. Therefore, for the Nu number we have

$$\mathrm{Nu}=f(\mathrm{Gr},\mathrm{Re},\mathrm{Pr},\alpha) \quad (6)$$

where the angle α of the flat plate with respect to the gravity vector is introduced explicitly to indicate that in the mixed-flow domain the Nu number is a function of orientation, too. For a flat plate, a semi-empirical correlation is given by

$$\mathrm{Nu}=[\mathrm{Nu}_{forced}^n(\mathrm{Re},\mathrm{Pr})+\mathrm{Nu}_{free}^n(\mathrm{Gr},\mathrm{Pr},\alpha)]^{1/n} \quad (7)$$

with n typically between 1 and 3. This correlation was originally proposed by Churchill [15], and later generalized by others, for instance by Chen [16].

In the current geometry, with α fixed at 90 deg and Gr$=290$, $\mathrm{Nu}_{free}\approx$constant$\approx 3.24$ [17].

For air, the Prandtl number can be considered as fixed and equal to 0.71 in the temperature range under consideration; hence, in this case Nu_{forced} depends on Re only. For a flat plate, we may write $\mathrm{Nu}_{forced}=c_0\,\mathrm{Re}^{0.5}$; using Eq. (7) turns Eq. (5) into

$$\Phi_H=[((c_0\mathrm{Re}^{0.5})^n+3.24^n)^{1/n}\cdot\lambda(A_w/L)+c_1]\cdot\Delta T+c_2. \quad (8)$$

Although Eq. (7) was originally proposed to hold for a free flat plate, we will assume it may be valid for our geometry as well, where its behavior will be experimentally verified. Note that the mass flux, $\phi_m''=\rho u$, is related to the Re number as $(\eta/L)\mathrm{Re}=\phi_m''$.

2.2 Process II: Temperature Gradient Measurement. In the original design of the flow sensor, it was not primarily the change in the mean heat transfer coefficient, as measured from the change in the heater voltage, V_H, that was intended to be used as a measure for the flow signal, but the temperature gradient across its surface that would arise if placed in a flow [12].

This flow induced temperature gradient in the surface of the sensor is due to the fact that the local heat transfer coefficient h_x at the leading edge is different from that at the trailing edge. This follows directly from the relationship $h_x=-\lambda(\partial T/\partial y)/(T_w-T_f)$ where the fluid temperature gradient (evaluated at the sensor surface) is larger at the leading edge than at the trailing edge, due to the thermal boundary layer profile.

This difference in heat transfer coefficients, Δh_x, will induce a temperature gradient, ΔT_w, in the sensor surface, which is the source for the second sensor signal, V_{grad}, across the measurement bridge:

$$V_{grad}=V(\Delta h_x,\Delta T) \quad (9)$$

or stated differently

$$V_{grad}=g(\Delta \mathrm{Nu}_x,\Delta T) \quad (10)$$

where the function g relates the sensor output signal, V_{grad}, to the differences in the local Nu_x number and the sensor-fluid temperature difference, ΔT. This second output signal of the sensor, therefore, is also a function of both the mass flow, now contained in the *nonuniformity* of the local Nu number, and the sensor-fluid temperature difference, ΔT. Since there exists an a priori unknown, but fixed relation between the local Nu number Nu_x, and the overall Nu number, we will further drop the subscript from the local Nu number. We now write, in agreement with our previous discussion and using $\mathrm{Nu}=f(\mathrm{Gr},\mathrm{Re},\mathrm{Pr},\alpha)$

$$V_{grad}=g(\mathrm{Re},\mathrm{Gr},\Delta T) \quad (11)$$

where Pr as well as the angle α are assumed to be constant and therefore have been left out of this expression.

Although in theory Eq. (11) holds, in practice offset signals may be present that also contribute to the output signal. In a real world environment, Eq. (11) becomes

$$V_{\text{grad}} = g(\text{Re}, \text{Gr}, \Delta T) + E(U_1, U_2, \cdots, U_n) \tag{12}$$

where the function E is the so-called offset, i.e., the contribution of all additive disturbing effects on the sensor output signal. If the offset is a well defined constant, sensors may be designed with the possibility of offset compensation at the production site, for instance by suitable calibration. However, offset generally may vary (also known as drift) due to temperature variations, time, strain and stresses introduced by packaging, aging, etcetera. This creates a need for offset-reduction or drift-elimination methods that can be applied during each measurement. Especially at measurement of low air flow velocities, this influence may become relatively large.

In order to essentially eliminate this (bias) error function E, the VanPutten-Alternating Direction Method (VanPutten-ADM) [10,9,18,19] was applied. This procedure uses the bidirectional sensitivity of the current sensor, which can be realized with suitable electronics. This implies that the function g in Eq. (12) has either a positive or negative sign, depending on the direction of the flow applied to the *vector* sensor in contrast to the error function E, which is *not* dependent on the flow-sensor orientation. In practice, therefore, a measurement is performed with two different flow-sensor orientations,

$$V^1_{\text{grad}} = g(\text{Re}, \text{Gr}, \Delta T) + E(U_1, U_2, \cdots, U_n) \tag{13}$$

and

$$V^2_{\text{grad}} = -g(\text{Re}, \text{Gr}, \Delta T) + E(U_1, U_2, \cdots, U_n) \tag{14}$$

where subtraction of the signals yields the ADM-signal

$$V_{\text{ADM}} = 2g(\text{Re}, \text{Gr}, \Delta T) + \epsilon. \tag{15}$$

The additive drift effect has now been reduced to the difference over the time interval Δt between the two measurements, with $\epsilon = (\partial E/\partial t)\Delta t \ll E$, and an essentially *pure gradient measurement* has been realized [19].

We now propose the following semi-empirical relation [5] between the V_{ADM} voltage and the Re number and sensor-fluid temperature difference, ΔT, that explicitly defines V_{ADM} as

$$V_{\text{ADM}} = \sum_{i=1}^{N} a_i (\text{Re}^{0.5} \cdot \Delta T)^i \tag{16}$$

where now Nu is a function of the Re number, only. Since Gr was essentially fixed in our present experiments, a possible dependence on Gr is included in the values obtained for the coefficients.

We therefore have two expressions, given by the functions Φ_H and V_{ADM} in Eqs. (8) and (16) respectively, that are both functions of the Re number and the fluid-sensor temperature difference, ΔT. If the total heat loss and the gradient signal are independent, estimation of both Re and ΔT is feasible from simultaneous measurements of Φ_H and V_{ADM}. We will prove by experiment that this is indeed the case.

3 Methods

3.1 Experimental Procedure. The flow sensor is placed vertically inside the center of a horizontal stainless-steel tube with an internal diameter of 36 mm, as illustrated in Fig. 2.

It is connected to a revolving mechanism that could turn the sensor ± 180 deg in about 0.2 s. This realizes the two different flow sensor orientations, position 1 and position 2, respectively. The sensor is mounted onto a ceramic holder via 4 small glass-piles (size $0.2 \times 0.2 \times 0.2$ mm). Upstream, a Pt100 element is positioned to measure the air temperature. We use a very small sensor (1.3 mm) in order to reduce the possible effects on the flow profile in the tube. The revolving mechanism is controlled by a microcomputer, that on its turn is connected to the measurement computer, using LabView (National Instruments).

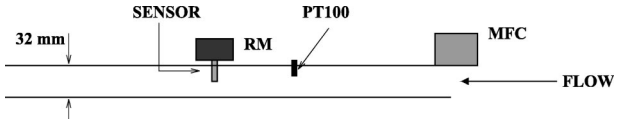

Fig. 2 Illustration of the measurement setup. The entrance length to the flow sensor is 1 meter, as well as the exit length. The mass flow controller (MFC) is placed upstream of the entrance length. RM=revolving mechanism. The temperature sensor is a Pt100 element, positioned upstream from the flow sensor.

A flow of ambient air is applied by use of a computer controlled mass flow controller (Bronckhorst Hytec, $0-20 \cdot 10^{-5}$ kg/s; 0–200 liters/min; $\text{Re}_L = 0-800$; $\text{Re}_D = 0-7200$); at the end of the flow tube, a rotary piston displacement meter is positioned as a reference (IRM-16, Instromet, Netherlands). This instrument allows volume measurements with an absolute error smaller than 0.3% of reading. From the volume displaced per unit time, the mass flow is calculated, using the universal gas law to calculate a standard volume. Although the sensor measures a local flow velocity in the tube, it is not so that the mass flow velocity is calculated from this point velocity measurement. Instead, an approach is chosen where the (fixed) relation between the local velocity and the mass flow is detected the displacement meter that acts as a reference for the calibration procedure in the total mass flow.

The Re_L numbers are calculated from the mean velocity in the flow tube and a characteristic length equal to the sensor size, $L = 4$ mm, where it is realized that our measurements are performed in both the laminar and the turbulent flow region, where different flow profiles are known to exist. Since the dynamic viscosity and the thermal conductivity vary less than $\approx 0.1\%$ per degree Celsius, they are assumed constant throughout the measurement procedure, with typical gas temperature variations smaller than ± 10°C.

After each change in the mass flow, a waiting period of 3 minutes is maintained for stabilization, after which a new flow measurement is performed. The flow and heater bridge signals, V_{grad} and V_H, respectively, and the output of the Pt100 temperature sensor are sampled at $f_s = 20$ Hz before 14-bit digitization. After each rotation of the flow sensor, sampling starts 1 second after the rotation and lasts for 7 seconds, up to the start of a new rotation; this procedure yields 140 data points per measurement frame.

The data obtained in the measurement windows are averaged and subsequent mean values are subtracted to obtain the V_{ADM}-signal. The heater bridge signal, V_H, as well as the Pt100 temperature, are also averaged over this 7 second measurement interval. Therefore, every 8 seconds three parameters are obtained. These data are written to file, together with the reference flow measured by the rotary piston displacement meter. A measurement continues for a few days, yielding a large dataset, typically containing a few hundred data points over a range of gas temperatures (typically 16–26°C), due to the natural fluctuations of the temperature in our laboratory.

The sensor operating temperature is derived by comparing the resistance value of the Wheatstone bridge under operating (i.e., heated) conditions with the value at ambient temperature. The dissipation in the measurement bridge, ϕ_M, is calculated from the reference voltage and the measurement bridge current. The total heat loss, Φ_H, is calculated from the heater bridge signal, according to

$$\Phi_H = V_H^2 / R_{\text{bridge}} + \phi_M, \tag{17}$$

where R_{bridge} is the resistance of the heater bridge under operating conditions.

3.2 Parameter Estimation. The final goal of the parameter estimation is to find the values of Re and ΔT given the total electrical dissipation, $P_{\text{tot}}=\Phi_H$ and the V_{ADM} signal, using Eqs. (8) and (16), repeated here for convenience

$$\begin{cases} \Phi_H=[((c_0\,\mathrm{Re}^{0.5})^n+3.24^n)^{1/n}\cdot\lambda(A/L)+c_1]\cdot\Delta T+c_2 \\ V_{\text{ADM}}=\sum_{i=1}^{N} a_i(\mathrm{Re}^{0.5}\cdot\Delta T)^i \end{cases} . \tag{18}$$

The estimation procedure consists of two steps. First, given the measured sets of Pt100 temperatures, T, Re numbers, V_{ADM} and Φ_H, the coefficients c_i, $(i=0,1,2)$ and a_i, $(i=1,...,N)$ and n are estimated using a non-linear fitting routine. Subsequently, applying Newton-Raphson's method to Eq. (18) with the now known coefficients, the temperature difference, $\Delta T=T_w-T_f$ and the Re number is determined. All routines are implemented in MatLab.

4 Results

To illustrate the typical signals that were measured in the experiment, we present in Fig. 3 the heater voltage, V_H, which is a measure for the total heat loss, and the sensor output voltage, V_{grad}, which contains the vectorial characteristics of the flow. The sensor was operated at a mean temperature of $T_w=68.1°\text{C}$. The dissipation in the measurement bridge was $P_M=0.096$ Watt $=$constant.

Figure 4 illustrates the temperature sensitivity of the sensor ADM-signal, V_{ADM}, and the total heat loss, Φ_H, as a function of the Re number for four different gas temperatures in the temperature range $T=18-24°\text{C}$. The temperature sensitivity of the gradient and total heat loss signal are approximately $3\%°\text{C}^{-1}$

The detailed characteristics near $\mathrm{Re}=0$ are presented in Fig. 5, showing the differences in sensitivity of the gradient signal, V_{ADM}, and the total heat loss signal, Φ_H. In this *mixed-flow* regime, with a significant contribution of the free convective forces to the heat transfer process [20,21], the gradient signal scales as a linear function of Re, while the power curve as a function of Re flattens, scaling as $\sim\mathrm{Re}^2$. This linear response of the gradient signal was also observed by others, for instance [22,23].

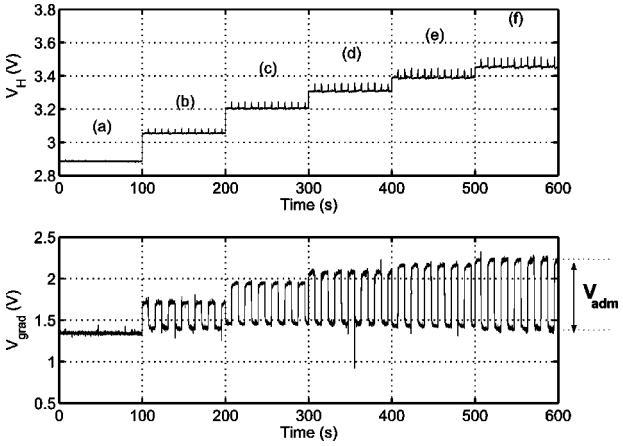

Fig. 3 Example of the heater voltage, V_H, and gradient signal, V_{grad}, from the sensor. The labels (a)–(f) denote 6 different flow velocities (0 to 20 SLM) (Re_L from 0 to 80) in steps of 4 SLM (or $\Delta R_L\approx 16$). The small spikes, visible in the heater signal, occur at the time that the sensor is turning 180°. During this rotation, it is temporarily positioned at a 90 deg angle with the forced flow component. In this position, the forced convected heat loss is increased, resulting in an increase in the heater voltage. The ADM signal relates to the top-top value of the amplitude of this gradient signal, as indicated in the graph for the flow velocity labeled with (f).

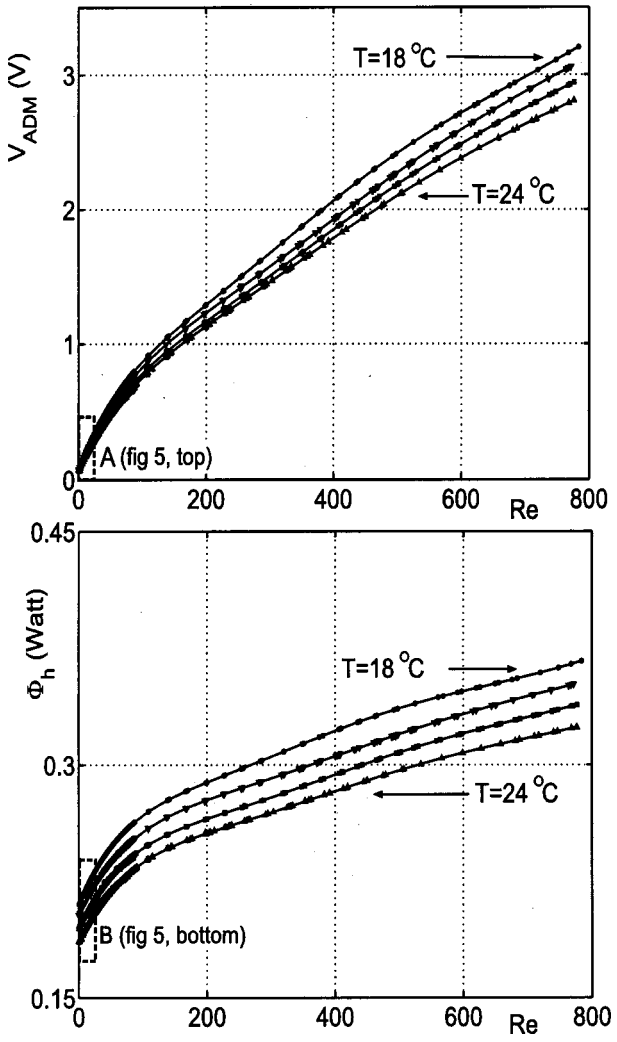

Fig. 4 Response curves for four different temperatures in the temperature range from 18 to 24°C. Only curves corresponding with even values of the temperature are shown. There is an increased density of measured values below Re≈80. Top: The gradient signal, V_{ADM}, as a function of Re. Bottom: total heat loss, Φ_H, as a function of Re. The detailed behavior of the response curves enclosed by the boxes A and B is shown in Fig. 5. Note, that the gradient signal, V_{ADM} is zero at Re=0, contrary to the total heat loss, Φ_H.

We remark, that the gain, G of our electronics was set to $G=1700$. The voltage across the measurement bridge at $\mathrm{Re}\approx 1$ was therefore about 10 μV, given the amplified signal amplitude of $\approx$17 mV. This implies that the temperature gradient in the sensor at these low Re numbers is in the order of a few mK [24].

In Fig. 6 we show the relation between the gradient signal and the total heat loss. Each combination of the gradient signal, V_{ADM}, and the total heat loss signal, Φ_H, corresponds to a single temperature, because the lines never intersect. This implies that the total heat loss, Φ_H and the gradient signal, V_{ADM}, are indeed independent signals.

To obtain a satisfactory forward estimate of the gradient signal, V_{ADM} in Eq. (16), the order of the polynomial was set to $N=8$. The coefficients in the expression for the heat loss found were $c_0=0.37\pm0.05$, $c_1=0.0027\pm0.0005$, and $c_2=0.011\pm0.005$ For n a value $n=0.62\pm0.01$ was found. Subsequently, Newton-Raphson's method was applied to Eq. (18), with the now known coefficients.

Results of the estimated values of Re and the gas temperature in

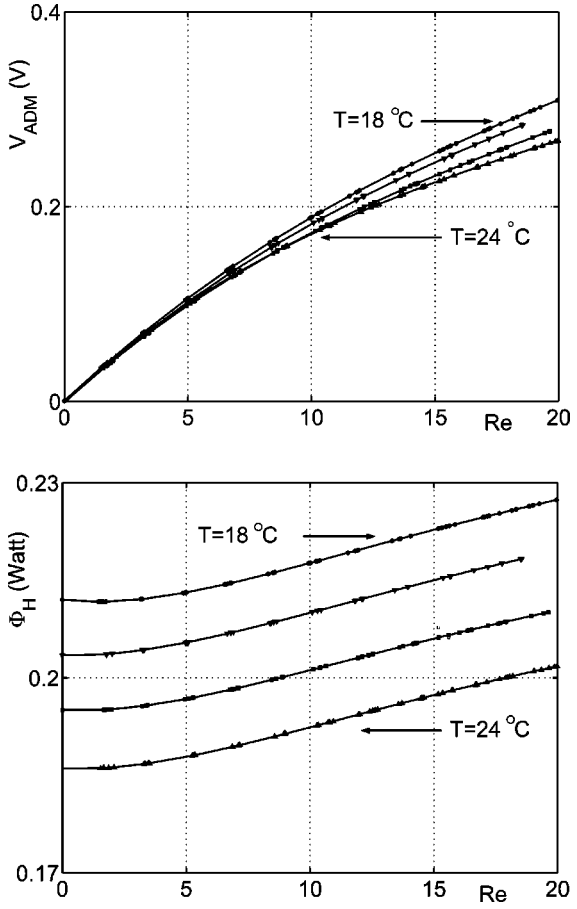

Fig. 5 Detail of the curves shown in Fig. 4 in the boxes A and B, respectively, showing the behavior of the gradient signal, V_{ADM} and the total heat loss, Φ_H, near Re=0. The gradient signal becomes a linear function of Re, while the heat loss behaves as an even function, scaling as $\sim Re^2$.

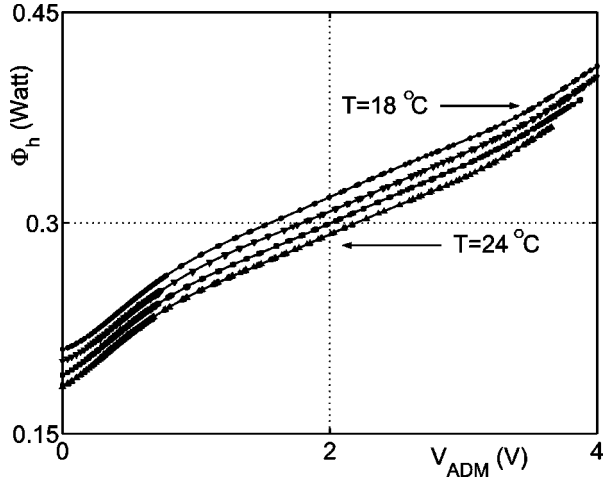

Fig. 6 Relation between the gradient signal, V_{ADM}, and the total heat loss, Φ_H, for four different temperatures in the temperature range 18–24°C; only values at even temperatures are displayed. Each point in the area enclosed by the V_{ADM} and the Φ_H axes correspond to a single temperature because the lines shown never intersect.

the flow range Re=0 to Re=800 are presented in Fig. 7. The standard deviation of the relative error in Re is 2.8%, the standard deviation of the absolute error in the temperature estimate is 0.32°C.

5 Discussion and Conclusions

Multi-parameter sensing may serve several purposes. For instance, in the application of thermal mass flow sensors, estimation of the gas temperature is necessary for mass flow measurements [3,4,25], with typical temperature sensitivities in the order of a few percent per degree Celsius [3,24]. Since the temperature of the fluid is in general not constant, continuous measurement of the fluid temperature needs to be realized; often, a separate temperature sensor is applied. Multi-parameter sensing, therefore, may apply to certain thermal mass flow sensors to circumvent the need for a separate temperature sensor in the measurement process. Obviously, this has beneficial consequences for mounting, packaging and calibration of the devices. For different applications, where an additional temperature sensor is used, it may allow *redundant* measurement of physical parameters, for instance temperature. This feature is important if continuous control of proper operation is important, for instance to reduce costs of preventive maintenance.

The current study was undertaken to investigate the possibility of multi-parameter sensing with a thermal heat flux sensor, that

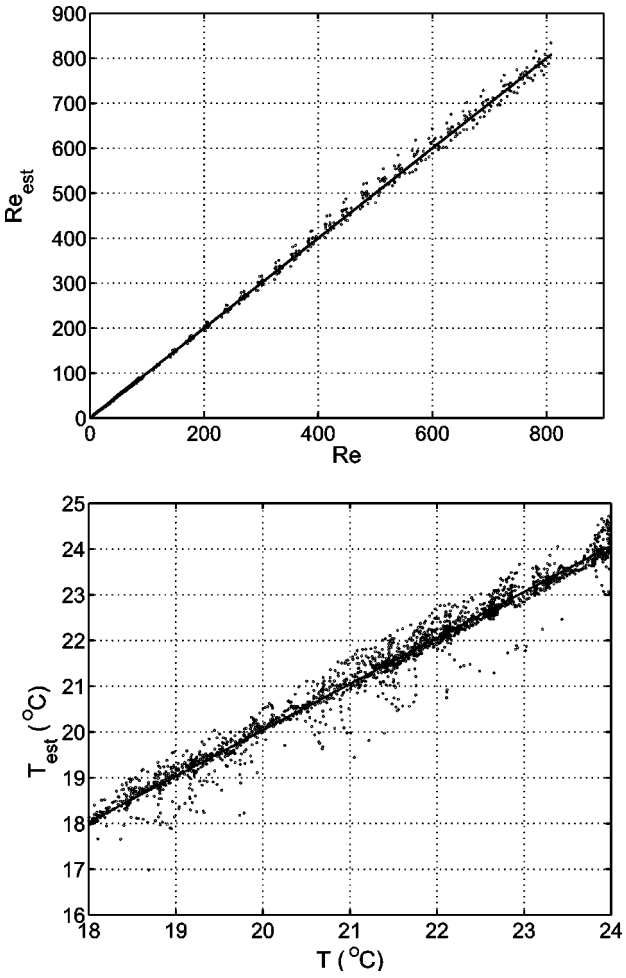

Fig. 7 Top: Estimated values of Re over the flow range Re=0 to Re=800. Bottom: Temperature estimates. The number of data points estimated was above 1900. The standard deviation of the relative error in the Re estimate is 2.8%. Temperature estimates are accurate within 0.64 K (2 standard deviations).

provides two sensor signals, *viz.* (i) a total heat loss signal, $\Phi_H = f(\mathrm{Re}, \Delta T)$ and (ii) a drift-free, pure gradient signal, $V_{\mathrm{ADM}} = g(\mathrm{Re}, \Delta T)$. As shown in Fig. 6, the total heat flow and the gradient signal are indeed independent, making multi-parameter sensing feasible.

Of course, several approaches exist to estimate the Re number and the temperature from these two signals, for instance by using a ''look-up'' table, using the relation between V_{ADM} and V_H as shown in Fig. 6. We decided to investigate the possibility of formulating explicit expressions for the gradient and total heat flow signal, that, after their parameters had been identified, could be used for the estimation of the Re number and the fluid-sensor temperature difference, ΔT.

The expressions presented in Eqs. (16) and (18) could satisfactorily describe the heat transfer processes over the complete flow range ($0 < \mathrm{Re} < 800$). For the coefficient, n, in Eq. (8) a value $n = 0.62$ was found; this value is somewhat smaller than the values obtained for a free, flat plate ($n = 1-3$). For the heat loss by radiation, we find $c_2 = 0.011 \pm 0.005$ Watt, which is realistic. The coefficient that accounts for the heat lost by conduction, $c_1 = 0.0027 \pm 0.0005\ \mathrm{J\,K^{-1}}$, is in agreement with previous measurements. For a typical sensor-fluid temperature difference of 40 K, this amounts to approximately 100 mWatt. Finally, we find that $c_0 = 0.37 \pm 0.05$. Subsequent application of Newton-Raphson's method realized Re-number estimates with a standard deviation of the relative error of 2.8% and temperature estimates accurate within 0.64 K (2 standard deviations) in the temperature range 18–24°C. Note, that if no temperature compensation had been applied, the error in the Re estimates would be about $3\%\,^{\circ}\mathrm{C}^{-1}$.

In summary, multi-parameter sensing can be realized with a thermal flow sensor, that allows measurement of two independent signals. As an application, this method may circumvent the need for an additional temperature sensor for mass flow measurements at varying gas temperatures. As an alternative, this multi-parameter sensing can be applied for self-diagnostics in those applications where a second temperature sensor is used. In that case, comparison between the ''flow sensor'' derived temperature and the temperature measured by the temperature sensor is possible. This is for instance important for long-term measurements or to assist in low-cost preventive maintenance.

Nomenclature

a = thermal diffusivity, $\mathrm{m^2\,s^{-1}}$
f = frequency, $\mathrm{s^{-1}}$
h = heat transfer coefficient, $\mathrm{W\,m^{-2}\,K^{-1}}$
t = time, s
u = velocity, $\mathrm{m\,s^{-1}}$
A = area, $\mathrm{m^2}$
E = additive drift, t.b.s.
H = heater bridge, -
I = current, Ampere
L = length, m
M = measurement bridge, -
P = power, W
R = resistance, Ω
T = temperature, °C or K
U = physical input, t.b.s
A_w = sensor area, $\mathrm{m^2}$
V_{grad} = gradient signal, V
V_h = heater signal, V
α = angle, rad
ϵ = rest value, t.b.s.
η = dynamic viscosity, $\mathrm{kg\,m^{-1}\,s^{-1}}$
ϕ = flow rate, t.b.s.
λ = thermal conductivity, $\mathrm{W\,m^{-1}\,K^{-1}}$
ν = kinematic viscosity, $\mathrm{m^2\,s^{-1}}$
ϕ_h = heat flow rate, W
ϕ_m = mass flow rate, $\mathrm{kg\,s^{-1}}$
ρ = density, $\mathrm{kg\,m^{-3}}$
θ = change in resistance value, Ω
Δ = difference, t.b.s.
ΔI = time interval, s
Φ = flow rate, t.b.s
Φ'' = flux, t.b.s
Θ = measurand, t.b.s.

Dimensionless Quantities

Gr = Grashof number, $gL^3\beta\Delta T/\nu^2$
Nu = Nusselt number, hL/λ
Pr = Prandtl number, ν/a
Re = Reynolds number, uD/ν

Subscripts

bridge = measurement bridge
cond = due to conduction
conv = due to convection
f = fluid
film = film
forced = forced convection
free = free convection
grad = gradient
h = heat or heater
m = mass
in = incoming
out = output or outgoing
rad = due to radiation
ref = reference
s = surface
w = surface
x = distance (m)
H = heater bridge
M = measurement bridge

Superscripts

ADM = ADM signal
1 = at position 1
2 = at position 2

Abbreviations

ADM = Alternating Direction Method
SLM = Standard Liter per Minute ($6{,}813\ 10^{-4}\ \mathrm{mol\,s^{-1}}$)
MFC = Mass Flow Controller

References

[1] Mettlen, D., Müller, A. (ed)., 1988, *Discharge and Velocity Measurement*, Balkema, Rotterdam.
[2] Sydenham, P. H. (ed.), 1983, *Handbook of Measurement Science, Vol 2, Practical Fundamentals*, Wiley, New York.
[3] Meijer, G. C. M. and Herwaarden, A. W. (eds.), 1994, *Thermal Sensors*, IOP Publishing, London.
[4] Göpel, W., Hesse, J., and Zemel, J. N. (eds.), 1990, *Sensors: A Comprehensive Survey, Vol. 4*, Thermal Sensors, VCH Verlagsgesellschaft GmbH, Weinheim.
[5] Van Putten, A. F. P., 1988, *Integrated Silicon Anemometers*, PhD thesis, Katholieke Universiteit Leuven, Belgium.
[6] Van Oudheusden, B., 1989, *Integrated Silicon Flow Sensors*, PhD thesis, Delft University of Technology, The Netherlands.
[7] Sze, S. M. (ed.), 1994, *Semiconductor Sensors*, Wiley, New York.
[8] Verhoeven, H.-J, 1995, *Smart Thermal Flow Sensors*, PhD thesis, Delft University of Technology, The Netherlands.
[9] Van Putten, M. J. A. M., Van Putten, M. H. P. M., and Van Putten, A. F. P., 1994, ''Full Additive Drift Elimination Using the Alternating Direction Method,'' Sens. Actuators, **44**, pp. 13–17.
[10] Van Putten, M. H. P. M., Van Putten, M. J. A. M., Van Putten, A. F. P. and Van Putten, P. F. A. M., 1995, ''Method for Drift Elimination in Sensors,'' *USA patent 5426969 and European patent application 94202293.0.*
[11] www.vpinstruments.com.
[12] Van Putten, A. F. P., 1980, ''Thermal Feedback Drives Sensor Bridge Simultaneously with Constant Supply Voltage and Current,'' IEEE Trans. Instrum. Meas., **39**, pp. 48–51.
[13] Van Putten, A. F. P., and Middelhoek, S., 1974, ''An Integrated Silicon Anemometer,'' Electron. Lett., **10**(21), pp. 425–426.
[14] Van Putten, A. F. P., 1990, ''Thermal Feedback Drives Sensor Bridge Simultaneously with Constant Supply Voltage and Current,'' IEEE Trans. Instrum. Meas., **39**, pp. 48–51.
[15] Churchill, S. W., 1977, ''A Comprehensive Correlating Equation for Laminar

Assisting Forced and Free Convection,'' AIChE J., **23**(1), pp. 10–16.
[16] Chen, T. S., Armaly, B. F., and Ramachandran, N., 1986, ''Correlations for Laminar Mixed Convection Flows on Vertical, Inclined and Horizontal Flat Plates,'' ASME J. Heat Transfer, **108**, pp. 835–840.
[17] Bird, R. B., Stewart, W. E. and Lightfoot, E. N., 1994, *Transport Phenomena*, Wiley, New York.
[18] Van Putten, M. J. A. M., 2000, ''*Flow Measurements with Thermal Silicon Sensors*,'' PhD thesis, Delft University of Technology, The Netherlands.
[19] Van Putten, M. J. A. M., and Van Putten, M. H. P. M., 2001, ''Facing Drift: A Comparison of Three Methods,'' Sens. Actuators, **90**, pp. 172–180.
[20] Van Putten, M. J. A. M., Van Putten, M. H. P. M., and Van Putten, A. F. P., 1999, ''Flow Measurements at $Gr/Re^2 \gg 1$ with Silicon Thermal Anemometry,'' IEEE Trans. Instrum. Meas., **48**(3), pp. 724–729.
[21] Van Putten, M. J. A. M., Kleijn, C. R., and Van den Akker, H. E. A., 2001, ''Heat Transfer and Temporal Behavior of the Laminar Mixed-Convection Flow Around a Ducted Flat-Plate Thermal Flow Sensor,'' Exp. Heat Transfer, **14**, pp. 229–250.
[22] Johnson, R. G., and Higashi, R. E., 1987, ''A Highly Sensitive Silicon Chip Microtransducer for Air Flow and Differential Pressure Sensing Applications,'' Sens. Actuators, **11**, pp. 63–72.
[23] Robadey, J., Paul, O., and Baltes, H., 1995, ''Two-Dimensional Integrated Gas Flow Sensors by CMOS IC Technology,'' J. Micromech. Microeng., **5**(3), pp. 243–250.
[24] Van Putten, M. J. A. M., Van Putten, M. H. P. M., Van Putten, A. F. P., Pompe, J. C., and Bruining, H. A., 1997, ''A Silicon Bidirectional Flow Sensor for Measuring Respiratory Flow,'' IEEE Trans. Biomed. Eng., 205–208.
[25] Toda, K., Sanemasa, I., and Ishikawa, K., 1996, ''Simple Temperature Compensation of Thermal Air-Flow Sensor,'' Sens. Actuators, **A57**, pp. 197–201.

A Universal, Nonintrusive Method for Correcting the Reading of a Flow Meter in Pipe Flow Disturbed by Installation Effects

C. Wildemann

W. Merzkirch

Lehrstuhl für Strömungslehre,
Universität Essen,
D-45117 Essen, Germany

K. Gersten

Institut für Thermo- und Fluiddynamik,
Ruhr-Universität Bochum,
D-44780 Bochum, Germany

A method is described that allows the correction of the reading of a flow meter that is exposed to pipe flow disturbed by installations upstream of the meter. The method is aimed at minimizing the distance between installation and meter and is based on characterizing the flow by "fundamental" disturbances, physically interpretable as vortical structures, and on the detection of these disturbances by a measuring device located slightly upstream of the meter. A functional relationship between fundamental disturbances and "error shift" of the meter is postulated, and its existence is demonstrated by a number of experiments. It is concluded that the correction method is applicable to any type of installation and flow meter. [DOI: 10.1115/1.1478065]

1 Introduction

Normally, flow meters are calibrated in fully developed pipe flow. For a practical use of the meter, existence of the same state of flow at the position of the meter must be secured, and this requires providing certain lengths of straight pipe upstream and downstream of the meter, as specified in the technical norms. These requirements are often not met in practice; the meter is then exposed to flow that is not fully developed, and measurement errors arise. Deviations from the fully developed flow state in the pipe are caused by installations, e.g., bends, valves, junctions, etc. Two principal approaches are known for using the flow meter with a minimum length of straight pipe between installation and meter, below the lengths prescribed by the norms. One is the use of a flow conditioner that is supposed to accelerate the redevelopment of the flow. The various types of disturbances of the fully developed velocity profile caused by installations disappear at different decay rates downstream of a conditioner; see, e.g., [1,2] and references therein.

The second approach is to calibrate the meter in the presence of the specific installation. This possibility was investigated systematically for orifice meters [3,4]. The velocity distribution downstream of various installations was measured and characterized. The reading of the orifice was then corrected as a function of chararcteristic numbers describing the deviation of the disturbed velocity profile from the fully developed state. While these approaches are dependent on the specific types of installation and meter, we describe here a correction procedure that is aimed at being more universal, independent of the knowledge about the specific installations and, in principle, applicable to any kind of flow meter.

Our approach is based on the theoretical results of Gersten and Klika [5] for laminar flow and Gersten and Papenfuss [6] for turbulent flow, who show that any disturbance caused by an installation is composed of a number of ''fundamental'' disturbances that decay downstream of the installation according to different decay laws. The local (axial) values of the magnitude of the fundamental disturbances characterize the local state of flow, i.e., the deviation from the fully developed state. This is equivalent to describing the state of flow by characteristic numbers, each of them representing one of the fundamental disturbances. In contrast to the characteristic numbers as they had been used, e.g., by Mattingly and Yeh [7] or Mickan et al. [8], the fundamental disturbances represent a specific vortex configuration in the flow, i.e., they have a real physical significance; see [5]. The idea is now that the state of the flow, expressed by a set of characteristic numbers, is measured slightly upstream of the flow meter, and that the reading of the meter can be corrected if a relationship between this reading and the set of characteristic numbers is known. Knowledge of this relationship is provided by a calibration: The difference between the discharge coefficient of the meter in fully developed flow, $C_{D\infty}$ (definition see below), and the discharge coefficient in disturbed flow, C_D, at the same value of the volumetric flow rate, is measured for a limited number of disturbances and flow rates. It must be proven that, once the relationship is established from this set of finite data values, the correction can be performed for any kind of disturbance caused by installations.

The relationship between C_D, characteristic numbers, and volumetric flow rate (or Reynolds number) must be determined for each type of meter to be used. We apply the procedure to the venturi and orifice flow meter. The deviation of the flow profile from the fully developed state is determined by measuring the azimuthal distribution of the wall shear stress along a circumference of the inner pipe wall, a short distance (<1 D) upstream of the flow meter. Using this quantity for characterizing the flow has the advantage that its value, which is known for fully developed flow, can be interpreted in physical terms, and that its measurement is nonintrusive, i.e., not related to an additional pressure drop. In the following we describe the characterization of the flow by the fundamental disturbances as defined by Gersten and Klika [5], the derivation of characteristic numbers by measuring the wall shear stress, and the establishment of the relationship for correcting the reading of the flow meter. The validity of the correction procedure is demonstrated by a number of experimental applications. Preliminary results of this approach were presented in two conference contributions [9,10].

2 Characterization of the Disturbed Flow

By means of a theoretical approach Gersten and Klika [5] as well as Gersten and Papenfuss [6] show that the disturbed flow in a pipe of circular cross section can be expressed as the composition of a basic flow pattern and a set of superimposed secondary patterns that are regarded as fundamental disturbances. Each of these disturbances is defined as a specific set of eigenfunctions of

Contributed by the Fluids Engineering Division for publication in the JOURNAL OF FLUIDS ENGINEERING. Manuscript received by the Fluids Engineering Division June 29, 2001; revised manuscript received February 28, 2002. Associate Editor: J. Katz.

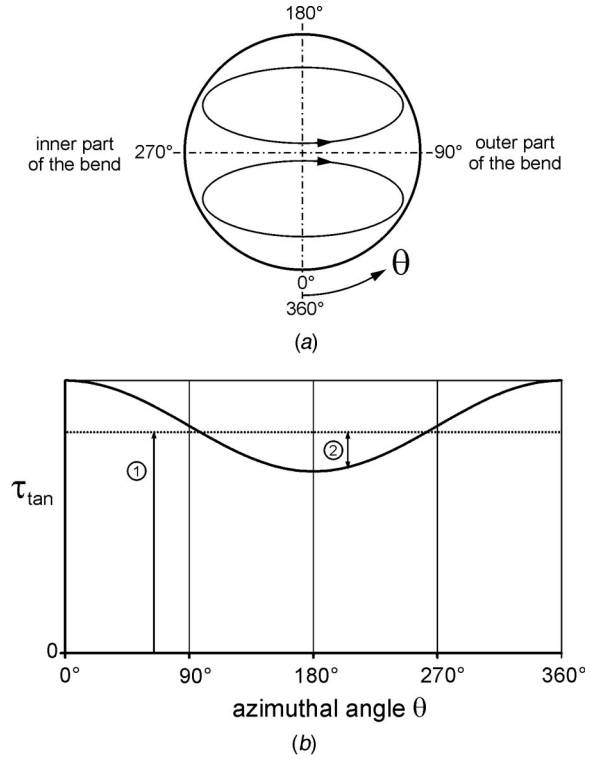

Fig. 1 (a) Pair of two counter-rotating vortices ("secondary flow") as caused by a 90 deg single bend and definition of the azimuthal angle with respect to the orientation of the bend. (b) Principal distribution of the tangential component of the wall shear stress downstream of the 2.9 deg out-of-plane bend: (1) contribution of swirl, (2) contribution of superimposed pair of counter-rotating vortices.

the problem and represents a specific vortical structure extending in the axial direction, e.g., pure swirl, a pair of two counter-rotating vortices ("secondary flow," see Fig. 1(*a*)), a quadruple of vortices, etc. The decay rates of the intensity of these vortices in the axial direction are different, e.g., the theory confirms the experimentally known fact that the decay rate of pure swirl is the lowest among all fundamental disturbances. Our aim is to characterize the state of the disturbed flow by measuring the wall shear stress along a circumference of the pipe and relating the measured result to the fundamental disturbances in Gersten and Papenfuss' theory.

The wall shear stress τ has two components, one in the axial and one in the azimuthal or tangential direction, τ_{ax} and $\tau_{\tan}$, that will be measured as functions of the azimuthal angle θ (see Fig. 1(a)). For fully developed flow one has $\tau_{ax}=\tau_\infty=\text{const}$ and $\tau_{\tan}=0$. Figure 1(b) shows the principal distribution of $\tau_{\tan}$ for swirl (in the figure designated as 1) plus the superimposed pair of counter-rotating vortices (designated as 2). For the purpose of flow characterization we develop the non-dimensional components of the wall shear stress, T, into Fourier series:

$$T_{ax}(\theta)=\frac{\tau_{ax}-\tau_\infty}{\tau_\infty}=a_{0ax}+\sum_{i=1}^{\infty}\left(a_{iax}\cos\left(i\frac{2\pi}{360}\theta\right)+b_{iax}\sin\left(i\frac{2\pi}{360}\theta\right)\right)$$

$$T_{\tan}(\theta)=\frac{\tau_{\tan}}{\tau_\infty}=a_{0\tan}+\sum_{i=1}^{\infty}\left(a_{i\tan}\cos\left(i\frac{2\pi}{360}\theta\right)+b_{i\tan}\sin\left(i\frac{2\pi}{360}\theta\right)\right) \quad (1)$$

It can be shown that the Fourier coefficients a_i, b_i can be associated with the eigensolutions of Gersten and Papenfuss' theory and the respective fundamental disturbances or vortex patterns. In particular, the following relationships exist:

Fourier coefficients	vortex pattern
a_{0ax}	ring vortex
$a_{0\tan}$	single axial vortex (pure swirl)
a_{1ax}, $a_{1\tan}$, b_{1ax}, $b_{1\tan}$	pair of counter-rotating vortices
a_{2ax}, $a_{2\tan}$, b_{2ax}, $b_{2\tan}$	quadruple of vortices

Gersten and Papenfuss [6] explain that disturbances associated with higher order coefficients $i>2$ decay very rapidly and can be disregarded for our further investigations. In the following we shall describe how a limited number of Fourier coefficients are determined from the measured distributions $T_{ax}(\theta)$ and $T_{\tan}(\theta)$. Important for the envisaged correction procedure is that a minimum of coefficients is sufficient for an efficient correction, i.e., that higher-order coefficients $(i>2)$ can be neglected.

3 Experiments

3.1 Flow Facility. The experiments are performed with air flow in a pipeline of circular cross section (diameter $D=100$ mm) at pipe Reynolds numbers ranging from $\text{Re}_D=5\cdot10^4$ to $\text{Re}_D=2.5\cdot10^5$. Higher values of the Reynolds number cannot be produced. This flow facility is equipped with a device allowing continuous reference measurements of the volumetric flow rate with an accuracy of $\pm0.25\%$. This device is based on a one-point measurement of the velocity profile in fully developed flow; for details of the flow facility see [11,12].

Three different installations are used for disturbing the flow in the pipe: a 90 deg single bend (radius of curvature of the centerline 1.5D), a $2\cdot90$ deg out-of-plane double bend, and a gate valve, i.e., a circular plate, inserted through a slit from above as a gate, with its plane normal to the pipe axis, thus blocking off a certain percentage of the pipe cross section.

3.2 Measurement of Wall Shear Stress. The wall shear stress τ is measured at various axial positions x/D downstream of the installations, ranging from $3\leqslant x/D\leqslant77$, and in fully developed flow. Sublayer fences [13,14] inserted in the inner pipe wall serve for measuring τ. They are calibrated in fully developed flow by making use of the balance between shear force and pressure force. Since it is necessary to determine two components of the wall shear stress (see Eq. (1)), two fences are used at each measuring position that are oriented at ±45 deg with respect to the direction of the pipe axis. The two components, τ_{ax} and $\tau_{\tan}$, are calculated with a formula describing the angular sensitivity of sublayer fences [14]. Application of this formula, which was derived in the boundary layer flow at a flat plate, appears justified because the ratio of fence height (0.15 mm) and pipe diameter (100 mm) is very small.

The azimuthal distribution $\tau(\theta)$ is measured along a circumference of the pipe, i.e., for a range of the azimuthal angle θ from 0 to 360 deg. For this purpose the two sublayer fences are inserted in a ring whose inner surface is flush with the inner pipe wall and which can be rotated around the pipe axis. At stationary flow conditions, τ is measured at angular intervals $\Delta\theta=5$ deg, i.e., at 72 equally spaced angular positions θ_i for the whole circumference.

Downstream of the 90 deg bend and the $2\cdot90$ deg out-of-plane double bend, these measurements are performed for the 5 downstream positions $x/D=3$, 5, 11, 21, and 41, and for the 4 Reynolds

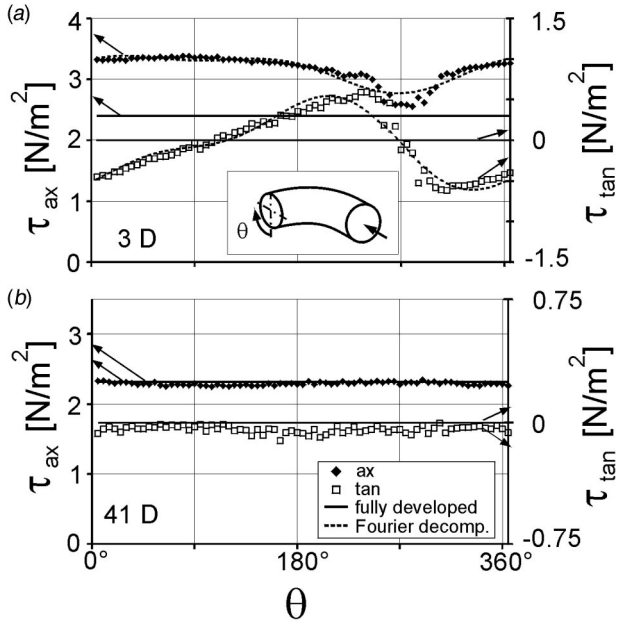

Fig. 2 Azimuthal distribution of wall shear stress downstream of the 90 deg single bend: Coordinate of the axial component, τ_{ax}, is on the left, coordinate of the tangential component, $\tau_{\tan}$, on the right. Pipe Reynolds number $Re_D=2.2\cdot10^5$. The values of τ_{ax} and $\tau_{\tan}(=0)$ for fully developed flow are indicated. (a) Axial distance from bend $x/D=3$, Fourier decomposition of τ_{ax} and $\tau_{\tan}$ is included. List of Fourier coefficients: $a_{0\tan}=-0.0206$, $a_{0ax}=0.319$, $a_{1\tan}=-0.199$, $a_{1ax}=0.0128$, $b_{1\tan}=-0.0080$, $b_{1ax}=0.112$, $a_{2\tan}=-0.0051$, $a_{2ax}=0.0517$, $b_{2\tan}=0.0781$, $b_{2ax}=-0.0003$. (b) $x/D=41$.

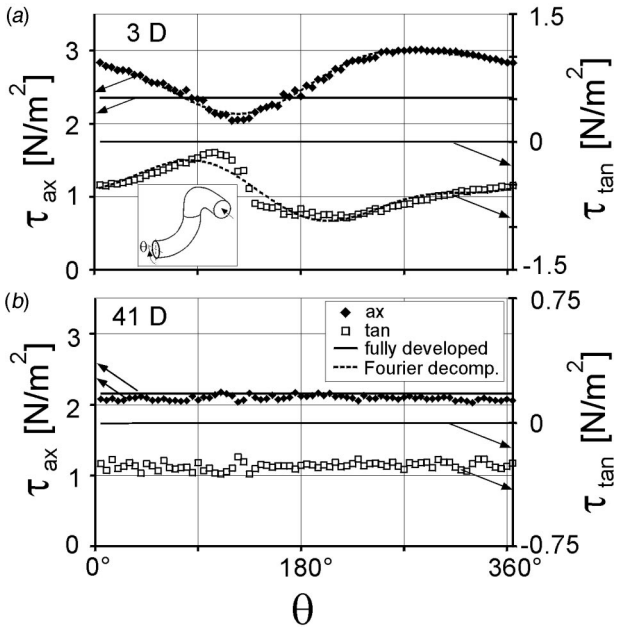

Fig. 3 Azimuthal distribution of wall shear stress downstream of the 2·90 deg out-of-plane double bend: The value of τ_{ax} for fully developed flow is indicated. (a) $x/D=3$, $Re_D=2.2\cdot10^5$. Fourier decomposition of τ_{ax} and $\tau_{\tan}$ is included. List of Fourier coefficients: $a_{0\tan}=-0.246$, $a_{0ax}=0.122$, $a_{1\tan}=0.0654$, $a_{1ax}=0.0838$, $b_{1\tan}=0.0974$, $b_{1ax}=-0.157$, $a_{2\tan}=-0.0553$, $a_{2ax}=0.0021$, $b_{2\tan}=-0.0145$, $b_{2ax}=0.0413$. (b) $x/D=41$, $Re_D=2.0\cdot10^5$.

numbers $Re_D/10^5=0.55$, 1.3, 2.2, and 2.45. From this variety of measured data we show only four typical distributions of $\tau_{ax}(\theta)$ and $\tau_{\tan}(\theta)$ in Figs. 2 and 3. Also shown is the Fourier decomposition of τ_{ax} and $\tau_{\tan}$; the Fourier coefficients are listed in the figure legend. The different scales for τ_{ax} on the left and $\tau_{\tan}$ on the right side of the diagrams should be noted. The distributions of τ_{ax} and $\tau_{\tan}$ are governed by the existence of the two counter-rotating vortices as shown in Fig 1(a,b). Therefore, $\tau_{\tan}$ changes its sign downstream of the 90 deg bend (Fig. 2(a)), while this quantity remains always negative downstream of the double bend due to the superimposed negative swirl (Fig. 3(a)). At $x/D=41$, τ_{ax} approaches closely its value for fully developed flow; this also applies to $\tau_{\tan}$ downstream of the single bend, i.e., $\tau_{\tan}\rightarrow0$ (Fig. 2(b)), while, for this position, $\tau_{\tan}$ assumes an almost constant negative value downstream of the double bend (Fig. 3(b)), thus giving evidence of the low decay rate of the swirl generated by the double bend.

Two sketches inserted in Figs. 2(a) and 3(a), respectively, indicate the spatial orientation of the bends with respect to the flow meter in the straight pipe section downstream of the installations. The four pressure taps for the venturi and orifice are located at the angular positions $\theta=0$, 90, 180, and 270 deg; the four pressure taps are connected by a hose such that a pressure value averaged along the circumference is measured.

3.3 Measurement of Discharge Coefficients. Three different flow meters are exposed to the flow disturbed by the three installations mentioned in Section 3.1: a venturi according to ISO 5167-1 with an opening diameter ratio $\beta=0.7$ and two orifices according to ISO 5167-1 with $\beta=0.65$ and $\beta=0.8$. The value $\beta=0.8$ is beyond the limits set by several norms for practical use of the orifice; this value was chosen here only for demonstrating the method with a meter that is known to have an uncertainty in C_D higher than normal. The differential pressure Δp at the flow meters is measured with a transducer (MKS Baratron 698) for which a value of the relative accuracy of $\pm0.1\%$ is given by the producer, while the air density ρ, necessary for deriving the discharge coefficient, is determined from a measurement of temperature and absolute pressure with a precision of $\pm0.15\%$. The discharge coefficient C_D of the meters, as defined by Eq. (1) in [15], is then calculated from the measured data Δp, ρ, the volumetric flow rate Q provided by the reference measurement (see Section 3.1), and the geometry of the meter (β, throat area).
A quantity

$$\Delta C_D=((C_D-C_{D\infty})/C_{D\infty})\cdot100\%, \tag{2}$$

in the literature often named ''error shift'' [3,7], with $C_{D\infty}$ being the discharge coefficient in fully developed flow, is determined for

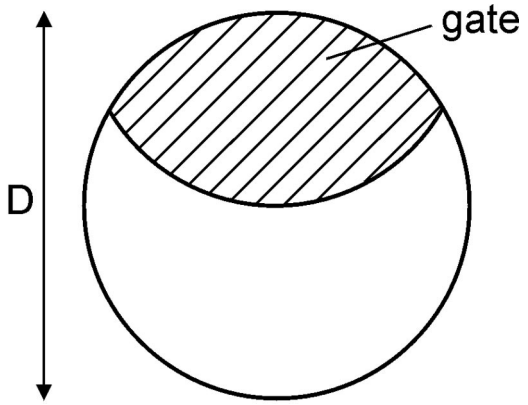

Fig. 4 Circular flat plate (gate valve) inserted from above into the pipe of diameter D as an installation

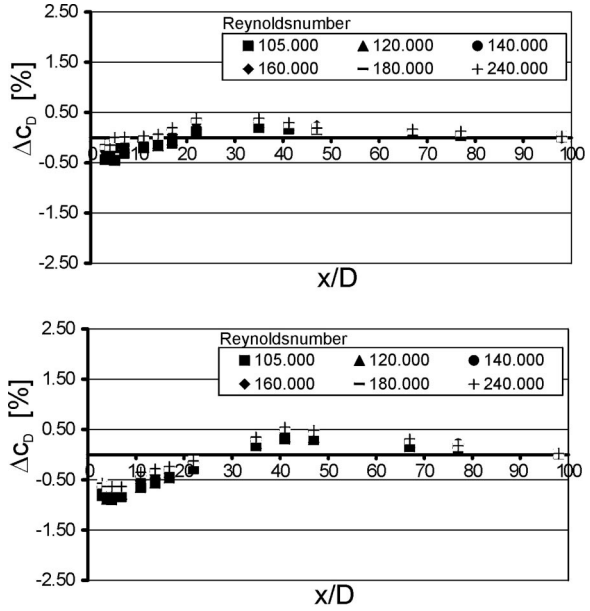

Fig. 5 Error shift ΔC_D measured for the venturi meter downstream of the 90 deg out-of-plane double bend (above) and the 90 deg single bend (below) as function of the axial distance x/D between installation and meter (horizontal scale)

all configurations of the installations, the indicated distances between flow meter and installation, and the 4 values of the pipe Reynolds number.

The gate, one of the three installations, was set at three different positions, such that the pipe cross section, which remained free, was 98.7%, 88.2%, and 67.2%. This is equivalent to the position of the lower edge of the circular plate inserted from above at 0.1D, 0.3D, and 0.5D (see Fig. 4).

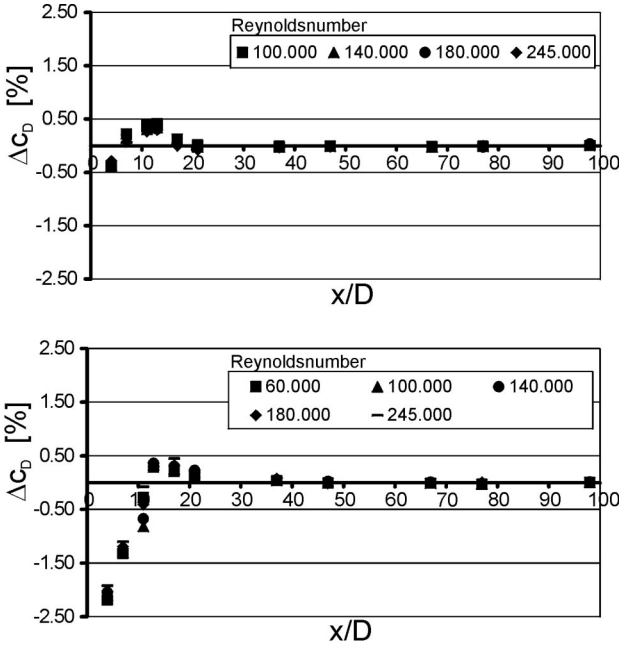

Fig. 6 Error shift ΔC_D measured for the $\beta=0.65$ orifice meter downstream of the 90 deg out-of-plane double bend (above) and the 90 deg single bend (below) as function of the axial distance x/D between installation and meter (horizontal scale)

As typical examples we show the values of ΔC_D measured at various axial distances x/D between installation and meter for venturi (Fig. 5) and the $\beta=0.65$ orifice (Fig. 6). The different scales for ΔC_D used in the two figures should be noted. Figures 5 and 6 indicate that the reading of both meters, venturi and orifice, is less affected by the disturbances caused by the 90 deg out-of-plane double bend, i.e., swirl, than by the disturbance due to the presence of a 90 deg single bend, i.e. ''secondary flow'' due to the counter-rotating vortices. Particularly for the venturi, the values of ΔC_D are of the same order as the uncertainty in the measurement of the volumetric flow rate. It is important to note that the values of ΔC_D shown represent a systematic difference to reproducible values of C_D. Here, their absolute numbers are not of any practical relevance, because they just serve to demonstrate the applicability and usefulness of the physical principle of correcting the reading of flow meters.

4 Relationship Between Error Shift and Flow Disturbance

According to our earlier assumption, a functional relationship exists, for a given meter, between the error shift ΔC_D, measured for the various installations, and the flow profile whose disturbance is characterized by the Fourier coefficients a_i, b_i (Eq. (1)). The Fourier coefficients are functions of the distance x/D between installation and meter. This dependence expresses the decay rate of the particular disturbance in axial direction. A further parameter on which a_i, b_i depend is the pipe Reynolds number Re_D, in our experiments a measure of the bulk velocity in the pipe or the volumetric flow rate. As an example of the derivation of the Fourier coefficients from the measured distributions $T_{ax}(\theta)$, $T_{\tan}(\theta)$, Fig. 7 shows the dependence of $a_{0\tan}$ and the combined coefficient $c_{1\tan}=\sqrt{(a^2{}_{1\tan}+b^2{}_{1\tan})}$ on the axial distance x/D for a Reynolds number $\mathrm{Re}_D=1\cdot10^5$; here, $a_{0\tan}$ represents the swirl whose low decay rate is evident, while $c_{1\tan}$ characterizes the vortex pair as caused by the single bend, and it is seen that this disturbance decays much faster in axial direction than the swirl.

The postulated functional relationship between ΔC_D, the Fourier coefficients and the Reynolds number is established by means of an artificial neural network. For this purpose we use a ''feed forward'' type network and the respective ''Matlab,'' version 5.0, software. The network is ''trained'' according to the Levenberg-Marquardt approximation with a selected, limited set of combinations of Fourier coefficients (up to order 2), related error shifts, and Reynolds number for each of the three meters. These data sets for the training are taken from a certain number of experiments performed with the three flow meters and the two bends, but without using the data measured with the gate valve as an installation.

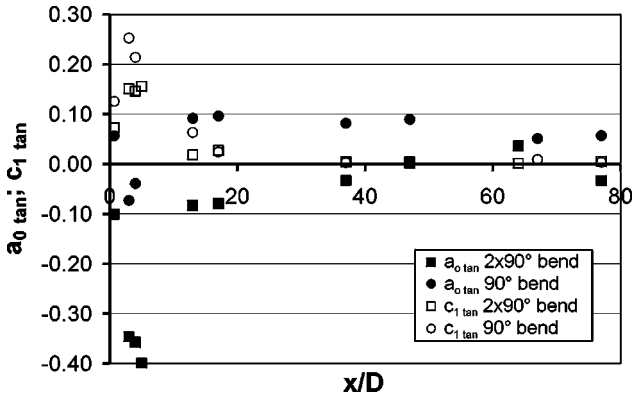

Fig. 7 Fourier coefficients a_0, $c_1=\sqrt{(a_1{}^2+b_1{}^2)}$ determined at various distances (horizontal scale) downstream of the 2·90 deg out-of-plane double bend and 90 deg single bend; pipe Reynolds number $\mathrm{Re}_D=1\cdot10^5$

The selection of the limited number of data from the complete data sets as input for the network was performed on the basis of a random choice program. The question for the further investigations is, how accurate can ΔC_D be predicted from a measured distribution of $T_{ax}(\theta)$, $T_{\tan}(\theta)$ for those cases, that were not used in the training of the neural network. For details of the selection and the training of the network, see [11]. The neural network is, of course, a substitution for a respective explicit relationship that is not available; the network is easy to implement and it can be used without difficulties.

5 Results

The "error shifts" predicted with the artificial neural network, $\Delta C_{D\,\mathrm{ANN}}$, and measured in our experiments, $\Delta C_{D\,\mathrm{exp}}$, are compared in Fig. 8 for the case of the venturi meter. Again $\Delta C_{D\,\mathrm{ANN}}$ is determined via the Fourier coefficients a_i, b_i from the measured distributions $T_{ax}(\theta)$, $T_{\tan}(\theta)$. The figure evidences which of the data were used for the training of the network and which are actually predicted. The data points shown include all positions x/D and Reynolds numbers as listed above. Ideally, all data points should lie on the oblique straight line through the origin. The scatter which is due to the experimental inaccuracies and the approximations by the neural network indicates the accuracy (or inaccuracy) in the prediction of ΔC_D. In order to quantify the precision of the prediciton we form the difference

$$\delta_{\Delta C} = \Delta C_{D\,\mathrm{exp}} - \Delta C_{D\,\mathrm{ANN}} \tag{3}$$

whose dimension is %, since ΔC_D is expressed in %, too, according to Eq. (2). Then, a probability density function (PDF) of $\delta_{\Delta C}$ is determined, see Fig. 9. From the pattern of the PDF and the area it includes one can derive that for 90% of the predictions the difference between the predicted and measured error shift is smaller than $\pm 0.18\%$, while for 100% of the predicitons this difference is smaller than $\pm 0.3\%$. From Figs. 8 and 9 it follows that the investigated venturi meter, when being exposed to the pipe flow disturbed by the present installations, measures the volume flow with an inaccuracy of $-1.0\% \leqslant \Delta C_D \leqslant +0.7\%$, and that this uncertainty range is reduced to $-0.3\% \leqslant \Delta C_D \leqslant +0.3\%$ with the device for correction that we have described.

The respective results for the two orifice meters are presented in Figs. 10 and 11. The measured error shifts are mostly negative and their absolute range is larger than that for the venturi. This confirms the known fact that the venturi is one of the most robust meters regarding the influence of flow disturbances (see, e.g., [16]). The orifice with $\beta = 0.8$ that is not defined in the norms has error shifts larger than that for the orifice with $\beta = 0.65$. From the PDF (not shown here) it follows that the uncertainty is reduced by the correction device to $-0.6\% \leqslant \Delta C_D \leqslant +0.6\%$, and for the orifice with $\beta = 0.65$ that is designed according to the norms to $-0.35\% \leqslant \Delta C_D \leqslant +0.35$.

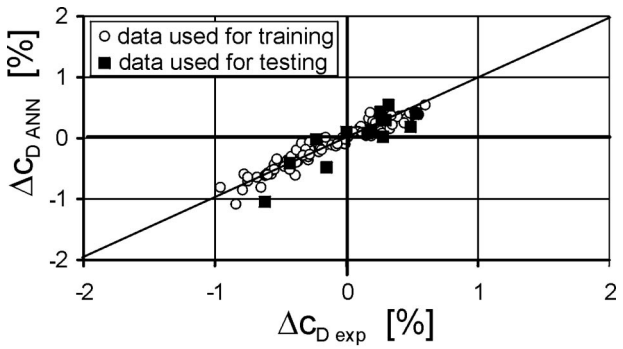

Fig. 8 Comparison of measured error shift, $\Delta C_{D\,\mathrm{exp}}$, and error shift predicted by the artificial neural network, $\Delta C_{D\,\mathrm{ANN}}$, for the venturi meter. The data that were used for the training of the ANN is marked as full squares.

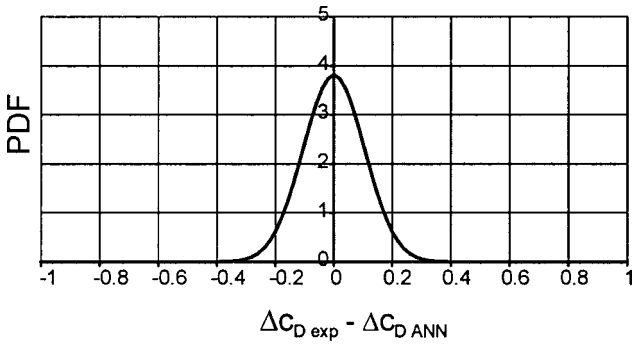

Fig. 9 Probability density function (PDF) of the scatter of the data shown in Fig. 7

Next we investigate how the device and procedure for correction perform when being applied to the flow disturbed by the installation whose data, i.e., the distributions $T_{ax}(\theta)$ and $T_{\tan}(\theta)$, were not used for "training" the artificial neural network. The installation is the gate sketched in Fig. 4 and used with the three different positions of the lower edge of the plate as described above. Also, the distance between installation and meter, x/D, and the Reynolds number were varied as indicated. These experiments were restricted to the venturi which is, among the three meters

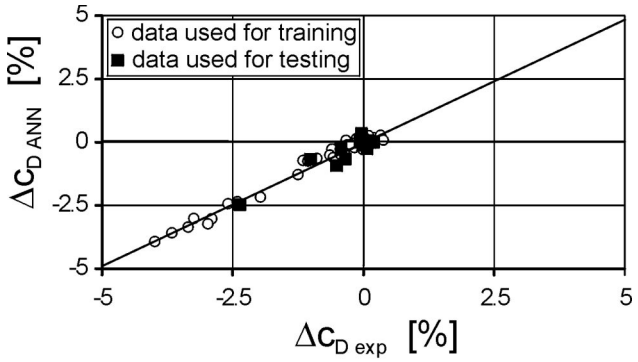

Fig. 10 Comparison of measured error shift, $\Delta C_{D\,\mathrm{exp}}$, and error shift predicted by the artificial neural network, $\Delta C_{D\,\mathrm{ANN}}$, for the $\beta = 0.8$ orifice meter. The data that were used for the training of the ANN is marked as full squares.

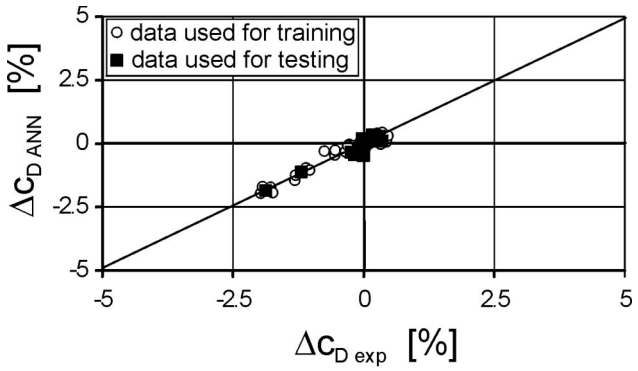

Fig. 11 Comparison of measured error shift, $\Delta C_{D\,\mathrm{exp}}$, and error shift predicted by the artificial neural network, $\Delta C_{D\,\mathrm{ANN}}$, for the $\beta = 0.65$ orifice meter. The data that were used for the training of the ANN is marked as full squares.

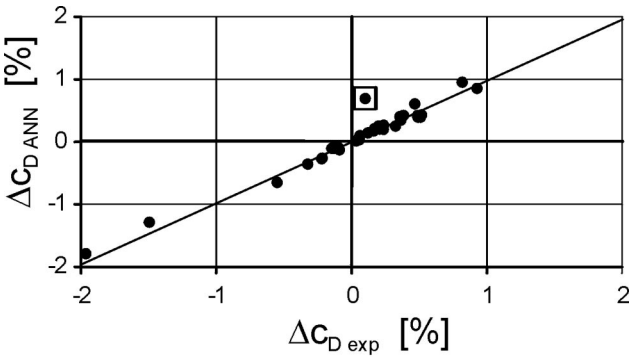

Fig. 12 Comparison of measured error shift, $\Delta C_{D\,\mathrm{exp}}$, and error shift predicted by the artificial neural network, $\Delta C_{D\,\mathrm{ANN}}$, for the gate (installation shown in Fig. 4). No data measured with this installation were used for the training of the ANN.

tested here, the least sensitive regarding disturbances. That is, the respective ΔC_D values for the orifices are expected to be larger than those for the venturi, thus providing a higher signal amplitude for the correction. We conclude that, if the correction performs well with the venturi, it should also work with those meters that are more severely affected by the disturbances than the venturi. The result, presented in Fig. 12, is very satisfactory and can be taken as a proof of the applicability of the principle used that any disturbance caused by an installation is composed of a finite number of fundamental disturbances.

In a practical application of this correction method it would be necessary to measure the wall shear stress (or a related quantity) with a set of stationary sensors along a circumference, as done here slightly upstream of the meter, and it is then of interest to minimize the number of sensors. For the results shown above we used the data of 72 measuring positions along the circumference for determining the distributions $T_{ax}(\theta)$ and $T_{\tan}(\theta)$. In order to provide information regarding the possible minimization of the number of measuring positions or sensors, we have also determined these distributions with data from a reduced number of measuring positions and used the new data for performing the correction procedure. The influence of the number of the measuring positions used, N, on the quality of predicting ΔC_D is investigated with the PDFs as they have been explained above. With decreasing number N the amplitude of the PDF's maximum decreases while the width increases, as shown in Fig. 13 for the venturi meter. From this presentation one can easily derive how the accuracy limits within which the corrected error shift ΔC_D is predicted vary with N.

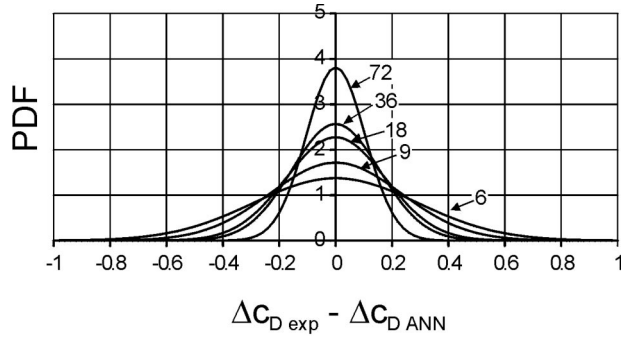

Fig. 13 Probability density functions (PDF) as defined and shown in Fig. 9 for different numbers of measuring positions used in determining the distributions $T_{ax}(\theta)$ and $T_{\tan}(\theta)$

6 Conclusions

We have described a method for correcting the reading of flow meters that are exposed to pipe flow disturbed due to the presence of an installation. The axial distance between installation and flow meter can be minimized to a few pipe diameters; the smallest distance we investigated was 3 pipe diameters. In contrast to flow conditioners that are also used for keeping this distance small, the presented method works without any additional pressure drop.

The principle of the method is based on the theoretically supported assumption that the disturbances caused by installations can be classified into fundamental disturbances, here: specific vortical structures, whose linear superposition allows characterization of the disturbed pipe flow. These fundamental disturbances are detected with a device, located slightly upstream of the meter, that, in our case, measures the azimuthal distribution of the two components of the wall shear stress. We postulate that a functional relationship exists between the set of detected characteristic disturbances and the ''error shift'' of the flow meter. This relationship is established by means of an artificial neural network, and the correction was successfully demonstrated, even for an installation that was, in principle, ''unknown'' to the network. We have taken this result as proof that the characterization of the disturbed flow by means of the fundamental disturbances is realistic. An advantage of characterizing the disturbed flow velocity profiles in the described way is that the fundamental disturbances used have a physical significance, namely vortical structures, which become evident in the measured distributions of the wall shear stress.

In developing and deriving the correction procedure, we have not made use of the physical significance of the quantitatively determined wall shear stress. The measured distributions of τ, shown in Figs. 2 and 3, are helpful for the physical interpretation of the correction procedure. But any signal giving quantitative evidence of the deviation from the fully developed state along the circumference could be used for the same purpose. This means that, for a practical application of the correction principle, the sublayer fences can be replaced by other sensors that must only fulfill the condition of having a reproducible sensitivity regarding changes of the wall shear stress. Inexpensive semiconductor sensors of the required type are available that can be considered for a practical realization. Technical details remain to be investigated for an adaptation of the correction principle to use in practice, e.g., minimization of the number of sensors along the circumference, optimization of the neural network and its training, replacing the neural network procedure with an algebraic functional relationship, further testing with a variety of different installations as well as different flow meters. The work presented here can be considered to deliver the physical basis for such developments, see [17]. Problems of compatibility of the method with rules set by technical norms should only become relevant when investigations of the mentioned technical details have arrived at satisfactory solutions.

Acknowledgment

This research was in part supported by a grant from Deutsche Forschungsgemeinschaft (DFG Az. Me 484/29, DFG Forschergruppe ''Strömungsmechanische Grundlagen der Durchflussmessung''). The authors thank Dr. Franka Schneider for helpful discussions.

References

[1] Laws, E. M., 1990, ''Flow Conditioning—A New Development,'' Flow Measurement and Instrumentation, **1**, pp. 165–170.
[2] Kalkühler, K., 1998, ''Experimente Zur Entwicklung Der Geschwindigkeitsprofile Und Turbulenzgrössen Hinter Verschiedenen Gleichrichtern,'' Dissertation, Universität Essen; also available as Fortschritt-Bericht VDI, Reihe 7, Nr. 339, VDI-Verlag, Düsseldorf.
[3] Mattingly, G. E., and Yeh, T. T., 1994, ''Pipeflow Downstream of a Reducer and Its Effect on Flowmeters,'' Flow Measurement and Instrumentation, **5**, pp. 181–187.
[4] Reader-Harris, M. J., Sattary, J. A., and Spearman, E. P., 1995, ''The Orifice

Plate Discharge Coefficient Equation—Further Work,'' Flow Measurement and Instrumentation, **6**, pp. 101–114.
[5] Gersten, K., and Klika, M., 1998, ''The Decay of Three-Dimensional Deviations From the Fully Developed State in Laminar Pipe Flow,'' *Advances in Fluid Mechanics and Turbomachinery*, H. J. Rath and C. Egbers, eds., Springer-Verlag, Heidelberg, pp. 17–28.
[6] Gersten, K., and Papenfuss, H. D., 2001, ''The Decay of Three-Dimensional Deviations From the Fully Developed State in Turbulent Pipe Flow,'' submitted to J. Fluid Mech.
[7] Mattingly, G. E., and Yeh, T. T., 1991, ''Effects of Pipe Elbows and Tube Bundles on Selected Types of Flow Meters,'' Flow Measurement and Instrumentation, **2**, pp. 4–13.
[8] Mickan, B., Wendt, G., Kramer, R., and Dopheide, D., 1996, ''Systematic Investigation of Pipe Flows and Installation Effects Using Laser Doppler Anemometry. Part II: The Effect of Disturbed Flow Profiles on Turbine Gas Meters—A Describing Empirical Model,'' Flow Measurement and Instrumentation, **7**, pp. 151–160.
[9] Wildemann, C., Merzkirch, W., and Gersten, K., 1998, ''Characterization and Correction of Installation Effects by Measuring Wall Shear Stress in Pipe Flow,'' *Proceedings FLOMEKO* 1998, Lund, Sweden, pp. 333–334.
[10] Wildemann, C., Merzkirch, W., and Gersten, K., 1999, ''A Systematic Approach for Correcting the Reading of a Flow Meter in Disturbed Pipe Flow,'' *Proceedings* 4th *Int. Symposium on Fluid Flow Measurement*, Denver, CO, USA.
[11] Wildemann, C., 2000, ''Ein System Zur Automatischen Korrektur Der Messabweichungen Von Durchflussmessgeräten Bei Gestörter Anströmung,'' Dissertation, Universität Essen; also available as *Fortschritt-Bericht VDI*, Reihe 8, Nr. 868, VDI-Verlag, Düsseldorf, 2001.
[12] Schlüter, Th., and Merzkirch, W., 1996, ''PIV Measurements of the Time-Averaged Flow Velocity Downstream of Flow Conditioners in a Pipeline,'' Flow Measurement and Instrumentation, **7**, pp. 173–179.
[13] Dengel, P., Fernholz, H. H., and Hess, M., 1987, ''Skin-Friction Measurements in Two-and Three-Dimensional Highly Turbulent Flows With Separation,'' *Advances in Turbulence*, G. Comte-Bellot, J. Mathieu, eds., Springer-Verlag, Heidelberg, pp. 470–479.
[14] Nitsche, W., 1994, *Strömungsmesstechnik*, Springer-Verlag, Berlin.
[15] Mattingly, G. E., 1983, ''Volume Flow Measurements,'' *Fluid Mechanics Measurements*, R. J. Goldstein, ed., Hemisphere, Washington, D.C., pp. 245–306.
[16] Baker, R. C., 2000), *Flow Measurement Handbook*, Cambridge University Press.
[17] Gersten, K., Merzkirch, W., and Wildemann, C., 2001, ''Verfahren Und Vorrichtung Zur Korrektur Fehlerhafter Messwerte Von Durchflussmessgeräten Infolge Gestörter Zuströmung,'' Patent no. 197 24 116.

A. Di Mascio
Research Scientist,
INSEAN, Via di Vallerano, 139,
00128, Rome, Italy

R. Paciorri
Research Scientist

B. Favini
Professor

Department of Mechanics and Aeronautics,
University of Rome "La Sapienza,"
Via Eudossiana, 18,
00184, Rome, Italy

Truncation Error Analysis in Turbulent Boundary Layers

The influence of turbulence model and numerical technique on RANS computations is discussed in the case of turbulent boundary layer flow on a flat plate. In particular, results are presented for a centered scheme with artificial dissipation and a ENO-type scheme with the Baldwin-Lomax and Spalart-Allmaras models. First, in an a priori analysis, the truncation errors are evaluated under the assumption of parallel Couette flow and some conclusions about mesh optimization and scheme performance are drawn. Then, the a posteriori analysis for the numerical solution of turbulent boundary layer on a flat plate is performed. Grid Convergence Index and convergence rate analysis confirm the a priori results. [DOI: 10.1115/1.1478564]

Introduction

The issues of accuracy and grid convergence of numerical solutions have direct implications in practical computations. In fact, the actual capability of any numerical algorithm to yield a reliable prediction in engineering applications strongly depends on the grid convergence rate of the numerical approximation. Two approaches can be used to obtain the required information: the *a priori* analysis, based on an estimate of the modified equation truncation error, and the *a posteriori* analysis, which relies on a generalization of the Richardson extrapolation.

The *a priori* analysis is the most useful tool to gain a clear view of the behavior of the numerical scheme, in that it allows a pointwise knowledge of the truncation error. Unfortunately, it requires the exact solution of the differential problem, which can be computed only in extremely simplified cases. On the contrary, the *a posteriori* analysis can be applied to analyze numerical solutions without any restriction about the flow structures (see e.g. [1] for a discussion about the main topics in this subject). Nevertheless, the *a posteriori* analysis alone cannot explain why a numerical solution has a large error, and consequently, how this error can be reduced.

In the present work, *a posteriori* analysis is performed on the numerical solutions of the turbulent boundary layer on a flat plate. In order to perform the *a priori* analysis, the parallel Couette flow assumption is introduced to reduce the governing equations to a simple ordinary differential equation, which allows the evaluation of the exact solutions. Since these two flows exhibit strong similarity in the inner region of the boundary layer, the combination of the *a priori* and the *a posteriori* analysis allows to understand the effect of numerical discretization and turbulence modeling on computed solutions, and to gain suggestions to efficiently reduce the numerical error in such region.

Two different numerical schemes and two different turbulence models have been selected. The two integration techniques are a centered scheme with artificial dissipation, implemented on the basis of the numerical models developed in [2,3], and a ENO-type scheme, derived from the general form given in [4]; both algorithms were adapted to the case of incompressible flow in the framework of the pseudo-compressibility formulation [5]. In both cases, the steady-state solution was gained by a Full Approximation Storage-Full Multi-grid (FAS-FMG) algorithm (see e.g. [6,7]). The turbulence models used in the simulations are the zero-equation by Baldwin and Lomax [8] and the one-equation model by Spalart and Allmaras [9].

Contributed by the Fluids Engineering Division for publication in the JOURNAL OF FLUIDS ENGINEERING. Manuscript received by the Fluids Engineering Division January 25, 1999; revised manuscript received February 6, 2002. Associate Editor: U. Ghia.

Mathematical and Numerical Models

The steady incompressible flow is computed as the asymptotic solution of the unsteady pseudo-compressible Reynolds averaged Navier-Stokes equations (RANSE)

$$\frac{\partial p}{\partial t}+\beta\frac{\partial u_l}{\partial x_l}=0$$

$$\frac{\partial u_l}{\partial t}+\frac{\partial u_l u_m}{\partial x_m}+\frac{\partial p}{\partial x_l}-\frac{\partial \tau_{lm}}{\partial x_m}=0 \quad l,m=1,2,3. \tag{1}$$

The system (1) is approximated by a cell-centered finite volume scheme. To this aim, the fluid domain D is divided into $N_i\times N_j\times N_k$ disjoint hexahedrons D_{ijk} such that $\cup D_{ijk}=D$. Then, by integrating the equations on each volume, we get, in vector form,

$$\int_{V_{ijk}}\frac{\partial \mathbf{q}}{\partial t}dV+\sum_{m=1}^{6}\int_{S_s}(\mathbf{F}_s^c+\mathbf{F}_s^v)dS=0 \tag{2}$$

where $\mathbf{q}=(p,u_1,u_2,u_3)^T$ is the vector of the state variables, S_s is the sth face of the finite volume D_{ijk}, whose measure is V_{ijk}, and

$$\mathbf{F}_s^c=(\beta(\mathbf{u}\cdot\mathbf{n}),\ \mathbf{u}(\mathbf{u}\cdot\mathbf{n})+p\mathbf{n})^T;$$

$$\mathbf{F}_s^v=(0,\ -\tau_{1l}n_l,\ -\tau_{2l}n_l,\ -\tau_{3l}n_l)^T. \tag{3}$$

The system of ordinary differential equations (2) is advanced in time by means of a multistage Runge-Kutta integration. Local time step and multi-grid were used to speed up convergence to the steady-state solution.

In order to obtain second-order accuracy in space, the convective and viscous fluxes are evaluated in the following way:

$$\int_{S_s}\mathbf{F}_s^c dS=\mathbf{F}_s^c|_0 A_s+O(\delta^2);\qquad \int_{S_s}\mathbf{F}_s^v dS=\mathbf{F}_s^v|_0 A_s+O(\delta^2) \tag{4}$$

where the subscript 0 means that the quantities are computed at the face center, A_s is the measure of S_s, δ is the diameter of S_s. The viscous stress tensor in Eq. (4) is approximated by centered differencing for both schemes, whereas two different discretizations of the convective terms are adopted.

In the centered scheme [2,3], Eulerian terms are computed, for instance, as

$$\mathbf{F}^c|_{i+1/2,j,k}=\mathbf{F}^c\left[\left(\frac{\mathbf{q}_{i,j,k}+\mathbf{q}_{i+1,j,k}}{2}\right)\right]+\varepsilon_4\lambda(\mathbf{q}_{i+2,j,k}-3\mathbf{q}_{i+1,j,k}+3\mathbf{q}_{i,j,k}-\mathbf{q}_{i-1,j,k}) \quad (5)$$

where $\varepsilon_4=O(1)$ is a coefficient to be assigned, and $\lambda=\mathbf{u}\cdot\mathbf{n}+\sqrt{(\mathbf{u}\cdot\mathbf{n})^2+\beta}$ is the largest eigenvalue of the Jacobian matrix of the flux vector.

In the ENO scheme [4], instead, the flux is computed by means of the solution of a Riemann problem

$$\mathbf{F}^c|_{i+1/2,j,k}=\hat{\mathbf{F}}(\mathbf{q}^L,\mathbf{q}^R) \quad (6)$$

whose left and right states are $\mathbf{q}^L,\mathbf{q}^R$, given by

$$\mathbf{q}_l=\mathbf{q}_{i,j,k}+\tfrac{1}{2}\,\mathrm{minmod}(\Delta_{i-1/2},\Delta_{i+1/2});$$

$$\mathbf{q}_r=\mathbf{q}_{i+1,j,k}-\tfrac{1}{2}\,\mathrm{minmod}(\Delta_{i+1/2},\Delta_{i+3/2}) \quad (7)$$

where $\Delta_{i+1/2}=\mathbf{q}_{i+1,j,k}-\mathbf{q}_{i,j,k}$ and minmod is a limiter function. In this scheme, an approximate solution of the Riemann problem was used. If the solution is smooth enough, both schemes are formally second order accurate in space; a detailed description can be found in [10].

Solutions of Turbulent Parallel Couette Flow

The fully developed turbulent flowfield on a flat plate in the immediate vicinity of the surface exhibits strong similarity with the turbulent parallel Couette flow. As a matter of fact, the universal laws of the turbulent boundary layer velocity profile, widely verified by experiments, are obtained under this assumption [11]. In this flow, the streamwise derivatives of all variables and the transverse velocity component are zero; as a consequence, the divergence constraint is automatically satisfied, and the transverse momentum equation shows that the pressure is constant. Therefore, only the streamwise momentum equation has to be solved that, close to the wall, reduces to

$$\frac{d}{dy^+}\left[(1+\nu_T^+)\frac{du^+}{dy^+}\right]=0, \quad (8)$$

with

$$u^+|_{y^+=0}=0; \quad \left.\frac{du^+}{dy^+}\right|_{y^+=0}=1$$

where the classical dimensionless variables are adopted:

$$u^+=\frac{\bar{u}}{u^*}; \quad y^+=y\frac{u^*}{\nu}; \quad \nu_T^+=\frac{\nu_T}{\nu}. \quad (9)$$

The use of the friction velocity u^* as reference variable transforms the original boundary value problem in an initial value problem with two boundary conditions assigned at $y^+=0$ that yields an universal velocity profile. The actual solution for each particular boundary value problem can be then obtained once u^* is computed by enforcing the boundary condition for u as $y\to\infty$.

The solution of Eq. (8) can be computed once ν_T^+ is specified. In particular in the Baldwin-Lomax model (B-L), we have

$$\nu_T^+=l^2\left|\frac{du^+}{dy^+}\right|; \quad l=ky^+(1-\exp(-y^+/26)), \quad (10)$$

and in the Spalart and Allmaras model (S-A), specialized for Couette flows, the turbulent viscosity is easily computed as

$$\nu_T^+=\frac{(ky^+)^4}{(ky^+)^3+(7.1)^3}. \quad (11)$$

The velocity profiles are computed by numerical integration of Eqs. (8) with (10) or (11). To this aim, Eq. (8), rewritten by analytical integration as

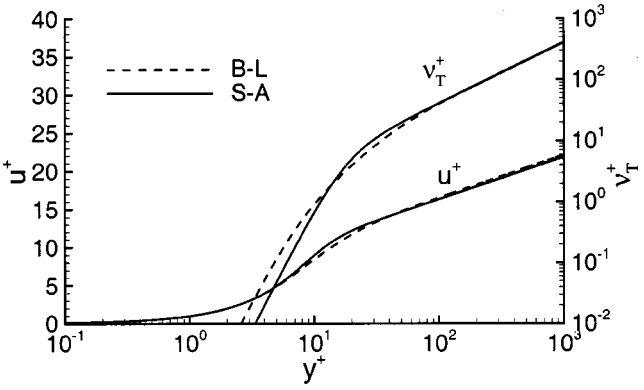

Fig. 1 Velocity profile and turbulent viscosity profile for the Spalart and Allmaras profile (solid line) and for the Baldwin and Lomax model (dashed line)

$$(1+\nu_T^+)\frac{du^+}{dy^+}=1, \quad (12)$$

is solved by trapezoidal rule. The integration step was constant and equal to $\Delta y^+=10^{-2}$. Verification was carried out by using two grid refinements with factor 2. The three solutions were graphically indistinguishable in Fig. 1, where the plots of $u^+(y^+)$ and $\nu_T^+(y^+)$ are reported.

Modified Equation for Turbulent Couette Flow

Let us consider a generic numerical scheme based on second order finite volume formulation with a high order artificial dissipation. For a turbulent Couette flow the numerical schemes reduce to

$$\left[\nu+\frac{\nu_{Ti}+\nu_{Ti+1}}{2}\right]\frac{u_{i+1}-u_i}{\Delta y}-\left[\nu+\frac{\nu_{Ti}+\nu_{Ti-1}}{2}\right]\frac{u_i-u_{i-1}}{\Delta y}+\varepsilon_4\lambda(u_{i+2}-4u_{i+1}+6u_i-4u_{i-1}+u_{i-2})=0, \quad (13)$$

where in actual calculations $\lambda=O(1)$ and ε_4 is $\ll 1$. This expression includes both the centered scheme and the ENO scheme which has $\varepsilon_4=0$. Note that the convective terms disappear as consequence of the assumption of parallel flow (see Eq. (8)); consequently, the centered and ENO scheme differ only for the artificial dissipation term.

By Taylor series expansion around x_i of the exact solution, we obtain the expression of the modified equation in dimensionless variables

$$\frac{d}{dy^+}\left[(1+\nu_T^+)\frac{du^+}{dy^+}\right]=E_2^+\Delta y^{+2}+\varepsilon_4E_3^+\Delta y^{+3}+E_4^+\Delta y^{+4}+O(\Delta y^{+5}), \quad (14)$$

where the coefficients E_2^+, E_3^+, and E_4^+ are

$$E_2^+=-\frac{1}{12}\left[(1+\nu_T^+)\frac{d^4u^+}{dy^{+4}}+2\frac{d\nu_T^+}{dy^+}\frac{d^3u^+}{dy^{+3}}+3\frac{d^2\nu_T^+}{dy^{+2}}\frac{d^2u^+}{dy^{+2}}+2\frac{d^3\nu_T^+}{dy^{+3}}\frac{du^+}{dy^+}\right],$$

$$E_3^+=-\lambda^+\frac{d^4u^+}{dy^{+4}},$$

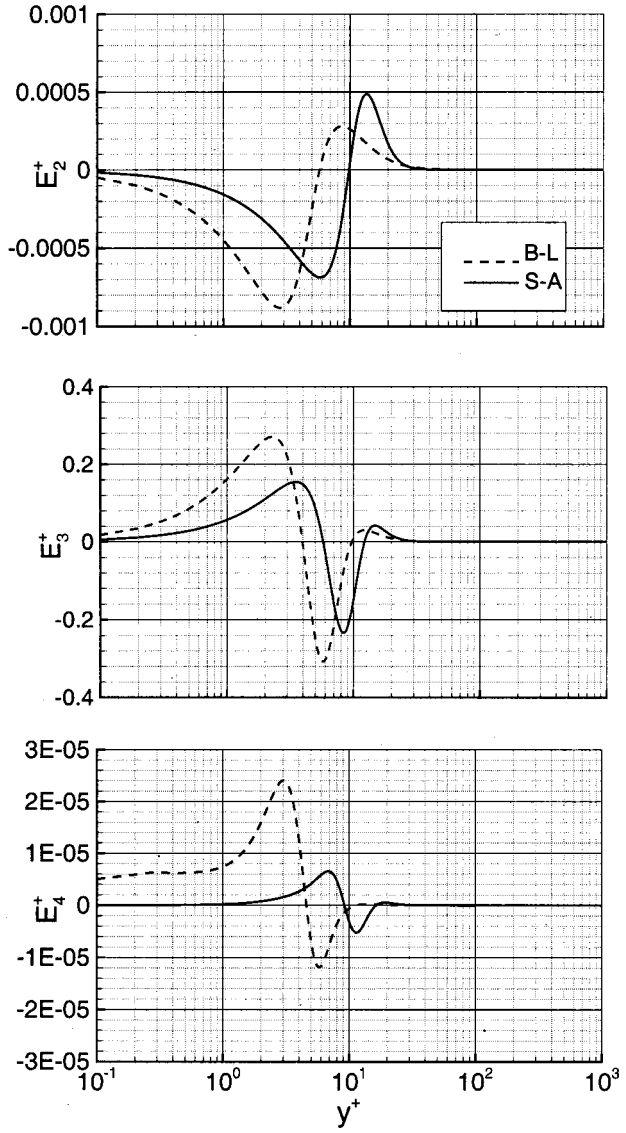

Fig. 2 Truncation error coefficients for the Spalart and Allmaras model (solid line) and for the Baldwin and Lomax model (dashed line)

$$E_4^+ = -\frac{1}{360}\left[(1+\nu_T^+)\frac{d^6u^+}{dy^{+6}} + 3\frac{d\nu_T^+}{dy^+}\frac{d^5u^+}{dy^{+5}} + \frac{15}{2}\frac{d^2\nu_T^+}{dy^{+2}}\frac{d^4u^+}{dy^{+4}} + 10\frac{d^3\nu_T^+}{dy^{+3}}\frac{d^3u^+}{dy^{+3}} + \frac{15}{2}\frac{d^4\nu_T^+}{dy^{+4}}\frac{d^2u^+}{dy^{+2}} + 3\frac{d^5\nu_T^+}{dy^{+5}}\frac{du^+}{dy^+}\right]$$

being $\lambda^+ \approx 30$ if $\lambda \approx 1$. It can be seen that only the third-order term depends on the artificial dissipation. In the case $\varepsilon_4 = 0$, Eq. (14) reduces to the modified equation of a second-order centered scheme for a standard diffusion problem. Moreover, coefficients E_i^+ depend on the turbulence model only through the eddy viscosity; then, their expressions remain valid for any Boussinesq closure. The coefficients E_i^+ for both turbulence models are shown in Fig. 2. The evaluation of coefficients E_i^+ has been performed by approximating the derivatives with centered finite differences of order two, using the values of u^+ and ν_T^+ computed as described in the previous section.

If Δy^+ is constant, the error expression is

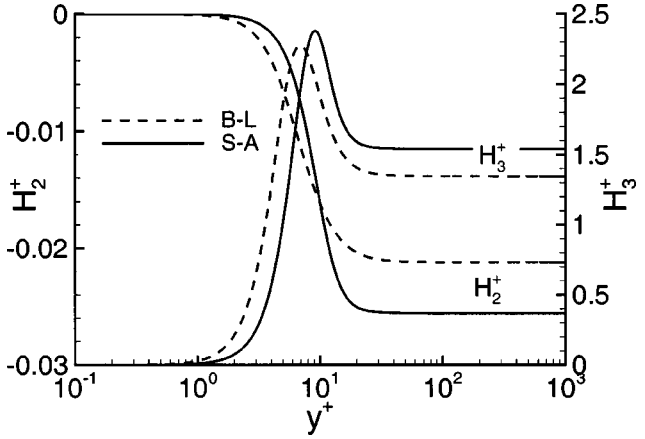

Fig. 3 Numerical error coefficients for the Spalart and Allmaras model (solid line) and for the Baldwin and Lomax model (dashed line)

$$u_n^+ - u_e^+ = H_2^+ \Delta y^{+2} + \varepsilon_4 H_3^+ \Delta y^{+3} + H_4^+ \Delta y^{+4} + O(\Delta y^{+5}) \tag{15}$$

where the coefficients H_i^+ are computed by a double integration of Eq. (14) (see Fig. 3)

$$H_i^+ = \int_0^{y^+} \frac{d\zeta}{1+\nu_T^+(\zeta)} \int_0^{\zeta} E_i(\eta)\, d\eta \tag{16}$$

and u_e^+, which is the exact solution, is given by

$$u_e^+ = \left.\frac{du^+}{dy^+}\right|_0 \int_0^{y^+} \frac{d\zeta}{1+\nu_T^+(\zeta)}. \tag{17}$$

As before, the solution u_e^+ and the numerical error coefficients H_i^+ are computed by the trapezoidal rule.

The behavior of H_i^+ and E_i^+ inside of the boundary layer is useful for understanding the convergence properties of the numerical schemes. It can be seen from Fig. 2 that, in the whole boundary layer, $|E_4^+| < 3\times 10^{-5}$, $|E_2^+| \gg |E_4^+|$ and E_3^+ is very large when compared to E_2^+; therefore the leading term of the truncation error will dominate on the third-order term only if the grid normal dimension Δy^+ and / or ε_4 are very small. For instance, if $\Delta y^+ = 2$ in the whole boundary layer (this is clearly unrealistic and optimistic in practical computations), the second and third-order term will be comparable in the log–layer even for $\varepsilon_4 = 1/128$.

Under the assumption $\Delta y^+ = \text{const}$, we have always $H_2^+ < 0$ and $H_3^+ > 0$. Then, when $\varepsilon_4 = 0$ (ENO scheme), $u_n^+ < u_e^+$ has to be expected. On the other hand, when $\varepsilon_4 \neq 0$ (centered scheme), the second and the third-order terms have opposite signs and therefore the sign of the numerical error depends on the values of ε_4 and Δy^+. An example can be seen in Fig. 4 for $\lambda^+ = 30$, $\Delta y^+ = 1.75$ and several values of ε_4. Of course, the presence of two error terms, with the same order of magnitude but opposite sign, can give rise to nonmonotonic convergence when decreasing the grid size.

The numerical error is almost constant in the log–layer (see Eq. (15), Eq. (16) and Fig. 3), since E_i^+ tends to zero for $y^+ > 20$ (see Fig. 2). For a given Δy^+, it can also be seen that the truncation error is large in the whole region $0 < y^+ < 20$. This fact suggests that, although in actual flow simulations memory requirements impose the use of nonuniform grids, the cell size should be kept small in this interval and not only in the laminar sublayer. The simplest mesh that fulfills this requirement is a uniform grid up to $y^+ < 20$, and a stretched grid only outside this region.

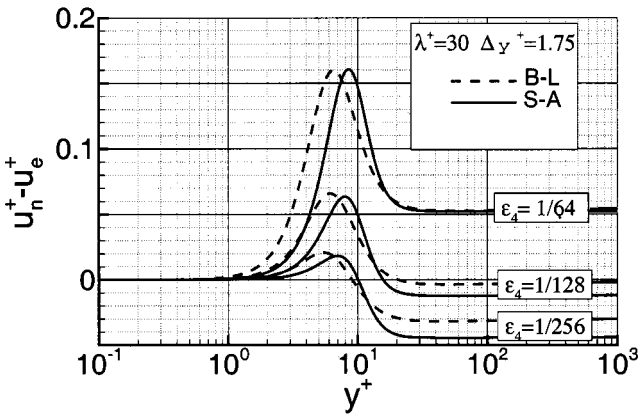

Fig. 4 Numerical error for $\lambda^+=30$, $\Delta y^+=1.75$ and $\varepsilon_4=1/64$, 1/128, 1/256

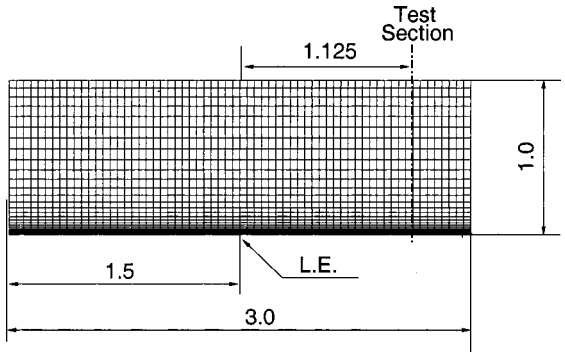

Fig. 5 Computational mesh

Richardson Extrapolation and Asymptotic Convergence

In general, the numerical solution errors can be evaluated by means of the *a posteriori* analysis, which is not restricted to simple cases, like *a priori* analysis. Indeed it does not require the knowledge of the exact solution. On the other side, it does not allow any general conclusion, being strictly related to the computed numerical solutions.

In the framework of the Richardson extrapolation, the observed convergence order $\tilde{n}$ of the numerical solution and an estimate $\tilde{u}_e$ of the exact solution u_e are evaluated as:

$$\tilde{n}=\log\frac{u_n^{4h}-u_n^{2h}}{u_n^{2h}-u_n^{h}}\Bigg/\log 2;\quad \tilde{u}_e=\frac{2^{\tilde{n}}u_n^{2h}-u_n^{h}}{2^{\tilde{n}}-1}. \tag{18}$$

When the numerical solutions u_n^{4h}, u_n^{2h}, and u_n^h are in the asymptotic range, the observed order $\tilde{n}$ tends to the actual order n, which generally does not differ from the formal one. In recent works, Roache [1] used the Richardson extrapolation concept to define the Grid Convergence Index (GCI) which represents a bandwidth error of the numerical solution. In particular, the GCI is defined as three times the difference between the numerical and the extrapolated solution $\tilde{u}_e$ computed assuming $\tilde{n}=n$

$$\mathrm{GCI}=3|u_n-\tilde{u}_e|. \tag{19}$$

Test Case Description and Computational Meshes

The *a posteriori* analysis is applied to the numerical solution of full turbulent boundary layer on a flat plate and, therefore, the hypothesis of parallel flow, exploited in the *a priori* approach, is abandoned. The numerical test case considered here is the incompressible flow on a flat plate for $\mathrm{Re}=10^7$. The computational domain is a rectangle area whose length is 3, width is 1 and the leading edge is 1.5 dimensionless units from the inlet section (see Fig. 5). The no-slip condition is applied to half length of the lower side, the symmetry condition to the remaining part. Uniform velocity was enforced at the inflow and at the upper boundary. Finally, extrapolation of velocity was used at the outflow boundary. The blockage effects were checked to be absent with the chosen location of the upper and upstream boundaries.

The numerical solutions were computed on four families of Cartesian meshes called G1, G2, G3, and G4. Each mesh family has three grid levels, the finest mesh being 64×64 for G1 and G3, and 128×128 for G2 and G4. The medium and coarse levels of each family were obtained by removing every other vertex from the previous finer level. In G1 and G2, the cells are clustered to the wall using the stretching law proposed in [12] in the whole boundary layer. The law parameters are set to yield a fine mesh width Δy_{min} at the wall and Δy_{max} in the far field. In G3 and G4 families, whose meshes are characterized by the same value of Δy_{min} and Δy_{max} and by the same number of cells of the G1 and G2 families respectively, the cells have constant spacing in the region $y^+<20$, while the grid step is stretched outside this inner zone according to the Vinokur law's. Of course, this particular grid configuration was chosen on the basis of the indications provided by the *a priori* analysis. More details about the fine meshes of each family are reported in Table 1.

Analysis of Numerical Results

The flow on a flat plate was computed by means of the two numerical schemes on the four mesh families described in the previous sections and using both the B-L and the S-A model. In the centered scheme simulations, several values of the parameter ε_4 have been considered, ranging from $\varepsilon_4=1/16$ to $\varepsilon_4=1/256$.

The qualitative convergence behavior for the dimensionless velocity profile in a selected test section is reported in Fig. 6 for the ENO scheme. This section, which is located at 1.125 unit from leading edge (see Fig. 5), is far enough from the leading edge to consider the local flow sufficiently close to the Couette flow condition. As expected from the sign of the coefficient H_2^+ (see Fig. 3), the numerical error $(u_n^+-u_e^+)$ is negative everywhere, and then the solution converges from below to its limit value.

Figure 7 shows the solutions computed with the centered scheme and $\varepsilon_4=1/64$ on the G3 meshes with the B-L model. In this case, the error being positive, the profiles tend to their limit values from above. Nevertheless, the behavior can change completely by varying ε_4. In Fig. 8, the solutions computed on the coarse mesh of G3 family with several values of ε_4 are reported. As expected, the solutions with large value of ε_4 have positive error whereas, as ε_4 is reduced, the solutions tend to the limit profile obtained with the ENO scheme, which is characterized everywhere by a negative error.

The quantitative convergence of the solution has been studied by means of the *a posteriori* analysis. In order to compute the local apparent convergence order $\tilde{n}$ and the GCI, the point value

Table 1 Characteristic data of the fine meshes of each family

	G1	G2	G3	G4
$n\times m$ of finest mesh	64×64	128×128	64×64	128×128
Δy_{min}	0.50E-5	1.8116E-6	0.50E-5	1.8116e-6
Δy_{max}	0.05	0.025	0.05	0.025
n cells with $\Delta y=\Delta y_{min}$	1	1	10	32
Vinokur's law	$y^+>0$	$y^+>0$	$y^+>20$	$y^+>20$

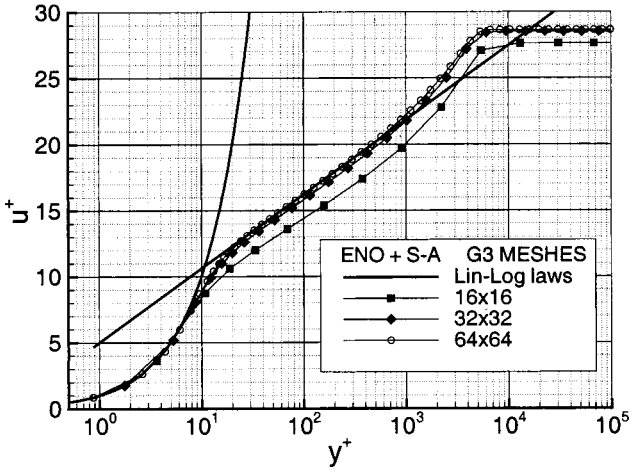

Fig. 6 Numerical solution with the ENO scheme and the Spalart and Allmaras model on three mesh levels

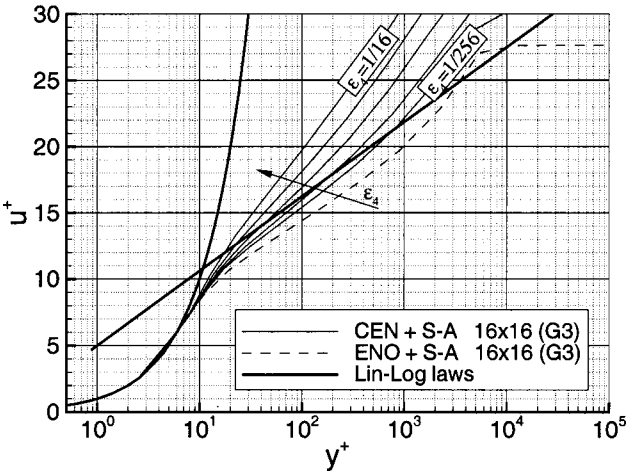

Fig. 8 Numerical solutions with the centered scheme and varying ε_4 and with the ENO scheme on a 16×16-G3 mesh

of the solution at each level was interpolated on the vertex of the coarsest grid by means of a bilinear interpolation (note that, both scheme being cell-centered, the control points for different grid levels do not coincide). This operation affects the numerical solution by means of a second-order error term whose coefficient is the same for each grid size; therefore, this interpolation does not corrupt the accuracy of the numerical solutions.

A comparative analysis of the convergence properties of the ENO scheme is reported in Fig. 9. In each diagram, the profile computed on the finest mesh is plotted; the positions of control points (that coincide with the vertices of the coarse grid) are marked by X. In all diagrams, the apparent order $\tilde{n}$ (circles) and the GCI of the finest solution (bars) are also reported. It can be noticed that the apparent convergence order $\tilde{n}$ for the ENO scheme computations is approximately constant in the log-layer. The observed convergence order $\tilde{n}$ is close to the formal one, as expected when the computed solutions are in the asymptotic range. Of course, $\tilde{n}$ is not exactly 2 because the higher order terms in the truncation error are nonzero for any finite grid size. The GCI is rather regular (and small) in the whole boundary layer. As expected, the use of the meshes G3 and G4 causes a remarkable reduction of the GCI.

The solutions computed with the centered scheme (with $\varepsilon_4=1/64$) on G1 and G3 meshes are shown in Fig. 10. The solutions computed on meshes G1 are quite different from the analytical law in the log-layer, in spite of the small GCI. In this case, the GCI fails to give a reasonable estimate of the bandwidth, because the solutions are not in the asymptotic range. It can be noticed that the values of $\tilde{n}$ are far from the theoretical value $n=2$ and moreover, at several points, it is even impossible to compute $\tilde{n}$, because monotonic convergence is not attained (see the lower diagrams of Fig. 10).

The use of meshes G3 reduces numerical errors also in this case. The error reduction has positive effects on the convergence

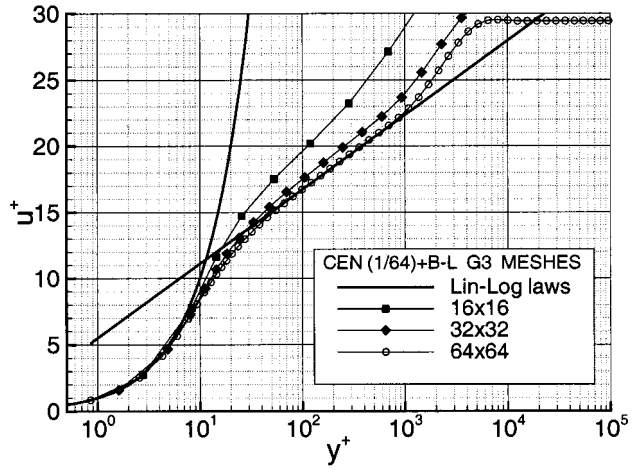

Fig. 7 Numerical solution with the centered scheme ($\varepsilon_4=1/64$) and the Baldwin and Lomax model on three mesh levels

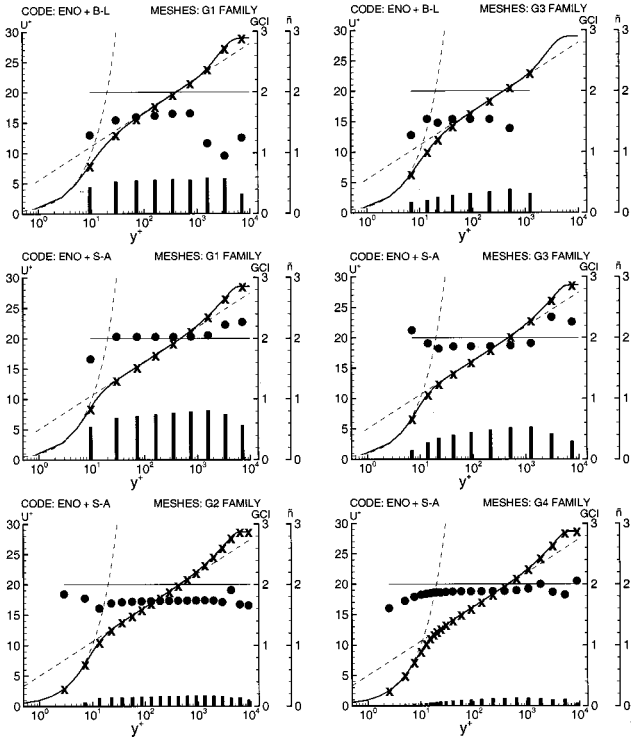

Fig. 9 Numerical solutions with the ENO scheme and mesh families G1 (left, top and middle) and G2 (left, bottom) and mesh families G3 (right, top and middle) and G4 (right, bottom) with Baldwin and Lomax model (top) and Spalart and Allmaras model (middle and bottom). Solid line: numerical solution. X: control points. Full circles: apparent convergence order. Bars: GCI.

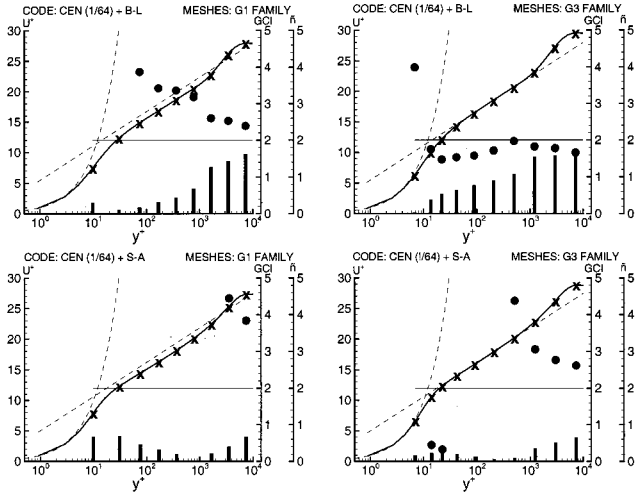

Fig. 10 Numerical solutions with the centered scheme ($\varepsilon_4 = 1/64$) and mesh families G1 (left) and mesh families G3 (right) with Baldwin and Lomax model (top) and Spalart and Allmaras model (bottom). Solid line: numerical solution. X: control points. Full circles: apparent convergence order. Bars: GCI.

Table 2 $C_f \times 100$ at $x = 1.125$; S-A Model, ENO scheme

Grid	G1	G2	G3	G4
16×16	$0.2965 \pm (0.1623)$		$0.2635 \pm (0.0631)$	
32×32	$0.2531 \pm (0.0322)$	$0.2497 \pm (0.0214)$	$0.2470 \pm (0.0135)$	$0.2450 \pm (0.0074)$
64×64	$0.2451 \pm (0.0081)$	$0.2445 \pm (0.0059)$	$0.2436 \pm (0.0034)$	$0.2430 \pm (0.0016)$
128×128		$0.2430 \pm (0.0015)$		$0.2426 \pm (0.0004)$
extrapolated	0.2432	0.2424	0.2427	0.2425
$\tilde{n}$	2.4295	1.8000	2.2906	2.2986

behavior especially when the B-L model is used. In particular, with the first control point excluded, the numerical solutions are in the asymptotic range and therefore the GCI provides realistic values of the error. Unfortunately, the error reduction on meshes G3 with the S-A model is not sufficient to achieve the asymptotic range.

The convergence behavior for the skin friction coefficient C_f is similar to that of velocity profiles. In Table 2, the results for C_f, calculated with the ENO scheme and the S-A model are summarized (the GCI is reported in brackets). It is evident that all numerical solutions are in the asymptotic range, the apparent order $\tilde{n}$ being always very close to $n=2$, and the convergence behavior is always monotonic. It can be noticed that the differences in the extrapolated values are very small for all mesh families; in particular, the C_fs computed with the finer mesh families G2 and G4 differ only for 0.0024% and therefore one of these values can be reasonably assumed as a reference value. It is possible to verify that this reference value is always inside the interval defined by the computed value and the GCI. Moreover, the error analysis confirms that, when $\Delta y^+ = \text{const}$ for $y^+ < 20$ (meshes G3 and G4), we have a better prediction without additional computational cost.

In Table 3, the values of C_f computed by the centered scheme on meshes G3 are analyzed when ε_4 is reduced. The apparent order $\tilde{n}$ is below the theoretical one up to $\varepsilon_4 = 1/32$, whereas it is much larger for smaller values of the artificial dissipation coefficient; moreover, the extrapolated values are very different from one another and none is close to the reference value. This anomalous behavior represents a typical example of how the addition of an artificial dissipation term corrupts a regular grid convergence and it confirms the *a priori* analysis conclusions. Indeed, the difference between the values computed with the centered scheme and with the ENO scheme on corresponding meshes can be assumed as a measure of the third-order term of the error, whereas the differences between the ENO computation and the reference value as a measure of the second-order term. As seen in the *a priori* analysis, the third-order term is never negligible with respect to the second one and, in addition, they have opposite sign. Although the computed C_fs seem to converge monotonically, the fact that $\tilde{n} \gg n$ for $\varepsilon_4 = 1/128$ and 1/256 and the over-prediction of C_f when compared with the reference value suggest that the asymptotic range has not yet attained. In this case, the rigorous procedure suggested in [13] for removing the artificial dissipation effects in numerical solutions is not useful, because the extrapolated 0-viscosity values do not converge monotonically (see the last column in Table 3).

Conclusion

The *a priori* analysis has proved that high order artificial dissipation terms in second-order accurate centered schemes can significantly spoil the actual rate of convergence of the numerical solutions of turbulent parallel Couette flow. This is due to the

Table 3 $C_f \times 100$ at $x = 1.1255$; S-A Model, Centered scheme, G3 mesh family

Grid	artificial dissipation coefficient ε_4					
	$\frac{1}{16}$	$\frac{1}{32}$	$\frac{1}{64}$	$\frac{1}{128}$	$\frac{1}{256}$	0 (Blottner)
16×16	$0.1187 \pm (0.3936)$	$0.1385 \pm (0.3334)$	$0.1640 \pm (0.2503)$	$0.1922 \pm (0.1591)$	$0.2177 \pm (0.0779)$	0.2432
32×32	$0.1896 \pm (0.1810)$	$0.2109 \pm (0.1162)$	$0.2266 \pm (0.0626)$	$0.2367 \pm (0.0256)$	$0.2425 \pm (0.0035)$	0.2482
64×64	$0.2349 \pm (0.0452)$	$0.2400 \pm (0.0291)$	$0.2422 \pm (0.0156)$	$0.2431 \pm (0.0064)$	$0.2433 \pm (0.0009)$	0.2436
extrapolated	0.3147	0.2595	0.2474	0.2442	0.2434	-
$\tilde{n}$	0.6475	1.3170	2.0006	2.7990	4.8063	-

third-order term in the truncation error, which is much larger than the leading second-order term. On the other hand, when considering ENO-type schemes, the third-order term disappears in parallel flows and the fourth-order term is much smaller than the second-order one. Consequently, the ENO scheme solutions are expected to be in the asymptotic range also in practical computations.

The *a posteriori* analysis of turbulent boundary layers shows that the Grid Convergence Index can sometimes fail to give a realistic estimate of the error bandwidth when the solutions are not in the asymptotic range, as seen in the case of centered scheme with artificial dissipation. Moreover, the asymptotic solution can be evaluated by means of the Richardson extrapolation only if the apparent convergence order is close to the theoretical value (although this condition is clearly not sufficient).

A careful design of the grid can be helpful in reducing the error without increasing the computational cost. The distribution of grid points should be driven by the truncation error, as proven by the computations performed with meshes G3 and G4. When the *a priori* analysis is not feasible, the truncation error can be estimated numerically (see, for instance [6]).

Acknowledgments

This work was supported by the Italian Ministry of Transportation and Navigation in the frame of INSEAN research plan 1997-99 and by the Italian Ministry of University and Technology Research.

Nomenclature

A_s = cell interface
$\mathbf{F}_s^c$ = Eulerian flux vector at cell face
$\mathbf{F}_s^v$ = viscous flux vector at cell face
k = von Karman constant
l = mixing length
$\mathbf{n}$ = $(n_1,n_2,n_3)^T$ normal unit vector
p = pressure
$\mathbf{q}$ = $(p,u_1,u_2,u_3)^T$ state variable vector
Re = Reynolds number
S_s = cell interface measure
$\mathbf{u}$ = $(u_1,u_2,u_3)^T=(u,v,w)^T$ velocity vector
u^* = $\sqrt{\nu(du/dy)|_w}$ friction velocity
$V_{i,j,k}$ = cell volume
x_i = ith coordinate
β = pseudo-compressibility factor
δ = cell interface diameter
$\Delta t_{i,j,k}$ = local time step
Δy = grid size
ε_4 = coefficient of artificial dissipation
E_i, H_i = error coefficients
λ = $\mathbf{u}\cdot\mathbf{n}+\sqrt{(\mathbf{u}\cdot\mathbf{n})^2+\beta}$ largest eigenvalue of flux Jacobian matrix
ν = kinematic viscosity
ν_T = turbulent viscosity
τ_{ij} = $(\nu+\nu_T)(\partial u_j/\partial x_i+\partial u_i/\partial x_j)$ viscous stress tensor

Superscripts

$+$ = nondimensional variables
$\sim$ = extrapolated estimate

References

[1] Roache, P. J., 1997, "Quantification of Uncertainty in Computational Fluid Dynamics," Annu. Rev. Fluid Mech., **29**, pp. 123–160.
[2] Jameson, A., Schmidt, W., and Turkel, E., 1981, "Numerical Solutions of the Euler Equations by Finite Volume Methods Using Runge-Kutta Time-Stepping Schemes," AIAA Paper 81-1259.
[3] Jameson, A., 1985, "Multigrid Algorithms for Compressible Flow Calculations" MAE Report 1743, Princeton University, Princeton, NJ.
[4] Harten, A., Engquist, B., Osher, S., and Chakravarthy, S. R., 1987, "Uniformly High Order Accurate Essentially Non-Oscillatory Schemes," J. Comput. Phys., **71**, pp. 231–303.
[5] Chorin, A., 1967, "A Numerical Method for Solving Incompressible Viscous Flow Problems," J. Comput. Phys., **2**, pp. 12–26.
[6] Brandt, A., 1984, "Multi-grid Techniques: 1984 Guide With Application to Fluid Dynamics," The Weizmann Institute of Science, Rehovot (Israel).
[7] Favini, B., Broglia, R., and Di Mascio, A., 1996, "Multigrid Acceleration of Second Order ENO Schemes From Low Subsonic to High Supersonic Flows," Int. J. Numer. Methods Fluids, **23**, pp. 589–606.
[8] Baldwin, B. S., and Lomax, H., 1978, "Thin Layer Approximation and Algebraic Model for Separated Turbulent Flows," AIAA Paper 78-257.
[9] Spalart, P. R., and Allmaras, S. R., 1994, "A One-Equation Turbulence Model for Aerodynamic Flows," La Recherche Aérospatiale, **121**, pp. 5–21.
[10] Di Mascio, A., Broglia, R., and Favini, B., 1998, "Numerical Simulation of Free-Surface Viscous Flow by ENO-Type Schemes," 3rd Int. Conf. on Hydrod., Oct. 1998, Seoul, Korea.
[11] Schlichting, H., 1960, *Boundary Layer Theory*, McGraw-Hill, New York.
[12] Vinokur, M., 1983, "On One Dimensional Stretching Function of Finite Difference Calculations," J. Comput. Phys., **50**, pp. 215–234.
[13] Blottner, F. G., 1990, "Accurate Navier-Stokes Results for Hypersonic Flow Over a Spherical Nosetip," J. Spacecr. Rockets, **27**, pp. 113–122.

Donald J. Bergstrom
Professor,
Department of Mechanical Engineering,
University of Saskatchewan,
57 Campus Drive,
Saskatoon, SK, Canada S7N 5A9
e-mail: Don_Bergstrom@engr.usask.ca

Nathan A. Kotey
Project Engineer,
Atomic Energy Canada Limited,
2251 Speakman Drive,
Mississauga, ON, Canada L5K 1B2
e-mail: koteyn@aecl.ca

Mark F. Tachie
Assistant Professor,
Department of Mechanical Engineering,
University of Manitoba,
15 Gillson Street,
Winnipeg, MB, Canada
e-mail: tachiemf@cc.umanitoba.ca

The Effects of Surface Roughness on the Mean Velocity Profile in a Turbulent Boundary Layer

Experimental measurements of the mean velocity profile in a canonical turbulent boundary layer are obtained for four different surface roughness conditions, as well as a smooth wall, at moderate Reynolds numbers in a wind tunnel. The mean streamwise velocity component is fitted to a correlation which allows both the strength of the wake, Π, and friction velocity, U_τ, to vary. The results show that the type of surface roughness affects the mean defect profile in the outer region of the turbulent boundary layer, as well as determining the value of the skin friction. The defect profiles normalized by the friction velocity were approximately independent of Reynolds number, while those normalized using the free stream velocity were not. The fact that the outer flow is significantly affected by the specific roughness characteristics at the wall implies that rough wall boundary layers are more complex than the wall similarity hypothesis would allow. [DOI: 10.1115/1.1493810]

Introduction

Turbulent boundary layers continue to be the subject of both experimental study and numerical simulation due to their prominence in most industrial and environmental flows. Very often in engineering applications, the transport rate of a scalar contaminant is also fixed by transport mechanisms occurring at the wall. For a smooth surface, the no-slip condition requires the relative velocity of the fluid at the surface to be zero. For a rough surface, the protrusion of the roughness elements into the surrounding flow complicates the interaction with the surface, both in terms of the mean and fluctuating velocity fields. In each case, the interaction of the wall and the outer flow appears to manifest itself as prototypical vortical structures which appear to be universal for near-wall turbulent flows.

Given their importance and also their complexity, turbulent boundary layers on rough surfaces have been extensively studied in the past, e.g., by Hama [1], Furuya and Fujita [2], Perry et al. [3], Bandyopadhyay and Watson [4], as well as the review paper by Raupach et al. [5]. Nonetheless, as pointed out in a recent paper by Patel [6], the treatment of rough surfaces by present modeling techniques is still deficient and additional laboratory investigations are required. One of the most important parameters required by an engineering analysis is the wall shear stress, or its equivalent the friction velocity, U_τ. The friction velocity is of practical value in so far as it represents the skin friction drag, and is also an essential scaling parameter for theoretical analysis of the mean velocity profile. Most engineering theories of near-wall turbulent flow postulate a universal velocity profile which is characterized by an overlap region where the mean streamwise velocity component varies logarithmically with the wall normal distance, i.e.,

$$U^+ = \frac{1}{\kappa} \ln y^+ + B \tag{1}$$

where $U^+ = U/U_\tau$, $y^+ = yU_\tau/\nu$ and U_τ is the friction velocity; $\kappa \approx 0.41$ and $B \approx 5.0$ are empirical constants. In this case, the wall normal distance is normalized by a viscous length scale associated with the smooth surface. More recently, various researchers, including Barenblatt [7] and George and Castillo [8], have presented theoretical arguments advocating a power-law velocity profile in the over-lap region. However, a logarithmic velocity profile has been traditionally used to describe boundary layers in mechanical engineering applications, and in fact does a very convincing job of collapsing the data for many different experiments. For example, it is the basis of the skin friction relation commonly used to calculate the pressure drop in fully developed duct flows. A related issue addressed by George and Castillo [8] is the choice of velocity scale in the outer flow region, which according to their theory is the freestream value, U_e, and not the friction velocity.

For a rough surface, the wall boundary condition becomes more complex. On the micro-scale, i.e., the scale of the roughness elements, the flow is no longer parallel to the ground plane. Instead, details of the flow in the roughness sublayer depend on the specific geometry of the roughness elements. For example, in the case of roughness configurations which resemble bluff body structures attached to a ground plane, the flow structure is dominated by the wakes created by the roughness elements. In general, the flow in the roughness sublayer is markedly different from that in the viscous sublayer of a smooth surface, and becomes spatially non-homogeneous just above the roughness elements. However, outside the roughness sublayer, it has been proposed that for sufficiently high Reynolds numbers the turbulent motion is not affected by the surface roughness [9]. The implications of this hypothesis—often referred to as the wall similarity hypothesis—would be very attractive for turbulence modeling, since it suggests that apart from a modification in the skin friction parameter, the mean flow structure remains the same. Unfortunately, there is an increasing amount of experimental evidence, e.g., Krogstad et al. [10], and Krogstad and Antonia [11], which in contrast to the hypothesis above suggests that roughness effects extend throughout the boundary layer.

An overly simplistic but pragmatic way to treat fully rough boundary layers is to replace the viscous length scale of the smooth wall with the mean roughness height, k. The resultant form of the mean velocity profile in the overlap region then becomes

$$U^+ = \frac{1}{\kappa} \ln(y/k) + B_k \tag{2}$$

Contributed by the Fluids Engineering Division for publication in the JOURNAL OF FLUIDS ENGINEERING. Manuscript received by the Fluids Engineering Division May 23, 2000; revised manuscript received January 30, 2002. Associate Editor: D. R. Williams.

where typically $B_k = 8.5$ [12]. The difference between the mean velocity profile on a smooth and rough surface, using Eqs. (1) and (2) is given by the relation

$$\Delta U^+ = \frac{1}{\kappa} \ln k^+ - 3.5 \tag{3}$$

where the change ΔU^+ represents a downward shift to the velocity profile plotted in inner coordinates. As White [12] points out, experiments on different types of rough walls have shown that its value varies with the type of roughness. In fact, as will be shown below, the effect of roughness extends beyond the over-lap region into the outer region of the boundary layer.

To explore the effects of roughness on the outer region of the boundary layer, following Krogstad et al. [10], we consider a composite mean velocity profile given by

$$U^+ = \frac{1}{\kappa} \ln y^+ + B - \Delta U^+ + \frac{2\Pi}{\kappa} w\left(\frac{y}{\delta}\right) \tag{4}$$

which consists of: the overlap profile, Eq. (1); the roughness shift, ΔU^+; and the wake function, $w(y/\delta)$, where Π represents the strength of the wake and δ is the boundary layer thickness. This profile represents the velocity throughout the boundary layer region outside the viscous or roughness sublayer, and as such is much more useful than the log-law for making comparisons to experimental data. The mean velocity profile in the outer region of the boundary layer is more conveniently analyzed in terms of its deviation from the value, U_e, at the outer edge, $y = \delta$. The mean defect profile is given by

$$U_e^+ - U^+ = \frac{2\Pi}{\kappa}\left[w(1) - w\left(\frac{y}{\delta}\right)\right] - \frac{1}{\kappa}\ln(y/\delta) \tag{5}$$

For a given form of the wake function, the mean velocity defect depends on two boundary layer parameters: 1) the strength of the wake, Π, and 2) the friction velocity, U_τ, both of which are influenced by surface roughness.

The study reported below investigates the effect of surface roughness on the velocity profile for three different types of roughness elements, i.e., sand grains, a wire screen, and a perforated plate, in a zero-pressure gradient boundary layer created in a wind tunnel. The results obtained clearly demonstrate that surface roughness systematically affects the velocity characteristics throughout the boundary layer. A companion study [13] considered a similar investigation in open channel flow using LDA measurements. Although the overall conclusions were the same, the specific results were influenced by some of the special features of open channel flow, i.e., a relatively high background turbulence intensity and finite depth of fluid. In contrast, the present study considers a zero-pressure gradient boundary layer flow at Reynolds numbers which were much higher than those that could be obtained in the open channel study. The remainder of the paper begins with a description of the experimental facility followed by a brief theoretical background. Next, the results are presented for five different flow fields—four rough and one smooth—at three different Reynolds numbers. Finally, some conclusions arising from the study are presented.

Experimental Facility

The experiments were performed in the high-speed test section (HSTS) of a single return wind tunnel with a 1129 mm $\times$912 mm rectangular cross-section. The test section was 2 m long, and the flow enters the HSTS from the low speed test section via a 7:1 contraction. This ensures that the upstream flow prior to meeting the ground plane is relatively undisturbed. The velocity measurements were obtained on a smooth surface as well as four types of rough surfaces. The smooth wall measurements were obtained on an elevated Medium Density Fiber (MDF) board which was screwed onto the floor of the wind tunnel. The MDF board has a rectangular cross-section, a width of 950 mm, a length of 1820 mm and a thickness of 25 mm. The leading edge is 20 mm from the entrance of the HSTS. Streamlined risers are used to maintain a 40 mm spacing between the bottom of the ground plane and the floor of the HSTS. These also ensure the cross-stream and stream-wise flatness to within 0.3 deg over the entire ground plane. The leading edge was carefully rounded to an elliptical profile in order to improve the quality of the flow. The board also served as the ground plane for the rough surfaces. Four different surface roughness conditions were examined:

1. A 1500 mm long and 550 mm wide steel plate (PS) with circular perforations arrayed in a hexagonal pattern. The plate was 1.4 mm thick with perforations 2.0 mm in diameter spaced 4.0 mm between centers giving an openness ratio of about 43%.
2. A 1440 mm long and 480 mm wide steel plate (PL) with circular perforations arrayed in a hexagonal pattern. The plate was 1.6 mm thick with perforations 4.8 mm in diameter spaced 6.3 mm between centers giving an openness ratio of about 53%.
3. A stainless-steel wire screen (WS) made of 0.6 mm wires with 7.0 mm-centerline spacing. The ratio of centerline spacing to wire diameter was about 12 and the openness ratio approximately 84%.
4. A sand grain roughness (SG) created from sand grains of 1.2 mm nominal mean diameter carefully attached to ensure a uniform distribution.

The boundary layer was tripped using 3 mm diameter pebbles glued onto a 15 mm strip of double-sided tape. This aids the development of a turbulent boundary layer close to the leading edge. The tape was placed 300 mm from the leading edge of the board and spanned the entire width of the board. The different roughness plates were attached to the ground plate adjacent to the 15 mm trip strip by means of double-sided tape. In order to investigate a fully developed flow in the stream-wise direction, velocity measurements were obtained at sections $x = 800$ mm and $x = 1000$ mm downstream of the trip using a Pitot-probe with a circular cross-section and a square end. The tip of the Pitot probe had outer and inner diameters of 1.07 mm and 0.60 mm, respectively. With the aid of the LabVIEW software, the exact position of the Pitot probe could be obtained by setting a reference position (say 0 mm) when the tip of the Pitot probe is positioned on the test surface. For a desired range and number of grid points, the program automatically moves the probe and stores its current position in a file together with the mean parameters sampled at each location.

At any location y in the boundary layer, velocity measurements were obtained by taking 5000 samples of the dynamic pressure at a sampling frequency of 1000 Hz using the Pitot probe. The effects of velocity or total pressure gradient, viscosity or Reynolds number based on Pitot probe diameter, turbulence and Pitot probe geometry on the Pitot probe measurements were considered as outlined in Chue [14]. However, corrections to the velocities calculated from these measurements were not implemented since they were small and tend to cancel [15]. The Pitot probe was aligned to the flow with the aid of a square to eliminate errors caused by yaw of Pitot probes [14]. Refined measurements were taken close to the wall to give adequate spatial resolution for an accurate determination of boundary layer integral parameters. The nominal free-stream turbulence intensity and pressure gradient were, respectively, 0.3% and -10 Pa/m. The nonuniformity of the freestream velocity profile was 0.5%.

For each surface, measurements were obtained at three different Reynolds numbers by varying the freestream velocity from 20 to 42 m/s. A summary of the test conditions is given in Table 1, where U_e is the freestream velocity, δ is the boundary layer thickness, θ is the momentum thickness, H is the shape parameter, Re_θ is the Reynolds number based on the momentum thickness, and x is the distance downstream of the trip. The boundary layer thick-

Table 1 Summary of test conditions

Test	Type of surface	U_e (m/s)	x (mm)	δ (mm)	θ (mm)	H	δ^+	Re_θ
SM1	Smooth	20.40	800	33.0	4.06	1.32	1640	5180
SM2	Smooth	30.48	800	33.5	3.82	1.32	23 90	7280
SM3	Smooth	41.91	1000	35.5	3.81	1.30	3370	9980
PS1	Perforated	20.30	1000	29.0	3.84	1.44	2080	4870
PS2	Perforated	31.53	800	27.0	3.86	1.41	3000	7610
PS3	Perforated	41.51	800	29.0	3.92	1.46	3820	10170
PL1	Perforated	20.51	800	30.0	4.43	1.65	2440	5680
PL2	Perforated	31.41	800	28.5	4.27	1.62	3390	8380
PL3	Perforated	41.88	800	30.0	4.48	1.64	4440	11730
SG1	Sand grain	20.33	800	30.0	4.41	1.60	2440	5603
SG2	Sand grain	30.74	800	29.0	4.18	1.63	3440	8030
SG3	Sand grain	41.51	800	29.5	4.37	1.62	4520	11340
WS1	Wire screen	20.93	1000	35.5	5.45	1.66	2730	7130
WS2	Wire screen	31.52	800	31.5	4.69	1.68	3600	9240
WS3	Wire screen	41.87	800	33.0	4.91	1.71	4850	12850

ness δ is defined as the location above the surface at which the local mean velocity is 99% of the freestream value. The dimensionless boundary layer thickness, δ^+ $(=\delta u_\tau/\nu)$, which measures the relative size of the outer and inner layers, is also included in the table. The Reynolds numbers considered in the rough wall tests are sufficiently high to minimize Reynolds number effects.

Determination of U_τ

Different indirect techniques are available for the determination of the wall shear stress or friction velocity U_τ at sufficiently high Reynolds numbers. For a smooth wall turbulent boundary layer $(\Delta U^+=0)$, the wall shear stress is commonly determined by fitting to the mean velocity profile measured near the wall using a so called ''Clauser plot.'' Previous rough wall experiments demonstrate that the Clauser technique may not be reliable [16]. For a turbulent boundary layer developing over a rough surface, Eq. (4) can be used to describe the mean velocity in which case description of a measured velocity profile on a rough wall requires the determination of three parameters namely: U_τ, ΔU^+, and Π. A reduction in the number of parameters to be fitted is obtained by choosing to work with the velocity defect form of the velocity profile given by Eq. (5). Recent experimental evidence of the dependence of Π on surface roughness suggests that for rough surfaces we should employ a correlation which enables both Π and U_τ to be fitted to experimental data in a way which acknowledges the coupling between them. In this regard, the commonly used profile of Hama [1] is deficient. Instead, following Krogstad et al. [10] we employed the formulation proposed by Finley et al. [17] and later used by both Granville [18] and Hancock and Bradshaw [19], namely:

$$w\left(\frac{y}{\delta}\right)=\frac{1}{2\Pi}\left[(1+6\Pi)-(1+4\Pi)\left(\frac{y}{\delta}\right)\right]\left(\frac{y}{\delta}\right)^2 \tag{6}$$

Of special importance in using Eqs. (5) and (6) in the profile matching is the explicit determination of the wake strength Π, and the expectation of a more accurate estimate of the friction velocity, U_τ. In the LDA measurements reported by Tachie et al. [13] for a smooth surface, the friction velocities obtained using Eq. (5) and Eq. (6) were compared to the corresponding values obtained using the velocity gradient in the viscous sublayer. The differences between the friction velocities obtained from the two methods were found to be within $\pm 4\%$.

For flow over a rough surface, a precise definition of y would discriminate between the distance measured from the top of the roughness elements and that measured from a virtual origin, ε, implied by the logarithmic velocity relation. However, the virtual origin is generally a small fraction of the roughness height, k, which itself is small relative to the boundary layer thickness δ. For example, Krogstad et al. [10] reported a typical value of $\varepsilon/k=0.25$ for their 0.69 mm thick wire screen measurement while a review of previous sand grain data by Nezu and Nakagawa [20] suggested $0.15<\varepsilon/k<0.30$. In the present experiments, the roughness height is about 2 to 6% of the boundary layer thickness. Therefore, except in the very near wall region where the value of ε is comparable to y, we estimate the effect of the virtual origin ε to be negligible over a significant portion of the flow. In this study, our focus is on the outer part of the flow and no attempt was made to determine ε. For the rough wall measurements reported herein, the wall normal distance, y, was measured relative to the nominal top of the roughness elements.

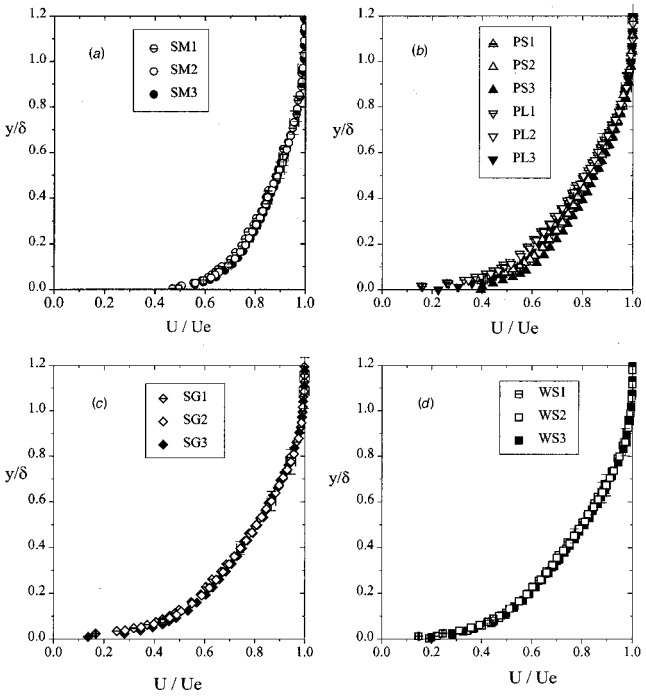

Fig. 1 Mean velocity profiles on smooth and rough surfaces in outer coordinates: (*a*) smooth, (*b*) perforated plate, (*c*) sand grain, and (*d*) wire screen. The error bars correspond to the intermediate Reynolds number data, i.e., SM2, PS2, PL2, SG2, and WS2.

The uncertainty in δ is estimated to be $\pm 7\%$. The uncertainty in the mean velocity is estimated to be less than 2%, and the uncertainty in the friction velocity U_τ is estimated to be 2 and 5% for the smooth and rough wall data, respectively. Error bars, representing the level of measurement uncertainty (at the 95% confidence level), are included for the mean velocity profiles in Fig. 1, and the defect profiles in Figs. 6 and 7, for the data at intermediate Reynolds numbers. Further details on uncertainty analysis are reported in Kotey [21].

Results and Discussion

The mean velocity profiles in outer coordinates are shown in Fig. 1. Figure 1(*a*) shows the profiles obtained on the smooth wall, while Fig. 1(*b*) shows the data for both the small (PS) and large (PL) perforations. The profiles obtained on the sand grain (SG) and the wire screen (WS) roughness are shown in Fig. 1(*c*) and Fig. 1(*d*), respectively. Also shown on each of these figures are the error bars corresponding to the intermediate Re_θ, i.e., SM2 (Fig. 1(*a*)), PS2 and PL2 (Fig. 1(*b*)), SG2 (Fig. 1(*c*)) and WS2 (Fig. 1(*d*)). With perhaps the exception of the wire screen roughness, all the profiles exhibit some Reynolds number effects. The Reynolds number effects are greatest for the two perforated plates (Fig. 1(*b*)). In most cases, these Reynolds number effects are confined to the very near-wall region. In the case of the smooth surface, for example, data obtained at the two higher Reynolds numbers (SM2 and SM3) collapse within measurement uncertainty except for $y/\delta<0.05$. The sand grain data for SG2 and SG3 also show a

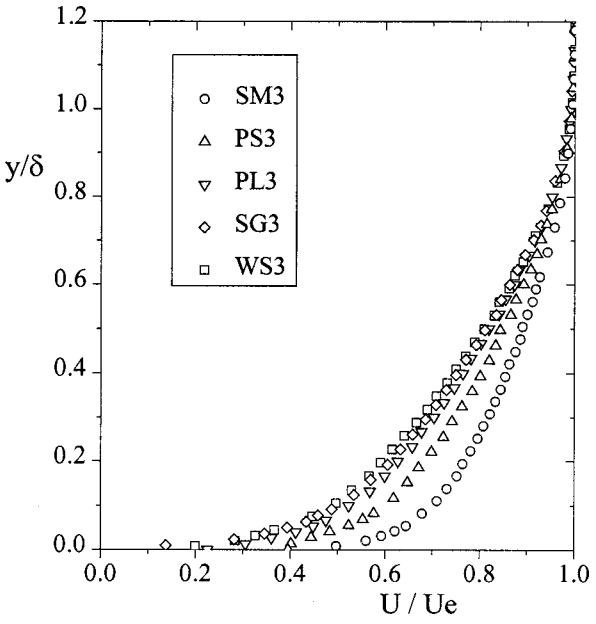

Fig. 2 Comparison of mean velocity profiles in outer coordinates for smooth and rough surfaces

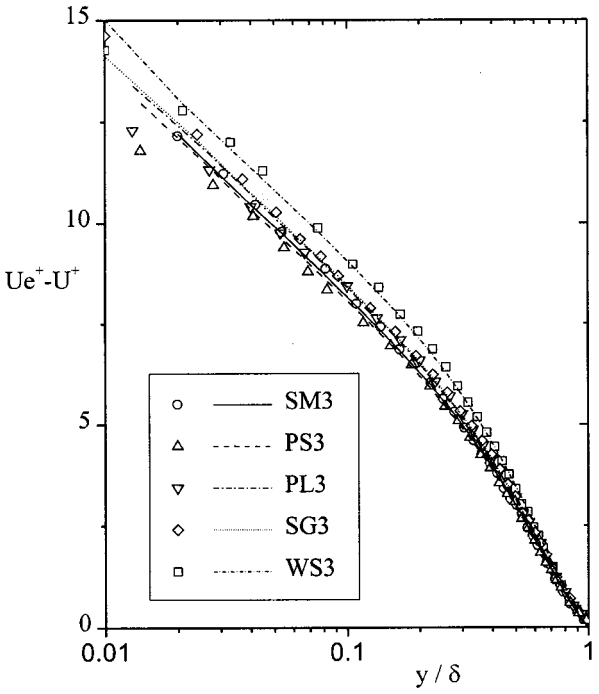

Fig. 3 Mean defect profiles for smooth and rough surfaces

similar collapse for $y/\delta > 0.1$. The lack of collapse very close to the wall may be partly attributed to the uncertainty in determining the exact location of the wall in the case of the smooth wall data, and an additional error associated with the virtual origin ε for the rough wall data.

Figure 2 compares the mean velocity profile for the smooth wall to those on the four different rough surfaces considered. In this figure, only the velocity profiles for the highest Re_θ are shown. Compared to the smooth wall profile, the rough wall profiles show significant deviation almost up to the outer edge of the boundary layer. It is of interest to observe that even though the wire screen has the smallest physical dimension, it causes the greatest alteration to the mean profile in comparison to the smooth wall data. The close agreement among PL3, SG3, and WS3 observed in Fig. 2 is also consistent with the approximately equal values of the dimensionless boundary layer thickness δ^+ and roughness shift ΔU^+ (see Tables 1 and 2), and suggests that irrespective of the specific form of surface geometry, the outer region of the mean profiles is similar if the roughness effect is the same. For the perforated plates, it is observed that a modest increase of about 20% in openness ratio causes significant modification of the mean velocity profiles.

The friction velocity U_τ in the present study was obtained by fitting a defect profile to the experimental data following Krogstad et al. [10]. This technique does not implicitly fix the strength of the wake (Π) and therefore allows the Π values to be optimized for each specific roughness geometry. Since the Reynolds numbers considered in the present experiments are sufficiently high, the validity of a log-law with $\kappa^{-1}=2.44$ was assumed for both the smooth and rough surfaces. Equations (5) and (6) were fitted to the experimental mean defect profile while ensuring that the friction velocity simultaneously ensured a log-linear relation with $\kappa^{-1}=2.44$. In view of the uncertainty in locating the wall (for the smooth surface) and the virtual origin (for the rough surfaces), data in the immediate vicinity of the wall or the roughness elements, i.e., $y<0.1\delta$, were not considered in the profile matching to obtain U_τ and Π. Figure 3 shows some typical fits to the experimental data. An assessment of goodness-of-fit using the chi-squared distribution indicated that the correlation fit the experimental data at a confidence level of 99.5% or better in the region of interest, i.e., $0.1 \leqslant y/\delta \leqslant 1$. As will be shown below, each roughness was characterized by a distinct defect profile. The values of the friction velocity U_τ and wake strength Π obtained for the present tests are summarized in Table 2. For a given surface, the Π values are independent of Re_θ. The rough-wall profiles show distinctly higher Π values compared to the value obtained for the smooth wall. The wire screen (WS) roughness, in spite of its smallest physical size, has the highest Π value. The present value of $\Pi=0.73$ for WS is comparable to the value of 0.7 reported in the recent study by Krogstad and Antonia [11] which considered a wire screen of similar physical size but with a smaller openness ratio at $\mathrm{Re}_\theta=12800$. Also shown in Table 2 are the skin friction coefficient C_f, the roughness shift ΔU^+ and the dimensionless roughness height k^+ $(=kU_\tau/\nu)$. The k values used for each surface were as follows: for each perforated plate, the plate thickness, i.e., $k_{PS}=1.4$ mm and $k_{PL}=1.6$ mm; for the sand grain surface, the mean diameter of the sand particles, $k_{SG}=1.2$ mm; and for the wire screen, the wire diameter, $k_{WS}=0.6$ mm.

Table 2 Summary of mean velocity parameters

Test	Re_θ	U_τ (m/s)	$C_f \times 10^3$	Π	ΔU^-	k
SM1	5176	0.795	3.04	0.55		
SM2	7277	1.140	2.80	0.54		
SM3	9980	1.520	2.63	0.54		
PS1	4872	1.110	5.98	0.56	7.5	97
PS2	7606	1.700	5.81	0.57	8.1	149
PS3	10170	2.170	5.47	0.56	8.2	190
PL1	5679	1.300	8.03	0.59	10.8	146
PL2	8383	1.900	7.32	0.59	10.8	214
PL3	11726	2.370	6.40	0.59	10.3	267
SG1	5603	1.300	8.18	0.60	11.1	98
SG2	8031	1.900	7.64	0.60	10.8	143
SG3	11337	2.450	6.97	0.60	11.1	184
WS1	7129	1.230	6.91	0.73	10.5	46
WS2	9239	1.830	6.74	0.73	11.1	69
WS3	12849	2.350	6.30	0.73	11.3	88

The velocity profiles normalized by the friction velocity obtained from matching the defect profile are shown in Fig. 4. For all profiles, near the wall, the data exhibit significant scatter, which can be attributed to an increased sensitivity to any uncertainty in the value of y. For the smooth wall profiles shown in Fig. 4(a), the extent of collapse with the law-of-the-wall increases as Re_θ increases, although it still remains only a small fraction of the

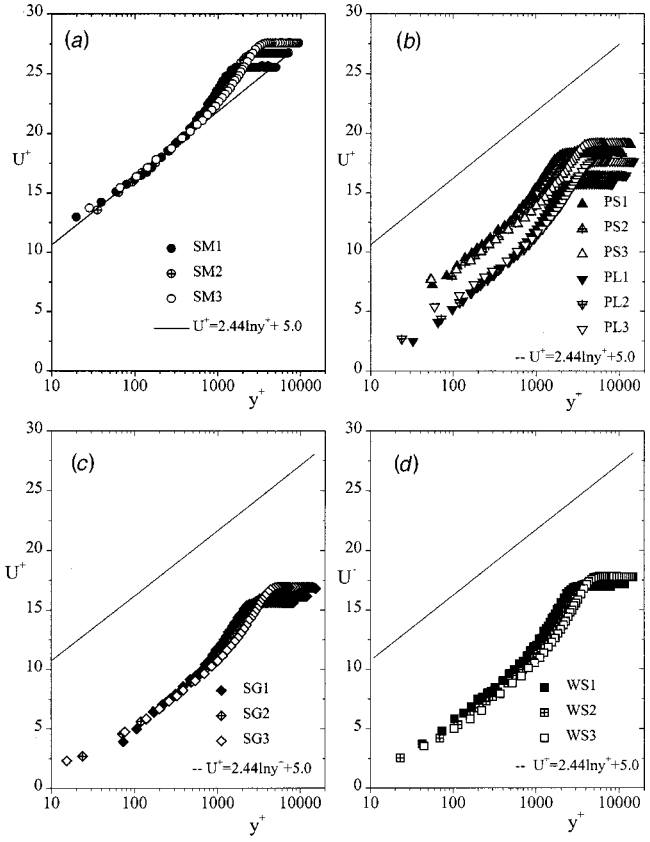

Fig. 4 Mean velocity profiles using inner coordinates: (*a*) smooth, (*b*) perforated plate, (*c*) sand grain, and (*d*) wire screen

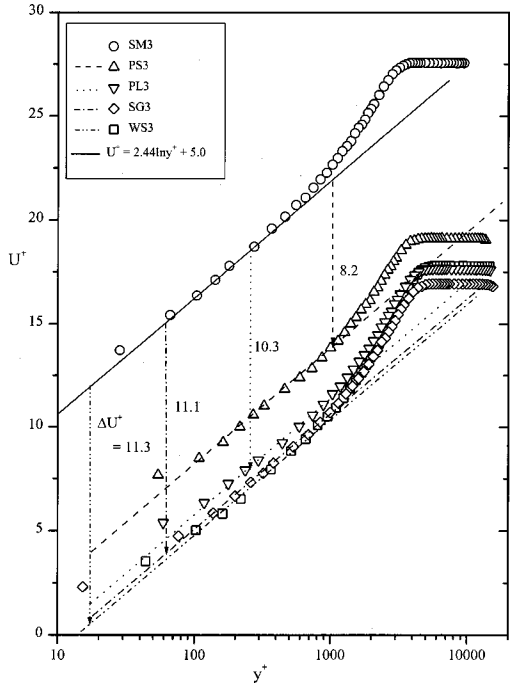

Fig. 5 Mean velocity profiles using inner coordinates for smooth and rough surfaces

width of the boundary layer. The mean profiles, shown in Fig. 4(*b*) for the perforated plates (PS and PL), Figure 4(*c*) for sand grain (SG) and Fig. 4(*d*) for wire screen (WS), all exhibit the expected downward-right shift with respect to the log law for a smooth surface. The rough wall profiles also show a more extended linear region at higher Re_θ, which is consistent with the higher values of δ^+. For the rough surfaces, especially PS and WS, there is a small scatter in the magnitude of the downward shift. However, the scatter in ΔU^+ (see Table 2) is well within the measurement uncertainty in the friction velocity (approximately 5%).

Figure 5 compares the velocity profiles obtained on both the smooth and rough surfaces for the highest Reynolds numbers. The small-perforated plate (PS) shows the smallest shift from the smooth wall data, while the wire screen, in spite of its smallest physical size, shows the highest roughness shift. It is also important to note that in spite of the small difference in the openness ratio for PS3 and PL3, the two profiles are quite distinct. More specifically, the roughness effect is higher for the larger perforation (PL) than for the smaller perforation (PS). In some ways, the roughness PL more resembles the SG and WS roughness than the PS roughness.

The mean defect profiles are shown in Fig. 6 for the five different surfaces considered. The friction velocity U_τ and the boundary layer thickness δ are used to scale the velocity and wall-normal distance, respectively. For each surface, the defect profiles nearly collapse onto each other. This is not surprising because the profile matching technique employed ensures a collapse with the law-of-the-wall in the overlap region.

Figure 7 shows the defect profiles scaled with freestream velocity U_e, which is the correct scaling according to the recent theory developed by George and Castillo [8] for smooth wall zero pressure gradient turbulent boundary layers. The theory also shows that the mean defect profiles in outer scaling must admit Reynolds number dependence except in the limit of infinite Reynolds numbers. Figure 7(*a*) shows the data obtained on the smooth surface at three values of Re_θ, while Fig. 7(*b*) shows the profiles on both the perforated plates. The sand grain (SG) and wire screen (WS) data are shown in Fig. 7(*c*) and 7(*d*), respectively. All the data, except perhaps those obtained on the wire screen roughness, show a Rey-

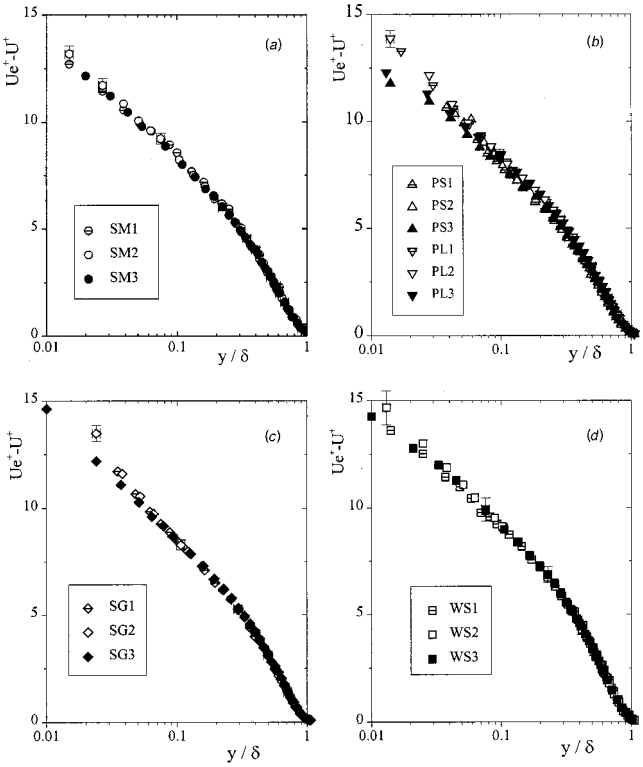

Fig. 6 Mean defect profiles using inner velocity scale: (*a*) smooth, (*b*) perforated plate, (*c*) sand grain, and (*d*) wire screen

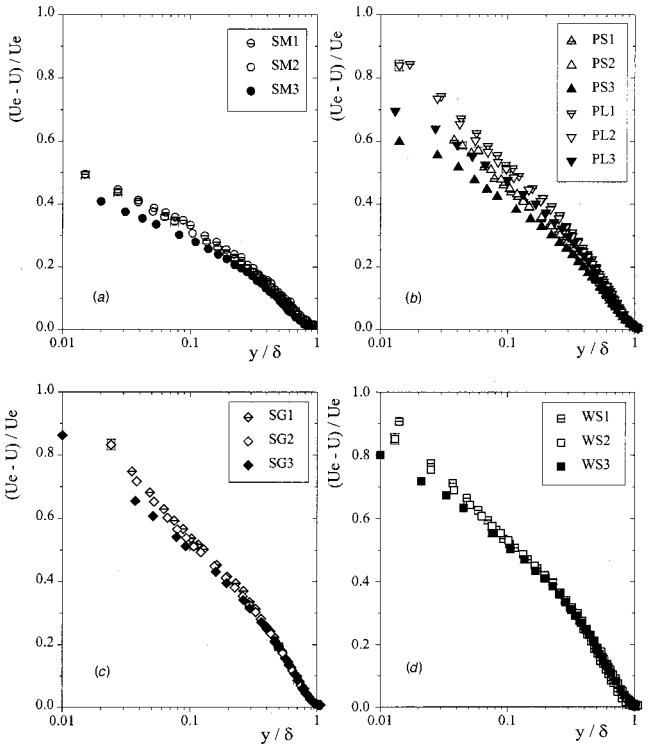

Fig. 7 Mean defect profiles using outer velocity scale: (*a*) smooth, (*b*) perforated plate, (*c*) sand grain, and (*d*) wire screen

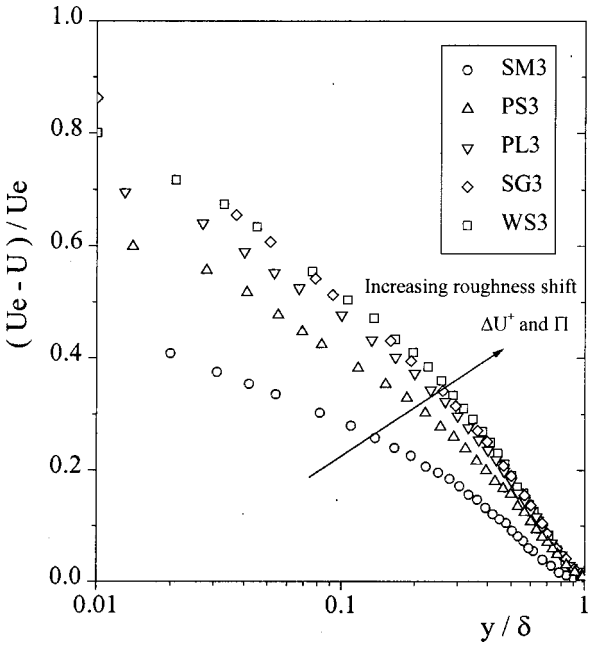

Fig. 8 Mean defect profiles for smooth and rough surfaces using outer coordinates

nolds number dependence. At similar y/δ, the normalized velocity defect decreases as Re_θ increases for a given surface roughness. This is in contradiction to the apparent Reynolds number independence observed in Fig. 6 which used the friction velocity obtained from profile matching as the normalizing velocity scale. Figure 7(*b*) reveals that even though PS and PL have the same form of surface roughness, the two sets of profiles are distinct as evidenced by the skin friction coefficients summarized in Table 2.

Figure 8 compares the mean defect profiles at the highest Re_θ for each surface geometry. As the roughness effect increases, there is a tendency for the defect profile to move upwards. The profiles for PL3, SG3, and WS3 collapse reasonably well for $y/\delta > 0.05$. It should be recalled that the C_f values as well as the roughness shifts ΔU^+ for these profiles are also nearly equal (see Table 2). The fair agreement observed for PL3, SG3, and WS3 in Figs. 2, 5, and 7 indicates that the mean velocity profiles are similar for similar roughness shift (ΔU^+), irrespective of the specific form of the roughness geometry.

Conclusions

The present paper reports additional measurements of the mean velocity profile in a zero-pressure gradient turbulent boundary layer on a rough surface at moderate Reynolds numbers. Specifically, measurements were made for a smooth surface and three different types of roughness elements: sand grains, a wire screen and two perforated plates. Comparison of the mean velocity and defect profiles indicated characteristic differences between the smooth and rough surfaces, as well as among the different rough surfaces. This observation suggests that any formulation, which presumes roughness effects to be limited to the roughness sublayer, may give inaccurate results for parameters such as the skin friction and wake strength. More generally, the fact that roughness effects penetrate into the outer region of the boundary layer argues against the notion of wall similarity and suggests that turbulence models for rough wall flows must incorporate the effects of roughness at the surface, which are complex. On the other hand, the results also show that irrespective of the specific roughness geometry, roughness conditions with approximately the same roughness shift, i.e., ΔU^+, have similar mean flow characteristics. Finally, we note that for a given surface condition, the mean velocity defect profiles normalized by the free-stream velocity show systematic Reynolds number dependence whereas the defect profiles normalized by the friction velocity are independent of Reynolds number.

Acknowledgments

The support of the Natural Sciences and Engineering Research Council of Canada via a research grant (DJB) and scholarship (MFT) is gratefully acknowledged.

References

[1] Hama, F. R., 1954, "Boundary Layer Characteristics for Smooth and Rough Surfaces," Trans. Soc. Naval Archit. Mar. Engnrs, **62**, pp. 333–358.
[2] Furuya, Y., and Fujita, H., 1967, "Turbulent Boundary Layers on a Wire-Screen Roughness," Bull. JSME, **10**, pp. 77–86.
[3] Perry, A. E., Lim, K. L., and Henbest, S. M., 1987, "An Experimental Study of the Turbulence Structure in Smooth- and Rough-Wall Boundary Layers," J. Fluid Mech., **177**, pp. 437–466.
[4] Bandyopadhyay, P. R., and Watson, R. D., 1988, "Structure of Rough Wall Turbulent Boundary Layers," Phys. Fluids, **31**, pp. 1877–1883.
[5] Raupach, M. R., Antonia, R. A., and Rajagopalan, S., 1991, "Rough Wall Turbulent Boundary Layers," Appl. Mech. Rev., **44**, pp. 1–25.
[6] Patel, V. C., 1998, "Perspective: Flow at High Reynolds Number and Over Rough Surfaces—Achilles Heel of CFD," ASME J. Fluids Eng., **120**, pp. 434–444.
[7] Barenblatt, G. I., 1993, "Scaling Laws for Fully Developed Turbulent Shear Flows. Part 1. Basic Hypothesis and Analysis," J. Fluid Mech., **248**, pp. 513–520.
[8] George, W. K., and Castillo, L., 1997, "Zero-Pressure-Gradient Turbulent Boundary Layer," Appl. Mech. Rev., **50**(11), pp. 689–729.
[9] Townsend, A. A., 1976, *The Structure of Turbulent Shear Flow*, Cambridge University Press, Cambridge, UK.
[10] Krogstad, P. A., Antonia, R. A., and Browne, L. W. B., 1992, "Comparison between Rough- and Smooth-Wall Turbulent Boundary Layers," J. Fluid Mech., **245**, pp. 599–617.
[11] Krogstad, P. A., and Antonia, R. A., 1999, "Surface Roughness Effects in Turbulent Boundary Layers," Exp. Fluids, **27**, pp. 450–460.

[12] White, F. M., 1974, *Viscous Fluid Flow*, McGraw-Hill, New York, NY.
[13] Tachie, M. F., Bergstrom, D. J., and Balachandar, R., 2000, ''Rough Wall Turbulent Boundary Layers in Shallow Open Channel Flow,'' ASME J. Fluids Eng., **122**, pp. 533–541.
[14] Chue, S. H., 1975, ''Pressure Probes for Fluid Measurement,'' Prog. Aerosp. Sci., **16**, pp. 147–223.
[15] Zagarola, M. V., 1996, ''Mean Flow Scaling in Turbulent Pipe Flow,'' Ph.D. thesis, Princeton University, Princeton, NJ.
[16] Perry, A. E., Schofield, W. H., and Joubert, P. N., 1969, ''Rough Wall Turbulent Boundary Layers,'' J. Fluid Mech., **37**, pp. 383–413.
[17] Finley, P. J., Chong, Phoe Khoo, and Jeck, Poh Chin, 1966, ''Velocity Measurements in a Thin Turbulent Wake Layer,'' La Houille Blanche, **21**, pp. 713–721.
[18] Granville, P. S., 1976, ''A Modified Law of the Wake for Turbulent Shear Layers,'' ASME J. Fluids Eng., **98**, pp. 578–580.
[19] Hancock, P. E., and Bradshaw, P., 1989, ''Turbulence Structure of a Boundary Layer beneath a Turbulent Freestream,'' J. Fluid Mech., **205**, pp. 45–76.
[20] Nezu, I., and Nakagawa, H., 1993, *Turbulence in Open-Channel Flows*, A. A. Balkema, Rotterdam.
[21] Kotey, N. A., 2001, ''Effects of Surface Roughness on the Mean Velocity Profile in a Turbulent Boundary Layer,'' M.Sc. thesis, University of Saskatchewan, Saskatoon, SK.

Analysis and Experiments on Three-Dimensional, Irregular Surface Roughness

J. A. van Rij

B. J. Belnap

P. M. Ligrani

Convective Heat Transfer Laboratory,
Department of Mechanical Engineering,
50 S. Central Campus Drive, MEB 2202,
University of Utah,
Salt Lake City, UT 84112

Randomly placed, nonuniform, three-dimensional roughness with irregular geometry and arrangement is analyzed. New correlations are presented for such roughness for determination of magnitudes of equivalent sand grain roughness size k_s from a modified version of the Sigal and Danberg parameter Λ_s. Also described are the numerical procedures employed to determine Λ_s from three-dimensional profilometry data. The sand grain roughness values determined with this approach are then compared with and verified by k_s magnitudes determined using: (i) analytic geometry for uniformly shaped roughness elements arranged in a regular pattern on a test surface, and (ii) measurements made with nonuniform, three-dimensional, irregular roughness with irregular geometry and arrangement. The experiments to obtain these measurements are conducted using this latter type of roughness placed on the walls of a two-dimensional channel. Skin friction coefficients are measured in this channel with three different types of rough surfaces on the top and bottom walls, and agree very well with values determined using the numerical procedures and existing correlations. The techniques described are valuable because they enable the determination of equivalent sand grain roughness magnitudes, for similar three-dimensional roughness, entirely from surface geometry after it is characterized by three-dimensional optical profilometry data. [DOI: 10.1115/1.1486222]

Introduction

The overall efficiency of machinery that involves the movement of a working fluid is dependent upon the energy losses which occur as the fluid moves past system components. Examples include gas turbine engines, steam turbines, compressors, heat exchangers, piping networks, ships, micro-scale devices, submarines, aircraft, missiles, re-entry vehicles, and passages for cooling electronic components. Surface roughness in these applications often increases the friction losses, aerodynamic losses, and thermal loading of system components. This can be either beneficial or detrimental depending upon the application. For example, for aircraft, ships, and external portions of turbine airfoils, aerodynamic losses and thermal loading should be as low as possible. However, for internal cooling passages of turbine airfoils, heat exchangers, and electronic cooling passages, increased heat transfer is beneficial, and naturally-occurring roughness, or manufactured customized surface roughness are often used.

Quantifying the characteristics of such roughness is important for all of the applications mentioned. Such quantifications take many forms, where one of the most widely used quantities is ''equivalent sand grain roughness''. The magnitude of equivalent sand grain roughness was first proposed and utilized by Nikuradse [1] and Schlichting [2] as the size of sand grains which give the same skin friction coefficients in internal passages as the roughness being evaluated. This measure of roughness size continues to be widely used in closure models for a variety of numerical prediction codes, as well as for many empirical correlations which are based on experimental data.

Coleman et al. [3] re-evaluated Schlichting's [2] surface roughness experiments by using more accurate and physically plausible assumptions in the analysis of the original experimental data to determine skin friction coefficients, $C_f/2$, and magnitudes of equivalent sand grain roughness, k_s. According to the authors, corrected values of $C_f/2$ are 0.5 to 75% higher, and corrected values of k_s are 26 to 555% higher than values originally presented by Schlichting [2]. Other investigators examine the roughness influences of a variety of objects, such as bars [4–8], ribs [9], circular rods [10,11], sand grains [1], spheres [2,12–14], hemispherical elements [2], cones [2], angles [2], pyramids, and screens. There have also been many studies on the effects of roughness of specific engineering surfaces such as turbine blades, re-entry vehicles, ship hulls, and various types of machined surfaces [15,16]. Examination of these studies reveals that there is no single parameter which is completely adequate for specifying all aspects of roughness geometry, and their effects on aerodynamic losses and surface skin friction coefficients. Height, shape, density, and manner of distribution of roughness elements are all needed to develop such a characterization.

Sigal and Danberg [17,18] made important advances in accounting for these roughness geometry considerations for uniformly-shaped roughness elements spread in a uniform pattern over a test surface. The authors define a roughness parameter, Λ_s, which is given by

$$\Lambda_s = \left(\frac{S}{S_f}\right)\left(\frac{A_f}{A_s}\right)^{-1.6} \tag{1}$$

where S is the reference area, or the area of the smooth surface before adding on the roughness, S_f is the total frontal area over the rough surface, A_f is the frontal area of a single roughness element, and A_s is the windward wetted surface area of a single roughness element. (S/S_f) is then a roughness density parameter and (A_f/A_s) is a roughness shape parameter. For ''two-dimensional roughness,'' the ratio of equivalent sand grain roughness to roughness height, k_s/k, for different ranges of Λ_s is given by

$$\frac{k_s}{k} = \begin{cases} 0.00321\Lambda_s^{4.925} & 1.400 \leqslant \Lambda_s \leqslant 4.890 \\ 8 & 4.890 \leqslant \Lambda_s \leqslant 13.25 \\ 151.71\Lambda_s^{-1.1379} & 13.25 \leqslant \Lambda_s \leqslant 100.00 \end{cases} \tag{2}$$

According to the authors [17,18], ''two-dimensional roughness'' refers to either bars, ribs, or circular rods, where each element (of

Contributed by the Fluids Engineering Division for publication in the JOURNAL OF FLUIDS ENGINEERING. Manuscript received by the Fluids Engineering Division July 23, 2001; revised manuscript received April 2, 2002. Associate Editor: K. Zaman.

each type of roughness) is placed on the surface perpendicular to the flow direction. With this approach, k_s is determined entirely from roughness geometry for surfaces with uniformly-sized and uniformly-shaped ''two-dimensional'' roughness elements arranged in a uniform pattern along a test surface. According to Sigal and Danberg [17], ''three-dimensional'' roughness consists of arrangements of spheres, hemispherical elements, cones, angles, pyramids, screens, or sand grains along a surface. However, no equation for the ratio of equivalent sand grain roughness to roughness height as dependent upon Λ_s is given by the authors for this type of roughness.

The objective of the present study is analysis of randomly placed, non-uniform, three-dimensional roughness with irregular geometry and arrangement. New correlations are presented for determination of magnitudes of equivalent sand grain roughness size from a modified version of the Sigal and Danberg parameter Λ_s for such roughness. Also described are the numerical procedures employed to determine Λ_s from three-dimensional profilometry data. The sand grain roughness values determined with this approach are then compared with *and verified by* k_s magnitudes determined using: (i) analytic geometry for uniformly-shaped roughness elements arranged in a regular pattern on a test surface, and (ii) new measurements made with non-uniform, three-dimensional, irregular roughness with irregular geometry and arrangement. These experiments are conducted using this latter type of roughness placed on the walls of a two-dimensional channel. These techniques are valuable because they allow the determination of equivalent sand grain roughness magnitudes for such irregular roughness, entirely from roughness geometry determined from three-dimensional optical profilometry data. Skin friction coefficients and friction losses are then determined for these surfaces using existing correlations [19–21], which agree very well with the new experimental results (which are also presented in this paper). Determination of such roughness characteristics from roughness geometry is important because it leads to reduced design uncertainties, lower production and part costs, and increased component life. The results are also beneficial for the analysis of different three-dimensional rough surface geometries, as well as for the development of numerical prediction models to account for the effects of roughness.

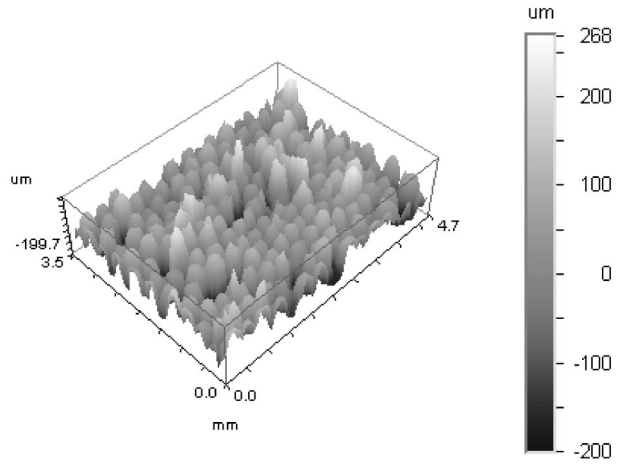

Fig. 1 Three-dimensional Wyko profilometry trace of a portion of the completely rough test surface

Rough Surfaces Tested

Three pairs of stainless steel test plates are tested in the study, each with a different type of surface: (i) smooth, (ii) three-dimensional roughness spread over the entire surface (hereafter, denoted ''completely rough''), and (iii) three-dimensional roughness arranged in a pattern on the test surface (hereafter, denoted ''patterned rough''). For this third, patterned rough surface, the rough parts of the surface pattern alternate with smooth regions, such that the surface is composed of alternate regions of the smooth and completely rough surfaces (i.e., surfaces (i) and (ii)). The smooth pair of surfaces is used to provide baseline data. Figure 1 shows an enlarged image of a portion of the completely rough test surface, obtained from three-dimensional optical profilometry data. Notice that the highest peak reaches to about 150 μm on the vertical scale. The irregularity, nonuniformity, and three-dimensional nature of the roughness elements, including their irregular arrangement, are evident from this plot.

Experimental Apparatus and Procedures

The components and dimensions of the flow facility employed for the study are shown in Fig. 2. The facility is open-circuit, subsonic, and constructed of polycarbonate material. The inlet of the facility consists of a rectangular bell mouth, followed by a honeycomb, and two screens. From the inlet section, the airflow enters a nozzle with 40 contraction ratio, and then into an inlet duct with the same cross-sectional dimensions as the test section (50.8 mm by 6.35 mm). This inlet duct is 0.864 m in length, which is equivalent to 76.5 hydraulic diameters, where hydraulic diameter is 11.3 mm. This assures that fully developed flow is present at the inlet of the test section, which follows, for all Reynolds numbers investigated. After the airflow exits the test section, it enters a square plenum. This plenum connects to a circular tube with an orifice plate at the center of its length. The flow then exits into a second square plenum. Attached to the opposite side of this plenum is a New York Blower Co. 7.5 HP, size 1808 suction blower that pulls the air through the wind tunnel. Two valves in the walls of the second plenum are used to adjust the air mass flow rate through the facility.

Details of the test section are given in Figs. 3 and 4. The test surfaces are located on the top and bottom walls of the test section. The sidewalls of the test section are made of smooth polycarbonate material. Static wall pressure taps are located on the sidewalls of the test section with streamwise spacing between adjacent taps of 2.54 cm. Each pressure tap is connected to a Celesco LCVR pressure transducer, which produces signals which are processed using a Celesco CD10D Carrier Demodulator. The resulting signals are then read using a Hewlett-Packard type 44422A data acquisition card, installed into a Hewlett-Packard HP 3497A data acquistion controller, which is operated by a Hewlett-Packard

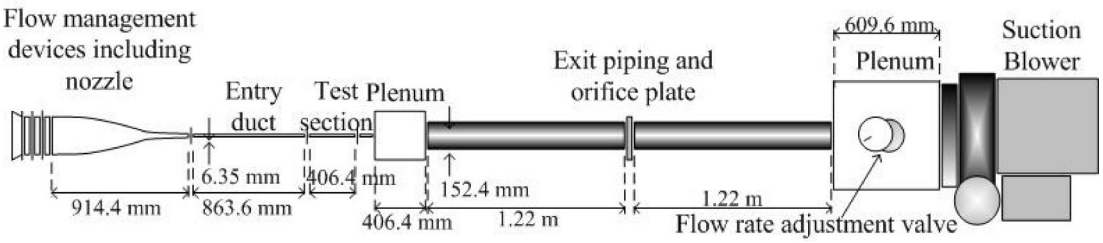

Fig. 2 Flow facility components and dimensions

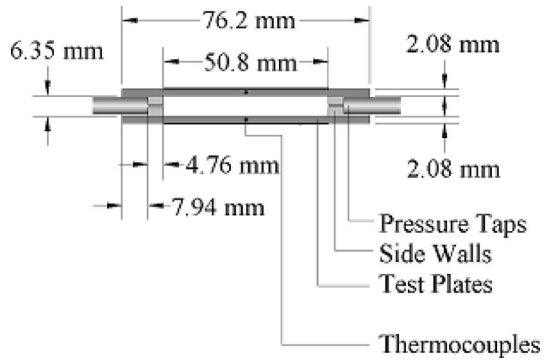

Fig. 3 Front cross-sectional view of the test section

Series 362 computer system. All pressure transducers are calibrated using a Meriam model 40GD10-WM inclined manometer as a standard. Approximately 50.8 mm upstream of the test section are three thermocouples centered in the channel to measure the inlet air recovery temperature. The voltage produced by each thermocouple is read using an HP44422T thermocouple card installed into the same Hewlett-Packard HP 3497A data acquisition controller used to acquire the pressure measurements.

The mass flow rate, spatially-averaged velocity, and Reynolds number through the test section are determined using the measured pressure drop across an ASME standard orifice plate. This pressure drop is measured using a Validyne 3–36 Model DP15-46 1546N1S4A, S/N103378 pressure transducer with a D269-94A diaphragm. Transducer signals are processed using Celesco CD10D Carrier-Demodulators, and read and acquired using the same devices described above. Standard ASME procedures are used to determine the mass flux, $\dot{m}$, spatially average velocity, V, and Reynolds number, Re_{Dh}, through the test section. With this arrangement, data are obtained at Reynolds numbers based on hydraulic diameter Re_{Dh} of 10,000, 15,000, 20,000, and 25,000.

To determine the experimental skin friction values for the rough test walls only, the smooth wall surface shear stress must first be determined. If $\Delta P/\Delta x$ is the average pressure drop per unit length, then the surface shear stress for all four smooth channel surfaces, τ_{smooth}, is determined using the following equation

$$\tau_{\mathrm{smooth}}=\frac{1}{2}\frac{\Delta P}{\Delta x}\left(\frac{b\cdot w}{b+w}\right) \tag{3}$$

where w is the spanwise width of the test section, and b is the height of the test section. With rough top and bottom walls and smooth sidewalls, the coefficient of friction (for the rough walls only) is determined using τ_{smooth}, and the equations given by

$$b\cdot w\cdot \Delta P=2\cdot b\cdot \Delta x\cdot \tau_{\mathrm{smooth}}+2\cdot w\cdot \Delta x\cdot \tau_{\mathrm{rough}} \tag{4}$$

$$\tau_{\mathrm{rough}}=\left(\frac{b}{2}\right)\left(\frac{\Delta P}{\Delta x}\right)-\left(\frac{b}{w}\right)\tau_{\mathrm{smooth}} \tag{5}$$

and

$$C_f/2=\tau_{\mathrm{rough}}/\rho V^2 \tag{6}$$

With this approach, the $C_f/2$ values given by Eq. (6) are unaffected by the sidewalls and are representative of the rough top and bottom test surfaces only.

Correlation for Three-Dimensional, Irregular Roughness

To determine the magnitude of equivalent sand grain roughness for ''three-dimensional roughness,'' an empirical relationship is needed for the dependence of k_s/k on Λ_s. As mentioned, such ''three-dimensional'' roughness is comprised of arrangements of spheres, hemispherical elements, cones, angles, pyramids, screens, or sand grains along a surface [17]. The three-dimensional roughness correlation used here is based on data from Schlichting's roughness experiments [2], after correction by Coleman et al. [3]. This correlation is plotted in Fig. 5 and given by the following equations

$$\frac{k_s}{k}=\begin{cases}1.583\times 10^{-5}\Lambda_s^{5.683} & \Lambda_s\leqslant 7.842\\ 1.802\Lambda_s^{0.03038} & 7.842\leqslant\Lambda_s\leqslant 28.12\\ 255.5\Lambda_s^{-1.454} & 28.12\leqslant\Lambda_s\end{cases} \tag{7}$$

Note that the form of these equations is similar to the one given by Sigal and Danberg for two-dimensional roughness [17] (i.e., Eq. (2)). From Fig. 5, it is evident that the above equations provide a good match to the experimental data for several types of roughness elements, especially for $\Lambda_s>28.1$. These include spheres, spherical segments, and cones. Equation (7) also applies to the non-uniform, irregular sand-grain-type roughness investigated experimentally as part of this study.

Numerical Procedures to Determine Rough Surface Geometry Parameters

The three-dimensional contour data, which are analyzed to characterize the rough surface, are initially produced using a Wyko high-resolution optical Surface Profilometer. With this device, roughness dimensions from 0.1 nm to several millimeters, with a vertical resolution as low as 0.1 nm, are recorded for each rough surface over areas of about 3.3 mm by 4.5 mm. This provides an order of magnitude improvement over conventional rough surface stylus profilometers which usually obtain rough surface data only along single lines.

The next step in the software used to analyze these data is calculation of the parameters that determine the surface's roughness parameter Λ_s, given by Eq. (1). First, the total reference area, S, is numerically calculated using the number of data points in each direction and the spacing between these data points. Then, for a surface of *uniform roughness elements* (which are also spaced uniformly), the values of A_f and A_s are determined numerically from the profilometer data. Note that these parameters

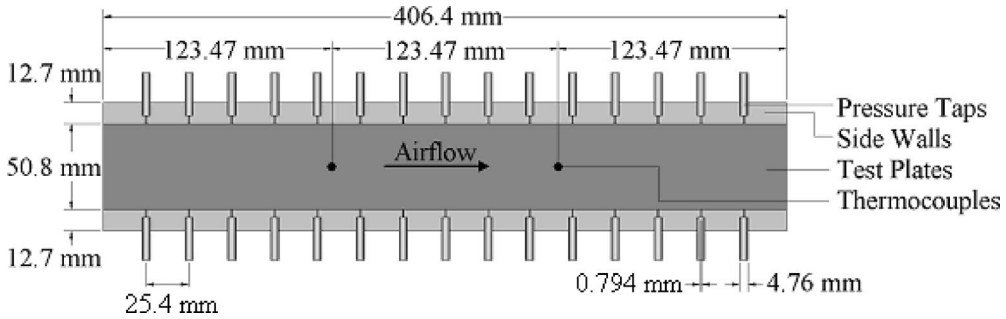

Fig. 4 Top view of the test section

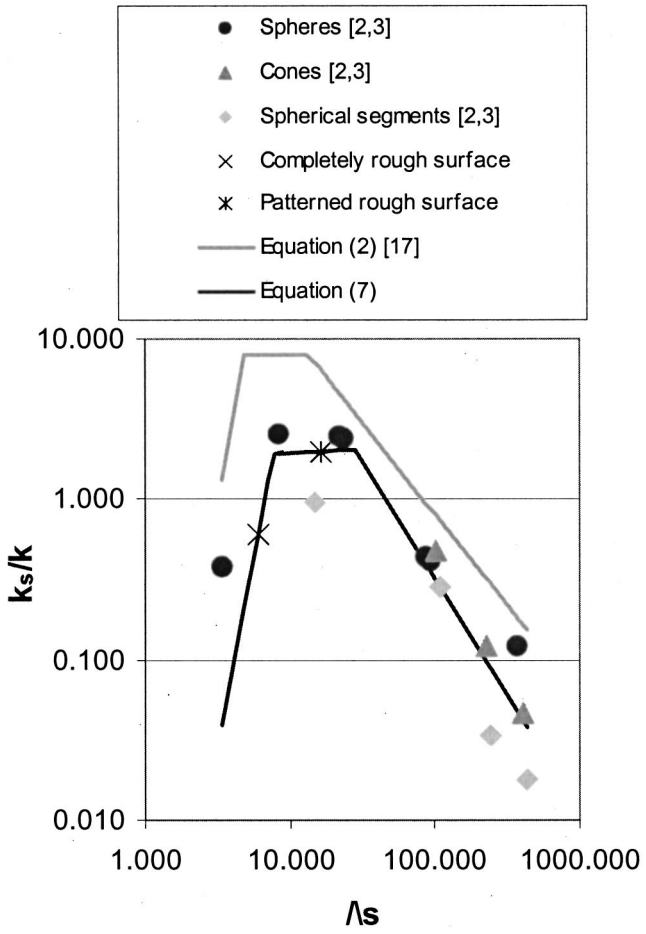

Fig. 5 Comparison of experimental results with Eq. (2), the correlation for "two-dimensional" roughness, and with Eq. (7), the correlation for "three-dimensional" roughness

can also be determined analytically because of relatively simple geometry of individual elements for this type of roughness. On a surface with *irregularly shaped and placed three-dimensional roughness elements*, the values of A_f and A_s differ from one roughness element to another. With this type of rough surface, the ratio of frontal area to windward wetted surface area of one roughness element A_f/A_s is replaced with the ratio of the total frontal area to the total windward wetted surface area for all the roughness elements on the surface, S_f/S_s, for determination of Λ_s. The roughness parameter equation given by Eq. (1) is thus modified to become

$$\Lambda_s = \left(\frac{S}{S_f}\right)\left(\frac{S_f}{S_s}\right)^{-1.6} \tag{8}$$

To calculate the total frontal area, S_f, and the total wetted surface area, S_s, the rough surface is numerically divided into finite element triangles. To calculate the total windward wetted surface area, S_s, the area of each surface triangle facing the direction of flow is summed. To calculate the total frontal area, S_f, each surface triangle facing the direction of flow is projected onto a plane perpendicular to the flow. The areas of all of these projected triangles are then summed. Because the flow can approach a roughness element from any direction, the total frontal and windward wetted surface areas are calculated in each of the four directions for each sample of rough wall data. The averages of these values are then used as the final values of S_f and S_s in Eq. (8) to determine the roughness parameter Λ_s. Eq. (7) is then employed to determine k_s/k.

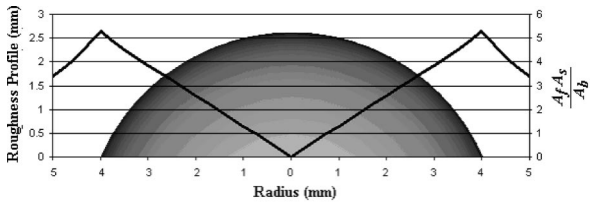

Fig. 6 Variation of roughness element area parameter, $A_f A_s/A_b$, with height of a spherical segment roughness element

To calculate the equivalent sand grain roughness size k_s, the roughness height k must be known. This k roughness height is easily determined for a surface comprised of uniformly-sized roughness elements. However, for a rough surface with irregularly sized and spaced elements, each roughness element height is different and there is no defined zero, or base value, from which to measure this height. Therefore, the surface's average roughness element height is used for k. To calculate this average roughness element height, all of the roughness elements on the surface are aligned by their maximum point and the profiles are ensemble-averaged to get an average roughness element profile. From this profile, the average roughness element height is determined.

To determine the base, or zero value, the height of the average roughness element profile is varied incrementally, starting from the highest point on the roughness element. At each height, the area parameter $A_f A_s/A_b$ is calculated, where A_b is base area of the averaged roughness element at a particular height. For a spherical segment roughness element, the variation of this area parameter with height is shown in Fig. 6. If the segment shown in this figure is a complete half sphere, then $A_f = \pi/2\,(d/2)^2$, $A_s = \pi(d/2)^2$, and $A_b = \pi(d/2)^2$, which gives $A_f A_s/A_b = \pi/2\,(d/2)^2$ at the outer edge of roughness element. From Fig. 6, it is then evident that the radius of the base area is correct when the area parameter $A_f A_s/A_b$ is maximum. This is because A_f and A_s then no longer increase as the $A_f A_s/A_b$ parameter is calculated on the flat region to the sides of the spherical segment (for distances from the center greater than 4 mm in Fig. 6).

Once the base or zero height is known, the average roughness element height k is then the difference between the maximum height and the height of this base area, both for elements like the one shown in Fig. 6, as well as for irregularly shaped elements determined from ensemble-averages.

Analytic Verification of Numerical Procedures

To provide checks on the procedures and accuracy of the numerical code used to calculate equivalent sand grain roughness magnitudes, k_s values for several of the roughness types, originally analyzed by Schlichting [2], are determined and compared to k_s magnitudes determined using analytic geometry. The surfaces considered are listed in Table 1. Figure 7 then shows the shapes,

Table 1 Schlichting's roughness dimensions and experimental results [2,3]

Surface	d μm	D μm	k μm	k' μm	k_s/k	k_s μm
Spherical Segments						
XIII	8000	40000	2600	-	0.02	46.80
XIV	8000	30000	2600	-	0.03	88.40
XV	8000	20000	2600	-	0.28	722.80
Cones						
XXIII	8000	40000	3750	4250	0.05	172.50
XXIV	8000	30000	3750	4250	0.12	457.50
XXV	8000	20000	3750	4250	0.47	1766.25

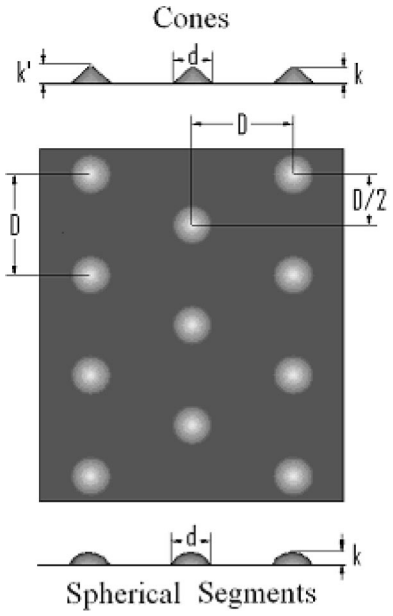

Fig. 7 Dimensions of Schlichting's roughness elements [2]. Geometric parameter values are given in Table 1.

sizes, and spacings for the two roughness shapes considered in this part of the study: cones and spherical segments. The analytic determination of k_s values from roughness geometry (with no numerical analyses) are made possible by the simplicity of the roughness element shapes shown in Fig. 7. The results of these efforts are listed in Table 2. To numerically determine magnitudes of equivalent sand grain roughness, data files (similar to ones resulting from Wyko profilometer output) are numerically generated for each roughness element listed in Table 1. The results of these numerical analyses, including k_s values, are then given in Table 3. The agreement with k_s values from Table 2 is very good, and verifies code procedures for uniformly shaped roughness elements of uniform size and spacing. Note that given in Tables 2 and 3 are magnitudes of S_f and S_s for a surface with one complete roughness element. For this situation, magnitudes of S_f and S_s are thus then the same as the magnitudes of A_f and A_s, respectively.

Note that there is no ambiguity in the determination of roughness height k for cone and spherical segment roughness. This is because the height is the same for each element for each of these types of roughness. Figure 7 shows how k is defined for the cone and spherical segment roughness elements. Notice that the tops of the cones are flat, and not pointed. The height of a cone, from the base to the imaginary point at the top, is then denoted by k'.

Experimental Results and Experimental Verification of Numerical Procedures

The experimental results for the three test surfaces (smooth, completely rough, patterned rough), at each flow condition investigated, are given in Table 4 and Fig. 8. Included in the table are static densities, average velocities, Reynolds numbers, and average streamwise pressure gradients. Figure 8 shows $C_f/2$ values which decrease with Re_{Dh} for each of the three test surfaces. At each Re_{Dh}, the smooth test plate gives the lowest $C_f/2$ values, and the patterned rough surface then gives the highest $C_f/2$ values. Notice that the smooth surface skin friction coefficients are in excellent agreement with values determined using a smooth duct correlation from Kays and Crawford [20].

To check the numerical procedures employed for equivalent sand grain roughness determination for irregular, three-dimensional roughness with nonuniform shapes and spacings, the results given in Table 4 and in Fig. 8 are compared to numerically determined values. The first step to accomplish this is *numerical* determination of k_s values for the completely rough surface and the patterned rough surface. Six Wyko profilometer samples are obtained from each of these surfaces. The results of the numerical analyses of each of these samples are given in Tables 5 and 6, along with average overall values. Numerically-averaged k_s/k magnitudes are also then plotted in Fig. 5, and show excellent agreement with the correlation for ''three-dimensional'' type roughness, given by Eq. (7).

Values of k_s from the numerical analyses are then used to determine magnitudes of roughness Reynolds numbers. Resulting values are given in Table 7 for the two rough surfaces investigated, for different Reynolds numbers based on channel hydraulic diameter. These are then employed in the Colebrook correlation for transitionally rough behavior [21] to determine skin friction coefficients. For transitionally rough flow ($5 \leqslant \mathrm{Re}_k \leqslant 70$), this equation is given by

Table 2 Analytic geometry analysis of Schlichting's [2,3] cone and spherical segment roughness

Surface	S μm^2	S_f μm^2	S_s μm^2	Λ_s	k_s/k	k_s μm
Spherical Segments						
XIII	1600000000	14976073	35751324	429.89	0.04	98.44
XIV	900000000	14976073	35751324	241.81	0.09	227.26
XV	400000000	14976073	35751324	107.47	0.28	739.01
Cones						
XXIII	1600000000	16764706	36163058	326.52	0.06	211.79
XXIV	900000000	16764706	36163058	183.67	0.13	488.95
XXV	400000000	16764706	36163058	81.631	0.42	1589.96

Table 3 Numerical analysis of Schlichting's [2,3] cone and spherical segment roughness

Surface	S μm^2	S_f μm^2	S_s μm^2	Λ_s	k_s/k	k_s μm
Spherical Segments						
XIII	1580851000	14972161	37002520	449.08	0.04	92.38
XIV	889228730	14976070	36723660	249.40	0.08	217.28
XV	395212800	14975760	36243780	108.54	0.28	728.44
Cones						
XXIII	1580851000	16766990	37782344	345.92	0.05	194.76
XXIV	889228730	16766850	37402500	191.46	0.12	460.30
XXV	395212800	16765432	36835583	83.06	0.41	1550.44

Table 4 Experimental results

Re_{Dh}	V m/s	ρ kg/m^3	$(\Delta P/\Delta x)_{avg}$ Pa/m	$C_f/2$
Smooth Surface				
10010	16.37	0.9998	372.72	0.003925
15163	24.80	0.9998	777.48	0.003568
19793	32.37	0.9998	1240.90	0.003342
25678	42.00	0.9998	2009.25	0.003215
Completely Rough Test Surface				
9950	15.98	1.0184	420.24	0.004627
15408	24.76	1.0178	933.78	0.004314
19604	31.47	1.0187	1484.49	0.004238
24935	39.93	1.0210	2346.57	0.004140
Patterned Rough Test Surface				
10032	16.17	1.0140	536.87	0.005930
15251	24.50	1.0180	1217.55	0.005888
19965	32.05	1.0190	2057.12	0.005822
25051	40.12	1.0210	3134.16	0.005624

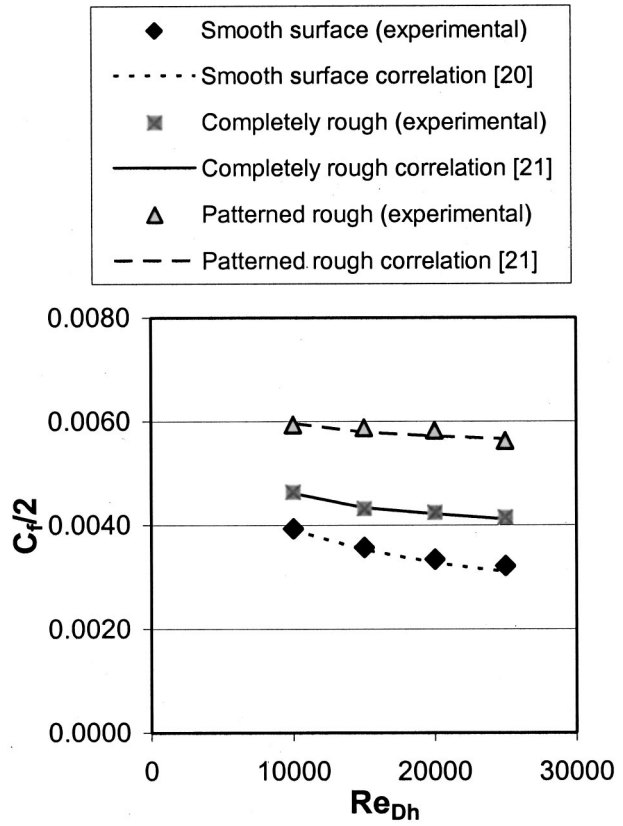

Fig. 8 Comparisons of experimentally and numerically determined skin friction coefficients

Table 5 Numerical results for completely rough surface samples

Surface	S μm^2	S_f μm^2	S_s μm^2	Λ_s	k_s/k	k μm	k_s μm
15 - 6-d-a	9773747	4699952	9656239	6.58	0.88	82.21	72.69
16 - 6-d-b	9773747	5103529	10244670	5.84	0.50	90.54	45.56
17 - 6-d-c	9773747	5325864	10555540	5.48	0.37	87.14	32.57
18 - 6-d-d	9773747	5200071	10330471	5.64	0.43	84.58	36.02
19 - 6-d-f	9773747	4608047	9488678	6.74	0.99	83.16	82.08
20 - 6-d-g	9773747	4890841	9927010	6.20	0.67	83.24	55.65
Average	9773747	4971384	10033768	6.05	0.59	85.14	50.23

Table 6 Numerical results for patterned rough surface samples

Surface	S μm^2	S_f μm^2	S_s μm^2	Λ_s	k_s/k	k μm	k_s μm
15 (2) - 6-d-a	9773747	1879981	3862496	16.45	1.98	82.21	162.84
16 (2) - 6-d-b	9773747	2041412	4097868	14.60	1.97	90.54	178.67
17 (2) - 6-d-c	9773747	2130346	4222216	13.71	1.97	87.14	171.62
18 (2) - 6-d-d	9773747	2080028	4132188	14.09	1.97	84.58	166.71
19 (2) - 6-d-f	9773747	1843219	3795471	16.84	1.98	83.16	164.82
20 (2) - 6-d-g	9773747	1956336	3970804	15.51	1.98	83.24	164.56
Average	9773747	1988554	4013507	15.12	1.98	85.14	168.20

Table 7 Experimental roughness Reynolds numbers, Re_k

Test Surface	Re_{Dh} 10000	15000	20000	25000
Completely rough	3.07	4.60	5.77	7:26
Patterned rough	11.45	17.16	22.30	27.85

Table 8 Comparison of numerical and experimental equivalent sand grain roughness sizes (μm)

Test Surface	Re_{Dh} 10000	15000	20000	25000	Average Experimental	Average Numerical
Completely rough	50.53	48.40	51.44	51.68	50.51	50.23
Patterned rough	163.64	174.82	177.21	163.82	169.87	168.2

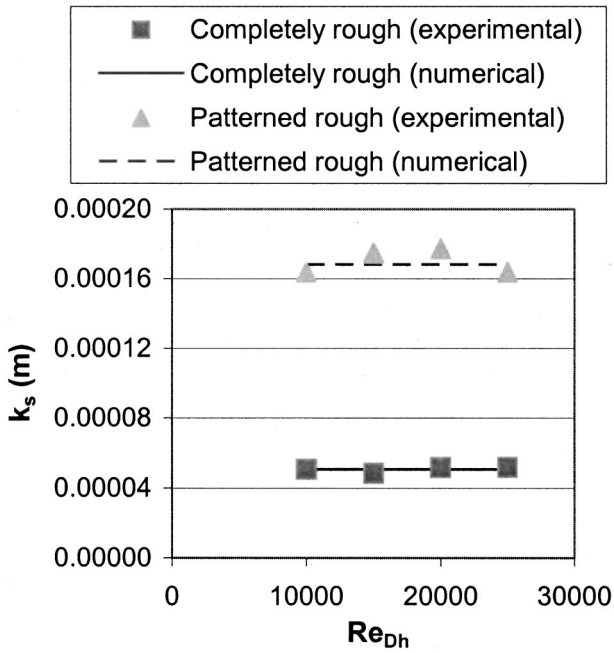

Fig. 9 Comparisons of experimentally and numerically determined k_s values

$$\frac{C_f}{2} = \left[-2.46 \ln\left(\left(\frac{k_s/D_h}{3.7} \right) + \frac{0.887}{\mathrm{Re}_{D_h}\sqrt{C_f/2}} \right) \right]^{-2} \tag{9}$$

Figure 8 shows that skin friction coefficients, determined using Eq. (9), are in excellent agreement with the experimental measurements.

From the experimental skin friction coefficients, experimentally determined equivalent sand grain roughness sizes are calculated using the skin friction equations, which depend upon Reynolds number [21]. Regardless of Re_{Dh}, the value of k_s is constant for each rough test surface. Thus, k_s values determined at each Re_{Dh} are averaged to get a final experimental k_s value for each test surface. These k_s values for each experimental flow condition and each rough test surface, as well as the numerically determined k_s values (from Tables 5 and 6), are presented and compared in Table 8 and in Fig. 9. The agreement between experimental and numerical values is excellent, which further verifies the validity of the k_s/k versus Λ_s correlation equation (7), which is also shown in Fig. 5. This agreement also validates the numerical code procedures employed for determination of equivalent sand grain roughness magnitudes for irregular, three-dimensional roughness with non-uniform arrangement and spacing.

Summary and Conclusions

A new numerical procedure is described to calculate the equivalent sand grain roughness k_s of three-dimensional rough surfaces with irregular geometry and arrangement. An analytic check of the numerical procedure and accuracy is provided by comparisons of numerically determined k_s values with analytic geometry results for several types of uniformly shaped and spaced roughness elements, originally investigated by Schlichting [2], and later analyzed further by Coleman et al. [3]. The resulting equivalent

sand grain roughness values differ by less than a few percent. Additional checks on the numerical procedures are provided by measurements made using two different surfaces with non-uniform, three-dimensional roughness with irregular geometry and arrangement. A total of three sets of test plates are tested in a two-dimensional channel, which are denoted smooth, completely rough, and patterned rough. The smooth wall surface provides baseline results. Measured in the two-dimensional channel flows are streamwise pressure gradient, and skin friction coefficients at Reynolds numbers based on hydraulic diameter Re_{Dh} of 10,000, 15,000, 20,000, and 25,000. Measured skin friction coefficients for these surfaces agree very well with existing correlations [19–21], which are based on roughness Reynolds numbers determined using k_s values calculated using the new numerical procedures. For both rough surfaces tested, the differences between these numerical equivalent sand grain roughness sizes, and values determined from the measurements is less than 1 percent for all Re_{Dh} considered.

These techniques are valuable because they enable the determination of equivalent sand grain roughness magnitudes, for such irregular roughness, entirely from roughness geometry after it is characterized using three-dimensional optical profilometry data. Determination of such roughness characteristics from roughness geometry is important because it leads to reduced design uncertainties, lower production and part costs, and increased component life in machinery which operate with moving fluids. The results are also beneficial for the analysis of different three-dimensional rough surface geometries, as well as for the development of numerical prediction models to account for the effects of roughness.

Acknowledgments

The work on the research reported in the paper began under sponsorship of a Faculty Fellowship provided by the Advanced Gas Turbine Systems Research Program of the South Carolina Institute for Energy Studies. Dr. Dan Fant was the SCIES program monitor. The later phases of the work were sponsored by General Electric Corporate Research and Development Center, and the National Science Foundation, Grant Number NSF-GOALI CTS-0086011. Dr. Kent Cueman was GE-CRD program monitor. Dr. Stefan Thynell and Dr. Richard Smith were the NSF Program monitors. Dr. Nessim Abauf is acknowledged for his valuable suggestions and discussions on the earliest portions of the research. Dr. Asher Sigal and Dr. Ron Bunker are acknowledged for several useful discussions which took place as the research was underway.

Nomenclature

A_b = roughness element base area
A_f = roughness element frontal area
A_s = roughness element windward wetted surface area
b = channel test section height
$C_f/2$ = skin friction coefficient, $\tau/\rho V^2$
d = base diameter of cone and spherical segment roughness elements
D = roughness element spacing
D_h = hydraulic diameter
k = roughness height
k' = adjusted roughness height for cones
k_s = equivalent sand grain roughness
Λ_s = Sigal and Danberg [17] roughness parameter, Eqs. (2) and (7)
ΔP = static pressure change
Re_{Dh} = hydraulic diameter Reynolds number, $V \cdot D_h / \nu$
Re_k = roughness Reynolds number, $Vk_s(C_f/2)^{1/2}/\nu$
S = rough surface flat reference area
S_f = total roughness frontal area
S_s = total roughness windward wetted surface area
Δx = incremental streamwise distance
V = spatially-averaged velocity
w = channel test section spanwise width
ν = kinematic viscosity
τ = surface shear stress
ρ = static density

Subscripts

avg = average value
rough = rough wall value
smooth = smooth wall value

References

[1] Nikuradse, J., 1933, ''Laws of Flow in Rough Pipes,'' NACA TM 1292, National Advisory Committee on Aeronautics.
[2] Schlichting, H., 1936, ''Experimental Investigation of the Problem of Surface Roughness,'' NACA TM-832, National Advisory Committee on Aeronautics.
[3] Coleman, H. W., Hodge, B. K., and Taylor, R. P., 1984, ''A Re-Evaluation of Schlichting's Surface Roughness Experiment,'' ASME J. Fluids Eng., **106**, pp. 60–65.
[4] Antonia, R. A., and Luxton, R. E., 1971, ''The Response of a Turbulent Boundary Layer to a Step Change in Surface Roughness, Pt. 1. Smooth to Rough,'' J. Fluid Mech., **48**, Part 4, pp. 721–762.
[5] Antonia, R. A., and Wood, D. H., 1975, ''Calculation of a Turbulent Boundary Layer Downstream of a Step Change in Surface Roughness,'' Aeronaut. Q., **26**, Part 3, pp. 202–210.
[6] Bettermann, D., 1966, ''Contribution a l'Etude de la Convection Force Turbulente le Long de Plaques Rugueuses,'' Int. J. Heat Mass Transf., **9**, pp. 153–164.
[7] Perry, A. E., and Joubert, P. N., 1963, ''Rough-Wall Boundary Layers an Adverse Pressure Gradients,'' J. Fluid Mech., **17**, Part 2, pp. 193–211.
[8] Pineau, F., Nguyen, V. D., Dickinson, J., and Belanger, J., 1987, ''Study of a Flow Over a Rough Surface with Passive Boundary-Layer Manipulators and Direct Wall Drag Measurements,'' AIAA Paper 87-0357, American Institute of Aeronautics and Astronautics.
[9] Han, J. C., Glickman, L. R., and Rohsenow, W. M., 1978, ''An Investigation of Heat Transfer and Friction for Rib-Roughened Surfaces,'' Int. J. Heat Mass Transf., **21**, pp. 1143–1156.
[10] Furuya, Y., Fujita, H., and Nakashima, H., 1987, ''Turbulent Boundary Layers on Plates Roughened by Wires in Equal Intervals,'' Perspectives in Turbulence Studies, pp. 223–249.
[11] Sherif, N., and Gumley, P., 1966, ''Heat-Transfer and Friction Properties of Surfaces with Discrete Roughnesses,'' Int. J. Heat Mass Transf., **9**, pp. 1297–1320.
[12] Pimenta, M. M., Moffat, R. J., and Kays, W. M., 1978, ''The Structure of a Boundary Layer on a Rough Wall With Blowing and Heat Transfer,'' ASME Paper No. 78-HT-3, AIAA-ASME Thermophysics and Heat Transfer Conference, Palo Alto.
[13] Coleman, H. W., Moffat, R. J., and Kays, W. M., 1977, ''The Accelerated Fully Rough Turbulent Boundary Layer,'' J. Fluid Mech., **82**, Part 3, pp. 507–528.
[14] Ligrani, P. M., and Moffat, R. J., 1986, ''Structure of Transitionally Rough and Fully Rough Turbulent Boundary Layers,'' J. Fluid Mech., **162**, pp. 69–98.
[15] Bogard, D. G., Schmidt, D. L., and Tabbita, M., 1998, ''Characterization and Laboratory Simulation of Turbine Airfoil Surface Roughness and Associated Heat Transfer,'' ASME J. Turbomach., **120**(2), pp. 337–342.
[16] Abuaf, N., Bunker, R. S., and Lee, C. P., 1998, ''Effects of Surface Roughness on Heat Transfer and Aerodynamic Performance of Turbine Airfoils,'' ASME J. Turbomach., **120**(3), pp. 522–529.
[17] Sigal, A., and Danberg, J. E., 1990, ''New Correlation of Roughness Density Effect on the Turbulent Boundary Layer,'' AIAA J., **28**, No. 3, pp. 554–556.
[18] Sigal, A., and Danberg, J. E., 1988, ''Analysis of Turbulent Boundary Layer Over Rough Surfaces With Application to Projectile Aerodynamics,'' Army Ballistic Research Lab, Aberdeen Proving Grounds MD, Technical Report BRL-TR-2977.
[19] Schlichting, H., 1991, *Boundary Layer Theory*, Seventh Edition, McGraw-Hill, New York.
[20] Kays, W. M., and Crawford, M. E., 1993, *Convective Heat and Mass Transfer*, Third Edition, McGraw-Hill, New York.
[21] Colebrook, C. F., 1938-1939, ''Turbulent Flow in Pipes, With Particular Reference to the Transition Between the Smooth and Rough Pipe Laws,'' J. Inst. Civil Engineers, London, **11**, pp. 133–156.

Inception of Turbulence in the Stokes Boundary Layer Over a Transpiring Wall

Joseph Majdalani
e-mail: maji@mu.edu
Assistant Professor,
Department of Mechanical and Industrial Engineering,
Marquette University,
Milwaukee, WI 53233

James Barron
Mechanical/Electrical Engineering Department Manager,
Lockwood, Andrews & Newnam, Inc.,
Dallas, TX 75219

William K. Van Moorhem
Professor,
Department of Mechanical Engineering,
University of Utah,
Salt Lake City, UT 84112

In this work, the onset of turbulence inside a rectangular chamber is investigated, with and without side-wall injection, in the presence of an oscillatory pressure gradient. Two techniques are used to define the transition from laminar to turbulent regimes: statistical analysis and flow visualization. Calibrated hot film anemometry and a computer data acquisition system are used to record and analyze acoustical flow data. Four classifications of flow regimes are reported: (a) laminar, (b) distorted laminar, (c) weakly turbulent, and (d) conditionally turbulent. Despite numerous attempts to promote turbulence, a fully turbulent flow does not develop at any of the driving frequencies tested. Statistical measurements reveal that a periodic drop in standard deviation of axial velocity fluctuations always occurs, indicating relaminarization within each cycle. Transition between flow regimes is assessed from the standard deviation of velocity data correlated as a function of the acoustic Reynolds number Re_A. *Under predominantly laminar conditions, the standard deviation is found to vary approximately with the square of the acoustic Reynolds number. Under turbulent conditions, the standard deviation becomes almost directly proportional to the acoustic Reynolds number. Inception of turbulence in the oscillatory flow with side-wall injection is found to be reproducible at the same critical value of* $Re_A \cong 200$. [DOI: 10.1115/1.1490375]

1 Introduction

In a solid rocket motor, it is both difficult and expensive to investigate the dynamic gas behavior associated with unsteady propellant burning. It is a well known fact that the presence of acoustic oscillations can affect the burning rate of known propellants, leading sometimes to undesirable combustion instabilities. In the current study, a cold-flow facility that employs solid carbon dioxide (dry ice) is constructed for the purpose of simulating the response of a solid propellant. The current research includes modifying an existing simulation facility to improve small experimental deficiencies reported previously. In addition, the work involves quantifying the occurrence of acoustically introduced turbulence and investigating flow phenomena that may exacerbate the onset of acoustic instabilities.

A variety of problems involving turbulent oscillatory flows are frequently encountered in the applied fields of acoustics and fluid mechanics. One emerging topic is closely tied to acoustic instability in solid rocket motors. In recent years, it has become accepted that an acoustic boundary layer or ''Stokes layer'' can stem from the oscillatory wave motion over a solid boundary [1,2]. In fact, the instability of such oscillatory layers has been examined by several researchers in both circular-port and rectangular channels [3–12]. However, most previous experiments have concentrated on the study of transitional Stokes layers over nontranspiring surfaces. At present, we hope to extend those studies by incorporating the effects of gas addition at the walls.

2 Basic Ideas

For nonporous solid boundaries, the thickness of the oscillatory Stokes layer δ is found to be of the order of $\sqrt{2\nu/\omega}$ (where ν and ω are the kinematic viscosity and circular frequency, respectively). Under such physical settings, early investigators have noted that the onset of turbulence is governed by the Reynolds number based on the thickness of the boundary layer, $\mathrm{Re}_\delta = \delta U_0/\nu$. This similarity parameter has also been termed ''the acoustic Reynolds number'' when written in the form

$$\mathrm{Re}_A = \sqrt{\pi}\,\mathrm{Re}_\delta = U_0/\sqrt{f\nu}. \tag{1}$$

In Eq. (1), U_0 is the amplitude of the oscillatory axial velocity component and $f=(2\pi\omega)$ is the frequency of oscillations.

Both experimental and theoretical analyses rise to a new level of difficulty when the boundaries surrounding the flow are made porous. This becomes necessary when analyzing the burning response of propellants modeled as transpiring surfaces. Imposition of a normal influx along the porous walls introduces an additional complexity that must be dealt with. In fact, the incoming mean flow interaction with the internal chamber acoustics can alter the flow considerably. From a physical standpoint, all parameters needed to characterize periodic flows remain valid here. The additional parameter of importance is the injection speed at the wall. On that account, the problem of predicting turbulence is expected to depend on the injection Reynolds number (based on the Stokes layer thickness and the injection velocity of the fluid). Investigations that correlate the turbulent character to the injection Reynolds number are hence necessary to help establish a clearer assessment of the flow stability criteria.

At the time of this writing, the oscillatory flow bounded by transpiring walls has been achieved experimentally by Traineau et al. [13], Ma et al. [14,15], Huesmann and Eckert [16], and Dunlap et al. [17–19]. Whereas Traineau and Ma have selected rectangular port chambers, Huesmann and Dunlap have employed circular-port tubes. Except for Ma's experiment, a pressurized gas injection was accomplished by forcing either air or nitrogen through sintered copper, aluminum or bronze plates. In all three experiments, the use of finely porous metal sheets was used to ensure both uniformity and homogeneity of mass addition.

In the current study, a different experimental technique is used to produce the desired mass addition. In fact, the sublimation of solid CO_2 is chosen over previously used simulation techniques for several reasons. Although weaker, the dynamic behavior of solid CO_2 is analogous to the behavior of an actual propellant. In a rocket motor, increasing the pressure results in an increase in the propellant burning rate and, as such, in the mass influx. Similarly,

Contributed by the Fluids Engineering Division for publication in the JOURNAL OF FLUIDS ENGINEERING. Manuscript received by the Fluids Engineering Division February 1, 2001; revised manuscript received February 21, 2002. Associate Editor: A. Prasad.

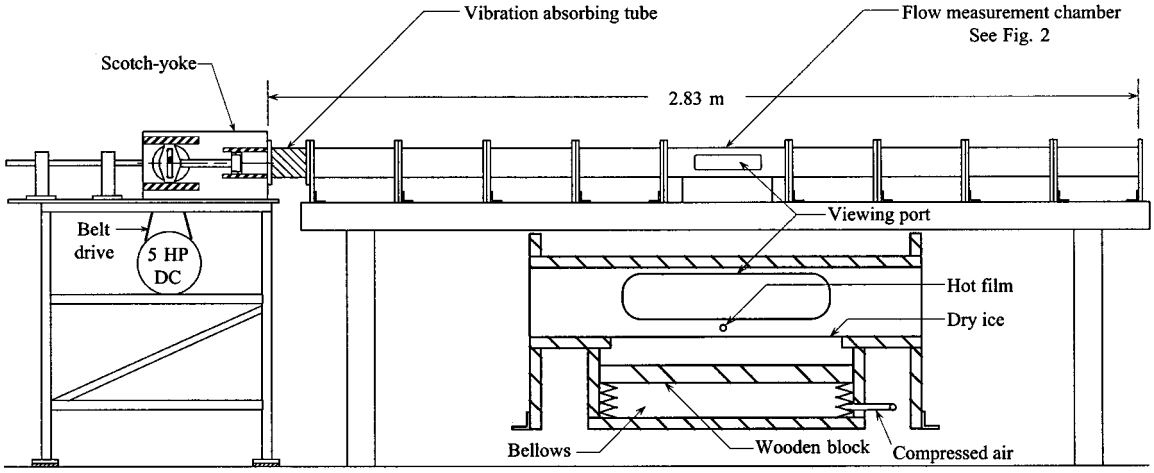

Fig. 1 Experimental apparatus. The inset shows a section view of the principal test chamber.

an increase in the pressure over the solid CO_2 results in an increase in the sublimation rate and, therefore, mass flow from the surface. This increase is due to the drop in heat of sublimation with increasing pressure. To the authors' knowledge, all other cold-flow facilities have simulated the combustion process by injecting a gas through porous walls. Under such circumstances, the pores must be choked to prevent acoustic energy from being lost into the walls. An increase in pressure above the porous walls results in either (a) unchoking of the pores and mass flow reduction or (b) a constant mass flow rate if the pores remain choked. These mechanisms may fail to capture some of the dynamic features associated with propellant burning. An even more serious problem is the possibility that the injection itself causes turbulence. The use of solid CO_2 eliminates the question of choking or unchoking at the pores and makes it ideally suited for simulating the behavior of a solid rocket motor propellant. In both an actual solid propellant rocket motor (SPRM) and a cold-flow simulation facility, the characteristic injection Reynolds number Re_i may be expressed in terms of the injection velocity (or injection Mach number M), kinematic viscosity, and frequency of the acoustic disturbance. Based on Eq. (1), the resulting expression takes the form $Re_i = \alpha M/\sqrt{f}$ where $\alpha = 3.27 \times 10^5$ $s^{-1/2}$ is a typical value for SPRMs [14,15]. In our simulation facility, we find $\alpha = 1.18 \times 10^5$ $s^{-1/2}$ to provide a comparable response. Moreover, when compared with the average injection Mach number of $M = 3 \times 10^{-3}$ reported in SPRMs, the value of $M = 2.4 \times 10^{-4}$ that we have achieved with commercial dry ice seems reasonable.

In addition to the novelty in effecting the gas evaporation from the walls, another advantage of this study is the careful selection of a Scotch-yoke wave generator that can produce purer harmonic waves than the rotary butterfly or slider-crank mechanisms used previously. Furthermore, unlike most previous experiments, the main focus of this experiment will be to characterize the flow regimes that arise prior to and during transition to turbulence in the presence of wall transpiration.

3 Experimental Apparatus

The SPRM simulation facility is a cold flow (nonreactive) facility in which solid carbon dioxide plays the role of the injectant. The use of solid carbon dioxide (CO_2 or dry ice) as the simulated propellant makes it possible to focus on the fluid mechanical aspects of the acoustic instability problem by separating the fluid mechanics from the combustion dynamics at the propellant surface. The SPRM facility used in our experiments is shown in Fig. 1. The flow chamber has a square cross section with an inside dimension of 7.62 by 7.62 centimeters. The flow chamber consists of eight interchangeable sections, a test section used for flow measurement, and a vibration isolating tube. The entire flow chamber is bolted to a granite table to minimize vibration. The interchangeable sections make it possible to vary the test section location, chamber length and system resonant frequency. For these experiments, the length is held constant at 2.83 meters corresponding to a resonant frequency of 49 Hz at a temperature of 27°C. For all experiments, the chamber is initially purged with room temperature CO_2 to remove the air. The CO_2 gas enters at one end of the flow chamber and exits the chamber at the opposite end through a small orifice. The orifice is closed with a valve prior to operating the wave generator.

The principal part of the flow chamber is a 43.2 cm long test section (see Fig. 2). The test section is placed near the center of the chamber where the acoustic velocity antinode (maximum velocity) occurs and a pressure node (pressure minimum) occurs for a standing wave. The inset in Fig. 1 shows a section view of the test section. The solid CO_2 employed in this experiment is a commercial dry ice block approximately 30 cm long, 5 cm deep, and 7.62 cm wide. Thus it can be seated snugly at the bottom of the test section. The dry ice rests on a wooden block and a bellows is used to maintain the top of the dry ice at the same level as the bottom of the test section. The bellows pushes the flat dry ice block with a constant supply air pressure of 3 psig. The bellows supply pressure is sufficiently large to eliminate appreciable vibrations of the dry ice block due to acoustic pressure oscillations. The dry ice can also be replaced by a fitted aluminum plate that makes the investigation of the flow field without side-wall injection possible. A glass view port is located on either side of the test section. As shown in Fig. 2, visual flow monitoring is facilitated through a glass view port. The axial velocity of the gas near the surface of

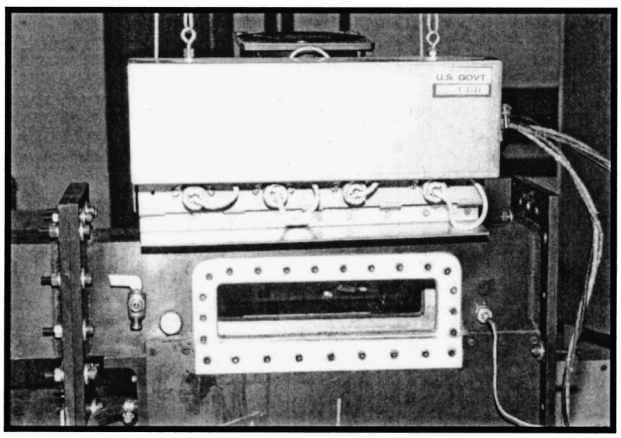

Fig. 2 Flow measurement chamber

the dry ice can be measured via hot film anemometry. A high frequency response hot film anemometer is mounted in the test section in order to measure local velocities. The hot film probe is typically centered above the dry ice and is mounted perpendicularly to, and approximately 0.8 cm above, the surface of the dry ice. This location is recommended by previous investigators who conducted oscillatory-flow experiments over nontranspiring surfaces [7–10]. These former studies have indicated that turbulence could diffuse into the entire flowfield once transition occurred. In our study, it is expected for turbulence to also convect into the entire field as a direct consequence of injection. Placing the probe inside the boundary layer region [20] is intended to more accurately capture the turbularization of the resulting acoustic boundary layer.

It should be noted that the vertical location of the probe is chosen to coincide with the point above the porous surface where the coupling between vorticity and acoustic waves is maximal. At that point the pairing of the waves leads to an overshoot in the total oscillatory velocity that ranges between 1.4–1.6 times the acoustic wave amplitude in the outer field—away from the walls. The axial location of the probe is also taken at the chamber midpoint where an acoustic velocity antinode is formed. As a result, the acoustic velocity amplitude that we measure is the largest that can be detected anywhere in the chamber. The proximity of the probe to the wall has thus enabled us to capture the total magnification in the fluctuating amplitude known as Richardson's overshoot [21]. This is due to the favorable pairing, near the porous wall, of pressure-driven and boundary-driven waves. Since the velocities measured are, in principle, the largest in the system, it seems unlikely for the flow to be turbulent when the Reynolds number based on the measured velocities indicates laminar conditions. To ensure that there are no spots where the oscillatory velocity exceeds the measured values, the probe was initially moved around until an ideal location was found at which the velocity was largest. This confirmed the theoretical speculation justifying its location based on acoustic theory.

In addition to the unsteady velocity, pressure oscillations in the flow chamber have also been measured. To that end, a pressure transducer was mounted at various locations in the chamber to record the pressure oscillations. In our experiments, the pressure transducer was located at the end of the flow chamber counterfacing the wave generator where maximum pressure is observed.

The sublimation of solid CO_2 was chosen over previously used simulation techniques for reasons stated earlier. Several modifications were implemented as improvements to the experiments done by others. For example, an experimental difficulty in Ma's [14,15] experiments was that a slider-crank mechanism (with a crankshaft, connecting rod and piston) was used to generate the acoustic environment. The slider-crank motion complicated the flow data by adding undesirable harmonics. As a remedy, a Scotch-yoke mechanism was designed and constructed to provide a purer sinusoidal piston motion. The Scotch-yoke piston motion provided acoustic flow data that was not complicated by additional harmonics (see the comparison presented in Fig. 3 for typical signals derived from either Scotch-yoke or slider-crank wave generators). This facilitated the development and implementation of a meaningful method for performing statistical analysis and reduced the likelihood of noise interference.

Another advantage of the current wave generator is that, when compared with former devices, the larger displacement volume of the Scotch yoke produces larger acoustic pressure amplitudes. Since the heat of sublimation for dry ice diminishes at higher pressures, increasing the pressure amplitude increases the rate of sublimation. The enhanced pressure-sensitivity of dry-ice improves the model's ability to mimic a propellant's pressure response. Unlike Ma's model [14,15], the enhanced pressure sensitivity obviates the need to use infrared heating lamps to speed up the sublimation process. The absence of an infrared lamp is also beneficial in improving the accuracy of required measurements.

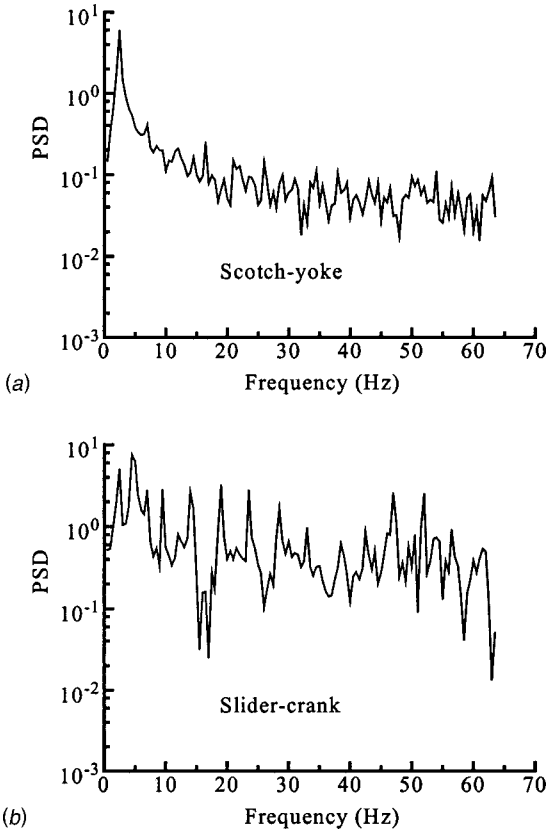

Fig. 3 Power Spectral Density (PSD) of pressure data using (*a*) Scotch-yoke and (*b*) slider-crank mechanisms. By comparison, the Scotch yoke provides a purer signal containing less harmonics and noise interference.

Here, they cannot be biased by heat interference with signals gathered from the hot films. In fact, both pressure and velocity data acquired in the experiments are Fourier analyzed to verify the reliability of the driving mechanism.

Two oscillatory flow conditions are investigated in our rectangular test section after purging it with CO_2 gas. The two conditions are: (1) oscillatory flow with side-wall injection and (2) oscillatory flow without side-wall injection. Experiments with side-wall injection are performed for driving frequencies between 2.2 and 50.8 Hz. These result in an acoustic Reynolds number (Re_A) ranging between 80 and 2200. Experiments without side-wall injection are performed for driving frequencies between 2.3 and 44.8 Hz, and $50 < Re_A < 500$. In each of these studies, four types of flow regimes are observed: laminar, distorted laminar, weakly turbulent, and conditionally turbulent.

4 Transition to Turbulence

Two different methods are utilized to predict the occurrence of turbulence: statistical analysis of acoustic flow data and flow visualization. The statistical analysis of acoustic data provides a systematic method of quantifying the occurrence of turbulence.

In order to perform a statistical analysis of the data, between 10 and 15 data sets are collected at each piston driving frequency. Each data set consists of 512 data points that are collected during a time period of approximately two driving piston cycles. Since the piston frequency ranges between 2.2 and 50.8 Hz, the sampling frequency has been varied between 512 and 10,240 Hz. Each of the 10 to 15 data sets at a given piston driving frequency is started at the same point in the mechanical driving cycle. The data sets are superimposed and the mean and standard deviation

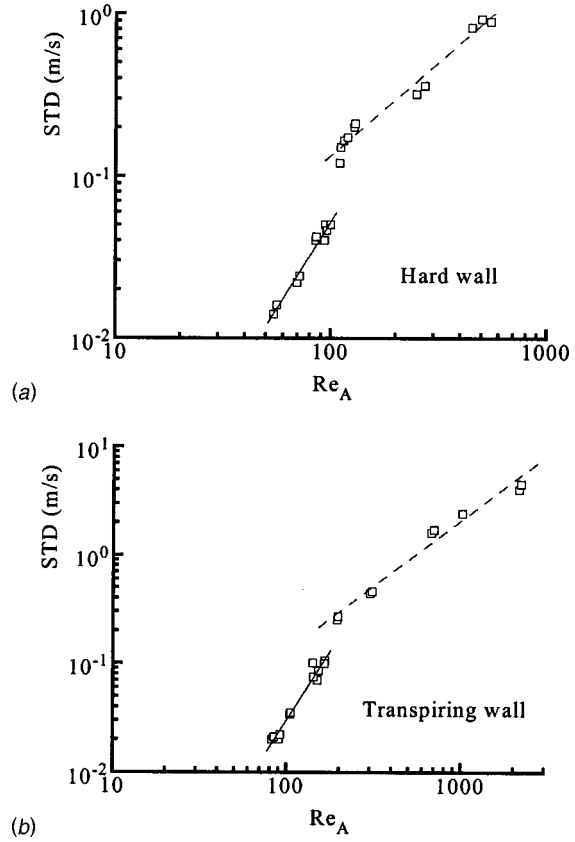

Fig. 4 Standard deviation σ versus acoustic Reynolds number Re_A for experimental data (□) acquired over (*a*) hard walls, and (*b*) transpiring walls. Assuming a logarithmic power law ($\sigma \sim Re_A^b$), linear least-squares indicate the presence of two regions. The first is characterized by $b \cong 2.2$ and is predominantly laminar (——). In the second region, *b* drops to approximately 1.1, ushering a turbulent flow behavior (— — —).

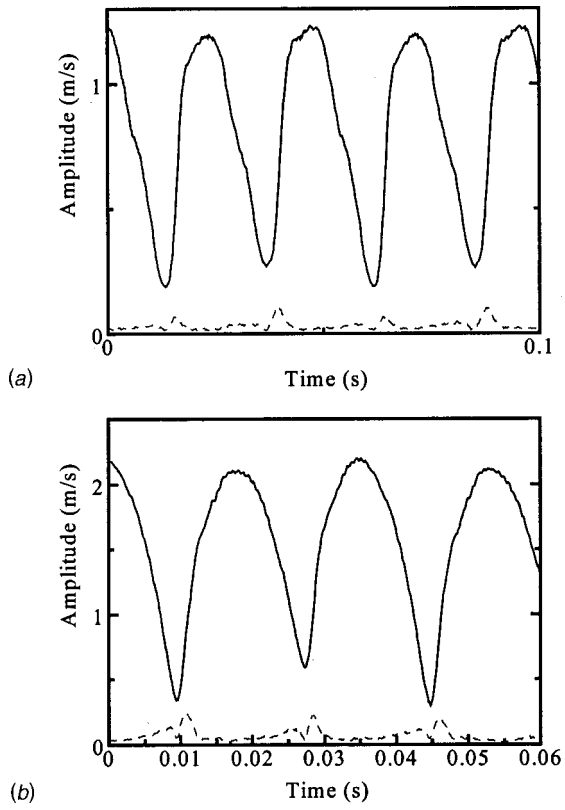

Fig. 5 Using nontranspiring walls, velocity (——) and standard deviations (— — —) are shown for $Re_A = 95$ and 130. The two cases correspond to (*a*) laminar, and (*b*) distorted laminar flow regimes.

are determined as a function of time. The maximum standard deviation over the sampling time is also determined.

Calibration of the hot film anemometer is carefully achieved. The sensing elements are delicate mechanically and analog output signals have a tendency to drift. Hence, frequent checks of probe calibration have been regularly performed to ensure consistency in measurements. Hot film anemometers are quite repeatable so accuracy is a function of how closely the calibration conditions are being reproduced in the flow to be measured. For this reason, calibration is performed before each data set is acquired after purging the entire chamber with carbon dioxide. A flow generator with a plenum chamber and an ASME nozzle are used to get a known gas velocity for calibration. The nozzle exit velocity is determined from Bernoulli's equation. An assumption that the static pressure of the gas exiting the nozzle is equal to the outside atmospheric pressure is used. A calibration relationship is determined between known velocity and bridge voltage with the hot film probe located at the nozzle exit. The relationship is nonlinear (approximately a 1/4 power relation).

4.1 Statistical Analysis

4.1.1 Hard Wall. The maximum standard deviation as a function of acoustic Reynolds number is shown in Fig. 4. For experiments without side-wall injection and $Re_A < 110$, Fig. 4(*a*) indicates that the flow is laminar. The reason is this. An almost linear power law relationship appears to exist between the standard deviation and the Reynolds number. This relationship is of the form $\sigma = a\, Re_A^b$, where σ is the standard deviation and *a* and *b* are constants. The power law exponent found from least-squares indicates that the standard deviation varies approximately with the square of the acoustic Reynolds number for the laminar case. The standard deviation of the laminar flow is very small (approximately 4% of the maximum velocity amplitude). This is clearly illustrated in Fig. 5 for two typical signals recorded at frequencies of 21 and 36.4 Hz. It should be noted that, in assessing the level of turbulence, the standard deviations near velocity nodes are filtered out. This is done to block out the relatively large standard deviations that are brought about by insignificant fluctuations in the correspondingly near-zero velocity amplitudes.

In our study, distorted laminar flow is observed for $110 < Re_A < 275$. The largest standard deviations seem to occur in the accelerating and decelerating phases in this regime. The standard deviation for distorted laminar flow is slightly larger than for laminar flow. In fact, a weakly turbulent flow is realized at $Re_A = 275$. The standard deviations are larger than those for the laminar or distorted laminar cases and the maximum standard deviation occurs at the velocity peaks. A slightly smaller standard deviation is observed in the accelerating phase where turbulence is generated. During the decelerating phase of the same cycle, a sudden drop in standard deviation is noted. This observation indicates that the flow returns to laminar during part of the cycle. The largest standard deviation without side-wall injection occurs in the $Re_A = 500$ case in which conditionally turbulent flow is achieved. During each cycle, the maximum standard deviation occurs in the decelerating phase where turbulence is generated. In the conditionally turbulent regime, turbulent bursts occur just after the velocity peaks in the decelerating phase. These turbulent bursts are identified by a large standard deviation that appears suddenly, persists for a short time, and then decreases rapidly as the flow returns to laminar. As seen in Fig. 4(*a*) the power law coefficient *b* relating σ to Re_A drops to near unity in the region corresponding to $Re_A > 110$. In that range, repeated experiments seem to indicate

that the standard deviation becomes of the order of the acoustic Reynolds number as large amplitude turbulence begins to grow.

4.1.2 Transpiring Wall. Maximum standard deviation as a function of the acoustic Reynolds number is shown in Fig. 4(*b*) for experiments with side-wall injection. For $Re_A < 140$ the flow is laminar. An almost linear power law relationship also appears to exist between the standard deviation and the acoustic Reynolds number for the side-wall injection case. The power law exponent is approximately 2.2 for the laminar case. The standard deviation of the laminar flow is very small (approximately 4% of the maximum velocity amplitude). Distorted laminar flow is observed for $140 < Re_A < 200$. The largest standard deviations occur in the accelerating and decelerating phases. The standard deviation for distorted laminar flow is slightly larger than for laminar flow. Weakly turbulent flow is observed for $200 < Re_A < 680$. The maximum standard deviation in this regime occurs at the velocity peaks and a slightly smaller standard deviation is observed in the accelerating phase where turbulence is generated. The standard deviation becomes small during the decelerating phase when relaminarization occurs. Conditionally turbulent flow is observed for $680 < Re_A < 2200$. In this regime, the maximum standard deviation occurs in the decelerating phase where turbulence is produced. In the conditionally turbulent regime, turbulent bursts occur just after the velocity peaks in the decelerating phase. These turbulent bursts are identified by a large standard deviation that appears suddenly, persists for a short time, and then decreases rapidly as the flow returns to laminar. At $Re_A = 2200$, the flow is turbulent during most of the cycle; however, fully turbulent flow is not observed in any of the experiments. In every case, flow is either laminar or relaminarization is seen to occur during a part of the oscillatory cycle. This happens when the periodic amplitude drops below some threshold value. As seen in Fig. 4(*b*) the power law exponent b relating σ to Re_A decreases to about 1.1 in the region corresponding to $Re_A > 200$. In that region, turbulence begins to dominate during a cycle. Typical signals that illustrate the relative size of the standard deviation in each of the four flow categories are shown in Fig. 6. Note that, in Fig. 6(*d*), a subharmonic presence begins to appear in the mean velocity signal at $Re_A = 2200$. Thus as turbulence is approached, fractional, as well as integer multiples of the resonant frequency are triggered in the chamber. This effect is accompanied by turbulent bursts and a broad spectral behavior. In addition to being based on relative magnitudes of standard deviations, our flow classification is substantiated by standard flow visualization. This qualitative assessment tool is described next.

4.2 Flow Visualization. Flow visualization is employed to examine the flow patterns arising in experiments with dry ice in the test section. In fact, under steady state operating conditions, a fog-like layer can be observed above the dry ice. The presence of the fog layer is caused by the water (approximately 1% by weight) that is used to bind the dry ice together during manufacturing. The behavior of the ''fog'' in the flow chamber has been useful both in visualizing the oscillatory Stokes layer, and in qualitatively determining the critical Reynolds number at which transition to turbulence occurs. The flow is considered turbulent when the flow field exhibits high intensity mixing and solid CO_2 particles leave the dry ice surface due to local high intensity instability. Evidently, flow visualization alone is the least conclusive method of detecting turbulence since the analysis is qualitative and the results are somewhat subjective. However, when coupled with statistical measures, it can prove to be quite insightful.

Figure 7 illustrates the general structure of the fog layer during the transitional stages leading to turbulence. The fog layer appears to be uniform across the test section for driving frequencies less than 30 Hz ($Re_A < 200$). The flow also appears to be stable with no indication of mixing (Fig. 7(*a*)). At approximately 30 Hz ($Re_A = 200$), solid CO_2 particles are observed to leave the dry ice surface due to local high intensity instability (Fig. 7(*b*)). For driv-

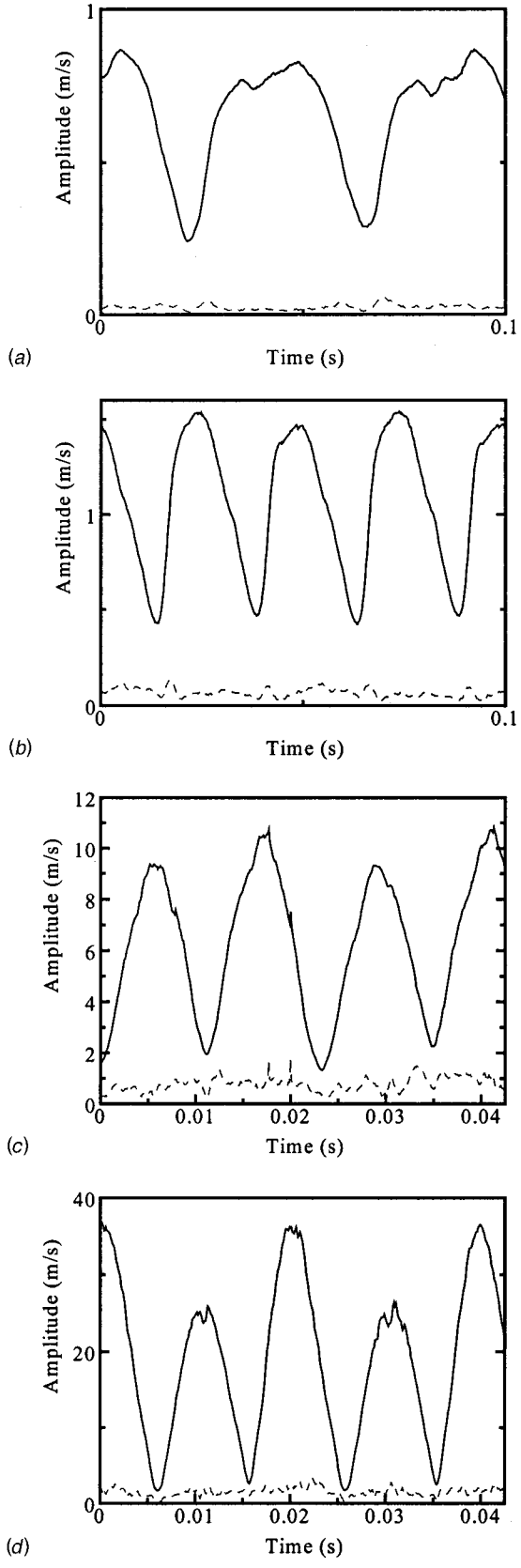

Fig. 6 Using transpiring walls, velocity (——) and standard deviations (— — —) are shown for $Re_A = 105$, 145, 675 and 2200. The four cases correspond to (*a*) laminar, (*b*) distorted laminar, (*c*) weakly turbulent, and (*d*) conditionally turbulent regimes.

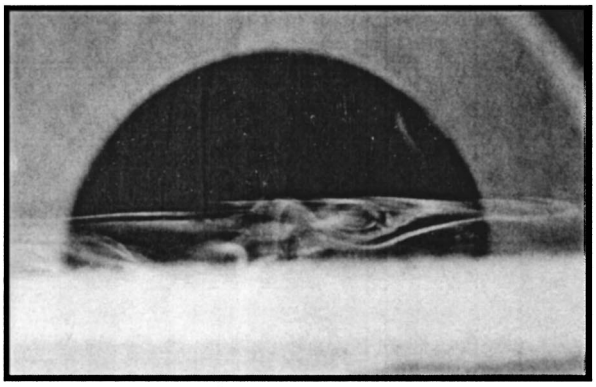

(*a*) **laminar fog layer**

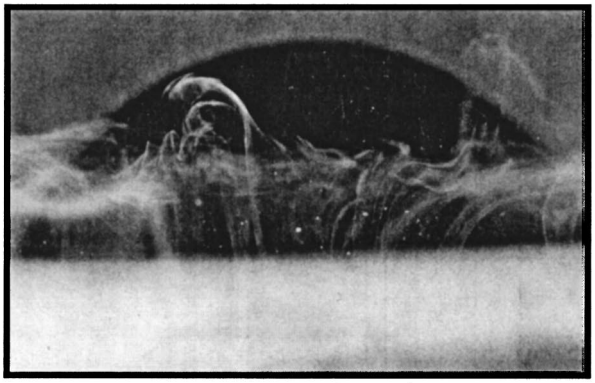

(*b*) **distorted laminar**

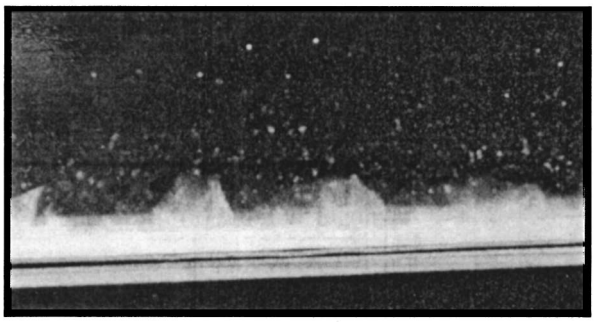

(*c*) **weakly turbulent**

Fig. 7 Flow visualization of the oscillatory Stokes layer over a transpiring surface. The close-ups illustrate the detailed structure of the fog layer in (*a*) laminar, (*b*) distorted laminar, and (*c*) weakly turbulent flow regimes.

ing frequencies above 30 Hz, the two-dimensional wave propagation is no longer present. The fog layer motion is chaotic and three-dimensional. We conclude that, at driving frequencies greater than 30 Hz, turbulence begins to grow. As the driving frequency is varied from 30 Hz to 42 Hz ($200<\mathrm{Re}_A<680$), the number of particles ejected from the dry ice surface into the flow field increases and mixing becomes more vigorous as the driving frequency is augmented (Fig. 7(*c*)). For flow above approximately a 42 Hz driving frequency ($\mathrm{Re}_A=680$), the fog is no longer visible due to intense mixing. From flow visualization, the critical frequency for transition to turbulence is approximately 30 Hz. This value is in good agreement with the statistical analysis of the hot film data. In fact, weakly turbulent flow is first seen at 30.4 Hz ($\mathrm{Re}_A=200$) using statistical analysis. These results are summarized in Fig. 8 where the four distinct patterns of flow are illustrated. Due to the preponderance of Reynolds number ranges, Table 1 is provided to summarize our findings. It should be noted that the dark semi-circular shapes in Figs. 7(*a-b*) are due to a black mask that was placed in the background to improve photographic quality. In Figs. 7(*a-b*), the photographic resolution is such that the mask is visible. In Fig. 7(*c*), however, the resolution is increased, thus placing the mask border outside the field-of-view. In Fig. 8, the black mask is no longer needed as the camera is moved out.

Table 1 Summary of experimental observations over different ranges of the acoustic Reynolds number. Results include conclusions from statistical analysis and flow visualization of the Stokes layer over both hard and transpiring walls.

Range of Re_A	Classification of flow regime	Power law exponent	CO_2 present	Flow observed
Oscillatory flow over transpiring walls				
< 140	Laminar	2.2	Yes	A uniform fog layer is visible
140-200	Distorted laminar	1.1	Yes	Particles are seen leaving the dry ice surface
200-680	Weakly turbulent	1.1	Yes	Vigorous mixing and intense particle ejection
680-2200	Conditionally turbulent	1.1	Yes	The fog layer is no longer visible
Oscillatory flow over hard walls				
< 110	Laminar	2.1	No	Invisible air
110-275	Distorted laminar	1.1	No	Invisible air
275-390	Weakly turbulent	1.1	No	Invisible air
390-500	Conditionally turbulent	1.1	No	Invisible air

5 Conclusions

In the current investigation, several experimental deficiencies of previous studies have been addressed. An apparatus that incorporates a nearly pure harmonic wave generator has been successfully constructed and utilized. Substituting the typical slider-crank mechanism by a Scotch yoke led to the remission of undesirable harmonics produced in previous experiments. A data acquisition system controlled by a computer network was capable of collecting many samples of acoustic velocity and pressure data at consecutive cycles and driving frequencies. The method of data collection facilitated statistical analysis of the acoustic data.

The onset of turbulence was investigated for an oscillating flow in a rectangular geometry both with and without side-wall injection. Side-wall injection at the transpiring surface was simulated by the sublimation process of dry ice. This was justified by the fact that sublimating dry ice exhibited many desirable features that we wished to explore. These features include (1) its ability to simulate the burning of a solid rocket propellant; (2) its noninterference with the natural system frequency; (3) its resistance to acoustic dissipation; and (4) its safe handling advantages. Calibrated hot film anemometry was used to record the velocity amplitude near the dry ice surface. Two techniques were used to define the transition from laminar to turbulent regimes: statistical analysis and flow visualization. Results depended on computer data acquisition and hot film anemometry.

For oscillatory flows over hard walls, Hino and coworkers [7–10] had observed four distinct flow categories in their experiments. These were: (a) laminar, (b) distorted laminar, (c) weakly turbulent, and (d) conditionally turbulent regimes. A fully turbulent flow could not be achieved. In order to maintain consistency, the structures observed in the current experiments were classified in the same four categories. It is hoped that this choice will help to standardize the ever-growing nomenclature in periodic flow studies.

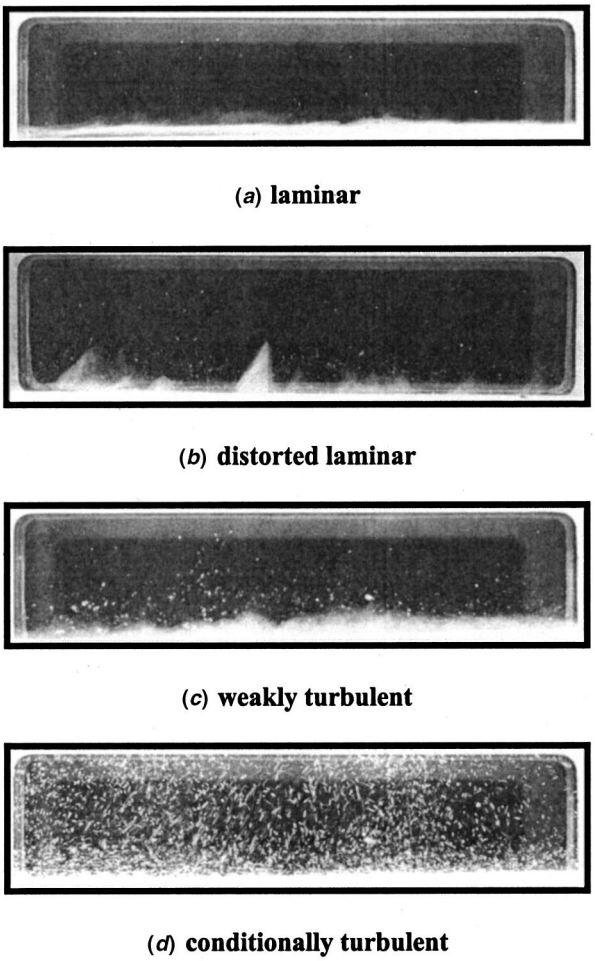

Fig. 8 Flow visualization of the four distinct phases preceding turbulence. Patterns indicate (*a*) laminar, (*b*) distorted laminar, (*c*) weakly turbulent, and (*d*) conditionally turbulent flow regimes.

It should be noted that the inability to stimulate a fully turbulent condition is consistent with the findings of other researchers. According to a comprehensive survey by Davis [22], turbulence in oscillatory flows could be expected around $\mathrm{Re}_A = 890$ or $\mathrm{Re}_\delta \approx 500$ (see Eq. (1)). In our experiment, the largest Re_A of 500 fell short of the established critical value. As such, it could only lead to conditionally turbulent conditions. The documented difficulties in achieving instability may be attributed to the Stokes layer being very stable to small disturbances over a very broad range of Re_A. As an example, one may cite the results reported by von Kerczek and Davis [23]. Accordingly, a stable state was observed up to $\mathrm{Re}_A = 1420$ ($\mathrm{Re}_\delta \approx 800$), thus exceeding the average threshold for instability. Nonetheless, since the Stokes layer can become unstable to disturbances of sufficiently large amplitudes, it is likely for an unconditionally turbulent regime to be achieved at higher Re_A.

The statistical flow analysis showed that the fully turbulent flow regime was not developed even at the highest frequencies permitted by our wave generator. A relaminarization occurred within every cycle when the velocity amplitude diminished below a certain value. As explained earlier, this result is consistent with observations reported in studies with nonporous walls. The reader is referred, for instance, to the literature survey by Hino and coworkers [7–10].

Through statistical analysis and flow visualization, turbularization of the Stokes layer with side-wall injection was reproducible and repeatable at a critical acoustic Reynolds number of 200. Another important indicator of turbulence was found to be the clear shifting in the power law relationship between the maximum standard deviation and Re_A.

Acknowledgments

The authors wish to thank the editor and anonymous referees for their very useful suggestions. We also thank Dr. David Flanagan of Thiokol Inc. for supporting this work by an IR&D grant.

References

[1] Majdalani, J., and Van Moorhem, W. K., 1998, "Improved Time-Dependent Flowfield Solution for Solid Rocket Motors," AIAA J., **36**(2), pp. 241–248.
[2] Majdalani, J., 1999, "The Boundary Layer Structure in Cylindrical Rocket Motors," AIAA J., **37**(4), pp. 505–508.
[3] Vincent, G. E., 1957, "Contribution to the Study of Sediment Transport on a Horizontal Bed Due to Wave Action," *Proceedings of the Conference on Coastal Engineering*, Vol. 16, pp. 326–335.
[4] Collins, J. I., 1963, "Inception of Turbulence at the Bed under Periodic Gravity Waves," J. Geophys. Res., **68**, pp. 6007–6014.
[5] Sergeev, S. I., 1966, "Fluid Oscillations in Pipes at Moderate Reynolds Numbers," Fluid Dyn., **1**, pp. 21–22.
[6] Merkli, P., and Thomann, H., 1975, "Transition to Turbulence in Oscillating Pipe Flow," J. Fluid Mech., **68**, pp. 567–575.
[7] Hino, M., and Sawamoto, M., 1975, "Linear Stability Analysis of an Oscillatory Flow between Parallel Plates," *Proceedings of the 7th Symposium on Turbulence*, pp. 1–7.
[8] Hino, M., Sawamoto, M., and Takasu, S., 1976, "Experiments on Transition to Turbulence in an Oscillatory Pipe Flow," J. Fluid Mech., **75**, pp. 193–207.
[9] Hino, M., Kashiwayanagi, M., Nakayama, A., and Hara, T., 1983, "Experiments on the Turbulence Statistics and the Structure of a Reciprocating Oscillatory Flow," J. Fluid Mech., **131**, pp. 193–207.
[10] Hino, M., Fukunishi, Y., and Meng, Y., 1990, "Experimental Study of a Three-Dimensional Large-Scale Structure in a Reciprocating Oscillatory Flow," Fluid Dyn. Res., **6**, pp. 261–275.
[11] Ohmi, M., Iguchi, M., Kakehashi, K., and Masuda, T., 1982, "Transition to Turbulence and Velocity Distribution in an Oscillating Pipe Flow," Bull. JSME, **25**, pp. 365–371.
[12] Akhavan-Alizadeh, R., 1987, "An Investigation of Transition and Turbulence in Oscillatory Stokes Layers," Ph.D. dissertation, MIT.
[13] Traineau, J. C., Hervat, P., and Kuentzmann, P., 1986, "Cold-Flow Simulation of a Two-Dimensional Nozzleless Solid-Rocket Motor," *AIAA* 86–1447.
[14] Ma, Y., Van Moorhem, W. K., and Shorthill, R. W., 1990, "Innovative Method of Investigating the Role of Turbulence in the Velocity Coupling Phenomenon," ASME J. Vibr. Acoust., **112**(4), pp. 550–555.
[15] Ma, Y., Van Moorhem, W. K., and Shorthill, R. W., 1991, "Experimental Investigation of Velocity Coupling in Combustion Instability," J. Propul. Power, **7**(5), pp. 692–699.
[16] Huesmann, K., and Eckert, E. R. G., 1990, "Studies of the Laminar Flow and the Transition to Turbulence in Porous Tubes with Uniform Injection through the Tube Wall," J. Propul. Power, **6**(6), pp. 690–705.
[17] Dunlap, R., Willoughby, P. G., and Hermsen, R. W., 1974, "Flowfield in the Combustion Chamber of a Solid Propellant Rocket Motor," AIAA J., **12**(10), pp. 1440–1445.
[18] Dunlap, R., Sabnis, J. S., Beddini, R. A., Flandro, G. A., Brown, R. S., Gibeling, H. J., Blackner, A. M., Waugh, R. C., and McDonald, H., 1985, "Internal Flow Field Investigation," *U.S. Air Force Rocket Propulsion Laboratory* No. TR-85-079.
[19] Dunlap, R., Blackner, A. M., Waugh, R. C., Brown, R. S., and Willoughby, P. G., 1990, "Internal Flow Field Studies in a Simulated Cylindrical Port Rocket Chamber," J. Propul. Power, **6**(6), pp. 690–704.
[20] Barron, J., Majdalani, J., and Van Moorhem, W. K., 2000, "A Novel Investigation of the Oscillatory Field over a Transpiring Surface," J. Sov. Laser Res., **235**(2), pp. 281–297.
[21] Richardson, E. G., 1928, "The Amplitude of Sound Waves in Resonators," Proc. Phys. Soc., **40**(27), pp. 206–220.
[22] Davis, S. H., 1976, "The Stability of Time-Periodic Flows," Annu. Rev. Fluid Mech., **8**, pp. 57–74.
[23] von Kerczek, C., and Davis, S. H., 1974, "Linear Stability Theory of Oscillatory Stokes Layers," J. Fluid Mech., **62**(4), pp. 753–773.

R. M. Sadri[1]

J. M. Floryan
Professor

The University of Western Ontario,
Department of Mechanical
and Materials Engineering,
London, Ontario N6A 5B9, Canada

Accurate Evaluation of the Loss Coefficient and the Entrance Length of the Inlet Region of a Channel

Evaluations of loss coefficient and entrance length in the inlet region of a channel are presented. Correlations and numerical values of these quantities are provided for Reynolds number ranging from 0.01 to 2200. The results provide an accurate benchmark for engineering design. [DOI: 10.1115/1.1493813]

1 Introduction

The understanding of the behavior of flow in the inlet region of a channel is one of the classical problems in fluid mechanics. In spite of a large number of investigations, a rational resolution of the problem still remains unknown. It is believed that an ad-hoc modeling of upstream effects is the main source of discrepancies in the literature [1].

The common approaches to model the entry flow in a channel assume (A) a parallel flow with a uniform velocity distribution at the inlet (uniform entry flow), (B) a uniform velocity with zero vorticity at the inlet (irrotational entry flow), and (C) a stream tube with uniform flow far upstream which corresponds to flow in an infinite number of channels (cascade entry flow). The above models are described in the review by Shah and London [1]. The fourth model [2], type (D), accounts for the upstream flow by treating the channel entry as an inviscid sink.

None of the above models represents a realistic description of the upstream flow and its effects on flow development inside the channel. To remove uncertainties associated with this problem, Sadri [3] presented a thorough investigation of entry flow in a channel for Reynolds number ranging from 0.01 to 2200. To account for the effects of upstream flow, the inlet boundary conditions were defined based on a far-field asymptotic solution described by Jeffery-Hamel flow. The flow fields upstream and downstream of the channel entry were determined simultaneously by solving the Navier-Stokes equations numerically.

The situation arising in the entrance region is significant in many engineering applications. For example, a reliable estimate of the size of a compact heat exchanger depends on the correct evaluation of heat transfer coefficients and the total pressure drop characteristics through the channel entry [4]. The design of flow-intake devices relies on a reliable analysis of pressure loss in the inlet region of channels. Entry flow condition also occurs in microchannels because the length of microchannels is shorter than the entrance length for fully developed flow [5]. For a review of the application of entry flow in bioscience, the reader may refer to Zou and Liu [6].

Information in the literature regarding the pressure loss is generally provided based on incremental pressure drop $K(\infty)$. A variety of solution methods to determine this quantity have been reported in previous studies. Bodoia and Osterle [7] assumed plug flow at the entrance, solved numerically boundary layer equations and obtained incremental pressure drop $K(\infty)$ at high Reynolds numbers. Schmidt and Zeldin [8] used the same model of the entry flow, solved the complete Navier-Stokes equations and obtained values for $37.5 \leqslant Re \leqslant 3750$. Their results at $Re=3750$ can be compared with the studies based on the solution of boundary layer equations. Han [9] determined incremental pressure drop on the basis of approximate solution of boundary layer equations. Sparrow et al. [10] reported the results based on linearizing convective terms in the momentum equations. Schlichting [11,12] patched the boundary layer solution near the entrance with a perturbation of the fully developed flow far downstream and obtained $K(\infty)$. Collins and Schowalter [13] included the effects of higher-order terms and obtained identical result as Bodoia and Osterle [7]. Chen [14] used an integral approach and obtained a correlation for $K(\infty)$, which is in good agreement with the results obtained from numerical solution of boundary layer equations. Nguyen and Maclaine-Cross [15] modeled the upstream flow as a stream tube, solved the complete Navier-Stokes equations for $15 \leqslant Re \leqslant 750$, and provided a correlation for $K(\infty)$ in this range of Reynolds number. Lundgren et al. [16] developed a linearization method that does not require knowledge of velocity at the inlet and obtained $K(\infty)$.

Experimental analyses are performed for flows in rectangular ducts of different aspect ratios. Beavers et al. [17] considered ducts of aspect ratio 51 and flows with $600 \leqslant Re \leqslant 1125$. A comprehensive review of prior contributions in evaluating incremental pressure drop for various cross sections is given by Shah and London [1].

Evaluation of entrance length (the distance from the channel inlet where the flow attains its fully developed form) has been carried out by a number of authors. Morihara and Cheng [18], Narang and Krishnamoorthy [19], and Chen [14] predicted the entrance length based on the uniform entrance velocity assumption. Sparrow and Anderson [2] obtained the entrance length for Reynolds number ranging from 0.375 to 375.

The available data for pressure loss and hydrodynamic entrance length suffer from various degrees of approximations either in modeling the inlet flow (types A-D) or the solution method. Therefore, the purpose of this study is to present an accurate evaluation of the pressure loss and hydrodynamic entrance length in the entry region of a channel. This paper is organized as follows. The model of the entry flow is described in Section 2. The numerical method used is discussed in Section 3. A discussion of results is presented in Section 4, including description of flow pattern in Section 4.1, analysis of pressure drop in Section 4.2, and correlations for loss coefficient in Section 4.2.1. Section 4.3 provides an evaluation of entrance length in the upstream and downstream regions. Section 5 gives a summary of the main conclusions.

[1]Present Address: Bombardier Aerospace, 1800 Marcel-Laurin Blvd., Bld. 123, Saint Laurent, Quebec H4R 1K2, Canada.

Contributed by the Fluids Engineering Division for publication in the JOURNAL OF FLUIDS ENGINEERING. Manuscript received by the Fluids Engineering Division March 31, 2000; revised manuscript received January 14, 2002. Associate Editor: U. Ghia.

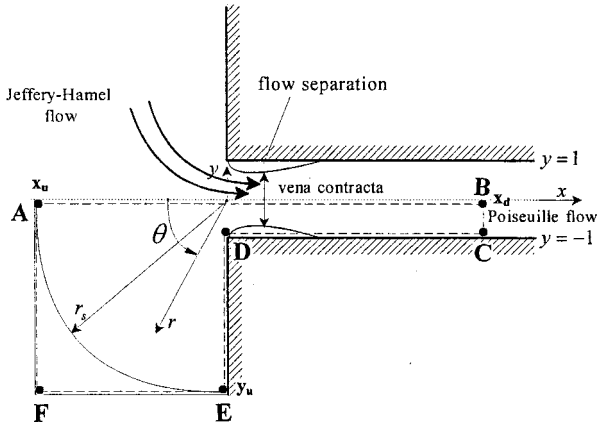

Fig. 1 Flow pattern in a sharp-edged entrance

2 Problem Formulation

Consider two-dimensional, steady flow in the inlet zone of a straight channel of width $2H$ (Fig. 1). The fluid is incompressible with density ρ, dynamic viscosity μ, and kinematic viscosity ν. The origin of the reference Cartesian system (x,y) is placed at the channel entry with the x-axis overlapping with the centerline of the channel. The origin of the auxiliary reference polar coordinate system (r,θ) is placed at $(x,y)=(0,0)$ with θ overlapping with the negative x-axis (Fig. 1). The problem is scaled using the maximum velocity U far inside the channel $(x\rightarrow+\infty)$ as the velocity scale, ρU^2 as the pressure scale and H as the length scale. The dimensionless velocity vector $\bar{v}$ has components (u,v) in the (x,y) reference system and (u_r,u_θ) in the (r,θ) reference system. The Reynolds number is defined as $\mathrm{Re}=UH/\nu$. The field equations consist of the Navier-Stokes and the continuity equations in the form

$$(\bar{v}.\nabla)\bar{v}=-\nabla p+\mathrm{Re}^{-1}\nabla^2\bar{v}, \tag{1a}$$

$$\nabla.\bar{v}=0, \tag{1b}$$

where p denotes pressure and ∇ stands for the nabla operator.

At a large distance downstream from the inlet $(x\rightarrow+\infty)$ the form of the flow is well described by the Poiseuille solution. Upstream from the channel inlet $(r\rightarrow\infty,-\pi/2\leqslant\theta\leqslant\pi/2)$ the flow field approaches the Jeffery-Hamel flow (Jeffery [20]; Hamel [21]).

The relevant boundary conditions have the form

$$u=v=0 \quad \text{at } x=0, \quad y\geqslant 1, \quad y\leqslant -1, \tag{2a}$$

$$u=v=0 \quad \text{at } x\geqslant 0, \quad y=\pm 1, \tag{2b}$$

$$u_r\rightarrow F(\theta)/r, \quad u_\theta\rightarrow 0 \text{ as } r\rightarrow\infty, \quad -\pi/2\leqslant\theta\leqslant\pi/2, \tag{3}$$

$$u\rightarrow 1-y^2, \quad v\rightarrow 0 \text{ as } x\rightarrow\infty, \quad -1\leqslant y\leqslant 1, \tag{4}$$

where $F(\theta)$ is determined from the Jeffery-Hamel solution with the same mass flux as the Poiseuille flow inside the channel (see Appendix A). Conditions (2*a*,*b*) describe the no-slip and no-penetration conditions at the walls. The inflow boundary conditions (3) are defined based on the solution of Jeffery-Hamel flow. The outflow boundary condition (4) are based on the Poiseuille flow.

3 Numerical Method

The governing equations are expressed in terms of the stream function ψ and vorticity ζ as

$$\nabla^2\zeta=\mathrm{Re}(\psi_y\zeta_x-\psi_x\zeta_y), \tag{5a}$$

$$\nabla^2\psi=-\zeta, \tag{5b}$$

where $u=\psi_y, v=-\psi_x, \zeta=v_x-u_y$ and subscripts denote derivatives. The solution domain has been reduced by half due to symmetry and is bounded by lines ABCDEF in Fig. 1. The relevant boundary conditions have the form

$$\psi=\frac{2}{3}, \quad \zeta=0 \qquad \text{on line AB}, \tag{6}$$

$$\psi=y-\frac{y^3}{3}+\frac{2}{3}, \quad \zeta=2y \quad \text{on line BC}, \tag{7}$$

$$\psi=0, \quad \frac{\partial\psi}{\partial y}=0 \qquad \text{on line CD}, \tag{8}$$

$$\psi=0, \quad \frac{\partial\psi}{\partial x}=0 \qquad \text{on line DE}, \tag{9}$$

$$\psi,\zeta \quad \text{known from Jeffery-Hamel flow on line EFA.} \tag{10}$$

In numerical calculations, the solution domain must be finite and thus physical condition (7) must be applied at a finite distance x_d. This distance must be large enough so that one can study evolution of the computed flow towards its asymptotic state as x increases. The criterion defining this distance is not unique. For example, the criterion frequently found in the literature stating that the fully developed flow is reached when the centerline velocity attains 99% of its asymptotic value [14,18,19,22,23] produces far too short computational domain. The criterion found to be most useful involves centerline pressure gradient $\mathrm{Re}\,dp/dx$, which has the expected value of -2 for large enough x. The length x_d of the computational domain was judged sufficient when the computed value of $\mathrm{Re}\,dp/dx$ agreed with the value predicted by the small perturbation theory (see Section 4.3.2) over a significant part of the outflow zone of the channel. The selected values of x_d range from 1 for $\mathrm{Re}=0.01$, through 93.96 at $\mathrm{Re}=500$ to 397.97 at $\mathrm{Re}=2200$.

The location of the inlet boundary conditions was selected by comparing the numerical solution with the small perturbation solution described in Appendix B using an analogous procedure. The selected locations of the inlet conditions are $x_u=y_u=20$ for $\mathrm{Re}<1$, $x_u=y_u=12$ for $1\leqslant\mathrm{Re}\leqslant 50$ and $x_u=y_u=10$ for $\mathrm{Re}>50$.

Comparison of the required size of the computational domain upstream and downstream from the channel entry shows that the size of the entrance zone increases inside the channel, but decreases outside the channel as Re increases.

Because of the large size of the solution domain, and because of the large range of gradients of flow quantities within the flow domain, use of a grid with a variable step size was found to be mandatory. The required grid distribution was achieved through a carefully selected mapping of the (x, y) flow domain onto the (ξ, η) computational domain. The structure of the mapping is described by Sadri [3].

A uniform, square grid in the computational domain and compact fourth-order finite-difference scheme [24] were used for discretization purposes. The grid size $h=0.025$ provided the desired accuracy for the flow parameters of interest, as determined through grid convergence studies (see Fig. 2). This grid size combined with the transformations resulted in a large grid density in the vicinity of the inlet and around the solid walls. The corresponding grid spacing in the physical domain varied from $\Delta y=0.0125$ around $y=-1$ to $\Delta y=0.0437$ around $y=0$, and $\Delta y=0.0125043$ around $y=y_u$. The grid spacing in the x-direction was $\Delta x=0.0125043$ around $x=0$, $\Delta x=0.7054$ around $x=x_d$, and $\Delta x=0.0593$ around $x=x_u$. The largest grid used contained $\sim 10^5$ grid points. The discretized equations were solved using iterative method with the convergence criterion for the residuum Res of (5) at each grid point set at $\mathrm{Res}<10^{-7}$.

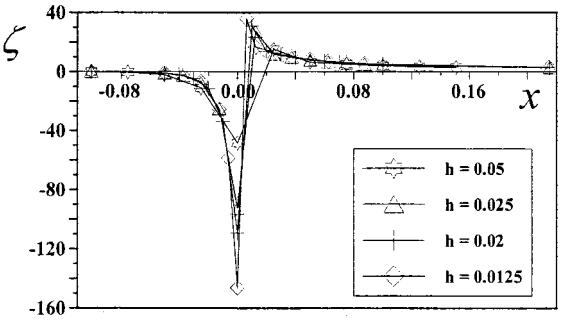

Fig. 2 Distribution of vorticity ζ along the line $y=-1$ for Re =1000 obtained with different grid sizes h

An additional difficulty arose due to the presence of the sharp corner at point D (see Fig. 1) where the vorticity is singular. An inappropriate numerical treatment of this point may lead to a large error in the computed flow field, especially in the separation zone [25]. This problem has been solved by taking the analytical solution of the flow field in the small neighborhood of the corner [26] and matching it with a purely numerical solution away from the corner. Several possible matching procedures are described by Floryan and Czechowski [25] but only one gives acceptable results for higher values of Re as determined by the grid convergence studies. This procedure involves assigning a value of vorticity to the grid point overlapping with the corner, which can be subsequently used in the discretization formulas. Results of the grid convergence studies displayed in Fig. 2 demonstrate that the above method correctly captures singular behavior of vorticity and that the grid independent results can be obtained very close to the corner. A detailed description of the above method and its implementation to the present study can be found in Sadri [3].

4 Results and Discussion

4.1 Flow Pattern. Interpretation of results is simplified by displaying pressure distribution along the channel centerline. This pressure has been determined from the known velocity field through numerical integration of the streamwise momentum equation and is displayed in Fig. 3. At large distance upstream ($x\rightarrow-\infty$), the pressure approaches the ambient pressure as described by the Jeffery-Hamel solution. As fluid is drawn into the channel, an entrance pressure drop begins to appear upstream of the channel inlet, owing to the combined effects of the fluid acceleration towards the entrance and wall shear stress. Two different flow characteristics may be distinguished depending on the magnitude of Re. At Re<137, when the flow does not separate, the axial pressure decreases monotonically as fluid enters the channel [3]. At Re>137, when the flow separates, there is a more pronounced pressure drop at the entrance associated with flow acceleration due to formation of vena contracta (see Fig. 1), followed by pressure recovery downstream of vena contracta. Further downstream, pressure begins to decrease linearly as the fully developed flow begins to form.

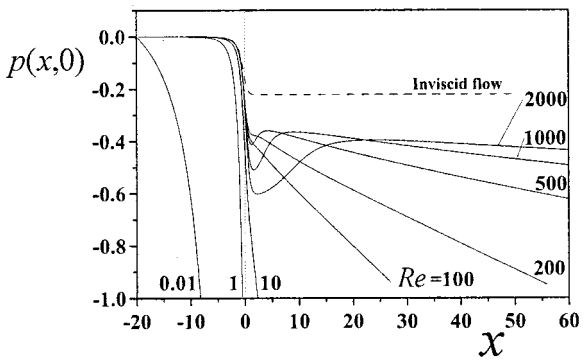

Fig. 3 Pressure distribution along the channel centerline, 0.01≤Re≤2000

The behavior of the inviscid flow is quantitatively different from the behavior of the viscous flow as illustrated in Fig. 3. Following the sudden pressure drop at the entrance region, pressure approaches its asymptotic value almost immediately downstream from the channel entrance. The (inviscid) pressure drop occurs because of the change of kinetic energy (Bernoulli effect). The head loss in the entrance in this case is zero due to absence of viscosity.

4.2 Analysis of Pressure Drop. The analysis of pressure loss due to flow development can be performed using the one-dimensional energy equation in the form

$$p_0+\alpha_0\frac{\overline{u_0^2}}{2}=p(x)+\alpha(x)\frac{\overline{u^2}}{2}+f\frac{x}{D}\frac{\overline{u^2}}{2}+k(x)\frac{\overline{u^2}}{2}, \qquad (11)$$

where $p(x)$ denotes the local pressure, $\overline{u}$ is the average velocity, subscript 0 stands for the condition upstream of the channel inlet, $\alpha(x)$ is the kinetic energy correction coefficient, f is the friction factor, x is the distance from the inlet in the downstream direction, D is the hydraulic diameter and $k(x)$ denotes additional (entrance) losses. It is important to note that (11) is only valid for one-dimensional flow and the application of this equation in the neighborhood of the inlet results in an approximation whose validity remains to be judged.

Far upstream of the channel inlet, the amount of kinetic energy of the flow is negligible and (11) can be rearranged into the following form

$$\frac{p_0-p(x)}{\overline{u^2}/2}=\alpha(x)+f\frac{x}{D}+k(x). \qquad (12)$$

It is apparent that $k(x)$ can be evaluated only if $\alpha(x)$ is known throughout the entire entrance region. The $\alpha(x)$ is computed from the known velocity field. The numerical evaluation of the integral $\int_{-1}^{1}(u^2+v^2)u/2dy$ at each x-location gives distribution of kinetic energy of the stream, which, after division by 8/27, i.e., kinetic energy of the stream assuming constant velocity equal to the average velocity, produces $\alpha(x)$. The reader may note that the integral takes the value of 16/35 in the case of Poiseuille flow and results in $\alpha(\infty)=54/35$ [27].

Equation (12) indicates that the total local pressure drop consists of three parts: (i) change of kinetic energy, (ii) losses represented by a fully developed flow starting at $x=0$, and (iii) additional (entrance) losses accounted for by $k(x)$. Figure 4 illustrates each of the above elements for Re=2200. It can be seen that as $x\rightarrow\infty$, $\alpha(x)$ approaches the asymptotic (Poiseuille) value of $\alpha(x)=54/35$ [27]. A plot of pressure drop for an inviscid flow is shown for comparison. The pressure loss for such flow is zero and the pressure drop is only due to the change of kinetic energy. Far downstream of the channel entry the velocity profile is uniform and $\alpha_{inviscid}=1$. The difference between $\alpha(\infty)$ and $\alpha_{inviscid}$ accounts for the difference between the kinetic energy of the real fluid and the inviscid fluid. In the next section we present the results for the loss coefficient $k(x)$.

4.2.1 Loss Coefficient. The distribution of $k(x)$ is shown in Fig. 5. With increasing downstream distance, $k(x)$ rises sharply at first and then levels off at a constant value, which characterizes the total entrance loss. When k reaches this constant value, the hydrodynamic development of the flow is complete and this fact could be used to define the length of the channel entrance zone.

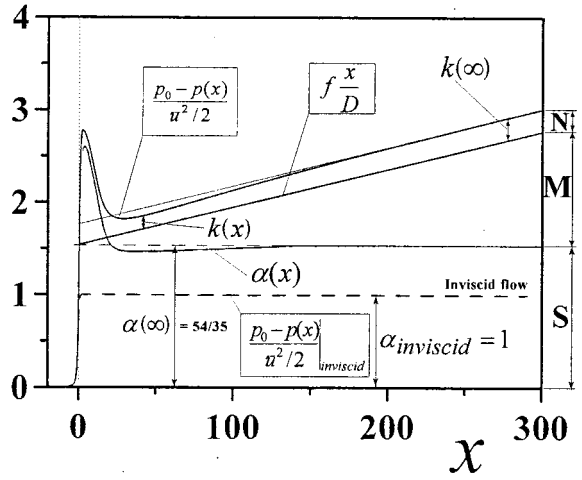

Fig. 4 Pressure drop along the centerline of the channel for Re=2200. S denotes the pressure drop due to the change of the kinetic energy, M stands for the pressure drop associated with the Poiseuille flow, and N denotes the additional pressure drop occurring due to the entrance effects.

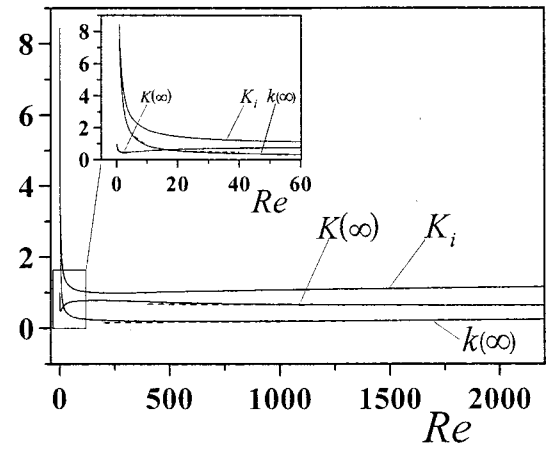

Fig. 6 Variations of the loss coefficient $k(\infty)$, the incremental pressure drop $K(\infty)$ and the additional pressure loss coefficient K_i as a function of Re. Dashed lines denote correlations given in Section 4.2.1.

A plot of the fully developed values of k as a function of Re is shown in Fig. 6. At first $k(\infty)$ decreases sharply as Re increases until it attains a local minimum at Re≈700 and then it begins to increase with further increase of Re. The results show that for Re>1000, $k(\infty)$ increases as a linear function. The available results lead to correlations in the form (see Fig. 6)

$$k(\infty)=7.208\,\mathrm{Re}^{-1}+4.729\times10^{-4}\,\mathrm{Re}+0.168\pm2.98\%,\quad 1\leqslant\mathrm{Re}\leqslant100. \tag{13a}$$

$$k(\infty)=10.604\,\mathrm{Re}^{-1}+2.592\times10^{-5}\,\mathrm{Re}+0.160.07\%,\quad 100<\mathrm{Re}\leqslant1000. \tag{13b}$$

$$k(\infty)=4.183\times10^{-5}\,\mathrm{Re}+0.152\pm0.2\%,\quad 1000<\mathrm{Re}\leqslant2200. \tag{13c}$$

A comparison between the present numerical results and the results available in the literature is carried out using a modified form of (11) written as

$$\frac{p_0-p(x)}{\bar{u}^2/2}=f\frac{x}{D}+K(x)+K_i, \tag{14}$$

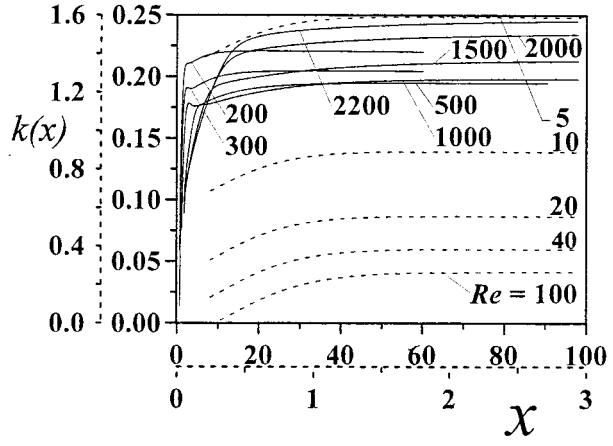

Fig. 5 Distribution of the loss coefficient along the channel

where $K(x)$ is referred to in the literature as the incremental pressure drop [7–13,15,16] and accounts for flow variations starting from the channel entrance ($x=0$). The detailed description of $K(x)$ and how it is computed are given in Appendix C. The reader may note that $K(x)$ captures only partial entrance losses, i.e., those occurring inside the channel. The quantity K_i is introduced to account for the losses not included in $K(x)$ and could be viewed as an error to the incremental pressure drop reported in the literature. Comparison of (12) and (14) shows that

$$k(x)=K(x)+K_i-\alpha(x), \tag{15a}$$

$$k(\infty)=K(\infty)+K_i-54/35. \tag{15b}$$

The values of K_i and fully developed values of $K(\infty)$ as a function of Reynolds number are given in Table 1 and Fig. 6. It can be seen that K_i at first decreases, reaches a minimum of 0.465 around Re≈3, then increases and reaches a maximum of 0.777 around Re≈150, and subsequently decreases again with further increase of Re. The shape of the curve suggests that $K(\infty)$ approaches an asymptote at high Reynolds number. The available results permit writing a correlation in the form (see also Fig. 6)

$$K(\infty)=0.107\,\mathrm{Re}^{-1}-1.427\times10^{-4}\,\mathrm{Re}+0.797\pm1.1\%,\quad 100\leqslant\mathrm{Re}\leqslant1000, \tag{16a}$$

$$K(\infty)=-2.35\times10^{-5}\,\mathrm{Re}+0.684\pm0.28\%,\quad 1000<\mathrm{Re}\leqslant2200. \tag{16b}$$

Values of K_i shown in the same figure demonstrate that error in the estimation of pressure loss using $K(\infty)$ could reach several hundred percent at very small Reynolds numbers, while at Re ≈2000 it decreases to about 50%. This error is usually mitigated by adding one head loss to account for pressure loss due to inviscid acceleration of fluid entering the channel from surroundings.

Comparisons between the present values of $K(\infty)$ and those available in the literature are presented in Table 1. Chen [14] presented a correlation in the form of $K(\infty)=0.64+14.25\,\mathrm{Re}^{-1}$. Nguyen and Maclaine-Cross [15] provided correlation in the form $K(\infty)=0.6779+1.7218\,\mathrm{Re}^{-1}$ for 15≤Re≤750. Shah and London [1] recommended $K(\infty)=0.674$ for large values of Re. The differences between the above results and the present ones are either due to various idealizations of the inflow boundary conditions, or due to different approximations used in determining the solution, or both.

Beavers et al. [17] performed a large number of experiments in ducts of aspect ratio 51 and flows with 600≤Re≤1125. These

Table 1 The entrance loss coefficient $k(\infty)$, the incremental pressure drop $K(\infty)$ and the additional loss coefficient $K_i(\infty)$. Superscripts denote the values of the incremental pressure drop coefficient reported in the literature, i.e.,[1]Nguyen and Maclaine-Cross [15],[2]Schmidt and Zeldin [8],[3]Bodoia and Osterle [7],[4]Han [9],[5]Schlichting [11,12],[6]Sparrow et al. [10],[7]Lundgren et al. [16],[8]Collins and Schowalter [13]. References [7–9] assume that $K(\infty)$ is reached where velocity reaches 99% of its asymptotic value, [11–13] assume this to happen for 98% of the asymptotic value, [10,16] use expansions and thus do not define where $K(\infty)$ is reached, [15] computes numerically $\lim_{x\to\infty} K(x)$ where it is assumed that the limit is attained where changes of $K(x)$ are below the numerical accuracy.

Re	$k(\infty)$	$K(\infty)$	$K_i(\infty)$
0.01	745.9	12.45	734.99
0.2	37.15	0.97	37.72
0.5	14.89	0.617	15.81
1	7.405	0.508	8.439
5	1.588	0.485	2.646
10	0.89	0.552	1.882
15	0.667	0.606, 0.7954[1]	1.603
22.5	0.518	0.660, 0.7522[1]	1.401
30	0.442	0.694, 0.7329[1]	1.291
37.5	0.394	0.71, 0.7224[1], 0.74[2]	1.225
100	0.266	0.77	1.035
187.5	0.221	0.776, 0.698[2]	0.987
375	0.198	0.746, 0.6828[1]	0.994
500	0.195	0.72	1.015
750	0.194	0.686, 0.6817[1]	1.05
1000	0.197	0.666	1.073
1500	0.213	0.647	1.108
2000	0.236	0.638	1.141
2200	0.247	0.635	1.154
↓		0.6779[1], 0.669[2], 0.676[3], 0.85[4], 0.601[5], 0.686[6], 0.6857[7], 0.676[8]	

authors concluded that $K(\infty)$ is essentially independent of Re for these values of Re and estimated it to be $K(\infty)\approx 0.61$. This value is lower than those obtained in the present analysis. The most likely reason for this difference is the use of rounded entrance in the experiment that eliminates flow separation. The dependence of $K(\infty)$ on Re in this flow regime is probably too weak to be registered by experimental techniques used.

4.3 Entrance Length. In the problem under investigation, the flow fields far upstream and downstream of the channel entry approach the Jeffery-Hamel flow and the Poiseuille flow, respectively. However, the existence of the sharp-edged, finite-size entrance changes the flow character close to the inlet. Analysis of the entrance length consists of determining the distance where the flow attains its asymptotic states in the both upstream and downstream directions. We begin our analysis by looking at the entrance length in the upstream zone.

4.3.1 Upstream Zone. The flow approaching the channel entry begins to be affected by the inlet geometry at a certain distance upstream and departs from the Jeffery-Hamel form. Sufficiently far upstream, the flow may be represented by a superposition of the Jeffery-Hamel flow and small perturbations. The decay of these perturbations is governed by an eigenvalue problem described in Appendix B and is proportional to r^{λ} where the eigenvalues λ indicate the rate of decay. In general, eigenvalues are complex and correspond to symmetric and antisymmetric modes. The dominant eigenvalues of interest, i.e., those with the smallest negative real parts corresponding to both modes, are displayed in Fig. 7. For $\mathrm{Re}<0.8$ the symmetric eigenvalue is real. As Re increases, this eigenvalue becomes complex and for $\mathrm{Re}>8.3$, it becomes real again. The existence of a range of complex eigenvalues suggests formation of a complex flow pattern for $0.8<\mathrm{Re}\leqslant 8.3$. When $\mathrm{Re}\to 0$, the magnitude of the dominant eigenvalue

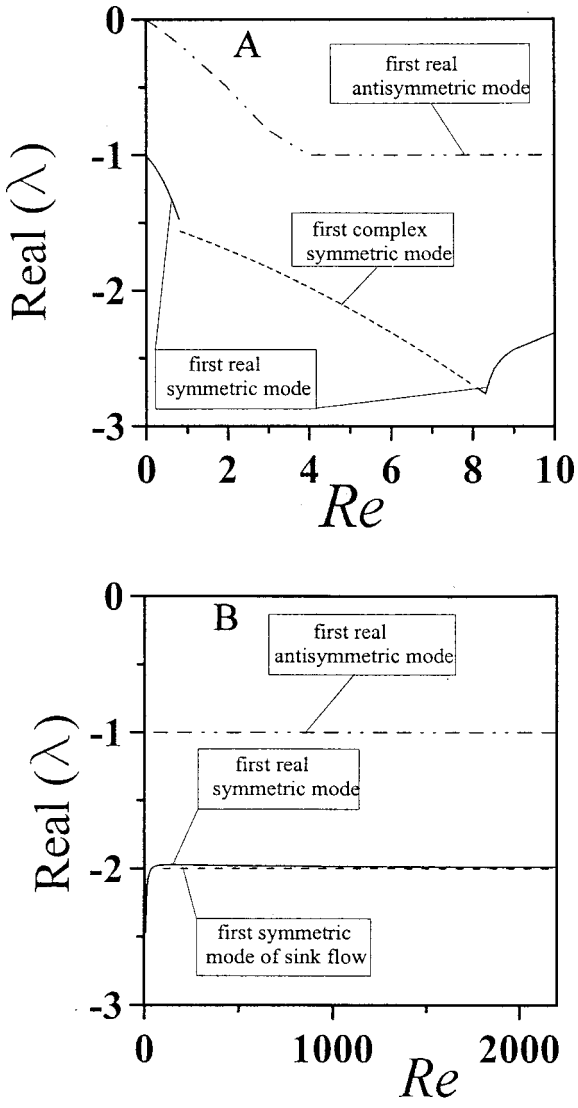

Fig. 7 Variations of the eigenvalues describing decay of the perturbations of Jeffery-Hamel flow. Figure 6(*a*)-0⩽Re⩽10, Fig. 6(*b*)-0⩽Re⩽∞.

decreases indicating a slower rate of decay of perturbations and suggesting the need to increase the size of the computational box, in agreement with the numerical experiments reported in Section 2. The antisymmetric eigenvalue attains its asymptotic value very rapidly, i.e., it is equal to -1 already for $\mathrm{Re}\geqslant 4$. The magnitudes of the eigenvalues show that the anti-symmetric mode always decreases slower with r than the symmetric one. Such mode is likely to be found when the channel entry does not satisfy the symmetry condition.

Figure 7 shows that for $\mathrm{Re}\geqslant 50$, the dominant eigenvalues of the Jeffery-Hamel flow approach the dominant eigenvalue of the sink flow. This indicates that potential sink flow provides an adequate representation of the inlet boundary conditions for $\mathrm{Re}\geqslant 50$. Sparrow and Anderson [2] studied the flow in an identical geometry and used a potential sink to set up the inlet boundary conditions. Figure 7 shows that for small Re the dominant eigenvalues are significantly different from the inviscid eigenvalue and thus a simple sink cannot correctly represent the oncoming flow. Furthermore, these authors increased the size of the inlet domain as Re was increased. The eigenvalues of the first symmetric mode approaches -2 for large Re suggesting no need to use a large computational domain.

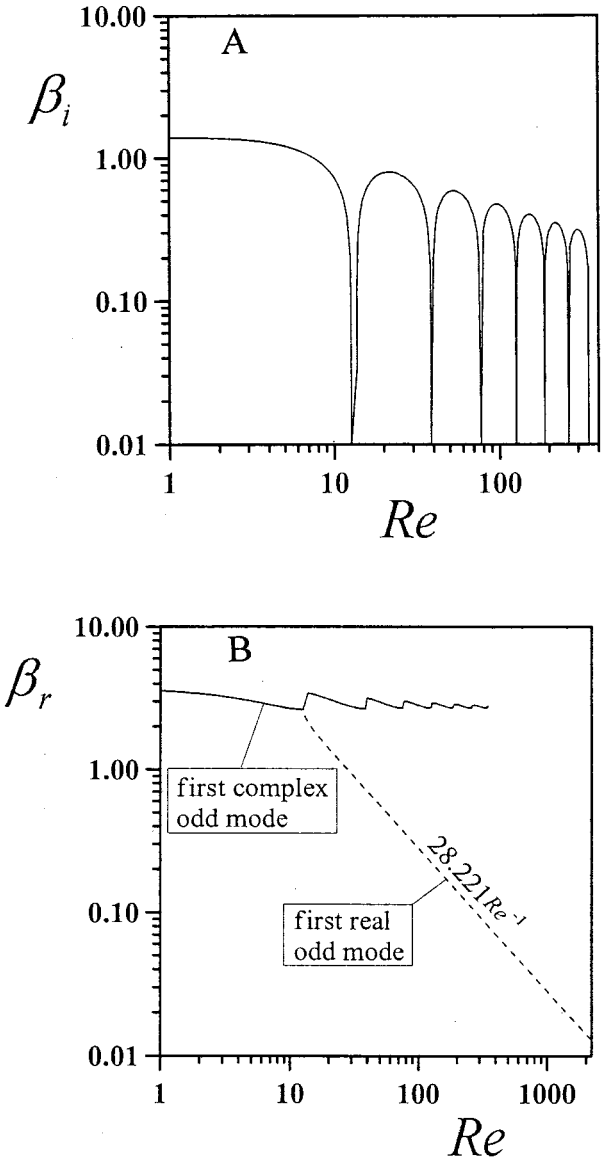

Fig. 8 Variations of the eigenvalues describing decay of the perturbations in the Poiseuille flow as a function of Re. Figure 7(*a*)-imaginary part β_i; Fig. 7(*b*)-real part β_r.

Table 2 The entrance length, based on criteria (A) and (D). Superscripts denote the values of the entrance length reported in the literature, i.e.,[1]Morihara and Cheng [18],[2]Narang and Krishnamoorthy [19],[3]Schlichting [12],[4]Chen [14],[5]Sparrow and Anderson [2],[6]Brandt and Gillis [30]. All references use criterion A, except references [12], [30] which use criterion based on 98% and 97% of the asymptotic velocity, respectively.

	L_e			
Re	Present work (A)	Present work (D)	others	A_r
0.01	0.489	1.00		
0.375	0.495	1.06	0.54[5]	
0.75	0.5	1.12	1.302[1]	
			1.282[2]	
			0.08[3]	
			1.63[4]	
3.75	0.51	1.265	0.6[5]	
5	0.525	1.29	0.53[3]	
7.5	0.56	1.34	1.847[2],	
			0.8[3]	
			2.18[4]	
10	0.616	1.39	1.06[3]	
15	0.75	1.51	2.237[1]	
			2.22[2]	
			1.6[3]	
			3.0[4]	
			2.26[6]	
18.75	0.87	1.61	1.1[5]	
37.5	2.48	4.49	5.45[2]	
			4.0[3]	
			5.82[4]	
			2.6[5]	
50	3.9	6.77	5.33[3]	0.018
75	6.75	10.85	8.99[2]	0.016
100	9.54	15.00	10.6[3]	0.014
112.5	10.86	17.22	10.8[5]	0.013
150	15.06	23.31	18.06[1]	0.0109
			16.7[2]	
			18.23[6]	
375	39.68	60.00	48.85[2]	0.0051
			38.6[5]	
500	53.05	81.97	53.3[3]	0.00392
750	79.86	121.48	91.08[2]	0.00265
1000	106.07	160.45	106.6[3]	0.00192
1500	155.51	237.36	171.6[1]	0.0012
			168.8[2]	
			160[3]	
2000	199.46	312.08	213.3[3]	0.000805

4.3.2 Downstream Zone. Far downstream of the channel entry, the flow may be represented as a sum of the Poiseuille flow and a small perturbation. The decay of these perturbations deep inside the channel occurs in an exponential manner and is governed by an eigenvalue equation where the eigenvalues indicate the rate of decay of perturbations. In general, eigenvalues are complex ($\beta=\beta_r+i\beta_i$) and represent odd and even solutions. In the present study only odd solutions are of interest due to the assumed symmetry of flow. A plot of eigenvalues of interest, i.e., those with the smallest positive real part is displayed in Fig. 8. These eigenvalues correspond to the slowest decaying perturbations, which are expected to describe the flow evolution deep inside the channel. At low Reynolds number all eigenvalues are complex and disturbances associated with them decay in an oscillatory manner. As the Reynolds number is increased, the eigenvalues undergo a number of branching processes switching between being complex and real (and vice versa). As Re$\rightarrow\infty$, there exist one real $O(1/\mathrm{Re})$ and one complex $O(\mathrm{Re}^{-1/7})$ eigenvalue families (not shown). Perturbations associated with eigenvalues $O(\mathrm{Re}^{-1/7})$ are damped out rapidly and eigenvalues $O(1/\mathrm{Re})$ become dominant. Far downstream of the channel entry, relation of the form

$$\left.\frac{\partial p}{\partial x}\right|_{y=0}+\frac{2}{\mathrm{Re}}\approx A_r\exp(-\beta_r x), \tag{17}$$

approximates the decay of perturbations of pressure gradient. The value of the exponent β_r for large values of Re is given as $\beta_r \approx 28.221/\mathrm{Re}$. The values of A_r for a range of Reynolds numbers are given in Table 2.

The available numerical as well as perturbation results presented above permit determination of the channel entry zone L_e. The selection criterion is not unique and the entry length can be defined as corresponding to a location where centerline velocity reaches (A) 99%, (B) 99.5%, (C) 99.9% of its asymptotic value, respectively, (D) where $\mathrm{Re}\,\partial p/\partial x|_{y=0}$ reaches 99% of its asymptotic value, (E) where $K(x)$ reaches 95% of the fully developed value, (F) where $|(\partial p/\partial x)_{y=0}+2/\mathrm{Re}|=\exp(-10)$, or (G) where $|(\partial p/\partial x)_{y=0}+2/\mathrm{Re}-A_r\exp(-\beta_r x)|=10^{-4}$. The existing theoretical analyses use either criterion (A) [14,18,19,22,23] or criterion (E) [28,15] (the last authors required 99% of the fully developed value). Experimental works rely either on criterion (E) [17] or on the asymptotic value of the pressure gradient $\partial p/\partial x$ [10,29]. We have introduced criteria (B), (C) in order to give more insight into the physical properties of the flow. Criteria (F) and

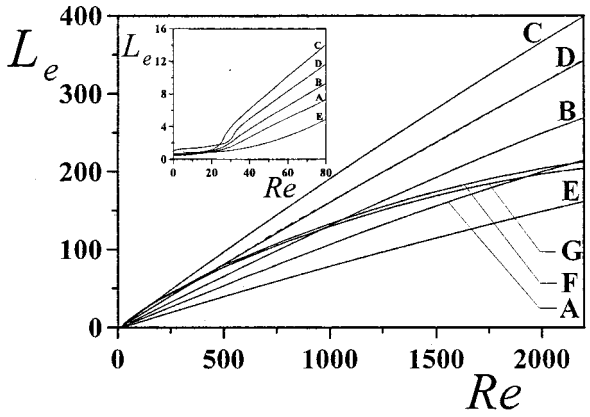

Fig. 9 Variations of the length of the channel entrance zone as a function of Re. Letters A, . . . , G correspond to the different criteria used to determine the length of the entrance zone, discussed in Section 4.3.2. Dashed lines correspond to the correlations developed in the present study. The numerical method used does not provide sufficient accuracy for application of the criteria F and G when Re<80 and thus the corresponding curves are omitted from the insert plot.

(G) are directly related to the perturbation analysis of the flow (Eq. 17). Criterion (G) estimates also the flow area where nonlinear effects are important.

The variations of the entrance length evaluated on the basis of the above criteria as a function of Re are displayed in Fig. 9, and the numerical values based on criteria (A) and (D) determined in the present analysis and found in the literature are given in Table 2. Figure 9 shows that L_e is not very sensitive to variations of Reynolds number if Re$<$20. Three out of four criteria that can be applied under such conditions, i.e., A, B, C, and E, produce very similar L_e. This lack of sensitivity can be explained by noting that for Re$<$20 the real parts of the dominant eigenvalues are quite large leading to a very rapid flow development where the difference between the flow development at various values of Re is below resolution of the criteria used. Criteria F cannot be used under such conditions due to the finite accuracy of the numerical results. For 20$<$Re$<$30 there is a transition in the character of variations of L_e as a function of Re. The reader may note that the magnitude of dominant eigenvalue changes quite rapidly with Re. When Re$\geqslant$30, the dominant eigenvalues are much smaller ($O(\mathrm{Re}^{-1})$), they decrease in a regular manner and they are fairly insensitive to variations of Re i.e., small change of Re causes only a small change in the magnitude of the eigenvalue. Because of that the flow development occurs at a slower rate over a much longer distance and the computed L_e changes smoothly with Re. All criteria used exhibit good sensitivity, however, they lead to different values of L_e (see Fig. 9) with criterion C giving the upper bound for L_e.

The available results permit us to write correlations for L_e using criterion D in the form

$$L_e = 0.166\,\mathrm{Re} - 1.619 \pm 0.1\%, \quad 50 \leqslant \mathrm{Re} < 100, \qquad (18a)$$

$$L_e = -121.617\,\mathrm{Re}^{-1} + 0.163\,\mathrm{Re} - 0.126 \pm 1.3\%, \quad 100 \leqslant \mathrm{Re} \leqslant 1000, \qquad (18b)$$

$$L_e = -1892.249\,\mathrm{Re}^{-1} + 0.151\,\mathrm{Re} + 11.726 \pm 0.5\%, \quad 1000 \leqslant \mathrm{Re} \leqslant 2200. \qquad (18c)$$

Correlations found in the literature have the forms: (i) $L_e = 8/75$ [11–12,23]; (ii) $L_e = 0.1128\,\mathrm{Re}$ [18]; (iii) $L_e = 0.1173\,\mathrm{Re}$ [7]; (iv) $L_e = 0.1179\,\mathrm{Re}$ [30]; (v) $L_e = 0.1125\,\mathrm{Re}$ [31]; (vi) $L_e = 0.16\,\mathrm{Re}$ [17]; $L_e = 0.06272\,\mathrm{Re}$ [28]; (vii) $L_e = 0.79/(0.053\,\mathrm{Re}+1)+0.071$ [14]; and (viii) $L_e = 2.5 + 0.235\,\mathrm{Re}$ [22], with the first seven claimed to be valid for large Re only.

Table 2 provides comparison between results available in the literature based on criterion (A) and the present ones. Analyses based on the uniform entrance velocity assumption [14,18,19] generally over-predict L_e. This assumption decouples the upstream and downstream regions of channel entry. At low values of Re the neglected diffusion of vorticity in the upstream region plays a significant role in the flow development. This is highlighted by good agreement with the results of Sparrow and Anderson [2] for Re$>$30 who accounted for the upstream flow region. At higher values of Re, the existing analyses [11,18,19] generally over predict L_e. At high values of Re the flow develops a vena contracta, which results in higher velocity in the inviscid core, more intense mixing and more rapid flow development. Uniform velocity assumption cannot account for this effect and leads to larger L_e. These conclusions are supported by the results of Emery and Chen [29], who considered sharp-edged entrance as a method to reduce the entry length. Comparison of the present results with Morihara and Cheng [18] and Narang and Krishnamoorthy [19] for Re$=$1500 shows that effects associated with flow separation reduce flow development length by about 10%.

5 Conclusions

An analysis of loss coefficient in the inlet region of a channel is presented. Results indicate that behavior of loss coefficient is significantly different at low and high Reynolds number. Correlation for additional pressure losses associated with the entrance effects is given. It is shown that the existing correlations significantly under predict the losses at low Re due to omission of the upstream flow development.

Correlation for the length of the entry zone is given. It is shown that the existing correlations over predict the entry length at low Re due to omission of the upstream flow development, and at high values of Re due to omission of the flow separation effects.

Acknowledgments

The NSERC of Canada supported this research. Computations were performed using the Cray J90se at the University of Western Ontario. The authors would also like to thank P.J.D. Roberts for his assistance in the editing of this work.

Nomenclature

α = kinetic energy correction factor
α_0 = kinetic energy correction factor far upstream of the channel inlet
α_1 = kinetic energy correction factor at the inlet
β = $\beta_r + i\beta_i$ dominant eigenvalue downstream of the channel entry
λ = dominant eigenvalue in the upstream region
$\overline{u}$ = average velocity
μ = dynamic viscosity
ν = kinematic viscosity
ρ = density
θ = polar coordinate
ξ = streamwise coordinate in the computational plane
η = transverse coordinate in the computational plane
A_r = constant in defined in Eq. (17)
D = hydraulic diameter
E_k = kinetic energy
f = friction factor
H = half-channel width, reference length scale
h = finite-difference grid size in the computational plane
$K(x)$ = incremental pressure drop
k = entrance loss
$k(\infty)$ = fully developed entrance loss
$K(\infty)$ = fully developed incremental pressure drop

K_1 = entrance loss between far upstream and inlet
K_i = additional pressure drop not accounted by incremental pressure drop
K_{1x} = entrance loss between inlet and location x inside the channel
L_e = entrance length
p = pressure
p_0 = pressure far upstream of the channel inlet
p_1 = pressure at the inlet
Q = volume flux
r = polar coordinate
r_s = radial distance
Re = Reynolds number $=UH/\nu$
U = maximum velocity far inside the channel; reference velocity scale
u = velocity component in the x-direction
u_r = radial velocity component in polar coordinate
u_θ = angular velocity component in polar coordinate
v = velocity component in the y-direction
$\bar{v}$ = velocity vector
x = Cartesian coordinate in the streamwise direction
x_d = channel length in the downstream direction
x_u = size of the inlet domain in the x-direction
Δx = grid spacing in the x-direction in the physical plane
y = Cartesian coordinate in the normal-to-the-wall direction
y_u = size of the inlet domain in the y-direction
Δy = grid spacing in the y-direction in the physical plane

Appendix A

Consider flow driven by a sink located on a solid wall at $y=0$. The wall overlaps with the y-axis. The fluid is located in the left half-plane. The flow is purely radial and can be expressed in the polar reference system in the form

$$u_r=F(\theta)/r, \quad u_\theta=0, \tag{A1}$$

where r is the distance from the origin. Substitution of (*A*1) into the Navier-Stokes equations and elimination of pressure leads to the following problem

$$F'''+2\,\mathrm{Re}\,FF'+4F'=0. \tag{A2}$$

The no-slip boundary equations can be expressed as

$$F=0 \quad \text{at} \quad \theta=\pm\pi/2. \tag{A3}$$

The total volume flux flowing into the sink must be equal to the volume flux flowing through the channel, which leads to an additional condition in the form

$$\int_{-\pi/2}^{\pi/2} F\,d\theta=-4/3. \tag{A4}$$

Equation (*A*2) subject to condition (*A*3)-(*A*4) has to be solved numerically.

Appendix B

The flow far upstream of the channel is represented as

$$\begin{aligned} u_r(r,\theta)&=U_r(r,\theta)+u_r'(r,\theta),\\ u_\theta(r,\theta)&=u_\theta'(r,\theta),\\ p(r,\theta)&=P(r,\theta)+p'(r,\theta), \end{aligned} \tag{B1}$$

where $U_r(r,\theta)$ and $P(r,\theta)$ denote the radial velocity and the pressure of the Jeffrey-Hamel flow, respectively, and primes denote small perturbations. The perturbations can be assumed in the form

$$\begin{aligned} u_r'(r,\theta)&=Mr^{\lambda-1}\hat{u}_r(\theta)+\text{c.c.},\\ u_\theta'(r,\theta)&=Mr^{\lambda-1}\hat{u}_\theta(\theta)+\text{c.c.},\\ p'(r,\theta)&=Mr^{\lambda-2}\hat{p}(\theta)+\text{c.c.}, \end{aligned} \tag{B2}$$

where M is an arbitrary (complex) constant and c.c stands for the complex conjugate. Substitution of (*B*1) into the field equations expressed in polar coordinates, linearization and substitution of (*B*2) into the resulting equations followed by elimination of pressure give

$$\begin{aligned} D^4\hat{u}_\theta+(\lambda^2+(\lambda-2)^2)D^2\hat{u}_\theta+\lambda^2(\lambda-2)^2\hat{u}_\theta-\mathrm{Re}(\lambda-2)F(D^2\hat{u}_\theta\\ +\lambda^2\hat{u}_\theta)+\lambda\,\mathrm{Re}\,D^2F\hat{u}_\theta+2\,\mathrm{Re}\,DFD\hat{u}_\theta=0, \end{aligned} \tag{B3}$$

subject to the boundary conditions

$$\hat{u}_\theta=0, \quad D\hat{u}_\theta=0 \quad \text{at} \quad \theta=\pm\pi/2, \tag{B4}$$

where D denotes derivative $d/d\theta$. Equation (*B*3) with boundary conditions (*B*4) represents an eigenvalue problem for λ to be solved numerically. The solution procedure used is described in Sadri [3].

Appendix C

Consider three points on a streamline overlapping with the axis of the channel with point 0 at $x=-\infty$, point 1 at the inlet ($x=0$) and point 2 inside the channel at location x. Equation (12) written between points 0-1 and 1-2 results in

$$\frac{p_0-p_1}{\bar{u}_1^2/2}=\alpha_1+K_1, \tag{C1a}$$

$$\frac{p_1-p(x)}{\bar{u}_1^2/2}=f\frac{x}{D}+\alpha(x)-\alpha_1+K_{1x}(x), \tag{C1b}$$

where $K_{1x}(x)$ accounts for the entrance losses between points 1 and 2, K_1 accounts for the entrance losses between points 0 and 1, and α_1 is evaluated from its definition using the actual velocity distribution at the channel cross-section at $x=0$. The incremental pressure drop used in the literature is defined as

$$K(x)=\alpha(x)-\alpha_1+K_{1x}(x), \tag{C2}$$

where it is evaluated assuming uniform velocity distribution at the entrance, i.e., $u|_{x=0}=\text{const}$. The reader should note that in the present study, $K(x)$ is evaluated using the actual computed velocity distribution at $x=0$. Adding (*C*1) and (*C*2) results in (14) where $K_i=\alpha_1+K_1$ accounts for the losses not included in $K(x)$.

References

[1] Shah, R. K., and London, A. L., 1978, *Advances in Heat Transfer, Laminar Flow Forced Convection in Ducts*, Academic Press, New York.
[2] Sparrow, E. M., and Anderson, C. E., 1977, "Effect Of Upstream Flow Processes On Hydrodynamic Development In A Duct," ASME J. Fluids Eng., **99**, pp. 556–560.
[3] Sadri, R. M., 1997, "Channel Entrance Flow," Ph.D. thesis, The University of Western Ontario, London, Ontario, Canada.
[4] Kays, W. M., and London, A. L., 1984, *Compact Heat Exchangers*, McGraw-Hill, New York.
[5] Gravesen, P., Branebjerg, J., and Jensen, O. S., 1993, "Microfluidic-a Review," J. Micromech. Microeng., **3**, pp. 168–182.
[6] Zou, Q., Liu, Z., and Goldberg, I. S., 1993, "On Non-Axisymmetric Entry Flow At Very Low Reynolds Numbers," Math. Biosci., **113**, pp. 245–260.
[7] Bodoia, J. R., and Osterle, J. F., 1961, "Finite Difference Analysis Of Plane Poiseuille And Couette Flow Developments," Appl. Sci. Res., **10**, pp. 265–276.
[8] Schmidt, F. W., and Zeldin, B., 1969, "Laminar Flows In Inlet Sections Of Tubes And Ducts," American Institute of Chemical Engineers Journal, **15**, pp. 612–614.
[9] Han, L. S., 1960, "Hydrodynamic Entrance Lengths For Incompressible Laminar Flow In Rectangular Ducts," ASME J. Appl. Mech., **27**, pp. 403–409.
[10] Sparrow, E. M., Liu, S. H., and Lundgren, T. S., 1964, "Flow Development In The Hydrodynamic Entrance Region Of Tubes And Ducts," Phys. Fluids, **7**, pp. 338–347.
[11] Schlichting, H., 1934, "Laminare Kanaleinlaufstömung," Zeitschrift für angewandte Mathematik und Mechanik, **14**, pp. 368–373.

[12] Schlichting, H., 1973, *Boundary Layer Theory*, McGraw-Hill, New York.
[13] Collins, M., and Schowalter, W. R., 1962, ''Laminar Flow In The Inlet Region Of A Straight Channel,'' Phys. Fluids, **5**, pp. 222–228.
[14] Chen, R. Y., 1973, ''Flow In The Entrance Region At Low Reynolds Numbers,'' ASME J. Fluids Eng., **95**, pp. 153–158.
[15] Nguyen, T. V., and Maclaine-Cross, I. L., 1988, ''Incremental Pressure Drop Number In Parallel-Plate Heat Exchangers,'' ASME J. Fluids Eng., **110**, pp. 93–96.
[16] Lundgren, T. S., Sparrow, E. M., and Starr, J. B., 1964, ''Pressure Drop Due To The Entrance Region In Ducts Of Arbitrary Cross Section,'' ASME J. Basic Eng., **88**, pp. 620–626.
[17] Beavers, G. S., Sparrow, E. M., and Magnusun, R. A., 1970, ''Experiments On Hydrodynamically Developing Flow In Rectangular Ducts Of Arbitrary Aspect Ratio,'' Int. J. Heat Mass Transf., **13**, pp. 689–702.
[18] Morihara, H. K., and Cheng, R. T., 1973, ''Numerical Solution Of The Viscous Flow In The Entrance Region Of Parallel Plates,'' J. Comput. Phys., **11**, pp. 550–572.
[19] Narang, B. S., and Krishnamoorthy, G., 1976, ''Laminar Flow In The Entrance Region Of Parallel Plates,'' ASME J. Appl. Mech., **43**, pp. 186–188.
[20] Jeffery, G., 1915, ''The Two-Dimensional Steady Motion Of A Viscous Fluid,'' Philos. Mag., **6**, pp. 455–465.
[21] Hamel, G., 1916, ''Spiralfömrige Bewegungen zäher Flüssigheiten,'' Jahresbericht der Deutschen Math. Vereinigung,, **3**, pp. 34–60.
[22] Atkinson, B., Brocklebank, M. P., Card, C. C. H., and Smith, J. M., 1969, ''Low Reynolds Number Developing Flows,'' American Institute of Chemical Engineers Journal,, **15**, pp. 548–553.
[23] Williamson, J. W., 1969, ''Decay Of Symmetrical Laminar Distorted Profiles Between Flat Parallel Plates,'' ASME J. Basic Eng., **91**, pp. 558–560.
[24] Rokicki, J., and Floryan, J. M., 1999, ''Higher-Order Unstructured Domain Decomposition Method For The Navier-Stokes Equations,'' Comput. Fluids, **28**, pp. 87–120.
[25] Floryan, J. M., and Czechowski, L., 1995, ''On The Numerical Treatment Of Corner Singularity In The Vorticity Field,'' J. Comput. Phys., **118**, pp. 168–182.
[26] Moffat, H. K., 1964, ''Viscous And Resistive Eddies Near A Sharp Corner,'' J. Fluid Mech., **18**, pp. 1–18.
[27] Fox, R. W., McDonald, A. T., 1989, *Introduction to Fluid Mechanics*, Wiley, New York.
[28] McComas, S. T., 1967, ''Hydrodynamic Entrance Length For Ducts Of Arbitrary Cross Section,'' ASME J. Basic Eng., **89**, pp. 847–850.
[29] Emery, A. F., and Chen, C. S., 1968, ''An Experimental Investigation Of Possible Methods To Reduce Laminar Entry Length,'' ASME J. Basic Eng., **90**, pp. 134–137.
[30] Brandt, A., and Gillis, J., 1966, ''Magnetohydrodynamic Flow In The Inlet Region Of A Straight Channel,'' Phys. Fluids, **9**, pp. 690–699.
[31] Hwang, C. L., and Fan, L. T., 1978, ''A Finite Difference Analysis Of Laminar Magneto-Hydrodynamic Flow In The Entrance Region Of A Flat Rectangular Duct,'' Appl. Sci. Res., Sect., **13**, pp. 329–343.

Spreading of Nonuniform Jets in Wind

S. Bhattacharyya
Department of Mathematics,
Indian Institute of Technology,
Kharagpur, 721302, West Bengal, India

F. T. Smith
Mathematics Department,
University College London,
Gower Street,
London, WC1E 6BT, U.K.

The steady flow due to a nonuniform source in an otherwise uniform stream is studied, the source taking the form of an upstream-pointing and a downstream-pointing slender jet, or sheet-jet. The planar-model setting is described, along with applications, and then viscous flow computations are presented. The results show that the sheet-jet source together with the entrainment into the jets upstream and downstream induce an almost sink-like response in the overall flow, in contrast with the effects of a uniform source. The response yields a small eddy at the higher Reynolds numbers of the computations and suggests that large-scale eddies may occur for increased Reynolds numbers; yet the uniform-source model predicts the upstream stagnation point and some other features well.
[DOI: 10.1115/1.1478063]

Introduction

The effect of a free stream on the flow emanating, in both the upstream and downstream directions, from a localized source is the present concern. As well as intrinsic interest in the problem there is practical interest also in terms of vent emissions from manufacturing plants into wind and in design of interior ventilation, as well as in the use of so-called water and air knives, shields and curtains for cleaning or protecting certain confined spaces. The spreading of fluid injected into an oncoming stream also covers the outer motion induced by the fast wing flapping of flying insects and birds. The typical Reynolds number Re varies from moderate to large in all these cases and other relevant applications, and many involve an inner local length scale and an outer scale. One example of this is in the flapping just mentioned, and another interesting case is for numerous rotor blade [1–13] and similar motions, e.g. [14] for animals with smaller typical Re, where the impact of side or head winds on flight during hovering or near-hovering conditions is significant for take-off and landing close to the ground or a floating platform. A common approach there is to focus on complex local flows possible near a helicopter blade for instance, such as with tip vortices. Our approach is to start more simply in order to increase understanding of the total flow structure more, as described in the paragraphs below, specifically for SLENDER rotating blades in the presence of *slight* wind or forward travel; although the direct application to helicopter blade flows may thus be limited a global picture of the flow in this context is provided by the current study in conjunction with previous studies.

On a local scale (see Fig. 1(*a*)) close to the blades the flow in near-hover is then past multiple successive blades almost aligned with each other's wakes, in a rotating frame. Most flow studies are on properties for an isolated blade. Inviscid fluid flow computations or direct numerical simulation at relatively low Re, and some experimental work, are discussed usually for the helicopter setting by [1–6], an interesting review being given by [7]. Theoretical works on wind effects as well as on multiple rotor blade interactions and global flow structure are few, especially concerning viscous features. The paper [8] considers three-dimensional rotating configurations of blades, such as for a cut disk, with normal symmetry and negligible free stream. The planar-flow investigation [9] admits normal nonsymmetry and notes that a quasi-periodic local flow solution emerges for the case of many blades. Many is found to mean more than about 4 in practice, indicating this case as one of practical value (see also[10,11]). Multi-blade motions are also addressed by [12] with interaction between pressure and the efflux into the outer inviscid motion. This interaction, which allows for regular flow separations, can cover an entire blade and couple short-blade and long-wake effects. The concern of [13] is with normal nonsymmetry under interaction past successive blades and wakes, and the implications for lift and drag, with each blade positioned not far from the centerline of the preceding wake.

The above investigations all omit the influence of a wind or overall free stream, however, in the context of rotary motions. Only a brief mention is made by [8] of such outer flow in the presence of comparatively strong rotation, in effect, where the influence of the free stream first enters at positions which are far outboard (Fig. 1(*a*,*b*)), i.e., at distances from the rotary system which are large compared with the maximum local rotary blade dimension. The far-outboard or more global area is important to understand and solve both in itself and because it provokes a back-effect on the local blade flows, which may be compared with the downwash in an actuator disk model and which in practice can drastically alter the flow characteristics there. A combination of theory and computation is felt to be desirable for the area, in order to develop physical and parametric understanding and suggest reasoned approximation approaches, given that the interactions involved between the local and the far outboard features can be very complex indeed. Our aim here is to accommodate the influence of a far-outboard free stream and to obtain increased understanding of the properties for the entire wake of the slender rotary system. This is of special interest at higher Re, where reliable models are required for more realistic configurations, and the question arises of how well the simple inviscid uniform-source model predicts flow features such as the upstream stagnation point, at various Re.

The setting for the present study is described in the next section, addressing first the local motion and then the consequent far-outboard flow, followed by the simpler model flow problem. The latter is for the steady planar laminar motion of an incompressible fluid subjected to a nonuniform sheet-jet source as input at the origin and to a uniform stream in the farfield. The computational method is presented in the section after that, where the numerical results and main flow properties are also discussed. Final comments are given in the concluding section, including the relevance of the current setting to the creation of large-scale eddies.

The Setting for the Jet-in-Wind Flow

For the context of rotary blades there are essentially two zones of interest at medium to high Reynolds numbers, one local to the blades and the other in the farfield or far outboard. Each is now considered in turn.

Contributed by the Fluids Engineering Division for publication in the JOURNAL OF FLUIDS ENGINEERING. Manuscript received by the Fluids Engineering Division March 29, 2001; revised manuscript received January 14, 2002. Associate Editor: T. B. Gatski.

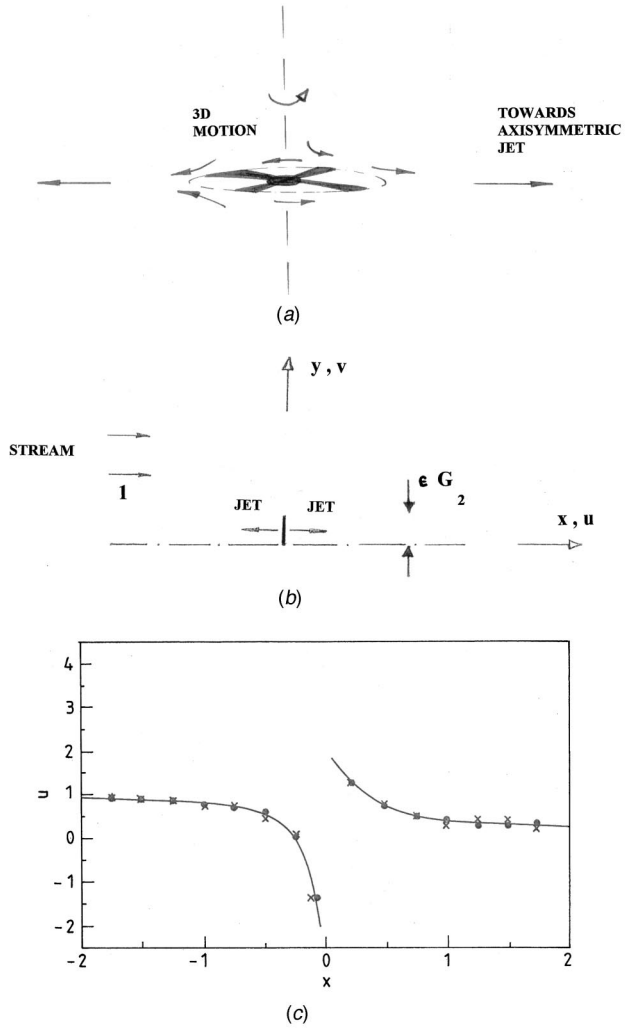

Fig. 1 Sketch of basic configuration for *slender* rotating-blade and similar motions: (*a*) local view near origin, where 3D hover details have effect; (*b*) outer problem addressed in present study, with jets of width ϵG_2 emerging outboard (non-uniform sheet-jets (2c) in a stream). (*c*) Gridsize effect on horizontal velocity along symmetry line: solid curve, grid 0.005×0.005; dots, 0.001×0.001; crosses, 0.01×0.01.

In the local motion around the system of thin, virtually horizontal, blades rotating rapidly about a vertical axis it is assumed that the flow velocities greatly exceed those of the effective free stream. This is in a frame moving with the rotating blades, and the above assumption corresponds to the relatively slow translation of the whole during take-off or landing for example. The blades themselves can be of radially increasing chord as for a cut circular disc or of fixed or nearly fixed chord as in rotorcraft applications but they have finite span (radius, measured horizontally from the axis of rotation). The effective free stream including any wind effects can be neglected here to a first approximation, leaving typical flow velocities of the order of the maximum rotation speed at most, as in [8] and related papers. The fluid rotates and centrifuges outwards radially on the multiple blades, in their multiple wakes and further outboard, i.e., at radii greater than the maximum span, in a manner which depends on the precise blade geometry and blade number in particular and is governed by thin-layer equations.

At sufficiently large radial distances, far outboard, what remains is a sheet-jet of similarity form in which the flow solution is *symmetric* about the vertical axis, independently of the number and shape of all the blades: see [8]. The far-outboard form here is dominated by the radial velocity (together with the smaller vertical velocity for continuity) with negligible azimuthal velocity but the characteristic vertical thickness increases linearly with radius due to viscous diffusion and in consequence the radial velocity itself within the sheet-jet decays algebraically. Hence at larger distances outboard the effective free-stream velocity, being approximately constant (say) although small, must make itself felt in turn, modifying the otherwise radial sheet-jet and introducing nonaxisymmetry again.

The far-outboard motion of concern, at the larger distances just mentioned, then has scales of length, velocity and pressure which are such that the three-dimensional thin-layer equations apply at first sight at least, the vertical extent being still small compared with the horizontal and the main pressure force remaining constant. The boundary conditions require matching to the assumed uniform free stream in the farfield, a stream which flows in the *x*-direction say, while the matching to the sheet-jet-like source is on approach to the origin in effect on this large-distance scale.

The source is thin, directed radially in the horizontal plane, but the resulting motion must be *nonaxisymmetric* because of the *x*-directed stream, in the current fixed frame. The motion is also complex, because separation of an unknown kind has to take place in part of the ''wind-facing'' half of the flow as the stream and jet oppose each other there and must produce a single stagnation point at least. The implied separation or flow reversal is likely to be of large scale, disrupting the original thin layer within the current outboard zone and yielding a global structure which is thicker in the vertical direction and whose form is as yet unknown. Likewise unknown or not immediately obvious is the mechanism for upstream influence in the thin layer ahead of the separation, given the absence of any solid surface in the current zone. By the same token, in part of the ''leeward'' half of the flow the stream and jet reinforce each other and the enhancement of the motion there is of interest.

With the theory faced by the above complexities as far as the far-outboard flow is concerned, the aim in the present work is to see if direct numerical simulations might act to provide further insight for the theory. It seems natural to start with the two-dimensional analogue of the setting described in the previous paragraph for the far outboard zone, an analogue which represents a fairly fundamental flow problem in its own right (Fig. 1(*b*)). This planar analogue also captures the essence of the original outboard three-dimensional problem while allowing far more accurate numerical solutions to be obtained.

Thus the appropriate continuity and Navier-Stokes equations are

$$\frac{\partial u}{\partial x}+\frac{\partial v}{\partial y}=0, \tag{1a}$$

$$\left(u\frac{\partial}{\partial x}+v\frac{\partial}{\partial y}\right)(u,v)=-\left(\frac{\partial p}{\partial x},\frac{\partial p}{\partial y}\right) \tag{1b}$$

$$+\mathrm{Re}^{-1}\nabla^2(u,v), \tag{1c}$$

for the nondimensional velocity components (u,v) in Cartesian coordinates (x,y), and the pressure p, where Re denotes the Reynolds number. The nondimensionalization is based on the dimensional freestream speed U^* and a characteristic distance ℓ^* obtained from comparing the mass flux $|\psi^*|$ of the jet and U^*, by analogy with the known properties of a uniform source in a stream. Thus the dimensional velocities and lengths are $U^*(u,v)$ and $\ell^*(x,y)$ respectively, where $\ell^*\equiv|\psi^*|/\alpha_1 U^*$, and $\mathrm{Re}\equiv U^*\ell^*/\nu^*$, with ν^* being the kinematic viscosity. In our case of (3) below the nondimensional parameter α_1 is represented by $L/3$ for convenience. The boundary conditions are

$$(u,v)\rightarrow(1,0) \text{ in the farfield,} \tag{2a}$$

$$\frac{\partial u}{\partial y} = v = 0 \quad \text{at} \quad y = 0, \tag{2b}$$

$$u \to \pm G_1(y/\epsilon)/\epsilon, \quad v \to 0, \quad \text{as} \quad x \to 0\pm \quad \text{for} \quad 0 \leqslant y \leqslant \epsilon G_2 . \tag{2c}$$

Clearly (2*a*,*b*) are required for the free-stream constraint and an assumed vertical symmetry in y. Condition (2*c*) represents an analogue, or approximation, to the matching with a sheet-jet at the origin described previously wherein ϵ is a small positive constant while the positive function G_1 and the positive constant G_2 are of order unity: see Fig. 1(b) and precise forms in the next section. The function G_1 is zero at the top $y = \epsilon G_2$ to represent a jet profile, has zero derivative at $y = 0$ for vertical symmetry, and is generally positive so that a source rather than a sink is implied, with jet velocities directed horizontally outward from the origin. The jet-width constant ϵ is broadly of a size comparable to $\mathrm{Re}^{-1/2}$ (see specific value below), the standard thin-layer scale for large Re, but otherwise measures the input jet width (or inverse velocity scale). The condition (2*c*) is also associated with a generalization of that for a conventional uniform point source since here substantial vorticity is introduced by means of the jets emerging in the upstream and downstream directions from the origin.

Computational Method and Solution Properties

We used the alternating-direction implicit scheme (ADI) in discretizing the fictitious time derivatives for this steady problem. A third-order upwind difference scheme is employed to discretize the convective terms in the vorticity transport equation. A central difference scheme is used for the second order diffusive terms. At every time step the Poisson equation for the stream function likewise derived from (1*a*–*c*) is solved through the successive over relaxation (SOR) method. A detailed description of the method is in [15], the resulting showing good agreement with theory.

To check on how much the numerical solution is dependent on grid size, the grid sizes around the obstacle were made to range between 0.001×0.001 and 0.01×0.01 at selected Reynolds numbers. The effects of grid sizes on the solution were found to be minimal: Fig. 1(c). We found that a grid size of 0.005×0.005 near the origin produces the optimal solution. The fictitious time step was taken as 0.001 originally but was then increased at subsequent times t.

The computational results are shown in Figs. 2–5. These are all for cases where (2c) has

$$G_1/\epsilon = [1 - (y/\epsilon)^2]L/(4\epsilon) \tag{3}$$

and the positive jet-strength parameter L is 0(1), while the jet-width constant ϵ is set as 0.1 throughout and G_2 is unity. Varying L corresponds to varying the strength and form of the input jets.

Figs. 2(a–c) shows the streamline solutions in close-up for the case $L = 1$ with Re equal to 50, 100, 130, respectively. The gradual increase in upstream influence (horizontally) and also in the vertical spread of injected fluid both near the origin and everywhere downstream are clear as Re is increased. Figure 3(a–c) is likewise for the value $L = 1$, presenting in turn vorticity contours at Re=100, the plots of the center-line velocity u along the x-axis ahead of and downstream of the jets source as Re is varied from 50 to 120, and the velocity vectors calculated for Re=130. The increase of upstream influence and vertical spread is again evident. Varying L to show the effects of the form of the sheet jets is found to largely confirm the above trends. The case $L = 2$ is addressed in Fig. 4(a–c) where, respectively, the streamlines at Re=50 and then velocity vectors at Re=30 and 50 are presented. An additional property, however, is that the enhanced L value now provokes an eddy of weakly recirculating motion which stretches from upstream to downstream of the origin, above the source(s). The same feature of an embrionic eddy is observed in the case $L = 3$: see Fig. 5(a–d) which shows the streamlines at Re=20, 30 (shown on a broader scale than in Fig. 4(a)) and the associated velocity vectors and which indicates an increasing of eddy size with Re increasing.

The results are somewhat reminiscent at first of a simple potential-flow-and-source model, at the higher values of Re. The model has complex potential $z + \Gamma$ ($\ln z - i\pi$) say where $z = x$

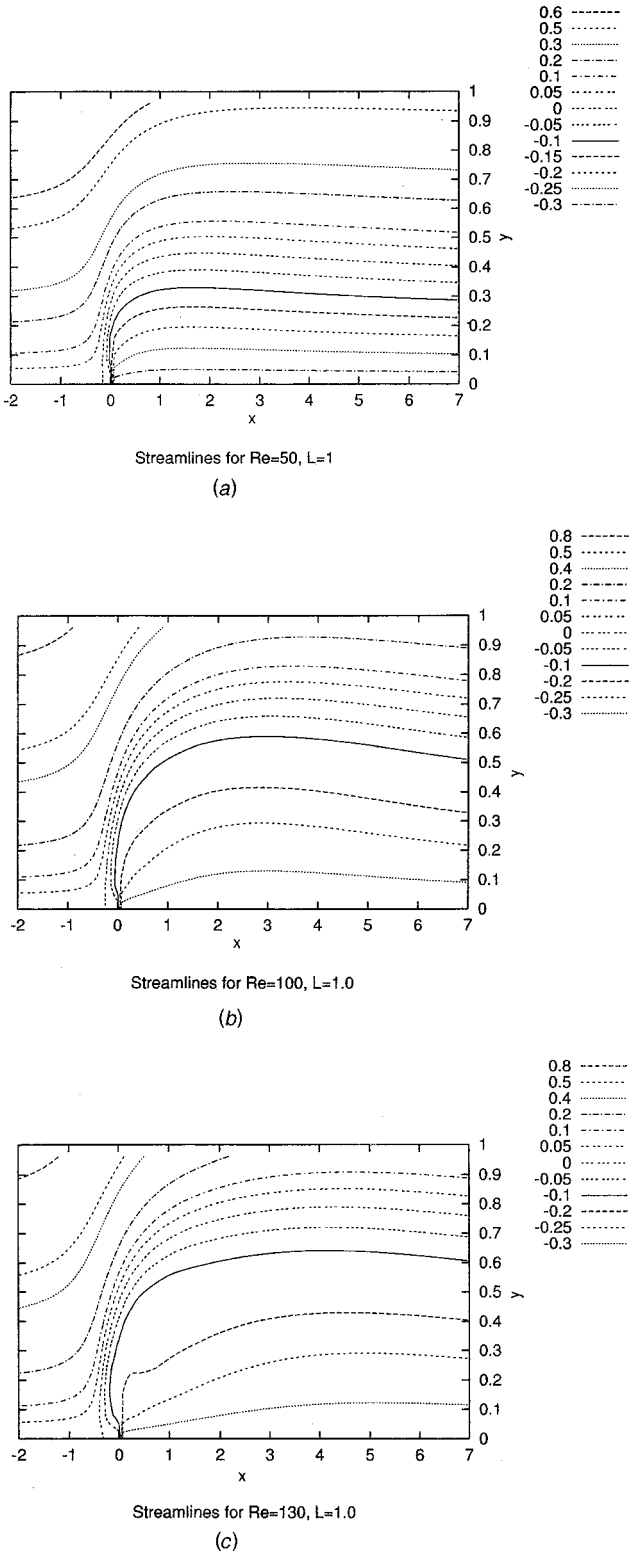

Fig. 2 Plots of computed streamlines for case $L = 1$. Reynolds number is (*a*) 50, (*b*) 100, (*c*) 130.

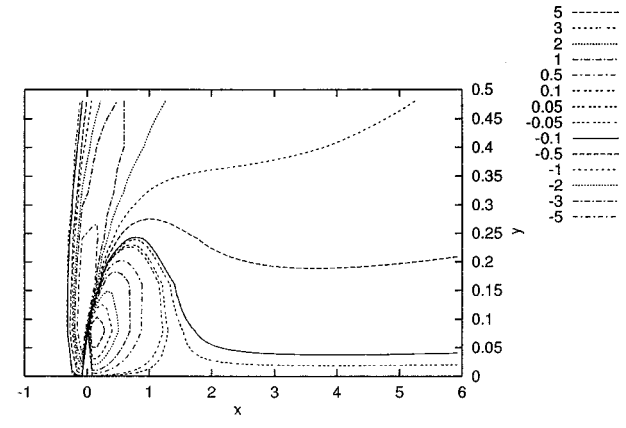

(*a*)

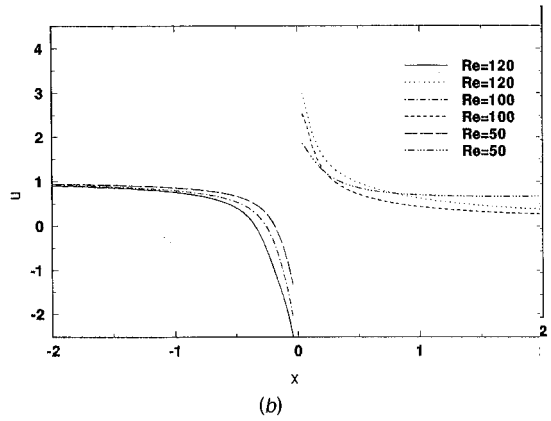

(*b*)

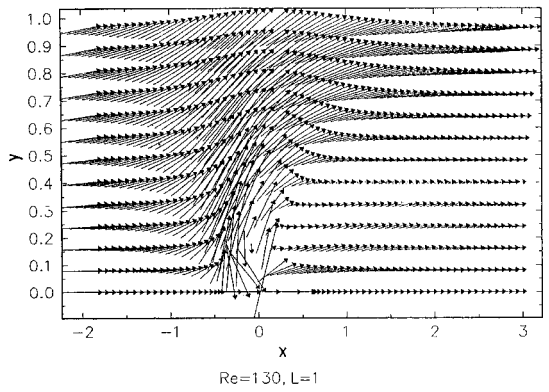

(*c*)

Fig. 3 For the case $L=1$: (*a*) vorticity contours at Re=100; (*b*) centerline velocity versus *x*, for various Re, upstream and downstream of source; (*c*) velocity vectors at Re=130

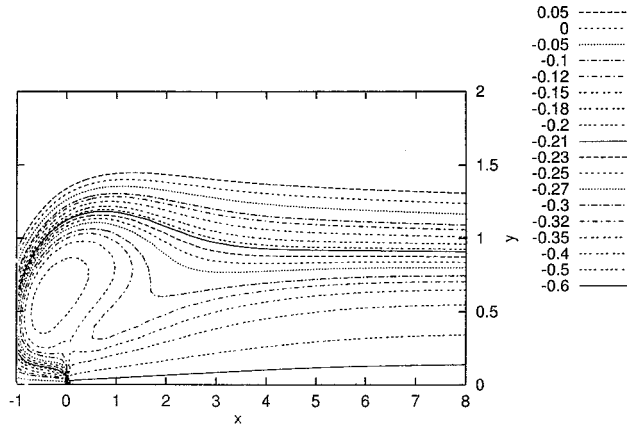

(*a*)

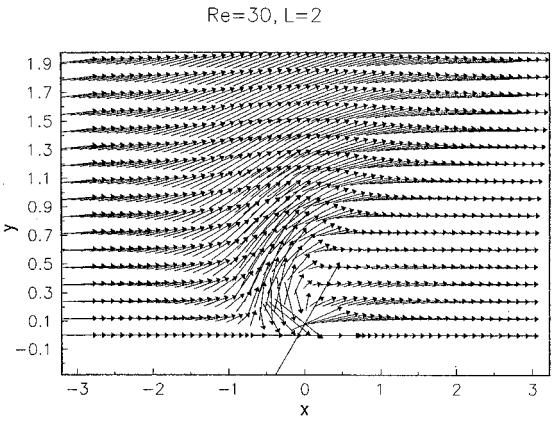

(*b*)

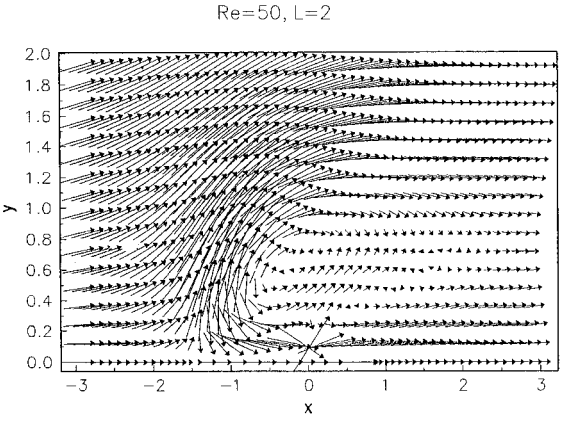

(*c*)

Fig. 4 For case $L=2$: (*a*) streamlines at Re=50; (*b*), (*c*) velocity vectors at Re=30, 50

$+iy$, so that $u-iv=1+\Gamma z^{-1}$, and Γ being positive represents the source strength. Hence $u=1+\Gamma r^{-1}\cos\theta$ in terms of plane polars ($x=r\cos\theta$,$y=r\sin\theta$), yielding u equal to $1-\Gamma r^{-1}$ upstream along $\theta=\pi$ and $1+\Gamma r^{-1}$ downstream along $\theta=0$. This trend for the induced u along the x-axis resembles the computational findings for u in the above figures. We note that the injected mass flux into the upper half plane is $\Gamma\pi$ here, as opposed to the $-\psi$ value $L/3$ along the positive x-axis in the computations. If the input source at the origin were indeed uniform in space then the potential-flow solution would be the appropriate solution of the Navier-Stokes equations, at least at high Re. Open separation would also be implied then. This is in the sense that the dividing streamline between source (injected) fluid and free-stream fluid would reach upstream as far as the stagnation point at $(x,y)=(-\Gamma,0)$ and then travel downstream in the upper half plane along the curve $y=\Gamma(\pi-\theta)$, asymptoting to the nonzero value $\Gamma\pi$ far downstream. There the gap between the x-axis and $y=\Gamma\pi$ far downstream would be filled with injected fluid all moving in the streamwise direction at unit velocity.

As it is, the input source is jet-like. Assuming that the input fluid stays in jets at first, and discounting any variation of the

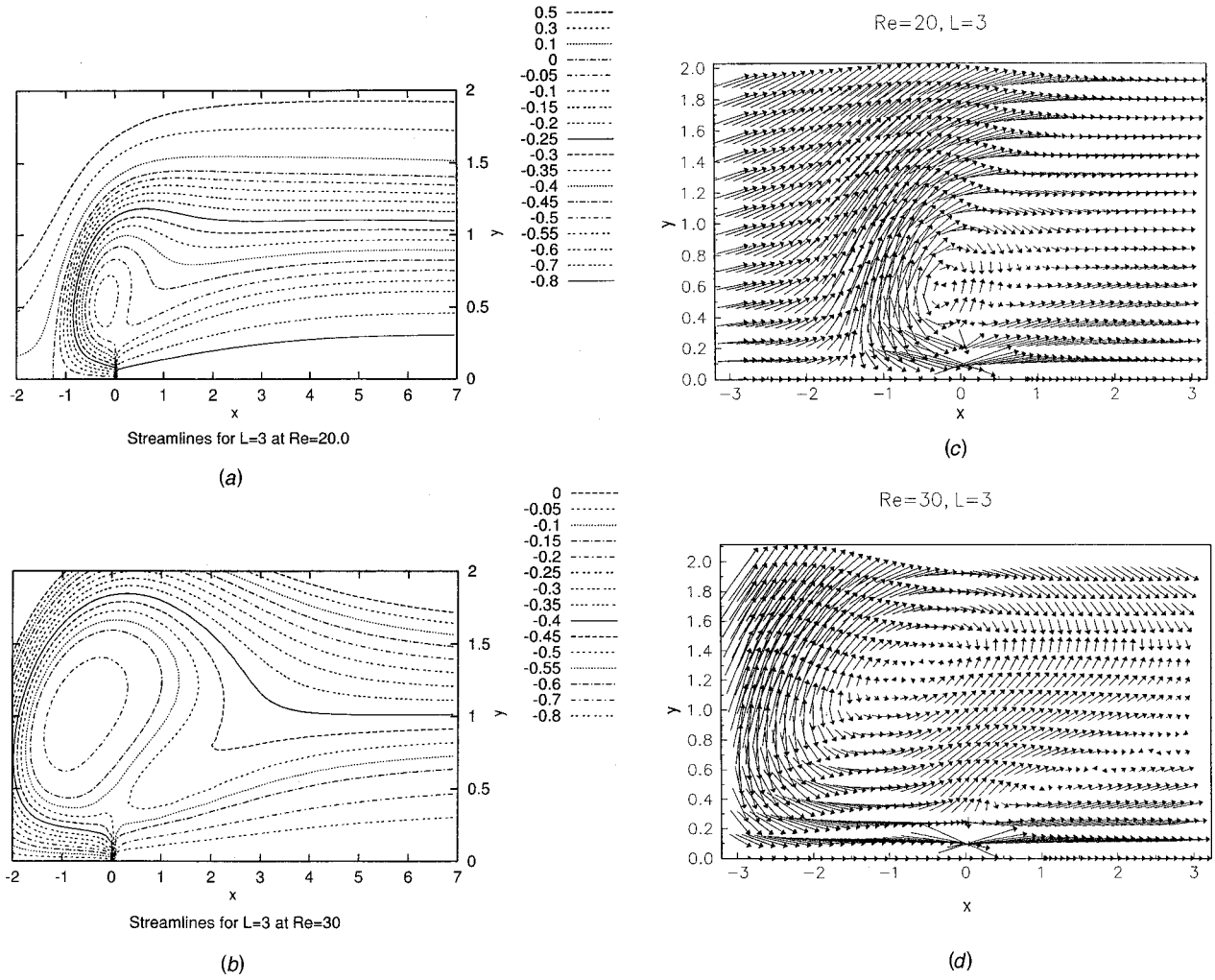

Fig. 5 The case $L=3$, showing (*a*, *b*) streamlines for Re=20, 30, and (*c*, *d*) velocity vectors for Re=20, 30

parameter ϵ with Re, we model the flow at moderate to large Re with four flow regions 1-4 in the main for the 0(1) length scale in x. These are brought about by the input jets and the positive entrainment into them, coupled with the uniform stream. Indeed, the physical basis for the present asymptotic argument lies in the prolonged thinness of the jets at moderately large Re. Region 1 begins as the upstream moving thin jet which is centered on the negative x-axis but, following stagnation and separation, thereafter is adjacent to the dividing streamline in the upper half plane where fluid from that jet and fluid from the free stream meet to form a thin free shear layer. Region 2 is the downstream moving thin jet, again emanating from the origin. Formally both of regions 1,2, expand slowly as $\mathrm{Re}^{-1/2}x^{2/3}$ at increasing positive x. Region 3 is a larger predominantly inviscid region, between 1,2, where the flow is driven by the need to supply entrainment (positive mass flux) into both 1,2. The thickness of region 3 is of order unity so that the typical pressures produced outside, in region 4 on the other side of the shear layer 1, are of order unity; region 4 is one of potential flow under a uniform stream, past the effective body shape formed by 3. The 0(1) pressures there are sufficient to affect the velocities by an 0(1) amount and in particular to reduce the velocity along the symmetry line $y=0$ from 1 far upstream to zero at the stagnation point along the negative x-axis. The same feature arises in different form in the potential-flow model of the previous paragraph. The entrainment required in region 3 however implies that at least some of the flow far downstream in 3 is reversed, in contrast with that of the earlier model, if the separation is open. If eddy closure occurs downstream, see also the computations, the suggestion is that a substantial recirculating eddy motion must be set up in order to supply the entrainment above. This relatively large closed-separation eddy is likely to be of the Prandtl-Batchelor or Sadovsky form as in [16–19] and it would seem to be indicated in embryo in the earlier computations. Again there is a contrast with the potential-flow model.

It is interesting to examine how well the uniform-source model performs, however, at the present Re values. The model simply equates the constant Γ with $L/(3\pi)$, due to the input mass flux. So the upstream stagnation point is predicted to lie at a distance $L/(3\pi)$ ahead of the source, i.e., a distance 0.106 for the case $L=1$. This predicted distance is quite near that observed in the computed results in Figs. 2 and 3 over the current range of Reynolds numbers. Also, the spread $\Gamma\pi$, i.e. $L/3$, i.e., 0.33 in the $L=1$ case, from the uniform-source model, is not far from that in the computational findings downstream. Indeed this spread is attained well sufficiently far downstream in the computations, as mass and momentum conservation require. The maximum spread in the computations exceeds that value considerably, however. This is essentially because of the vertical entrainment downwards in the sense of the figures presented, which is in line with the influences of the sheet-jets described in the previous paragraph and in some cases the presence of an induced eddy blocking the motion.

An alternative model for large Re should also be mentioned, namely that the dominant y-scale remains small of the order

$Re^{-1/2}$ throughout, which points instead to the boundary-layer equations holding throughout, with thin-layer flow sweeping not only upstream of but also directly over the input source. Such a suggestion is compelling but fraught with snags: on the mechanism for substantial upstream influence in the uniform stream, the separation process, the absence of 0(1) pressures due to the outer flow. Similar snags occur if the eddy closure is assumed to take place over a longer viscous distance downstream, with y of order unity, for although the boundary layer equations then apply there is again no mechanism to support a sufficiently strong pressure variation.

Final Comments

The simple uniform-source model clearly works well in many respects, quantitatively or qualitatively, even if it omits important effects such as entrainment and in some cases eddy formation. Concerning the original rotor and similar applications, the computational results provide some inkling of the wind effects sweeping over a rotor system (in the coordinate frame of the rotor), on a large scale, even if the present model may be more relevant in practice to other applications mentioned in the Introduction. The results also give some guidance to the theory, although the range of Reynolds numbers covered by accurate flow solutions is still relatively low. It would be helpful if this range could be extended upwards successfully. The computations do not highlight firmly yet a particular flow model valid for increasing Reynolds numbers but if the closed eddy with substantial velocities and pressures described in the previous section is the true limit then it is of some significance that the present inner-outer configuration provides a setting, for such an eddy, which is perhaps more realistic than that of conventional flow past a bluff body. The setting also provides insight into the general spreading of injected fluid in wind.

There is a further need eventually to extend the study to three dimensions, as discussed in the first two sections of the paper, concerned with the radial sheet-jet. This seems just as relevant in practice as the extension to unsteady motion, and perhaps more so. In three-dimensional flow, clearly part of the fluid from upstream can pass around the origin instead of having to pass over the origin. Another important extension, given the contexts of take-off and landing of rotorcraft and animals, is to incorporate the influences from nearby ground and other solid structures. Efforts in this direction are presented by [20].

Acknowledgments

Thanks are due to EPSRC, UK, for the funding of a Visiting Fellowship for S.B. to visit University College. Helpful referees' comments are gratefully acknowledged.

References

[1] Davis, S. S., and Chang, I.-C., 1986, "The Critical Role of Computational Fluid Dynamics in Rotary-Wing Dynamics," AIAA paper no. 86-0336.
[2] Strawn, R. C., and Caradonna, F. X., 1986, "Numerical Modeling of Rotor Flows With a Conservative Form of the Full-Potential Equations," AIAA paper no. 86-0079.
[3] Seddon, J., 1990, *Basic Helicopter Dynamics*, BSP Prof. Books.
[4] Brouwer, H. H., 1992, "On the Use of the Method of Matched Asymptotic Expansions in Propellor Aeronautics and Astronautics," J. Fluid Mech., **242**, pp. 117–144.
[5] Landgrebe, A. J., 1994, "New Direction in Rotorcraft Computational Aerodynamics Research in the U.S.," AGARD Rept. 1.
[6] Wake, B. E., and Baeder, J. D., 1994, "Evaluation of the TURNS Analysis for Hover Performance Prediction," Am. Helic. Soc. Aeromech. Spec. Conf., Jan., San Fransisco, CA.
[7] Conlisk, A. T., 1994, "Modern Helicopter Aerodynamics," Annu. Rev. Fluid Mech., **21**, pp. 515–567.
[8] Smith, F. T., and Timoshin, S. N., 1996a, "Blade-Wake Interactions and Rotary Boundary Layers," Proc. R. Soc. London, Ser. A, **A452**, pp. 1303–1329.
[9] Smith, F. T., and Timoshin, S. N., 1996b, "Planar Flows Past Thin Multi-Blade Configurations," J. Fluid Mech., **324**, pp. 355–377.
[10] Hawkings, D. L., and Lowson, M. V., 1974, "Theory of Open Supersonic Rotor Noise," J. Sound Vib., **36**, pp. 1–20.
[11] Parry, A. B., and Crighton, D. G., 1989, "Asymptotic Theory of Propellor Noise: 1. Subsonic Single-Rotation Propellor," AIAA J., **27**, pp. 1184–1190.
[12] Bowles, R. G. A., and Smith, F. T., 2000a, "Interactive Flow Past Multiple Blades and Wakes," Q. J. Mech. Appl. Math., **52**, pp. 1–45.
[13] Bowles, R. G. A., and Smith, F. T., 2000b, "Lifting Multi-Blade Flows with Interaction," J. Fluid Mech., **415**, pp. 203–226.
[14] Rayner, J. M. V., 1979, "A Vortex Theory of Animal Flight. Part 1. The Vortex Wake of a Hovering Animal," J. Fluid Mech., **91**, pp. 697–730.
[15] Bhattacharyya, S., Dennis, S. C. R., and Smith, F. T., 2001, "Separating Shear Flow Past a Surface-Mounted Blunt Obstacle," J. Engg. Math., **39**, pp. 47–62.
[16] Smith, F. T., 1985, "A Structure for Laminar Flow Past a Bluff Body at High Reynolds Number," J. Fluid Mech., **155**, pp. 175–191.
[17] Smith, F. T., 1986, "Concerning Inviscid Solutions for Large-Scale Separated Flows," J. Eng. Math., **20**, pp. 271–292.
[18] Peregrine, D. H., 1985, "A Note on the Steady High-Reynolds-Number Flow About a Circular Cylinder," J. Fluid Mech., **157**, pp. 493–500.
[19] Chernyshenko, S. I., 1998, "Asymptotic Theory of Global Separation," Appl. Mech. Rev., **51**, pp. 523–536.
[20] Purvis, R., 2002, "Rotor Blades and Ground Effect," Ph.D. thesis, Univ. of London.

Pascal Jay
Assistant Professor

Albert Magnin
CNRS Researcher

Jean Michel Piau
Professor

Laboratoire de Rhéologie,
BP 53, Domaine Universitaire,
38041 Grenoble Cedex 09, France

Numerical Simulation of Viscoplastic Fluid Flows Through an Axisymmetric Contraction

Flows of viscoplastic fluids through sudden, conical axisymmetric contraction are studied. A finite-element numerical simulation is performed using a biviscosity approximation. Inertia is neglected. The effects of yield stress are analyzed, as are those of shear-thinning, contraction angle, and contraction ratio. The pressure losses, detailed structure of the flow such as the rigid static and moving zones, and the vortex are given in relation to these parameters. Consistent comparisons are also made with the experimental results obtained in the laboratory. [DOI: 10.1115/1.1486472]

1 Introduction

Some fluids such as gels, slurries, and pastes exhibit no deformation under a certain level of stress and flow above. These fluids are called ''yield stress fluids'' or ''viscoplastic fluids.'' The Herschel-Bulkley and Bingham models (Prager [1]) are generally used to give an approximate representation of this type of behavior. At very high stress levels, the former is equivalent to a power law model and the latter to a Newtonian one. Plasticity renders numerical and experimental studies of this type of fluid highly specific and works on viscoplastic fluids are far less numerous than those on viscoelastic ones. Many publications, such as those by Nguyen and Boger [2], Wilson [3], Piau [4,5], and Barnes [6] discuss this field of research.

Several theoretical papers have been published on the behavior of viscoplastic fluids flowing through a contraction.

In the planar case, Coupez et al. [7] used an augmented Lagrangian method to solve flows of Bingham fluids. They calculated the yielded zone in the case of an 8:1 contraction with a 45 deg contraction angle. Bingham numbers varied between 4×10^{-2} and 20. Isayev and Huang [8] proposed a study of a viscoelastic plastic medium for a constant 4:1 contraction and expansion with entrance angles of 90, 45, and 15 deg. They give the yielded surface locations for different flow rates, the recirculation area in the entrance corner and the pressure. Gans [9] presents a lubrication-type analysis for a Bingham fluid in a contraction connecting two parallel plates for a variety of contraction ratios ranging from 1:1 to 4:1. He discusses the presence of a floating core in the downstream flow and shows the core length as a function of the contraction ratio.

With regard to axisymmetric conditions, Magnin and Piau [10] demonstrated the importance of yield stress on the flow structure and pressure drop both numerically and experimentally in the case of a 1:4 expansion and contraction. Mitsoulis et al. [11] have studied numerically the flow of a viscoplastic material through extrusion dies (contraction ratio of 10:1) by using a Herschel-Bulkley model. They have shown the extent and shape of the yielded/unyielded regions and the importance of viscous dissipation.

Abdali et al. [12] investigated the flow of a Bingham fluid for a 4:1 abrupt contraction in planar and axisymmetric dies. The yield stress was set at between 1 and 2.7, which corresponds to Bingham numbers (Bi) representing the yield effect (with the definition given in this work) from 1.95 to 264. Results were given concerning particularly the shape of the yielded surfaces, the entrance and exit correction and the swell ratio, in relation with the yield stress.

From a technological point of view, for example to design an industrial process, it is very important to know the structure of the flow and how it changes in accordance with the governing parameters. In some industrial cases (such as food and pharmaceutical products, etc.), it is necessary to eliminate rigid static zones or reduce the size of the vortex. To design the process, it is also necessary to know pressure losses.

The purpose of this paper is therefore to extend, supplement, and check the numerical results available (Magnin and Piau [10], Mitsoulis et al. [11], Abdali et al. [12]) concerning the flow of a viscoplastic fluid through sudden conical and axisymmetric contractions (Fig. 1) in isothermal conditions. This study is performed for a wide range of Bi numbers (from 0 to 100). The influence of contraction angle and of contraction ratio are also studied for a large number of cases. Contraction angles of between 20 and 90 deg were chosen and contraction ratios of between 2:1 and 8:1.

The first part discusses the methods used for the numerical modeling, i.e., the adaptation of the model, the characterization of unyielded zones, and pressure loss calculations, as well as the experimental apparatus. The second part presents and analyzes the results obtained for the detailed structure of the flow and pressure losses. The third part compares a number of numerical results with the experimental ones for different contraction angles.

2 Numerical Modeling

The axisymmetric incompressible flow of a viscoplastic fluid in isothermal conditions with no slip at the wall is considered. The governing equations of the flow are therefore the conservation of mass and momentum. Inertia is neglected. The finite-element program ''Polyflow'' developed by Fluent Inc. was used. This code is based on mixed pressure-velocity formulation, accepted algorithm for steady state viscous approximation. The resolution is based upon an iterative Newton scheme coupled with Picard iterations (Crochet et al. [13]). Convergence is achieved when the norm of the change in solution vector between successive iterations is less than 10^{-5}.

2.1 Adaptation of the Model. If we call $\mathbf{T}$ the extra-stress tensor, $\mathbf{D}$ the rate of deformation tensor, $\dot\gamma$ the rate of deformation intensity defined as a second invariant of $\mathbf{D}$ ($\dot\gamma=\sqrt{2\mathbf{D}:\mathbf{D}}$), τ_0 the yield stress, K the consistency factor, n the shear-thinning index, T_{II} the second invariant of $\mathbf{T}$ (defined by a relation similar to $\dot\gamma$), the Herschel-Bulkley model is defined by the equations:

$$\mathbf{T}=2\left(\frac{\tau_0}{\dot\gamma}+K\dot\gamma^{(n-1)}\right)\mathbf{D} \quad \text{if} \quad T_{II}>\tau_0^2$$

$$\mathbf{D}=0 \quad \text{if} \quad T_{II}\leq\tau_0^2 \tag{1}$$

Contributed by the Fluids Engineering Division for publication in the JOURNAL OF FLUIDS ENGINEERING. Manuscript received by the Fluids Engineering Division June 8, 2001; revised manuscript received March 20, 2002. Associate Editor: G. Marshall.

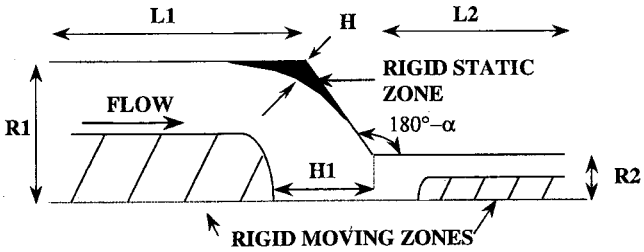

Fig. 1 Domain of the flow. Definition of R1, R2, L1, L2, α, H, and H1.

for the Bingham model n=1.

This model presents a singularity: the viscosity becomes infinite when the shear rate vanishes. Two solutions can be found in the literature to overcome this difficulty. The first one was proposed by Papanastasiou [14] and involves introducing an exponential part in the viscosity expression. This method has been widely used by numerous authors (Mitsoulis et al. [11], Loest et al. [15], Abdali et al. [12], Isayev and Huang [8], Beaulne and Mitsoulis [16], Burgos et al. [17,18], Alexandrou et al. [19]). It is also possible to introduce a biviscosity model as proposed by Lipscomb and Denn [20] and also extensively used by different authors (O'Donovan and Tanner [21], Magnin and Piau [10], Wilson [3], Vradis and Ötügen [22], Jay et al. [23]). Under a critical shear rate $\dot{\gamma}_c$, the viscosity is constant and equal to the viscosity obtained at $\dot{\gamma}=\dot{\gamma}_c$. Above $\dot{\gamma}_c$ the viscosity is given by the model. So Eqs. (1) become:

$$\mathbf{T}=2\left(\frac{\tau_0}{\dot{\gamma}}+K\dot{\gamma}^{(n-1)}\right)\mathbf{D} \quad \text{if} \quad \dot{\gamma}>\dot{\gamma}_c$$

$$\mathbf{T}=2\left(\frac{\tau_0}{\dot{\gamma}_c}+K\dot{\gamma}_c^{(n-1)}\right)\mathbf{D} \quad \text{if} \quad \dot{\gamma}\leqslant\dot{\gamma}_c \tag{2}$$

Burgos et al. [17], in a very detailed study, discussed the ability of a Herschel-Bulkley model transformed into a two-viscosity model or a Papanastasiou model (but also into the Bercovier and Engelman models) to determine the limits of the unyielded regions in the case of shear flow in a wedge between two rigid walls. They conclude that with a proper choice of the regularizing parameters, the regularized models can be used to both predict the bulk flow and describe the unyielded zones. And they add that Papanastasiou model predicts well the yield regions while the both the Papanastasiou and the biviscosity models predict well the stress field away from the yield stress.

In a previous paper (Jay et al. [23]), it has been shown in the case of a sudden axisymmetric expansion that with an optimal choice of the critical shear rate, it is also possible to achieve with a biviscosity model a good determination of the yield surface. The numerical simulations have been compared with both analytical solutions and experimental visualisations.

So this biviscosity model has been used still in this study.

2.2 Nondimensionalization. The problem was rendered dimensionless by scaling velocities with the average velocity V2 in the small tube, distances with the radius R2 of the same tube and the viscosity with *K*. The dimensionless flow rate is then equal to π.

As inertia is neglected, there are just two dimensionless numbers, *n*, the shear-thinning index and Bi, the Bingham number defined by:

$$\mathrm{Bi}=\frac{\tau_0}{K\left(\frac{V_2}{R_2}\right)^n} \tag{3}$$

2.3 Characterization of Vortex and Unyielded Zone. The stream function ψ is set to 0 at the wall. So the limit between the main flow and the vortex is determined by tracking the isoline $\psi=0$.

The limit of the yielded/unyielded zones is defined by $\dot{\gamma}=\dot{\gamma}_c$. Afterwards the unyielded zones in contact with the wall are called rigid static zones (here in the corner of the contraction) and the central ones are called rigid moving zones. In a preceding work (Jay et al. [23]) the value $\dot{\gamma}_c=10^{-5}$ has been determined. This value has been also used in this work.

2.4 Pressure Loss Measurement. Pressure losses were characterized by the equivalent entrance length defined by:

$$L_{\mathrm{eq}}=\frac{\Delta P_s}{2\sigma_{\omega_2}}=\frac{\Delta P-\Delta P1-\Delta P2}{2\sigma_{\omega_2}} \tag{4}$$

where ΔP_s represents the additional pressure loss due to the singularity; ΔP is the total pressure drop, $\Delta P1$ ($\Delta P2$) the pressure drop in fully developed Poiseuille flow in the entrance (exit) tube, and σ_{ω_2} the wall shear stress in the exit tube.

2.5 Meshes and Boundary Conditions. The aim is to study numerous geometries, so in order to reduce the influence of the meshes on the results and to achieve a reasonable CPU time, they must be designed carefully. The mesh influence on both the shape of the unyielded zones and the pressure losses has been then systematically studied. Figure 2 shows examples of meshes for three contraction angles. In the contraction part, the mesh is very refined in order to have a very accurate definition of the flow structure (unyielded zones and vortices). In this part, results are mesh independent. The rest of the mesh corresponding to the main flow has larger elements to keep a reasonable CPU time. In this part, the evolutions with the mesh of the characteristic lengths of the rigid moving zone (radius, establishing lengths, . . .) can be considered as negligible. Pressure losses are also mesh independent. For these three cases, the number of nodes is respectively of 4247, 5557, 7123, for the 20, 60, 90 deg contraction angle.

For all the meshes, the length of the small tube is 20 times R2 and the total length varies from 45 to 60 times R2 depending on the contraction ratio and angle. With these lengths, the fully developed conditions upstream and downstream are verified.

The no-slip condition is imposed at the wall.

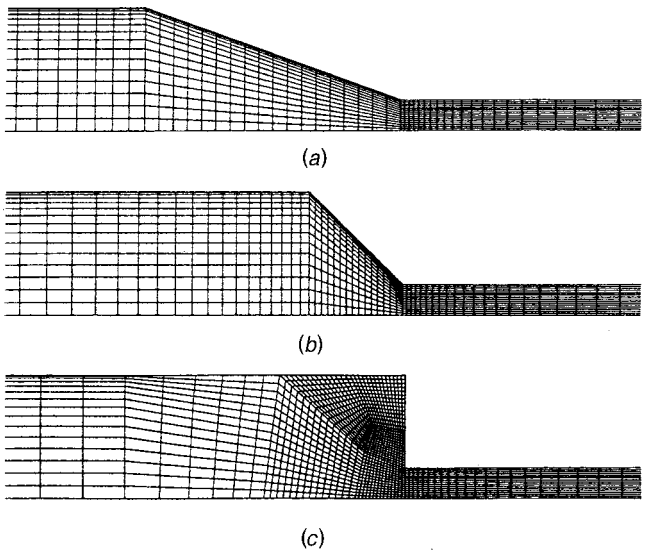

Fig. 2 Example of 3 meshes. Case of the 4:1 contraction ratio. (*a*) Contraction angle=20 deg 4247 nodes; (*b*) contraction angle=60 deg 5557 nodes; (*c*) contraction angle=90 deg 7123 nodes.

3 Experimental Setup

A specific experimental setup was designed and built at the Laboratoire de Rhéologie for the study of yield stress fluid flows through axisymmetric expansions and contractions (Belhadri et al. [24]). Original processes and technological solutions were used to overcome the problems occurring with yield stress. The polymer used, Carbopol 940, is a shear-thinning transparent yield stress fluid. It has been rheometrically characterized and shown to follow a Herschel-Bulkley model (Magnin and Piau [25]). Streamlines in the median plane were obtained by dispersing a tracer in the gel. The tracer was illuminated by a HeNe laser slit.

4 Results

4.1 Structure of the Flow. The flow of a viscoplastic fluid in a tube with a contraction has a particular structure. The fully developed flows in the entrance and exit tubes consist of peripheral viscous flow zones and ''central rigid moving zones.'' In the contraction corner, there is a vortex and/or a rigid static zone (Fig. 1). In these static and moving zones, the fluid does not flow and the shear stress is below the yield stress.

In this part, this structure is studied as a function of the shear-thinning index, the Bingham number, the contraction angle and the contraction ratio.

4.1.1 Influence of the Shear-Thinning Index. When the shear-thinning index decreases from $n=1$ (Bingham fluid) to $n=0.36$ (value obtained rheometrically for our experimental fluid) the same observations may be made as for an expansion flow (Jay et al. [23]); for Bi numbers lower than 1, the size of the rigid moving zones decreases drastically: the radius of these zones is almost halved from $n=1$ to $n=0.36$. In the corner, as for a purely shear-thinning fluid (Kim et al. [26]), the size of the vortex decreases drastically with the decrease in shear-thinning index. The same is true for the dimension of the rigid static zone. For greater Bi numbers (>10), there are few differences between $n=1$ and $n=0.36$.

4.1.2 Influence of the Bingham Number.

(a) Rigid moving zone

Figure 3 shows the overall change in flow versus the Bi number for $n=1$ (Bingham fluid). The structure of the flow is characterized principally by a central rigid moving zone both upstream and downstream. In the case of small Bi numbers (e.g., $\mathrm{Bi}=1$) the size of the downstream rigid moving zone is very limited. The upstream zone already takes up roughly 70% of the flow. On the other hand, for $\mathrm{Bi}=100$, these two zones take up a large part of the flow both upstream and downstream. When the Bingham number increases, the diameter of these zones increases but in addition, their extremities grow towards the corner. For the fully developed flows, it is possible to obtain the radius of the rigid moving zones analytically (Jay et al. [23]).

It is possible to notice on Fig. 3 that there are few differences between the radius of the upstream rigid moving zones in cases $\mathrm{Bi}=10$ and $\mathrm{Bi}=100$. It can be shown analytically that the difference in radius between these two cases is less than 4%. It is therefore natural not to observe differences in the figures for the two cases.

It is difficult to compare these results with equivalent ones from the literature because all of them have been calculated for planar geometries. For example, Abdali et al. [12] show the same type of figure but for a planar contraction. In this case, the dimensions of the unyielded zones are greater than in the present case, particularly for the larger Bi numbers, for which almost all the die is occupied by the unyielded zone.

(b) Rigid static zone and vortex

Figure 4 also shows the changes occurring in the morphology of flow versus Bi number but by zooming on the corner. As shown numerically by Crochet et al. [13] and experimentally by Nguyen and Boger [27], a vortex is found in the corner for $\mathrm{Bi}=0$ (Newtonian fluid). As the Bi number increases, the vortex is gradually replaced by a rigid static zone via a particular transition. For $\mathrm{Bi}=0.008$, two rigid static zones appear on the figure: one in the corner and the other at the break point between the main flow and the vortex. For $\mathrm{Bi}=0.01$ these two zones combine to create a single larger rigid static zone. The vortex has then disappeared. For larger Bi numbers, the rigid static zone increases until it occupies all the corner of the contraction for $\mathrm{Bi}=100$. It can be noted that the appearance of two rigid static zones has never been reported in the literature but was also found experimentally in our laboratory in the case of an expansion flow.

4.1.3 Influence of the Contraction Angle. Figure 5 shows the same overall change in flow structure but versus the contraction angle and for a constant Bi number ($\mathrm{Bi}=10$). When the contraction angle decreases, the extremity of the upstream central rigid moving zone is pushed slightly upstream. Its diameter does not change. There is also no modification in the diameter of the downstream zone.

On the other hand, greater changes occur in the rigid static zone in the corner. Its size decreases drastically with the angle. For $\alpha=90$ deg, the rigid static zone occupies a large part of the corner. For $\alpha=60$ deg, this zone is considerably reduced and almost invisible. For $\alpha=20$ deg, no static zone is visible.

The contraction angle therefore plays a major role in determining whether or not a rigid static zone occurs; this is interesting to study systematically by drawing up a map.

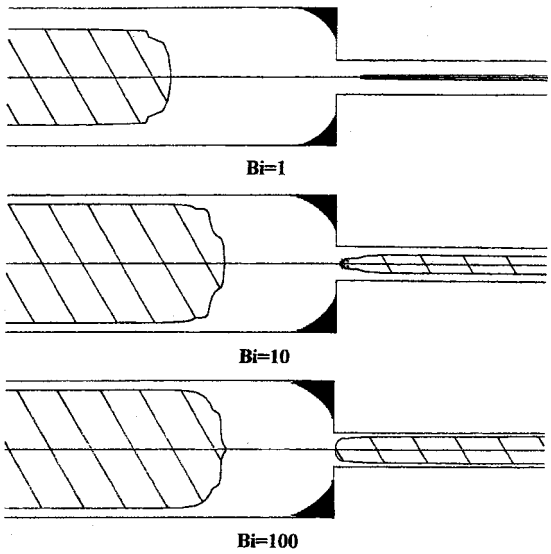

Fig. 3 Influence of Bi on the overall structure of the flow. Rigid static zone in black. Rigid moving zone hatched. n=1.

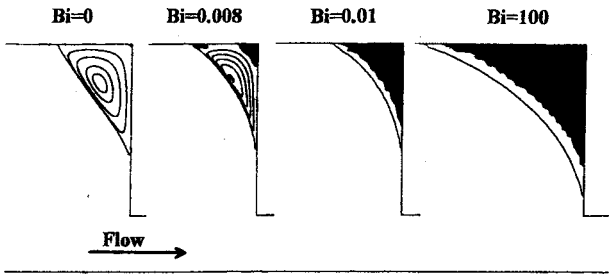

Fig. 4 Change in flow in relation to the Bi number. Zoom on the corner. n=1.

4.1.4 Map of Vortex and Rigid Static Zones. From a technical point of view, as seen previously, it is necessary to reduce the dimensions of the rigid static zone. Numerically, as seen in Figs. 4 and 5, it is possible to determine the presence or absence of a vortex or rigid static zone as a function of the Bi number and angle. It is also possible to define the transition between these two zones. After a systematic analysis of the morphology of the flows, for Bi numbers between 10^{-4} and 10 and contraction angles between 45 and 90 deg, a map of the flow structure was prepared for $n=1$ (Fig. 6). The continuous line corresponds to the limit of appearance of the static zone and the dotted line to that of the vortex. It is assumed that there is no rigid static zone when the dimension H (Fig. 1) is lower than the radius R1 divided by 30. Below this value, these zones cannot be detected. The vortex appears for $\alpha=65$ deg in the Newtonian case and disappears for $\alpha=90$ deg and $\mathrm{Bi}=0.01$. The limit of the rigid static zone goes from $\alpha=90$ deg, $\mathrm{Bi}=0.0008$ to $\alpha=45$ deg, $\mathrm{Bi}=5$. It is also possible to observe the zone where the vortex with static zone co-exist, as described previously.

The shear thinning index has obviously an important effect on this map obtained for $n=1$. If it is decreased, i.e., if the fluid becomes shear thinning, as explained previously and shown by Kim et al. [26]for an sudden contraction, the size of the vortex reduces drastically. It has been also shown, but in the case of a creeping flow through an expansion, that there is a reduction of the unyielded zones size. So for this map, the area both of the ''vortex zone'' and of ''rigid static zone'' must certainly decrease. The dotted line corresponding to the vortex zone (Fig. 6) must displace toward great angles and the continuous one corresponding to the rigid static zone toward the great Bi numbers.

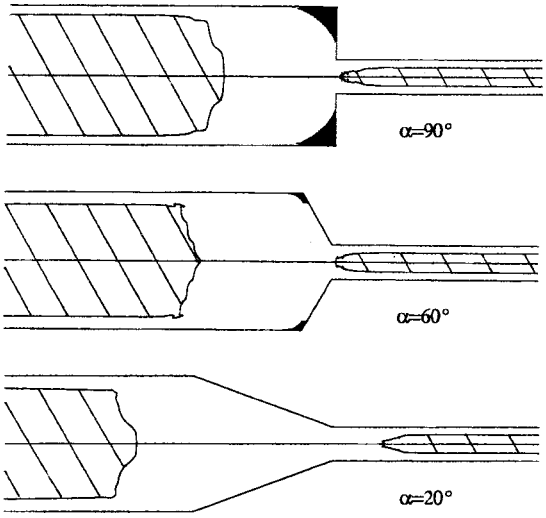

Fig. 5 Influence of contraction angle on flow structure for a 4:1 contraction ratio and Bi=10. n=1.

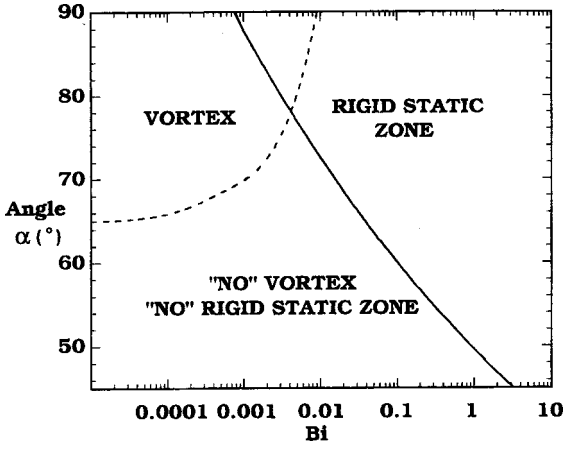

Fig. 6 Map showing the appearance of the vortex and rigid static zone. 4:1 contraction ratio. n=1.

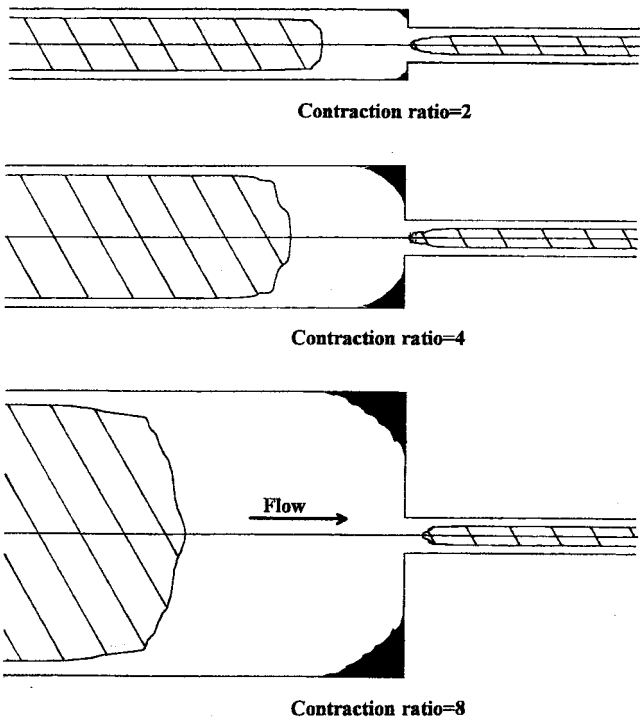

Fig. 7 Influence of contraction ratio on flow structure. Bi=10. $\alpha=90$ deg. n=1.

4.1.5 Influence of the Contraction Ratio. The influence of the contraction ratio on flow morphology was also analyzed. Figure 7 shows these changes. When the contraction ratio increases, the size of the rigid static zone in the corner (H, see Fig. 1) also increases. The extremity of the upstream rigid moving zone (H1) is pushed back. On the other hand, the position of the extremity of the downstream rigid zone changes very little.

4.2 Pressure Losses. From an industrial point of view, it is useful to know the pressure losses associated with the different flow structures. In this part, these are evaluated (they are represented by Leq defined in Section 2.4). The effects of Bi number, contraction angle and contraction ratio are investigated.

When Leq is expressed as a function of the Bi number, the reference value is obtained for the Newtonian case. For a 4:1 abrupt contraction, this value varies from 0.49 to 0.69 in the literature (Boger [28]). The final value chosen by this author is 0.589. In this work, the Leq value found to be 0.55 with the mesh defined above.

The influence of the Bi number on pressure losses is shown on Fig. 8. Below $\mathrm{Bi}=10^{-1}$, Leq is nearly constant. It begins to increase up to this value. At this point, the rigid central zone begins to grow and therefore so do the pressure losses. For the abrupt contraction, Leq increases from the value of 0.55 obtained for $\mathrm{Bi}=0$ to the value of 2.1 obtained for $\mathrm{Bi}=100$. These results were also compared with those obtained by Abdali et al. [12] for the case of a sudden contraction. The results are very close (with a difference of between 0% and 12.5%) over a wide range of Bi numbers (between 10^{-1} and 100).

The effect of the contraction angle is shown on Fig. 9. The value of Leq increases when the contraction angle decreases. For

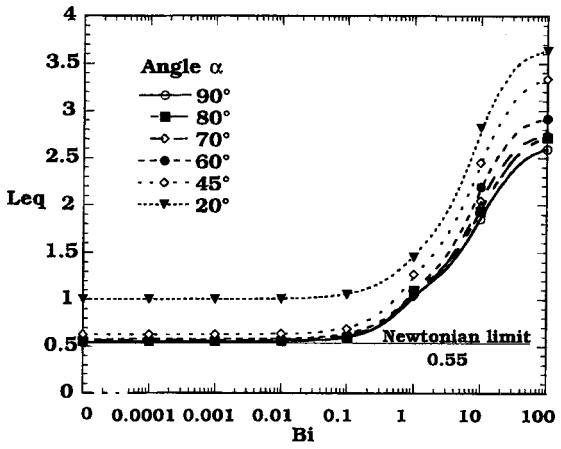

Fig. 8 Leq versus Bi number for different contraction angles. 4:1 contraction ratio. n=1. Newtonian limit for $\alpha=90$ deg: Leq=0.55.

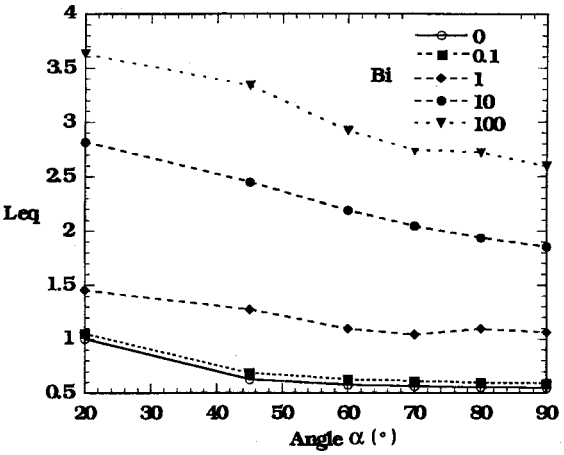

Fig. 9 Leq versus contraction angle for different Bi numbers. 4:1 contraction ratio. n=1.

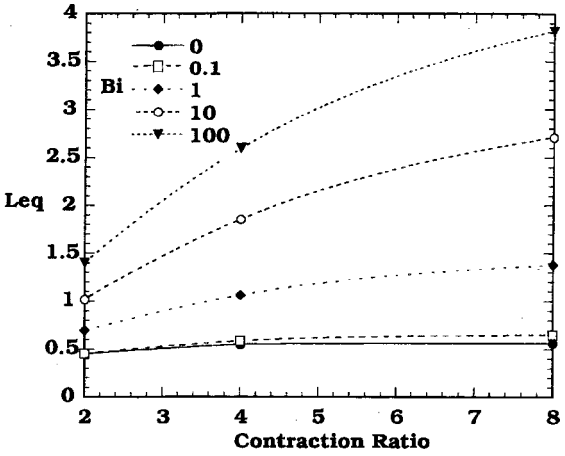

Fig. 10 Leq versus contraction ratio for different Bi numbers. $\alpha=90$ deg. n=1.

Bi=100, the Leq increases from 2.1 for 90 deg to 3.65 for 20 deg. This can be explained by the fact than the pressure loss has a component that is proportional to the length of the conical part and this component grows when the angle decreases. So when the contraction angle decreases, the pressure loss and consequently Leq rise (because σ_{ω_2} remains unchanged). This effect does not depend on the Bi number.

The change in Leq versus contraction ratio is shown in Fig. 10 for different Bi numbers. Leq is an increasing function of the contraction ratio. When this rises, it seems that each curve tends asymptotically towards a limit value. The asymptote seems to be reached the quickest for the smallest Bi numbers. As previously, it may be noted than the largest Leq are obtained for the highest Bi. For a contraction ratio 8:1, a value of 4 is almost obtained for a Bi number equal to 100.

4.3 Comparisons With Experimental Visualizations. Experimental investigations of viscoplastic fluid flows through transparent dies are currently being carried out in our Laboratory. It is thus possible to compare experimental and numerical results. We have compared our numerical results with experimental ones obtained with a gel, the rheometric properties of which fit well with the Herschel-Bulkley model. Figure 11 shows three different cases obtained for different angles and different Bi numbers. Experimentally, it is easy to observe the central flow and the streamlines (obtained by introducing tracers into the gel). In the corner, no particle is seen to be shifting: so there is indeed a rigid static zone created by the yield stress. It may be noted that this zone decreases with the angle. For $\alpha=45$ deg, this zone has almost disappeared.

There is a relatively good agreement between the shape of the rigid static zones obtained experimentally and numerically. Nevertheless, the numerical approach seems to overestimate the dimension slightly. For example, the length H (Fig. 1) is about 10–12% greater in the numerical case than in the experimental one.

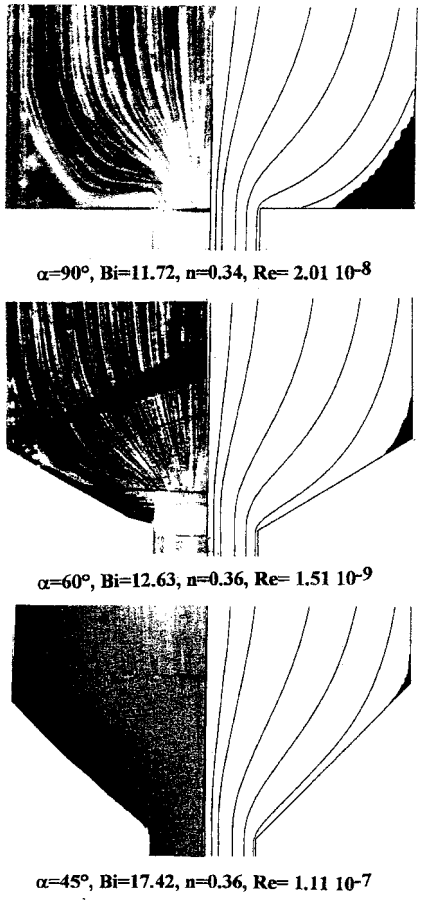

Fig. 11 Comparison of numerical and experimental results

5 Conclusions

Numerical simulations of viscoplastic fluid flows through axisymmetric contractions were performed with a biviscosity approximation of the Herschel-Bulkley model. Inertia was neglected. The effects of yield stress (for Bi numbers from 0 to 100), contraction ratio (from 2:1 to 8:1) and contraction angle (between 20 deg and 90 deg) on flow structure and pressure losses were determined quantitatively.

The structure of the flow is highly dependent on yield stress. When this increases, the size of the rigid moving and static zones increases drastically. An intermediate structure between the vortex and the rigid static zone was observed in the corner, with two rigid static zones and a vortex. The rigid static zones disappear in the case of very small contraction angles. A map has been proposed for predicting flow structure as a function of Bi number and contraction angle.

Pressure loss also depends on the same parameters. It is almost constant while the Bi number is smaller than 10^{-1}. On the other hand, for greater values the increase in Leq is very significant. Because of the increase in the length of the conical part, pressure loss decreases with the angle, especially in the case of high Bi numbers.

In order to validate these numerical results, comparisons are made with experimental results. A relatively good agreement was found.

Nomenclature

$\mathbf{T}$ = extra-stress tensor
$\mathbf{D}$ = rate of deformation tensor
$\dot{\gamma}$ = shear rate (s^{-1})
$\dot{\gamma}_c$ = critical shear rate (s^{-1})
τ_0 = yield stress (Pa)
K = consistency factor) ($Pa.s^n$)
n = shear-thinning index
T_{II} = second invariant of $\mathbf{T}$
V = average velocity ($m.s^{-1}$)
R = radius (m)
Bi = Bingham number
Leq = equivalent entrance length
ΔP_s = additional pressure loss due to the singularity (Pa)
ΔP = total pressure drop (Pa)
σ_ω = Wall shear stress (Pa)
α = contraction angle (degree)

Subscripts

1 = entrance tube
2 = exit tube

References

[1] Prager, W., 1961, *Introduction to Mechanics of Continua*, Ginn, Boston.
[2] Nguyen, Q. D., and Boger, D. V., 1992, "Measuring the Flow Properties of Yield Stress Fluids," Annu. Rev. Fluid Mech., **24**, pp. 47–88.
[3] Wilson, S. D. R., 1993, "Squeezing Flow of Bingham Material," J. Fluid Mech., **47**, pp. 211–219.
[4] Piau, J. M., 1996, "Flow of a Yield Stress Fluid in a Long Domain. Application to Flow on an Inclined Plane," J. Rheol., **40**, pp. 711–723.
[5] Piau, J. M., 1998, "Crucial Elements of Yield Stress Fluid Rheology," *Dynamic Complex Fluids*, Royal Society and Imperial Press, M. Adams, ed., pp. 353–374.
[6] Barnes, H. A., 1999, "The Yield Stress—a Review or $\pi\alpha\nu\tau\alpha\ \rho\epsilon\iota$—Everything Flows?" J. Non-Newtonian Fluid Mech., **81**, pp. 133–178.
[7] Coupez, T., Zine, M. A., and Agassant, J. F., 1994, "Numerical Simulation of Bingham Fluid Flow," Proceedings of the 4th European Rheology Conference, Seville, pp. 341–343.
[8] Isayev, A. I., and Huang, Y. H., 1993, "Two-Dimensional Planar Flow of a Viscoelastic Plastic Medium," Rheol. Acta, **32**, pp. 181–191.
[9] Gans, R. F., 1999, "On the Flow of a Yield Strength Fluid Through a Contraction," J. Non-Newtonian Fluid Mech., **81**, pp. 184–195.
[10] Magnin, A., and Piau, J. M., 1992, "Flow of Yield Stress Fluids Through a Sudden Change of Section," *Theoretical and Applied Rheology*, P. Moldenaers and R. Keunings, eds., Elsevier, Amsterdam pp. 195–197.
[11] Mitsoulis, E., Abdali, S. S., and Markatos, N. C., 1993, "Flow Simulation of Herschel-Bulkley Fluids Through Extrusion Dies," Can. J. Chem. Eng., **71**, pp. 147–160.
[12] Abdali, S. S., Mitsoulis, E., and Markatos, N. C., 1992, "Entry and Exit Flows of Bingham Fluids," J. Rheol., **36**, pp. 389–407.
[13] Crochet, M. J., Davies, A. R., and Walters, K., 1984, "*Numerical Simulation of Non-Newtonian Flows*," Elsevier, Amsterdam.
[14] Papanastasiou, T. C., 1987, "Flow of Material With Yield," J. Rheol., **31**, pp. 385–404.
[15] Loest, H., Lipp, R., and Mitsoulis, E., 1994, "Numerical Flow Simulation of Viscoplastic Slurries and Design Criteria for a Tape Casting Unit," J. Am. Ceram. Soc., **77**, pp. 254–262.
[16] Beaulne, M., and Mitsoulis, E., 1997, "Creeping Motion of a Sphere in Tubes Filled With Herschel-Bulkley Fluids," J. Non-Newtonian Fluid Mech., **72**, pp. 55–71.
[17] Burgos, G. R., Alexandrou, A. N., and Entov, V., 1999, "On the Determination of Yield Surfaces in Herschel-Bulkley Fluids," J. Rheol., **43**, pp. 463–483.
[18] Burgos, G. R., and Alexandrou, A. N., 1999, "Flow Development of Herschel-Bulkley Fluids in a Sudden Three-Dimensional Square Expansion," J. Rheol., **43**, pp. 485–498.
[19] Alexandrou, A. N., McGilvreay, T. M., and Burgos, G., 2001, "Steady Herschel-Bulkley Fluid Flow in Three-Dimensional Expansions," J. Non-Newtonian Fluid Mech., **100**, pp. 77–96.
[20] Lipscomb, G. G., and Denn, M. M., 1984, "Flow of Bingham Fluids in Complex Geometries," J. Non-Newtonian Fluid Mech., **14**, pp. 337–346.
[21] O'Donovan, E. J., and Tanner, R. I., 1984, "Numerical Study of the Bingham Squeeze Film Problem," J. Non-Newtonian Fluid Mech., **15**, pp. 75–83.
[22] Vradis, G. C., and Otugen, M. V., 1997, "The Axisymmetric Sudden Expansion Flow of a Non-Newtonian Viscoplastic Fluid," ASME J. Fluids Eng., **119**, pp. 193–199.
[23] Jay, P., Magnin, A., and Piau, J. M., 2001, "Viscoplastic Fluid Flow Through a Sudden Axisymmetric Expansion," AIChE J., **47**(10), pp. 2155–2166.
[24] Belhadri, M., Magnin, A., and Piau, J. M., 1994, Actes du 8$^{\text{ème}}$ Colloque TIFAN, Toulouse, 7, pp. 29–38.
[25] Magnin, A., and Piau, J. M., 1990, "Cone Plate Rheometry of a Yield Stress Fluid. Measurement of an Aqueous Gel," J. Non-Newtonian Fluid Mech., **36**, pp. 85–108.
[26] Kim-E, M. E., Brown, R. A., and Armstrong, R. C., 1983, "The Roles of Inertia and Shear Thinning in Flow of Inelastic Liquid Through an Axisymmetric Contraction," J. Non-Newtonian Fluid Mech., **13**, pp. 41–63.
[27] Nguyen, H., and Boger, D. V., 1979, "The Kinematics and Stability of Die Entry Flows," J. Non-Newtonian Fluid Mech., **5**, pp. 353–368.
[28] Boger, D. V., 1987, "Viscoelastic Flows Through Contractions," Annu. Rev. Fluid Mech., **19**, pp. 157–182.

Yong H. Im
Graduate Student
e-mail:iyh@postech.ac.kr

Kang Y. Huh[1]
Professor
e-mail:huh@postech.ac.kr

Department of Mechanical Engineering,
Pohang University of Science & Technology,
Pohang, Kyungbuk, Korea

Kwang-Yong Kim
Professor,
Department of Mechanical Engineering,
Inha University, Inch-eon,
Kyungki, Korea
e-mail: kykim@inha.ac.kr

Analysis of Impinging and Countercurrent Stagnating Flows by Reynolds Stress Model

Numerical simulation is performed for stagnating turbulent flows of impinging and countercurrent jets by the Reynolds stress model (RSM). Results are compared with those of the $k-\varepsilon$ model and available data to assess the flow characteristics and turbulence models. Three variants of the RSM tested are those of Gibson and Launder (GL), Craft and Launder (GL-CL) and Speziale, Sarkar and Gatski (SSG). As is well known, the $k-\varepsilon$ model significantly overestimates turbulent kinetic energy near the wall. Although the RSM is superior to the $k-\varepsilon$ model, it shows considerable difference according to how the redistributive pressure-strain term is modeled. Results of the RSM for countercurrent jets are improved with the modified coefficients for the dissipation rate, $C_{\varepsilon 1}$ and $C_{\varepsilon 2}$, suggested by Champion and Libby. Anisotropic states of the stress near the stagnation region are assessed in terms of an anisotropy invariant map (AIM). [DOI: 10.1115/1.1493815]

1 Introduction

There have been recent investigations on stagnating turbulent flows, which involve turbulence mechanisms different from those in simple shear flows [1]. The stagnating flow configuration has provided a challenging test case for a few turbulence models in the literature [1–4]. In stagnating flows production of turbulence is attributed to normal strain instead of cross-stream shear with strong effects of streamline curvature. Stagnating laminar and turbulent flows provide a floating flame with easy optical access and a homogeneous mean rate of strain that can be easily adjusted in experiment. The countercurrent flow configuration has the additional advantage that the complexities arising from heat loss or chemistry effects on the wall are excluded. Proper understanding of the flow characteristics is essential for such applications in order to achieve enhanced heat and mass transfer [1,4,5,6] or analysis of stabilized floating flames [7–10].

Experimental efforts have been made to gain an insight and to provide database in stagnating turbulent flows. Gutmark et al. [11] measured mean velocity and Reynolds stress components with their energy budget in a wall impinging jet. The results indicated selective stretching of vortices causing anisotropy near the wall. Cooper et al. [12] provided well-documented turbulence statistics by hot wire anemometry in the stagnation region of a wall impinging jet. Ueda et al. [13] also provided similar data by LDV (Laser Doppler Velocimetry) with and without a turbulence generator in a wall impinging jet. Nishino et al. [14] provided the turbulent statistics by PTV (Particle Tracking Velocimetry) for a water jet injected on a wall. Cho et al. [8] and Escudie et al. [9] reported data on flow field and a premixed flame brush stabilized in a wall impinging jet. Kostiuk et al. [7,15] and Mounaim-Rousselle and Gokalp [16] made measurements of mean flow, turbulent intensity, and a premixed flame in nonreacting and reacting countercurrent jets.

Numerical predictions were made with the $k-\varepsilon$ model for a semi-confined wall impinging jet by Ashforth-Frost and Jambunathan [17]. The heat transfer rate was significantly overpredicted due to excessive production of turbulence at the stagnation region. Rabbitt [18] improved the results with a modified nonlinear $k-\varepsilon$ model, although the turbulence statistics in the stagnation region were still in error. The second-order closures with a modified wall reflection term produced better results than the $k-\varepsilon$ model for the highly anisotropic turbulent flow in a wall impinging jet [1–3]. The SSG [19] with a quadratic pressure-strain term gave good results in various flow configurations such as a backward-facing step [20] and a free jet flow with swirl [21]. Champion and Libby [22] identified three distinct regions in a wall impinging jet, i.e., viscous sublayer (Region I), shear layer (Region II), and external streaming zone (Region III). They applied the asymptotic series expansion method [22–24] in each region to obtain matching solutions and recently extended the analysis to calculate Reynolds stress and scalar flux in a turbulent reacting flow [25]. In this paper, numerical simulations are performed to assess the flow characteristics and turbulence models in impinging and countercurrent jets. The three different RSM's, which are termed as GL [26], GL-CL [1] and SSG [19], are compared with the $k-\varepsilon$ model and against available data in the literature [9,12,15,16].

2 Analytical Models

The transport equation for the Reynolds stress, $\overline{u_i u_j}$, takes the following form,

$$\frac{D\overline{u_i u_j}}{Dt} = P_{ij} + D_{ij} - \varepsilon_{ij} + \phi_{ij} = -\left(\overline{u_i u_k}\frac{\partial U_j}{\partial x_k} + \overline{u_j u_k}\frac{\partial U_i}{\partial x_k} \right) - \frac{\partial}{\partial x_k}\left[\overline{u_i u_j u_k} + \frac{1}{\rho}(\overline{p' u_i}\delta_{jk} + \overline{p' u_j}\delta_{ik}) - \nu \frac{\partial \overline{u_i u_j}}{\partial x_k} \right] - 2\nu \overline{\frac{\partial u_i}{\partial x_k}\frac{\partial u_j}{\partial x_k}} + \overline{\frac{p'}{\rho}\left(\frac{\partial u_i}{\partial x_j} + \frac{\partial u_j}{\partial x_i} \right)}. \quad (1)$$

The production term, P_{ij}, does not require any modeling while the diffusion term, D_{ij}, is given by the gradient diffusion model of Daly and Harlow [27] as

$$D_{ij} = \frac{\partial}{\partial x_k}\left(C_s \overline{u_l u_k}\frac{k}{\varepsilon}\frac{\partial \overline{u_i u_j}}{\partial x_l} \right). \quad (2)$$

Modeling is required for the pressure-strain term, ϕ_{ij}, which involves fluctuations of pressure and velocity gradient. A linear pressure-strain model may be given in the following general form,

$$\phi_{ij} = \phi_{ij1} + \phi_{ij2} + \phi^w_{ij1} + \phi^w_{ij2}. \quad (3)$$

In the GL each term is modeled as [26]

[1]Corresponding Author.

Contributed by the Fluids Engineering Division for publication in the JOURNAL OF FLUIDS ENGINEERING. Manuscript received by the Fluid Engineering Division, February 21, 2001; revised manuscript received March 18, 2002. Associate Editor: T. Gatski.

Table 1 Model constants in turbulence models

Model	Model constants
GL	$C_1=1.8$, $C_2=0.6$, $C_{1w}=0.5$, $C_{2w}=0.3$, $C_{\varepsilon 1}=1.44$, $C_{\varepsilon 2}=1.92$, $C_\varepsilon=0.18$, $C_l=2.5$
GL-CL	$C_1=1.8$, $C_2=0.6$, $C_{1w}=0.5$, $C_{2w}=0.08$, $C'_{2w}=0.1$, $C''_{2w}=0.4$, $C_{\varepsilon 1}=1.44$, $C_{\varepsilon 2}=1.92$, $C_\varepsilon=0.18$, $C_l=2.5$
SSG	$C_1=3.4$, $C_1^*=1.8$, $C_2=4.2$, $C_3=0.8$, $C_3^*=1.3$, $C_4=1.25$, $C_5=0.4$, $C_{\varepsilon 1}=1.44$, $C_{\varepsilon 2}=1.83$, $C_\varepsilon=0.183$

$$\phi_{ij1}=-C_1\frac{\varepsilon}{k}\left(\overline{u_iu_j}-\frac{2}{3}k\delta_{ij}\right) \tag{4}$$

$$\phi_{ij2}=-C_2\left(P_{ij}-\frac{1}{3}P_{kk}\delta_{ij}\right) \tag{5}$$

$$\phi^w_{ij1}=C_{1w}\frac{\varepsilon}{k}\left(\overline{u_mu_l}\,n_mn_l\delta_{ij}-\frac{3}{2}\overline{u_iu_m}\,n_mn_j-\frac{3}{2}\overline{u_ju_m}\,n_mn_i\right)f_y \tag{6}$$

$$\phi^w_{ij2}=C_{2w}\left(\phi_{ml2}n_mn_l\delta_{ij}-\frac{3}{2}\phi_{im2}n_mn_j-\frac{3}{2}\phi_{jm2}n_mn_i\right)f_y \tag{7}$$

$$f_y=\frac{k^{3/2}}{C_l\varepsilon y}. \tag{8}$$

The model constants are listed in Table 1. n_i is the normal component of a unit vector on the wall. f_y is a length scale function in terms of the closest distance to the wall. ϕ_{ij1} is the return-to-isotropy term given by Rotta [28]. ϕ_{ij2} is the rapid pressure-strain term representing contribution of the mean rate of strain. The wall reflection term, ϕ^w_{ij}, is responsible for redistribution of energy among Reynolds stress components near the wall. It dampens the Reynolds stress components normal to the wall, while enhancing those parallel to the wall.

Craft et al. [1] proposed a modified form of the wall reflection term in a wall impinging jet. The model of Craft et al., termed as GL-CL, is identical to the GL except for ϕ^w_{ij2}, which is given as

$$\begin{aligned}\phi^w_{ij2}=&-C_{2w}\frac{\partial U_l}{\partial x_m}\overline{u_lu_m}(n_qn_q\delta_{ij}-3n_in_j)f_y\\&-C'_{2w}k\left(\frac{\partial U_k}{\partial x_m}n_ln_ka_{lm}\delta_{ij}-\frac{3}{2}\frac{\partial U_i}{\partial x_m}n_ln_ja_{lm}\right.\\&\left.-\frac{3}{2}\frac{\partial U_j}{\partial x_m}n_ln_ia_{lm}\right)f_y\\&+C''_{2w}k\frac{\partial U_l}{\partial x_m}n_ln_m\left(n_in_j-\frac{1}{3}n_qn_q\delta_{ij}\right)f_y.\end{aligned} \tag{9}$$

The model constants of the GL-CL are listed in Table 1.

In the SSG [19] the pressure-strain term is modeled as

$$\begin{aligned}\phi_{ij}=&-(C_1\varepsilon+C_1^*P)b_{ij}+C_2\varepsilon\left(b_{ik}b_{kj}-\frac{1}{3}b_{kl}b_{kl}\delta_{ij}\right)+(C_3\\&-C_3^*\mathrm{II}_b^{1/2})kS_{ij}+C_4k\left(b_{ik}S_{jk}+b_{jk}S_{ik}-\frac{2}{3}b_{kl}S_{kl}\delta_{ij}\right)\\&+C_5k(b_{ik}W_{jk}+b_{jk}W_{ik})\end{aligned} \tag{10}$$

$$P=-\overline{u_iu_j}\frac{\partial U_i}{\partial x_j} \tag{11}$$

$$\mathrm{II}_b=b_{ij}b_{ij}. \tag{12}$$

The model constants in the above are listed in Table 1. Note that ϕ_{ij} is given as a quadratic function in terms of the Reynolds stress. The GL and the GL-CL are linear pressure-strain models, while the SSG is a quadratic model. b_{ij}, S_{ij}, and W_{ij} denote anisotropy of the Reynolds stress, mean rate of strain and mean vorticity tensor, which are, respectively, defined as

$$b_{ij}=\frac{\overline{u_iu_j}}{2k}-\frac{1}{3}\delta_{ij} \tag{13}$$

$$S_{ij}=\frac{1}{2}\left(\frac{\partial U_i}{\partial x_j}+\frac{\partial U_j}{\partial x_i}\right) \tag{14}$$

$$W_{ij}=\frac{1}{2}\left(\frac{\partial U_i}{\partial x_j}-\frac{\partial U_j}{\partial x_i}\right). \tag{15}$$

The linear part of the return-to-isotropy term is supplemented by a production based rapid term with the constant, C_1^*, and a variable isotropic rapid term with the constant, C_3^*. There is no need to consider the length scale function for the wall reflection effect in the SSG.

The Kolmogorov hypothesis of local isotropy is invoked for modeling of the dissipation rate tensor, ε_{ij}, as

$$\varepsilon_{ij}=\tfrac{2}{3}\delta_{ij}\varepsilon \tag{16}$$

where ε is the scalar dissipation rate of turbulent kinetic energy obtained from the transport equation,

$$\frac{D\varepsilon}{Dt}=\frac{\partial}{\partial x_j}\left(C_\varepsilon\frac{k}{\varepsilon}\overline{u_ju_l}\frac{\partial\varepsilon}{\partial x_l}\right)+C_{\varepsilon 1}\frac{\varepsilon}{k}P-C_{\varepsilon 2}\frac{\varepsilon^2}{k}. \tag{17}$$

The constants employed are $C_{\varepsilon 1}=1.44$, $C_{\varepsilon 2}=1.92$.

It was shown in the asymptotic analysis by Champion and Libby [24] that the empirical constants, $C_{\varepsilon 1}$ and $C_{\varepsilon 2}$, should approach the same limit at the stagnation plane. To satisfy the limiting behavior they adopted the distribution functions of $C_{\varepsilon 1}$ and $C_{\varepsilon 2}$ given as

$$C^*_{\varepsilon 1}=C_{\varepsilon 0}-(C_{\varepsilon 0}-C_{\varepsilon 1})[1-\exp(-8\varsigma^2)] \tag{18}$$

$$C^*_{\varepsilon 2}=C_{\varepsilon 0}-(C_{\varepsilon 0}-C_{\varepsilon 2})[1-\exp(-8\varsigma^2)] \tag{19}$$

where $C_{\varepsilon 0}=2.27$ [24]. The dimensionless coordinate from the stagnation plane is defined as

$$\varsigma=\frac{y}{H/2}. \tag{20}$$

$C^*_{\varepsilon 1}$ and $C^*_{\varepsilon 2}$ approach their standard values as ς increases from the plane. On the other hand, they approach a common value, $C_{\varepsilon 0}$, as $\varsigma\to 0$. These modified constants are applied only in the range, $r\leqslant R/2$, while the standard values for $C_{\varepsilon 1}$ and $C_{\varepsilon 2}$ are retrieved in $r\geqslant R/2$, where an outward radial jet develops away from the axis with a dominant shear stress.

3 Numerical Methods

The Reynolds averaged continuity, momentum, and turbulence equations are solved in a 2-D axisymmetric domain by the finite volume method (FVM). The SIMPLE algorithm [29] is adopted with a staggered grid to prevent decoupling of Reynolds stress, velocity and pressure fields [30]. The Reynolds shear stress is defined at the corner vertices of a control volume, while the Reynolds normal stress is defined at the center of the volume as shown in Fig. 1. To reduce false numerical diffusion the convection term is discretized by the second order, bounded TVD scheme originally proposed by Van Leer [31]. The grid refinement from 60×130 to 90×195 does not produce any noticeable change in the results for Escudie et al. [9] in Fig. 2. The grid systems in Table 2 may be considered as fine enough to provide acceptable, grid independent solutions. The convergence criterion is that the residuals for all major solution variables should be less than 10^{-8}.

The computational domain and boundary conditions are shown in Fig. 3 and 4. The symmetry boundary condition is employed on the axis and the countercurrent stagnation plane. The pressure boundary condition is employed on the upper and right bound-

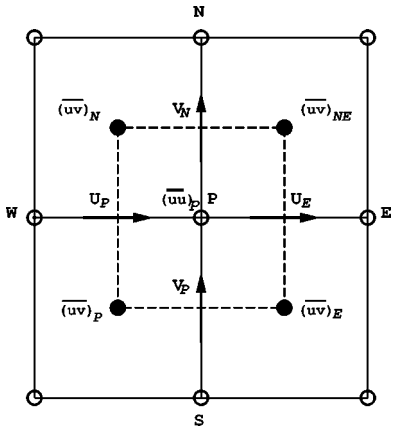

Fig. 1 Schematic diagram of a staggered grid

aries. An auxiliary transport equation is solved for turbulent kinetic energy, k, to provide the boundary condition for the Reynolds stress on the wall [32]. The wall function method is used on the wall with a matching point in the log law region ($11.225 < y^+ < 100$) [3]. The turbulent kinetic energy thus obtained is used only for boundary condition, nowhere else in the solution procedure. The Reynolds stress on the wall is given by an empirical formula, $\overline{u_i u_j} = C_{ij} k$, where C_{ij} is obtained from experiments. The dissipation rate, ε, adjacent to the wall is algebraically given in terms of the distance to the wall [32]. Craft et al. [1] adopted a different approach by defining an interface between the regions of second moment closure and eddy viscosity approximation. Continuity of shear stress, turbulent kinetic energy, and dissipation rate was enforced at the interface, which is at a fixed distance from the wall. Craft et al. used the low Reynolds number $k-\varepsilon$ model [33] to account for existence of the viscous sublayer.

4 Test Cases

The test cases in this paper are the impinging jets in Cooper et al. [12] and Escudie et al. [9] and the countercurrent jets in Kostiuk et al. [15] and Mounaim-Rousselle et al. [16]. All the experimental conditions are summarized in Table 3. Schematic diagrams for the experimental setup are shown in Figs. 3 and 4. The cases of Cooper et al. have been used as benchmark test cases of a wall impinging jet in the literature [1–3]. They have a feature that the jet issues from a long pipe with a fully developed exit profile. Preliminary calculations were performed to obtain the inlet conditions from the pipe [1].

A perforated plate was placed to make a uniform profile at the nozzle exit in all the other cases. In Escudie et al. the measured turbulent intensity was 7% of the local mean velocity and the

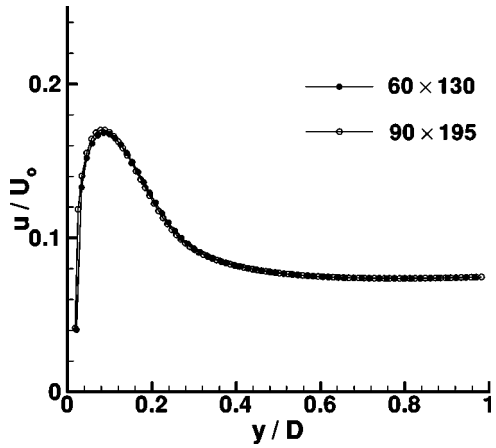

Fig. 2 Grid sensitivity results for the impinging jet of Escudie et al. [9]

Table 2 Grid systems

	Cooper et al. [12]	Escudie et al. [9]	Kostiuk et al. [15]			Mounaim-Rousselle et al. [16]
			Case A	Case B	Case C	
Grid	55×130	60×130	60×120	60×120	40×120	50×200

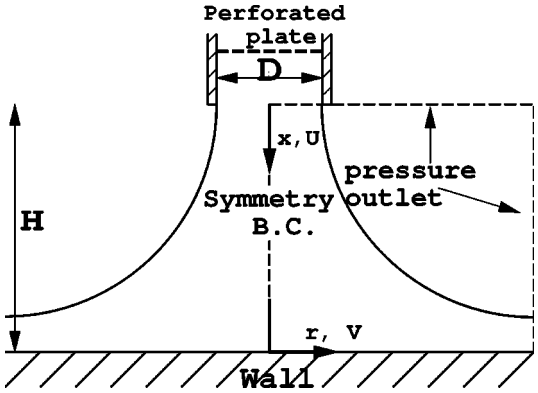

Fig. 3 Schematic diagram of an impinging jet

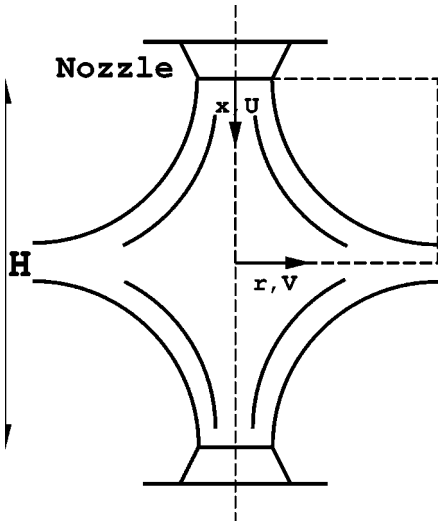

Fig. 4 Schematic diagram of a countercurrent jet

Table 3 Simulation conditions

			U_o (U_b) (m/s)	H (mm)	D (mm)	l_t (mm)	u'/U_o (%)	$a_b(a)$ (s^{-1})
Impinging jets	Cooper et al. [12]		12.68	52	26	–	–	487
	Escudie et al. [9]		4	66	66	4.0	7.0	121
Counter current jets	Kostiuk et al. [15]	Case A	9	70	35	2.0	9.4	205
		Case B	8	55	35	2.45	6.8	270
		Case C	8	20	35	2.45	6.8	550
	Mounaim-Rousselle et al. [16]		4.5	30	25	8	13	213

* For Cooper et al. l_t and u'/U_o have spatial distribution profiles from preliminary calculations.

integral length scale was deduced as 4 mm from the Taylor's hypothesis. In Kostiuk et al. they were estimated from the following correlations [10],

$$l_t = 0.774(x/d)^{0.5} \tag{21}$$

$$\log(u/U_0) = -0.367 - \log(x/d)^{0.8} \tag{22}$$

where x denotes the distance from the perforated plate and d is the hole diameter of the perforated plate. The inlet condition had to be adjusted for Case C of Kostiuk et al. [15], since the correlations showed some discrepancy with the measurements near the nozzle. In Mounaim-Rousselle et al. [16] turbulent intensity and integral length scale at the nozzle exit were measured as 13% of mean flow velocity and 8 mm, respectively. The Reynolds stress

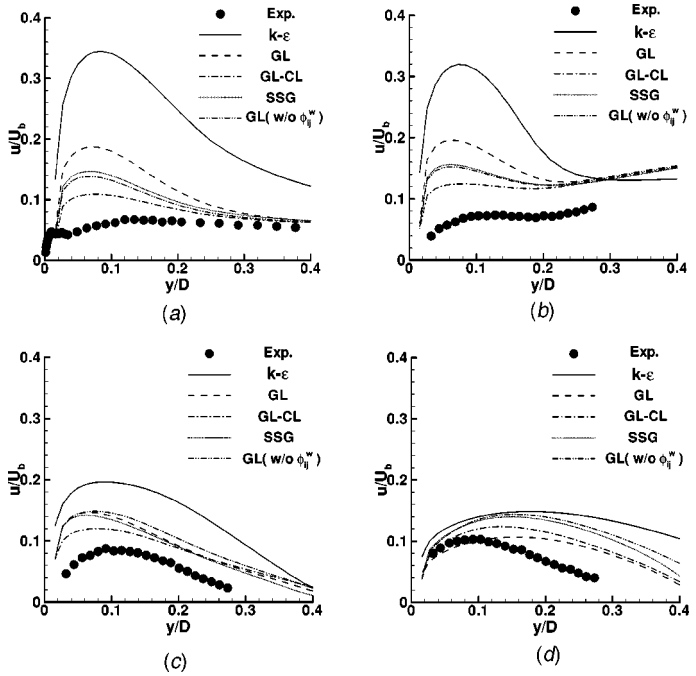

Fig. 5 Axial turbulent intensity components in the impinging jet of Cooper et al. [12]. (*a*) r/D=0; (*b*) r/D=0.5; (*c*) r/D=1.0; (*d*) r/D=2.5.

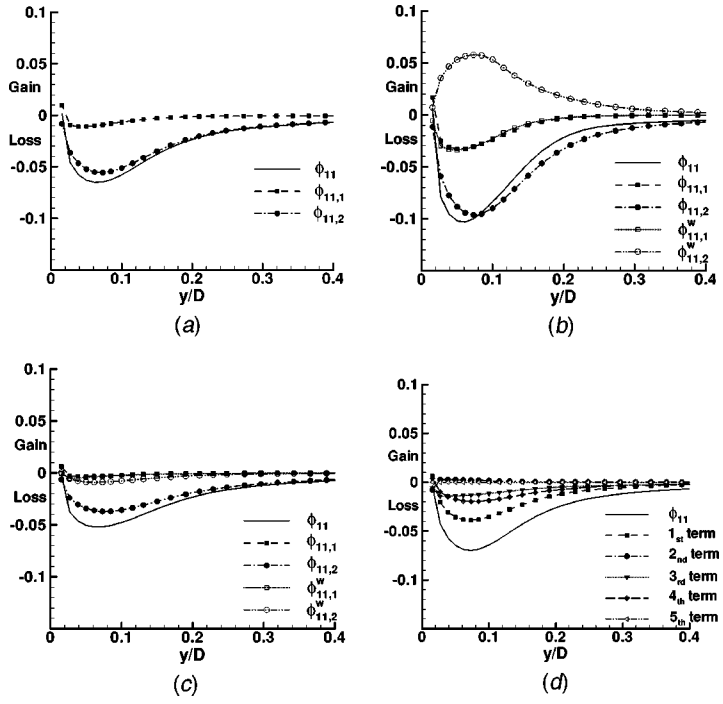

Fig. 6 Budget of the pressure-strain term for $\overline{uu}$ at r/D=0 in the impinging jet of Cooper et al. [12]. (*a*) GL (w/o wall reflection term); (*b*) GL; (*c*) GL-CL; (*d*) SSG.

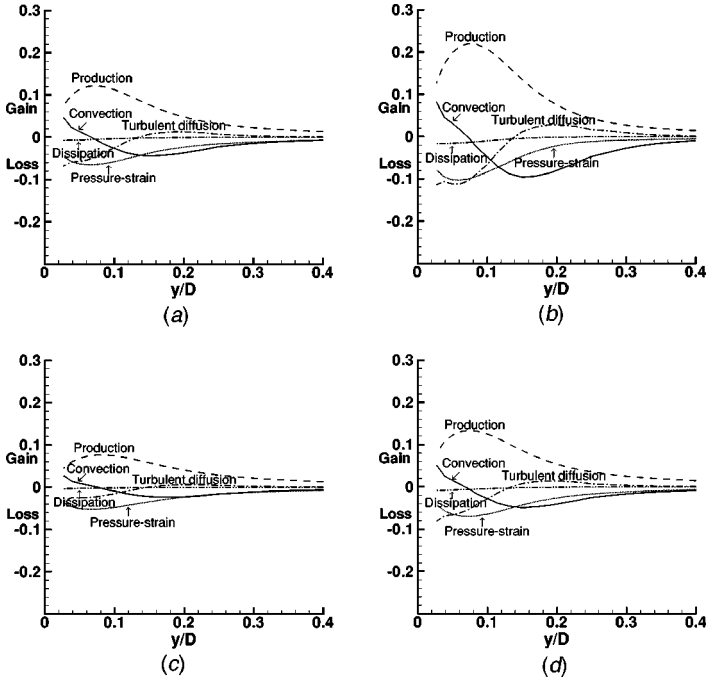

Fig. 7 Comparison of the terms for $\overline{uu}$ at r/D=0 in the impinging jet of Cooper et al. [12]. (*a*) GL (w/o wall reflection term); (*b*) GL; (*c*) GL-CL; (*d*) SSG.

and dissipation rate at the inlet are estimated from the given turbulent intensity and integral length scale by the following isotropic relationships,

$$\overline{uu}=\overline{vv}=\overline{ww}=\frac{2}{3}k \tag{23}$$

$$\overline{uv}=0 \tag{24}$$

$$\varepsilon=C_{\mu}^{3/4}\frac{k^{3/2}}{l_t}. \tag{25}$$

5 Results and Discussions

Figures 5–11 show predictions and measurements for the impinging jet in Cooper et al. [12]. All the models tend to overesti-

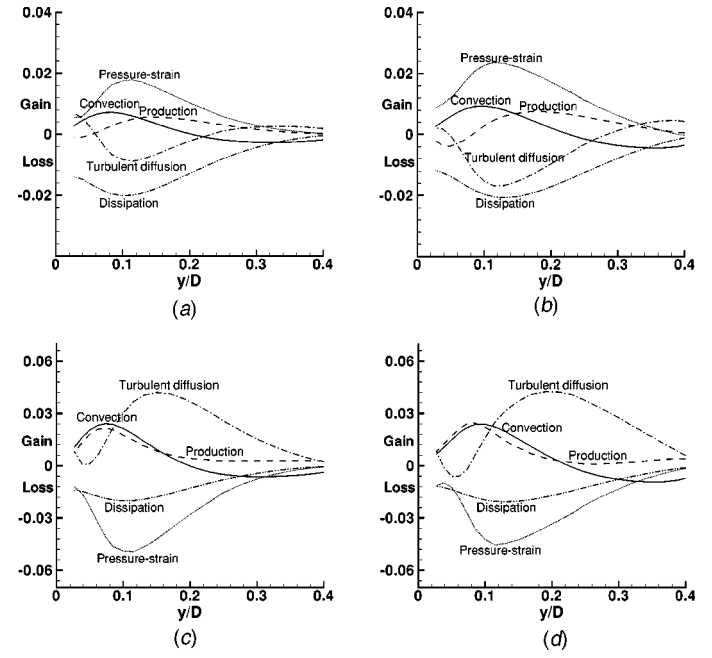

Fig. 8 Comparison of the terms for $\overline{uu}$ and $\overline{vv}$ at r/D=2.5 in the impinging jet of Cooper et al. [12]. (*a*) $\overline{uu}$ in GL-CL; (*b*) $\overline{uu}$ in SSG; (*c*) $\overline{vv}$ in GL-CL; (*d*) $\overline{vv}$ in SSG.

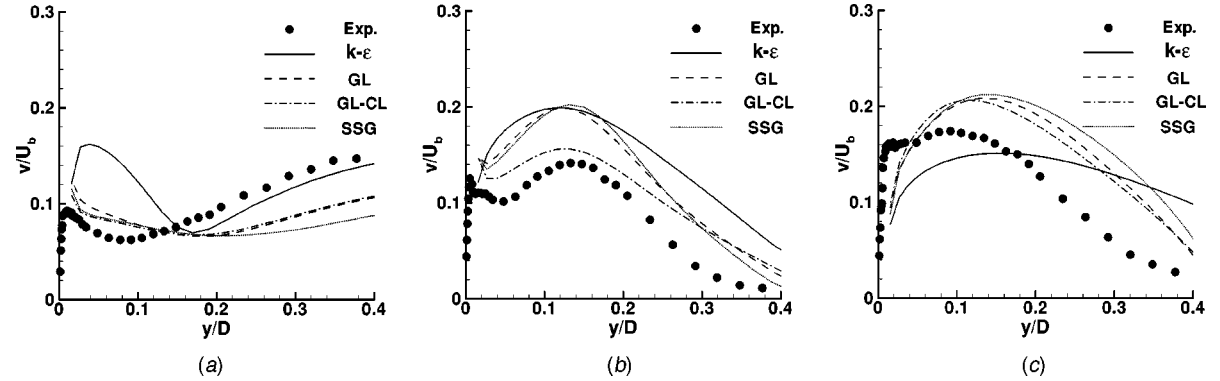

Fig. 9 Radial turbulent intensity components in the impinging jet of Cooper et al. [12]. (*a*) r/D=0.5; (*b*) r/D=1.0; (*c*) r/D=2.5.

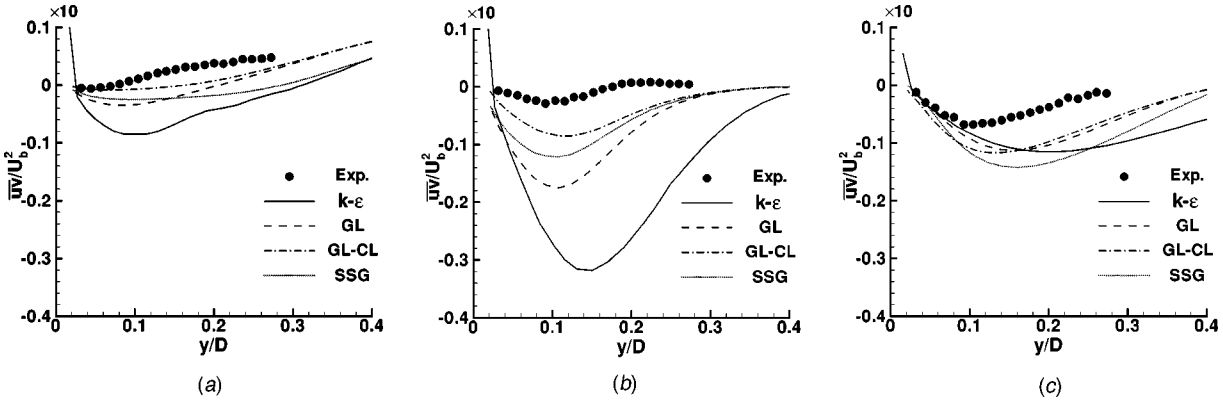

Fig. 10 Reynolds shear stresses in the impinging jet of Cooper et al. [12]. (*a*) r/D=0.5; (*b*) r/D=1.0; (*c*) r/D=2.5.

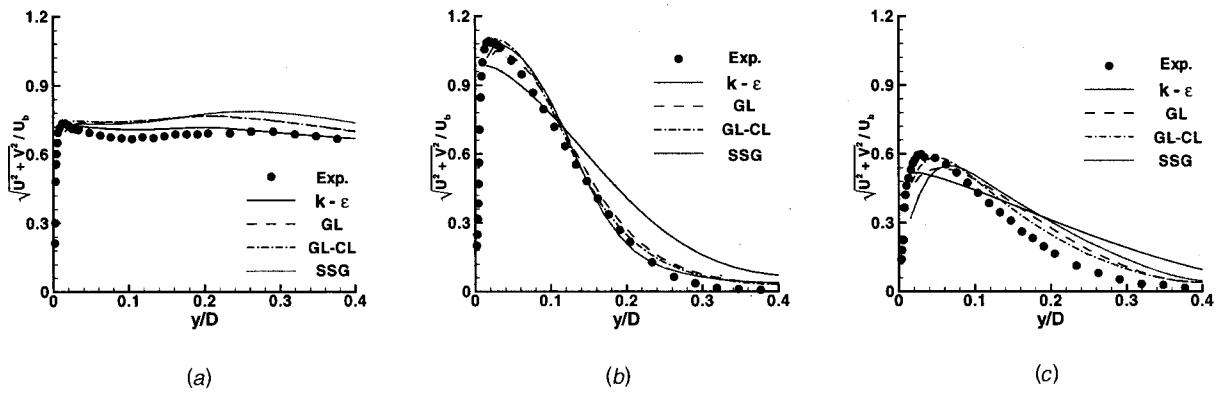

Fig. 11 Mean velocity profiles in the impinging jet of Cooper et al. [12]. (*a*) r/D=0.5; (*b*) r/D=1.0; (*c*) r/D=2.5.

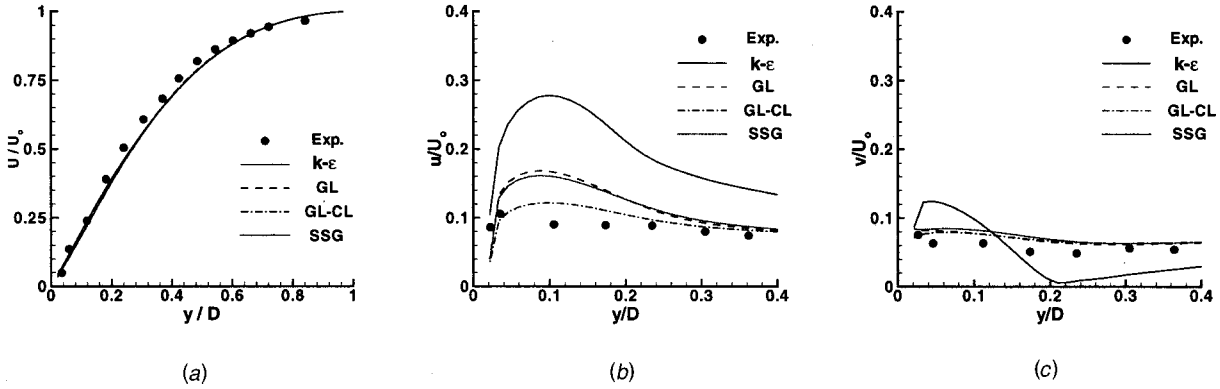

Fig. 12 Mean and turbulent intensity components on the axis in the impinging jet of Escudie et al. [9]. (*a*) Mean velocity; (*b*) axial turbulent intensity component; (*c*) radial turbulent intensity component.

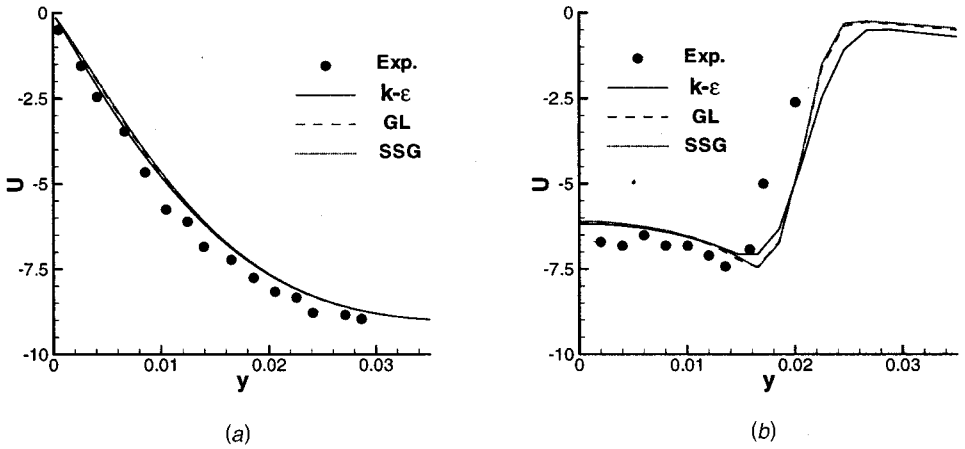

Fig. 13 Mean axial velocities in the countercurrent jets of Kostiuk et al. [15]. (*a*) On the axis; (*b*) 1.4 cm above the stagnation plane.

mate axial turbulent intensity near the wall. Results of the GL become worse closer to the axis in Fig. 5, due to an erroneous wall reflection term [1]. The SSG performs better than the GL, while it is comparable with the GL with no wall reflection term. The wall reflection term of the GL, however, contributes to a more accurate solution, as the flow develops into a radial wall jet.

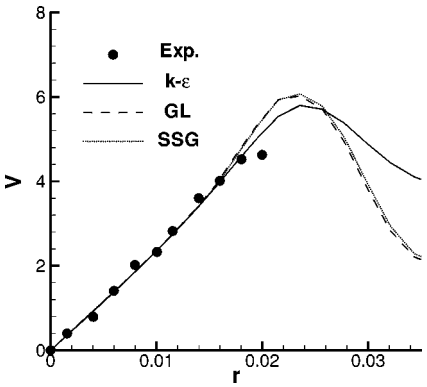

Fig. 14 Mean radial velocities in the countercurrent jets of Kostiuk et al. [15], 0.6 cm above the stagnation plane

Energy budgets for the pressure-strain term of the RSM are given in Fig. 6. The term, $\phi_{11,2}^{w}$, of the GL reduces the effect of $\phi_{11,2}$ near the stagnation plane, while that of the GL-CL does the opposite role of enhancing $\phi_{11,2}$. This is in accordance with the reasoning of Craft et al. [1]. Note that the best results are obtained with the modified wall reflection term of the GL-CL in Fig. 5.

Figure 7 shows budgets for the axial stress component, $\overline{uu}$, along the axis. Abrupt production of turbulence by normal strain is primarily balanced by the redistributive pressure-strain term. The other terms, i.e., convection, turbulent diffusion, and dissipation, in Eq. (1) are not as large as the production and the redistribution term. Note that the GL has the largest negative total pressure-strain term, ϕ_{11}, in Fig. 6 (*b*). It acts as a sink in the $\overline{uu}$ equation, which is, however, dominated by overpredicted production in the GL. Overestimated $\overline{uu}$ due to the wrong wall reflection term contributes to the production, $-\overline{uu}\,\partial U/\partial x$. This is why the GL results in the largest axial turbulent intensity, u, near the stagnation plane. The GL-CL, on the other hand, results in the smallest u with the smallest production term for $\overline{uu}$ in Fig. 7 (*c*).

In Fig. 8 a different feature is observed in the radial wall jet developing away from the axis. Energy is supplied by a shear stress, while the dissipation term exerts a significant influence on the overall budget. Transfer of turbulence energy occurs in the reverse way from the stream component, $\overline{vv}$, to the cross-stream component, $\overline{uu}$, in the wall jet.

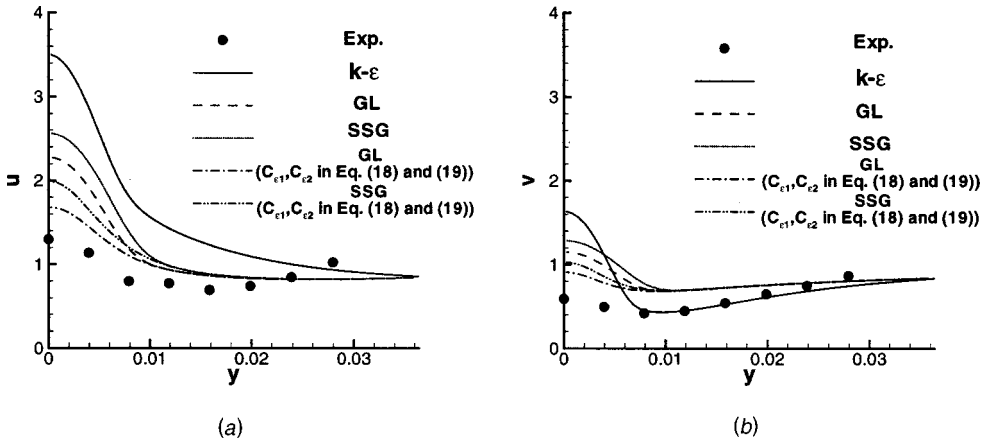

Fig. 15 Axial and radial turbulent intensity components on the axis of Case A in the countercurrent jets of Kostiuk et al. [15]. (*a*) Axial turbulent intensity component; (*b*) radial turbulent intensity component.

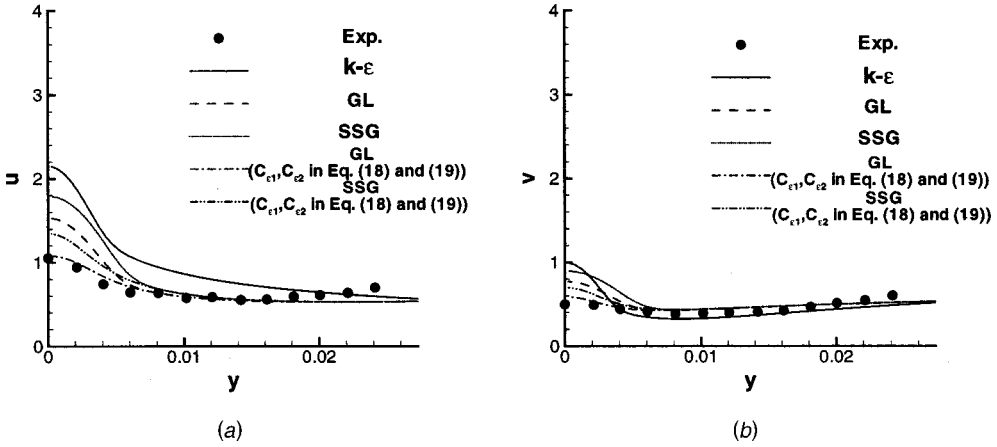

Fig. 16 Axial and radial turbulent intensity components on the axis for Case B in the countercurrent jets of Kostiuk et al. [15]. (*a*) Axial turbulent intensity component; (*b*) radial turbulent intensity component.

Figure 9 shows the radial turbulent intensity, v, for Cooper et al. [12]. Predictions in Fig. 9 are better than those for the axial component in Fig. 5. The GL-CL shows the closest agreement with data, while the $k-\varepsilon$ model is the worst. Reynolds shear stress and mean velocity are shown in Figs. 10 and 11, respectively. Excessive mixing is observed for the $k-\varepsilon$ model in Fig. 11. The SSG also overestimates mixing around $r/D=2.5$, where a radial wall jet develops. It may be related with the overpredicted Reynolds shear stresses in Fig. 10 (c).

Figure 12 shows mean velocity and axial and radial components of turbulent intensity for the impinging jet in Escudie et al. [9]. The GL-CL again gives the best agreement, while the results show a similar trend to those in Cooper et al. [12]. Uniform mean and turbulence quantities are assumed at the nozzle exit. The exit profile does not have any noticeable effect on the results near the wall.

As noted in the above, the SSG is not satisfactory enough in an impinging jet, although it has been validated in flows such as a backward facing step [20] and a strongly swirling flow [21,34]. According to the energy budget in Fig. 7, it is crucial whether the abruptly produced turbulence energy is properly redistributed to other directional components. Redistribution of turbulence energy occurs mainly by the rapid pressure-strain term, which is modeled as proportional to production with an arbitrary coefficient C_2 in the GL. In the SSG the production based rapid term, $-C_1^* P b_{ij}$, in Eq. (10) is dominant over the other terms as shown in Fig. 6 (d). The quadratic slow term with the coefficient C_2 gives substantial influence in a swirling flow [21], while it has a negligible effect in a stagnating flow. Redistribution by the production based rapid term depends on anisotropy of the Reynolds stress. Since b_{11} in the stagnation region is estimated to be less than 0.39 from measurement, the redistributed turbulence energy in the SSG cannot be larger than that in the GL.

Another possibility for poor performance of the SSG may be the modeled dissipation equation of an ad hoc nature, which currently accompanies all three RSM's. In the present study we tried the modified coefficients, $C_{\varepsilon 1}$ and $C_{\varepsilon 2}$, as proposed by Champion and Libby [22]. Validation is performed for the countercurrent flows in Kostiuk et al. [15] and Mounaim-Rousselle et al. [16]. It is difficult to apply the functional forms suggested by Champion and Libby [22] to a wall impinging jet, because the viscous sublayer cannot be resolved with the wall function method used throughout this paper.

Figures 13–18 show results for the countercurrent jets in Kostiuk et al. [15]. The GL and the GL-CL are identical here, since there is no wall reflection term involved. Figure 13 (a) shows a profile of mean axial velocity along the axis. Mean axial and radial velocity in Fig. 13 (b) and 14 are, respectively, at 1.4 cm and 0.6 cm above the stagnation plane, where data are available. Note that mean axial velocity increases linearly

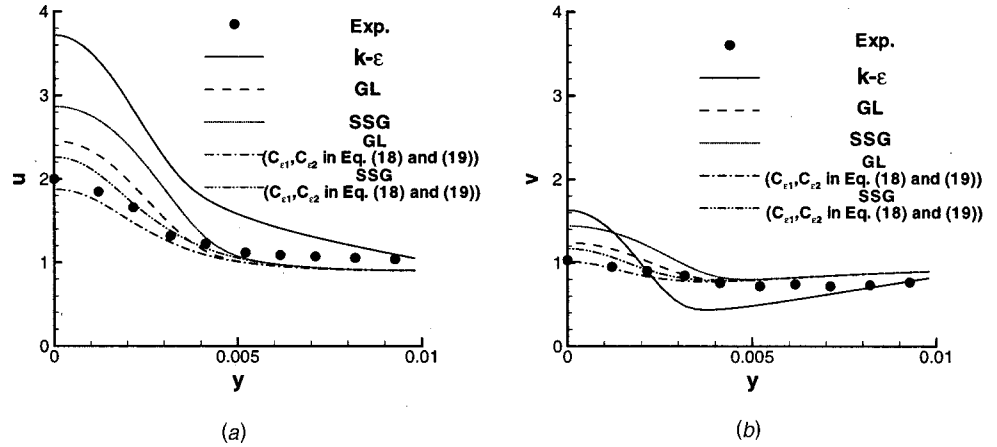

Fig. 17 Axial and radial turbulent intensity components on the axis for Case C in the countercurrent jets of Kostiuk et al. [15]. (*a*) Axial turbulent intensity component; (*b*) radial turbulent intensity component.

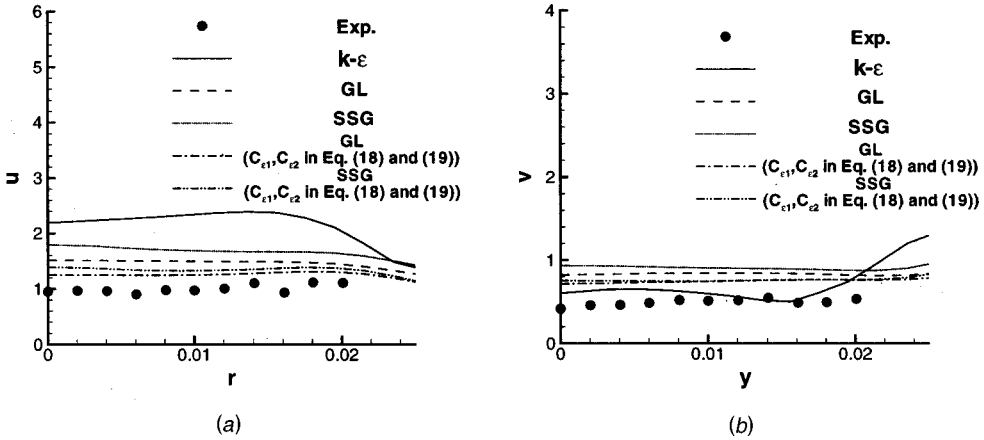

Fig. 18 Axial and radial turbulent intensity components at 0.6 cm above the stagnation plane for Case A in the countercurrent jets of Kostiuk et al. [15]. (*a*) Axial turbulent intensity component; (*b*) radial turbulent intensity component.

from the stagnation plane, while mean radial velocity increases linearly from the axis. A uniform bulk strain rate is assumed as a parameter to characterize the flow field in a similarity solution procedure [23,24].

There are three cases, A, B, and C, with different bulk strain rates in terms of the exit velocity and the distance between nozzles in Kostiuk et al. [15]. Axial and radial components of turbulent intensity are shown for the three cases in Fig. 15, 16, and 17, respectively. As in Cooper et al., simulation results tend to overestimate turbulent intensity near the stagnation plane. Discrepancy near the nozzle exit is due to inaccurate experimental correlations for inlet turbulence quantities. No measurements were made at the nozzle exit in Kostiuk et al. [15].

In Figs. 15–17 the $k-\varepsilon$ model significantly over predicts turbulent intensity as expected for the case with a large bulk strain rate. The production rate is proportional to the square of a normal strain rate in a stagnating flow. The SSG and the GL produce comparable results in reasonable agreement with measurements. Improvement is made by the modified $C_{\varepsilon 1}$ and $C_{\varepsilon 2}$ for both the GL and the SSG, although the SSG is still not any better than the linear pressure-strain model, GL.

Figure 18 shows axial and the radial components of turbulent intensity at 0.6 cm above the stagnation plane. They are uniform and planar near the axis, which is a desirable feature for a flame stabilized in a stagnation flow [15]. The turbulent intensity by the $k-\varepsilon$ model increases slightly in the radial direction. It is evident that an anisotropic structure of turbulence results in superior performance of the RSM's. It is shown that improvement is made by the modified coefficients in the dissipation equation not only on the axis but also at a distance from the axis.

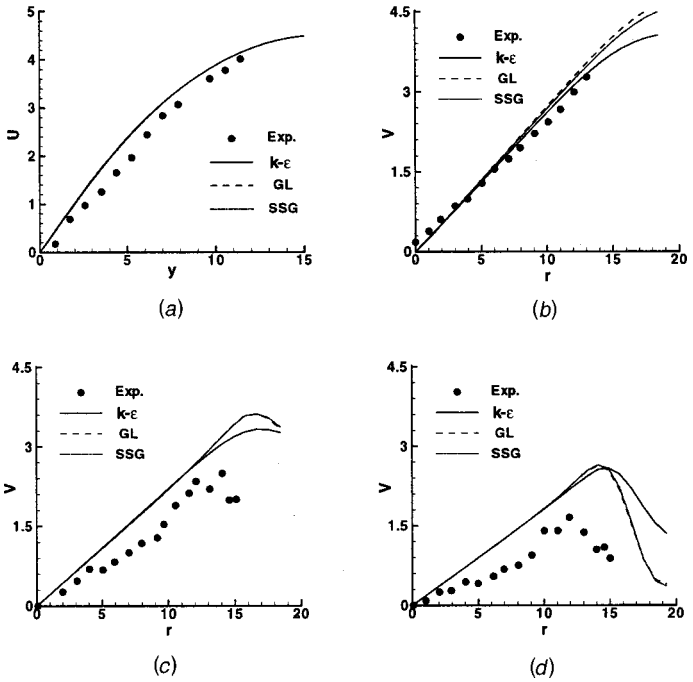

Fig. 19 Mean axial and radial velocities in the countercurrent jets of Mounaim-Rousselle et al. [16]. (*a*) On the axis; (*b*) on the stagnation plane; (*c*) 0.4 cm above the stagnation plane; (*d*) 0.6 cm above the stagnation plane.

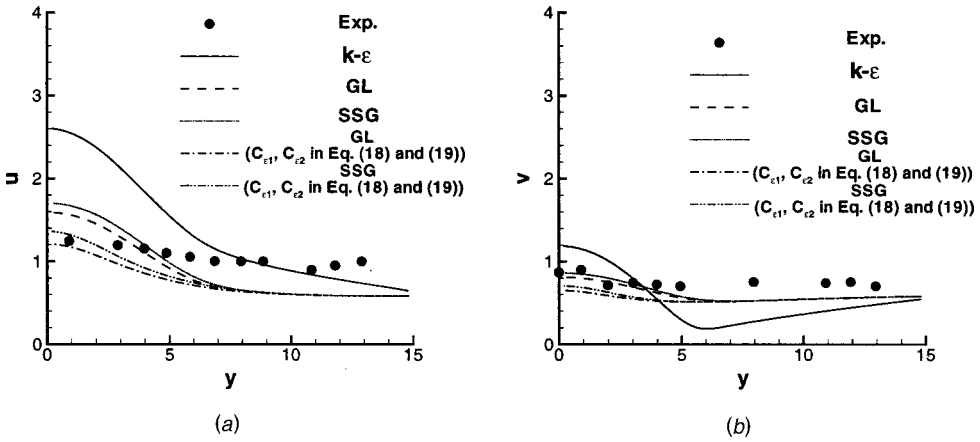

Fig. 20 Axial and radial turbulent intensity components on the axis in the countercurrent jets of Mounaim-Rousselle et al. [16]. (*a*) Axial turbulent intensity component; (*b*) radial turbulent intensity component.

Figures 19–23 show results for the countercurrent jets in Mounaim-Rousselle et al. [16]. Figure 19 (*a*) shows mean axial velocity along the axis. Mean radial velocity is shown in Fig. 19 (*b*) to Fig. 19 (*d*) on the stagnation plane and at 0.4 cm and 0.6 cm above the stagnation plane. The RSM's and the $k-\varepsilon$ model do not show any noticeable difference for mean axial velocity on the axis. The results for mean radial velocity are almost identical near the axis, while there occurs deviation as the flow develops into an outward radial jet. Discrepancy with data also tends to increase as the distance increases from the stagnation plane.

The axial and radial components of turbulent intensity are shown along the axis in Fig. 20. The overall trend is similar to that in Kostiuk et al. Discrepancy at the stagnation plane is attributed to different turbulence models, since the same inlet conditions were employed. Figure 21 shows uniform profiles of axial and radial turbulent intensities on the stagnation plane. The RSM's slightly overestimate the axial components near the axis, while the radial components show better agreement with data. The modified coefficients, $C_{\varepsilon 1}$ and $C_{\varepsilon 2}$, for the dissipation rate contribute to substantial improvement in the stagnation region as well as away from the axis.

Figure 22 shows turbulent kinetic energy and the ratio of axial and radial components of turbulent intensity on the stagnation plane. The $k-\varepsilon$ model shows poor prediction of turbulent kinetic energy, especially near the axis. Comparable results for the ratio of axial and radial components in Fig. 22 (*b*) are only due to highly overestimated turbulent intensities.

Figure 23 shows radial profiles of the dissipation rate on the stagnation plane and at 0.2 cm and 0.4 cm above the stagnation plane. There is significant discrepancy between measurements and the results of the $k-\varepsilon$ model. Although the RSM's produce better results than the $k-\varepsilon$ model, they fail to predict the dissipation rate increasing toward the axis on the stagnation plane in Fig. 23 (*a*). It is interesting to note that the results with the modified $C_{\varepsilon 1}$ and $C_{\varepsilon 2}$ show such increase near the stagnation region, although not in quantitative agreement with measurement.

Anisotropic states of the Reynolds stress in impinging and countercurrent jets are assessed by AIM's in Figs. 24 and 25. In an impinging jet on a wall the Reynolds stress becomes anisotropic along the axisymmetric expansion line, as the flow expands from the nozzle exit in Fig. 24. It then returns to an isotropic state along the axisymmetric expansion line near the wall. Recently, Nishino et al. [14] showed in their measurements that it eventually moves to another anisotropic state along the axisymmetric contraction line on the wall. Champion and Libby [22] found similar behavior in their mathematical analysis. The flow was anisotropic at the outer edge of the Region II due to evolution of turbulence from

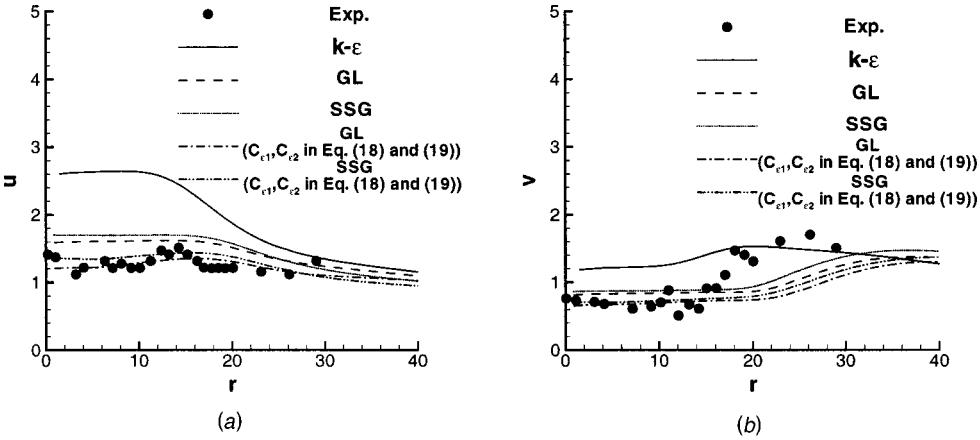

Fig. 21 Axial and radial turbulent intensity components on the stagnation plane in the countercurrent jets of Mounaim-Rousselle et al. [16]. (*a*) Axial turbulent intensity component; (*b*) radial turbulent intensity component.

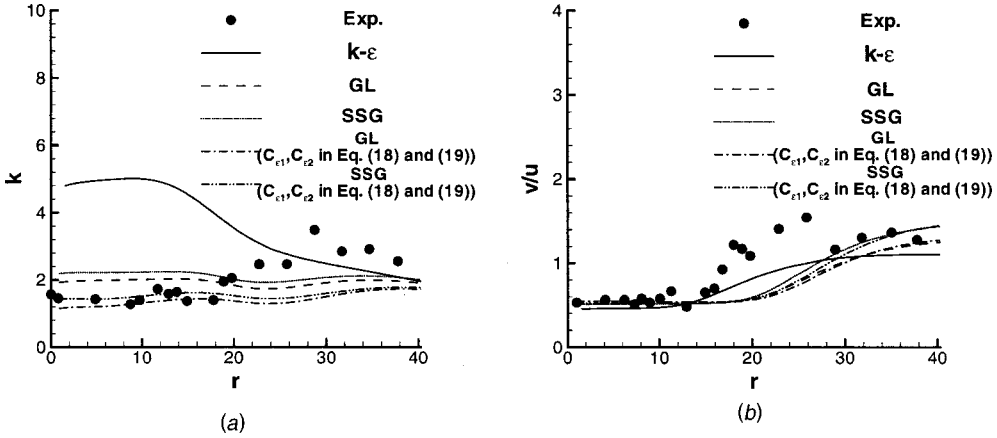

Fig. 22 Turbulent kinetic energy and the ratio of axial and radial turbulent intensity components on the stagnation plane in the countercurrent jets of Mounaim-Rousselle et al. [16]. (*a*) k; (*b*) *v*/*u*.

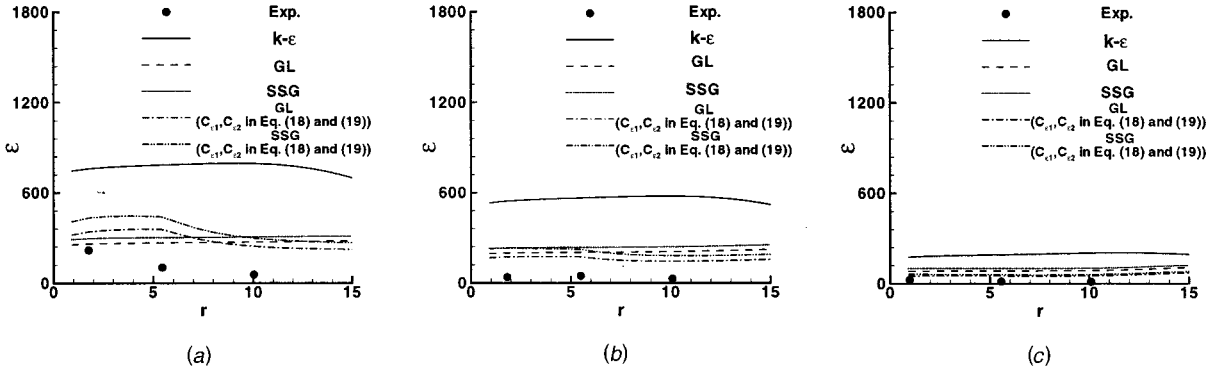

Fig. 23 The radial profiles of turbulent dissipation rate on and above the stagnation plane in the countercurrent jets of Mounaim-Rousselle et al. [16]. (*a*) On the stagnation plane; (*b*) 0.2 cm above the stagnation plane; (*c*) 0.4 cm above the stagnation plane.

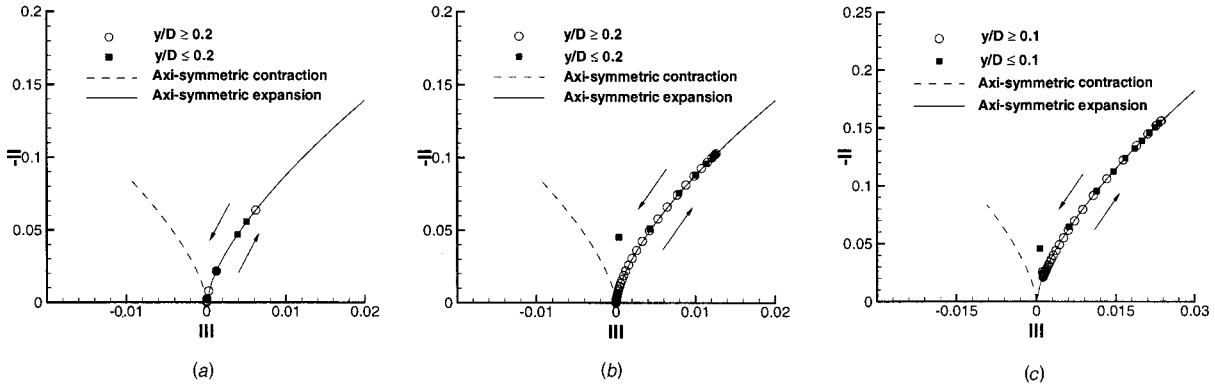

Fig. 24 AIM for the impinging jets. (*a*) Experiments for the impinging jet of Escudie et al. [9]; (*b*) predictions for the impinging jet of Escudie et al. [9]; (*c*) predictions for the impinging jet of Cooper et al. [12].

the exit. It changed to an isotropic state in the Region II to satisfy the matching condition and then became anisotropic again in the viscous sublayer, Region I, adjacent to the wall.

Calculated endpoints near the wall show minor deviation from the axisymmetric expansion line in Figs. 24 (*b*) and (*c*). It is due to the inappropriate values of C_{ij}, which were calibrated against flows parallel to a wall. The Reynolds stress does not reach an isotropic state at the endpoints, which are in the log law region in Fig. 24. The wall function method does not provide such resolution for the inner region including the viscous sublayer. The Reynolds stress moves along the axisymmetric expansion line monotonically in Fig. 25, until the flow stagnates at the stagnation plane. The degree of anisotropy on the stagnation plane is approximately proportional to the distance from the nozzle under the same conditions otherwise.

6 Conclusion

Numerical simulation is performed to evaluate the three RSM's, GL, GL-CL, and SSG, and the $k-\varepsilon$ model against available data in the literature for impinging and countercurrent turbulent jets.

1 The RSM's are superior to the $k-\varepsilon$ model near the stagnation region, where the production and the redistribution term are dominant to determine turbulence properties. The dissipation term

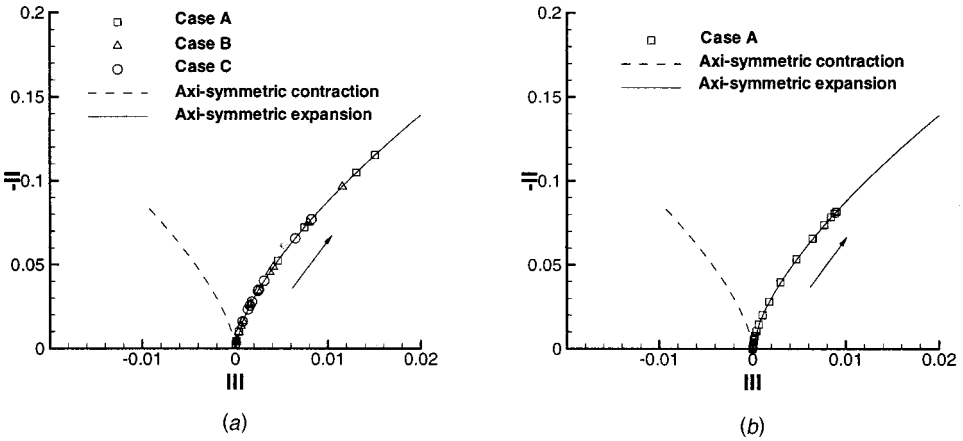

Fig. 25 AIM for the countercurrent jets. (*a*) Experiments for the countercurrent jets of Kostiuk et al. [15]; (*b*) predictions for the countercurrent jets of Kostiuk et al. [15].

turns out to be of a small magnitude in comparison with the former two terms in the energy budget. Results show that the predictive capabilities of the RSM's depend largely on modeling of the redistributive pressure-strain term in a stagnating flow.

2 The GL-CL with a modified wall reflection term showed the best performance among the three RSM's. The term, ϕ_{ij2}^{w}, in the GL works in the wrong way to suppress redistribution of the produced turbulence energy in the axial direction. Against the initial expectation, the SSG turned out not to be satisfactory enough in a stagnating flow. The SSG suffers from the common problem of underpredicted redistribution of turbulence energy.

3 Results of the RSM's are improved by adopting the modified coefficients for the dissipation rate, $C_{\varepsilon 1}$ and $C_{\varepsilon 2}$, suggested by Champion and Libby. Substantial improvement is obtained in the stagnation region for a range of the mean rate of strain in countercurrent jets. Standard values for $C_{\varepsilon 1}$ and $C_{\varepsilon 2}$ are retrieved in $r \geqslant R/2$ to produce comparable results in a radial jet away from the axis.

4 The AIM shows different anisotropic stress fields for impinging and countercurrent jets. In countercurrent jets the Reynolds stress becomes anisotropic from the nozzle exit along the axisymmetric expansion line. In impinging jets it returns to an isotropic state again as the flow stagnates on the wall. Although the wall function treatment cannot provide such resolution, it moves to another anisotropic state along the axisymmetric contraction line in the viscous sublayer.

Nomenclature

a = mean rate of strain ($a = 2U_0/H$)
a_b = bulk strain rate
a_{ij} = anisotropic stress ($a_{ij} = \overline{u_i u_j}/k - 2/3\delta_{ij}$)
b_{ij} = anisotropy of the Reynolds stress
C's = model constants in turbulence models
D_{ij} = diffusion term in the Reynolds stress transport equation
D = nozzle diameter
d = hole diameter of the perforated plate
f_y = length scale function
H = distance between nozzles or height above a plate
k = turbulent kinetic energy
l_t = integral length scale
n_i = normal component of a unit vector on the wall
P_{ij} = production rate of the Reynolds stress
P = production rate of turbulent kinetic energy ($P = 0.5P_{kk}$)
r = radial distance
S_{ij} = mean rate of strain
$\overline{u_i u_j}$ = Reynolds stress
u, v = turbulent intensity components
u_τ = friction velocity ($u_\tau = \sqrt{\tau_w/\rho}$)
U, V = mean velocity components
U_0 = mean velocity at the nozzle exit
U_b = bulk velocity at the nozzle exit
W_{ij} = mean vorticity tensor
x = distance from the perforated plate to the nozzle exit
x_i = coordinate direction
y = distance from the wall or stagnation plane
y^+ = nondimensional distance from the wall ($y^+ = \rho u_\tau y/\mu$)
II,III = second and third invariants of b_{ij}
δ_{ij} = Kronecker delta
ρ = density
τ_w = wall shear stress
ε = scalar dissipation rate of turbulent kinetic energy
ε_{ij} = dissipation rate tensor of the Reynolds stress
ν = kinematic viscosity
ϕ_{ij} = pressure-strain correlation

References

[1] Craft, T. J., Graham, L. J. W., and Launder, B. E., 1993, "Impinging Jet Studies for Turbulence Model Assessment-II. An Examination of the Performance of Four Turbulence Models," Int. J. Heat Mass Transf., **36**(10), pp. 2685–2697.

[2] Dianat, M., Fairweather, M., and Jones, W. P., 1996, "Predictions of Axisymmetric and Two-Dimensional Impinging Turbulent Jets," Int. J. Heat Fluid Flow, **17**, pp. 530–538.

[3] Dianat, M., Fairweather, M., and Jones, W. P., 1996, "Reynolds Stress Closure Applied to Axisymmetric Impinging Turbulent Jets," Theor. Comput. Fluid Dyn., **8**, pp. 435–447.

[4] Craft, T. J., and Launder, B. E., 1991, "Computation of Impinging Flows using Second-Moment Closures," 8th Symp. on Turbulent Shear Flows, 8–5.

[5] Parneix, S., Behnia, M., and Durbin, P. A., 1999, "Predictions of Turbulent Heat Transfer in an Axisymmetric Jet Impinging on a Heated Pedestal," ASME J. Heat Transfer, **121**, pp. 43–49.

[6] Behnia, M., Parneix, S., Shabany, Y., and Durbin, P. A., 1999, "Numerical Study of Turbulent Heat Transfer in Confined and Unconfined Impinging Jets," Int. J. Heat Fluid Flow, **20**, pp. 1–9.

[7] Kostiuk, L. W., Bray, K. N. C., and Cheng, R. K., 1993, "Experimental Study of Premixed Turbulent Combustion in Opposed Streams. Part II-Reacting Flow Field and Extinction," Combust. Flame, **92**, pp. 396–409.

[8] Cho, P., Law, C. K., Hertzberg, J. R., and Cheng, R. K., 1986, "Structure and Propagation of Turbulent Premixed Flames Stabilized in a Stagnation Flow," 21th Symp. (international) on Combustion, pp. 1493–1499.

[9] Escudie, D., Haddar, E., and Brun, M., 1999, "Influence of Strain Rate on a Premixed Turbulent Flame Stabilized in a Stagnating Flow," Exp. Fluids, **27**, pp. 533–541.

[10] Lee, E., Choi, C. R., and Huh, K. Y., 1998, "Application of the Coherent Flamelet Model to Counterflow Turbulent Premixed Combustion and Extinction," Combust. Sci. Technol., **138**, pp. 1–25.

[11] Gutmark, E., Wolfshtein, M., and Wygnanski, I., 1978, "The Plane Turbulent Impinging Jet," J. Fluid Mech., **88**, Part A, pp. 737–756.

[12] Cooper, D., Jackson, D. C., Launder, B. E., and Liao, G. X., 1993, "Impinging

Jet Studies for Turbulence Model Assessment-I. Flow-Field Experiments,'' Int. J. Heat Mass Transf., **36**(10), pp. 2675–2684.
[13] Ueda, T., Imaizumi, H., Mizomoto, M., and Shepherd, I. G., 1997, ''Velocity Statistics along the Stagnation Line of an Axisymmetric Stagnating Turbulent Flow,'' Exp. Fluids, **22**, pp. 473–481.
[14] Nishino, K., Samada, M., Kasuya, K., and Torii, K., 1996, ''Turbulence Statistics in the Stagnation Region of an Axisymmetric Impinging Jet Flow,'' Int. J. Heat Fluid Flow, **17**, pp. 193–201.
[15] Kostiuk, L. W., Bray, K. N. C., and Cheng, R. K., 1993, ''Experimental Study of Premixed Turbulent Combustion in Opposed Streams. Part I-Nonreacting Flow Field,'' Combust. Flame, **92**, pp. 377–395.
[16] Mounaim-Rousselle, C., and Gokalp, I., 1994, ''Strain Effects on the Structure of Counterflowing Turbulent Premixed Flames,'' 25th Symp. (international) on Combustion, pp. 1199–1205.
[17] Ashforth-Frost, S., and Jambunathan, K., 1996, ''Numerical Prediction of Semi-Confined Jet Impingement and Comparison with Experimental Data,'' Int. J. Numer. Methods Fluids, **23**, pp. 295–306.
[18] Rabbitt, M. J., 1997, ''Some Validation of Standard, Modified and Non-linear $k-\epsilon$ Turbulence Models,'' Int. J. Numer. Methods Fluids, **24**, pp. 965–986.
[19] Speziale, C. G., Sarkar, S., and Gatski, T. B., 1991, ''Modelling the Pressure-Strain Correlation of Turbulence: an Invariant Dynamic Systems Approach,'' J. Fluid Mech., **227**, pp. 245–272.
[20] Basara, B., and Younis, B. A., 1995, ''Assessment of the SSG Pressure-Strain Model in Two-Dimensional Turbulent Separated Flows,'' Appl. Sci. Res., **55**, pp. 39–61.
[21] Younis, B. A., Gatski, T. B., and Speziale, C. G., 1996, ''Assessment of the SSG Pressure-Strain Model in Free Turbulent Jets with and without Swirl,'' ASME J. Fluids Eng., **118**, pp. 800–809.
[22] Champion, M., and Libby, P. A., 1994, ''Reynolds Stress Description of Opposed and Impinging Turbulent Jets II. Axisymmetric Jets Impinging on Nearby Walls,'' Phys. Fluids, **6**(5), pp. 1805–1819.
[23] Champion, M., and Libby, P. A., 1991, ''Asymptotic Analysis of Stagnating Turbulent Flows,'' AIAA J., **29**(1), pp. 16–24.
[24] Champion, M., and Libby, P. A., 1993, ''Reynolds Stress Description of Opposed and Impinging Turbulent Jets. Part I. Closely Spaced Opposed Jets,'' Phys. Fluids A, **5**(1), pp. 203–216.
[25] Bray, K. N. C., Champion, M., and Libby, P. A., 2000, ''Premixed Flames in Stagnating Turbulence Part IV: A New Theory for the Reynolds Stresses and Reynolds Fluxes Applied to Impinging Flows,'' Combust. Flame, **120**, pp. 1–18.
[26] Gibson, M. M., and Launder, B. E., 1978, ''Ground Effects on Pressure Fluctuations in the Atmospheric Boundary Layer,'' J. Fluid Mech., **86**, pp. 491–511.
[27] Daly, B. J., and Harlow, F. H., 1970, ''Transport Equations in Turbulence,'' Phys. Fluids, **13**, pp. 2634–2649.
[28] Rotta, J. C., 1951, ''Statistische Theorie Nichthomogener Turbulenz,'' Z. Phys., **129**, pp. 547–572.
[29] Patankar, S. V., and Spalding, D. B., 1972, ''A Calculation Procedure for Heat, Mass and Momentum Transfer in Three-Dimensional Parabolic Flows,'' Int. J. Heat Mass Transf., **15**, pp. 1787–1805.
[30] Libby, P. A., and Williams, F. A., 1993, *Turbulent Reacting Flows*, Academic Press, pp. 309–374.
[31] Van Leer, B., 1974, ''Towards the Ultimate Conservative Difference Scheme. II: Monotonicity and Conservation Combined in a Second-Order Scheme,'' J. Comput. Phys., **14**, pp. 361–370.
[32] FLUENT Users' Manual Version 5, Fluent Europe Ltd. Sheffield, UK, 1998.
[33] Launder, B. E., and Sharma, B. I., 1974, Lett. Heat Mass Transfer, **1**, pp. 131–138.
[34] Chen, J. C., and Lin, C. A., 1999, ''Computations of Strongly Swirling Flows with Second Moment Closures,'' Int. J. Numer. Methods Fluids, **30**, pp. 493–508.

Effect of Radial Clearance on the Flow Between Corotating Disks in Fixed Cylindrical Enclosures

Mohammad Al-Shannag

Joan Herrero

Universitat Rovira i Virgili,
Department of Chemical Engineering,
43006 Tarragona,
Catalonia, Spain

Joseph A. C. Humphrey[1]
Department of Mechanical and Aerospace Engineering,
University of Virginia,
Charlottesville, VA 22904-4746

Francesc Giralt
Universitat Rovira i Virgili,
Department of Chemical Engineering,
43006 Tarragona,
Catalonia, Spain

Numerical results are obtained for the isothermal laminar flow of air between a pair of disks attached to and rotating with a hub in a fixed cylindrical enclosure. The presence of radial clearances or "gaps" between the rims of the disks and the curved enclosure wall, and the finite thickness of the disks, are considered in the calculations. The gaps allow time- and circumferentially-dependent axially-directed air flow exchanges between the contiguous inter-disk spaces. As a consequence, axisymmetric calculations of the flow, whether using boundary conditions in the gaps or extended to include the entire flow domain, fail to faithfully reproduce the experimentally measured radial variations of the mean and rms circumferential velocity components in the inter-disk space. Likewise, three-dimensional calculations using the symmetry-plane boundary condition in the gaps also fail to reproduce these variations. In contrast, computationally intensive three-dimensional calculations of the entire flow domain, including the gaps, yield results in very good agreement with the measured mean and rms velocities. These three-dimensional calculations reveal large velocity fluctuations in the gap regions accompanied by corresponding large fluctuations of the inter-disk flow, reflecting a destabilization of the structure and dynamics of the latter by the former. The axisymmetric calculations as well as those using the symmetry-plane condition in the gap are included in this study principally to elucidate their shortcomings in simulating the three-dimensional flows considered; they are not the main goal of the study. Notwithstanding, the physically approximate, full domain axisymmetric calculations yield useful qualitative results. They show that increasing gap size decreases disk surface shear and the associated disk torque coefficient, but at the cost of destabilizing the inter-disk flow. This observation is in agreement with earlier findings and is better understood as the result of the present study.
[DOI: 10.1115/1.1487355]

Introduction

Problem Statement. The unobstructed motion of a fluid driven by a pair of coaxial disks corotating in a fixed cylindrical enclosure is of fundamental interest and has interesting mixing applications. This configuration has also been proposed as a first approximation for modeling the bulk flow of air in disk drives; see Schuler et al. [1], Abrahamson et al. [2], and Humphrey et al. [3] for early reviews and Herrero et al. [4,5] for more recent references. Of interest here is the case shown in Fig. 1 which includes the two end spaces defined by the outer surface of each disk and the flat (top or bottom) fixed enclosure wall facing it. The disks are attached to a hub and rotate at constant angular velocity, Ω, such that the Reynolds number is $\mathrm{Re}=\Omega R_2^2/\nu$, where R_2 is the radius of the disks and ν is the kinematic viscosity of the fluid. The presence of a small gap of width A between the rim of each disk and the curved enclosure wall allows axial flow exchanges between the contiguous inter-disk and disk/end-wall spaces. Notwithstanding, earlier work relating to disk drives has mostly ignored, assumed negligible, or oversimplified the effect of the gaps on the inter-disk and disk/end-wall flows. This investigation is concerned with quantifying the effect of the gaps on the structure and dynamics of the flows in these regions as well as on the torque required to rotate the disks.

Background. Many recent experimental fluid mechanics studies of coaxial disks corotating in cylindrical enclosures have typically involved several disks in a stack and have focused on visualizing and measuring the velocity field. Although necessary to allow disk rotation, in these studies the effects of the gaps on the flow have not been systematically investigated. An exception is the work by Hudson and Eibeck [6] who measured the total torque required to corotate a stack of N disks ($N=1$, 3 and 5) as a function of the Reynolds number, Re, the dimensionless inter-disk spacing, H/R_2, and the dimensionless gap width, A/R_2. (Abrahamson et al. [2], Hudson and Eibeck [6], Humphrey et al. [7] and others have also investigated the influence of an obstruction on the inter-disk flow but that effect is not considered here.) Hudson and Eibeck [6] found a weak dependence of the torque on the gap width for values $A/R_2<0.08$ and $H/R_2<0.2$ when $8\times10^4<\mathrm{Re}<2.8\times10^5$. Analytical investigations by Schuler et al. [1] and Humphrey et al. [7], and numerical studies by Humphrey et al. [8], Iglesias and Humphrey [9] and Herrero et al. [4,5] have assumed $A=0$, or have imposed a symmetry-plane or a periodic-plane boundary condition in the gap regions. In spite of these simplifications, these studies have quantified the nature and characteristics of the unsteady, 3D, vortical flow between a pair of corotating disks as a function of H/R_2 and Re. In particular, Iglesias and Humphrey [9] show that the presence of gaps lowers the threshold value of Re required for transition from a steady axisymmetric flow to the corresponding unsteady axisymmetric flow. Similarly, Herrero et al. [4] show that, for fixed H/R_2, the flow between a pair of corotating disks evolves from a steady axisymmetric state to an unsteady 3D state with increasing Re. (Henceforth, in this communication all references to ''axisymmetric'' flow imply a 2D flow that is circumferentially symmetric.)

The assumption of a symmetry-plane boundary condition in the gaps precludes axial flow through them. This limitation is somewhat relieved by resorting to a periodic-plane boundary condition

[1]Corresponding author.

Contributed by the Fluids Engineering Division for publication in the JOURNAL OF FLUIDS ENGINEERING. Manuscript received by the Fluids Engineering Division August 2, 1999; revised manuscript received February 1, 2002. Associate Editor: U. Ghia.

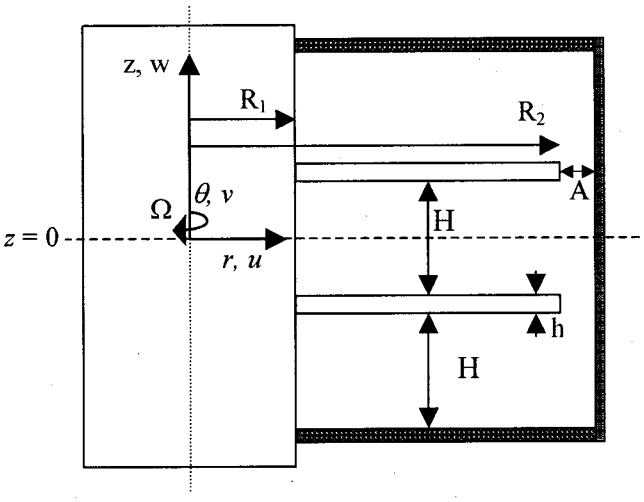

Fig. 1 Sketch of the flow configuration investigated numerically. The geometrical parameters shown match those of the test section investigated experimentally by Schuler et al. [1] in which: $R_1=56.4$ mm, $R_2=105$ mm, $H=9.53$ mm, $h=1.91$ mm and $A=2.7$ mm. In this study calculations are performed for five gap sizes ($A/R_2=0.0064$, 0.013, 0.026, 0.052 and 0.077) with $Re=2.1\times10^4$.

but, to be applied in a logically consistent manner, such a condition requires the assumption of axisymmetric flow. The result is a flow across the gaps that may change its axial sense of motion with time but which, instantaneously, is everywhere (circumferentially) directed in the same (axial) direction. It is clear that the imposition of a symmetry-plane or periodic-plane boundary condition in the gaps leads to unrealistic constraints on fluid motion and, in particular, that such conditions do not apply to the gaps associated with the two end disks in an enclosure.

The calculations performed by Tzeng and Fromm [10] and by Humphrey et al. [7] apply to a stack of disks where the gap regions are part of the calculation domain. While limited to axisymmetric flows, the results point to the importance of avoiding artificial gap boundary conditions by including the gap regions in the calculation domain. The problem then becomes one of ensuring sufficient grid refinement to obtain accurate results throughout the entire flow field, but especially in the gap regions which affect the accuracy of the calculations elsewhere in the domain.

Purpose of This Study. As will be shown, the presence of gaps between the rims of the corotating disks and the fixed curved enclosure wall in the geometry of Fig. 1 significantly affects the structure and dynamics of the flow in the inter-disk space. Earlier attempts to match measurements and calculations of the mean and rms circumferential velocity components in the inter-disk space have met with mixed success. For example, Fig. 4 (discussed below) provides a comparison between measurements and calculations of these two quantities along the mid-plane, $Z=0$, of the center pair of disks in a stack of N disks. The measurements are obtained in a stack with $N=4$ disks while all the calculations have been made in a stack with $N=2$ disks; otherwise, the measured and calculated flow conditions correspond exactly. The measurements are from Schuler et al. [1] for a geometry with the dimensions given in Fig. 1 and a disk speed of rotation of 300 rpm corresponding to $Re=2.1\times10^4$. Of immediate interest here is the comparison between these measurements and the 3D calculations of Humphrey et al. [8], performed for a pair of disks of zero thickness using a symmetry-plane boundary condition in the gaps. (In this and the following figures, $R=r/R_2$, $Z=z/H$, $U=\langle u\rangle/\Omega R_2$, $U_{\rm rms}=u_{\rm rms}/\Omega R_2$, $V=\langle v\rangle/\Omega R_2$, $V_{\rm rms}=v_{\rm rms}/\Omega R_2$, $W=\langle w\rangle/\Omega R_2$, and $W_{\rm rms}=w_{\rm rms}/\Omega R_2$, where "$\langle\ \rangle$" and the subscript "rms" denote the mean and rms values of the velocity components.) Both the calculated mean and rms circumferential velocities show qualitative agreement with the experimental data but significant discrepancies arise, particularly for the rms velocity. The rms measurements (and calculations) peak markedly at three distinct radial locations where flow unsteadiness contributes to the velocity fluctuations. The large experimental values of the rms at $R\leqslant0.75$ contrast with the results obtained from both theoretical and numerical analyses performed to date which predict solid body rotation conditions for the flow in this region.

The purpose of this study is to accurately assess the effects of the gaps on the flow in a fixed cylindrical enclosure containing a pair of corotating disks. The geometry of interest is that of Fig. 1, where the linear dimensions correspond to the experiment of Schuler et al. [1] assuming two disks, as opposed to four, in the enclosure. The structure and dynamics of the flow, as well as the variation of the disk torque coefficient, C_M, are analyzed numerically as a function of A/R_2 for a fixed value of $Re=2.1\times10^4$. Both axisymmetric and 3D calculations are performed and the effects on the flow of imposing symmetry-plane or periodic-plane boundary conditions in the gaps are examined. The axisymmetric calculations as well as those using the symmetry-plane condition in the gap are included in this study for completeness. They elucidate the shortcomings in simulating the three-dimensional flows considered; they are not the main goal of the study. Notwithstanding, as will be shown, the physically approximate, full domain axisymmetric calculations yield useful qualitative results.

Conservation Equations

The constant property, unsteady, axisymmetric or 3D, laminar flow of air is assumed. The corresponding mass and momentum conservation equations expressed relative to a fixed cylindrical coordinate system (see Fig. 1) are:

mass:

$$\frac{\partial w}{\partial z}+\frac{\partial u}{\partial r}+\frac{u}{r}+\frac{1}{r}\frac{\partial v}{\partial\theta}=0 \tag{1}$$

r-momentum:

$$\frac{Du}{Dt}=-\frac{1}{\rho}\frac{\partial p}{\partial r}+\nu\left\{\frac{\partial}{\partial r}\left(\frac{1}{r}\frac{\partial}{\partial r}[ru]\right)+\frac{1}{r}\frac{\partial^2 u}{\partial\theta^2}-\frac{2}{r^2}\frac{\partial v}{\partial\theta}+\frac{\partial^2 u}{\partial z^2}\right\}+\nu^2/r \tag{2}$$

θ-momentum:

$$\frac{Dv}{Dt}=-\frac{1}{\rho r}\frac{\partial p}{\partial\theta}+\nu\left\{\frac{\partial}{\partial r}\left(\frac{1}{r}\frac{\partial}{\partial r}[rv]\right)+\frac{1}{r^2}\frac{\partial^2 v}{\partial\theta^2}+\frac{2}{r^2}\frac{\partial u}{\partial\theta}+\frac{\partial^2 v}{\partial z^2}\right\}-uv/r \tag{3}$$

z-momentum:

$$\frac{Dw}{Dt}=-\frac{1}{\rho}\frac{\partial p}{\partial z}+\nu\left\{\frac{1}{r}\frac{\partial}{\partial r}\left(r\frac{\partial w}{\partial r}\right)+\frac{1}{r^2}\frac{\partial^2 w}{\partial\theta^2}+\frac{\partial^2 w}{\partial z^2}\right\} \tag{4}$$

In Eqs. (2)–(4), u, v, w are the velocity components in the r, θ, and z coordinate directions, p is pressure, and t is time. D/Dt denotes the operator $[\partial/\partial t+w(\partial/\partial z)+u(\partial/\partial r)+vr(\partial/\partial\theta)]$, not to be confused with the substantial derivative since the base vector variation terms have been placed on the right-hand side of these equations.

For both axisymmetric and 3D flows, Eqs. (1)–(4) are solved subject to the following boundary conditions,

$$u=w=0;\ v=\Omega r \quad \text{on all rotating surfaces (hub and disks)} \tag{5a}$$

$$u=v=w=0 \quad \text{on all fixed surfaces (curved, top and bottom walls of the enclosure)} \tag{5b}$$

The conditions for the 3D flows investigated in this work lead to aperiodic, modulated motions corresponding to "Region II" type flows in the study by Herrero et al. [4]. Therefore, it is necessary to resolve the entire flow field in the circumferential coordinate direction; that is, over a 360 degree θ domain. For this, circumferentially-periodic boundary conditions are imposed for the three velocity components in the θ-coordinate direction.

For those flow calculations restricted to the inter-disk space, one of the following two boundary conditions is implemented in the gap, $R_2 < r < R_2 + A$:

(a) Symmetry-plane:

$$\frac{\partial u}{\partial z} = \frac{\partial v}{\partial z} = w = 0 \quad \text{at} \quad z = \pm (H+h)/2 \tag{6}$$

(a) Periodic-plane:

$$(u,v,w,p)_{z=-(H+h)/2} = (u,v,w,p)_{z=(H+h)/2} \tag{7}$$

Numerical Algorithm

The calculations have been performed using an upgraded version of the CUTEFLOWS numerical algorithm developed for unsteady, constant property, 2D and 3D flows. CUTEFLOWS (Computing Unsteady Three-dimensional Elliptic Flows) is second-order accurate in both space and time and has been extensively tested and used for a wide variety of problems; see Humphrey et al. [8], Iglesias and Humphrey [9], Herrero et al. [4,5] and the references therein. The upgraded algorithm is fourth-order accurate in both space and time. Both algorithms are based on a staggered-grid, control-volume discretization approach for deriving finite difference forms of the conservation equations in terms of their primitive variables. Mass conservation yields a discrete Poisson equation that is solved for pressure using the conjugate gradient method. The upgraded algorithm uses an upstream-biased differencing scheme (Rai and Moin [11]) for the convection terms. The spatially discretized momentum conservation equations are explicitly integrated in time by means of a fourth-order Runge-Kutta scheme. Like the original CUTEFLOWS code, the upgraded algorithm is capable of reproducing all known features of the unsteady, 3D, vortical flow between a pair of corotating disks. For further details see the references cited above.

Effect of Grid Refinement. The grid independence of the calculated results is established first for the case of axisymmetric flow. For this, the case with a gap ratio $A/R_2 = 0.026$ is investigated for the conditions shown in Fig. 1, corresponding to the experiment of Schuler et al. [1]. This case is solved using increasingly refined $(R\text{-}Z)$ grids until the numerical results for the two finest grids essentially coincide. (Meaning that maximum discrepancies between calculated velocity components on the finest two grids are less than 5%, the average being 2%.) These are full domain calculations with no boundary conditions imposed in the gaps. We comment below on the results obtained for this case on three grids referred to as "coarse," "medium" and "fine."

In all cases the grids are nonuniform in the R and Z directions. They are constructed as in Herrero et al. [4] who calculated the flow between a pair of disks with the dimensions of Fig. 1 but with $A = 0$. As in that work, current near-wall node densities allow for the presence of at least five nodes in the disk Ekman layers and the curved wall boundary layer. In the inter-disk space and in each of the disk/end-wall spaces, the spacing between nodes increases linearly from each wall by a grid expansion factor not larger than 1.2. In addition, the grid spacing is not allowed to exceed 5% of the total distance covered by the grid in the radial and axial directions. Table 1 summarizes the minimum and maximum spacings and expansion factors used in the tests conducted for $A/R_2 = 0.026$. In the gap regions the grid is distributed uniformly in the radial and axial directions, with a spacing equal to the minimum spacing listed in Table 1. All calculations are performed using a dimensionless integration time step, $\Delta\tau = \Omega\ \Delta t$, set to $\Delta\tau \leqslant 0.003$. This time step corresponds to a physical displacement equal to or less than 5.4 degrees for a disk rotating at 300 rpm ($\Omega = 10\ \pi$ rad/s) and guarantees stable and accurate convergence.

Table 1 Minimum and maximum spacing and expansion factors used in the axisymmetric flow calculations with $A/R_2 = 0.026$

Coordinate	Grid (Nodes)	Minimum Spacing, mm	Maximum Spacing, mm	Expansion factor
R-direction	Coarse (90)	0.15000	0.88955	1.20
	Medium (118)	0.12273	0.68972	1.10
	Fine (182)	0.07500	0.49968	1.05
Z-direction	Coarse (132)	0.14690	0.47530	1.20
	Medium (164)	0.12273	0.25720	1.10
	Fine (240)	0.07346	0.24562	1.05

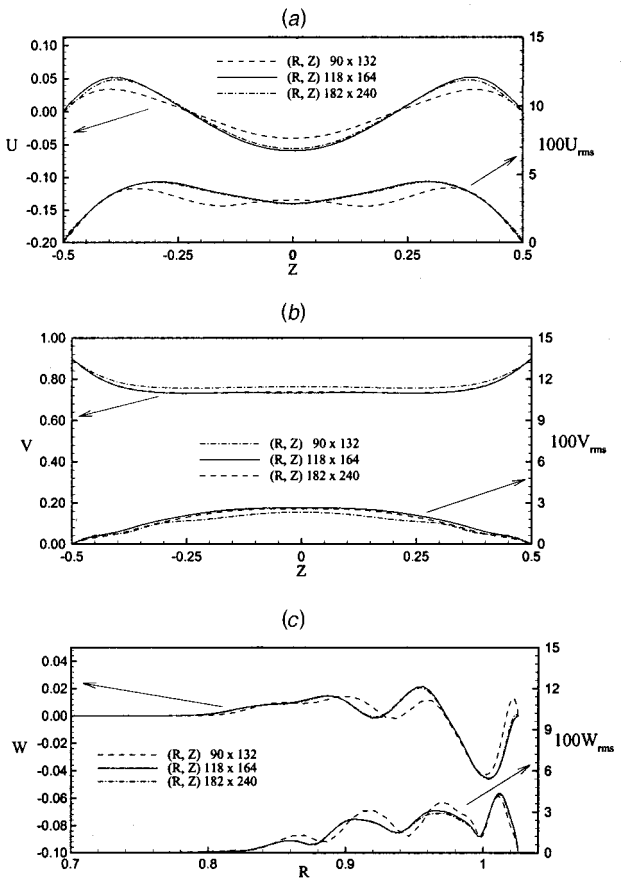

Fig. 2 Effect of grid refinement on axisymmetric calculations of the mean and rms velocities for $Re = 2.1 \times 10^4$ with $A/R_2 = 0.026$. (a) Axial profiles of radial velocity components at $R = 1.0$. (b) Axial profiles of the circumferential velocity components at $R = 0.9$. (c) Radial profiles of the axial velocity components at $Z = 0.25$.

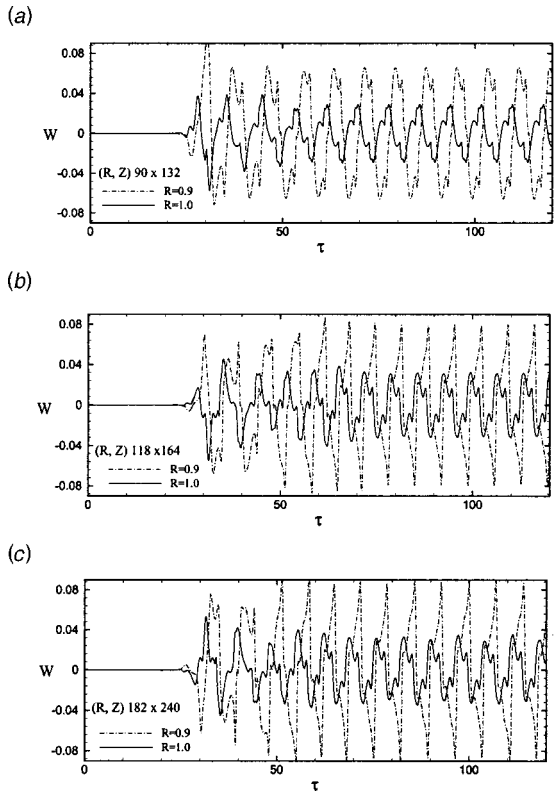

Fig. 3 Effect of grid refinement on the time dependence of the axial velocity component at $Z=0$ for $R=0.90$ and 1.0. Calculation conditions correspond to Fig. 2.

Figures 2(*a*)-(*c*) and 3(*a*)-(*c*) show the axisymmetric flow results obtained for the case with $A/R_2=0.026$ on the three grids. Profiles of the mean and rms velocity components are compared in Figs. 2(*a*)-(*c*). It is clear from these two figures, particularly in the gap regions shown in Fig. 2(*c*), that the results of the coarse grid (90×132) and the medium grid (118×164) do not agree. However, the results of the medium grid essentially coincide with those obtained with the fine grid (182×240). Time records of the dimensionless axial velocity component corresponding to two mid-plane locations with $R=0.9$ and $R=1.0$ are shown in Figs. 3(*a*)-(*c*). While the coarse grid does not accurately resolve the velocity oscillations and amplitudes, the records obtained on the medium and fine grids are in very good agreement. From these tests we conclude that a nonuniform grid consisting of 118×164 (R-Z) nodes is sufficiently accurate for axisymmetric calculations of the flow with $A/R_2=0.026$. Table 2 shows the values of the (R-Z) grids used for each of the axisymmetric cases investigated.

For the 3D calculations, tests are performed for the case with $A/R_2=0.026$ using the above 118×164 (R-Z) grid in combination with 64 or 128 equally spaced grid nodes in the θ direction. The differences between the results obtained with these two grids are sufficiently small (on average, less than 2% for the mean and less than 4% for the rms) to allow calculations of the cases with $A/R_2=0.026$ and $A/R_2=0.013$ using 64 nodes in the θ direction. (Note that setting 64 nodes in the θ direction yields a circumferential grid refinement that is more than twice that employed by Humphrey et al. [8].) The adequacy of the final 3D grids used is further confirmed by the goodness of the mean and rms velocity results obtained for the case with $A/R_2=0.026$ (Fig. 7, discussed below) relative to the experimental measurements.

Table 2 Grid nodes used in the axisymmetric flow calculations of the various A/R_2 cases

Coordinate	A/R_2				
	0.0064	0.013	0.026	0.052	0.077
R-direction (nodes)	104	108	118	140	162
Z-direction (nodes)	164	164	164	164	164

Results

The dimensions of the geometry shown in Fig. 1 match those of the experiment performed by Schuler et al. [1] for which $A/R_2=0.026$. In addition to this case, detailed calculations are performed for the case with $A/R_2=0.013$ to further elucidate the effects of the gap on the flow. Cases with other values of A/R_2 (0.0064, 0.013, 0.026, 0.052 and 0.077) are also examined for their effects on the disk torque coefficient. In order to vary A/R_2 for these cases, the quantity A is changed by varying the inside radius of the cylindrical enclosure. Each calculation case, corresponding to a particular value of A/R_2, is started from a fluid at rest and extended over a time period long enough to ensure a statistically stationary flow. A single disk angular velocity is considered corresponding to the experimental value of 300 rpm ($\mathrm{Re}=2.1\times10^4$).

Effect of the Gaps on the Flow Structure and Dynamics The structure and dynamics of the flow are investigated in detail for two gap ratios ($A/R_2=0.026$ and 0.013). The geometry with $A/R_2=0.026$ is solved first, by restricting attention to the inter-disk space and imposing symmetry-plane or periodic-plane boundary conditions in the gaps. For this: (i) axisymmetric and 3D calculations are performed with the symmetry-plane condition

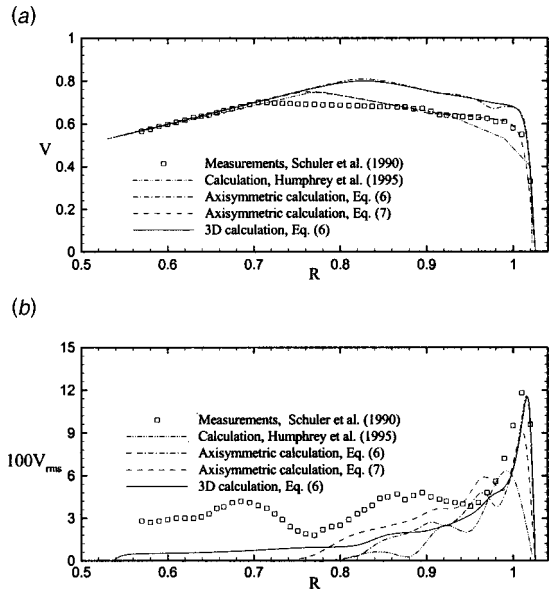

Fig. 4 Measured and calculated radial profiles of the mean (*a*) and rms (*b*) circumferential velocities along the inter-disk mid-plane, $Z=0$, for the case with $A/R_2=0.026$. Calculations are restricted to the inter-disk space of Fig. 1 using symmetry-plane (Eq. (6)) or periodic-plane (Eq. (7)), boundary conditions in the gaps. The axisymmetric results are averaged over time and the 3D results (and the measurements) are averaged over time and in the circumferential direction. The 3D calculations by Humphrey et al. [8] are for a pair of disks of zero thickness using symmetry-plane boundary conditions in the gaps.

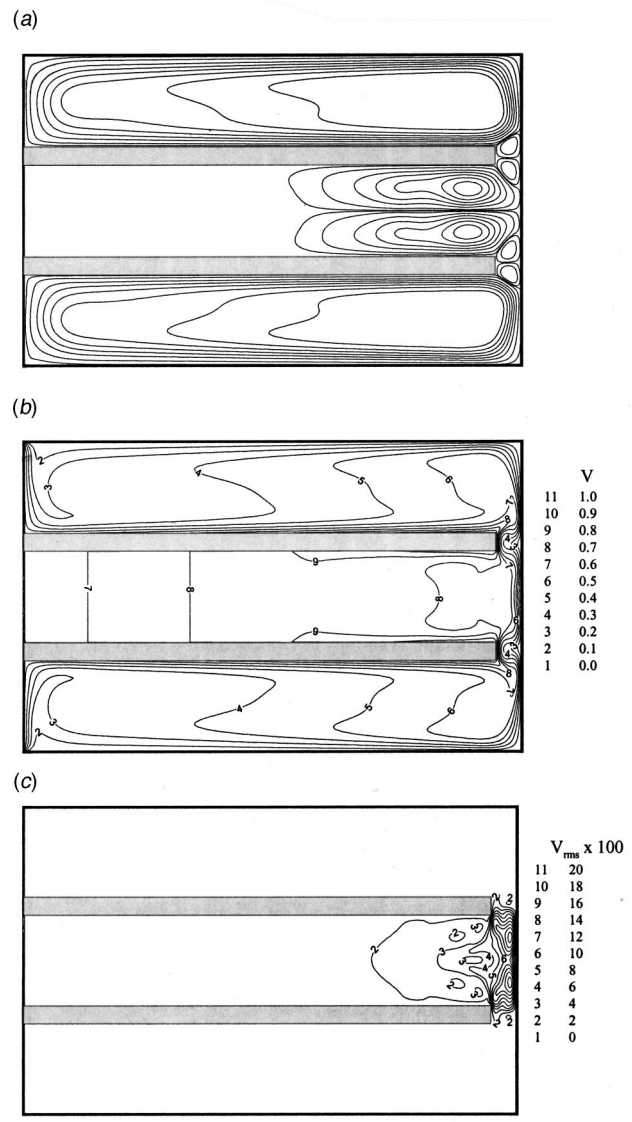

Fig. 5 Cross-stream distributions of the time-averaged flow obtained in a full domain axisymmetric calculation for the geometry of Fig. 1 with $A/R_2=0.026$. (a) Cross-stream flow streamlines (unlabeled). (b) Contours of the mean circumferential velocity component. (c) Contours of the rms circumferential velocity component.

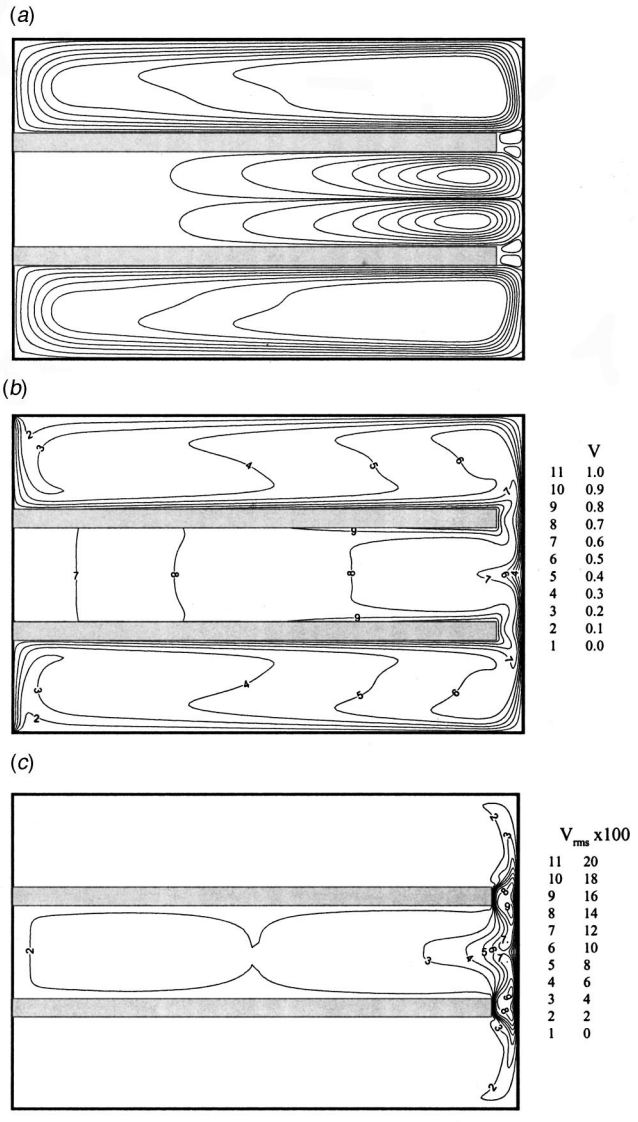

Fig. 6 Cross-stream distributions of the time- and circumferentially-averaged flow obtained in a full domain 3D calculation for the geometry of Fig. 1 with $A/R_2=0.26$. (a) Cross-stream flow streamlines based on the axial and radial velocity components (unlabeled). (b) Contours of the mean circumferential velocity component. (c) Contours of the rms circumferential velocity component.

(Eq. (6)); and, (ii) axisymmetric calculations are performed with the periodic-plane condition (Eq. (7)). Radial profiles of the mean and rms circumferential velocity components calculated along the mid-plane ($Z=0$) are plotted in Figs. 4(a) and (b). The best overall calculation of the mean is obtained assuming axisymmetric flow and using the periodic-plane boundary condition. Both the axisymmetric and 3D results using the symmetry-plane boundary condition significantly overpredict the mean. The best near-wall calculations of the rms are obtained with the symmetry-plane condition, but neither set of boundary conditions yields accurate predictions of the rms for $R<0.98$. Notwithstanding, it is clear that by allowing axisymmetric flow reversals in the gaps the periodic-plane boundary condition better reproduces the trend for the large rms values arising at $R<0.94$. In contrast, with the symmetry-plane condition imposed it makes little difference to the calculation of the mean velocity whether the inter-disk flow is treated as axisymmetric or 3D, the differences between these two sets of results being almost indistinguishable.

In spite of the somewhat better results obtained for the flow in the inter-disk space, especially the mean velocity, when computed with a periodic-plane boundary condition applied in the gaps, the axisymmetric flow assumption is highly constraining. Similarly, irrespective of whether the inter-disk flow is calculated as axisymmetric or 3D, the imposition of a symmetry-plane boundary condition in the gaps is also very limiting. As shown below, these shortcomings are removed in two steps, first by extending the axisymmetric calculation to encompass the entire flow domain, thus removing the need to specify a gap boundary condition, and then by removing the axisymmetric constraint and performing a 3D calculation.

Figures 5(a)–(c) present time-averages of the cross-stream flow streamlines and of the mean and rms circumferential velocity components for an axisymmetric calculation of the entire flow domain. Figures 6(a)–(c) show the same quantities for the corresponding 3D calculation, where the quantities plotted have been averaged both with respect to time and along the circumferential

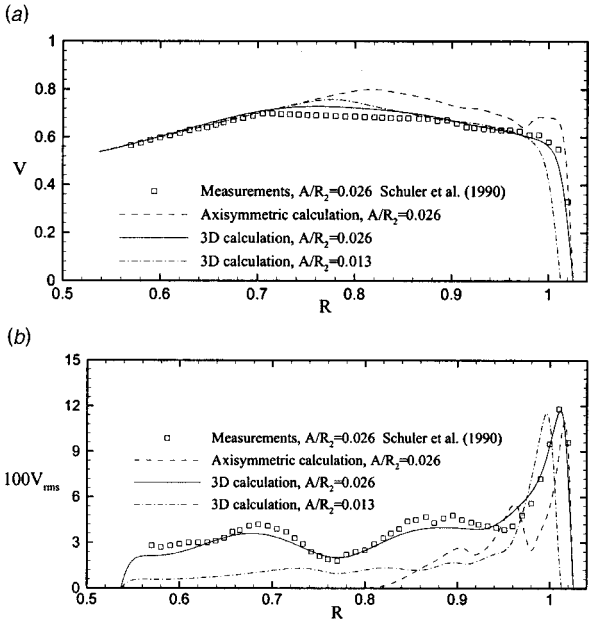

Fig. 7 Measured and calculated radial profiles of the mean circumferential velocity (a) and rms (b) along the inter-disk mid-plane, $Z=0$. These are full domain calculations corresponding to the geometry of Fig. 1 with $A/R_2=0.013$ and 0.026. The axisymmetric results are averaged over time and 3D results (and the measurements) are averaged over time and in the circumferential direction.

coordinate direction. Although these axisymmetric and 3D calculations yield unsteady flows (with the 3D results showing relatively strong departures from time-periodicity), the mean velocity plots are fairly similar with the main cross-stream flows in the inter-disk and disk-end wall spaces being determined by the strong radial outflows along the disk Ekman layers. These radial outflows are also responsible for the additional pair of much smaller cross-stream flows arising in the gap regions. In contrast, distributions of the rms, shown in Figs. 5(*c*) and 6(*c*), reveal larger levels of this quantity in the inter-disk space for the 3D calculation case compared to the axisymmetric. In particular, the 3D results show stronger radial and axial penetrations, driven by the cross-stream flows between the disks and in the gaps, of fluid with low circumferential velocity and high rms. Such penetrations induce a small departure of the mean flow from the condition of solid body rotation for $R<0.8$. Both the axisymmetric and 3D calculations yield rms levels larger than 10% near the curved enclosure wall and as high as 20% in the gaps. Although not shown here, the intensity of the strongly sheared flow in and around the gaps varies significantly with time.

Radial profiles of full domain mean and rms circumferential velocities obtained along the inter-disk mid-plane are compared in Figs. 7(*a*) and (*b*) with corresponding experimental results. (Also shown are the results obtained in a 3D calculation with $A/R_2=0.013$, discussed below.) It is clear that removing the specification of a gap boundary condition *and* extending the calculation dimensionality to predict a fully unconstrained 3D flow leads to significantly improved results for *both* the mean and rms velocities for *all* values of *R*. The circumferential dependence of the full domain 3D flow is illustrated in Figs. 8(*a*)–(*d*). These plots show cross-stream flow streamlines (derived from the cross-stream velocity components) for the same instant in time at four θ-planes. The plots reveal a main cross-stream flow that oscillates strongly about the inter-disk mid-plane and which is accompanied by significant axial displacements of fluid in the gaps. The circumferentially-dependent axial flows in the gaps induce large nonaxisymmetric variations in the cellular structures of the cross-

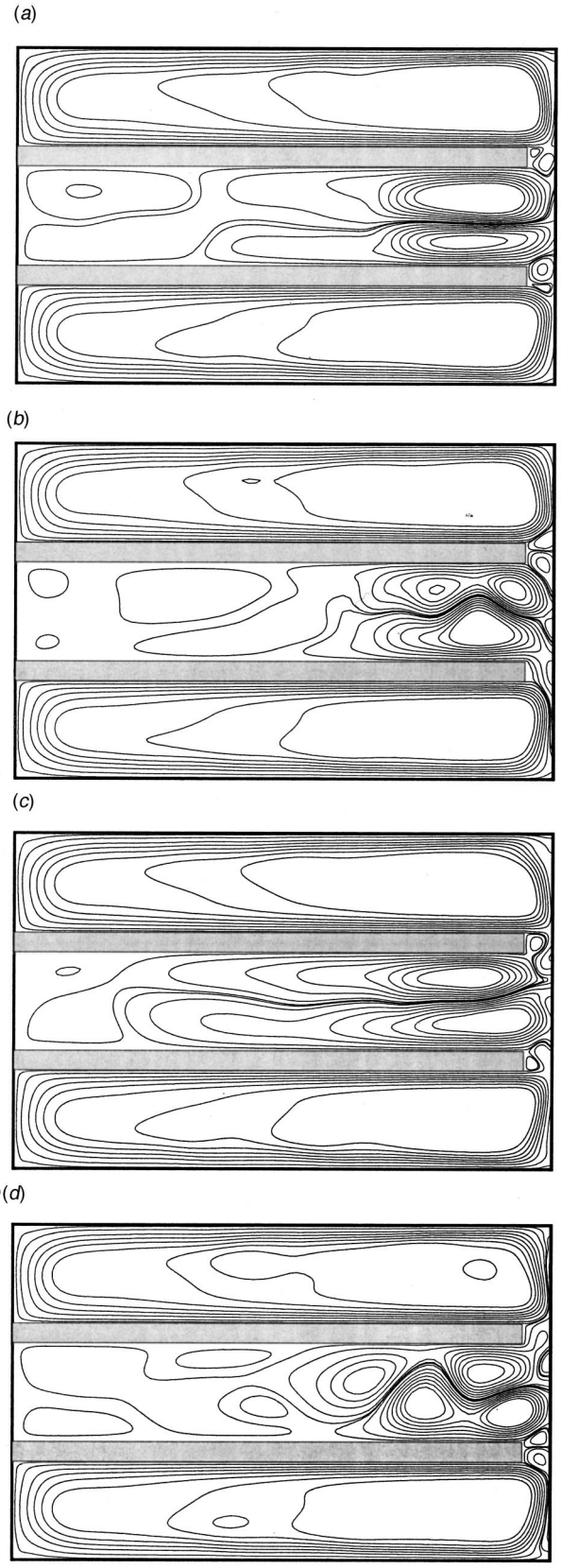

Fig. 8 Instantaneous cross-stream flow streamlines (unlabeled) corresponding to the full domain 3D calculation conditions of Fig. 6 ($A/R_2=0.026$). Contours are plotted at selected (R-Z) planes corresponding to: (a) $\theta=0.72\pi$; (b) 0.84 π; (c) 1.03 π; (d) 1.91 π.

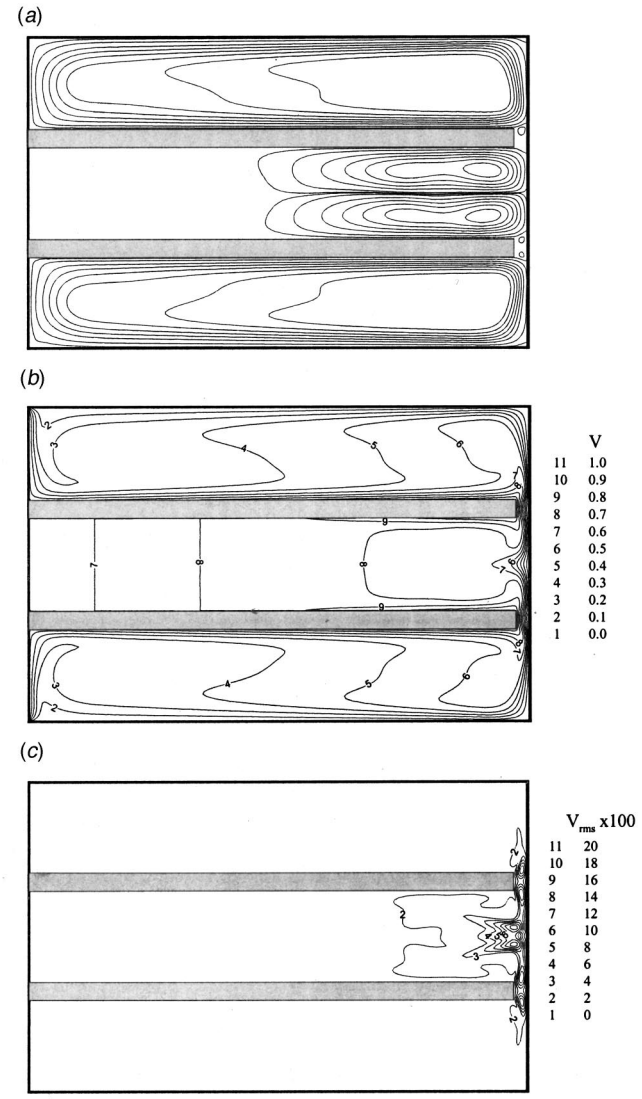

Fig. 9 Cross-stream distributions of the time- and circumferentially-averaged flow obtained in a full domain 3D calculation for the geometry of Fig. 1 with $A/R_2=0.013$. (a) Cross-stream flow streamlines based on the axial and radial velocity components (unlabeled). (b) Contours of the mean circumferential velocity component. (c) Contours of the rms circumferential velocity component.

stream flow in the inter-disk space and, to a smaller extent, in the end-wall spaces. The depth of penetration toward the hub of the oscillatory mid-plane flow varies with time and from plane to plane, leading to the large values of the rms observed in the inter-disk space. Such variations in the inter-disk space are not pre dicted assuming axisymmetric flow (regardless of whether gap boundary conditions are imposed or not), nor are they predicted by a 3D flow calculation using the symmetry-plane boundary condition.

Axisymmetric and 3D full domain calculations of the case with $A/R_2=0.013$ both yield time varying flows but their respectively averaged velocity fields are practically indistinguishable. Time- and θ-averaged values of cross-stream flow streamlines, and of the mean and rms circumferential velocities, are plotted in Fig. 9. A comparison between these results and those obtained for $A/R_2=0.026$, in Figs. 6(*a*)–(*c*), shows similar spatial distributions for the mean velocity but somewhat different ones for the rms. In particular, while both cases have equally high values of the rms in the gaps, the case with $A/R_2=0.013$ has significantly lower values of the rms in the bulk of the inter-disk space; see Fig. 7(*b*) also.

Effect of the Gaps on the Disk Torque Coefficient. The disk torque coefficient, C_M, is a dimensionless measure of the total torque required to rotate a disk and includes: (a) the torques associated with each of the flat surfaces of a disk; (b) the torque associated with the rim surface of a disk; and, (c) the torques due to the sections of the hub associated with a disk.

In the present geometry each of the two disks has an ''inner'' surface (I) that faces the surface of the opposite corotating disk, and an ''outer'' surface (O) that faces a fixed flat enclosure wall. It makes sense to define the above three contributions to the torque coefficient for *each* of the two surfaces of a disk. Thus, call $C^I_{M,disk}$ the mean torque acting on the inner surface of a disk, $C^I_{M,rim}$ the mean torque acting on the peripheral half-surface of the rim associated with the inner surface of a disk, and $C^I_{M,hub}$ the mean torque acting on the peripheral half-surface of the hub associated with the inner surface of a disk. The corresponding quantities for the outer surface of a disk are $C^O_{M,disk}$, $C^O_{M,rim}$, and $C^O_{M,hub}$. These quantities are calculated from the following expressions:

$$C^{I,O}_{M,disk}=\frac{\int_0^{2\pi}\int_{R_1}^{R_2}\mu\left|\frac{\partial\nu}{\partial z}\right|r^2 dr d\theta}{1/2\rho\Omega^2R_2^5} \tag{8a}$$

$$C^{I,O}_{M,rim}=\frac{\int_0^{2\pi}\int_{z_1}^{z_2}\mu\left|\frac{\partial\nu}{\partial r}\right|R_2^2 dz d\theta}{1/2\rho\Omega^2R_2^5}. \tag{8b}$$

$$C^{I,O}_{M,hub}=\frac{\int_0^{2\pi}\int_{z_1}^{z_2}\mu\left|\frac{\partial\nu}{\partial r}\right|R_1^2 dz d\theta}{1/2\rho\Omega^2R_2^5} \tag{8c}$$

where the vertical bars denote time-averaged wall values of the velocity gradients indicated. In these expressions the superscript ''I'' denotes the disk, rim, or hub surfaces associated with the inner surface of a disk and the superscript ''O'' denotes the disk, rim, or hub surfaces associated with the outer surface of a disk. Thus, with reference to Fig. 1, $C^I_{M,disk}$ is evaluated at $z=\pm H/2$ and $C^O_{M,disk}$ at $z=\pm(H/2+h)$; $C^I_{M,rim}$ is evaluated from $z_1=\pm H/2$ to $z_2=\pm(H/2+h/2)$ and $C^O_{M,rim}$ from $z_1=\pm(H/2+h/2)$ to $z_2=\pm(H/2+h)$; $C^I_{M,hub}$ is evaluated from $z_1=0$ to $z_2=\pm H/2$ and $C^O_{M,hub}$ from $z_1=\pm(H/2+h)$ to $z_2=\pm(3H/2+h)$.

From the above equations it is possible to obtain the following quantities:

Mean torque coefficient for a disk near the middle of a stack of disks in a cylindrical enclosure

$$C^{MD}_M=2(C^I_{M,disk}+C^I_{M,rim}+C^I_{M,hub}) \tag{9a}$$

Mean torque coefficient for a single disk in a cylindrical enclosure

$$C^{SD}_M=2(C^O_{M,disk}+C^O_{M,rim}+C^O_{M,hub}) \tag{9b}$$

Mean torque coefficient for a disk at the end of a stack of disks in a cylindrical enclosure

$$C^{ED}_M=(C^I_{M,disk}+C^O_{M,disk}+C^I_{M,rim}+C^O_{M,rim}+C^I_{M,hub}+C^O_{M,hub})=1/2(C^{MD}_M+C^{SD}_M) \tag{9c}$$

Mean torque coefficient for a stack of N disks in a cylindrical enclosure

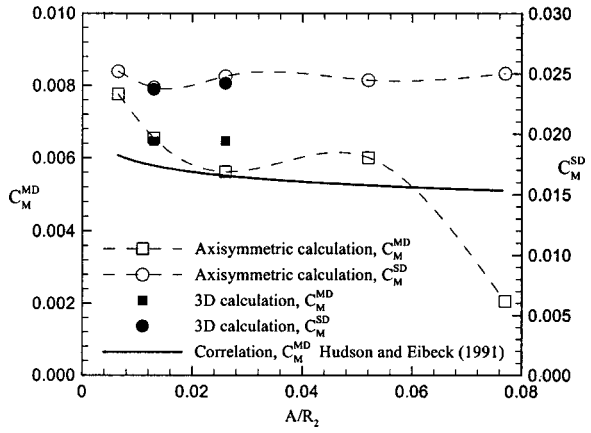

Fig. 10 Variations of the disk torque coefficients C_M^{MD} and C_M^{SD} (defined in the text) as a function of A/R_2 for full domain axisymmetric and 3D calculations. Also shown is the experimental fit for C_M^{MD} obtained by Hudson and Eibeck [6]. The axisymmetric calculations are connected by dotted lines to help visualize the qualitative trends in the data but the lines are not to be interpreted as "best fits" to the numerical data.

$$C_M^{Stack}=(N-2)C_M^{MD}+2C_M^{ED}=(N-1)C_M^{MD}+C_M^{SD} \qquad (9d)$$

Note that in the above four equations it is implied that the various contributions to the torque coefficient are additive and the results discussed below support this assumption.

Calculated values of C_M^{MD} and C_M^{SD} are given in Fig. 10 where they are plotted as a function of the gap ratio A/R_2. In all cases $\mathrm{Re}=2.1\times10^4$ and both full domain axisymmetric and 3D values are presented, the latter being limited to two gap sizes because of the long calculation times involved. As expected, the calculations show that $C_M^{SD}>C_M^{MD}$, by a factor as large as four at intermediate values of A/R_2. They also reveal an insensitivity of C_M^{SD} with respect to the gap size. In the A/R_2 range investigated we find $C_M^{SD}\approx0.024$, in close agreement with the results obtained using the single disk correlations of Daily and Nece [12] ($C_M^{SD}=0.020$), Hudson and Eibeck [6] ($C_M^{SD}=0.021$), and Humphrey et al. [7] ($C_M^{SD}=0.020$) by setting $\mathrm{Re}=2.1\times10^4$.

The figure also compares present calculations of C_M^{MD} with the correlation proposed by Hudson and Eibeck [6] for $\mathrm{Re}>8\times10^4$. The correlation is given by $C_M^{MD}=0.46\,\mathrm{Re}^{-0.35}(H/R_2)^{0.5}(A/R_2)^{-0.07}$ and, as observed for C_M^{SD}, shows a very weak dependence on A/R_2. Agreement between the calculations and the experimental fit varies between 1% and 15% in the range $0.010<A/R_2<0.060$. In contrast, the calculated value of C_M^{MD} for the largest gap explored, $A/R_2=0.077$, is significantly smaller than the value given by the fit. The discrepancy is partly due to the lower Re of the current study (large gaps in disk flows at high Re are expected to facilitate turbulent exchanges of momentum that can significantly increase the disk torque coefficient), but may also be attributed to the over-constraining assumption of axisymmetric flow. In this respect, while there is good agreement between the axisymmetric and 3D calculations of C_M^{MD} and C_M^{SD} for the case with $A/R_2=0.013$, a 12% discrepancy arises between the values for C_M^{MD} for the more critical case with $A/R_2=0.026$. As discussed further above, such a discrepancy is explained by the inability of the axisymmetric calculations to fully capture the physics of the inter-disk flow for $A/R_2=0.026$. Thus, while the axisymmetric calculations follow the empirical trend and predict decreasing C_M^{MD} with increasing A/R_2, they should only be used for qualitative guidance, especially for large values of A/R_2.

Increasing A/R_2 might be viewed as a convenient way to reduce the torque, and hence the power requirement of a stack of disks. However, the rms values in Fig. 7(*b*) show that such a reduction will come at the expense of a more unstable inter-disk flow. A related observation has been made by Humphrey et al. [7] who show that the inwards radial displacement of fluid with high circumferential momentum works to reduce total disk torque at the cost of destabilizing fluid motion in the inter-disk space. That study also supports the observation made here, that axial transport of circumferential momentum across the gaps can significantly alter the structure and dynamics of the inter-disk flow while not significantly affecting the flows in the disk-end wall spaces.

Concluding Remarks

Present numerical calculations show that the structure and dynamics of the flow in the space between a pair of disks corotating in a fixed cylindrical enclosure at $\mathrm{Re}=2.1\times10^4$ are sensitive to the size of the gaps between the rims of the disks and the curved enclosure wall. This is due to axial transport of circumferential momentum between the inter-disk spaces connected by the gaps. In this regard, regardless of the imposition or not of symmetry-plane or periodic-plane boundary conditions in the gaps, the assumption of axisymmetric flow yields results that, while numerically accurate, fail to faithfully reproduce measured variations of the mean and rms circumferential velocities. Likewise, a 3D calculation using the symmetry-plane boundary condition in the gaps also fails to reproduce the variations observed in the measurements. In contrast, a 3D calculation of the flow including the gaps and the inter-disk spaces as parts of an interconnected flow domain yields mean and rms velocities in very good agreement with the corresponding measurements.

At a qualitative level, present full domain axisymmetric calculations suggest that increasing A/R_2 works to significantly reduce the disk torque coefficient, but at the expense of increasing flow unsteadiness as revealed by the calculations of the rms circumferential velocity. This observation agrees with previous related findings and suggests that while disk torque may be significantly reduced by increasing gap size, the reduction may come at the expense of a significantly destabilized flow due to the enhanced axial exchanges of momentum through the gaps. However, it is important to keep in mind that, because of the differences in flow structure and dynamics predicted by axisymmetric and 3D calculations, respectively, axisymmetric values of the disk momentum coefficient are not reliable at a quantitative level, especially for large values of A/R_2. For accurate predictions of all flow behavior, computationally intensive full domain 3D calculations are required, even for integral quantities such as the disk momentum coefficient.

From a practical standpoint, present calculations suggest that Eqs. 9(*a*)–(*d*) can be used together with previously reported empirical correlations, analytical equations or full domain 3D numerical results to predict the torque coefficients associated with one or more disks corotating in a cylindrical enclosure. However, because most previous results have been obtained for conditions corresponding to moderate and high values of the Reynolds numbers, as illustrated here, their use to predict torque at lower values of Reynolds than for which they were derived must be viewed with caution.

Acknowledgments

Financial support for this investigation was provided by the Spanish government to MS, JH and FG through projects DGES-PB96-1011 and DGESYC-PPQ2000-1339, and through a grant received by JACH from the National Storage Industry Consortium. MS gratefully acknowledges a research travel grant to conduct research at UVA provided by the Catalan government.

References

[1] Schuler, C. A., Usry, W., Weber, B., Humphrey, J. A. C., and Greif, R., 1990, ''On the flow in the unobstructed space between shrouded corotating disks,'' Phys. Fluids A, **2**, pp. 1760–1770.

[2] Abrahamson, S. D., Chiang, C., and Eaton, J. K., 1991, ''Flow Structure in Head Disk Assemblies and Implications for Design,'' Adv. Inf. Storage Syst., **1**, pp. 7111–7132.

[3] Humphrey, J. A. C., Chang, C.-J., Li, H., and Schuler, C. A., 1991, ''Unobstructed and obstructed rotating disk flows: A summary review relevant to information storage systems,'' Adv. Inf. Storage Syst., **1**, pp. 79–110.

[4] Herrero, J., Giralt, F., and Humphrey, J. A. C., 1999-a, ''Influence of the geometry on the structure of the flow between a pair of corotating disks,'' Phys. Fluids, **110**, pp. 88–96.

[5] Herrero, J., Giralt, F., and Humphrey, J. A. C., 1999-b, ''Non-isothermal laminar flow and heat transfer between disks corotating in a fixed enclosure,'' Int. J. Heat Mass Transf., **42**, pp. 3291–3306.

[6] Hudson, A. J., and Eibeck, P. A., 1991, ''Torque measurements of corotating disks in an axisymmetric enclosure,'' ASME J. Fluids Eng., **113**, pp. 648–653.

[7] Humphrey, J. A. C., Schuler, C. A., and Iglesias, I., 1992, ''Analysis of viscous dissipation in disk storage systems and similar flow configurations,'' Phys. Fluids A, **4**, pp. 1415–1427.

[8] Humphrey, J. A. C., Schuler, C. A., and Webster, D. R., 1995, ''Unsteady laminar flow between a pair of disks corotating in a fixed cylindrical enclosure,'' Phys. Fluids, **7**, pp. 1225–1240.

[9] Iglesias, I. and Humphrey, J. A. C., 1998, ''Two- and three-dimensional laminar flows between disks co-rotating in a fixed cylindrical enclosure,'' Int. J. Numer. Methods Fluids, **26**, pp. 581–603.

[10] Tzeng, H.-M., and Fromm, J. E., 1990, ''Airflow study in a cylindrical enclosure containing multiple corotating disks,'' IBM Research Division, Report RJ 7334 (68815).

[11] Rai, M. M., and Moin, P., 1991, ''Direct Simulations of Turbulent Flows Using Finite-Difference Schemes,'' J. Comput. Phys., **96**, pp. 15–53.

[12] Daily, J. W. and Nece, R. E., 1960, ''Chamber dimension effects on induced flow and frictional resistance of enclosed rotating disks,'' ASME J. Basic Eng., **82**, 217–232.

A Comparison of Second-Moment Closure Models in the Prediction of Vortex Shedding From a Square Cylinder Near a Wall

Anthony G. Straatman

Robert J. Martinuzzi

The Advanced Fluid Mechanics Research Group,
Department of Mechanical
& Materials Engineering,
The University of Western Ontario,
London, Ontario N6A 5B9, Canada

A computational study is presented that examines the capability of various second-moment closure models in the prediction of two-dimensional, nonstationary flow around a square cylinder in proximity to a wall. The linear return-to-isotropy/isotropization-of-production model ($RTI+IP$) and the nonlinear SSG pressure-strain models were combined with the DH and modified LUM diffusion models in the computations. In terms of global activity, the drag is well-predicted in terms of both magnitude and variation with cylinder-to-wall gap width S/D. The Strouhal number St was reasonably well-predicted in terms of magnitude, but the predicted trend with decreasing S/D was incorrect for all model combinations. The lift was not well-predicted in terms of magnitude or trend. Prediction of the detailed flow structure in the vicinity of the cylinder and in the wake was favourable, though the magnitudes of some velocity and Reynolds-stress components were over-predicted. It was argued that the large differences between the results at the intermediate gap width may be due to the difference between the measured and predicted critical gap widths. On the basis of the predicted global and detailed activity, the modified LUM model combined with the nonlinear SSG model was suggested as being the most viable combination for future studies. [DOI: 10.1115/1.1490127]

Keywords: Vortex Shedding, Transient RANS, Second-Moment Closure, Nonstationary Flow

1 Introduction

Turbulent vortex shedding from a square cylinder is a classical case of a nonstationary, periodic flow that has received considerable attention in the past. This flow is attractive from a research perspective because it is rich in physics and can be studied both computationally and experimentally. Briefly, when the cylinder is placed in a uniform stream, counter-rotating vortices are alternatively shed from opposite faces of the cylinder giving rise to a periodic vortex shedding pattern in the cylinder wake. When the cylinder is placed in the proximity of a wall, the nonstationary activity around the cylinder is modified and, for very small cylinder-to-wall gap widths, the periodicity can be completely suppressed rendering the flow stationary.

A number of computational studies have been carried out in the recent past to examine the capability of different unsteady Reynolds Averaged Navier Stokes (RANS) turbulence models to predict the nonstationary flow around a square cylinder, both isolated and in proximity to a wall. This flow lends itself well to unsteady or transient RANS modelling because of the clear separation between the scales of the coherent, periodic motions and the random turbulent motions. Franke and Rodi [1] considered turbulent vortex shedding from an isolated cylinder at a Reynolds number $Re_D=22{,}000$ using different RANS-based turbulence models. Their study concluded that within the scope of RANS-based models, full Reynolds-stress models give the best predictions; the standard $k-\epsilon$ model was not satisfactory due to an over-prediction of turbulence production at the stagnation region on the front face of the cylinder. Bosch and Rodi [2] performed computations of vortex shedding around a square cylinder near a wall and found that better predictions could be obtained using a $k-\epsilon$ model provided the Kato-Launder formulation for production was used. Other computational studies of the isolated square cylinder have been conducted by Bosch and Rodi [3], Lee and Bienkiewicz [4], Bouris and Bergeles [5], Thomas and Williams [6], and Peng and Hwang [7]. Bosch and Rodi [3] found that the two-layer $k-\epsilon$ model was slightly better than that using wall-functions and that the predicted results are very sensitive to the choice of inlet conditions. The remaining studies employed three-dimensional Large Eddy Simulation (LES) models for flow predictions of the isolated cylinder. In models. However, a further comparative study by Rodi [8] noted that LES predictions require approximately 25 times more computational effort than unsteady Reynolds-stress models and almost 650 times more effort than unsteady $k-\epsilon$ models.

While many of the above-mentioned papers have been devoted to exploring the capability of turbulence models, comparisons to experimental data have been limited. In most cases, comparisons are made for the shedding frequency in terms of the Strouhal number, time-averaged lift and drag coefficients, and the phase-averaged lateral velocity along the cylinder centerline. In some cases, additional comparisons were made for phase-averaged velocity vectors or phase-averaged velocity profiles in the near-wake of the cylinder, however, none include comparisons for the time-averaged velocities and Reynolds stress components, or the pressure distribution on the wall or around the cylinder. Accurate prediction of the Reynolds stresses is essential for this problem since the turbulence intensities may greatly affect the near- and far-wake structure of the flow. Furthermore, the structure of the velocity field directly affects the vorticity field, which is of interest when examining the suppression of vortex shedding at small cylinder-to-wall gap widths.

The present study takes a critical look at the capability of second-moment closure models for predicting two-dimensional, non-stationary flow around the square cylinder near a wall. Two popular pressure-strain relations and two diffusion models are

Contributed by the Fluids Engineering Division for publication in the JOURNAL OF FLUIDS ENGINEERING. Manuscript received by the Fluids Engineering Division November 2, 2001; revised manuscript received April 3, 2002. Associate Editor: J. Marshall.

used. In the present study, only high-Re variants of the turbulence models are considered. While low-Re models have been shown to improve predictions, particularly in regions of separation and reattachment, it is of more immediate importance to understand the capabilities of the high-Re models since almost all computations of industrial significance are computed in this manner. Comprehensive comparisons are made with the experimental data of Wu and Martinuzzi [9] for unsteady and time-averaged quantities in the assessment of models. The paper is organized such that the mathematical formulation is presented first, followed by a description of the turbulence models, the numerical formulation, data processing and results and discussion.

2 Mathematical Formulation

With the exception of Direct Numerical Simulations (DNS), the prediction of turbulent flows involves solving the conservation of mass and momentum equations coupled with a turbulence model. When the solution of a stationary turbulent flow is sought, the conservation equations are cast in their usual time-averaged form and the dependent variables are interpreted as

$$\Phi(x_i,t)=\overline{\Phi(x_i)}+\phi(x_i,t), \tag{1}$$

where $\Phi(x_i,t)$ is the total instantaneous scalar value, $\overline{\Phi(x_i)}$ is the time average of Φ over a long period, $\phi(x_i,t)$ is the instantaneous fluctuating component of Φ, x_i is the spatial coordinate and t is time. When a nonstationary, periodic flow is considered, Hussain [10] suggests that a more suitable representation for incompressible flows is a decomposition of the type

$$\Phi(x_i,t)=\overline{\Phi}(x_i)+\phi_c(x_i,t)+\phi(x_i,t)=\langle\Phi(x_i,t)\rangle+\phi(x_i,t) \tag{2}$$

where $\phi_c(x_i,t)$ is the organized, periodic component of the flow and $\phi(x_i,t)$ is the contribution of the small-scale or random turbulent motions. For conciseness, the time-averaged and organized periodic components are combined to form the phase-averaged term $\langle\Phi(x_i,t)\rangle$, as is shown in the final expression of Eq. (2). The $\langle\ \rangle$ brackets are used hereafter to denote phase-averaging. Using this decomposition for the velocities and pressure, and subsequent phase-averaging, the conservation equations in Cartesian tensor notation take the form

$$\frac{\partial}{\partial x_i}(\rho\langle U_i\rangle)=0 \tag{3}$$

and

$$\frac{\partial}{\partial t}(\rho\langle U_i\rangle)+\frac{\partial}{\partial x_k}(\rho\langle U_k\rangle\langle U_i\rangle)=-\frac{\partial\langle P\rangle}{\partial x_k}\delta_{ik}+\mu\frac{\partial^2}{\partial x_k^2}(\langle U_i\rangle)-\frac{\partial}{\partial x_k}(\rho\langle u_iu_k\rangle) \tag{4}$$

where $\langle U_i\rangle$ is the phase-averaged fluid velocity in the x_k direction, $\langle P\rangle$ is the phase-averaged pressure, ρ and μ are the fluid density and dynamic viscosity, respectively, and δ_{ik} is the Kronecher delta. The second-order term on the right hand side of the momentum equation is the phase-averaged Reynolds-stress term. This term is an artifact of the Reynolds- and phase-averaging processes and in this formulation, represents the total unresolved turbulence.

In the present study, a second-moment or full stress-transport closure is used to model the unresolved turbulence in the momentum balance. Using a second-moment turbulence closure, no approximation for $\langle u_iu_k\rangle$ is introduced in the momentum equation and thus, a transport equation must be solved for each nonzero component of the Reynolds-stress tensor. The Reynolds-stress transport equation is given as

$$\frac{\partial\langle u_iu_j\rangle}{\partial t}+\langle U\rangle_k\frac{\partial\langle u_iu_j\rangle}{\partial x_k}=\underbrace{-\left(\langle u_iu_k\rangle\frac{\partial\langle U\rangle_j}{\partial x_k}+\langle u_ju_k\rangle\frac{\partial\langle U\rangle_i}{\partial x_k}\right)}_{\mathcal{P}_{ij}}+\mathcal{D}_{ij}+\pi_{ij}-\epsilon_{ij} \tag{5}$$

where $\langle u_iu_j\rangle$ is the phase-averaged Reynolds-stress term (per ρ). The left side of Eq. (5) represents the substantial or convective derivative of $\langle u_iu_j\rangle$ while the terms on the right side represent the rates of production $\mathcal{P}_{ij}$, diffusion $\mathcal{D}_{ij}$, pressure-strain π_{ij}, and homogeneous dissipation ϵ_{ij} of $\langle u_iu_j\rangle$. The convection and production require no approximation, but the remaining processes must be modelled to close the equation set at the second-moment level. The diffusion process is approximated in this work using either the modified LUM model suggested by Straatman [11] or the commonly used Daly and Harlow [12] model. The diffusion process in Eq. (5) is given in its exact form (neglecting molecular diffusion) as

$$\mathcal{D}_{ij}=\frac{\partial}{\partial x_k}\left(-\langle u_iu_ju_k\rangle-\frac{\langle p'u_j\rangle}{\rho}\delta_{ik}-\frac{\langle p'u_i\rangle}{\rho}\delta_{jk}\right) \tag{6}$$

where $\langle u_iu_ju_k\rangle$ is the turbulent transport and p' is the fluctuating pressure. The pressure-velocity terms represent pressure-diffusion. Using the modified LUM model, the turbulent transport is approximated by

$$-\langle u_iu_ju_k\rangle=C_{s1}\frac{\langle k\rangle}{\langle\epsilon\rangle}[\mathcal{G}_{ijk}+C_{s2}(\mathcal{G}_i\delta_{jk}+\mathcal{G}_j\delta_{ik}+\mathcal{G}_k\delta_{ij})] \tag{7}$$

where $\mathcal{G}_{ijk}$ is a third-order tensor given by

$$\mathcal{G}_{ijk}=\left(\langle u_iu_l\rangle\frac{\partial\langle u_ju_k\rangle}{\partial x_l}+\langle u_ju_l\rangle\frac{\partial\langle u_iu_k\rangle}{\partial x_l}+\langle u_ku_l\rangle\frac{\partial\langle u_iu_j\rangle}{\partial x_l}\right) \tag{8}$$

and $\mathcal{G}_i=\mathcal{G}_{imm}$. The pressure-diffusion component of $\mathcal{D}_{ij}$ is modelled as

$$-\frac{1}{\rho}\langle p'u_k\rangle=P_D\langle u_ku_mu_m\rangle \tag{9}$$

Using the Daly and Harlow [12] (hereafter DH) relation, the turbulent transport and pressure-diffusion terms are modelled as

$$-\langle u_iu_ju_k\rangle=C_s^{DH}\frac{\langle k\rangle}{\langle\epsilon\rangle}\left(\langle u_ku_l\rangle\frac{\partial\langle u_iu_j\rangle}{\partial x_l}\right) \tag{10}$$

and

$$-\frac{1}{\rho}\langle p'u_k\rangle=0, \tag{11}$$

respectively.

The pressure-strain process is modelled in the present work using either the return-to-isotropy/isotropization-of-production (hereafter *RTI*) relations or the Speziale et al. [13] (hereafter *SSG*) relation. The *RTI* relation is given as

$$\pi_{ij}=-C_1^L\epsilon a_{ij}-C_2^L\left(\mathcal{P}_{ij}-\frac{1}{3}\mathcal{P}_{kk}\delta_{ij}\right)+\pi_{ij,w} \tag{12}$$

Table 1 Coefficients for the diffusion and pressure–strain models

C_{s1}	C_{s2}	P_D	C^{DH}	C_1^L	C_2^L	C_1'	C_2'	C_μ	κ
0.098	0.31	0.142	0.22	1.8	0.6	0.5	0.3	0.09	0.41

C_1	C_1^*	C_2	C_3	C_3^*	C_4	C_5
1.7	0.9	1.05	0.8	0.65	0.625	0.2

where $\pi_{ij,w}$ accounts for the observed effect of solid boundaries on the turbulence. The standard form for $\pi_{ij,w}$ is

$$\pi_{ij,w}=\left[C_1'\frac{\epsilon}{k}\left(\overline{u_n u_n}\delta_{ij}-\frac{3}{2}\overline{u_n u_i}\delta_{nj}-\frac{3}{2}\overline{u_n u_j}\delta_{ni}\right)+C_2'\left(\pi_{nn,2}\delta_{ij}-\frac{3}{2}\pi_{ni,2}\delta_{nj}-\frac{3}{2}\pi_{nj,2}\delta_{ni}\right)\right]\cdot f \quad (13)$$

in which C_1' and C_2' are coefficients and the function f is defined as $f=(l/x_n)$, where l is the local length scale of the turbulence defined by $l=\kappa k^{3/2}/\epsilon C_\mu$, and x_n is the normal distance to the wall. The SSG relation is given as

$$\pi_{ij}=-\left(C_1\langle\epsilon\rangle+\frac{1}{2}C_1^*\mathcal{P}_{kk}\right)a_{ij}+C_2\langle\epsilon\rangle\left(a_{ik}a_{kj}-\frac{1}{3}A_2\delta_{ij}\right)+(C_3-C_3^*A_2^{1/2})\langle k\rangle S_{ij}+C_4\langle k\rangle\left(a_{ik}S_{jk}+a_{jk}S_{ik}-\frac{2}{3}a_{kl}S_{kl}\delta_{ij}\right)+C_5\langle k\rangle(a_{ik}W_{jk}+a_{jk}W_{ik}) \quad (14)$$

In Eqs. (12) and (14), $\langle k\rangle$ $(=\frac{1}{2}\langle u_i u_i\rangle)$ is the phase-averaged turbulent kinetic energy and $\langle\epsilon\rangle$ is the phase-averaged, homogeneous dissipation rate of $\langle k\rangle$. The additional terms in the pressure-strain models are given as

$$a_{ij}=\frac{\langle u_i u_j\rangle}{\langle k\rangle}-\frac{2}{3}\delta_{ij},\quad A_2=a_{ik}a_{ki},$$

$$S_{ij}=\frac{1}{2}\left(\frac{\partial\langle U_i\rangle}{\partial x_j}+\frac{\partial\langle U_j\rangle}{\partial x_i}\right),\quad W_{ij}=\frac{1}{2}\left(\frac{\partial\langle U_i\rangle}{\partial x_j}-\frac{\partial\langle U_j\rangle}{\partial x_i}\right)$$

Coefficients for the diffusion and pressure-strain models in the Reynold-stress equation are given in Table 1.

The dissipation rate of $\langle u_i u_j\rangle$ is modelled as

$$\epsilon_{ij}=\frac{2}{3}\langle\epsilon\rangle\delta_{ij} \quad (15)$$

The phase-averaged, homogeneous dissipation rate, $\langle\epsilon\rangle$, is then obtained from the modelled transport equation:

$$\frac{\partial\langle\epsilon\rangle}{\partial t}+\langle U\rangle_k\frac{\partial\langle\epsilon\rangle}{\partial x_k}=\frac{\partial}{\partial x_k}\left[C_\epsilon\frac{\langle k\rangle}{\langle\epsilon\rangle}\left(\langle u_k u_l\rangle\frac{\partial\langle\epsilon\rangle}{\partial x_l}\right)\right]+\frac{1}{2}C_{\epsilon 1}\frac{\langle\epsilon\rangle}{\langle k\rangle}\mathcal{P}_{kk}-C_{\epsilon 2}\frac{\langle\epsilon\rangle^2}{\langle k\rangle} \quad (16)$$

where $\{C_\epsilon, C_{\epsilon 1}, C_{\epsilon 2}\}=\{0.14, 1.44, 1.83\}$.

Discretization of the governing field equations was done using the finite-volume approach of Patankar [14] except with a collocated variable arrangement. The scheme was essentially second-order in space and first-order in time. Convective fluxes in the momentum equations were approximated using the QUICK scheme of Leonard [15], while in the turbulence equations, the upstream differencing scheme with Peclet weighting was used. Complete details of the discretization procedure and the implementation of the second-moment closure model are given in Straatman [16] and are not repeated here.

3 Processing of Turbulence Statistics

While the link between the time-averaged and the phase-averaged statistics is given by Eq. (2) it is not entirely trivial to convert from one to another. That is, if the equations are solved in a phase-averaged framework, then assumptions have inherently been made about some of the components. For example, the time-averaged Reynolds-stress component $\overline{u_1 u_1}$ is formed by

$$\overline{u_1 u_1}=\frac{1}{T}\int_0^T(U_1-\overline{U}_1)^2dt \quad (17)$$

which, after substitution of Eq. (2) becomes

$$\overline{u_1 u_1}=\frac{1}{T}\int_0^T(U_{1c}^2+2u_1U_{1c}+u_1u_1)dt \quad (18)$$

The first term in Eq. (18) represents the correlation between the organized periodic velocity component and itself. This term can become quite large, particularly in cases where large-scale periodic motions exist. The second term represents a correlation between the instantaneous fluctuating velocity, u_1, which is part of the unresolved turbulence, and the organized periodic velocity, U_{1c}. This term can be neglected on the basis of the differing time scales between coherent and incoherent motions (Hussain [10]). The final component in Eq. (18) represents the phase-averaged fluctuating velocity. Thus, the expression for $\overline{u_1 u_1}$ is simplified to

$$\overline{u_1 u_1}=\frac{1}{T}\int_0^T(U_{1c}^2)dt+\frac{1}{T}\int_0^T(u_1u_1)dt \quad (19)$$

and since $U_{1c}=\langle U_1\rangle-\overline{U}_1$, we obtain

$$\overline{u_1 u_1}=\overline{(\langle U_1\rangle-\overline{U}_1)^2}+\overline{\langle u_1u_1\rangle} \quad (20)$$

In a similar manner, the expressions for $\overline{u_2u_2}$ and $\overline{u_1u_2}$ are, respectively

$$\overline{u_2u_2}=\frac{1}{T}\int_0^T(U_{2c}^2)dt+\frac{1}{T}\int_0^T(u_2u_2)dt=\overline{(\langle U_2\rangle-\overline{U}_2)^2}+\overline{\langle u_2u_2\rangle} \quad (21)$$

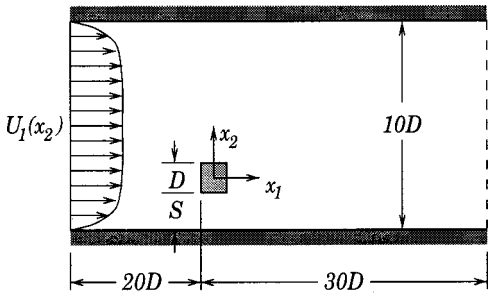

Fig. 1 Schematic representation of the square cylinder geometry showing the coordinate system and all important parameters

Table 2 Summary of spatial and temporal independence study. All computations were done using the *DH+RTI* combination of models.

Grid Dimensions	Δt^*	St	C_L	C_D
106×80	0.073	0.136	−0.300	2.275
150×113	0.073	0.139	−0.292	2.382
214×140	0.073	0.126	−0.271	2.478
150×113	0.037	0.138	−0.286	2.369
150×113	0.018	0.134	−0.286	2.334

Table 3 Summary of shedding frequencies given in terms of the Strouhal number, St, predicted by all model combinations and those measured by Wu and Martinuzzi [9].

Models	$S/D=1$	$S/D=0.5$
LUM+RTI	0.140	0.117
LUM+SSG	0.149	0.113
DH+RTI	0.138	steady
DH+SSG	0.164	0.112
Experiment	0.133	0.140

$$\overline{u_1u_2}=\frac{1}{T}\int_0^T(U_{1c}U_{2c})dt+\frac{1}{T}\int_0^T(u_1u_2)dt$$
$$=\overline{(\langle U_1\rangle-\overline{U_1})(\langle U_2\rangle-\overline{U_2})}+\overline{\langle u_1u_2\rangle} \quad (22)$$

4 The Computations

A schematic of the geometric configuration considered is given in Fig. 1. Boundary conditions for all variables were applied over the edges of the computational domain. At all wall boundaries (i.e., top and bottom of tunnel and cylinder faces), the viscous sublayer was bridged using standard wall-functions. The values of y^+ were checked after the initial computations to ensure that the control-volumes adjacent to the walls were large enough to yield $y^+>20$ over a majority of the wall boundaries. Obviously, this condition was difficult to ensure since the flow field was unsteady and there were regions of separation and reattachment. Thus, a reasonable compromise was to ensure acceptable values of y^+ for the time-averaged results. At the outlet of the domain, Neumann conditions were used for all variables, with the exception of pressure, which was set to zero. Simulations with the outlet plane at several locations from 10*D* to 40*D* downstream of the cylinder were conducted to ensure that the boundary conditions did not significantly influence the flow in the vicinity of the cylinder. The computations were done for a Reynolds number $\mathrm{Re}_D=U_oD/\nu=23{,}000$ to replicate the experimental conditions of Wu and Martinuzzi [9]. The inlet conditions were set based on the requirement that the boundary layer thickness δ/D be approximately 1.5 at the position of the cylinder. This value was used along with a simple developing boundary layer expression to extrapolate what the inlet value of δ/D should be to yield $\delta/D=1.5$ at the position of the cylinder. The shape of the inlet velocity profile was then formed by assuming fully-turbulent flow; the magnitude of the inlet velocity was set to give a Reynolds number of $\mathrm{Re}_D=23{,}000$. The turbulence intensity at the inlet was set to 1% in accordance with the experiments of Wu and Martinuzzi [9]. An estimate for the dissipation rate was obtained from $\langle\epsilon\rangle=0.61k^{3/2}/5D$, based on the imposition of essentially homogeneous turbulence at the inlet.

To ensure that the results were independent of the grid density and the time-step size, computations were made on grids of 106×80, 150×113 and 214×140 with dimensionless time-step sizes of $\Delta t^*=\Delta tU_o/D=0.073$, 0.037 and 0.018. All calculations were done using the *DH+RTI* combination of models. Table 2 summarizes the shedding frequency, quantified in terms of the Strouhal number $\mathrm{St}=fD/U_c$, and the time-averaged lift and drag coefficients for all cases considered in the grid and time independence study. It is evident from the table that the Strouhal number and the lift and drag coefficients are not strongly affected by changes in spatial or temporal discretization; the results from all cases for any one quantity are within 10%. Based on the tabulated results, the simulations on the intermediate grid with a time-step size $\Delta t=0.037$ are spatially converged to ≈7% and temporally converged to better than 1% (based on results from the intermediate grid). A further comparison of time-averaged velocity profiles at several positions at and behind the cylinder (not shown) indicated only very small difference between the results on the intermediate and fine grids and virtually no difference between those of all three time-step sizes. Because of the nonstationarity of the flow and the time-step sizes considered, it is also conceivable that too small a time-step could introduce *random* effects that are not part of the phase-average. Such effects are manifest as cycle-to-cycle variations, which by the formulation used, are not allowed. Thus, continually reducing the time-step size will not necessarily yield a more temporally-converged solution. Too small a time-step may lead to a solution that contains excessive variation from one cycle to the next, or a solution that appears to have no periodicity at all. All cases presented subsequently were computed on the intermediate grid and initiated as time-dependent calculations using $\Delta t^*=\Delta tU_o/D=0.037$, and allowed to develop for the given control parameters. In cases where significant cycle-to-cycle variations resulted, computations were run with larger time-step sizes until the variations diminished, and subsequent time-averaging was done over several periods to average out the variations that remained. For the nonstationary cases, a nominally *regular* or periodic result could typically be obtained within 10,000–15,000 time-steps, which corresponds to approximately 50–80 shedding events.

The convergence of the discretized equations within a time-step was based on the normalized residuals. For each equation, the absolute residuals in each finite-volume were normalized by the average magnitude of the dependent variable to maintain a consistent convergence level. A time-step was considered converged when the maximum residuals for the mass-momentum equations was below 10^{-3}. At this convergence level, the average normalized residuals were below 5×10^{-5} for all variables, including the Reynolds-stresses and the dissipation rate.

5 Results and Discussion

Computations were run for gap widths $S/D=1.0$, 0.5, and 0.25 using all combinations of models. As stated in the previous section, all computations were conducted for a Reynolds number $\mathrm{Re}=23{,}000$. In this section, results are presented for the global dynamic activity (shedding frequency), the integrated temporal activity (lift, drag) and for the time-averaged activity (pressure, velocities) in the vicinity of the cylinder and along the lower wall. The computed results are compared to the experimental data of

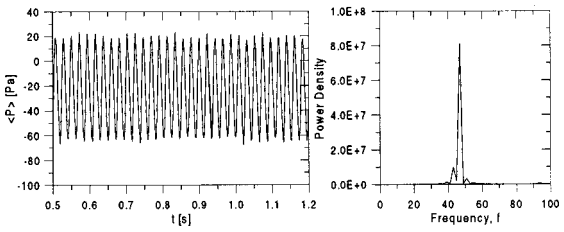

Fig. 2 Plot showing the temporal variation of pressure for on point on the upper face of the cylinder for *S/D*=1 computed using *DH*, *RTI+IP*. The figure on the right shows the result of the FFT conducted on the temporal pressure signal.

Table 4 Summary of time–averaged lift and drag coefficients, $\overline{C_L}/\overline{C_D}$, predicted by all model combinations and those measured by Wu and Martinuzzi [9].

Models	$S/D=1$	$S/D=0.5$	$S/D=0.25$
$LUM+RTI$	−0.455/2.360	−0.221/1.847	−0.242/1.224
$LUM+SSG$	−0.580/2.538	−0.137/1.906	−0.328/1.184
$DH+RTI$	−0.286/2.369	−0.257/1.485	−0.193/1.223
$DH+SSG$	−0.599/2.520	−0.173/1.859	−0.299/1.186
Experiment	−0.202/2.180	−0.495/1.657	−0.422/1.471

Wu and Martinuzzi [9] to assess the performance of models. Observations of the computed results are presented followed by a general discussion of the models used.

5.1 Shedding Frequency. Table 3 gives a summary of the predicted shedding frequencies from the different model combinations and from the experiments of Wu and Martinuzzi [9]. Results are only shown for the two larger gap widths since the flow for $S/D=0.25$ was predicted to be stationary for all model combinations, in accordance with the experiments. The Strouhal number was computed as $\mathrm{St}=fD/U_c$, where f is the frequency of vortex shedding, D is the cylinder dimension and U_c is the streamwise velocity, corrected for blockage. The frequency f was obtained by conducting a fast-Fourier-transform (FFT) on a continuous pressure signal from several points in the flow field. Figure 2 shows a sample of the temporally varying pressure for one point on the upper surface of the cylinder. Included in the figure is the result of the FFT for that pressure signal. The FFT gives a very clear peak at the shedding frequency, as might be expected for a computed signal. For the largest gap width considered, $S/D=1$, the predicted results shown in Table 3 are similar, with the exception of that predicted using $DH+SSG$. The common result is within approximately 10% of the experimental results shown, while that predicted using $DH+SSG$ is approximately 25% too high. For $S/D=0.5$, the experiments indicate that St is larger than that for $S/D=1$, while the computed results show unilaterally that the shedding frequency decreases by about 20%. The $DH+RTI$ models predict a stationary result for this case, which is not consistent with experiments. As mentioned above, for $S/D=0.25$, the flow is predicted to be stationary using all model combinations.

5.2 Lift and Drag. The lift and drag coefficients were obtained by integrating the pressure forces, on the upper and lower (lift) and front and back (drag) faces of the cylinder for each time level. The resulting lift and drag coefficients were computed as

$$\langle C_L\rangle=\frac{\langle F_{lift}\rangle}{\frac{1}{2}\rho U_o^2},\quad \langle C_D\rangle=\frac{\langle F_{drag}\rangle}{\frac{1}{2}\rho U_o^2} \tag{23}$$

where $\langle F_{lift}\rangle$ and $\langle F_{drag}\rangle$ are the integrated, phase-averaged lift and drag forces, respectively. The time-averaged results were then obtained by averaging the phase-averaged results over several periods. Table 4 gives a summary of the time-averaged lift and drag coefficients predicted by all model combinations along with the values obtained by Wu and Martinuzzi [9]. The predicted values for the lift and drag are shown to be somewhat dependent on the model combination chosen for the computation. Considering the $S/D=1$ case, negative lift is predicted by all combinations. The experiments also indicate a negative value. While the $DH+RTI$ combination is closest to the experimental value, the absolute value of the lift is not necessarily the value of most interest. The experimental results indicate that as the cylinder approaches the wall from $S/D=1$, the lift coefficient becomes more negative. The increased negative lift is due to the fluid acceleration and subsequent pressure drop in the gap between the cylinder and the wall. As S/D is further reduced, experiments indicate that the lift coefficient reaches a local minimum followed by an increase that eventually becomes positive as S/D approaches zero. Bailey [17] reports a local minimum in the lift coefficient occuring in the range $0.4\geqslant S/D\geqslant 0.47$ and a minimum value of approximately -0.65. Computationally, no model combination appears to predict this trend correctly; all of the computational results suggest that $\overline{C_L}$ increases with decreasing S/D, however, this could simply be due to a difference in the predicted position of the local minimum. A more detailed investigation of the variation of lift through the suppression regime is given by Martinuzzi and Straatman [18].

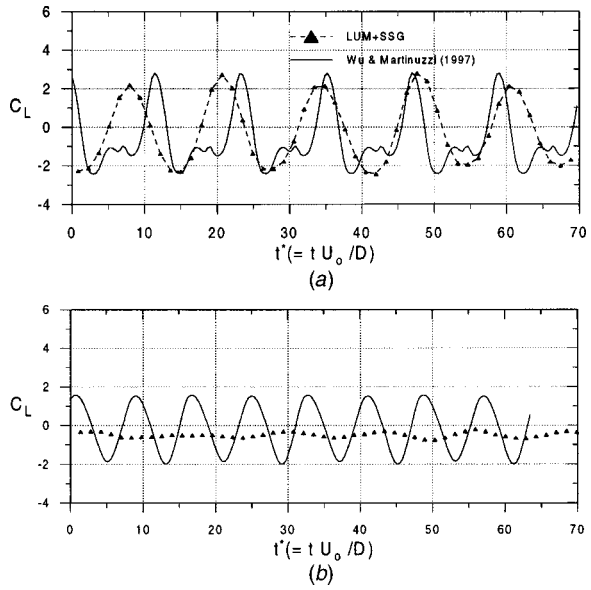

Fig. 3 Plot comparing the temporal variation of lift, $\langle C_L\rangle$, for (*a*) $S/D=1$ and (*b*) $S/D=0.5$ predicted using the $LUM+SSG$ model combination and compared to the measured results of Wu and Martinuzzi [9]

Figure 3(*a*) gives the phase-averaged lift predicted using $LUM+SSG$ for $S/D=1$, as compared to experimental data. Here, it is evident that while the predicted results are slightly out of phase with the measured variation (due to the difference in St), the predicted minima and maxima are in good agreement. It is also evident from the figure that the computed result is not perfectly *regular* (or sinusoidal-like), as might be anticipated. The regularity of the computed results was found to be highly dependent on the gap-width considered, and much less dependent on the model combination chosen. In fact, for $S/D=1$ all model combinations yielded irregular, but periodic time traces for the phase-averaged lift and drag. Results of lift computed using the other model combinations are similar to that shown in Fig. 3 except with (very) slightly different maxima and minima. Results of $\langle C_L\rangle$ for $S/D=0.5$ computed using $LUM+SSG$ are shown in Fig. 3(*b*), again compared to experiments. For this case, the computed results are almost perfectly regular and periodic, but are at best in qualitative agreement with the measured result; the model significantly over-predicts the amplitude of $\langle C_L\rangle$. The $LUM+RTI$ and $DH+SSG$ combinations yield results similar to $LUM+SSG$ except with the mean shifted down slightly, as is evident from the time-averaged results, but the $DH+RTI$ combination predicts a stationary result for this case. The substantial difference in amplitude between the measured and predicted $\langle C_L\rangle$ at $S/D=0.5$ can be partly attributed to the difference between the observed and predicted point at which shedding is suppressed, as suggested above. The suppression of vortex shedding is a process that occurs over a range of S/D (see Bailey [17], Martinuzzi and Straatman [18]) in which all global characteristics of the flow field change. Since the model does not predict the same critical S/D (that re-

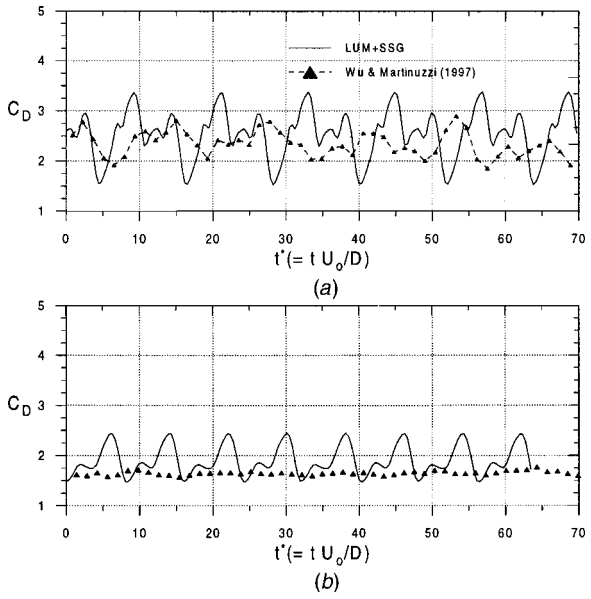

Fig. 4 Plot comparing the temporal variation of drag, $\langle C_D \rangle$, for (*a*) $S/D=1$ and (*b*) $S/D=0.5$ predicted using the *LUM+RTI* model combination and compared to the measured results of Wu and Martinuzzi [9]

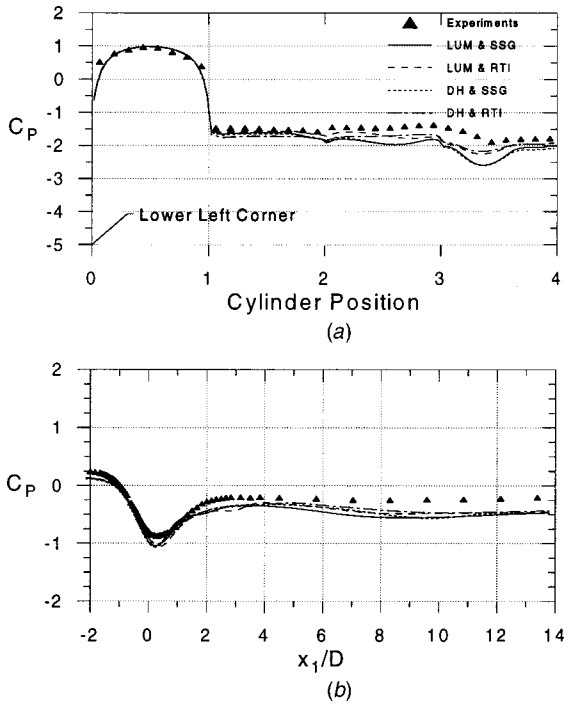

Fig. 5 Plots comparing the predicted time-averaged pressure variation around the cylinder (*a*) and along the lower wall (*b*) with the experimental results of Wu and Martinuzzi [9]

quired to suppress vortex shedding), differences in the amplitude of the lift (and drag) may be artificially high. The trends, however, may still be well-predicted.

The time-averaged drag coefficients are predicted favourably by all model combinations, as is made evident in Table 4. For the nonstationary cases ($S/D=1,0.5$), the predicted drag is generally slightly higher than the experimental values, while for the stationary case ($S/D=0.25$), the predicted drag is lower than that measured. This is due to the discrepancy between the size of the predicted and measured wake, as will be shown subsequently. All model combinations predict $\overline{C_D}$ decreasing with decreasing gap width, in accordance with the experimental results. Samples of the phase-averaged drag predicted using $LUM+SSG$ are shown in Fig. 4 along with experimental data. For $S/D=1$, both the measured and computed results are somewhat irregular. The model over-predicts the amplitude of the drag oscillations, but both the measured and predicted results are centered about approximately the same mean. For $S/D=0.5$, the model significantly over-predicts the amplitude of the drag oscillations, but this, again, could simply be due to the difference between the predicted and observed suppression points. Other model combinations give similar results, with the exception of $DH+RTI$, which predicts no temporal variation.

5.3 Pressure Coefficients. Pressure coefficients were computed as $\langle C_P \rangle = (\langle P \rangle - P_o)/\frac{1}{2}\rho U_o^2$ over all surfaces of the cylinder and along the lower wall. Here, $\langle P \rangle$ is the predicted phase-averaged pressure, P_o is the reference inlet pressure and ρ is the fluid density. The time-averaged pressure coefficients were obtained by averaging the phase-averaged coefficients over several periods. Figure 5 shows the predicted time-averaged pressure variations around the cylinder and along the lower wall for all model combinations compared to the experiments of Wu and Martinuzzi [9] for the case of $S/D=1$. Across the front face, all models predict $\overline{C_P} \approx 1$, as expected because of the stagnation flow in this region. Along the remaining faces, the model predictions are similar and in reasonable accordance with the experimental results. The most notable deviations between the predicted and measured results occur over the back and bottom faces, where all model combinations over-predict the negative $\overline{C_P}$. The trends, however, are still in good agreement. The over-prediction of negative $\overline{C_P}$ on the back face explains the over-prediction of cylinder drag, while the over-prediction of negative $\overline{C_P}$ on the lower face serves to explain the over-prediction of negative lift (see Table 4). The SSG model is seen to yield slightly worse results for $\overline{C_P}$, although overall no single combination is seen to give superior predictions.

The pressure along the lower wall is predicted reasonably well by all model combinations, although all combinations slightly over-predict the negative $\overline{C_P}$ under the cylinder and in the recovery region.

5.4 Velocity and Reynolds-Stresses. Figures 6–8 compare the predicted time-averaged velocity and Reynolds-stress profiles with those measured by Wu and Martinuzzi [9] for several positions at and behind the cylinder. For the $S/D=1$ case, the streamwise velocities are favourably predicted by all combinations, although near $x_1/D=4$, the size of the wall-jet is under-predicted leading to a flatter profile near the wall. The trends in the vertical velocities are well predicted except near $x_1/D=4$, where near the wall the fluid motion is predicted to be opposite that measured. In general, all model combinations tend to over-predict the vertical velocity in the wall-jet region, but then relax to nearly flat profiles beyond the wake ($x_1/D=4$), in accordance with the experiments. The Reynolds-stress components are generally over-predicted by all models in the near-wake region, but then relax to realistic values beyond the wake. Trends in the Reynolds-stress distributions are essentially correct.

Figure 7, corresponding to $S/D=0.5$, shows larger discrepancies between the model predicitions, particularly for the $DH+RTI$ combination, which yields a stationary result for this case. In terms of trends, the remaining combinations generally capture the shapes of the profiles, but, as with the case of $S/D=1$, the magnitudes of the velocity components in some positions are over-predicted. The most notable deviations occur in the near-wake, $x_1/D=1,2$, where the models (with the exception of $DH+RTI$) show full periodic shedding and the experiments yield a very low-amplitude, periodic flow field. This serves to reconcile

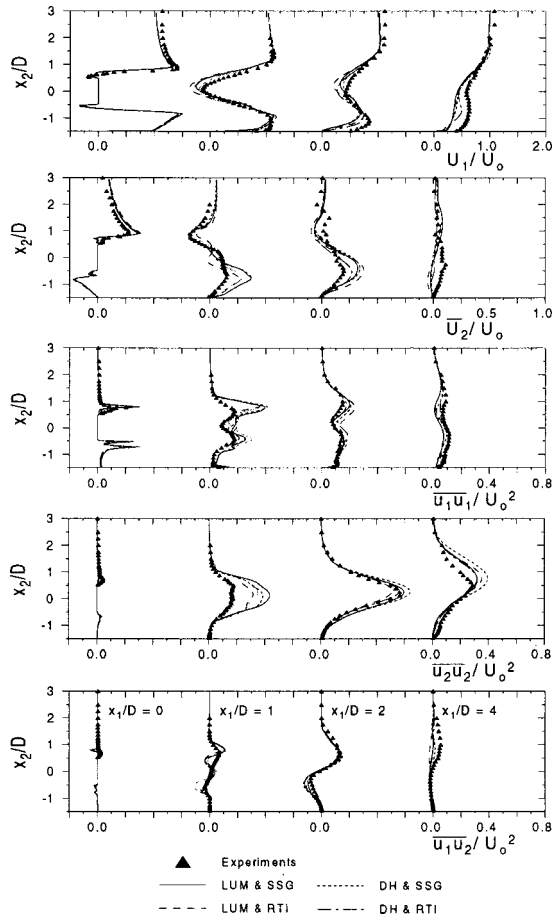

Fig. 6 Profiles of the mean velocities and the $\overline{u_1u_1}$, $\overline{u_2u_2}$ and $\overline{u_1u_2}$ Reynolds-stresses, all normalized by the inlet velocity U_o, for the case of $S/D=1.0$. Included for comparison are the experimental results of Wu and Martinuzzi [9]. All data are for the axial positions indicated in the $\overline{u_1u_2}$ plot.

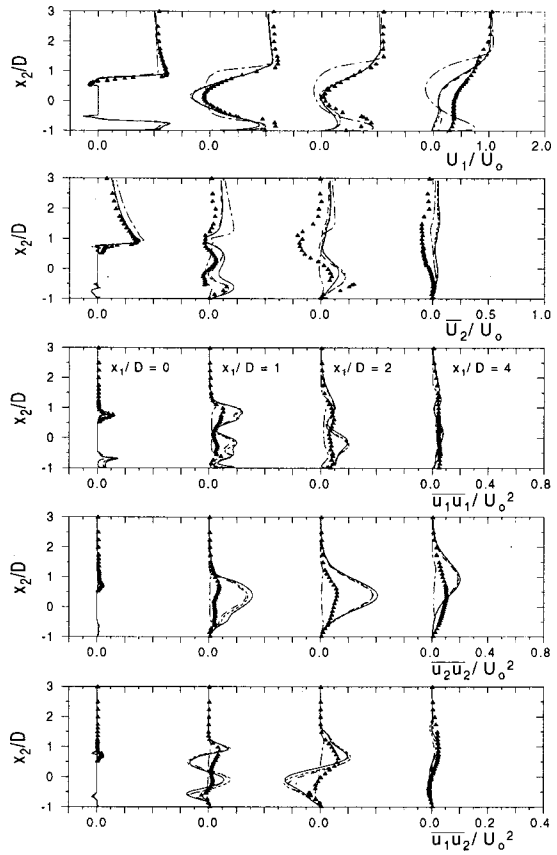

Fig. 7 Profiles of the mean velocities and the $\overline{u_1u_1}$, $\overline{u_2u_2}$ and $\overline{u_1u_2}$ Reynolds-stresses, all normalized by the inlet velocity U_o, for the case of $S/D=0.5$. Included for comparison are the experimental results of Wu and Martinuzzi [9]. Legend and axial positions same as in Fig. 6.

differences between the measured and predicted vertical velocities, and the $\overline{u_2u_2}$ and $\overline{u_1u_2}$ components of the Reynolds stress tensor. Note again, however, that these deviations may be artificially high due to the difference between the observed and predicted suppression points.

For the stationary case ($S/D=0.25$) shown in Fig. 8, the velocities and Reynolds-stresses are in reasonable agreement in terms of both trends and magnitudes. The largest deviation for this case is the over-prediction of the wake size behind the cylinder, which is made evident by the shape of the velocity profiles beyond $x_1/D=2$. In the computations, the shear layers do not decay significantly until beyond $x_1/D>5$, whereas the experiments show nearly a complete disappearance of the wake by this point. Surprisingly, the turbulence quantities in the far-wake are not over-predicted, even though there remains significant shear in the predicted mean flow field. This is likely due to the under-prediction of the normal and shear stresses in the near-wake region, which are subsequently transported downstream.

5.5 General Discussion. Considering all of the computed cases, the prediction of the flow structure using a second-moment turbulence is seen to be reasonable. In terms of global quantities, the drag appears to be the most faithfully reproduced. While the drag forces were slightly higher than those measured, owing to the under-prediction of pressure behind the cylinder, the predicted trend for decreasing S/D was correct for all model combinations. Trends predicted for the lift and the shedding frequency were not seen to be consistent with measurements, however, further study is warranted to explore the variations of St and $\overline{C_D}$ through the entire suppression regime. In terms of flow details, the variations of the individual stress components were generally well-predicted with differences in some regions, most notably the near-wake.

Though diffusive transport is not a dominant influence in much of the flow field, the modified LUM model was shown to perform slightly better than the DH model. Foremost, it was shown that the DH model yields a stationary result at too large a gap width when combined with the linear $RTI+IP$ relation, while yielding a nonstationary result when combined with SSG. The nonstationarity of the flow field is dependent on temporal instabilities and relative circulation strength (proportional to vorticity) in the upper and lower shear layers. Since the DH model is well-known to over-predict lateral diffusion in other types of flows (e.g., jets, mixing layers), it is likely that the flow becomes stationary too soon as a result of lateral transport of vorticity and thus, premature decaying of the shear layers. The nonlinear SSG model was seen to retain flow non-stationarity for $S/D=0.5$, however it is likely that this combination would still yield a stationary result prematurely. Thus, the present study is consistent with previous studies (Straatman et al. [19], Straatman [11]) that suggest the modified LUM model is the best available model for diffusion in a second-moment closure.

The influence of the pressure-strain model is thought to be much more important in the prediction of the flow since the turbulence is highly anisotropic and local structures are strongly influenced by wall interaction. Having stated this, only subtle differences were observed between the linear $RTI+IP$ model and the non-linear SSG model. Globally, the nonlinear model was seen to make the flow remain non-stationary for smaller S/D

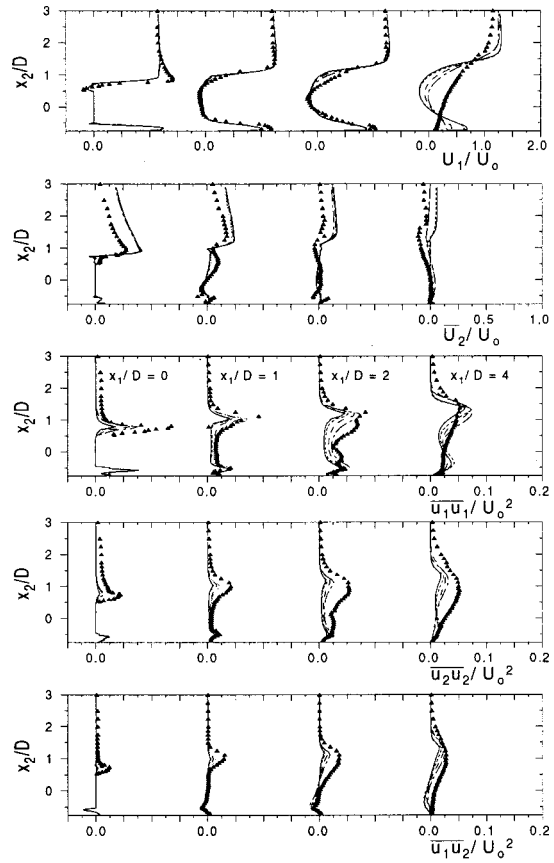

Fig. 8 Profiles of the mean velocities and the $\overline{u_1u_1}$, $\overline{u_2u_2}$ and $\overline{u_1u_2}$ Reynolds-stresses, all normalized by the inlet velocity U_o, for the case of $S/D=0.25$. Included for comparison are the experimental results of Wu and Martinuzzi [9]. Legend and axial positions same as in Fig. 6.

when combined with the *DH* diffusion model. In terms of flow structure, all model combinations over-predict the negative $\overline{C_P}$ on both the cylinder (back and bottom) and wall, the *SSG* model being slightly worse than *RTI*. The prediction of flow details in the wake region were not seen to be strongly dependent on the pressure-strain model. Furthermore, all combinations of models were seen to over-predict the size of the wake for the stationary flow case. Also of note is the fact that no difference in computational effort was required for the present calculations, despite the fact that the *SSG* model has been described as being more computationally *stiff* than the linear *RTI+IP* model. While there is no overwhelming evidence from the present study to suggest one model over the other, the *SSG* model has the advantage that it is easier to implement since there is no need to implement wall-reflection terms. Thus, within the scope of a high-Re_t framework, the *SSG* model appears to be a reasonable choice for modelling pressure-strain.

It is likely that the use of a low-Re_t closure model would improve the predictions in the wake, since the flow structure behind the cylinder is largely dependent on the turbulence produced on the walls of the cylinder and the separation and reattachment points on the lower wall. That is, since the turbulence in the wake is mainly that produced on the cylinder walls, better predictions of the unresolved turbulence on the walls may lead to improvements in the time-averaged turbulence statistics behind the cylinder. Although it is well-known that that wall-functions are ill-suited for predicting flows with separation and reattachment, it is still important to see their effect since most calculations of industrial relevance have and will continue to use only high-Re_t variants of turbulence models. Given that some of the important trends are properly reproduced, the second-moment closure does still serve as the best existing method for modelling the unresolved turbulence in unsteady RANS predictions.

6 Concluding Remarks

Computations of the two-dimensional, nonstationary flow field around a square cylinder in proximity to a wall were carried out using several combinations of second-moment turbulence closure models in an effort to assess the performance of the different models. The results of the computations were then systematically compared to similar results obtained experimentally by Wu and Martinuzzi [9]. The following conclusions are noted:

1 The flows for the large gap widths ($S/D=1,0.5$) were predicted to be non-stationary for most cases, in accordance with experiments. The only exception was the stationary prediction by *DH+RTI* for the case of $S/D=0.5$. For the small gap width, $S/D=0.25$, all models yielded a stationary result, in accordance with experiments. The shedding frequency was predicted reasonably well for the largest gap width, with the exception of *DH+SSG*, which over-predicted St by 25%. As the gap width was reduced, all model combinations that yielded a non-stationary result showed a decrease in the shedding frequency, while the experiments show a slight increase.
2 The absolute lift on the cylinder was not particularly well predicted. Predictions of the time-averaged lift were as much as 300% off and all model combinations predict $\overline{C_L}$ increasing with increasing S/D, opposite to that shown experimentally. However, temporal variations of the lift were shown to be in good agreement in terms of the minima and maxima for $S/D=1$. For $S/D=0.5$, the amplitude of the $\langle C_L \rangle$ oscillations were over-predicted, but it was argued that this may be due to the difference between the observed and predicted critical S/D.
3 The drag on the cylinder was predicted reasonably well in terms of absolute value and trend. All model combinations predict $\overline{C_D}$ decreasing with decreasing S/D.
4 Pressure coefficients were predicted favourably by all model combinations.
5 Comparisons of time-averaged velocities and Reynolds-stresses at several positions at and behind the cylinder indicate that details of the flow structure are not always well-predicted using second-moment closure models. For the $S/D=1$ case, predictions of the velocity and shear stress components were well predicted in terms of magnitude and trends, however the normal stress components were over-predicted in the near wake region. The $S/D=0.5$ case showed larger discrepancies between models, since the *DH+RTI* combination gives a stationary result, whereas all other combinations give a non-stationary result, in accordance with experiments. For $S/D=0.25$, all model combinations predict a stationary flow, but the size of the cylinder wake is over-predicted. It is felt that this might be improved upon using a low-Re_t model instead of wall-functions.

Acknowledgments

The authors gratefully acknowledge financial support received from the Natural Sciences and Engineering Research Council of Canada.

References

[1] Franke, R., and Rodi, W., 1993, "Calculation of Vortex Shedding Past a Square Cylinder With Various Turbulence Models," in *Turbulent Shear Flows 8*, F. Durst, et al., eds., Springer, New York, pp. 189–204.
[2] Bosch, G., and Rodi, W., 1996, "Simulation of Vortex Shedding Past a Square Cylinder Near a Wall," Int. J. Heat Fluid Flow, **17**(3), pp. 267–275.
[3] Bosch, G., and Rodi, W., 1998, "Simulation of Vortex Shedding Past a Square Cylinder with Different Turbulence Models," Int. J. Numer. Methods Fluids, **28**, pp. 601–616.

[4] Lee, S., and Bienkiewicz, B., 1998, ''Finite Element Implementation of Large Eddy Simulation for Separated Flows,'' J. Wind. Eng. Ind. Aerodyn., **77**, pp. 603–617.
[5] Bouris, D., and Bergeles, G., 1999, ''2D LES of Vortex Shedding From a Square Cylinder,'' J. Wind. Eng. Ind. Aerodyn., **80**, pp. 31–46.
[6] Thomas, T. G., and Williams, J. J. R., 1999, ''Large Eddy Simulation of Vortex Shedding From Cubic Obstacle,'' Journal of Aerospace Engineering, **12**(4), pp. 113–121.
[7] Peng, Y. F., and Hwang, R. R., 1999, ''A Numerical Study on Turbulent Vortex Shedding Flows Around a Cubical Form,'' J. Chin. Inst. Eng., **22**(5), pp. 639–648.
[8] Rodi, W., 1998, ''Comparison of LES and RANS Calculations of the Flow Around Bluff Bodies,'' J. Wind. Eng. Ind. Aerodyn., **69**, pp. 55–75.
[9] Wu, K. C. Q., and Martinuzzi, R. J., 1997, ''Experimental Study of the Turbulent Wake Flow behind a Square Cylinder near a Wall,'' Paper FEDSM97-3151, Proc. *ASME FED Summer Meeting*, Vancouver, British Columbia, Canada.
[10] Hussain, A. K. M. F., 1983, ''Coherent Structures, Reality and Myth,'' Phys. Fluids, **26**(10), pp. 2816–2849.
[11] Straatman, A. G., 1999, ''A Modified Model for Diffusion in Second-Moment Turbulence Closures,'' ASME J. Fluids Eng., **121**(4), pp. 747–756.
[12] Daly, B. J., and Harlow, F. H., 1970, ''Transport Equations in Turbulence,'' Phys. Fluids, **13**(11), pp. 2634–2649.
[13] Speziale, C. G., Sarkar, S., and Gatski, T. B., 1991, ''Modelling the Pressure-Strain Correlation of Turbulence: An Invariant Dynamical Systems Approach,'' J. Fluid Mech., **227**, pp. 245–272.
[14] Patankar, S. V., 1980, *Numerical Heat Transfer and Fluid Flow*, Hemisphere Publishing.
[15] Leonard, B. P., 1979, ''A Stable and Accurate Convection Modelling Procedure Based on Quadratic Upstream Interpolation,'' Comput. Methods Appl. Mech. Eng., **19**, pp. 59–98.
[16] Straatman, A. G., 2001, ''Implementation and Validation of the Modified LUM Diffusion Model in a Second-Moment Closure,'' *Proc. 9th Annual Conference of the CFD Society of Canada*, Waterloo, Ontario, Canada, pp. 511–517.
[17] Bailey, S. C. C., 2001, ''Experimental Investigation of the Pressure Distribution for a Square Cylinder near a Solid Boundary,'' M.E.Sc. thesis, The University of Western Ontario, London, Canada.
[18] Martinuzzi, R. J., and Straatman, A. G., ''A Study of the Onset/Suppression of Vortex Shedding from a Square Cylinder in Proximity to a Wall,'' Submitted for publication to ASME J. Fluids Eng., Apr. 2002.
[19] Straatman, A. G., Stubley, G. D., and Raithby, G. D., 1998, ''Examination of Diffusion Modelling using Zero-Mean-Shear Turbulence,'' AIAA J., **36**(6), pp. 929–935.

A Study of Vortex Shedding in a Staggered Tube Array for Steady and Pulsating Cross-Flow

E. Konstantinidis

S. Balabani

M. Yianneskis[1]

Department of Mechanical Engineering,
King's College London,
Strand, London WC2R 2LS, United Kingdom

This paper describes an experimental investigation of the vortex shedding phenomena in a staggered tube array with streamwise and transverse spacing to diameter ratios of 2.1 and 3.6, respectively. LDA measurements were employed to monitor the flow fluctuations and a visualization technique was implemented to reveal the underlying flow patterns in the array for steady and pulsating cross-flow. The results obtained in steady flow are in general agreement with results from previous investigations and show that vortex shedding occurs at two distinct frequencies in the front and inner rows. A lower frequency component was detected at the exit of the array, which has not been previously identified. Pulsating flow caused the frequency of vortex shedding to lock-on at the subharmonic of the imposed frequency. In the lock-on range, vortex shedding from all the tubes was synchronized and in-phase and velocity fluctuations at the shedding frequency increased considerably compared to their counterparts in steady flow. [DOI: 10.1115/1.1487359]

Introduction

Vortex shedding occurs at discrete frequencies inside tube arrays over a wide range of configurations and Reynolds numbers. The mechanism and the frequency of vortex shedding have been the subject of many previous experimental studies. The main reason behind this interest has been the excitation of flow-induced vibrations and noise in heat exchanger tube arrays and associated problems for industry. References [1–3] provide comprehensive reviews on the topic. The excitation mechanisms have been identified and classified as (a) turbulent buffeting, (b) Strouhal periodicity, (c) fluid-elastic instability and (d) acoustic resonance [2].

The Strouhal periodicity mechanism is often referred to as vortex or vorticity shedding in the literature. It is demonstrated as a narrow-band discrete event in the turbulence and pressure spectra with a frequency that varies linearly with flow velocity yielding a constant Strouhal number. Recent flow visualization studies have demonstrated that the discrete frequencies observed inside tube arrays are associated with periodic vortex shedding in the space between the tubes [4–11]. Coincidence of this flow frequency with a structural frequency of a tube in the array can excite tube vibrations in liquid flows whereas coincidence with an acoustic frequency can excite acoustic resonance and noise in gas flows. When resonance occurs, the vortex shedding frequency is locked-on with the resonance frequency and the Strouhal number may attain values different than its constant value at nonresonant conditions.

Weaver and Abd-Rabbo [4] observed symmetric vortex shedding inside a square tube array in connection with large amplitude streamwise tube vibrations. The mechanism of vortex formation had a fluid-elastic origin and vortex shedding was synchronized with the tube motion. The associated Strouhal number was one-half of that expected from published data for rigid arrays. Price et al. [5] noticed that vortex shedding was triggered by the motion of a flexible cylinder in a parallel triangular array with a pitch ratio of 1.375 whereas the flow in the rigid array had little or no vortical motion. The flexible cylinder was positioned in either the third or fifth row and was supported in such a way so that it was free to move in the transverse direction only. The possibility that the initial vibration of the cylinder might be due to a combination of excitation mechanisms was put forward and it was pointed out that vortex shedding can be due to a number of different mechanisms.

Weaver et al. [6] showed that the Strouhal number data in the literature for rotated square arrays fit relatively well into two curves as a function of the pitch ratio, eliminating data stemming from resonant conditions. Their experimental results indicated a higher Strouhal number due to vortex shedding from the first row of tubes and a lower Strouhal number due to vortex shedding from the second row. It was argued that vortex shedding occurs at distinct frequencies in the first and second rows because of the different local flow characteristics that affect the magnitude of the velocity near the separation point and the wake width which both correlate with the shedding frequency according to a ''universal Strouhal number'' [12].

Ziada and Oengören [7] and Polak and Weaver [8] studied the vortex shedding phenomena in normal triangular arrays and observed two different Strouhal numbers that stemmed from different vortex shedding frequencies in the front and inner rows. The former authors noted that for high Reynolds number and intermediate pitch ratios the low frequency component dominated the entire array, whereas the latter noted that for small pitch ratios only the high frequency component was detected. Both studies provided charts and empirical formulas for the prediction of the two Strouhal numbers as a function of the pitch ratio that agree well with other published data. Experimental results for parallel triangular arrays published recently [9] display three frequency components associated with shear layer instability, alternating vortex shedding and large-scale alternating vortex shedding. Therefore, the chart of Strouhal numbers as a function of the pitch ratio contains three curves.

The data in the literature provide a relatively complete picture of the expected Strouhal numbers in heat exchangers with rotated square, parallel and normal triangular tube arrays although some uncertainty remains over the associated mechanisms. Different heat exchanger designs still require data to be obtained from experiments as the Strouhal number depends on tube arrangement, spacing between the tubes -both normal to and in the direction of the flow-, location in the array and even Reynolds number. In practice, the flow in actual heat exchangers may contain turbulent fluctuations or even disturbances at distinct frequencies, as for instance in flows delivered by reciprocating pumps. Little attention has been paid on the effect of upstream turbulence in tube

[1]Corresponding author. e-mail: michael.yianneskis@kcl.ac.uk

Contributed by the Fluids Engineering Division for publication in the JOURNAL OF FLUIDS ENGINEERING. Manuscript received by the Fluids Engineering Division August 2, 2000; revised manuscript received April 2, 2002. Associate Editor: J. Bridges.

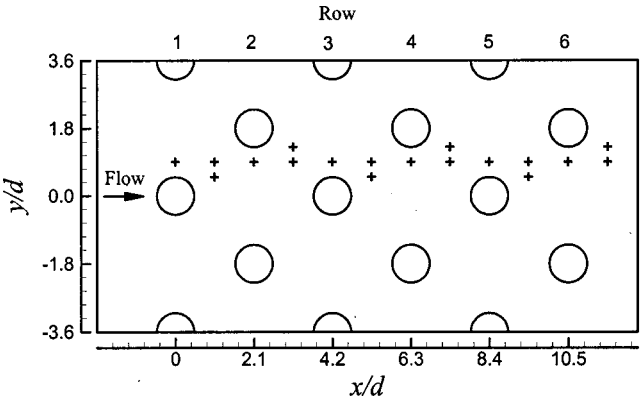

Fig. 1 Schematic cross-section of the tube array. The coordinate system employed is also shown and crosses indicate the measurement locations.

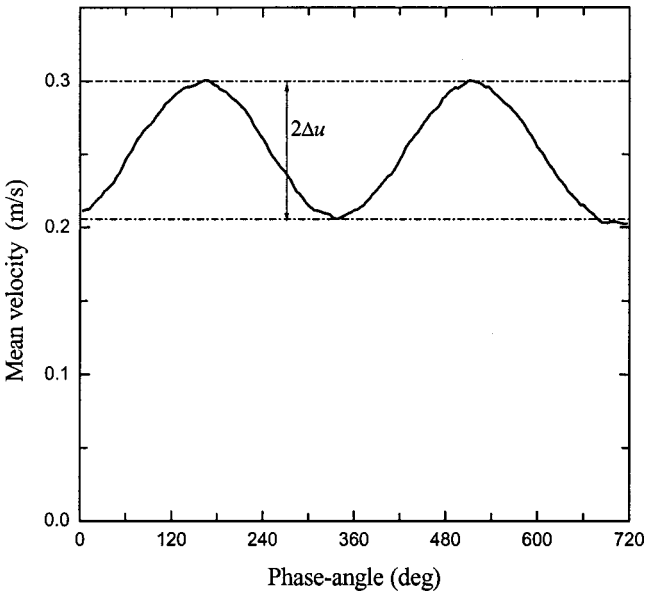

Fig. 2 Mean velocity profile with respect to a constant phase in the pulsation cycle obtained at the reference point upstream of the tube array

arrays. High upstream turbulence levels have been shown to influence the Strouhal mechanism in in-line arrays [10] and turbulence grids have been proposed as a means of destroying flow periodicity in tube arrays [2]. The effect of imposed flow disturbances at distinct frequencies (streamwise pulsations) has been previously studied for an in-line array by the authors [11]. It was found that vortex shedding locked-on at the sub-harmonic of the imposed pulsation frequency and vigorous shedding was incited in the gap between the tubes of the first and the second row whereas for steady approaching flow the gap was shielded by the shear layers that reattached onto the second-row tube.

The present study examines the constant Strouhal number mechanism in a rigid staggered tube array placed normal to a turbulent stream. The study comprised velocity measurements and flow visualisation. LDA measurements were employed to provide time-resolved velocity data in various locations in the array. The frequency of the periodic flow phenomena was identified from the amplitude spectra of the velocity data. The effects of flow disturbances at distinct frequencies, i.e., of pulsating flow, on Strouhal numbers and flow characteristics were investigated over a wide range of conditions. The motivation for studying the effect of pulsating flow was to explore the potential to modify the flow characteristics with a view to augment heat transfer in industrial heat exchangers; this requires a sound understanding of the pertinent fluid mechanics. The objective was to establish if the vortex shedding in staggered arrays is influenced by the frequency of the imposed pulsation and determine the range of parameters for which this might occur. No such data are available in the literature to the best of the authors' knowledge.

Experimental Facility

The staggered tube array used in the experiments is shown in Fig. 1. The configuration is similar to the one used by Weaver et al. [6] to study the vortex shedding phenomena in a rotated square array. The 72-mm square test section was made of acrylic plastic to allow optical access and the tubes were circular cylinders of the same material with diameter $d=10$ mm. The cylinders were fitted horizontally in the test section and rigidly mounted on the walls to eliminate vibration. The array comprised six rows and half cylinders were mounted on the test section walls to simulate an infinite array and minimize wall effects. The streamwise and transverse spacings were 21 and 36 mm, respectively. This gave a pitch ratio, i.e., the closest center-to-center distance of the tubes normalized with the tube diameter, of 2.77 which was neither a normal triangular nor a rotated square but an intermediate arrangement. Preliminary LDA measurements of the mean and r.m.s. velocity were carried out across the entire width of the test section and at various spanwise stations to check the flow in the tube array and determine the measurement locations for the study of the spectral characteristics. These measurements indicated that the time-averaged flow is symmetric with respect to the middle tube column and two-dimensional on the central span of the tubes.

The experiments were conducted in a closed-circuit water tunnel used previously in steady flow experiments [13,14], modified to produce pulsating flow. The flow in the tunnel was driven by a centrifugal pump delivering flow velocities up to 0.93 ms^{-1} adjustable with a bypass valve. A bifurcation in the circuit divided the flow into two branches and a rotating valve could periodically block the flow passage of one branch, thereby producing unsteadiness with a profile similar to a sinusoidal pulsation (see Fig. 2). The frequency of the pulsation was adjusted by the speed of the rotating valve via a variable speed motor. Control valves adjusted the relative amounts of steady/pulsed flow. With the present experimental setup, the mean flow velocity, the frequency and the amplitude of the pulsation could be adjusted independently and in continuous increments.

The upstream flow had a fully developed turbulent profile that was identical for both steady and pulsating flow. The bulk flow velocity upstream of the array, U_b, was measured with a variable area rotameter in steady flow. Reading the flow-rate from the scale of the rotameter resulted in an uncertainty in the estimation of the flow velocity of ± 0.009 ms^{-1} whereas bias was negligible. In pulsating flow the upstream velocity could not be monitored with the rotameter and measurements of the velocity at the reference point using the laser-Doppler anemometer described below were used instead. The reference point was $2.1d$ upstream of the array and in the centreline of the test section. The magnitude of the velocity at the reference point, denoted U_o in short, was calibrated against the rotameter readings in steady flow. The results of the calibration were then used to determine the bulk flow velocity in pulsating flow according to the relationship $U_b=0.79U_o$ with an uncertainty $\pm 0.05U_b$ for $U_b \geqslant 0.20$ ms^{-1} and ± 0.01 ms^{-1} for $U_b < 0.20$ ms^{-1}. The frequency of pulsation was monitored via an optical encoder with 2000 pulses per revolution attached to the shaft of the rotating valve. The pulsation frequency of the flow was twice the rotating frequency of the valve as the periodic blockage repeated itself each half cycle and was constant within ± 0.01 Hz during each set of experiments. The amplitude of the pulsation was deduced from the variation of the mean flow at the reference point as shown in Fig. 2. It should be noted that the

profile in Fig. 2 was obtained by phase-averaging the velocity fluctuations with respect to the pulsation phase. Turbulent fluctuations superimposed on the variation of the mean flow are therefore averaged out.

Time-resolved velocity data of the interstitial flow were obtained using a dual beam Laser Doppler Anemometer (LDA) with a 10 mW He-Ne laser source. The anemometer was operated in forward scatter and a photomultiplier collected the scattered light form particles crossing the control volume, 466 μm in length and 48.8 μm in diameter. Naturally occurring impurities in the tap water served as light-scattering particles. The produced signal was processed using a TSI frequency counter, model 1990B, interfaced to a computer with appropriate data acquisition software and the digital data were stored on the computer for subsequent analysis with the commercial software MatLab™. The number of samples acquired at each measurement location was 1.2×10^4 and the average data rate of the random inter-arrival times of particles through the measuring volume varied from 0.3−1.2 kHz depending on the measurement location and flow velocity. The raw random data were re-sampled at equal time intervals using a zero-order interpolation technique (''nearest neighbor''). A resample rate slightly less than the average data rate was used. Spectra of the velocity fluctuations were obtained by the method of fast Fourier transforms. The spectral resolution employed was set at 0.1 Hz for all the spectra presented in this paper, which is sufficient to resolve the fluctuations associated with the vortex shedding phenomena in detail. However, tests with different spectral resolutions have yielded the same results. Block-averaging was employed to reduce the variability of the spectra; the number of blocks was a function of the data (re-sample) rate due to the fixed resolution. As a result, the number of blocks used was higher for lower data rates (e.g., four blocks were used at 0.3 kHz) than for the higher data rates (e.g., no averaging was employed at 1.2 kHz).

In order to visualize the interstitial flow between the tubes, an Argon-Ion laser sheet was used to illuminate the test section at right angles to the axes of the tubes and midway in the test section and the flow was seeded with 0.015-mm diameter hollow glass particles. Because of the half tubes on the side-walls, the interstitial flow could be illuminated only with light passing through the cylinders and thus lighting was not homogeneous, producing light and dark patches. The glass particles were neutrally buoyant and followed the flow faithfully. Video recordings of the flow were taken using a CCD video camera with a zoom lens and individual frames of the video were obtained by digitising the video frames with a video grabber.

Experimental Results

Vortex Shedding in Steady Flow. The experiments commenced with steady flow tests. For a given flow velocity, time-resolved LDA measurements were taken at the locations indicated by the crosses in Fig. 1. These locations were along the flow lane between the staggered tubes and at the edge of the shear layers separating from the tubes. Typical spectra at one measurement location are shown in Fig. 3 for the range of gap velocities examined in steady flow. The gap velocity, U_g, is defined as the average velocity in the minimum gap between tubes in a transverse row and is equal to $1.385U_b$ by continuity. The Reynolds number, Re, employed in this study is based on the gap velocity and tube diameter ($\mathrm{Re}=U_g d/\nu=10^4 U_g$, where ν is the kinematic viscosity of water). There is clearly a string of peaks in the spectra of Fig. 3 that can be attributed to vortex shedding with the center frequency varying linearly with the gap velocity. Averaging the spectra over a longer period would clearly produce a smooth and well-defined peak [15]. The amplitude of the velocity fluctuations due to vortex shedding increases with increasing the gap velocity and background turbulence levels also increase in the same fashion.

The spectra obtained at the measurement locations along the flow lane between the tubes for a gap velocity of 0.53 ms^{-1} (Re $=5300$) are shown in Fig. 4, in order to identify the dominant periodic phenomena present in the array and their source. Three spectral peaks can be identified at 17.7, 12,8 and 9.2 Hz denoted f_{S1}, f_{S2}, and f_{S3}, respectively. The f_{S1} peak appears at the second row ($x/d=2.1$) and disappears after the fourth row ($x/d=6.3$) whereas the f_{S2} peak appears also at the second row but persists throughout the array. The f_{S3} peak appears only at the last measurement location at the exit of the array alongside f_{S2}. Spectra obtained at different Reynolds numbers produced very similar data except that the frequency of the peaks varied linearly with the gap velocity. As mentioned in the Introduction, it is known that vortex shedding from the tubes in the front rows occurs at a higher frequency than in inner rows. The present results support this observation. The tubes in the front rows shed vortices at the high frequency, f_{S1} and the inner tubes shed vortices at the medium frequency, f_{S2}. The low frequency peak, f_{S3}, was observed only at the exit of the array. This lower frequency, f_{S3}, may be attributed to an exit or collective effect [16,17], the explanation provided being simply that the wake of the last tube is not confined by surrounding tubes. Measurements at the edge of the shear layers separating from the tubes, not shown here for economy of presentation, showed that: (a) the f_{S1} and f_{S2} components were detected in the wake of both the 1st and 2nd row, (b) rows 3 to 5 gave rise only to the f_{S2} component, and (c) only the f_{S3} component was detected in the shear layer of the last row. These results help elucidate the source of the different components. Therefore, it seems appropriate that the results of this study be usefully categorized in terms of the three observed frequency components f_{S1}, f_{S2}, and f_{S3}.

Figure 5 shows the variation of the amplitude of the f_{S1} and f_{S2} components as a function of row depth and gap velocity. It can be seen that the amplitude of both components generally increases

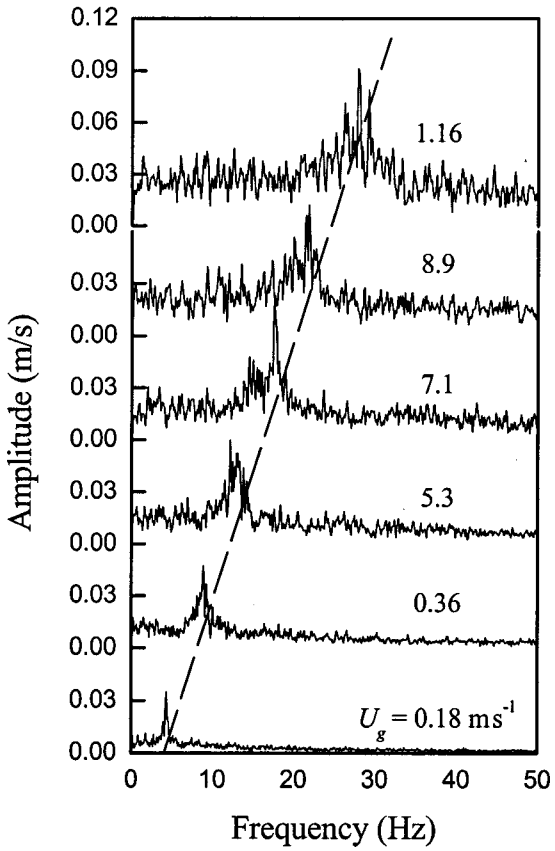

Fig. 3 Spectra of the streamwise velocity fluctuations for different gap velocities at the location: $x/d=7.35$, $y/d=0.9$ (steady flow). The Reynolds number is $\mathrm{Re}=10^4\times U_g$.

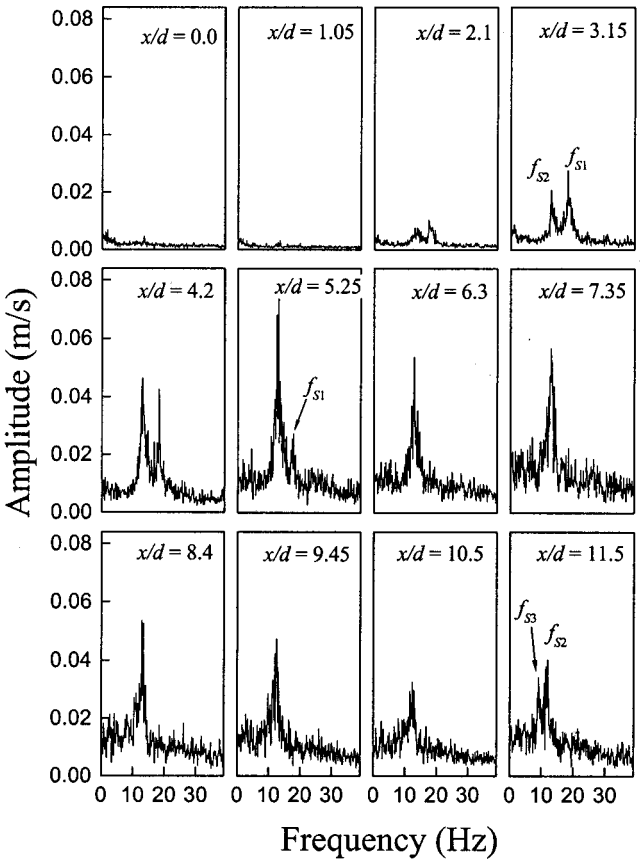

Fig. 4 Development of the streamwise velocity spectra along the flow lane between the staggered tubes for steady flow and U_g=0.53 ms^{-1} (Re=5300)

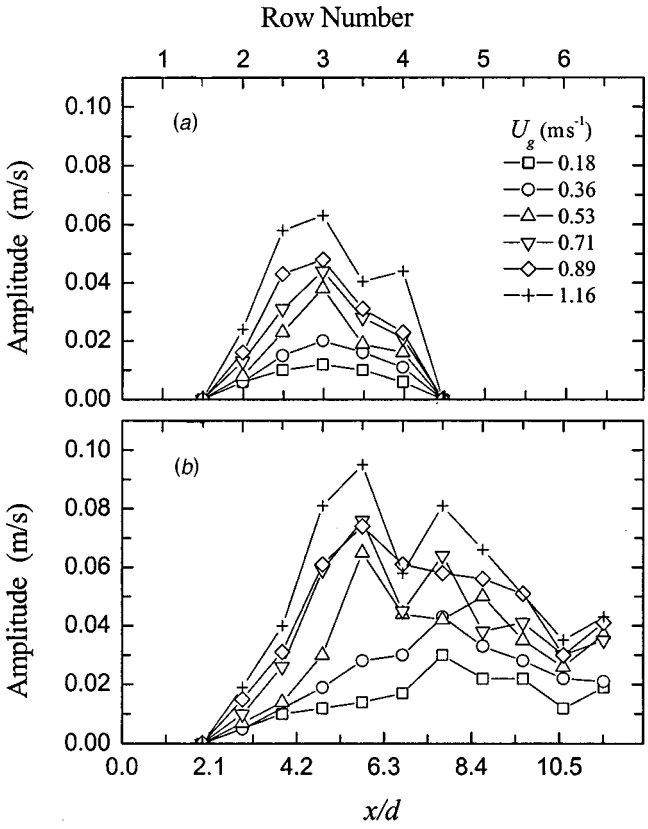

Fig. 5 The variation of the amplitude of velocity fluctuations at the shedding frequency as a function of the location in the array and Reynolds number (steady flow); (a) f_{S1} component and (b) f_{S2} component

with increasing velocity. The f_{S1} component increases behind the first row, reaches a maximum at the third row, then decreases and disappears after the fourth row for all velocities tested (Fig. 5(*a*)). The f_{S2} component reaches a maximum between the fourth and the fifth row for U_g=0.18 and 0.36 m s^{-1} and between the third and the fourth row for the higher velocities indicating a more complex development of the flow at higher Re (Fig. 5(*b*)). These characteristics contrast with the development of the flow in an in-line array of the same streamwise and transverse spacing where velocity fluctuations gain strength gradually with row depth [11].

The variation of the frequency of the three vortex shedding components as a function of the gap velocity is shown in Fig. 6. There is clearly a linear relationship between the frequency of each component and the gap velocity, as expected. The corresponding Strouhal numbers for each component, $S=f_S d/U_g$, based on gap velocity and tube diameter are 0.33, 0.24 and 0.17 with uncertainty estimates of 0.011, 0.008, and 0.013 for the f_{S1}, f_{S2}, and f_{S3} components, respectively. The reported Strouhal numbers are the averages over the different measurement locations and velocities and uncertainty estimates are based on 95% confidence levels computed according to the methods proposed by Abernethy et al. [18].

Direct comparison of the Strouhal numbers obtained in this study with others in literature is not possible due to the particular spacings involved. However, comparison may be made with the results of Weaver et al. [6] for a rotated square array with a pitch ratio of 2.83 that is similar to that of the present array. The longitudinal and transverse spacings were 2.0 and 4.0, respectively, and the corresponding Strouhal numbers were 0.42 and 0.32 based on upstream velocity. These compare well with the corresponding values of 0.46 and 0.33 based on the upstream velocity found in this study.

Effect of Flow Pulsation. According to published results on the pulsating cross-flow over a single stationary circular cylinder [19–21], the frequency of vortex shedding is expected to lock-on

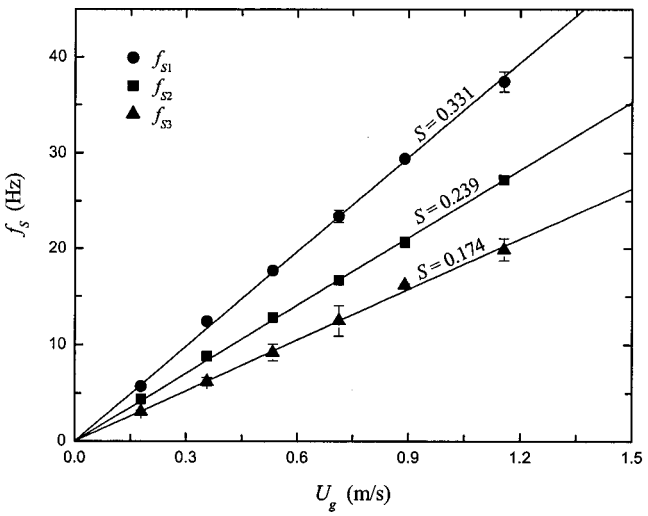

Fig. 6 Variation of the dominant frequency components detected in the array as a function of the gap velocity for steady flow

Table 1 Conditions for pulsating flow experiments

Set	U_g (ms^{-1})	f_P (Hz)	Δ_u (ms^{-1})	f_{S1} (Hz)	f_{S2} (Hz)	f_{S3} (Hz)
1	0.98	7.3	0.01	31.4	23.3	16.2
2	0.97	8.0	0.01	31.8	23.5	16.7
3	0.96	10.1	0.02	31.8	22.6	16.2
4	0.98	11.3	0.01	31.6	23.0	17.3
5	0.80	8.3	0.04	26.9	18.5	13.9
6	0.79	10.0	0.05	25.1	18.3	13.1
7	0.78	11.9	0.02	24.7	18.7	14.2
8	0.54	7.4	0.06	14.7	12.8	9.7
9	0.55	9.0	0.09	12.9	12.3	9.0
10	0.56	10.3	0.06	13.5	11.9	8.6
11	0.53	11.9	0.04	14.8	12.3	8.8
12	0.39	10.8	0.03	11.1	9.4	6.2
13	0.28	9.9	0.09	5.0	5.1	5.0
14	0.25	9.9	0.05	5.0	5.0	4.8
15	0.20	10.1	0.05	5.0	5.1	3.4
16	0.18	10.1	0.04	5.1	5.0	3.0

at the subharmonic of the pulsation frequency, f_P, when the imposed frequency is nearly twice the unforced or natural vortex shedding frequency, f_N. This frequency-locking phenomenon is commonly termed lock-on. In the subcritical flow regime, the Strouhal number has approximately a constant value of 0.20 and lock-on occurs for values of the reduced frequency of pulsation, $S_P = f_P d/U_g$, around 0.40, independently of Reynolds number. In view of the substantial differences in the Strouhal numbers in the array with that of a single cylinder, it was decided that in the present experiments the flow conditions should be selected such that the reduced pulsation frequency would cover a wide range of values in order to adequately resolve the interaction of the multiple Strouhal periodicities with the imposed pulsations. This was achieved by varying the pulsation frequency and/or the gap velocity, which was necessitated by the fact that sinusoidal pulsation waveforms, as that shown in Fig. 2, could be achieved only for frequencies between 8 and 12 Hz [22]. On the other hand, the choice of pulsation amplitude was rather arbitrary.

For the pulsating flow experiments, the rotating valve was set into operation. With the rotating frequency set at the desired value the flow velocity and the pulsation amplitude were adjusted by the control valves. The flow conditions were monitored with the control volume of the anemometer positioned at the reference point. After the flow conditions were adjusted, the control volume was moved inside the test section in order to take measurements at the same locations as in steady flow (Fig. 1). When the measurements were completed the flow conditions were altered and the entire process repeated.

The pulsating flow experiments are summarized in Table 1. Table 1 also shows the frequencies of the forced vortex shedding, i.e., for pulsating flow, in accordance with the steady—unforced—flow results given in the previous section: a high frequency component, f_{S1}, a medium frequency component, f_{S2} and a low frequency component, f_{S3}, as observed in the turbulence spectra. The results shown in Table 1 are difficult to interpret because all three parameters, i.e., velocity, frequency and amplitude, are different between each set of experiments. In order to clarify the results, the variation of the measured Strouhal number for each component is plotted as a function of the reduced (nondimensional) frequency $S_P = f_P d/U_g$ and amplitude $\varepsilon = \Delta u/(2\pi f_P d)$ in Fig. 7. The size of the symbols is proportional to the value of the reduced amplitude, which can be inferred from Table 1. It can be seen that for low reduced frequencies and amplitudes there is virtually no (or small) effect of the pulsation on Strouhal numbers. As the reduced frequency and/or amplitude are increased, the Strouhal numbers gradually decrease below their unforced value indicated by the dotted lines in each subplot of Fig. 7. This effect is more pronounced for the f_{S1} component whose Strouhal number decreases substantially from its unforced value (Fig. 7(*a*)). A further increase in the reduced frequency causes lock-on at half

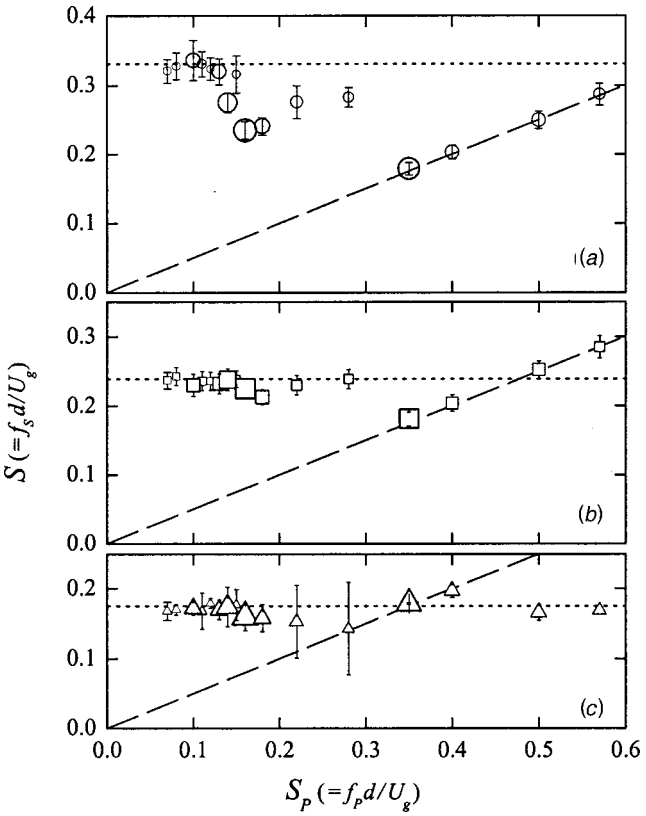

Fig. 7 Strouhal number, S, as a function of the reduced frequency of pulsation, S_P. The size of the symbols is proportional to the value of the reduced amplitude, ε. (a) f_{S1}, (b) f_{S2} and (c) f_{S3}.

the pulsation frequency or equivalently $S = 0.5\,S_P$, a relationship that is indicated by the dashed straight lines in Fig. 7 (lock-on is first observed for the f_{S3} component, i.e., in the last row, but it is intermittent as indicated by the associated error bars in Fig. 7(*c*)). At lock-on, the multiple Strouhal numbers transform to a single Strouhal periodicity in the array. For reduced frequencies greater than 0.48, the Strouhal numbers for the f_{S1} and f_{S2} components remain locked-on whereas that of f_{S3} component recovers its unforced value. Based on the published data on pulsating flow over a single cylinder [19–21], it might be expected that a further increase of the reduced frequency would cause the Strouhal numbers of all components to recover their unforced value. The conditions (reduced frequency and amplitude) at which vortex lock-on ceases require further investigation as this is of importance in predicting vortex resonance in heat exchanger tube arrays. Interestingly, when vortex shedding in the front rows is locked-on at the subharmonic of the pulsation frequency, the inner, but not the last, rows of the array exhibit the same behavior. This observation together with the lower Strouhal number at the exit of the array serve to emphasize that the flow characteristics at this location are not representative of the flow characteristics inside the array. It might also be argued that vortex shedding lock-on in the front rows induces strong oscillating velocity fields which will tend to synchronize vortex shedding in the array, especially in the presence of a forcing frequency.

The results obtained in this study are compared with those of Barbi et al. [20] in Fig. 8. Since their data are for a single cylinder in cross-flow, the comparison is made only for the response of the first-row cylinder (f_{S1} component) which might display similarities with a single cylinder. The ratio of the forced vortex shedding frequency to the unforced shedding frequency, f_S/f_N, is plotted as a function of the ratio of the pulsating to the unforced shedding

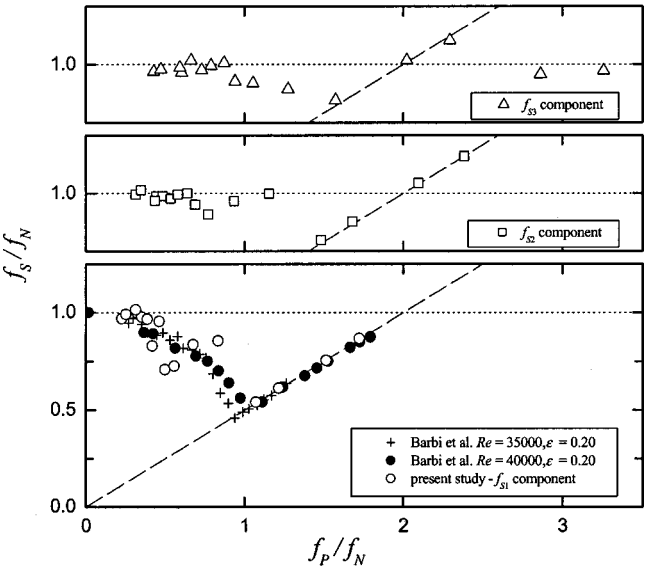

Fig. 8 The variation of f_S/f_N as a function of f_P/f_N for each frequency component and comparison with single cylinder results

frequency, f_P/f_N. For completeness, the variation for the other components is shown in different subplots. The present results agree well with those of Barbi et al., if the variation in the reduced amplitude of pulsation in the present study is taken into account. It is worthwhile to note that lock-on starts at a lower value of the frequency ratio f_P/f_N for the f_{S1} component than for the f_{S2} component.

Figure 9 shows representative spectra of the velocity measurements obtained at lock-on. The spectra are characterized by two spikes that correspond to f_P and $f_P/2$, i.e., at the pulsation and the single forced vortex shedding frequency in the array, respectively. The spikes have a very narrow bandwidth and background turbulence levels appear relatively lower than in the steady flow spectra presented in Figs. 3 and 4. These features of lock-on are characteristic of vortex resonance and indicate a well-organized flow pattern that repeats almost identically from cycle to cycle. Similar phenomena have been observed when the frequency of vortex shedding from a single cylinder is locked-on at the frequency of either a sound field or imposed flow pulsations [15,23]. From published data in references [15,19], it might be expected that the correlation of the velocity fluctuations along the span of the tubes increased with lock-on.

The bounds of lock-on from previous investigations of either pulsating flow over a single stationary cylinder or a cylinder oscillating in the direction of a uniform flow together with those from the present study are shown in Fig. 10. The vertical axis is the ratio of the amplitude of the cylinder to its diameter for the case of cylinder oscillations ($2a/d$) or its equivalent for flow oscillations (2ε) and the horizontal axis is the frequency ratio f_P/f_N. The unforced vortex shedding frequency was derived from the unforced Strouhal numbers and the three frequency components are represented by different symbols. The solid symbols represent lock-on. It can be seen that lock-on starts at lower f_P/f_N values than the bounds of lock-on for a single cylinder suggest. The reason for this might be that in the case of a confined flow as in the tube array, the pulsation amplitude is amplified as the flow enters the array. Therefore, the effective amplitude should be taken into account.

Figure 11 shows the variation of the amplitude of the velocity fluctuations associated with the three vortex-shedding components, normalized with the gap velocity, as a function of the reduced pulsation frequency, S_P. The results presented correspond

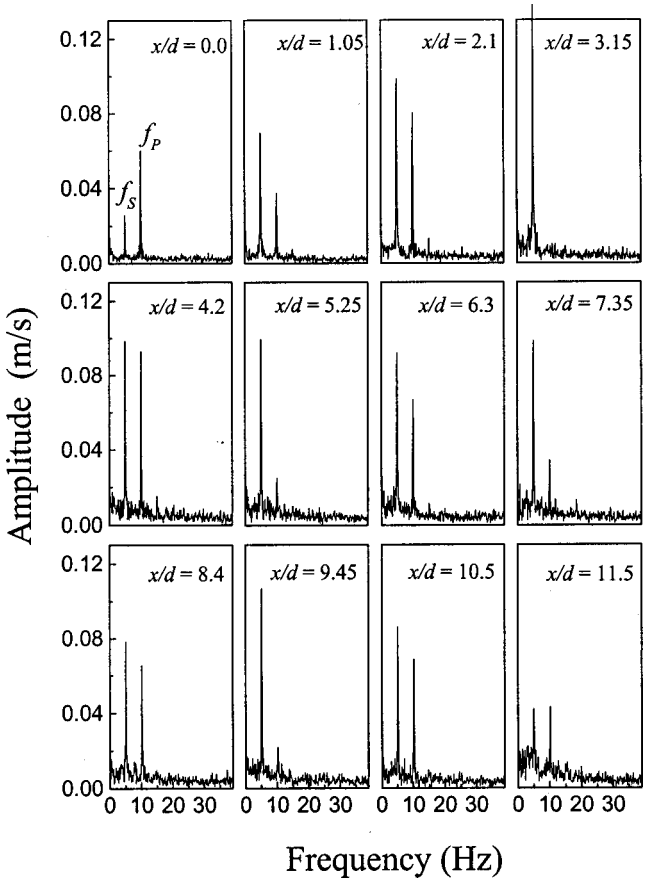

Fig. 9 Development of the streamwise velocity spectra along the flow lane between the staggered tubes for pulsating flow Re=2500; S_P=0.40; ε=0.08

to one measurement location in the flow lane for each component ($x/d = 2.1$ for f_{S1}; 6.4 for f_{S2}; 11.5 for f_{S3}) and the solid symbols again indicate lock-on. The symbols with a vertical bar through them correspond to conditions in which the pulsation frequency and vortex shedding frequency were coincident; therefore the fluctuations at the shedding frequency appear amplified. It is observed that there is a considerable increase in the amplitude of the velocity fluctuations associated with vortex shedding in the lock-on range, particularly for the f_{S1} component, i.e., in the front rows. It must be said that the variation of the normalized amplitude of the velocity fluctuations as a function of the gap velocity (or Reynolds number) was negligible in steady flow compared to its variation for pulsating flow shown in Fig. 11. Therefore the observed increase is solely due to changes of the flow field brought about by the pulsating flow and it is Reynolds number independent. Although there is a dependence of the results on the pulsation amplitude, it appears that the increase in the velocity fluctuations depends primarily on the reduced frequency. This implies that even relatively small amplitude disturbances can excite large amplitude velocity fluctuations if their frequency can couple with the vortex shedding frequency. Since the velocity fluctuations induce pressure fluctuations, it might be expected that the fluid forces exerted on the tubes increase substantially when lock-on occurs, which might be even more pronounced if there is a strong correlation of the velocity fluctuations along the span of the tubes.

Flow Visualization. Flow visualization was implemented to shed light into the mechanics of both steady and pulsating flow through the array. The areas of interest were selected based on the spectral analysis results presented in the previous sections. The

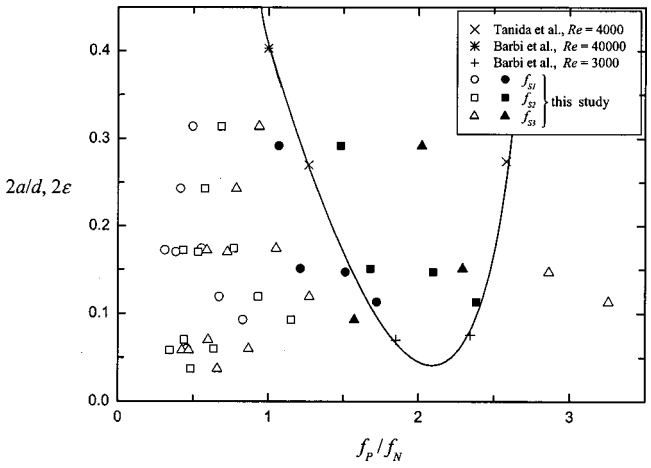

Fig. 10 Limits of lock-on for a cylinder oscillating in-line with the flow (from Tanida et al. reported in [20]), a stationary cylinder subjected to pulsating cross-flow (from Barbi et al. [20]) and present experimental data. Each symbol represents an experimental set and the different symbols represent the different frequency components. Solid symbols indicate experiments for which lock-on occurred.

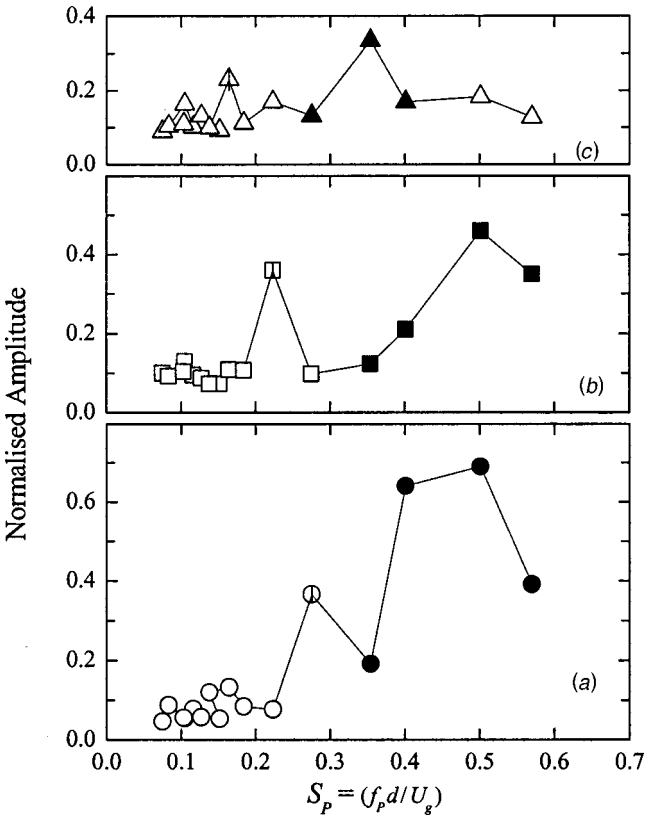

Fig. 11 The variation of the amplitude of the velocity fluctuations at the shedding frequency as a function of the reduced pulsation frequency. Results are normalized with the gap velocity and solid symbols indicate experiments for which lock-on occurred; (a) f_{S1} at $x/d=2.1$ (b) f_{S2} at $x/d=6.4$ and (c) f_{S3} at $x/d=11.3$ ($y/d=0.9$ in all cases).

visualization study was conducted for Re=1400, 2200, and 11000 in steady flow. In this Re range, the flow characteristics were similar as might be expected from the spectral analysis. Therefore, only selected results for Re=1400 are presented here. Figure 12 displays coherent vortices forming in the wake of the tube in the first row in (a) alternating and (b) symmetric manner with respect to the wake centerline. A region of low velocity on the plane of observation is discerned between the tube and the area where the vortices are formed. The flow pattern depicted in Fig. 12(*a*) was promoted when vortex shedding from the tubes in the second row occurred in-phase, i.e., from the same side of the tubes, as shown in Fig. 13(*b*). Inversely, out-of-phase vortex shedding from the tubes in the second row (Fig. 13(*a*)) promoted symmetric formation of the vortices in the wake of the tube in the first row. In both cases, these patterns resulted in large-scale vortices being ob served. Most of the time, however, the flow exhibited an intermediate structure between these described above with rather random characteristics. In subsequent rows, alternating vortex shedding was observed but the formation region was very close to the surface of the tubes and the vortices were less well formed. Ziada and Oengören [7] have reported extensive flow visualization results in normal triangular arrays. Both symmetric and alternating vortex shedding modes were observed but in contrast to the present study, these occurred behind the second row tubes depending on the phase of vortex shedding from the first row tubes where only alternating vortex shedding occurred. Although, the above differences might be related to the different geometries and spacings employed, the number of tubes per row or even, whether the first row is comprised by an even or odd number of tubes might also play a role in the observed patterns. Both studies agree in that behind the third row and further downstream (inner rows) only alternating vortex shedding occurs at the f_{S2} component (lower frequency than in the front rows).

The pulsating flow was also visualized for lock-on conditions (Re=2300; $S_P=0.44$; $\varepsilon=0.04$). The flow pattern around the first-row tube is illustrated in Fig. 14 that shows a sequence of images in a vortex shedding cycle. At time $t=0$ a fully-grown vortex is formed on the left-hand-side of the cylinder and a smaller vortex is attached on the surface of the cylinder on the other side. At the next instant, $t=0.04$ s, the shear layer on the right-hand-side restricts the supply of vorticity to the large vortex which is conse-

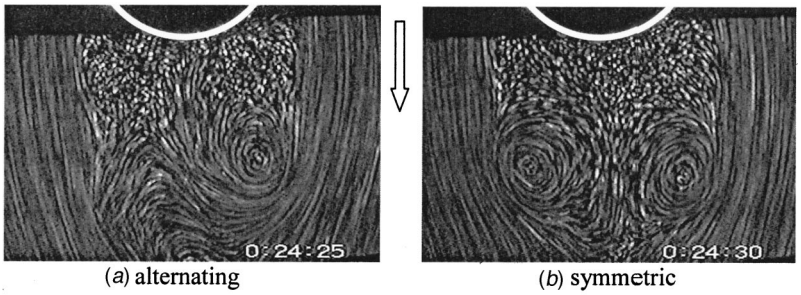

Fig. 12 Visualization of the wake behind the first row tube for steady flow; Re=1400

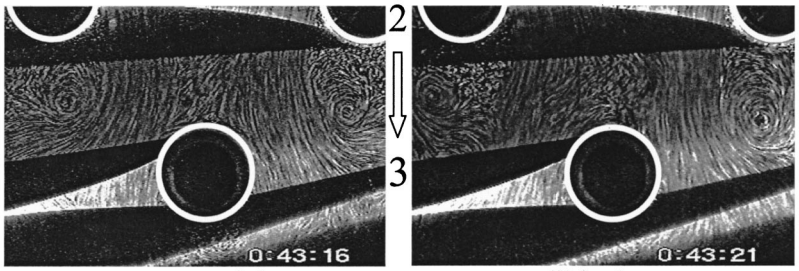

(*a*) out-of-phase (*b*) in-phase

Fig. 13 Vortex shedding patterns in the second row for steady flow; Re =1400

quently shed. As the vortex is shed, the shear layer moves in the opposite direction and unfolds ($t=0.08$ s). This results in the formation of a clockwise vortex, which at $t=0.12$ s is about to be shed producing the mirror image of the first frame with respect to the wake centerline. This process is essentially the same as the formation of vortices in the wake of a cylinder in unconfined flow as described by Gerrard [24]. It contrasts sharply the flow patterns observed around the first row in steady flow but resembles weakly the flow patterns observed behind the third and downstream rows. Note that the region of low velocity fluid observed in steady flow is replaced by vigorous activity and that the wake is virtually indistinguishable from the high velocity fluid in the flow lanes. The same pattern was observed for all tube rows but was somewhat obscured further downstream due to the increasing turbulence levels. In fact, a global picture of the flow showed that vortex shedding from all the tubes in the array was synchronized and in-phase, i.e., occurred at the same instant from the same side of the tubes as might be expected due to the frequency-locking. The present findings display remarkable similarity with the effects of transverse free surface waves on the flow patterns in normal triangular arrays observed by Ziada and Oengören [7]. They also found that when the vortex shedding frequency locked-on at a frequency of the surface waves, alternating vortex shedding from all tubes was synchronised and in-phase.

Discussion

The spectral analysis showed that the frequency of vortex shedding locks-on at the sub-harmonic of the pulsation frequency. This reflected the vigorous alternating vortex shedding featured in the flow visualization experiments that indicated a considerable decrease in the formation region of the vortices in the wake of the first-row tube. Gerrard [23] suggested that two characteristic length scales determine the vortex shedding frequency: the vortex formation length and the width to which the free shear layers diffuse. Armstrong et al. [25] found a reduction in the formation length from $1.2d$ to $0.9d$ behind a single cylinder when vortex shedding locked-on with an external perturbation of the flow, i.e., flow pulsation. The influence of the pulsating flow on the vortex formation length in the array is explored briefly in the following.

Several definitions of the vortex formation length have been proposed in the literature, which are epitomized in Griffin [26]. These are based on results obtained with hot-wire anemometry. One of the most commonly employed definitions states that the end of the vortex formation region is determined by the location of the maximum of the streamwise velocity fluctuations at twice the shedding frequency on the wake centerline. Measurements of the streamwise velocity fluctuations on the wake centreline were difficult to obtain close to the surface of the tubes. However, mea-

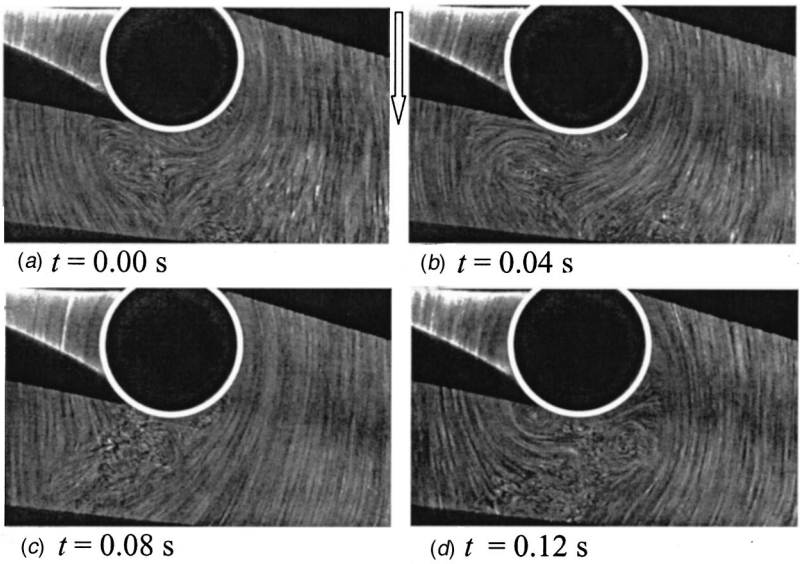

Fig. 14 Time sequence illustrating alternating vortex shedding in the first row for flow conditions for which the shedding frequency locked-on at the subharmonic of the pulsation frequency; Re=2300; $S_P=0.44$; $\varepsilon=0.04$

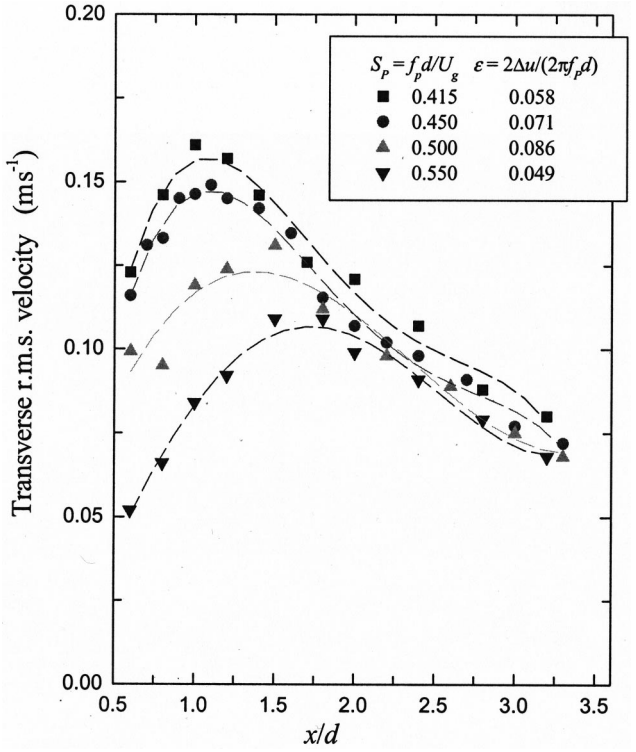

Fig. 15 Root-mean-square of transverse velocity fluctuations measured along the centerline in the wake of the first row for different pulsating flow conditions

surements of the transverse velocity fluctuations should provide similar information for reasons that bear upon the physical description of the vortex formation process, as described in detail by Gerrard [24]. Thus, in the present work, measurements of the transverse velocity were obtained in the wake of the first-row tube and the results are presented in Fig. 15. Possible amplitude effects on the results were kept to a minimum by confining the value of the reduced amplitude within a narrow range. It can be seen in Fig. 15 that the position of the maximum transverse velocity fluctuations moves closer to the surface of the tube, which is at $x/d = 0.5$, from $1.75d$ behind the tube center to $1.0d$ as the reduced pulsation frequency is decreased from 0.55 to 0.415. This corresponds to a substantial reduction in the formation length. Remarkably, the reduction in the formation length is greater at a reduced frequency of 0.415 which is roughly twice the Strouhal number of a single cylinder rather than at twice the unforced Strouhal number of the f_{S1} component detected in first row. This, taken in tandem with the flow visualization observations, suggests that the origin of vortex shedding lock-on might be the same in the array as in a single cylinder. It might be argued that the modification of the local flow characteristics imposed by the geometrical constraints in tube arrays influences the parameters that determine the frequency of vortex shedding. These parameters might be either the formation length and the diffusion width as proposed by Gerrard [24] or the velocity just outside separation and the wake width as proposed by Griffin [12]. For instance, Weaver et al. [6] used Griffin's [12] concept of a 'universal Strouhal number' to show that the Strouhal number has the same value for the first and the second rows of a staggered array despite the measured frequencies being different. Strictly speaking, the results presented are applicable only to the geometry studied. Tentatively, the results might be extended to arrays with smaller pitch ratio since the data in the literature suggest that the mechanism of vortex shedding remains the same except for very small pitch ratios. However, further experiments are required to confirm this observation.

Conclusions

The vortex shedding phenomena in a staggered tube array were investigated using LDA measurements and a visualisation technique. The frequency of vortex shedding and the amplitude of the associated velocity fluctuations were determined for steady and pulsating cross-flow. Two dominant frequency components f_{S1} and f_{S2} were observed inside the array for steady flow. The Strouhal numbers for these components were 0.33 and 0.24 and originated from vortex shedding from the front and inner rows respectively as confirmed by flow visualization. A lower frequency component f_{S3} with a Strouhal number of 0.17 was detected at the exit of the array but this is thought to be irrelevant to the periodic flow phenomena inside the array. The flow patterns associated with these components were similar to those observed in rotated square and normal triangular tube arrays. Pulsating flow caused the frequency of vortex shedding to occur at frequencies different than the natural or unforced frequencies observed in steady flow. This frequency shift was more prominent for the f_{S1} component. When the flow was pulsed at reduced frequencies approximately between $0.35 < S_P < 0.55$ (a range that depends on the pulsation amplitude), the frequency of vortex shedding inside the array locked-on at the subharmonic of the pulsation frequency, except for the tubes in the last row in which lock-on was observed for a narrower range. A further increase in the reduced frequency is expected to result in a gradual transition to natural vortex shedding as before the onset of lock-on. In the lock-on range, vortex shedding from all the tubes was synchronised and in-phase and velocity fluctuations at the shedding frequency increased considerably compared to their counterparts in steady flow. Such increased levels of velocity fluctuations may lead to unaccounted loads and failure in heat exchangers tube arrays but, on the other hand, they might also increase heat transfer from the tubes, as the flow is more active. A possible explanation of the observed phenomena was proposed which was based on the variation of the vortex formation length, which was found to decrease consistently in the lock-on range.

Acknowledgments

This research was sponsored by the Engineering and Physical Sciences Research Council (EPSRC) under contract no GR/L60937.

References

[1] Paidoussis, M. P., 1983, "A Review of Flow-Induced Vibrations in Reactors and Reactor Components," Nucl. Eng. Des., **74**, pp. 31–60.
[2] Weaver, D. S., and Fitzpatrick, J. A., 1988, "A Review of Cross-Flow Induced Vibrations in Heat Exchanger Tube Arrays," J. Fluids Struct., **2**, pp. 73–93.
[3] Moretti, P. M., 1993, "Flow-Induced Vibrations in Arrays of Cylinders," Annu. Rev. Fluid Mech., **25**, pp. 99–114.
[4] Weaver, D. S., and Abd-Rabbo, A., 1985, "A Flow Visualization Study of a Square Array of Tubes in Water Cross-Flow," ASME J. Fluids Eng., **107**, pp. 354–363.
[5] Price, S. J., Paidoussis, M. P., and Mark, B., 1995, "Flow Visualization of the Interstitial Cross-Flow Through Parallel Triangular and Rotated Square Arrays of Cylinders," J. Sound Vib., **181**, pp. 85–98.
[6] Weaver, D. S., Lian, H. Y., and Huang, X. Y., 1993, "Vortex Shedding in Rotated Square Arrays," J. Fluids Struct., **7**, pp. 107–121.
[7] Ziada, S., and Oengören, A., 1998, "An In-Depth Study of Vortex Shedding, Acoustic Resonance and Turbulent Forces in Normal Triangle Tube Arrays," J. Fluids Struct., **12**, pp. 717–758.
[8] Polak, D. R., and Weaver, D. S., 1995, "Vortex Shedding in Normal Triangular Tube Arrays," J. Fluids Struct., **9**, pp. 1–17.
[9] Ziada, S., and Oengören, A., 2000, "Flow Periodicity and Acoustic Resonance in Parallel Triangle Tube Bundles," J. Fluids Struct., **14**, pp. 197–219.
[10] Ziada, S., and Oengören, A., 1993, "Vortex Shedding in an In-Line Tube Bundle With Large Tube Spacings," J. Fluids Struct., **7**, pp. 661–687.
[11] Konstantinidis, E., Castiglia, D., Balabani, S., and Yianneskis, M., 2000, "On the Flow and Vortex Shedding Characteristics of an In-Line Tube Bundle in Steady and Pulsating Crossflow," Trans. Inst. Chem. Eng., **78**(A), pp. 1129–1138.
[12] Griffin, O. M., 1981, "Universal Similarity in the Wakes of Stationary and Vibrating Bluff Structures," ASME J. Fluids Eng., **103**, pp. 52–58.
[13] Balabani, S., and Yianneskis, M., 1996, "An Experimental Study of the Mean Flow and Turbulence Structure of Cross-flow Over Tube Bundles," Proc. Inst. Mech. Eng., Part C: Mech. Eng. Sci., **210**, pp. 317–331.

[14] Balabani, S., and Yianneskis, M., 1997, ''Vortex Shedding and Turbulence Scales in Staggered Tube Bundle Flows,'' Can. J. Chem. Eng., **75**, pp. 823–831.
[15] Blevins, R. D., 1985, ''The Effect of Sound on Vortex Shedding From Cylinders,'' J. Fluid Mech., **161**, pp. 217–237.
[16] Hetz, A. A., Dhaubhadel, M. N., and Telionis, D. P., 1991, ''Vortex Shedding Over 5 In-Line Cylinders,'' J. Fluids Struct., **5**, pp. 243–257.
[17] Hoyt, J. W., and Sellin, R. H. J., 1997, ''Flow Over Tube Banks-A Visualization Study,'' ASME J. Fluids Eng., **119**, pp. 480–483.
[18] Abernethy, R. B., Benedict, R. P., and Dowdell, R. B., 1985, ''ASME Measurement Uncertainty,'' ASME J. Fluids Eng., **107**, pp. 161–164.
[19] Armstrong, B. J., Barnes, F. H., and Grant, I., 1986, ''The Effect of a Perturbation on the Flow Over a Bluff Cylinder,'' Phys. Fluids, **29**, pp. 2095–2102.
[20] Barbi, C., Favier, D. P., Maresca, C. A., and Telionis, D. P., 1986, ''Vortex Shedding and Lock-on of a Circular-Cylinder in Oscillatory Flow,'' J. Fluid Mech., **170**, pp. 527–544.
[21] Griffin, O. M., and Hall, M. S., 1991, ''Vortex Shedding Lock-on and Flow-Control in Bluff Body Wakes-Review,'' ASME J. Fluids Eng., **113**, pp. 526–537.
[22] Konstantinidis, E., 2001, ''Pulsating flow in cylinder arrays,'' PhD thesis, King's College London, University of London.
[23] Telionis, D. P., Gundappa, M., and Diller, T. E., 1992, ''On the Organization of Flow and Heat-Transfer in the Near Wake of a Circular-Cylinder in Steady and Pulsed Flow,'' ASME J. Fluids Eng., **114**, pp. 48–355.
[24] Gerrard, J. H., 1966, ''The Mechanics of the Formation Region of Vortices Behind Bluff Bodies,'' J. Fluid Mech., **25**, pp. 401–413.
[25] Armstrong, B. J., Barnes, F. H., and Grant, I., 1987, ''A Comparison of the Structure of the Wake Behind a Circular-Cylinder in a Steady Flow With that in a Perturbed Flow,'' Phys. Fluids, **30**, pp. 19–26.
[26] Griffin, O. M., 1995, ''A Note on Bluff-Body Vortex Formation,'' J. Fluid Mech., **284**, pp. 217–224.

Heather L. McClusky
Mary V. Holloway
Donald E. Beasley
Fellow ASME

Thermal-Fluid Sciences Research Laboratory,
Department of Mechanical Engineering,
Clemson University,
Clemson, SC 29634

Michael E. Conner
Westinghouse Nuclear Fuel,
5801 Bluff Road,
Columbia, SC 29250

Development of Swirling Flow in a Rod Bundle Subchannel

Experimental measurements of the axial development of swirling flow in a rod bundle subchannel are presented. Swirling flow was introduced in the subchannel from a split vane pair located on the downstream edge of the support grid. Particle image velocimetry using an optical borescope yielded full-field lateral velocity data. Lateral flow fields and axial vorticity fields at axial locations ranging from 4.2 to 25.5 hydraulic diameters downstream of the support grid were examined for a Reynolds number of 2.8×10^4. The lateral velocity fields show that the swirling flow was initially centered in the subchannel. As the flow developed in the axial direction, the swirling flow migrated away from the center of the subchannel. Radial distributions of azimuthal velocity and circulation are presented relative to the centroid of vorticity, and are compared to that of a Lamb-Oseen vortex. The angular momentum decreased as the flow developed in the axial direction. The spatial decay rate of the angular momentum is compared to that of decaying, swirling flow in a pipe. [DOI: 10.1115/1.1478066]

1 Introduction

The configuration of the core of a pressurized water reactor consists of fuel rods that are assembled into rod bundles using support grids placed at axial locations along the length of the bundle. The fuel rods are cooled by forced convection where the thermal energy from fuel rods is transferred to the coolant as the coolant flows in the axial direction parallel to the fuel rods. There are numerous factors that are important to the thermal-hydraulic performance of a nuclear fuel bundle design, including pressure drop, flow distribution, and heat transfer and flow boiling characteristics. The heat transfer and flow boiling characteristics are directly a result of the development of the local flow field in the rod bundle. The flow field in a pressurized water reactor is highly three-dimensional and complex. This paper examines the local fluid dynamics in a model rod bundle that is representative of the core of a pressurized water reactor. Specifically, the lateral velocity fields downstream of a support grid are experimentally measured using particle image velocimetry. Insight into the flow field is gained from both a global analysis of integral parameters of the velocity fields and a local analysis of the details of the flow structure.

Local physics of the velocity field immediately downstream of a support grid include flow deceleration, velocity boundary layer development on the surface of the fuel rods, and elevated levels of turbulent velocity fluctuations. In this region, the local single-phase heat transfer coefficients are significantly higher than the local heat transfer coefficients further downstream in the bundle (for example, see Marek and Rehme [1]). The average heat transfer coefficient for the entire rod bundle is increased by this local enhancement. The local and average heat transfer coefficients may be further increased by the superposition of swirling flow on the axial flow. Heat transfer augmentation due to swirling flow was first documented in 1896 by Whitman [2]. Whitman [2] showed that implementing twisted tape inserts in the tubes of a steam boiler significantly increased the thermal efficiency of the boiler. To enhance single-phase forced convection and to increase the critical heat flux limit in a pressurized water reactor, support grids are designed with vanes placed on the downstream edge of the grid to create a lateral velocity field or swirling flow. Such local changes to the velocity field persist in the streamwise direction and affect the overall performance of the reactor. Yao et al. [3] and Armfield [4] showed local enhancement of single-phase heat transfer from the addition of swirling flow in rod bundles. For operating conditions where regions of the reactor produce flow boiling, de Crécy [5] demonstrated that swirling flow allows significantly higher critical heat fluxes than purely axial flow.

Valuable insight into the mechanism of heat transfer enhancement in a fuel bundle may be gained from knowledge of the velocity fields. For example, Yao et al. [3] developed a single-phase heat transfer correlation to predict the local heat transfer rate downstream of a support grid with vanes designed to generate swirling flow. The heat transfer enhancement was modeled as the superposition of grid effects and vane effects. The axial decay rate of the heat transfer coefficient was modeled in this manner. The development of the local heat transfer rate due to swirling flow generated by the vanes was modeled using the spatial decay rate of swirling flow in a pipe (Kreith and Sonju [6]). The decay rate of the swirling flow is a secondary effect in this correlation.

Flow at low temperature and pressure in a 5×5 rod bundle is employed in the present investigation to experimentally model fluid flow in the core of a pressurized water reactor. The side view and end view of the 5×5 rod bundle are shown in Figs. 1(*a*) and 1(*b*). The flow is conditioned using support grids without vanes. As illustrated in Fig. 1(*a*) the first two support grids are the conditioning grids, and the third grid is the test grid. Vanes are located on the downstream edge of the test grid. Figure 1(*b*) shows the end view of the 5×5 rod bundle, and a single subchannel is labeled. A subchannel is defined as the flow area between four adjacent rods bounded by the four surrounding rods and the rod pitch. The subchannel geometry is illustrated in Fig. 2 by the dotted lines. Figure 2 provides the dimensions of a subchannel for the 5×5 rod bundle. Each vane is 4 mm wide and 3.6 mm long, and the hydraulic diameter is 11.78 mm. Lateral velocities in a rod bundle subchannel are generated from vanes placed on the grid and located in each subchannel. Numerous types of vanes have been designed to produce lateral velocities or swirling flow in rod bundle subchannels. Split-vane pairs are utilized in the present study, and the two-dimensional projection of a single split-vane pair is shown in Fig. 2. Split-vane pairs may produce swirling flow in the subchannel and/or cross flow among neighboring subchannels. In the present study, only the vanes of the split-vane pair in subchannel A (Fig. 1) are configured to form a 30 deg angle relative to the axial direction. The vanes in all remaining subchannels were oriented at an angle of 0 deg relative to the axial direc-

Contributed by the Fluids Engineering Division for publication in the JOURNAL OF FLUIDS ENGINEERING. Manuscript received by the Fluids Engineering Division May 15, 2001; revised manuscript received February 26, 2002. Associate Editor: K. Zaman.

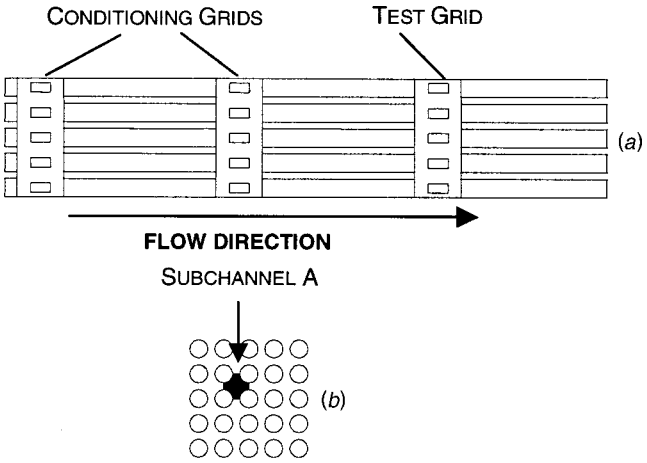

Fig. 1 Rod bundle configuration: (*a*) Side view; (*b*) end view as viewed from the outlet

tion. In this configuration, cross flow among neighboring subchannels is minimized and swirling flow dominates the flow field in subchannel A.

To capture the development of the full-field lateral velocity distribution in the subchannel, a particle image velocimetry (PIV) measurement system was developed. The small size of the subchannel and the geometry of the rod bundle provide unique challenges for optical access to the lateral flow field. To adapt this measurement technique to the subchannel geometry, a forward viewing, optical borescope was used to transmit images of the tracer particles in the flow field to the camera. The borescope was inserted into subchannel A from the outlet of the test section. PIV measurements of the lateral flow fields at six axial locations in subchannel A of the rod bundle are utilized to study the characteristics of the lateral velocity field. Time-averaged lateral velocity fields are analyzed to determine the axial vorticity. From these full-field representations of the lateral velocity field and the axial vorticity field, the centroid of vorticity, the radial profile of azimuthal velocity, and the radial distribution of circulation are computed for each axial location. Also, the spatial decay of angular momentum in the axial direction is determined for the flow in the subchannel. The purposes of this investigation are to document the development of the lateral velocity field downstream of a split-vane pair in a subchannel, and to compare this flow field with fundamental flow fields including tip vortices shed from an airfoil, swirling pipe flow, and analytical vortex flows.

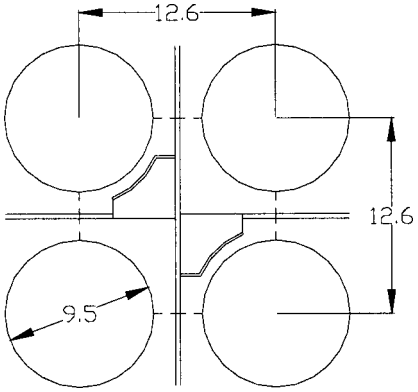

Fig. 2 Illustration of a subchannel (dimensions in mm) D_h=11.78 mm

2 Background

Fundamental vortical and swirling flows such as decaying, swirling flow in a pipe and trailing vortices from airfoils are similar to the flow field of the present study and provide a fundamental basis for comparison. An important distinction among these three flow fields is the effect of solid boundaries on the developing flow field. The present literature review focuses primarily on the physics of unconfined vortex flows and the physics of confined decaying, swirling flows. In addition, investigations of local velocity measurements in a rod bundle subchannel using laser Doppler anemometry are discussed.

The unconfined vortex flows reviewed here focus on the development of a tip vortex shed from an airfoil or hydrofoil. Using a holographic PIV technique, Green and Acosta [7] studied both near and far velocity fields of a wing tip vortex shed from a NACA 66-209 hydrofoil. Far field results showed the axial velocity deficit or surplus in the vortex core was dependent on the angle of attack. They attributed the observed vortex unsteadiness to regions of acceleration and deceleration in the core of the vortex. Shekarriz et al. [8] measured axial and lateral velocity components in the near field of a tip vortex shed from an NACA 66-209 hydrofoil. The authors implemented particle tracking to measure the lateral velocities and high density PIV for axial velocity measurements. In this study, comparison among instantaneous velocity fields showed temporal and spatial variations in the location of the tip vortex center; such variations are termed vortex wandering. Devenport et al. [9] employed a four-sensor hot wire probe for velocity measurements of a tip vortex shed from an NACA-0012 airfoil. They developed and implemented a technique to quantify the effects of vortex wandering on fixed probe measurements. Application of the technique to their data showed that the wandering amplitude was approximately 30% of the core radius and the effect of the fixed probe measurement was to increase the core radius and decrease the maximum azimuthal velocity magnitude. For the range of axial locations examined, the shape of the measured radial profiles of velocity, the maximum azimuthal velocity magnitude, and the core radius exhibited minor changes as the flow developed in the streamwise direction. Chen et al. [10] documented the development of a tip vortex shed from a hydrofoil as well as the development of a corotating vortex pair shed from a flapped hydrofoil. They acquired full-field velocity data by processing PIV data using Lagrangian particle tracking. Radial profiles of azimuthal velocity, and circulation proved to agree quantitatively with a Lamb-Oseen vortex. Chen et al. [10] used the moments of axial vorticity to demonstrate the three-dimensional nature of the vortex dynamics. Specifically, the third and fourth moments of axial vorticity showed large fluctuations in time.

Fundamental studies of decaying, swirling flow in a pipe may lend insight into the behavior of swirling flow in a subchannel of a rod bundle. Kreith and Sonju [6] compared experimental results of decaying, swirling flow in a pipe to an analytical solution of the θ-direction momentum equation. The experimental facility utilized a twisted tape insert located at the pipe inlet to produce decaying, swirling flow in a pipe. A separation of variables technique was employed to analytically solve the axisymmetric Reynolds averaged θ-direction momentum equation with an eddy diffusivity turbulence model. The initial condition for the analytical model was based on the measured velocity data of Smithberg and Landis [11]. Comparison between the spatial decay rate of angular momentum from their experiment and their model showed good agreement for all axial locations. In addition, Kreith and Sonju [6] stated that their analytical results for the radial profiles of azimuthal velocity distributions qualitatively agreed with the azimuthal velocity measurements of Musolf [12] for axial distances less than 20 diameters from the pipe inlet. Algifri et al. [13] utilized a multiple-position single inclined hot wire technique to measure the three mean velocity components and the six components of the turbulent stress tensor in decaying, swirling flow in a pipe. A radial cascade of vanes was used as the swirl generator. As

the flow developed in the axial direction, the radial location of the maximum azimuthal velocity moved closer to the wall. The data of Algifri et al. [13] showed that the location of maximum azimuthal velocity was strongly dependent on the local swirl level and only slightly dependent on the Reynolds number. Kitoh [14] studied decaying, swirling flow in a pipe generated using a radial cascade of vanes. Two experimental facilities were employed to obtain time-averaged mean velocity data, the turbulent stress tensor, and the wall shear stress. Kitoh [14] showed that the production of turbulent kinetic energy in decaying, swirling flow in a pipe is larger than that of fully developed axial flow in a pipe. Kitoh [14] hypothesized that increase in the production of turbulent kinetic energy results in higher heat transfer rates. Chang and Dhir [15] experimentally measured time-averaged velocity data and turbulence characteristics of swirling pipe flow using hot wire anemometry. The decaying, swirling flow was generated using pure tangential injection. Chang and Dhir [15] showed that the inlet azimuthal to total momentum flux ratio (M_t/M_T) influences the axial development of the flow. An axial velocity deficit is present in the central region of the decaying swirling flows of Algifri et al. [13], Kitoh [14], and Chang and Dhir [15].

Other investigators have employed laser-based measurement techniques to characterize specific swirling flow fields. Frigerio and Hart [16] obtained velocity and vorticity fields using digital PIV cinematography for a swirling flow designed to simulate a combustor. They studied the temporal characteristics of the axial flow fields; lateral flow fields were not presented. Xiong and Merzkirch [17] employed a borescope to accomplish PIV measurements of the swirling flow generated by two consecutive out of plane 90 deg bends in a pipe. Time-dependent flow structures in this pipe flow were resolved. The importance of selecting an appropriate time delay and interrogation region size for this complex flow was emphasized. Lozano et al. [18] employed holographic PIV to characterize swirling flows created in a cylindrical enclosure with the bottom rotating.

A limited number of studies have examined flow fields in rod bundles either experimentally or through computational simulations. Karoutas et al. [19] compared computational predictions and laser Doppler anemometry measurements of the velocities for two support grid designs, including a grid with split-vane pairs. The computational model consisted of a single subchannel with periodic boundary conditions. Predicted axial and lateral velocities agreed reasonably well with the experimental results. Herer [20] employed laser Doppler anemometry to measure mean axial velocity and turbulence intensity in a 5×5 rod bundle downstream of a support grid that had vanes. The lateral and axial velocity data of Karoutas et al. [19] and Herer [20] are, in general, consistent. As far as is known, no previous study has employed PIV to document full-field lateral velocity data downstream of a split-vane pair in a rod bundle subchannel.

3 Measurement Technique and Experimental Facility

Particle Image Velocimetry (PIV) is employed to measure the development of the lateral velocity fields in the rod bundle subchannel. PIV is a velocity measurement technique utilizing a temporal sequence of recorded images of tracer particles in the flow field to obtain the velocity field. A light source, typically a pulsed laser, is used to illuminate and freeze the tracer particles in the flow field. Details of the experimental facility, rod bundle assembly, and PIV measurement method are described in the following.

3.1 Experimental Facility. Figure 3 shows a schematic diagram of the test facility. Water was used as the working fluid. Major components of the closed-loop facility include a constant head tank, pump, flowmeter, metering valves, and test section. A 15 hp, variable speed Gould pump and a large volume constant head tank ensured constant flow rates in the facility. The volumetric flow rate was measured using a Sponsler turbine type flowmeter (Model SP3-CP-PHIL-A-4X) having a range of 0 to 2.46 m^3/min and a manufacturer stated accuracy of $\pm2\%$. The average

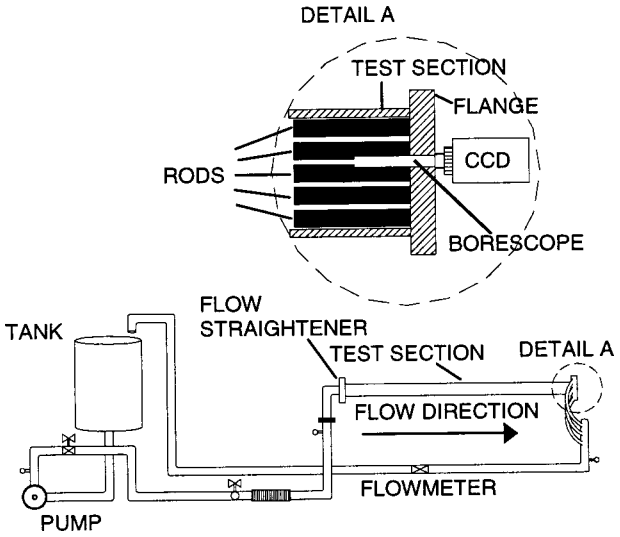

Fig. 3 Drawing of the experimental facility

axial velocity was calculated based on the open flow area in the rod bundle and the measured volumetric flow rate. For all measured lateral velocity fields in this study, the average axial velocity was 2.4 m/s. The water temperature was held constant at 20°C using a heat exchanger placed in the constant head tank. A flow straightener was placed at the inlet of the test section.

Measurements were acquired in a subchannel of a 5×5 rod bundle located in the test section. The Lexan test section had a square flow area of 42.3 cm^2 and was 1.64 m long. The rod bundle, as shown in Fig. 1, was constructed out of 9.5 mm diameter rods that were assembled in support grids on a square array having a pitch of 12.6 mm. Three support grids were placed at intervals of 508 mm along the length of the rods, with the first grid located 90 mm from the test section inlet. The first two support grids conditioned the flow and did not have vanes, and the third grid was the test grid with a split-vane pair located in subchannel A (Fig. 1) to superimpose large-scale swirl on the axial velocity. Lateral velocity fields generated from the split-vane pair were examined at axial locations downstream of the third grid. Optical access for the laser sheet to subchannel A was achieved through the transparent Lexan housing and hybrid zircaloy/quartz rods. The hybrid rods were zircaloy at the inlet to the test section and transitioned to quartz approximately 15 mm upstream of the third grid. An optical borescope (ITI, Inc.) was implemented to image the tracer particles in a lateral plane in the rod bundle subchannel. The forward viewing borescope has a viewing angle of 10 deg, a diameter of 6 mm, and is 0.648 m long. The borescope was inserted into the subchannel from the exit of the test section (Fig. 3).

3.2 Full-Field Velocity Measurement Technique. PIV utilizes measurements of the fundamental variables defining velocity, displacement and time, to obtain full-field velocity data. Raffel et al. [21] provides an overview of image acquisition techniques as well as post processing and image evaluation methods. In the present investigation, high density PIV (Adrian [22]) was implemented using a cross-correlation analysis technique. Keane and Adrian [23] describe the cross-correlation image analysis technique in detail.

In the present study, a Spectra-Physics Nd:YAG laser (PIV-400) was used as the light source. The Nd:YAG laser produces two pulses of light at a wavelength of 532 nm with a repetition rate of 10 Hz. For each laser beam, the pulse duration is less than 10 ns, and the pulse energy is 450 mJ. A Four Channel Digital Delay/Pulse Generator (Stanford Research Systems Model DG 535) controlled the timing between the laser pulses. The flow was seeded

with neutrally buoyant fluorescent particles having a diameter ranging from 20 to 40 μm. The tracer particles were manufactured in the Laboratory for Experimental Fluid Mechanics at Johns Hopkins University and contain two dyes, rhodamine 6G and dichloro-fluorescein, that fluoresce in 532 nm wavelength light. To illuminate a lateral plane of particles in the flow field, an optical slit controlled the width of the laser beam and a cylindrical lens expanded the beam into a laser sheet that was directed into the test section. Images were acquired using a Kodak Megaplus ES 1.0/SC camera having a resolution of 1008×1018 pixels and a frame rate of 30 Hz. Each image of the lateral flow field projected onto this CCD from the borescope was circular with a diameter of 525 pixels. The camera was operated in Triggered Double Exposure mode to record each exposure of the particle images on separate frames for cross correlation analysis. The Four Channel Digital Delay/Pulse Generator controlled the timing sequence for the laser, camera, and frame grabber board. In the present study, the time delay between pulses was 125 μs, and the laser sheet width was 3.5 mm. The working distance from the optical borescope to the laser sheet was 130 mm, and the pixel calibration for the borescope in water at this working distance was 28.16 μm/pixel. To reduce out-of-plane loss of correlation in highly three-dimensional flows, such as the flow field of the present study, Raffel et al. [21] recommend that the out of plane particle displacement remain less than 30% of the laser sheet thickness. For the present axial velocity and time delay, the axial displacement of the particles is approximately 10% of the laser sheet thickness.

VISIFLOW software was employed to acquire and analyze the digital image pairs. Each image pair was analyzed using the cross-correlation technique to calculate a single instantaneous velocity field. The interrogation regions were 32 pixels square and a 50% overlap between interrogation regions was employed. A time sequence of instantaneous full field velocity data was acquired at each axial location. Time-averaged velocity fields are presented in this paper, and are representative of the average velocity field. Two important considerations in time-averaging are the unsteadiness of the flow and the number of instantaneous velocity fields used in the time averaging process. Examination of consecutive instantaneous velocity fields revealed that the lateral velocity field is unsteady in time. The spatial magnitude of unsteadiness is small compared to the size of the subchannel. The time-averaged velocity fields resulting from repeated, independent PIV measurements of the velocity fields were compared. The time-averaged velocity fields were essentially identical upon repeated measurements. Thus, it may be concluded that time-averaging procedure provides an accurate representation of the average velocity field. In addition, the statistical significance of the number of instantaneous velocity fields employed in the averaging process was studied. The time-averaging process was repeated for acquisition of five to fifty image pairs; this resulted in five to fifty instantaneous velocity fields. There were no differences in the time-averaged flow fields upon increasing the number of images pairs beyond ten.

For the data presented in this paper, twenty-six frames of data were acquired at each axial location. The resulting thirteen instantaneous lateral velocity fields were time-averaged. The time-averaged data are presented at axial locations of 50, 100, 150, 200, 250, and 300 mm downstream of the third grid (subchannel hydraulic diameter is 11.78 mm). An upper bound on the uncertainty in the magnitude of each velocity vector is ±10% as calculated using a Kline-McKlintock [24] approach. This approach considers the uncertainty in the measured particle displacement between image pairs and the measured time delay. The dominant factor in this estimate is the resolution of the particle displacement. The resolution is ±1/2 pixel or 14.08 μm. Velocity measurements of a known calibration flow field using both a camera lens and the optical borescope were within ±3% of the calibration values. Therefore, a conservative estimate of the uncertainty in the magnitude of each velocity vector is estimated as ±6%.

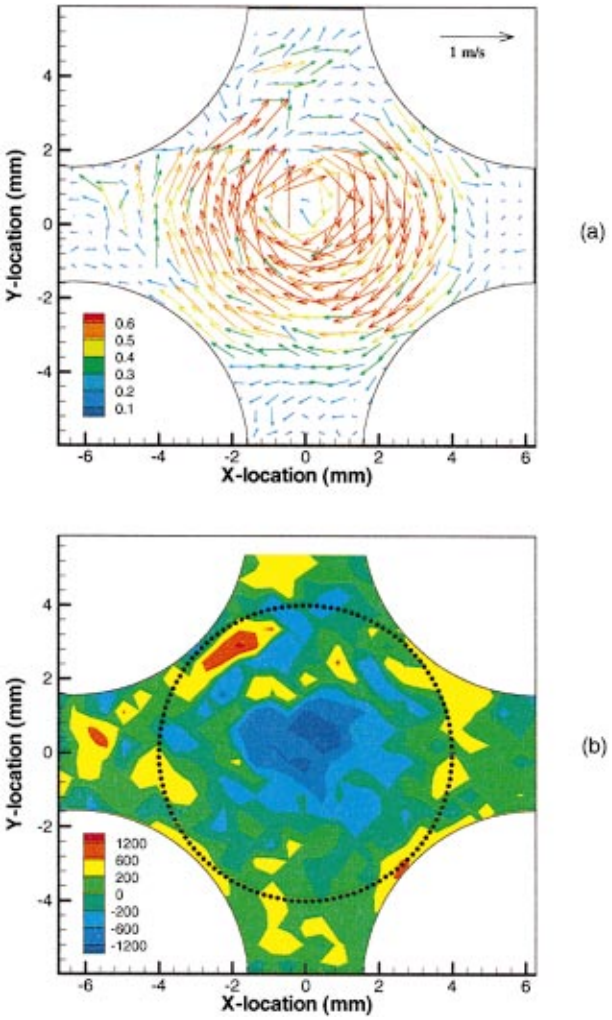

Fig. 4 (*a*) Lateral velocity field (m/s) at an axial location of $4.2D_h$(50 mm); (*b*) Corresponding axial vorticity field (1/s)

4 Results

Lateral velocity fields measured using PIV for six axial locations downstream of the support grid at a Re_{Dh} of 2.8×10^4 are presented; these describe the development of the swirling flow in the rod bundle subchannel. Full-field data showing the lateral velocity and axial vorticity fields are reported for $z/D_h=4.2$, 12.7, and 21.2. The axial vorticity was calculated using a first-order central-difference scheme and the uncertainty is ±12%. To characterize the swirling flow at $z/D_h=4.2$, 8.5, 12.7, 16.9, 21.2, and 25.5, radial distributions of azimuthal velocity and circulation, and the axial decay of angular momentum are presented. The origin of the radial coordinate is placed at the center of the swirling flow as determined by the centroid of vorticity. The location of the centroid of vorticity is also used to show the spatial migration of the swirling flow as the flow develops in the axial direction. The results of the present investigation are compared to the flow dynamics of a wing tip vortex, decaying, swirling flow in a pipe, and a Lamb-Oseen vortex.

4.1 Lateral Velocity and Axial Vorticity Fields. Figures 4, 5, and 6 present the lateral velocity fields and axial vorticity fields at $z/D_h=4.2$, 12.7, and 21.2. The velocity vectors are colored according to velocity magnitude and the midpoint of each velocity vector is located at the center of the corresponding interrogation region. As stated previously, to study swirling flow generated from a split-vane pair with minimal cross flow among neighboring

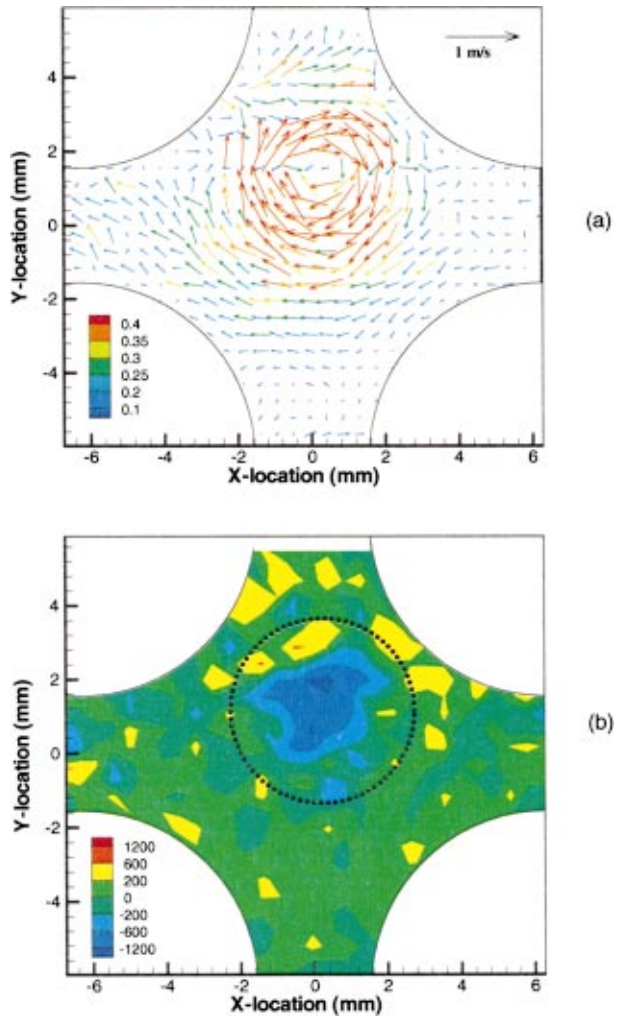

Fig. 5 (*a*) Lateral velocity field (m/s) at an axial location of $12.7D_h$(150 mm); (*b*) Corresponding axial vorticity field (1/s)

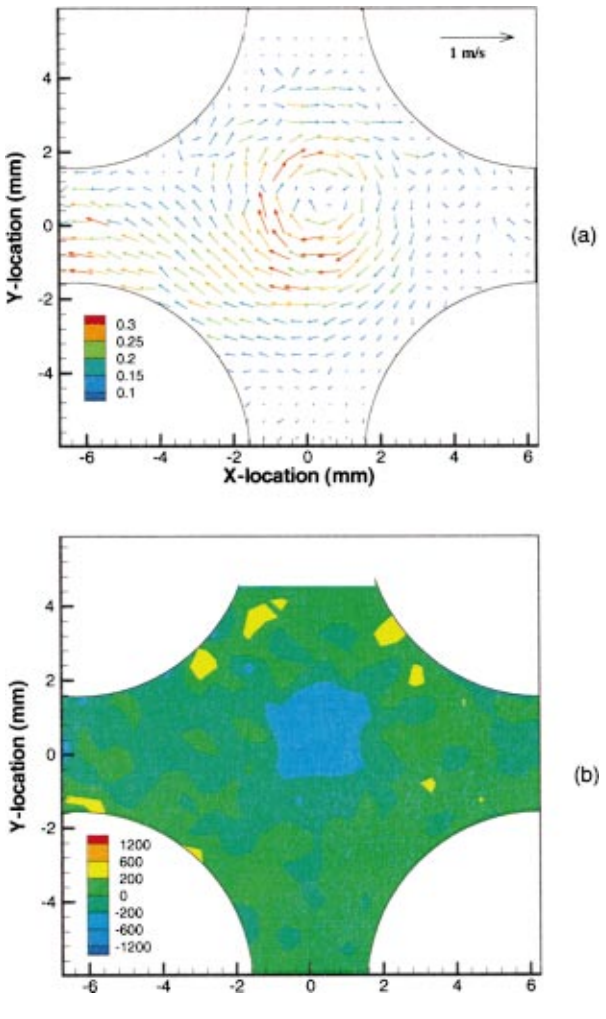

Fig. 6 (*a*) Lateral velocity field (m/s) at an axial location of $21.2D_h$(250 mm); (*b*) Corresponding axial vorticity field (1/s)

subchannels, only the vanes in subchannel A (Fig. 1) were configured to produce swirl. The velocity magnitude associated with the swirling flow in the subchannel is significantly larger than the velocity magnitude in the rod gaps. This indicates that cross-flow among neighboring subchannels was minimized. Evident in the lateral velocity fields of Figs. 4, 5, and 6 is the clockwise direction of the azimuthal velocity created by the orientation of the vane pair in this subchannel. The corresponding axial vorticity fields in Figs. 4, 5, and 6 are each characterized by an area of large magnitude vorticity surrounded by a region of nearly zero vorticity. Such a vorticity field characterizes a classical vortex. Specifically, Saffman [25] states that in the most general terms, "vortex" refers to a region of concentrated vorticity in an otherwise irrotational flow.

Figure 4 shows the lateral velocity field and corresponding axial vorticity at $z/D_h=4.2$, which is 50 mm downstream of the trailing edge of the support grid and 43.8 mm from the tips of the split-vane pair. At this axial location, the average magnitude of the lateral velocity is on the order of 0.6 m/s over the extent of the subchannel and the velocity magnitude in the rod gaps is 0.15 m/s. The axial vorticity field of Fig. 4(*b*) has a region of concentrated vorticity with a value of $-1200\ s^{-1}$. This region is located near the center of the subchannel and is surrounded by essentially irrotational flow ($-200\ s^{-1} \leqslant \omega_z \leqslant 200\ s^{-1}$). Figure 5 presents the velocity and vorticity fields for an axial location of $z/D_h=12.7$ ($z=150$ mm). At this location, the lateral velocities have diminished to 0.35 m/s. Comparison of Fig. 5(*b*) with Fig. 4(*b*) shows a reduced region of concentrated vorticity; however, the largest magnitude remains near $1200\ s^{-1}$. In contrast to $z/D_h=4.2$, the concentrated region of vorticity is located in a northeast region of the subchannel. The lateral velocity field and axial vorticity for $z/D_h=21.2$ ($z=250$ mm) is provided in Fig. 6. Figures 4(*a*) and 6(*a*) show that the magnitudes of lateral velocities at $z/D_h=21.2$ downstream of the support grid are less than 30% of the measured value at $z/D_h=4.2$. The region of concentrated vorticity is smaller than $z/D_h=12.7$ and the largest magnitude of vorticity is $600\ s^{-1}$. The concentrated region of vorticity remains in the northeast region of the subchannel. At an axial location of $z/D_h=25.5$ ($z=300$ mm) the velocity magnitude is on the order of 0.2 m/s. As the flow develops in the axial direction, the swirling flow does not remain in the center of the subchannel and there is a strong outflow in the west rod gap. In general, the velocity fields of the present study have similar trends as Karoutas et al. [19]. In addition, the relative magnitude of the maximum lateral velocity in the subchannel to the axial velocity of the present study and data of Karoutas et al. [19] agree. To document the development of the swirling flow in the subchannel, integral measures of the lateral velocity and axial vorticity fields are presented for all six axial locations.

4.2 Integral Analysis of Velocity and Vorticity Fields. Integral measures of the velocity fields are employed to locate the center of the swirling flow and to describe the axial development of the swirling flow. A Cartesian coordinate system is employed to

present the PIV data and is adopted to present the integral measures. For each axial location, the integral measures include the centroid of vorticity, the azimuthal velocity distribution, the circulation distribution, and the total angular momentum. In order to quantify radial distributions of azimuthally averaged velocity and circulation, it is necessary to locate an origin for the radial coordinate at the center of the swirling flow. The centroid of vorticity accurately represents the center of the swirling flow for the case where the total vorticity is non-zero (Saffman [25]). The centroid of vorticity is defined as

$$\overline{X_c} = \frac{\int\int_R x\omega_z dxdy}{\int\int_R \omega_z dxdy} \quad \overline{Y_c} = \frac{\int\int_R y\omega_z dxdy}{\int\int_R \omega_z dxdy}. \tag{1}$$

This calculation is performed over a circular area. The center of region R is located at the center of the subchannel as illustrated in Fig. 4(b). The circular region has a radius of 4 mm and includes velocity data for the region of the subchannel and does not include the data in the rod gaps. For further analysis of the lateral velocity data, the origin of the radial coordinate is located at the centroid of vorticity $(\overline{X_c}, \overline{Y_c})$.

The radial distribution of azimuthal velocity is determined by azimuthally averaging the velocity field. The averaging is accomplished using all of the velocity vectors in the region defined by a circle of radius 2.5 mm centered at the centroid of vorticity, thereby imposing symmetry. All velocity vectors in this region are used as input to a fourth-order polynomial curve-fit. An example of a typical region is shown in Fig. 5(b). The azimuthal velocity profiles are a representative average profile for all the vectors in the region. Circulation is defined as the flux of vorticity through the surface R or

$$\Gamma = \int\int_R \omega_z dxdy. \tag{2}$$

Circulation is calculated for the regions R bounded by circles having radii of 0.5, 1.0, 1.5, 2.0, and 2.5 mm and centered at the centroid of vorticity. The average circulation profile results from calculation of the circulation at the five regions stated above. The average circulation profiles are presented for each axial location. Angular momentum calculations utilized a region enclosed by a circle having a radius of 2.5 mm located at the centroid of vorticity. For a constant density flow, angular momentum may be defined as

$$\Omega = \frac{\int\int_R rV_\theta dxdy}{\int\int_R dxdy}. \tag{3}$$

4.3 Results of Integral Measures of the Lateral Velocity and Axial Vorticity Fields. Table 1 provides the location of the centroid of vorticity relative to the center of the subchannel for the six axial locations of the present study. Figures 4(b), 5(b), and 6(b) show the axial vorticity for three of the cases. As presented above, with axial development of the swirling flow the centroid of vorticity migrates toward the rod north and east of the subchannel center. This movement may affect local heat transfer rates from each of the four surrounding rods.

Figure 7 shows radial profiles of the azimuthal velocity for z/D_h from 4.2 to 25.5. Azimuthal velocity increases with radius until reaching a maximum, and then decreases with increasing radius. Figure 8 shows the corresponding circulation profiles. For each axial location, circulation increases with radial distance from the centroid of vorticity of the swirling flow. The radial profiles of azimuthal velocity and circulation from the present flow are compared with analytical forms for vortex flows. Both Chen et al. [10] and Kitoh [14] characterized swirling flows through similar comparisons. The qualitative behavior of azimuthal velocity and circulation shown in Figs. 7 and 8 is consistent with both a Rankine vortex and a Lamb-Oseen vortex. A Rankine vortex is a circular vortex patch in an irrotational fluid (Saffman [25] and Lamb [26]). The azimuthal velocity distribution of a Rankine vortex is the superposition of a forced vortex and a free vortex, or

$$V_\theta(r) = \frac{1}{2}\omega_0 r \quad 0 \leq r \leq a$$

$$V_\theta(r) = \frac{1}{2}\omega_0 \frac{a^2}{r} \quad a \leq r \leq R_0 \tag{4}$$

Table 1 Centroid of vorticity relative to the center of the subchannel

$\frac{z}{D_h}$	$\overline{X_c} - x_s$ (mm)	$\overline{Y_c} - y_s$ (mm)
4.2	0.01	0.37
8.5	0.21	1.05
12.7	0.24	1.15
17.0	0.37	1.24
21.2	0.13	1.27
25.5	- 0.09	0.67

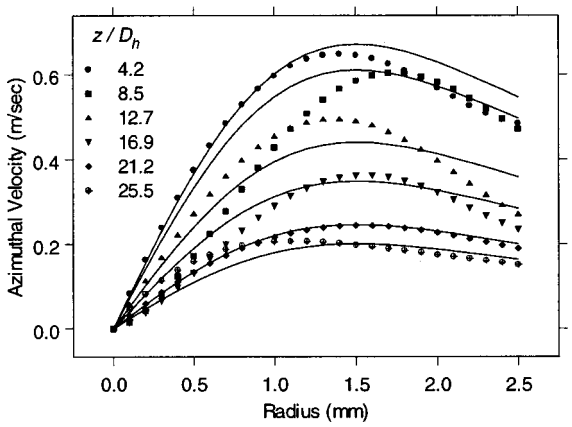

Fig. 7 Azimuthal velocity profiles

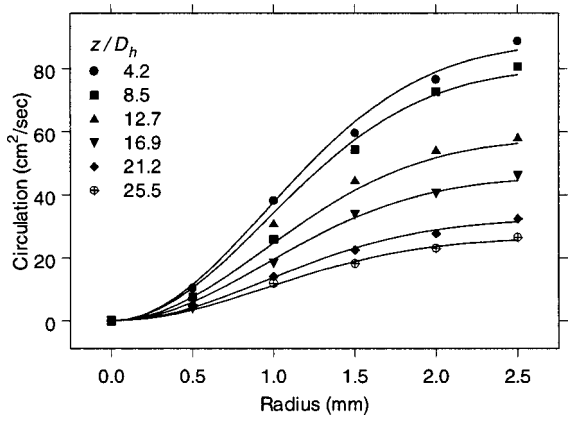

Fig. 8 Circulation profiles

Table 2 Velocity magnitude comparison of the data of the present investigation with decaying, swirling flow in a pipe

Investigation	Re_{Dh}	$\frac{z}{D_h}$	$\frac{V_{\theta,\max}}{V_{avg}}$	$\frac{M_t}{M_T}$
Present study	2.8×10^4	12.7	0.21	-
Kreith and Sonju [6]	4.8×10^4	10	0.38	-
Kitoh [14]	6.0×10^4	12.3	1.6	-
Chang and Dhir [15]	1.25×10^4	10	2.0	2.67
	1.25×10^4	10	4.8	7.84

where ω_0 is the axial vorticity. A continuous function representing the piecewise continuous Rankine vortex is

$$V_\theta(r) = C(1-e^{-r^2/B^2}), \tag{5}$$

where C and B are constants. A Lamb-Oseen vortex is a one-dimensional time dependent viscous vortex (Saffman [25] and Lamb [26]). The exact solution to the vorticity transport equation predicts the azimuthal velocity distribution as

$$V_\theta(r,t) = \frac{\Gamma_0}{2\pi r}(1-e^{-r^2/4\upsilon t}) \tag{6}$$

where Γ_0 is the asymptotic limit of circulation. The azimuthal velocity distribution of a Lamb-Oseen vortex is affected by viscous diffusion in time.

A Lamb-Oseen vortex was adopted as the basis for characterizing the azimuthal velocity profiles at each axial location. To predict the measured azimuthal velocity and circulation profiles from the analytical distribution of a Lamb-Oseen vortex, a coordinate transformation from time to space was performed by replacing t with z/V_{avg}. Under this coordinate transformation, the parameter $4\upsilon t$ ranged from 9.18×10^{-8} m^2 at 50 mm to 5.51×10^{-7} m^2 at 300 mm. The asymptotic value of circulation, Γ_0, was taken as the circulation at $r=2.5$ mm. The resulting analytical predictions for the radial distributions of azimuthal velocity and circulation significantly under-predicted the measured values. However, following Chen et al. [10] the parameter $4\upsilon t$ was taken as a constant, and an improved prediction of the data resulted from using 1.8×10^{-6} m^2 as the value of $4\upsilon t$ for all axial locations. The resulting distributions are shown in Figs. 7 and 8 for azimuthal velocity and circulation, respectively. The distribution of circulation is well described by the Lamb-Oseen vortex (Fig. 8). The azimuthal velocity profiles show reasonable agreement (Fig. 7). These comparisons will be useful in the discussion that follows.

The measured azimuthal velocity profiles in decaying swirling pipe flow studies are qualitatively similar to the azimuthal profiles of the present study. Kitoh [14] and Chang and Dhir [15] suggest that azimuthal velocity profiles may be divided into a core region and an annular region. In the core region, azimuthal velocity increases linearly with radius. The azimuthal velocity in the annular region is described by a decrease in azimuthal velocity with radius. Chang and Dhir [15] state that for their measured data, very near the center of the core region, the azimuthal velocity is quantitatively a forced vortex, while near the outer edge of the annular region the azimuthal velocity quantitatively follows the velocity profile of a free vortex. However, an extensive transition region between the free vortex and forced vortex velocity profiles exists in their measured data. Kitoh [14] qualitatively compares his measured data with a Rankine vortex and the data agree in the core and annular regions. These observations were consistent with the data of the present study.

Further insight into the nature of the swirling flow in the subchannel of the rod bundle can be gained through detailed comparison with the characteristics of the velocity field in swirling pipe flow. Table 2 compares the magnitude of the maximum azimuthal velocity of the present study with the data of Kreith and Sonju [6], Kitoh [14], and Chang and Dhir [15] for a representative axial location of either 10, 12.3, or 12.7 diameters from the inlet. The normalized maximum azimuthal velocity magnitudes ($V_{\theta,\max}/V_{avg}$) of the present data range from 0.27 at $z/D_h=4.2$ to 0.09 at $z/D_h=25.5$ for a $\mathrm{Re}_{Dh}=2.8\times10^4$. In the present data $V_{\theta,\max}/V_{avg}$ decays from 0.27 at $z/D_h=4.2$ to 0.21 at $z/D_h=12.7$. The magnitude of the present data at $z/D_h=12.7$ compared well with the analytical results of Kreith and Sonju [6]. The analytical results of Kreith and Sonju [6] modeled swirling flow generated from a twisted tape insert. The pure tangential injection method of Chang and Dhir [15] clearly had larger azimuthal velocity magnitudes, and showed a direct correlation between maximum azimuthal velocity magnitude and inlet swirl level as characterized by M_t/M_T. Kitoh [14] used a radial cascade of vanes to produce swirling flow. The maximum azimuthal velocity of Kitoh [14] compared well with the data of Chang and Dhir [15] at the lower momentum flux ratio (Table 2).

The radial location of the maximum azimuthal velocity is utilized to further compare the radial distributions of azimuthal velocity. Chang and Dhir [15] show that for tangential injection in swirling pipe flow the radial location associated with the maximum azimuthal velocity moves toward the center of the pipe with increasing axial location, and should occur at a non-dimensional radius between 0.4 and 0.7. The analytical results of Kreith and Sonju [6] for swirling flow in a pipe indicate the maximum azimuthal velocity occurs at a non-dimensional radius of 0.8 for the range of axial locations examined. The present data show that the locations of the maximum azimuthal velocity range from a non-dimensional radial location (R_s/R) of 0.44 to 0.68 with no consistent trend with axial location. The radial location of the maximum azimuthal velocity compares favorably with studies of decaying, swirling flow in a pipe; however, there is no trend in the change of the location of the maximum azimuthal velocity with increasing downstream distance.

Previous studies of unconfined tip vortex dynamics have demonstrated azimuthal velocity profiles that are qualitatively similar to those presented in this study. In the unconfined tip vortex studies, the rotational motion of the vortex shed from an airfoil entrains the surrounding wake into a spiral, thus creating a radial distribution of azimuthal velocity. The radial profiles of azimuthal velocity are linear in the vortex region, reach a maximum, then the azimuthal velocity decreases in the wake region. The hot wire data of Devenport et al. [9] show that the axial development of the flow is very slow in such an unconfined vortex flow. For axial locations of 5 to 30 chordlengths downstream, the magnitude of the maximum azimuthal velocity decreases by only 7% and the vortex radius remains essentially constant. Chen et al. [10] studied the behavior of a single vortex shed from a hydrofoil and a vortex pair shed from a flapped hydrofoil. The development of the radial profile of the azimuthal velocity of the single vortex compared well with a Lamb-Oseen vortex. Prior to interaction and merger, each vortex shed from the two edges of the flapped airfoil individually followed the behavior of a Lamb-Oseen vortex at radial locations away from the center of the cores. Table 3 compares the magnitude of the maximum azimuthal velocity of the present study with Devenport et al. [9] and Chen et al. [10]. As shown in Table 3, the normalized maximum azimuthal velocities of the present study compare well with Devenport et al. [9]. The velocity magnitudes of Chen et al. [10] are significantly less.

Accurate prediction of the axial decay rate of the velocity field is important for determining local heat transfer rates in the rod bundle. The development of the average azimuthal velocity in the axial direction of the present study is compared with the confined and unconfined vortex flows. The axial development of decaying, swirling flow in a pipe is similar to that of the present flow and is presented prior to discussion of the unconfined vortex flows. Figure 9 illustrates the axial decay of angular momentum in the rod bundle subchannel. The angular momentum decays from 11.4 to

Table 3 Velocity magnitude comparison of the data of the present investigation with tip vortex flow

Investigation	Re_c	$\alpha(°)$	$\frac{V_{\theta,max}}{V_\infty}$
Present study	2.8×10^4 *	-	0.27 to 0.09 **
Devenport et al. [9]	5.3×10^5	2.5	0.16
	5.3×10^5	5.0	0.27
Chen et al. [10] (unflapped)	8.2×10^5	4	0.0625
Chen et al. [10] (flapped – tip vortex)	8.2×10^5	4	0.0813
(flapped – flap vortex)	8.2×10^5	4	0.0375
	* Re_{Dh}		** $\frac{V_{\theta,max}}{V_{avg}}$

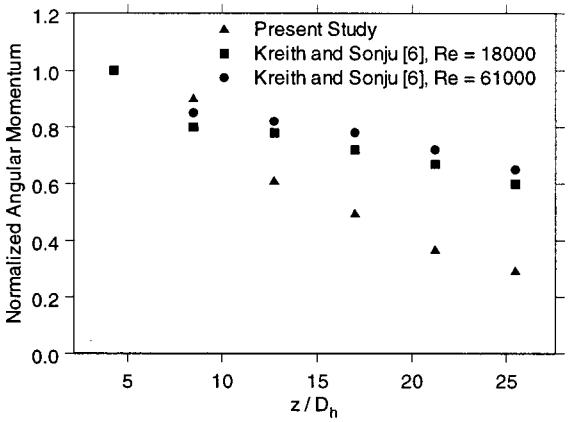

Fig. 10 Comparison of the axial decay rate of the present study with [6]

3.2 cm^2/s over the 300 mm span. Previous investigations of swirling pipe flow characterize the decay rate of angular momentum with axial location both empirically and analytically using an exponential function (Kreith and Sonju [6]). For the data in Fig. 9, the decay of the angular momentum in the axial direction is characterized as

$$\Omega(z/D_h) = 15.5\exp[-0.063(z/D_h)] \tag{7}$$

In general, quantitative comparison of this decay rate with that previously discussed for decaying, swirling flow in a pipe cannot be made without appropriate nondimensionalization. The angular momentum data in Fig. 10 are normalized by the angular momentum at $z/D_h = 4.2$. Figure 10 compares the normalized angular momentum decay rate of the present study with analytical results of the decaying swirling pipe flow study of Kreith and Sonju [6]. Comparison is made with this data because the normalized maximum azimuthal velocity magnitude compared well with the data of the present study at $z/D_h = 10$. In Fig. 10, two sets of data from Kreith and Sonju [6] are presented to show the influence of Reynolds number on the decay rate of the normalized angular momentum. Swirling flow in a rod bundle subchannel decays at a faster rate than the data in for decaying, swirling flow in a pipe measured by Kreith and Sonju [6], which was generated using a twisted tape insert. Chang and Dhir [15] (in Fig. 10 of [15]) showed that the decay rate of the angular momentum is larger than that measured by Kitoh [14].

The development of the azimuthal velocity in the unconfined tip vortex flows is quite different than the development of the present flow field and the flow field in decaying, swirling flow in a pipe. Chen et al. [10] showed that the vortex persists for 314 chordlengths while the tip vortex in the investigation of Devenport et al. [9] persisted for 30 chordlengths. The differences may result from the differences in the experimental set up as Devenport et al. [9] used a single wing configuration while Chen et al. [10] used a single flapped wing. The maximum azimuthal velocity of a wing tip vortex is uninfluenced by momentum diffusion from solid boundaries, and therefore the angular momentum decays at a much slower rate than the present flow field. The data of the present study clearly show that the axial development of the flow in the subchannel is characterized by a significant reduction in the azimuthal velocity magnitude.

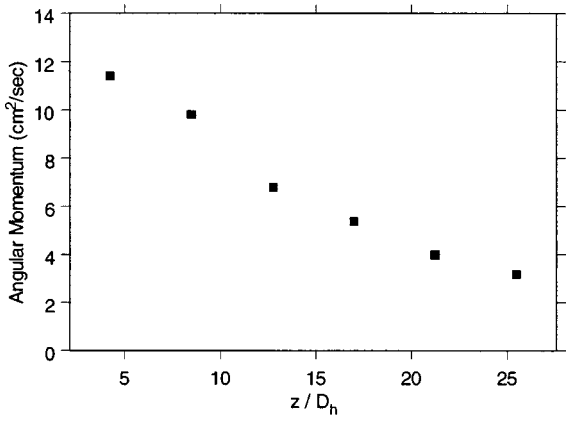

Fig. 9 Decay of angular momentum

The present azimuthal velocity fields are consistent with analytical forms for a vortex; however, the flow displays a unique axial development associated with the rod bundle geometry. In summary, comparison of the present data with the velocity fields in swirling flow in a pipe and velocity fields of a tip vortex shed from airfoils suggest that the significant parameters affecting decay rate for swirling flow are initial angular momentum, or swirl, and the type and degree of confinement.

5 Conclusions

The lateral velocity fields in a rod bundle subchannel generated from a split-vane pair were measured for $Re_{Dh}=2.8\times10^4$ using particle image velocimetry. Full-field lateral velocity and axial vorticity fields were presented for axial locations of 4.2, 12.7, and 21.2 hydraulic diameters. Integral parameters (radial profiles of azimuthal velocity and circulation, and axial decay of angular momentum) of the lateral velocity fields were presented for axial locations from 4.2 to 25.5 hydraulic diameters in increments of 4.2 hydraulic diameters. The centroid of vorticity for the swirling flow in the subchannel was utilized as the origin for calculation of the integral parameters.

The maximum azimuthal velocities were 27% and 9% of the axial velocity for 4.2 and 25.5 hydraulic diameters downstream of the support grid, respectively. The axial vorticity fields showed that the swirling flow generated by the split-vane pair is qualitatively consistent with the definition of a classical vortex. As the swirling flow developed in the subchannel, the centroid of vorticity did not remain in the center of the subchannel, but migrated toward one of the four surrounding rods. As measured in the radial direction from the centroid of vorticity at each axial location, the azimuthal velocity increased to a maximum then decreased. Circulation profiles increased from the centroid of vorticity to the edge of the region, and the maximum value of circulation decayed with axial location. The azimuthal velocity and circulation data were fit to a Lamb-Oseen vortex. The azimuthal velocity profiles of the present study, of swirling pipe flow, and of a wing tip vortex

qualitatively agreed. Normalized maximum azimuthal velocity magnitudes of the present study compared well with decaying swirling pipe flow generated using a twisted tape insert, and a tip vortex shed from a single wing. Angular momentum for the present flow decayed at a faster rate than that in decaying, swirling flow in a pipe.

Acknowledgments

The financial support of Westinghouse Nuclear Fuel is gratefully acknowledged. Professor James A. Liburdy was instrumental in the development of the PIV method employed in this work. Dr. Timothy A. Conover contributed to the data analysis process. This material is based in part upon work supported under a National Science Foundation Fellowship to the second author.

Nomenclature

a = radius at which the vorticity of the Rankine vortex becomes constant
B = constant in the continuous function for the Rankine vortex
C = constant in the continuous function for the Rankine vortex
D_h = hydraulic diameter (m)
M_t = azimuthal momentum flux (kg/sm^2)
M_T = total momentum flux (kg/sm^2)
r = radius (m)
R = region of integration
R_s = radius at maximum azimuthal velocity (m)
Re_c = Reynolds number based on chord length
Re_{Dh} = axial Reynolds number based on hydraulic diameter
R_0 = radius at the outer edge of the Rankine vortex (m)
t = time (s)
V_{avg} = average axial velocity (m/s)
V_∞ = free-stream velocity (m/s)
V_θ = azimuthal velocity (m/s)
x = x coordinate (m)
x_s = x coordinate locating the center of the subchannel (m)
$\overline{X}_c$ = x coordinate of centroid of vorticity (m)
$\overline{Y}_c$ = y coordinate of centroid of vorticity (m)
y = y coordinate (m)
y_s = y coordinate locating the center of the subchannel (m)
z = streamwise direction (m)
α = angle of attack (°)
ν = kinematic viscosity (m^2/s)
ω_z = axial vorticity (s^{-1})
ω_0 = axial vorticity for the Rankine vortex (s^{-1})
Γ_0 = asymptotic circulation (cm^2/s)
Ω = angular momentum (cm^2/s)

References

[1] Marek, J., and K. Rehme, 1979, ''Heat Transfer in Smooth and Roughened Rod Bundles Near Spacer Grids,'' *Proceedings of the ASME Winter Annual Meeting: Fluid Flow and Heat Transfer Over Rod or Tube Bundles*, December, New York, New York, pp. 163–170.
[2] Whitman, J. M., 1896, ''The Effect of Retarders in Fire Tubes of Steam Boilers,'' Trans. ASME, **17**, pp. 450–470.
[3] Yao, S. C., Hochreiter, L. E., and Leech, W. J., 1982, ''Heat Transfer Augmentation in Rod Bundles Near Spacer Grids,'' ASME J. Heat Transfer, **104**, pp. 76–81.
[4] Armfield, M. V., 2001, ''Effects of Support Grid Design on Local, Single-Phase Turbulent Heat Transfer in Rod Bundles,'' M. S. thesis, Clemson University, Clemson, SC.
[5] de Crécy, F., 1994, ''The Effect of Grid Assembly Mixing Vanes on Critical Heat Flux Values and Azimuthal Location in Fuel Assemblies,'' Nucl. Eng. Des., **149**, pp. 233–241.
[6] Kreith, F., and Sonju, O. K., 1965, ''The Decay of a Turbulent Swirl in a Pipe,'' J. Fluid Mech., **22**, pp. 257–271.
[7] Green, S. I., and Acosta, A. J., 1991, ''Unsteady Flow in Trailing Vortices,'' J. Fluid Mech., **227**, pp. 107–134.
[8] Shekarriz, A., Fu, T. C., and Katz, J., 1993, ''Near-field Behavior of a Tip Vortex,'' AIAA J., **31**, pp. 112–118.
[9] Devenport, W. J., Rife, M. C., Liapis, S. I., and Follin, G. J., 1996, ''The Structure and Development of a Wing-Tip Vortex,'' J. Fluid Mech., **312**, pp. 67–106.
[10] Chen, A. L., Jabob, J. D., and Savas, Ö., 1999, ''Dynamics of Corotating Vortex Pairs in the Wakes of Flapped Airfoils,'' J. Fluid Mech., **382**, pp. 155–193.
[11] Smithberg, E., and Landis, F., 1964, ''Friction and Forced Convection Heat-Transfer Characteristics in Tubes with Twisted Tape Swirl Generators,'' ASME J. Heat Transfer, **86**, pp. 39–49.
[12] Musolf, A. O., 1963, ''An Experimental Investigation of the Decay of a Turbulent Swirl Flow in a Pipe,'' Thesis, University of Colorado.
[13] Algifri, A. H., Bhardwaj, R. K., and Rao, Y. V. N., 1988, ''Turbulence Measurements in Decaying Swirl Flow in a Pipe,'' Appl. Sci. Res., **45**, pp. 233–250.
[14] Kitoh, O., 1991, ''Experimental Study of Turbulent Swirling Flow in a Straight Pipe,'' J. Fluid Mech., **225**, pp. 445–479.
[15] Chang, F., and Dhir, V. K., 1994, ''Turbulent Flow Field in Tangentially Injected Swirl Flows in Tubes,'' Int. J. Heat Fluid Flow, **15**, pp. 346–356.
[16] Frigerio, F., and Hart, D. P., 1997, ''Velocity Field Measurements of a Confined Swirling Flow using Digital Particle Image Velocimetry Cinematography,'' *Proceedings of the ASME Fluids Engineering Summer Meeting*, June, Vancouver, British Columbia, Paper No. FEDSM97-3225.
[17] Xiong, W., and Merzkirch, W., 1999, ''PIV Experiments using an Endoscope for Studying Pipe Flow,'' Journal of Flow Visualization and Image Processing, **6**, pp. 167–175.
[18] Lozano, A., Kostas, J., and Soria, J., 1999, ''Use of Holography in Particle Image Velocity Measurements in Swirling Flow,'' Exp. Fluids, **27**, pp. 251–261.
[19] Karoutas, Z., Gu, C., and Schölin, B., 1995, ''3-D Flow Analysis for Design of Nuclear Fuel Spacer,'' *Proceedings of the Seventh International Meeting on Nuclear Reactor Thermal-Hydraulics*, Sept., Saratoga Springs, New York, **4**, pp. 3153–3174.
[20] Herer, C., 1991, ''3-D Flow Measurements in Nuclear Fuel Rod Bundles using Laser Doppler Velocimetry,'' *Proceedings of the ASME FED Fluid Measurements and Instrumentation Forum*, **108**, pp. 95–97.
[21] Raffel, M., Willert, C., and Kompenhans, J., 1998, *Particle Image Velocimetry*, Springer, Berlin.
[22] Adrain, R. J., 1991, ''Particle-Imaging Techniques for Experimental Fluid Mechanics,'' Annu. Rev. Fluid Mech., **23**, pp. 261–304.
[23] Keane, R. D., and Adrian, R. J., 1992, ''Theory of Cross-Correlation Analysis of PIV Images,'' Appl. Sci. Res., **49**, pp. 191–215.
[24] Kline, S. J., and McClintock, F. A., 1953, ''Describing Uncertainty in Single-Sample Experiments,'' Mech. Eng. (Am. Soc. Mech. Eng.), pp. 3–8.
[25] Saffman, P. G., 1992, *Vortex Dynamics*, Cambridge University Press, United Kingdom.
[26] Lamb, H., 1932, *Hydrodynamics*, Cambridge University Press, United Kingdom.

Homayun K. Navaz
Associate Professor of Mechanical Engineering,
Kettering University,
Flint, MI 48504

Ramin Faramarzi
Refrigeration and Thermal Test Center
Project Manager,
Southern California Edison Company,
Irwindale, CA 91702

Morteza Gharib
Professor of Aeronautics,
California Institute of Technology,
Pasadena, CA 91125

Dana Dabiri
Research Scientist,
California Institute of Technology,
Pasadena, CA 91125

Darius Modarress
President,
Viosense Corporation,
Pasadena, CA 91106

The Application of Advanced Methods in Analyzing the Performance of the Air Curtain in a Refrigerated Display Case

Computational Fluid Dynamics (CFD) modeling is effectively coupled with the experimental technique of Digital Particle Image Velocimetry (DPIV), to study the flowfield characteristics and performance of the air curtain of a medium-temperature open vertical refrigerated display case used in supermarkets. A global comparison of the flowfield and quantification of the entrained air into the case indicate that there is a considerable amount of cold air spillage from a typical display case that is replaced by the ambient warm entrained air across the air curtain, lowering the energy efficiency of the case. The computational model that is developed from the marriage of CFD and DPIV techniques provides a reliable simulation tool that can be used for the design optimization of air curtains. A correct estimate of the infiltration rate by changing different parameters in a validated computational simulation model will provide a feasible tool for minimizing the spillage of the cold air, and thereby designing more energy efficient open display cases.
[DOI: 10.1115/1.1478586]

Introduction

Refrigerated display cases are extensively used in supermarkets and grocery stores. Recirculated cold air is used to keep the case contents at a desired preset temperature, while allowing customers unhindered access to the refrigerated food. Cold air is supplied into the case at the top through a discharge grill, and is recirculated through a return air grill at the bottom. Figures 1(*a*) and 1(*b*), show schematics of the display case with discharge and return air grills, and corresponding dimensions. The primary function of the cold air stream is to create a barrier between the outside warm air and the inside cold air. The effectiveness of the air curtain may depend on several factors including: the discharge air angle of throw, discharge air velocity (DAV), discharge air grill width, dimensional characteristics of the honey comb located at the discharge air grill, display case geometry, return air system, discharge air temperature (DAT), and number of air bands.

Laboratory tests have shown that infiltration constitutes the largest cooling load component of an open vertical display case [1]. So far, there has been no comprehensive qualitative and quantitative study of the flowfield parameters and structure for display cases. Stribling et al. [2] have made an attempt to combine the CFD and experimental results to study the velocity and turbulence in a display case. Their research indicates some discrepancies between the experimental and computational results, and they attribute that to the order of the numerical scheme and the grid resolution. Their hybrid approach of combining the computational and experimental methods to tackle the display case problem is genuine, but it is not conclusive. They have also recommended further research in this area.

One of the important aspects of such hybrid studies must be geared towards the optimized design of display cases, i.e., minimizing the infiltration of the outside air or better performance of the air curtain, and therefore energy savings. A cost effective optimization process requires a numerical simulation tool such as CFD methodology. On the other hand, reasonable confidence in CFD results must be built through validation with ''good'' experimental data, therefore necessitating a combined, or a hybrid, study. The CFD technology can be utilized with a reasonable degree of confidence only if it is properly anchored on actual and accurate data.

Earlier experimental studies by the Southern California Edison (SCE) Company recognized the importance of optimized design of display cases and its significant impact on energy savings. These studies prompted SCE to sponsor further research in the area of display case flowfield modeling. Therefore, a joint effort by SCE, California Institute of Technology (CalTech), and Kettering University was initiated. SCE established the base case scenarios by conducting tests at its sophisticated Refrigeration and Thermal Test Center (RTTC). CalTech conducted the DPIV effort, and Kettering University was mainly responsible for the CFD modeling. The Digital Particle Image Velocimetry experimental technique was utilized for flow visualization, quantitative measurements of the velocity profile, and entrainment calculations. The ROYA© [3] computer code was the simulation tool for the CFD modeling. In this paper, we intend to address the importance of the problem and its potential impact on energy savings, validate the CFD code with experimental data in a global manner, and utilize the numerical simulation to estimate the infiltration rate as a function of two operating variables: the inlet air velocity, and temperature. This parametric study can be utilized to develop compact equations for the infiltration rate as a function of the inlet air velocity and temperature. Such equations are quite important and useful to manufacturers in the design of their cooling systems. Furthermore, this work will pave the road for minimization of the infiltration rate, i.e., optimization of the vertical display case design.

Initial Tests

The control environment and data acquisition system of SCE's RTTC was utilized to establish the foundation of the project. The controlled environment room is an isolated thermal zone served by independent cooling, heating and humidification systems. This allows simulation of various indoor conditions of a supermarket. The sensible cooling load representing people and other heat gain sources is provided by a constant volume direct expansion system

Contributed by the Fluids Engineering Division for publication in the JOURNAL OF FLUIDS ENGINEERING. Manuscript received by the Fluids Engineering Division March 14, 2001; revised manuscript received January 14, 2002. Associate Editor: A. K. Prasad.

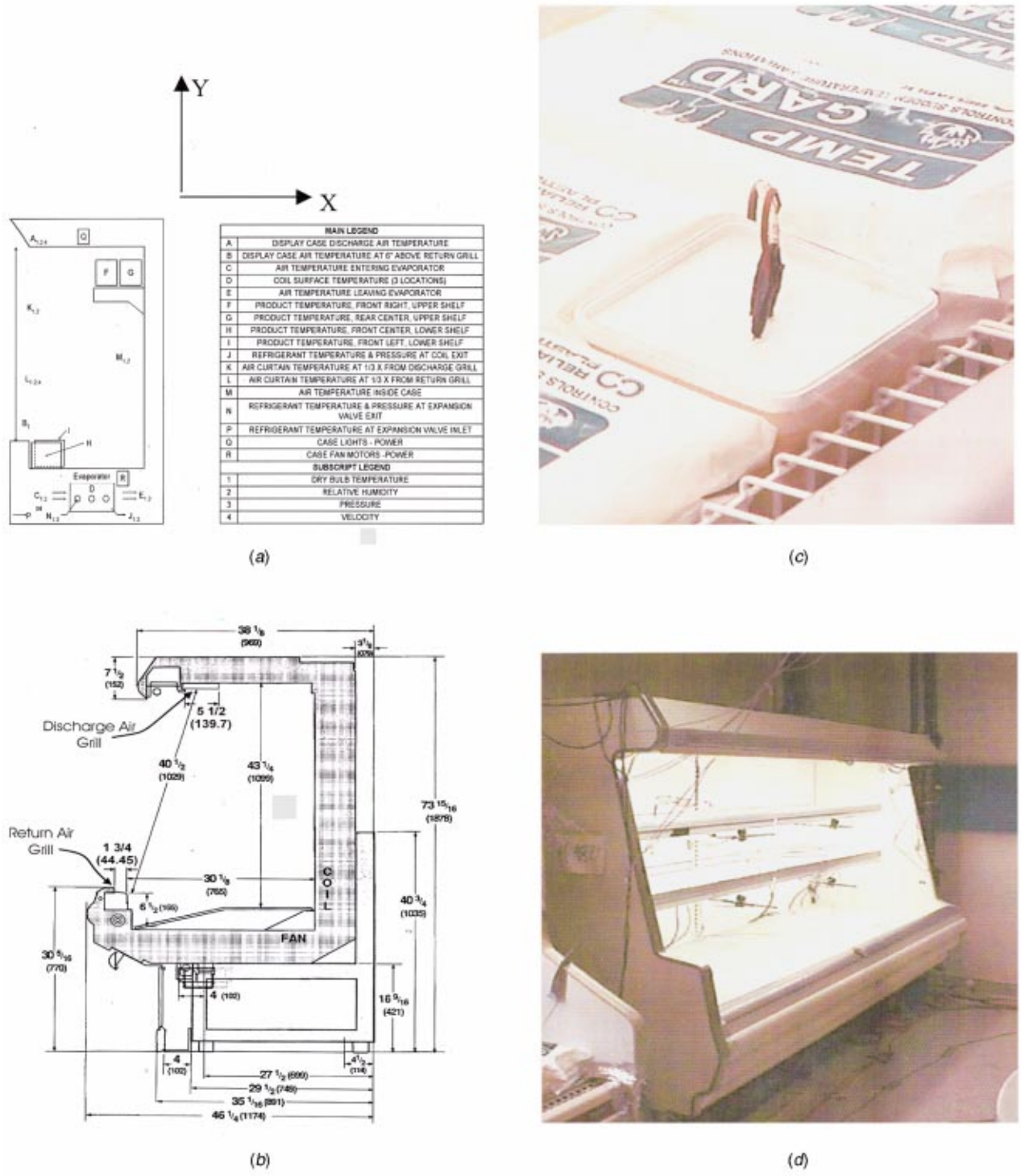

Fig. 1 (a) Case schematics and sensor locations with discharge and return grills. (b) Schematic of the display case with dimensions. (c) Simulator and dummy products used in the display case. (d) Multi-deck display case used in the present study.

reclaiming the waste refrigeration heat via a six-row coil. Auxiliary electric heaters located in the down-stream of the heat reclaim coils provide additional heating when required. While the air is conditioned to a desired thermostatic set point, an advanced ultrasonic humidification unit introduces precise amounts of moisture to the air surrounding the display case, representing the latent load due to outside air and people.

Discharge air velocity and temperature were selected as an initial set of test variables to ascertain the order of infiltration dependency on momentum and/or energy components of airflow. A series of initial tests were conducted to develop critical temperature and velocity readings within the display case. The fan blade pitch of the evaporator was changed from 34° to 11° to develop two discharge air velocity readings. Additionally, the refrigeration system suction pressure was changed from 53 psig (365.37 kPa gage) to 49 psig (337.80 kPa gage), resulting in 29.09°F

Table 1 Parameters used for each scenario

Test Scenario	Fan blade pitch	Measured average temperature °F (°C)	Reynolds number at $\frac{1}{2}$ of air curtain
1	34° (DAV* = 0.68 ms^{-1})	27.63 (−2.43)	26,766.
2	34° (DAV* = 0.68 ms^{-1})	29.09 (−1.62)	26,030.
3	11° (DAV* = 0.57 ms^{-1})	27.63 (−2.43)	23,144.

*Measured at discharge air grill.

(−1.62°C) and 27.63°F (−2.43°C) discharge air temperature, respectively, while DAV remained at 133 ft-min^{-1}, or 0.68 ms^{-1}. All modifications took place while the indoor condition of the room was maintained at 70°F (21.1°C) dry bulb (DB) and 45% relative humidity (RH).

All tests were conducted under American Society of Heating and Air-Conditioning Engineers (ASHRAE) Standard 72-1983, which prescribes a uniform method of testing of open refrigerators for food stores. This standard dictates that the air movement must be parallel to the plane of the opening of the display case and there should not be any external air drafts blowing into the refrigerated display case. The lighting intensity of the controlled environment room should be no less than 75 foot-candles (22.86 m-candle) at the center of the test fixture opening at a distance of one foot from the air curtain. This standard further dictates that the display case shall be filled with test package (or product simulator) and dummy products to simulate the presence of food product in the cases. According to ASHRAE Standard 72- 1983, food products are composed of 80 to 90 percent water, fibrous materials, and salt. A plastic container completely filled with a sponge material that is soaked in a brine solution of water and salt (6% by mass) was used to simulate the product. Figure 1(*c*) shows the simulator and dummy products.

Table 1 shows the parameters used for each test. In Test Scenarios 1 and 2, the fan speed is the same, i.e., the velocity of the inlet air remains constant while its average discharge air temperature varies. The comparison of these two test scenarios along with the results of parametric studies will be used to determine the temperature dependency of the volumetric flow rate of infiltrating air. In Test Scenario 3, the average temperature of the discharge air is maintained at the same value as the Test Scenario 1. However, with a smaller fan blade pitch, the average discharge air velocity was reduced. The comparison of these two tests will be used to determine the velocity dependency of the entering air.

Experimental Method

Digital Particle Image Velocimetry (DPIV) is a technique that is capable of measuring fluid velocity within a two-dimensional domain, unlike the hotwire or Laser Doppler Velocimetry (LDV) probe measurements that are single point measurement techniques. The present experiment was performed using FlowVision, a state-of-the-art DPIV system provided by General Pixels.

An Nd:Yag laser is used in combination with sheet generating optics to illuminate the cross-section of the flow of interest. The flow is then seeded with reflective particles that are small enough to accurately follow the flow. Upon illumination, the particles within the laser sheet reflect laser light. A camera situated at 90 degrees from the incident laser sheet captures the images within the laser sheet. These sequential images are recorded and post-processed, as explained below, to obtain the velocity and streamline fields.

The FlowVision implementation of the DPIV method is the cross-correlation technique, implying that sequential pairs are processed to produce a velocity field. For each sequential pair, a small interrogation window sub-samples a portion of each of the images at the same locations and a cross-correlation is performed, resulting in the average shift of particles within the interrogation windows. This interrogation is then, through calibration, converted into a velocity vector. The interrogation window is systematically moved through the sequential images to produce a vector field. Once the vector field is obtained through time, they are averaged to produce the mean velocity flows and streamlines. More detailed information about the DPIV technique can be found in Willert and Gharib [4], Westerweel, Dabiri and Gharib [5], and Gharib and Dabiri [6].

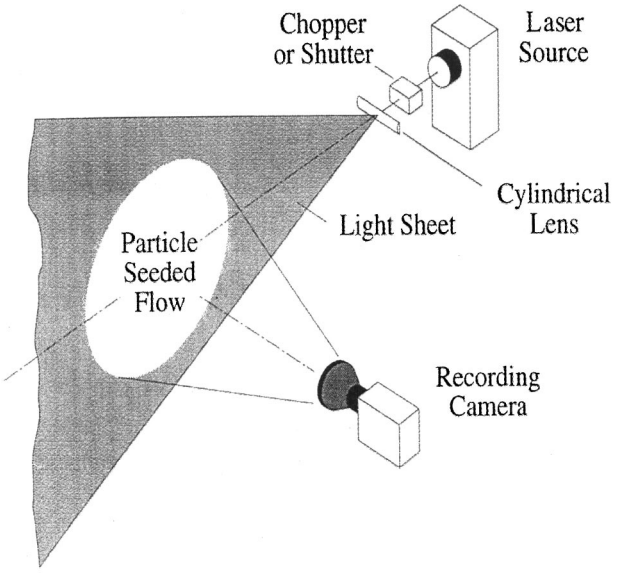

Fig. 2 Typical DPIV experimental setup

For the present experiment, a 768*480 pixel camera acquired images at 30 frames per second. A 120-mJ Nd:Yag laser is used to create a laser sheet and illuminate the area of interest. As the work is done in air, smoke is used to generate finely particulated flow. A cross-section of the middle of a typical multi-deck display case is illuminated (see Figs. 1(*d*) and 2), roughly spanning an area of 40 by 40 inches (1.01×1.01 meters). The measurements were done near the mid-section of the case and away from the end plates to avoid any corner effects. In order to properly and accurately image the jet curtain emanating from the top of the display case, the whole flow regime was broken down into 20 separate and overlapping regions, each of which was interrogated with FlowVision. For each of the 20 sections, 1000 images were acquired, and their results were averaged. The images were interrogated using a 32 by 32 pixel window, with a 50% overlap ratio resulting in 1440 vectors per region. A typical experimental setup using FlowVision is shown in Fig. 2. The resolution of the PIV velocity measurements is 1% of the measured velocity. This number reflects the magnitude of the error in the experimental data.

Computational Method

In general, computational fluid dynamics (CFD) is a methodology by which the conservation, or Navier-Stokes (NS), equations are solved. The method primarily consists of approximating the exact partial derivatives by a finite change of a variable in time

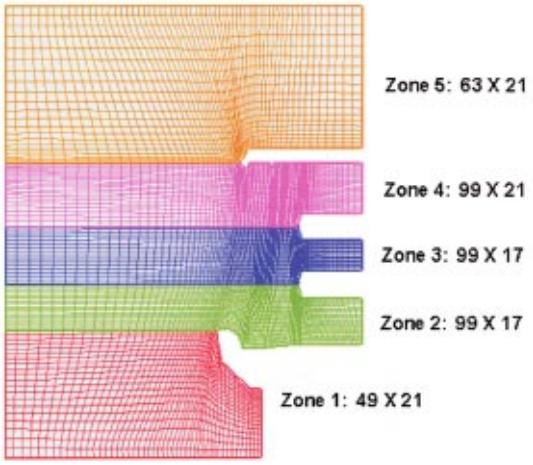

Fig. 3 Computational grid and zones

and/or space. Although CFD provides a powerful tool for simulation of a problem, it is still an approximation and requires validation with experimental data.

The ROYA© computer program has been the simulation tool for this research. This code is a Navier-Stokes (NS) solver for compressible and incompressible flows with chemical reaction capabilities based on a structured grid. The earlier version of this code, called Liquid Thrust Chamber Performance (LTCP), was developed for the National Aeronautics and Space Administration (NASA) in the early to mid-90's [7] for dense spray combustion in liquid rocket engines. However, the algorithm is quite versatile, and the code has been exercised over a wide range of flow regimes from creeping to subsonic and supersonic flows with and without chemistry, for a wide range of applications [8, 9]. The discretization scheme is fully implicit, and the left (L) and right (R) states of the inviscid fluxes are based on the Total Variation Diminishing (TVD) method. Either the Lax-Friedrichs (LF) or the Van-Leer (VL) method can be implemented to calculate the total inviscid fluxes by combining the left and right states. Two turbulence models, Cebeci-Smith algebraic, and low Reynolds number k-ε, are embedded in the code. The solver is second order accurate in time and space. However, the spatial accuracy can be increased to fourth order. The method becomes first order in space across a shock due to the implementation of the flux limiter.

The display case is enclosed in a room (test area). The computational domain is composed of the entire room and the display case. The upper and lower boundaries are assumed to be no-slip adiabatic walls. The left boundary (see Fig. 3) is mainly a no-slip adiabatic wall except the lower part that is open to the atmosphere with a specified backpressure. The entire domain is decomposed into five zones as seen from Fig. 3. In the numerical simulation model, there is not any recirculating air through the ductwork. There is a constant supply of air through the discharge grill at measured velocities i.e., both components of velocity profiles across the grill are specified as taken by measurements (U and V). The measurements are taken in the middle of the display case to be compatible with the two-dimensional CFD analysis. The discharged air temperature is also measured and specified as a boundary condition for the CFD code. Due to the elliptic nature of the equations, it is evident that the density has to be specified using the information taken from the interior nodes and cannot be prescribed at the boundary. A backpressure that produces a mass flow rate equal to the integrated input flow rate from the supply grill, and back panel is selected by running the CFD code several times. This is a subsonic outflow, and only one flow variable, in this case pressure, can be specified. The rest of the information (U, V, and T) has to be taken from the interior nodes. Since the net mass flow rate into the case should be zero, any spillage can directly be related to the entrained air. There is a supply of cold air through a perforated back panel with a very small inlet velocity (see Fig. 1(d)). In the simulation model, the amount of this cold air supply is uniformly distributed throughout the back panel. Since the mass balance is of the primary interest of this work, the net inflow of mass into the display case could not be compromised in the calculations. However, the uniform distribution of mass over the back panel will somewhat affect the temperature distribution in the display case and will cause a minor shift in the position of the cold air curtain as it will be seen from the results.

The amount of mass supplied from the discharge air grill and perforated back panel must be equal to the mass leaving the domain from the return air grill. Therefore, the amount of air leaving the display case by spillage can be marked by a negative axial velocity component (U), and the amount of air entering the display case can be marked by a positive axial component of velocity. The integrated mass flow across the negative U stencil represents the amount of spillage. This quantity is equal to the amount of mass flow rate across the positive U stencil. Calculation of the infiltration rate via the DPIV method verifies our numerical simulation method.

In the present analysis the Chien k-ε turbulence model for low Reynolds number is used. To carry the model to the wall a high-resolution grid is needed that causes a significant increase in the computational time. To avoid this problem, the two-equation k-ε model is used for the core flow and is linked to Cebeci-Smith algebraic model near the wall region. Although this method requires more programming skills, it is generally more advantageous over the law-of-the-wall approach. The edge of the sub layer where the algebraic and k-ε models are coupled can be determined by the Baldwin-Lomax vorticity, or total enthalpy criteria. These methods are described in [10, 11].

In the simulation model, the turbulence production term (k) was assumed to be 7.5% of the square of the average total velocity, i.e., $k=0.075\overline{V}^2$. Turbulent dissipation was taken from the one equation model, i.e., $\varepsilon=C_D k^{2/3}/\ell$, where ℓ is the mixing length taken from the previous time step ($\ell=\nu_T/\sqrt{k}$), and C_D is the closure coefficient taken to be 0.08. These boundary conditions will reproduce the same turbulence intensity as measured data at the discharge air grill.

Verification and Validation of Results

Two components of the inlet air jet velocity profile near the discharge grill are shown in Fig. 4. At the discharge grill, the velocity is not uniform. For a perfectly symmetrical and undisturbed flow, the maximum vertical velocity occurs at the center and changes to zero at the wall. However, due to the subsonic nature of the flowfield, i.e., the elliptic characteristic of the NS

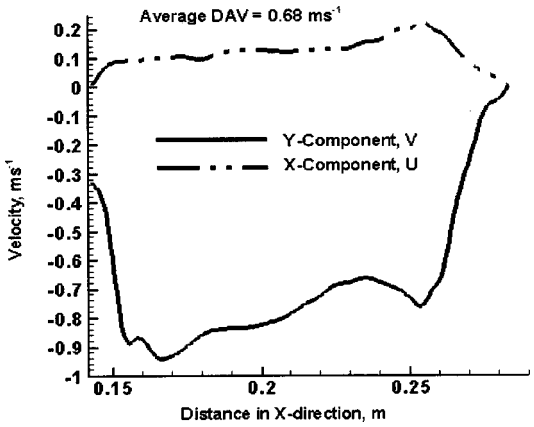

Fig. 4 Air velocity profile at the display case outlet for Scenario 1

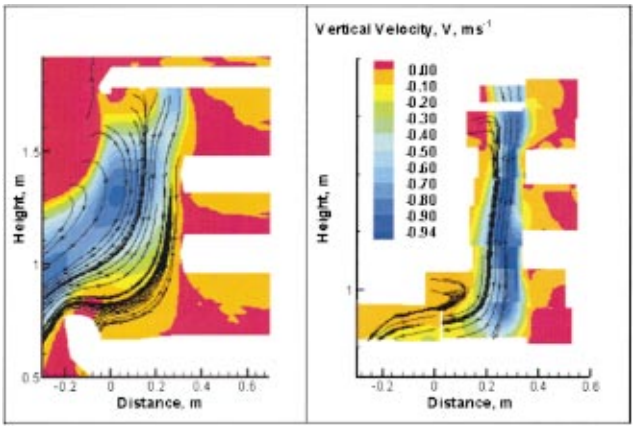

Fig. 5 Mean velocity and streamline fields for Scenario 1

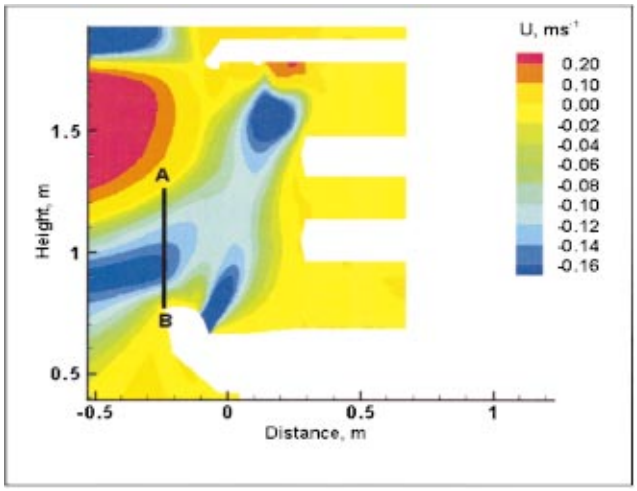

Fig. 6 Axial velocity contours at the opening

equations, this ideal profile will be disturbed. Furthermore, the cold air discharge velocity profile depends on the movement of air throughout the entire domain, that is, the display case and ambient air. The horizontal component is seen to be positive, indicating that the flow is moving towards the display case at the edge of the grill. This may be a result of the design of the discharge grill geometry. The velocity boundary conditions for the CFD analysis were taken from this measurement. In CFD modeling, the products in the display case were also included and they were treated as a no-slip adiabatic wall. Although the surface temperature of the products can be measured and used as a boundary condition in the CFD code, it was decided to adopt a simple adiabatic wall condition due to small effects of temperature on the infiltration rate.

Figure 5 compares the predicted and observed vertical velocity contours and streamlines. Note that the velocity scales are identical for computational and experimental results. Streamlines obtained by CFD and experimental results reveal the nature of the interaction of the two-dimensional jet flow with the surrounding area. The streamlines emanating from the jet at the top of the display case are turned into the display case. This jet then flows downward across the edges of the upper shelves, and onto the lower shelf. When the jet reaches the lower shelf, it turns toward the left and outside of the display case. The vertical velocity contours show that the flow between the shelves is rather stagnant and hardly moves as compared with the air curtain. Therefore, it is postulated that it may take some time before steady-state temperatures are reached between the shelves once the refrigeration system is turned on. Streamline and velocity plots in Fig. 5 show that, for the most part, the jet is rather effective in creating an air curtain. However, this curtain does spill over at the lower part of the display case near the return air grill. This provokes an entrainment from ambient air. The spillage to the outside of the case is a source of discomfort to people in the vicinity. There is not a straightforward way to quantify the amount of the entrained ambient air.

As can be seen from Fig. 5, the entrained air is entering into the display case through a mixing process. This mixing mechanism for air contributes to the amount of the entrained ambient air. Figure 6 is a contour plot of the axial component of the velocity, and will provide the key to this calculation. Basically the entrained air replaces the amount of air that is spilled over from the display case. It is clear that the x-component of the velocity, U going toward the left, i.e., the negative x-direction, is the sole contributor to the spillage phenomenon in the numerical simulation as it was described earlier. Therefore, a line that originates from the bottom edge of the opening and extends to a location where $U=0$ before it becomes positive, i.e., spans over all negative values of U, represents the surface that the air is moving through and resulting in spillage. The AB line in Fig. 6 marks the negative U stencil. Therefore, integrating the velocity over this area will yield the volumetric flow rate of the spilled air that is equivalent to the entrained ambient air or the infiltration rate.

As was mentioned earlier, it is quite important to predict the amount of warm air that flows into the display case due to the overspill of the cold air. This infiltration rate is most likely a function of velocity for a given geometry and design. The continuity equation determines the amount of mass that is being transported from one location to another. For a fixed geometry, the characteristic length or area remains constant. On the other hand, due to the relatively incompressible nature of the flow, small temperature changes of the supplied cold air, and the fixed ambient air temperature, the density variation has a second order effect on the mass flow rate. Therefore, velocity emerges as the main flowfield parameter that controls the mass flow rate, that is, the infiltration of the ambient air into the display case. Furthermore a quantitative comparison between CFD and DPIV results for both components of velocity along the opening of the display case becomes indispensable. Figure 7 compares components of velocity that are extracted from the field data along a line that connects the bottom part of the display case near the return air grill to the discharge air grill. In Fig. 7, the data is extracted from Fig. 5 via the Tecplot©

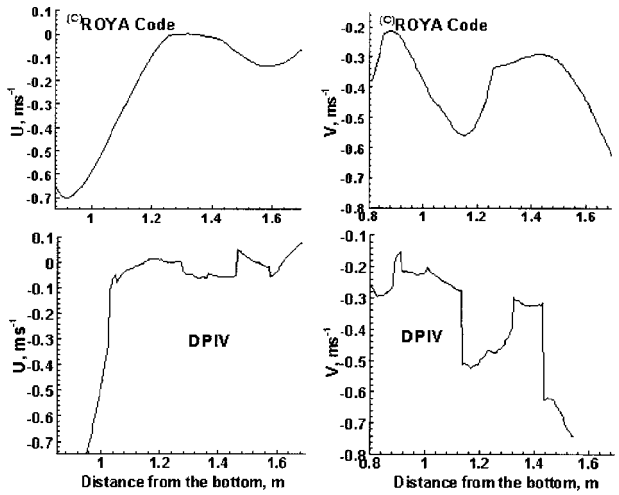

Fig. 7 Components of velocity profile along the display case opening as predicted by the CFD and DPIV techniques for Scenario 1

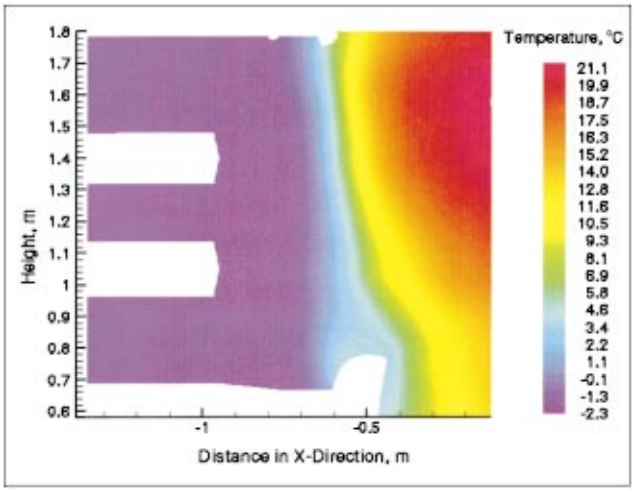

Fig. 8 CFD results for temperature contours in Scenario 1

program. In DPIV, the overall flowfield behavior is mapped by combining several frames. However, these frames may not be connected perfectly, i.e., there might be a gap, or slight overlap between frames. For these reasons, sometimes a sudden jump in the experimental results may be observed as the data is being extracted on a continuous line along the opening. A good agreement between the CFD model prediction and DPIV results can be observed.

It should be noted that we are performing a ''global'' comparison because the flowfield quantities such as the velocity components and turbulence intensity are not compared at a specific location. However, the end results, i.e., the infiltration rate and temperature field are of great practical importance, and conform part of the main focus of this paper. The comparison of the local velocity and turbulence intensity was performed, and will be the subject of another article. However, it should be mentioned that the rms (Root Mean Square) of the components of the velocity at the discharge grill is about $0.04\ \mathrm{ms}^{-1}$, i.e., nearly 6% of the average velocity that reflects a turbulence intensity of 0.06. This quantity increases to $0.178\ \mathrm{ms}^{-1}$ in the shear layer and in the vicinity of edges. This quantity corresponds to a turbulence intensity of about 20%.

Figure 8 shows the temperature distribution predicted by the CFD model. The surroundings or far-field temperature is assumed to be 70°F (21.1°C). The space above the upper shelf is maintained as the coldest spot in the entire display case. This can be attributed to the positive component of axial velocity at the discharge grill as is seen in Fig. 4. Furthermore, Fig. 5 reveals somewhat stagnant air over the shelves contributing to fairly uniform cold temperature after achieving steady-state operation. However, this pattern breaks down toward the bottom shelf, due to a relative increase in mixing length and consequently the turbulence intensity. The onset of the break down of the jet emanating from the discharge grill is a function of the jet velocity, and also the structure of the mixing region that contributes to the infiltration of the outside air. That is, as the vortex that is mainly responsible for the mixing becomes closer to the display case, it will ''sandwich'' the jet, which causes a reduction in the mixing length, therefore resulting in a more ''stable'' jet. So, it is quite possible that jets that possess lower velocities may break down earlier and spread the cold air over a wider region due to a ''weaker'' vortex structure in front of them. It can also be seen that temperature outside the display case is colder than the surroundings due to the overspill. This temperature is about 60°F (15.6°C) in the immediate vicinity of the case, and increases to about 70°F (21.1°C) at about 2 ft (0.61 m) away from the middle of the case.

To develop confidence in the CFD prediction for the temperature field, the Refrigeration and Thermal Test Center at SCE performed an infrared imaging of the display case, and also closely monitored and maintained the DAV and DAT to establish a benchmarking set of data for CFD temperature profile validation. Figure 9 shows the infrared image of the display case with its corresponding temperature field. The infrared temperature readings were calibrated by nine thermocouples located on various locations on the surface of the flat plate, which is a black cardboard with emissivity of 0.96. This plate was located in the middle of air curtain. These thermocouples are traceable to the National Institute of Standards and Technology's standards.

A good comparison between the observed and measured data and its CFD counterpart in Fig. 8 can be observed. It can also be seen that the IR image has a lower resolution than the post-

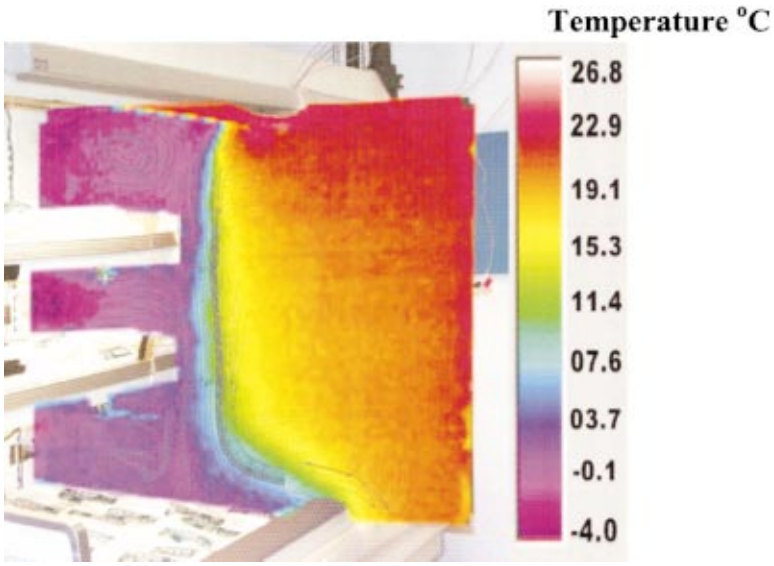

Fig. 9 Infrared image of the tested display case with corresponding temperature profile

Table 2 Point data comparison for temperature in test scenario 1

Location	RAT (°C)	ACT 1/3 (°C)	ACT 2/3 (°C)	Product temperature: Bottom front (°C)	Bottom rear (°C)	Top front (°C)	Top rear (°C)
Measured	5	7.7	5.5	3	−0.1	−1.6	−2.1
CFD	6	7.8	6	2.8	−0.5	−1.9	−2.2

processed CFD results. Furthermore, the field data comparison shows a good ''global'' agreement, i.e., they demonstrate that the air curtain is fairly effective in maintaining the temperature inside the display case over an acceptable range. The inside cold temperature gradually reaches the ambient air temperature due to the existing mixing region in front of the display case. It was mentioned earlier that in the computational model there is a supply of cold air distributed uniformly throughout the back panel. This has caused a slight shifting of the cold air curtain towards the outside of the case. The exact modeling of the perforated back panel is also possible, but time consuming. Since the effects of the temperature is fairly minor and most likely of the higher numerical order on the infiltration rate, no further refinements of the computational modeling of the back panel was performed. However, this global comparison is not sufficient and should be complemented by the point data comparison. To obtain such data, temperature sensors were placed at 1/3 and 2/3 distance of the opening from the discharge air grill or the air curtain temperature (ACT) (see Fig. 1), and at the front and back locations of the bottom and top shelves. One sensor was also placed at the returned air grill location. The computational data can directly be extracted from the temperature contour plot by probing the field. The outcome of the measurements and computation is shown in Table 2.

The purpose of Test Scenario 2 is to demonstrate the dependency of the flowfield variables on the discharge air temperature. Therefore, the velocity of the air at the discharge grill is kept the same as Test Scenario 1, while its average temperature is increased by slightly more than 2°F (0.81°C) as indicated in Table 1. The results of CFD and DPIV studies reveal that the flowfield structure and variables are almost identical to those of Test Scenario 1. The calculated infiltration rate showed about 0.1% and 0.8% decrease for DPIV and CFD results, respectively. How-

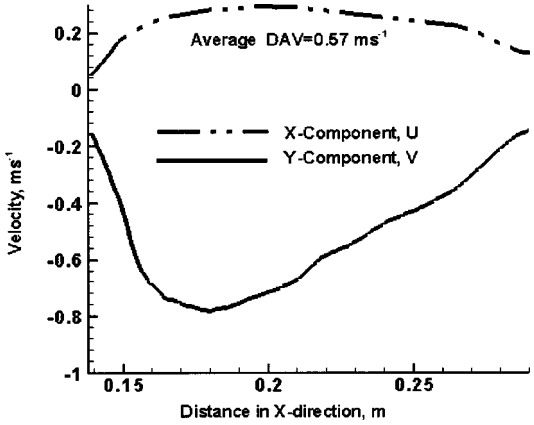

Fig. 10 Velocity profile at the discharge grill for test Scenario 3 predicted by the DPIV technique

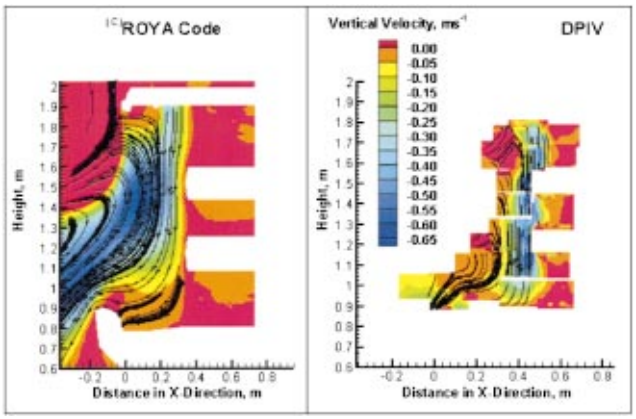

Fig. 11 Mean vertical velocity and streamline fields for test Scenario 3

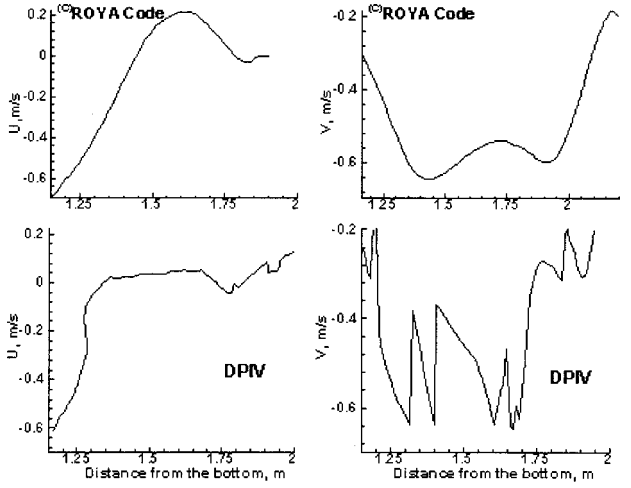

Fig. 12 Components of velocity profile along the display case opening as predicted by the CFD and DPIV techniques for Test Scenario 3

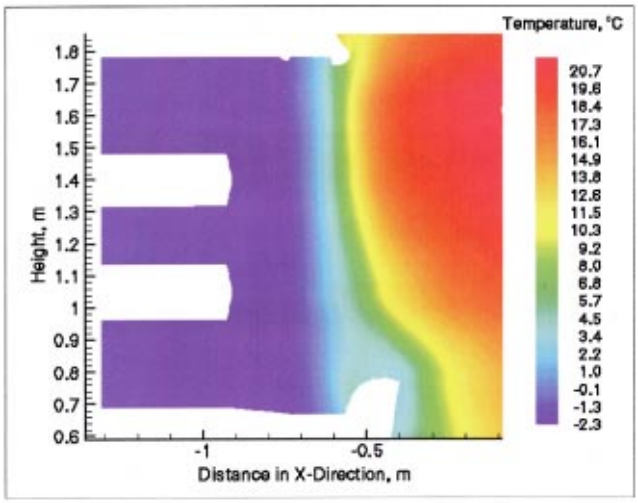

Fig. 13 Temperature contours for test Scenario 3

Table 3 Volumetric flow rate of entrained air in CFM and m^3s^{-1}

Method	Test Scenario 1	Test Scenario 2	Test Scenario 3
DPIV	249.5(0.117751)	249.3(0.1176565)	218.8(0.1032621)
Entrained/Discharged	46.05%	46.56%	47.90%
CFD	251.8(0.118836)	249.9(0.1179397)	221.4(0.1044891)
Entrained/Discharged	47.02%	46.67%	48.47%

ever, no significant global change in the velocity profiles and streamline structure could be detected. Therefore, for the sake of brevity, no graphical display of streamlines and velocity contours is presented.

In Test Scenario 3, the inlet velocity of air at the discharge grill is lowered while the temperature is maintained the same as Test Scenario 1. Figure 10 shows the velocity profile at the discharge grill based on DPIV results. The same velocity profile was used as a boundary condition for the CFD analysis. The results of this Test Scenario 3 will lead to determining the dependency of the infiltration rate and temperature distribution on the momentum of the inlet air. It should also be added the reference coordinates for each test case is self-contained and not necessarily identical for each test case.

Figure 11 compares the vertical velocity contours and streamlines for the CFD and DPIV results. It seems that the flow structure and pattern resemble Test Scenario 1. However, the magnitude of the vertical velocity changes, therefore affecting the infiltration rate of the ambient air. The streamlines in the computational and experimental studies indicate that the inlet jet is still able to act as a curtain, traveling across the edge of the shelves, and downward onto the bottom shelf. The jet then turns to the left, and while some of the flow is brought back through a return grill, most of the jet is seen to be flowing over the edge of the display case to the outside. Though the inlet cold air velocity is smaller than Test Scenario 1, it is still able to entrain ambient air.

The quantitative comparison between the DPIV and CFD results for velocity components, similar to those in Test Scenario 1, is shown in Fig. 12. The velocity components show the same trend and magnitude for DPIV and CFD predictions, implying the accuracy of the CFD modeling.

Temperature contours for the Test Scenario 3 are shown in Fig. 13, and they basically indicate somewhat similar behavior as the Test Scenario 1. However, the colder temperature is further spread to the outside of the display case. This implies a less ''stable'' air curtain where a breakup of the flow is taking place before reaching to the bottom section. Furthermore, the air curtain spreads over a wider region after the onset of instability and causes a broader cold air band toward the bottom of the display case.

The volumetric flow rate of the entrained air into the display case is calculated for each of the above test scenarios using DPIV and CFD techniques independently. The entrained quantities are shown in Table 3. Computational and experimental methods yielded close results. Both approaches indicated that the entrainment rate is more sensitive to the magnitude of the DAV than the DAT. Furthermore, more than 40% of the total mass involved in the cooling is always ''fresh and warm'' ambient air that will significantly increase the cooling load.

Extension of Results

Reconciliation of the computational results with DPIV techniques developed a high degree of confidence in the CFD modeling approach used in this project. Based on the CFD methods used in this project, a parametric study has been performed to obtain the dependency of the infiltration rate of the ambient air on a wider range of the average velocity and temperature of the discharged air for the same geometrical configurations. For this purpose, the average discharged air velocity is varied from 90 to 180 ft-min^{-1} (0.4579 to 0.9144 ms^{-1}), and the average temperature ranges from 15 to 70°F (−9.45 to 21.12°C). In actual applications, however, open vertical, medium temperature display cases typically operate at much higher discharge air velocities than 90 ft-min^{-1} (0.4579 ms^{-1}).

The results of CFD simulation are graphically depicted in Fig. 14. The simulation results are curve fitted with a parabola, and again signifies the fact that the infiltration rate is a very weak function of the discharge air grill temperature and is mostly momentum driven. Furthermore, it can be seen that a decrease in the discharge air temperature will slightly increase the infiltration rate. The values in Table 3 can also be identified on this figure. However, it can be seen that the given parabola is very close to a line, and for simplicity and practical engineering problems a linear curve fit may be sufficient. Figure 15 shows a linear curve fit of

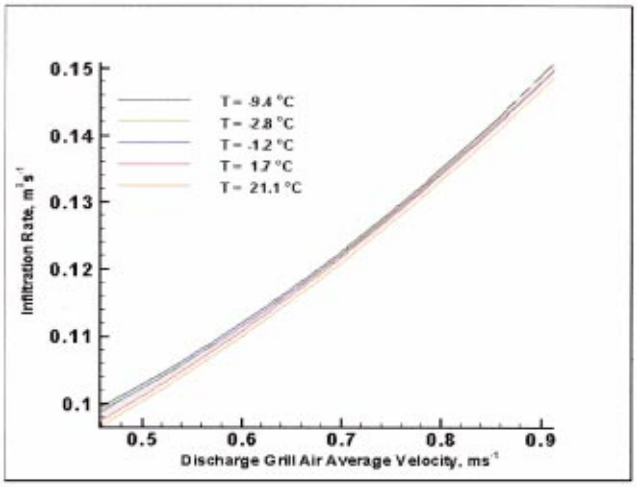

Fig. 14 Infiltration rate as a function of the discharge air average velocity and temperature by parabolic curve fit

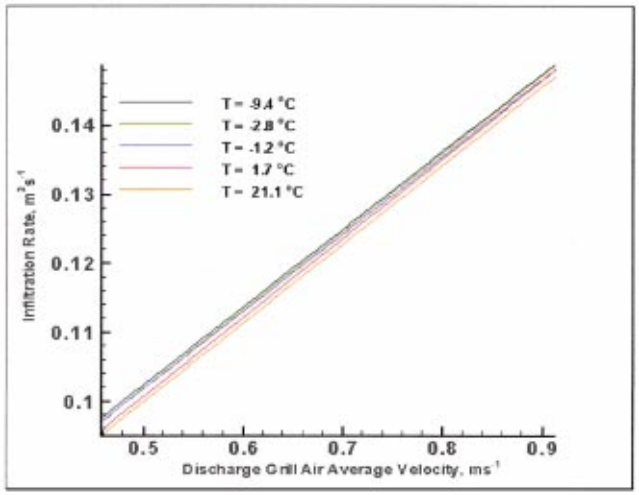

Fig. 15 Infiltration rate as a function of the discharge air average velocity and temperature by linear curve fit

the CFD simulation results, and they are very close to the results presented in Fig. 14. It can also be concluded that in cases where a high level of accuracy is not required, the temperature dependency of the infiltration rate might be thoroughly eliminated, and all curves or lines be collapsed into a single parabolic or linear curve. The maximum possible error in eliminating the temperature dependency can be calculated from either Fig. 14 or 15 to be about 2.5%. This can be evaluated from the volumetric flow rate difference between the minimum and maximum temperatures. The results of this parametric study provide information on the infiltration rate as a function of the discharge air velocity (DAV), and can be widely utilized by engineers to evaluate the cooling load and energy requirements for this particular display case. It is evident that the extension of these results to different display cases will provide valuable information to engineers, and will cut down the time consumed to evaluate cooling load calculations.

Conclusion

The combined computational and experimental study performed in this project demonstrates that calibrated CFD modeling can be used as a reliable and feasible tool for prediction of infiltration quantities in an open vertical display case. The project focused on examining the effects of DAV and DAT variation on the entrainment of air across the air curtain of one particular display case. Based on this approach, it was found that entrainment of air across the air curtain is predominantly momentum driven. Based on the results of this project, and without investigating the effects of other factors such as discharge air grill width or number of air bands, it can be concluded that changes that lead to better performance of the air curtain must primarily affect the momentum of the flowfield. This conclusion sets forth some of the options that are available for optimization of the air curtain design, such as the velocity distribution and its magnitude at the discharge grill. This paper also demonstrates that calibration of a CFD model with reliable and comprehensive experimental data is a prerequisite for generating reasonable and acceptable results. The marriage of the CFD simulation tool with powerful DPIV techniques can serve as an effective approach in design optimization of display case air curtains.

Nomenclature

ACT = Air Curtain Temperature
(1/3 X: at 1/3 of the opening distance from the top)
(2/3 X: at 2/3 of the opening distance from the top)
CFD = Computational Fluid Dynamics
CFM = Cubic Feet per Minute
DAT = Discharge Air Temperature
DAV = Discharge Air Velocity
DPIV = Digital Particle Image Velocimetry
LDV = Laser Doppler Velocimetry
NASA = National Aeronautics and Space Administration
NS = Navier-Stokes
RAT = Returned Air Temperature
RTTC = Refrigeration and Thermal Test Center

References

[1] Faramarzi, R., 1999, "Efficient Display Case Refrigeration," ASHRAE J., Nov., pp. 46–51.
[2] Stribling, D., Tassou, S. A., and Mariott, D., 1999, "A Two-Dimensional CFD Model of a Refrigerated Display Case," ASHRAE Trans., Nov., pp. 88–94.
[3] Navaz, H. K., 2000, ROYA©: A 2-D/3-D Code for Compressible, Incompressible Flows and Heat Transfer in Solids, Users Manual.
[4] Willert, C. E., and Gharib, M., 1991, "Digital Particle Image Velocimetry," Exp. Fluids, **10**, pp. 181–193.
[5] Westerweel, J., Dabiri, D., and Gharib, M., 1997, "The Effect of a Discrete Window Offset on the Accuracy of Cross-Correlation Analysis of PIV Recordings," Exp. Fluids, **23**, pp. 20–28.
[6] Gharib, M., and Dabiri, D., 1999, *An Overview of Digital Particle Image Velocimetry in Flow Visualization: Techniques and Examples*, Smiths, A. and Lim, T. T., eds.
[7] Navaz, H. K., and Dang, A. D., 1994, "The Development of the Liquid Thrust Chamber Performance (LTCP) Code for Turbulent Two-Phase Flow Combustion of Dense Sprays," Final Report Prepared for NASA/MSFC, Contract No. NAS8-38798.
[8] Navaz, H. K., and Berg, R. M., 1999, "Formulation of Navier-Stokes Equations for Moving Grid and Boundary," J. Propul. Power, **15**(1), Jan.–Feb.
[9] Navaz, H. K., and Berg, R. M., 1998, "Numerical Treatment of Multi-Phase Flow Equations with Chemistry and Stiff Source Terms," J. of Aerospace Science and Technology, **2**(3), Mar.–Apr., pp. 219–229.
[10] Dang, A. L., Navaz, H. K., and Coats, D. E., 1988, "PNS Solution of Non-Equilibrium Reacting Flow In Rocket Nozzles," 25th JANNAF Combustion Meeting, NASA/MSFC, Huntsville, AL.
[11] Berker, D. R., Coats, D. E., Dang, A. L., Dunn, S. S., and Navaz, H. K., 1990, "Viscous Interaction Performance Evaluation Routine for Nozzle Flows with Finite Rate Chemistry, (VIPER)," Final Report (Phase III) and Computer Users' Manual, Prepared for the Air Force Astronautics Laboratory, Edwards Air Force Base, California, Report No. AL-TR-90-042.

C. van Lookeren Campagne
Research Engineer

R. Nicodemus
Research Engineer

Robert Bosch GmbH,
Postfach 300 240,
D-70442 Stuttgart, Germany

G. J. de Bruin[1]
Research Engineer

D. Lohse
Professor

The University of Twente,
Department Applied Physics,
PO Box 217,
NL 7500 AE Enschede, Netherlands

A Method for Pressure Calculation in Ball Valves Containing Bubbles

A method of analyzing bubbly flow in a ball valve in a hydraulic circuit is presented. The dynamics of a single bubble can be well described by a quasi-static approximation of the Rayleigh-Plesset equation. Hence the presence of bubbles in low volume fractions can be modeled through an effective compressibility of the flow, which is easy to implement in commercial CFD packages. In the sample valve, a volume fraction of 4% air bubbles results in a mass flux reduction of up to 10%, as the bubbles expand due to the pressure drop in the valve and partly block it. [DOI: 10.1115/1.1486220]

1 Introduction

A common type of valve in mobile hydraulic systems is the ball valve (see Bosch [1]). Basically, it consists of a cone-shaped seat, where a ball can be pressed into the seat by a spring or a magnetically actuated poppet, see Fig. 1. Applying a sufficiently large pressure difference across the valve, the force holding the ball in the seat will be overcome and the valve opens.

A frequent design requirement is to maximize the mass flux during the time the valve is open. Gas bubbles in the flow can counteract this aim, because they expand when entering the low pressure regime and thus partially block the valve.

The aim of the work presented in this paper was to investigate, by analysis and simulation, how gas bubbles and liquid interact and affect the functioning of the valve. A number of simplifications have been imposed. First, the bubbles are assumed to consist of air. Any vapor fraction in the bubbles is neglected. Second, the formation of new bubbles is not examined. Dissolution of air, due to local temperature or pressure changes, is neglected. Third, no investigations were made into the size of the bubble nuclei entering the valve. Bubbles with ambient radii between 20 and 200 μm are assumed to be present in the valve. For the sample valve in this article, the maximum bubble size is limited by the hydraulic circuit of which it is a part. A typical length scale of the valve is 1 mm. Further characteristics of this example problem are the high viscosity, $\mu = 0.27\ \mathrm{kg\,m^{-1}\,s^{-1}}$, the surface tension at the interface air-liquid, $\sigma = 0.035\ \mathrm{N\,m^{-1}}$, and a 4% volume fraction of air. The speed of sound in the liquid without bubbles is $c_l = 1493\ \mathrm{m\,s^{-1}}$ and the density is $\rho_l = 1092\ \mathrm{kg\,m^{-3}}$.

The paper first examines how a single bubble reacts to the pressure field in the valve. In Section 3, a density function is constructed which describes the density of the air-liquid mixture as a function of the pressure. This approach is possible only because Section 2 shows the bubble dynamics to be of secondary importance for the sample valve. If this were not the case, the density at a point in the flow field would depend on the pressure at that point *and* on the pressure history along the streamline through the point in question. As the streamline is the result of the flow field being calculated, some complicated iterative process would then be needed to solve the problem.

Determining the volume-averaged density is still not straightforward, because it should depend on the bubble size distribution. Due to the surface tension, the total volume occupied by the gas bubbles is nonlinearly dependent on the pressure. Some knowledge of the number of bubbles present and the initial values of their radius seems necessary. However, it will be shown that, for the size of bubble assumed to be present in the sample valve, different distributions of bubble size lead to almost the same result. So one may choose the simplest.

Being now supplied with a well-justified pressure-density relation for the bubbly flow in the valve, we perform, in Section 4, a full numerical simulation of the flow through the sample valve with a commercial CFD-Package. Conclusions will be contained in Section 5.

2 Calculations on a Single Bubble

We first focus on a single bubble. It is assumed that the bubble travels along a streamline through the valve. The local pressure on the bubble is used as input to determine the development of the bubble radius.

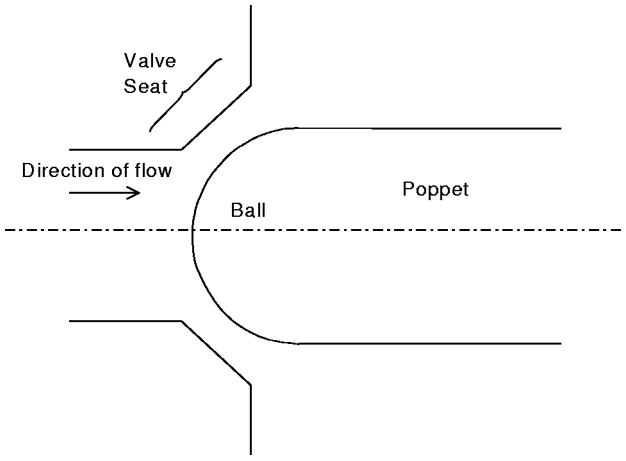

Fig. 1 Sketch of the main features of the ball valve

[1]Corresponding author.

Contributed by the Fluids Engineering Division for Publication in the JOURNAL OF FLUIDS ENGINEERING. Manuscript received by the Fluids Engineering Division May 19, 2000; revised manuscript received January 14, 2002. Associate Editor: Y. Matsumoto.

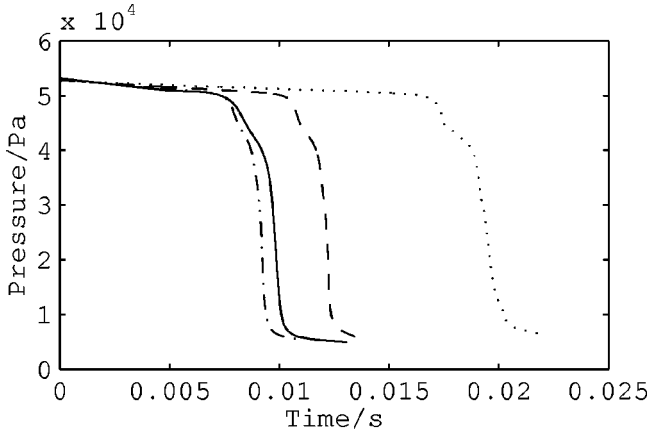

Fig. 2 Pressure development along four different streamlines in the example valve

2.1 The Driving Pressure of the Bubble. For the sample valve results of a 3D flow simulation were used to find the pressure along a streamline. The presence of the bubbles was not taken into account, but was based on a model for compressible flow.

Some examples of pressure development along streamlines through the valve in the fully open position are given in Fig. 2. The pressure drop occurs in two stages. The fluid motion through the valve has swirl and is not strictly rotational symmetric. Also a sealing lip in the seat of the sample valve makes the geometry and the flow more complicated. This leads to a pressure reduction in two stages, instead of the more straightforward pressure reduction one would get for a valve like the one in Fig. 1.

To be able to make some general statements, not limited to the present example, the bubble response is also calculated using some conceived functions as input, having the advantage that parameters can be varied.

As model function a pressure drop is taken, which is sufficiently smooth to pose no problems for the integration, see Fig. 3.

The pressures at the inlet and outlet of the ball valve are p_0 and p_1. This pressure drop occurs within a time interval Δt, being the time it takes the bubble to traverse the valve.

2.2 Bubble Dynamics. Using the terminology in Hilgenfeldt et al. [2], Leighton [3], and Brennen [4] the following equation will be referred to as the Rayleigh-Plesset equation:

$$\rho_l\left(R\ddot{R}+\frac{3}{2}\dot{R}^2\right)=p_{\text{gas}}-p_{\text{ext}}-\frac{4\mu\dot{R}}{R}-\frac{2\sigma}{R}+\frac{R}{c_l}\frac{d}{dt}p_{\text{gas}}. \quad (1)$$

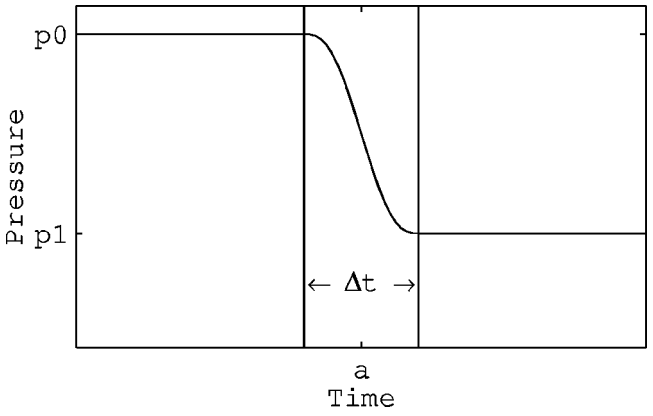

Fig. 3 Polynomial approximation of the pressure drop in the ball valve

Equation (1) takes the compressibility of the liquid into account to a limited extent, through the last term in the equation. This term represents the pressure associated with emitted sound waves.

As stated in the Introduction, two possible processes of mass transfer between fluid and bubble are neglected in the analysis: dissolution of air in/out the hydraulic liquid and evaporation/condensation of the hydraulic liquid.

The influence of phase changes of the hydraulic liquid is neglected, because the vapor pressure is much smaller than the pressure of air in the bubble. The values of the pressure before and after the valve are known (55,000 Pa and 5000 Pa respectively for the example). Since the value of the vapor pressure is of the order of several hundred Pa, it is reasonable to assume that the pressure never drops below the vapor pressure. The influence of gas dissolution is also neglected. The solubility is strongly dependent on temperature and weakly dependent on pressure. The temperature, however, remains constant in the example. Dissolved air can be released from the liquid by diffusion. The diffusion length scale is given by:

$$l=\sqrt{\pi D\Delta t}. \quad (2)$$

For the problem examined as an example, $D\sim 2.6\cdot 10^{-10}$ m^2 s^{-1}. Using a characteristic time scale of $\Delta t\sim 3\cdot 10^{-4}$ for the bubble dynamics, as calculated later on, the diffusion length scale is 0.5 μm, much smaller than the bubble radius: the influence of gas dissolution can therefore also be neglected.

The behavior of the pressure of the gas in the bubble is polytropic. Because the Péclet number $R\dot{R}/U\ll 1$, the isothermal limit (see Plesset and Prosperetti [5]) is considered:

$$p_{\text{gas}}=\frac{\left(p_0+\frac{2\sigma}{R_0}\right)(R_0^3-h^3)}{R^3-h^3}; \quad (3)$$

$h=R_0/8.85$ is the v.d. Waals' hard core radius.

The eigenfrequency ω of the bubble (Minnaert frequency) follows from linearizing the Rayleigh-Plesset equation (see Brennen [4]):

$$\omega^2=\frac{3R_1}{\rho_l}\left(p_0+\frac{2\sigma}{R_0}\right)\frac{(R_0^3-h^3)}{(R_1^3-h^3)^2}-\frac{2\sigma}{\rho_l R_1^3}. \quad (4)$$

A characteristic time scale based on the Minnaert frequency $\tau_c=2\pi/\omega$ will be needed later for comparison with other time scales, notably the time interval needed for the passage of the bubble through the valve.

The important aim of this research is to investigate how the bubble responds to a pressure drop: will the bubble expand and collapse violently (undesired) or does it exhibit a delayed expansion (favorable, since the expansion would take place behind the valve)? It will turn out that the latter is the case and that it is even possible to use a quasi-static approximation to describe the bubble behavior. This approximation, see e.g., Hilgenfeldt et al. [2], consists of dropping all derivatives with respect to time in the Rayleigh-Plesset equation

$$0=\left(p_0+\frac{2\sigma}{R_0}\right)\left(\frac{R_0^3-h^3}{R^3-h^3}\right)-\frac{2\sigma}{R}-p_{\text{ext}}(t), \quad (5a)$$

which is a simple fourth-order polynomial expression for $R(t)$.

Neglecting the hard core radius $h\ll R_0, R$, it reduces to a third-order polynomial

$$\frac{-p_{\text{ext}}(t)}{p_0}R^3-\frac{2\sigma}{p_0}R^2+\left(1+\frac{2\sigma}{R_0 p_0}\right)R_0^3=0. \quad (5b)$$

In this approximation $R(t)$ can be given analytically in terms of $p_{\text{ext}}(t)$.

A concept used in the study of the acoustical behavior of bubbles is the Blake radius (see e.g., Hilgenfeldt et al. [2] or Leighton [3]). Bubbles smaller than the Blake radius display quasi-harmonically oscillating behavior, larger ones exhibit rapid

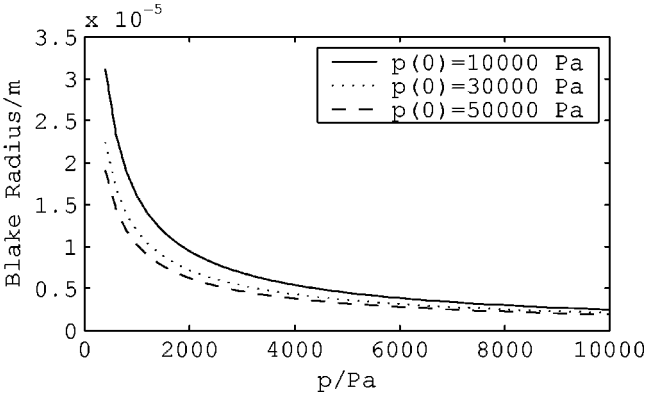

Fig. 4 Blake radius for different combinations of final and initial pressure

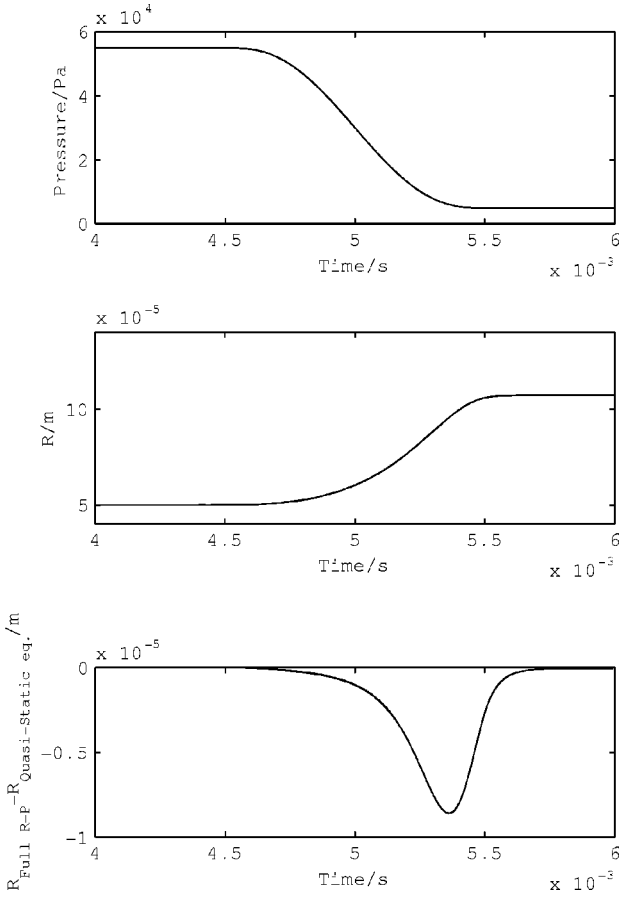

Fig. 5 Bubble radius response for a slow drop in pressure. $\Delta t = 1$ ms, $\tau_c = 28$ μs. (*a*) External pressure; (*b*) bubble radius development; (*c*) difference between the solution of the full Rayleigh-Plesset equation and the quasi-static approximation.

collapses. In the latter case, a complete description of the bubble behavior requires the use of the Rayleigh-Plesset Eq. (1), rather than Eq. (5).

The Blake radius as a function of the pressure amplitude can be calculated from Eq. (5*b*), see Eq. (3.4) in Hilgenfeldt et al. [6], and is displayed in Fig. 4. From that figure it can be concluded, that for the relatively small bubbles and small pressure amplitudes relevant to this study, the bubbles remain below the Blake threshold throughout.

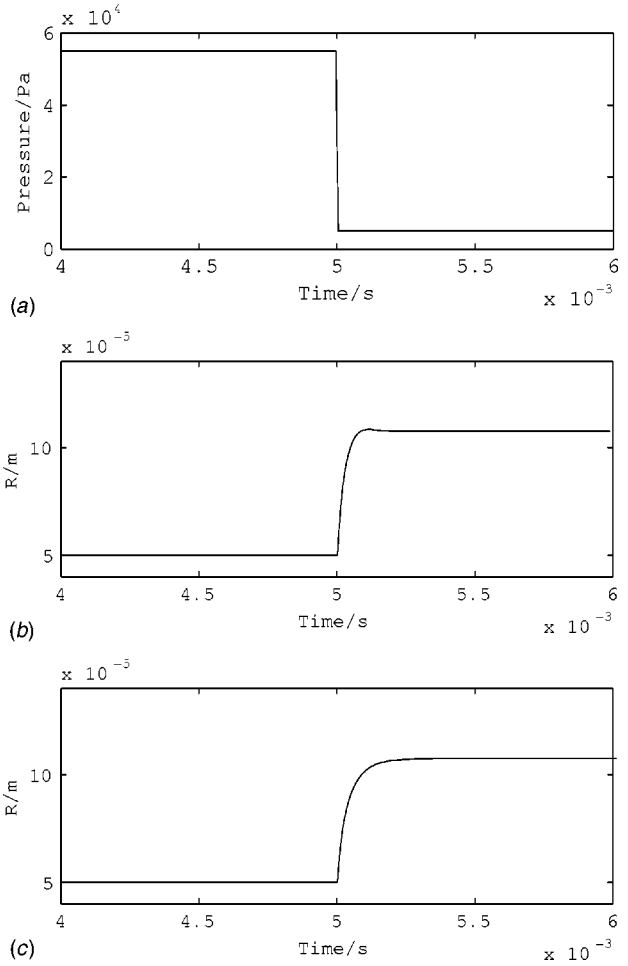

Fig. 6 Bubble radius response for a relatively steep drop in pressure. $\Delta t = 1$ μs, $\tau_c = 28$ μs. (*a*) External pressure; (*b*) bubble radius development for a relatively small value of the viscosity, $\mu = 0.17$ m^2 s^{-1}; (*c*) bubble radius development for a higher value of the viscosity, $\mu = 0.27$ m^2 s^{-1}.

To confirm this, the bubble dynamics were determined by numerically integrating the full ODE (1) with the model pressure function $p_{\text{ext}}(t)$ given in Fig. 3.

Three qualitative responses can occur, depending on the ratio of $\Delta t/\tau_c$ and on the value of the viscosity. Figures 5 and 6 show the response of a bubble with an initial radius of 50 μm. The bubble response is qualitatively independent of the initial bubble radius, but depends on the ratio of Δt and τ_c. If Δt is of the same order as τ_c or smaller, then the response will not follow the pressure closely. Figure 5 shows the bubble response for a pressure drop that occurs on a time scale comparable to that found along a streamline in the sample valve. The quasi-static approximation (5*b*) introduces only a small error, see Fig 5(*c*). The bubble response to steep pressure drops is shown in Fig. 6. If the viscosity is large, the bubble radius will lag behind the pressure, as in Fig. 6(*c*). For lower values of the viscosity, the bubble radius will exhibit overshoot, as demonstrated in Fig. 6(*b*). Figure 7 shows the bubble response to the pressure development actually found in the 3D simulation of the flow through the example valve. Larger pressure drops however can initiate much more violent bubble collapses and the quasi-static approximation would break down. Examples are jet cavitation (Cerutti et al. [7]), cloud cavitation (de Lange et al. [8]), edge cavitation (Young [9]), or sonoluminescence (Crum [10] and Brenner et al. [11]).

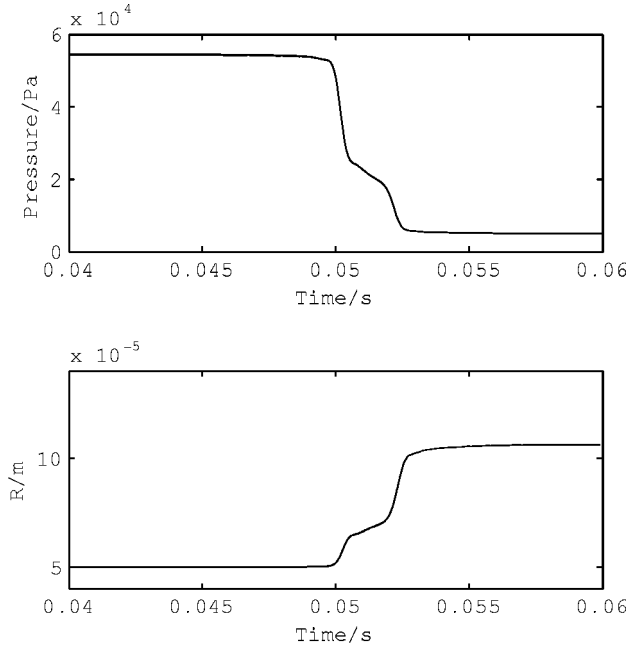

Fig. 7 Bubble radius response to the pressure development in the example valve. (*a*) External pressure; (*b*) bubble radius development.

2.3 Shape and Shape Stability. The Rayleigh-Plesset equation, describing the bubble in terms of its radius, assumes a spherical bubble. For the sample problem, some of the bubbles simply become too big to pass through the opened valve without deformation from the spherical shape. Another reason why the bubble might not be spherical is the pressure gradients in the seat area of the valve, leading to a pressure difference across the bubble, which might cause the bubble to lose its spherical shape. To estimate whether this is likely, a comparison with bubbles in a gravitational field is made by replacing in the usual Morton number $M=g\mu^4\Delta\rho/\rho^2\sigma^3$ and the Eötvös number $Eo=g\Delta\rho d^2/\sigma$ the buoyancy force per unit volume $g\Delta\rho$ simply by $|\nabla p|$. In addition to M and Eo, of course the Reynolds number $Re=\rho dU/\mu$ plays a role.

Clift et al. [12] give an overview which bubble shape to expect for a given set of values of the dimensionless variables. For the main flow area, away from the walls, pressure gradients in the sample valve are at most $4\cdot10^7\ \mathrm{Pa\,m^{-1}}$. For the bubbles small enough to fit into the valve opening $Re<1$ and the Morton number is of order 4000, putting those bubbles firmly in the spherical range.

Finally, the stability of the bubble to shape perturbations is examined. This tests whether the bubble returns to a spherical shape after a distortion of this initial shape. Following the analysis of Hilgenfeldt et al. [2] or Prosperetti [13], we find that decay times for the perturbation were found between 0.001 and 0.005 s. In this analysis, homogeneous conditions inside the bubble have been assumed, thus neglecting heat losses, which cause extra damping, see Hao et al. [14] or Brenner et al. [15]. The spherical shape of the bubble is therefore very stable.

3 Modeling the Density of a Bubbly Fluid

In the quasi-static approximation, the volume of a bubble at a certain point only depends on the pressure *at that point*. One can therefore look for a function to describe the density of the mixture of air and liquid in relation to the pressure. If we take surface tension into account, then the density will depend on the distribution of initial bubble sizes. A general formula for the density of a mixture of bubbles and liquid, where the initial volume fraction of air is x, is the following:

$$\rho=\frac{\rho_0}{(1-x)+\int_{R_{0,\min}}^{R_{0,\max}} f(R_0)\frac{4}{3}\pi R^3(R_0,p;p_0,\sigma)dR_0}. \tag{9}$$

Here, the function $f(R_0)$, describing the distribution of ambient radii, is defined as:

$$x=\int_{R_{0,\min}}^{R_{0,\max}} f(R_0)\frac{4}{3}\pi R_0^3 dR_0. \tag{10}$$

The initial density of the mixture at pressure p_0 is denoted as ρ_0. The expression used for R, is the quasi-static approximation of Eq. (5). When also surface tension is neglected, the density becomes independent of the ambient bubble radius distribution, and the following expression is found for the density:

$$\rho=\frac{\rho_0}{1-x+x\cdot p_0/p}. \tag{11}$$

However, going one step further and including the surface tension term, the relation between p and ρ becomes dependent on the bubble size distribution. Two bubble size distributions will be considered; a uniform distribution of bubble radii and a Gaussian distribution.

3.1 Uniform Distribution of Bubble Radii. For a uniform bubble size distribution the properly normalized distribution function is

$$f(R_0)=\frac{4x}{R_{\max}^4-R_{0,\min}^4}\frac{3}{4\pi}$$

and the density is described by the:

$$\rho=\frac{\rho_0}{1-x+\frac{4x}{R_{0,\max}^4-R_{0,\min}^4}\int_{R_{0,\min}}^{R_{0,\max}} R^3(R_0,p;p_0,\sigma)dR_0} \tag{12}$$

The integral cannot be evaluated analytically. One could numerically evaluate Eq. (12), but within a CFD-program this would lead to higher calculation times. Therefore we employ an approximation which allows for an analytical solution. We rewrite Eq. (5) as

$$\frac{R_0^3}{R^3}-\frac{p}{p_0}=\frac{2\sigma}{p_0R_0}\left(\frac{R_0}{R}-\frac{R_0^3}{R^3}\right). \tag{13}$$

and linearize around the root of the right hand side. The expression resulting for R is plugged into (12), which is then integrated numerically.

Differences between this method, the full numerical evaluation of the density via (12), and the approximation (11), which neglects surface tension, only arise for low values of the pressure. The difference between the three functions describing the density is, however, at most 0.5% for the sample problem.

3.2 Gaussian Distribution of Bubble Radii. Next an expression describing the density, when the bubble radius distribution is a Gaussian, was also developed. A narrow Gaussian would correspond to a situation where all the bubbles have the same radius. It is opposite to the previous uniform distribution, where all the radii occur equally often.

For simplicity, it is assumed that all bubble radii from R_c down to 0 can initially occur. The density depends on the parameters R_c, the radius b corresponding to the maximum of the Gaussian and λ is a parameter used to set the width of the Gaussian. The expression for the density found in this way is:

$$\rho = \frac{\rho_0}{1 - x + x \cdot \int_0^{R_c} A \cdot \exp\left(\frac{(R_0 - b)^2 \ln \lambda}{(R_c - b)^2}\right) \cdot \frac{4\pi}{3} R^3(R_0, p; p_0, \sigma) dR_0}, \tag{14}$$

where A is defined as:

$$A = \frac{1}{\int_0^{R_c} \frac{4\pi}{3} R_0^3 \exp\left(\frac{(R_0 - b)^2 \ln \lambda}{(R_c - b)^2}\right) dR_0}. \tag{15}$$

The density as described by Eq. (14), was evaluated numerically in order to compare it to the one found from Eq. (11) (the function that neglects surface tension). For a broad Gaussian lying within the range of bubble sizes expected for the example problem, differences between the two functions amount to at most 1%. However, if all the bubbles are smaller than 20 μm, then the difference can be up to 10%. In the last case, one cannot get away with neglecting the surface tension. However, a broader distribution of larger bubbles is assumed in the valve and so for the numerical simulation we can use Eq. (11) as the pressure density relation, and this is what is implemented in the commercial CFD code.

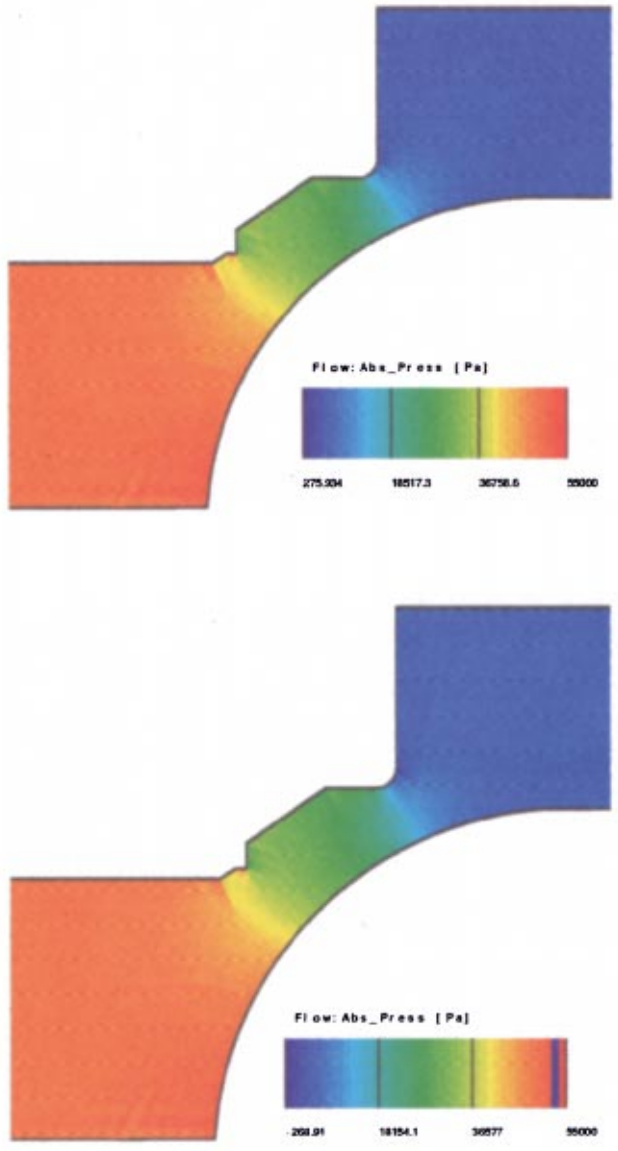

Fig. 8 Pressure field for the example valve. (*a*) With density function; (*b*) without density function.

4 Flow Simulations for the Example Ball Valve

The flow simulations alluded to in previous sections, were carried out using the commercially available CFD package AVL-Fire, a finite volume method. It is fully implicit, all terms containing no time derivatives are evaluated at the new time level. The spatial discretisation is of the hybrid type, switching between central and upstream differencing depending on the local cell Reynolds number. The velocity and pressure fields are linked by a SIMPLE (*S*emi-*I*mplicit *M*ethod for *P*ressure *L*inked *E*quations, see e.g., Ferziger et al. [16]). The resulting linear set of equations is solved by a Conjugate Gradient method for the velocity field. For the pressure a Gauss-Seidel method, combined with black-red SOR (*S*uccessive *O*ver *R*elaxation), is used.

The program can only carry out 3D flow simulations. It would have been possible to set up a geometry for the flow calculations based on the exact drawings of the valve. However, the geometry was simplified to a rotationally symmetrical valve. Only the flow in a 5 deg section was simulated. The program cannot switch to cylindrical coordinates, so the simplification could not really be exploited to the full extent. Indeed, taking such a small section creates a singularity at the valve axis, so the grid has to stop just short of the axis.

Although the flow field of interest is stationary, the flow simulation is that of a transient flow field. This has the advantage that the boundary conditions can be imposed gradually, to avoid sharp pressure gradients from occurring during the simulation. The final distribution of the pressure, resulting from the simulations for compressible two-phase flow, is given in Fig. 8(*a*). As pressure-density relation Eq. (11) was used, as justified in Sections 2 and 3. The pressure distribution in the incompressible monophase flow is given in Fig. 8(*b*).

In the compressible case, the mass flux is reduced by up to 10%, as shown in Fig. 9. This is a considerable amount for various applications. The reason is, of course, that incompressible flow can only respond to a pressure increase at the entrance of the valve by pushing the fluid through the valve, whereas compressible flow can also respond through compression, the bubbles being the origin of the effective compressibility here. This different behavior of compressible and incompressible flow can also be seen in the corresponding velocity fields in Fig. 10. The effect is most visible in the narrowest part of the valve, where a fluid particle experiences a pressure decrease and therefore expands in the compressible case, thus blocking the pathway and leading to a reduction of the velocity and the mass flow.

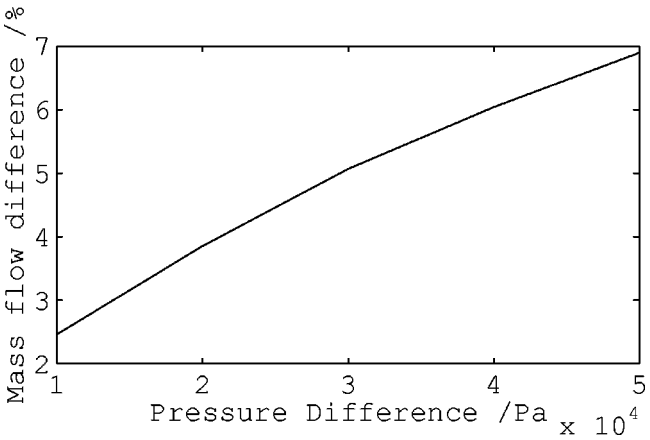

Fig. 9 Relative difference in the mass flow through the sample valve between the compressible and the incompressible calculation

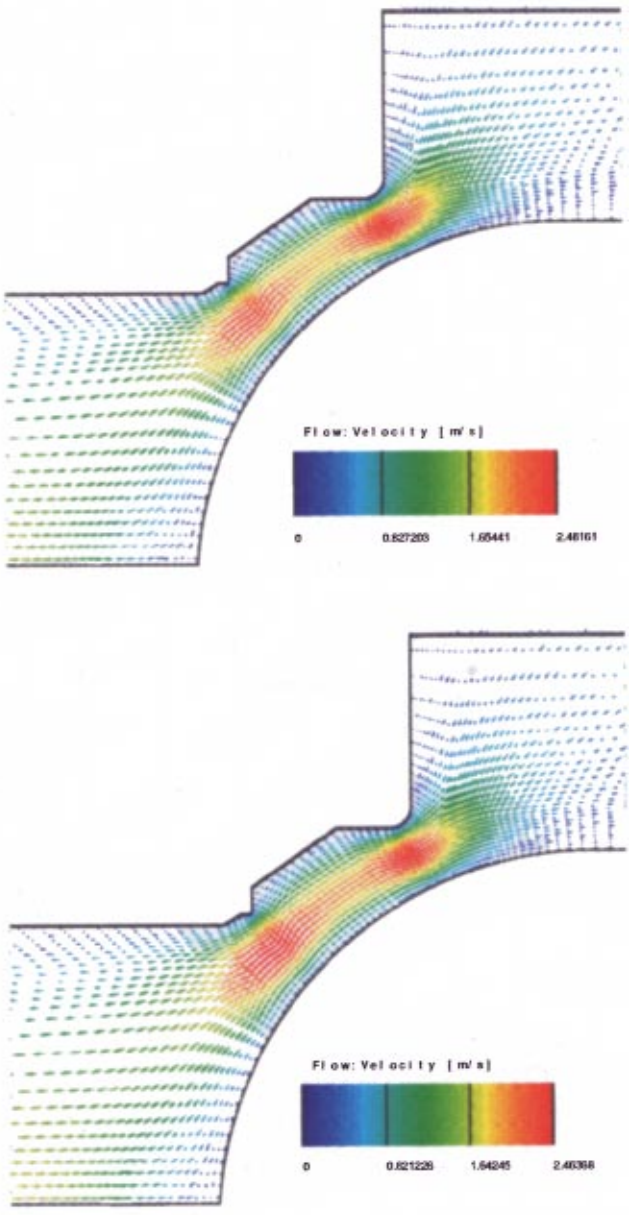

Fig. 10 Velocity vector field within the example valve. (*a*) With density function; (*b*) without density function.

5 Conclusions

In this work, the focus has been laid on calculations for a sample valve. In addition, some general conclusions concerning the procedure can be drawn, that are applicable to other ball valves as well.

First, one needs to have an idea of the properties of the bubbles. The content of the bubble was assumed to be air and a negligible amount of vapor. The size of these bubbles was determined by the dimensions of other elements in the hydraulic circuit. The amount of bubbles was determined from the measured volume fraction of air present.

The bubbles were assumed to be spherical, to be checked in retrospect. A means of doing this is to use perturbation analysis to investigate shape stability. Whether pressure gradients can lead to distortion, can be estimated by calculating the Reynolds number and the analogue of the Morton or Eötvös number. One should estimate, whether the geometry of the valve may lead to bubble deformations, as it obviously does, when the bubble gets too large to fit through the opened valve.

The next step is to specify the pressure drop over the valve, leading to the bubble expansion. The pressure experienced by the bubble as a function of time, is obtained by integrating the pressure along a streamline with a 3D code.

With that function describing the development of pressure in time, one can determine the development of the bubble radius in time. This was done for a number of model functions and for the pressure development extracted from the flow data. To determine the response of the bubble, the Rayleigh-Plesset equation was integrated.

For each bubble radius, a characteristic time scale can be calculated. The response of the bubble to the pressure drop depends on the ratio of the characteristic time scale and the time interval over which the pressure drops. For a fast pressure drop, the bubble can exhibit overshoot and will oscillate toward a final radius, if the viscosity is low. Alternatively, if the viscosity is high, the bubble can increase in size toward the final value, but lagging behind the pressure drop in time. If the pressure drop is not very steep, then the bubble response can be regarded as quasi-static. This is the case for the valve examined as an example. The time derivatives in the Rayleigh-Plesset equation can then be dropped, and one can employ the quasi-static approximation (5), where the presence of bubbles can be taken into account through a pressure-dependent density function.

The next step in the analysis is to find this expression for such a density function. We have shown that the distribution in initial bubble radius sizes has relatively little influence on the density function. If not all the bubbles are very small, surface tension can be neglected and one can use the simplest possible function to describe the density. It is a volume average over the liquid and the gas, neglecting the surface tension altogether. Such a description of the density of the hydraulic liquid with bubbles in it, is easy to implement in commercially available CFD codes like the AVL-Fire code used here.

For the sample valve the presence of bubbles in the flow, causing the effective compressibility, has a considerable blocking effect, reducing the mass flux by up to 10%. The reason is that the bubbles expand when experiencing the decrease of pressure in the valve and thus partly block the flow through the narrowest part of the valve.

In summary, one can see that the combination of parameters in the example valve is very favorable. It has turned out that one can take account of the presence of bubbles in a very simple way. In retrospect, splitting the problem into two parts, namely looking at the influence of bubbles on the flow and that of the flow on the bubbles separately, could have been avoided. Such a split has, however, been necessary just to prove this very fact.

References

[1] Bosch GmbH. R., 1995, ''*Kraftfahrttechnisches Handbuch*,'' 22nd edition.
[2] Hilgenfeldt, S., Lohse, D., and Brenner, M. P., 1996, ''Phase Diagrams for Sonoluminescing Bubbles,'' Phys. Fluids, **8**(11), pp. 2808–2826.
[3] Leighton, T., 1994, *The Acoustic Bubble*, Academic Press, London.
[4] Brennen, C. E., 1995, *Cavitation and Bubble Dynamics*, Oxford University Press, New York.
[5] Plesset, M., and Prosperetti, A., 1977, ''Bubble Dynamics and Cavitation,'' Annu. Rev. Fluid Mech., **9**, pp. 145–185.
[6] Hilgenfeldt, S., Brenner, M. P., Grossmann, S., and Lohse, D., 1998 ''Analysis of Rayleigh-Plesset Dynamics for Sonoluminescing Bubbles,'' J. Fluid Mech. **365**(10), pp. 171–204.
[7] Cerutti, S., Knio, O. M., and Katz, J., 2000, ''Numerical Study of Cavitation Inception in the Near Field of an Axisymmetric Jet at High Reynolds Number,'' Phys. Fluids, **12**(10), pp. 2444–2460.
[8] de Lange, D. F., de Bruin, G. J., and van Wijngaarden, L., 1993, ''Observations of cloud cavitation on a stationary 2D profile,'' Proc. IUTAM Symp.: Bubble Dynamics and Interface Phenomena, J. Blake et al., eds., Kluwer, pp. 241–246.
[9] Young, F. R., 1999, *Cavitation*, Imperial College Press, London.
[10] Crum, L., 1994, ''Sonoluminescence,'' Phys. Today, **47**(9), pp. 22–29.

[11] Brenner, M., Hilgenfeldt, S., and Lohse, D., 2002, ''Single-Bubble Sonoluminescence,'' Rev. Mod. Phys., **74**(2), pp. 425–484.
[12] Clift, R., Grace, J., and Weber, M., 1978, *Bubbles, Drops and Particles*, Academic Press, London.
[13] Prosperetti, A., 1977, ''Viscous Effects on Perturbed Spherical Flows,'' Q. Appl. Math., **25**, pp. 339–352.
[14] Hao, Y., and Prosperetti, A., 1999, ''The Effect of Viscosity on the Spherical Stability of Oscillating Gas Bubbles,'' Phys. Fluids, **11**(6), pp. 1309–1317.
[15] Brenner, M., Dupont, T., Hilgenfeldt, S., and Lohse, D., 1998, ''Reply on a Comment,'' Phys. Rev. Lett., **80**, pp. 3668–3669.
[16] Ferziger, J. H., and Peric, M., 1996, *Computational Methods for Fluid Dynamics*, Springer, Berlin.

Predicting Globe Control Valve Performance—Part I: CFD Modeling

James A. Davis
University of Arkansas,
Fayetteville, AR 72701

Mike Stewart
University of North Dakota,
Fargo, ND 58105

Computational Fluid Dynamics (CFD) tools are evaluated for use in industrial design applications by predicting primary control valve performance characteristics. The performance parameter of primary interest to the manufacturer is the flow coefficient, C_v. Valves having relative valve capacity factors between 2.5 and 13 were modeled. The control valve C_v was experimentally measured and numerically predicted. Both equal percentage and linear characteristic valves were represented in the study. The numerical (simulation) study presented in Part 1 showed that the valve C_v and the inherent valve characteristic could be accurately predicted using axisymmetric flow models over most of the plug travel. In addition, the study demonstrates the usefulness of simplified CFD analysis for relatively complex 3-D flows. [DOI: 10.1115/1.1490108]

1 Introduction

Control valves are used throughout the chemical process industry for controlling volumetric flow rates. One of the most common types of control valves is the single seat globe valve. It consists of three main components: body, trim, and actuator. The body of the valve houses the trim, which is made up of the plug and seat, and the actuator positions the plug. Efforts of this work were focused on the design of the trim. The trim of the control valve is responsible for the inherent valve flow characteristics. Different flow conditions require different shapes of the plug and seat to achieve optimum flow control. Past design strategies have relied heavily on experimental and to a lesser extent analytical techniques to design the trim. More recently, designers of fluid handling equipment have begun using Computational Fluid Dynamics (CFD) for product development and optimization. In this work control valve design tools were developed which utilize the technology of CFD. In particular, simplified analyses are used that would be more useful for smaller companies having fewer R & D resources.

This paper is one in a two part series. In the first paper the CFD results are primarily used to calculate control valve performance characteristics. The second paper focuses on details of the flow field such as pressure at a discrete point and jet behavior. In addition, the second paper uses flow visualization techniques for verification.

1.1 Literature Review. Despite the control valves relative importance in a control loop, little work has been published on control valve design. In an attempt to generalize losses through valves, the Crane Company's Technical Paper 410 [1] presents many analytical expressions that can be used to calculate flow and pressure relations. However, most of this information applies to valves that are fully opened and not used for flow control. Other work has been published on butterfly valves e.g., Takeyoshi et al. [2] developed an analytical method to predict flow characteristics based on the hub geometry and percent opening in a butterfly valve. Other work on butterfly valves includes Huang and Kim [3] who initially numerically modeled a butterfly valve as two dimensional and later modeled it in three dimensions. Calculating the loss coefficient from the converged flow field and comparing this coefficient to representative values verified their model.

Hydraulic valves differ from process control valves in application and design. Hydraulic valves are typically used for controlling pressures and therefore, are of the quick opening type of characteristics. Quick opening valves utilize plugs shaped in the form of a truncated cone with relatively large clearances between the plug and the seat. Or sometimes these valves utilize a disc for a poppet plug. Process control valves on the other hand are used for precise control of the fluid flowrate and are of the linear or equal percentage characteristic. These type valves usually have small clearances between the plug and the seat. Despite these differences, many of the flow phenomena in the hydraulic valve such as recirculation and jet separation and reattachment also occur in the process control valve. Therefore, it is instructive to review the literature in this area.

The experimental work of hydraulic valves extends back over many years. Johnston and Edge [4] studied forces on the valve plug as well as the pressure-flow characteristics for several different plug and seat arrangements. Schrenk [5] published work on the pressure-flow characteristics of poppet and disk valves. Stone [6] studied the characteristics of poppet valves with sharp-edged seats, small openings, and low Reynolds number. McCloy and McGuigan [7] studied the effects of the downstream chamber size in a two-dimensional model of a poppet. Oki and Kawakami [8] studied disk valves by issuing water jets into air.

Some researchers have attempted to analytically predict flow through poppet valves. Von Mises [9] predicted the contraction coefficient for flow through an orifice using potential flow. Fluid forces on the plug are often estimated using simple concepts of fluid momentum change through the valve [10]. Duggins [11] used potential flow to analyze the flow through a valve. These simplified techniques are often valuable for determining order of magnitude type calculations, but for high accuracy predictions, they can yield misleading results.

Recently CFD has been combined with experimental work to analyze hydraulic valves. Vaughan, Johnston, and Edge [12] modeled the valve reported experimentally by Johnston and Edge [4]. They found that the overall flow patterns and other parameters were predicted well for flows not dependent on jet separation and reattachment. Lee and Wellford [13] modeled a spring-loaded poppet valve with a valve body similar to a globe style valve in a two dimensional Cartesian coordinates system. His results showed how a jet may impinge on the roof of the valve body and cause a large-scale recirculation region in the pipe downstream of the valve.

Contributed by the Fluids Engineering Division for publication in the JOURNAL OF FLUIDS ENGINEERING. Manuscript received by the Fluids Engineering Division June 1, 2001; revised manuscript received April 3, 2002. Associate Editor: B. Schiavello.

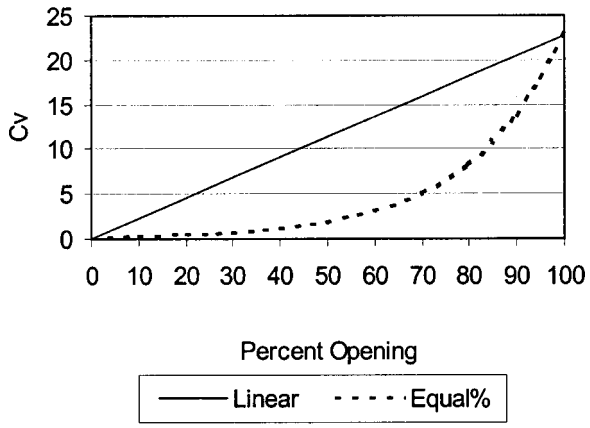

Fig. 1 Inherent valve characteristics

1.2 Objectives. The objectives of this work were to develop control valve design tools using CFD, and to verify these tools using experimental methods.

2 Theory

This section is divided into two parts. The first part discusses control valves from an application point of view and the second part discusses the turbulence model used in the study.

2.1 Control Valves. Two important control valve parameters are the overall flow coefficient C_v and the relative valve capacity factor C_d. In general the calculation methods for C_v are a function of the valve Reynolds number, Re_v. Another important concept in control valve application is characterization.

C_v. The flow coefficient C_v is a measure of the valve capacity. It is given by the ISA standard S75.01 [14] for incompressible, fully turbulent, noncavitating, and nonflashing flow as

$$C_v = 11.6q\sqrt{\frac{G_f}{\Delta P}} \tag{1}$$

The C_v is a dimensional quantity that has evolved through industry usage. In the English Engineering System of units the C_v is simply the number of gallons per minute of water that can flow through the valve with a pressure drop of one pound per square inch. However, in System International units this definition would not apply. Despite the somewhat ambiguous meaning of C_v, it has proven to be an acceptable indication of valve capacity. In the SI system the units of C_v are $(m^3/hr)/(kPa^{0.5})$.

Table 1 Valve description

Valve	Description	Rated C_v
Valve A	2.54 cm (1 in. nom. NPT), Seat radius 0.471 cm	2.5
Valve B	2.54 cm (1 in. nom. NPT), Seat radius 1.03 cm	4
Valve C	2.54 cm (1 in. nom. NPT), Seat radius 1.346 cm	13

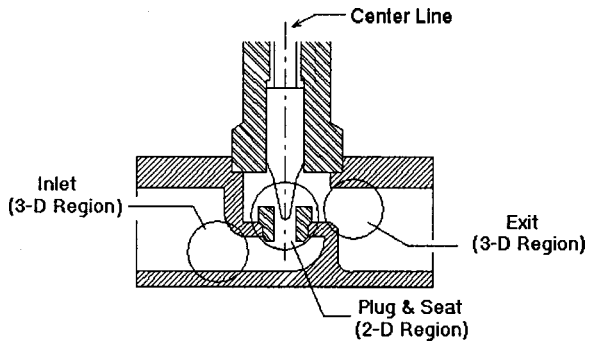

Fig. 2 Different regions of a control valve

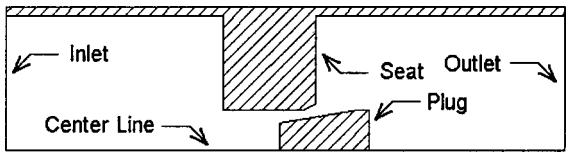

Fig. 3 Axisymmetric view of plug and seat region (rotated 90 degrees)

Re_v. Equation (1) is applicable to fully turbulent flow fields for which valve parameters become independent of the Reynolds number. However, due to its complex geometry, globe style control valves have no obvious characteristic dimension or velocity. Therefore, a valve Reynolds number (Re_v) is usually acceptable as a suitable parameter for predicting the point of transition to turbulence. Stiles [15] initially proposed the idea of using the diameter of a circular orifice with the same C_v as the control valve. This data was then correlated by an experimentally determined factor that corrected the dimension to an effective diameter. Using this concept the ISA [14] recommends

$$\mathrm{Re}_v = \frac{76{,}000F_d q}{\upsilon F_L^{1/2} C_v^{1/2}}\left[\frac{F_L^2 C_v^2}{(0.00214)D^4}+1\right]^{1/4} \tag{2}$$

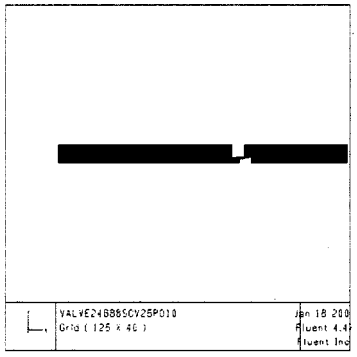

(*a*) Extent view.

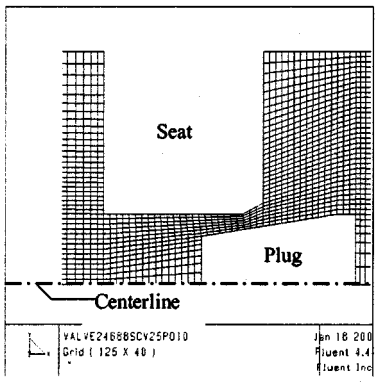

(*b*) Close up view of grid.

Fig. 4 Grid for valve A, 50 percent open (seat-plug region)

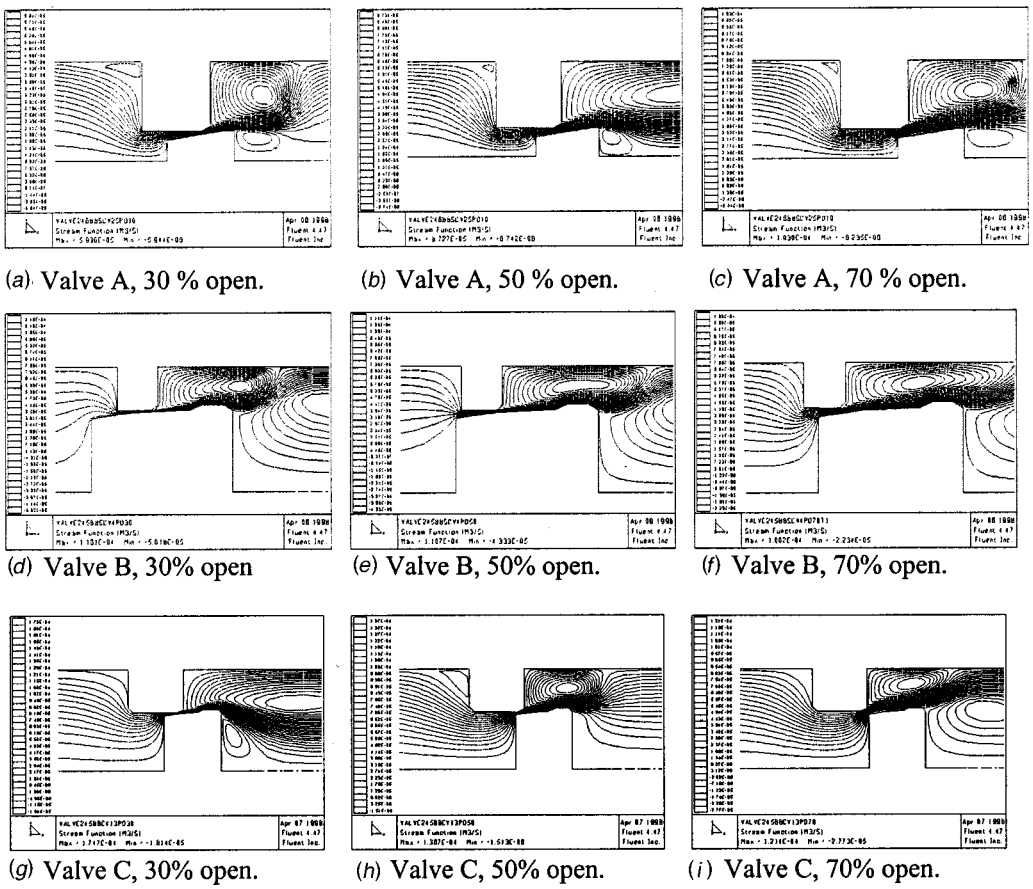

Fig. 5 Streamlines for valves A, B, and C (partial opening: 30 percent, 50 percent, 70 percent)

where F_d is a value that accounts for the effect of the valve geometry and F_L is a value that relates the overall pressure drop across the valve to the pressure drop at the vena contracta in the plug and seat area. Driskel [16] points out that for single seat globe style control valves fully turbulence occurs in regions of flow where $\mathrm{Re}_v > 10^4$.

C_d. The relative valve capacity factor is a measure of the valve capacity relative to its nominal pipe size. It is given by

$$C_d = \frac{C_v}{(0.0394D)^2} \tag{3}$$

and has units of $(\mathrm{m}^3/\mathrm{hr})/(\mathrm{kPa}^{0.5})/(\mathrm{mm}^2)$. Analogous to the C_v, the C_d is a quantity that has evolved through industry usage. Values of C_d do not normally exceed 11.

Valve Characteristic. The valve characteristic is a plot of the C_v versus percent opening of the valve. The plot is indicative of how the flow rate will change with a change in percent opening of the valve. The percent opening of the valve is a measure of how far the plug is stroked relative to its maximum stroke length. Characterization is used in control applications to better linearize the control loop. The two most commonly used characteristics are the linear, where flow rate increases linearly with valve plug travel, and equal percentage, where flow rate increases exponentially with valve plug travel. Both of these characteristics are shown in Fig. 1. Linear characteristics are used in applications where the majority of the system pressure drop occurs at the valve and equal percentage characteristics are used where the pressure drop across the valve could vary significantly.

2.2 Turbulence Model. Turbulence modeling is used to predict the Reynolds stresses in the governing equations. Researchers have developed many turbulence models. The model used in this study was the two equation K-ε model with the standard parameters [17]. Other turbulence models (RNG) were used but the effect on predictions was small [18].

3 Procedure

This project was divided into a numerical study and an experimental study. In the numerical study, three commercial globe valves were modeled using a CFD code developed by FLUENT, Inc. Then an experimental study was undertaken to verify these models. A description of the valves is given in Table 1. As seen in this table, all valves were 2.54 cm globe style control valves with rated C_v's (C_v at 100 percent open) ranging from 2.5 to 13. In globe style control valves, the widely varied range in rated C_v is accomplished by varying the size of the seat and plug, which is seen in Fig. 2. In addition, both linear and equal percentage trims were included in the study. Some of the details of the numerical study and the experimental study are discussed next.

3.1 Numerical Study. In the numerical study, valves A, B, and C were modeled axisymmetrically. Each valve was modeled with the plug positioned at different percent openings. These percent openings were in increments of ten percent and ranged from 10 to 100 percent open. The converged pressure and flow fields were used with Eq. (1) to calculate the valve C_v.

Geometry. A cross section of a single seat globe valve is shown in Fig. 2. From this figure three regions can be identified. The first region is a three-dimensional inlet region. The second one is a two dimensional axisymmetric plug and seat region. And the third one is a three-dimensional exit region. In this study the three dimensional valve was modeled as an axisymmetric valve.

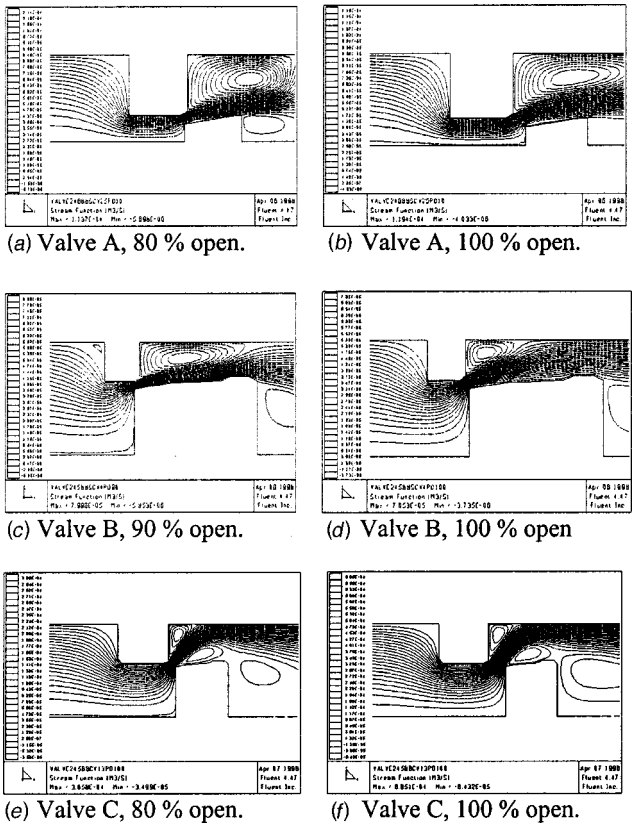

(*a*) Valve A, 80 % open. (*b*) Valve A, 100 % open.

(*c*) Valve B, 90 % open. (*d*) Valve B, 100 % open

(*e*) Valve C, 80 % open. (*f*) Valve C, 100 % open.

Fig. 6 Plug retracting from seat for valves A, B, and C

The plug and seat region was essentially axiymmetric and was well represented. The three-dimensional entrance and exit region was approximated using axisymmetric geometries. Upstream of the seat, the inlet pipe length divided by the valve radius (L/R) was 10, and downstream of the seat, the outlet pipe length divided by the valve radius was 6. In addition, symmetry was exploited at the centerline by only modeling half of the valve. The simplified axisymmetric model for valve A is shown in Fig. 3.

Grid. The grid used in the numerical study was a structured grid with body fitted coordinates (BFC). After an initial investigation for grid independence, a grid size of 40 by 25 was used. The nodes of the grid were clustered in the plug and seat regions since this was the area of largest flow gradients. In addition, an effort was made to reduce grid distortion. The effect of grid distortion is documented in previous research [19]. Figure 4(*a*) shows an extensive view of the grid and Fig. 4(*b*) shows an expanded view of the grid.

Boundary Conditions. Symmetry boundary conditions were used at the centerline. All solid boundaries were represented using no slip velocity conditions and log wall turbulence conditions. Inlet conditions were represented by uniform velocity sufficient to provide the required large Re_v flow. Turbulence intensity was set to 10 percent at the inlet. Test cases were run with 20 percent inlet conditions but no significant change in the predictions was observed. Outlet boundary conditions were set as uniform pressure. The pipe radius was used as the inlet length scale.

Numerical Accuracy. All conservation equations are discretized in FLUENT using a finite volume formulation with second order spatial accuracy. In areas having large flow velocities and cell sizes, a proportional upwinding scheme is used having first order spatial accuracy whenever full upwinding is required.

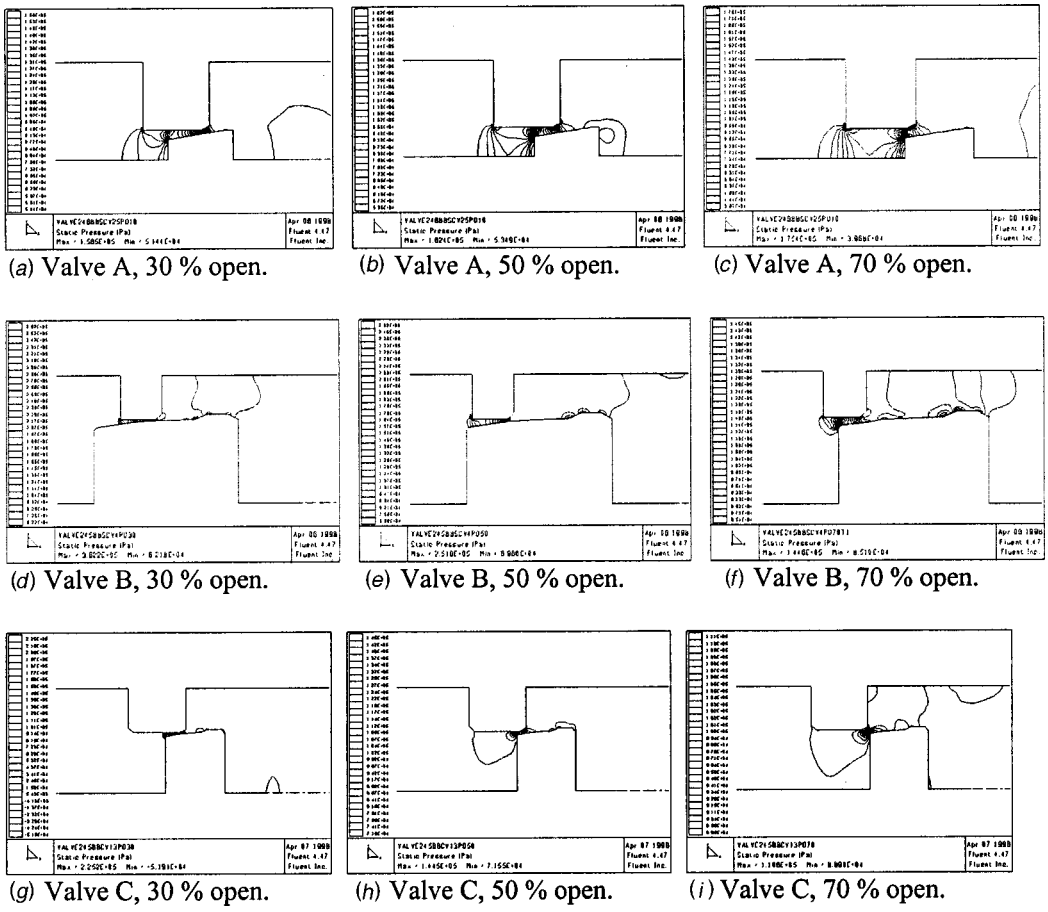

(*a*) Valve A, 30 % open. (*b*) Valve A, 50 % open. (*c*) Valve A, 70 % open.

(*d*) Valve B, 30 % open. (*e*) Valve B, 50 % open. (*f*) Valve B, 70 % open.

(*g*) Valve C, 30 % open. (*h*) Valve C, 50 % open. (*i*) Valve C, 70 % open.

Fig. 7 Pressure contours for valves A, B, and C (partial opening: 30 percent, 50 percent, 70 percent)

The effect of the reduced accuracy with upwinding would be evident during the grid resolution studies. Since there was no effect of grid refinement seen, the upwinding did not appear to affect the solutions. Continuity is satisfied using a SIMPLE (semi implicit pressure linked equations) algorithm. Normalized residuals were used for the convergence criteria, which was set at three orders of magnitude.

3.2 Experimental Study. The experimental study was undertaken to obtain an experimentally determined C_v for comparison to the numerically determined C_v. Details are found in Part 2 of the paper describing this research [20]. In Part 1 of the paper, some of the experimental results will be used to compare with the numerical predictions.

4 Results

The results of the numerical and experimental study are shown in Fig. 5–9. Figures 5–8 show the modeled streamlines and pressure contours, and Fig. 9 shows the inherent valve characteristics.

4.1 Streamlines. Figure 5 displays the numerically modeled streamlines for valves A, B, and C. Each valve is shown at openings of 30, 50, and 70 percent. In each case the flow initially accelerates through the plug and seat region, and then issues downstream in the form of a wall jet while remaining attached to the plug. In addition, a large recirculation region develops on the downstream side of the seat. As the valve percent open increases, the plug begins to retract beyond the plane of the seat as shown in Fig. 6 where valve A is shown at 80 and 100 percent open, valve B is shown at 90 and 100 percent open, and valve C is shown at 80 and 100 percent open. When this occurs the flow separates from the plug forming a second recirculation region between the jet and the plug. Then the flow either reattaches to the plug at some point downstream Figs. 6(*a*) and 6(*b*) or it issues as a free jet until impinging on the surface of the valve body, Figs. 6(*e*) and 6(*f*).

4.2 Pressure Contours. Figure 7 displays the numerically modeled pressure contours for valves A, B, and C. Each valve is shown at openings of 30, 50, and 70 percent. In each case the pressure decreases in the downstream direction with the largest pressure gradients occurring in the plug and seat region. Most of the contours are radial (relative to the centerline) which implies that the pressure field is primarily one dimensional with the axial (plug and stem) direction. No significant pressure changes are observed upstream of the seat and only minor changes are observed downstream of the seat. Minor pressure changes downstream of the seat imply little to no pressure recovery. This is both expected and desirable in a control valve.

Figure 8 shows the modeled pressure contours with the plug positioned at higher percent openings. As the plug starts to retract beyond the plane of the seat, the contours become two-dimensional and the gradients are less confined to the gap between the plug and seat. In addition, this phenomenon becomes more pronounced as the valve size (rated C_v) increases.

4.3 Inherent Valve Characteristics. Figure 9 displays the inherent valve characteristics for valves A, B, and C. In this figure the manufacturer's published values are plotted along with the numerical and experimental results. Over bars are used to represent the uncertainty in the experimental results. Details of this figure as well as the experimental uncertainty are discussed in more detail below.

Valve A. The experimental results in Fig. 9(*a*) show that valve A has a predominantly linear characteristic from 10 to 70 percent opening, and the numerical results show this trend from 10 to 80 percent opening. Both show a change in the characteristic type at higher percent openings. From 10 to 50 percent opening the numerical model over predicts the C_v. At higher percent openings (70 to 100 percent open) the numerical model under predicts the

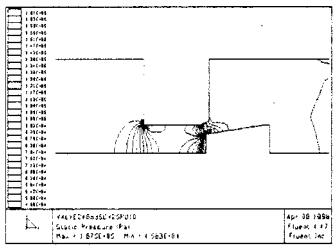

(*a*) Valve A, 80 % open.

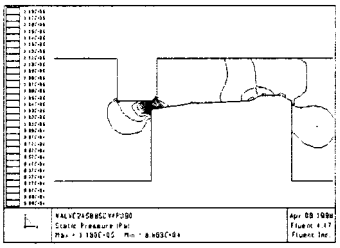

(*b*) Valve B, 90 % open.

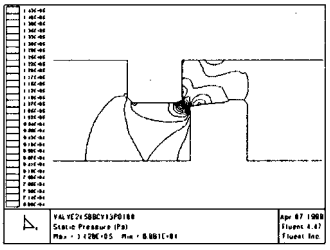

(*c*) Valve C, 80 % open.

Fig. 8 Plug retracting from seat for valves A, B, and C (pressure contours)

C_v. The experimental uncertainty for valve A changed with valve percent opening. When calculated as a percent of the measured C_v, the experimental uncertainty ranged from a minimum value of 2.14 percent error to a maximum value of 3.59 percent error. The minimum experimental error occurred at a valve opening of 10 percent, and the maximum experimental error occurred at a valve percent opening of 90 percent.

Valve B. The experimental results in Fig. 9(*b*) show that valve B has an equal percentage characteristic. At the lower percent openings there is good agreement between the numerical and the experimental results. However, at approximately 90 percent opening the difference in the numerical values and the experimental values start to increase significantly. The experimental uncertainty for valve B changed with valve percent opening. When calculated as a percent of the measured C_v, the experimental uncertainty ranged from a minimum value of 1.09 percent error to a maximum value of 8.47 percent error. The minimum experimental error occurred at a valve opening of 10 percent, and the maximum experimental error occurred at a valve percent opening of 100 percent.

Valve C. The experimental results in Fig. 9(*c*) show that valve C has an equal percentage characteristic. At the lower percent openings (10 to 60 percent) the numerical and experimental results have good agreement with the numerical model predicting a slightly higher value for the C_v. From 70 to 100 percent open the difference between the numerical and experimental values start to increase significantly. The experimental uncertainty for valve C changed with valve percent opening. When calculated as a percent of the measured C_v, the experimental uncertainty ranged from a minimum value of 2.09 percent error to a maximum value of

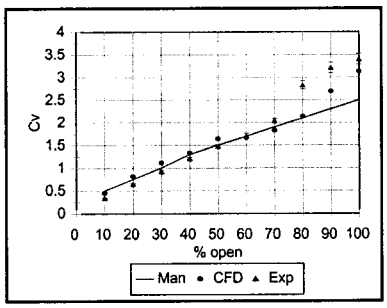

(*a*) Flow coefficient for Valve A (exp. uncertainty ranged from 2.14 to 3.59 percent error).

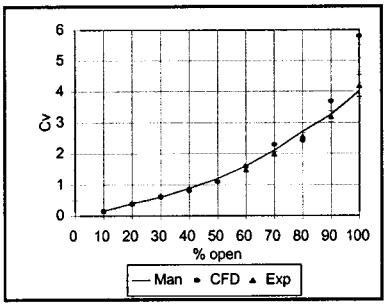

(*b*) Flow coefficient for Valve B (exp. uncertainty ranged from 1.09 to 8.47 percent error).

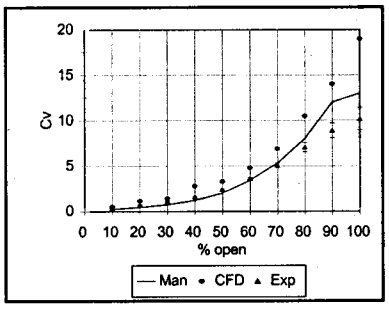

(*c*) Flow coefficient for Valve C (exp. uncertainty ranged from 2.09 to 11.96 percent error).

Fig. 9 Inherent valve characteristics for valves A, B, and C

11.96 percent error. The minimum experimental error occurred at a valve opening of 10 percent, and the maximum experimental error occurred at a valve percent opening of 100 percent.

General Trends. From these results two general observations are made regarding the inherent characteristic and the valve C_v. The first is that the numerically predicted inherent valve characteristic in all the valves qualitatively matches the experimentally determined inherent valve characteristic. The second observation is that the quantitative values of the experimentally determined C_v are in close agreement with the modeled values at the lower percent openings. However, at the higher percent openings, the discrepancy between the numerical and experimental values starts to increase. The discrepancy at higher percent openings is possibly explained by considering the plug position relative to the seat, which was previously shown, in Figs. 6 and 8. As the plug starts to retract beyond the plane of the seat, the flow field could possibly change from an axisymmetric flow field to a three-dimensional one. If this transition occurs, then the axisymmetric numerical model would naturally be in error at these percent openings.

5 Conclusions

Three commercial globe style control valves were modeled axisymmetrically using CFD. The valves modeled included both linear and equal percentage trims and included C_d ranges of 2.5 to 13.

From the results three conclusions were drawn. The first was that the simplified axisymmetric numerical model qualitatively predicted the inherent valve characteristic for globe style control valves. The second conclusion was that the axisymmetric numerical model quantitatively predicted the valve C_v over a large range of percent openings. The final conclusion was that after the plug retracted beyond the plane of the seat, the accuracy in predicting the C_v decreased significantly, but that this occurred only at the highest values of percent openings.

Nomenclature

C_d = relative valve capacity factor ($m^3/hr/kPa^{0.5}/mm^2$)
C_v = valve flow coefficient ($m^3/hr/kPa^{0.5}$)
D = internal diameter of pipe (mm)
F_d = valve style modifier (dimensionless)
F_L = pressure recovery factor (dimensionless)
G_f = liquid specific gravity (dimensionless)
ΔP = Pressure drop (kPa)
q = volumetric flow rate (m^3/hr)
$\mathrm{Re_v}$ = valve Reynolds number (dimensionless)
v = kinematic viscosity (centistokes)

References

[1] Crane Co., 1988, "Flow of Fluids," Technical paper 410, 24th Printing.
[2] Kimura, Takeyoshi et al., 1986, "Hydrodynamic Characteristics of a Butterfly Valve," Instrument Society of America Transactions, **24**(1), pp. 53–61.
[3] Huang, C., and Kim, R. H., 1996, "Three-Dimensional Analysis of Partially Open Butterfly Valve Flows," ASME J. Fluids Eng., **118**, pp. 562–568.
[4] Johnston, D. N., and Edge, K. A., 1991, "Experimental Investigation of Flow and Force Characteristics of Hydraulic Poppet and Disc Valves," Proc. Inst. Mech. Eng., **205**, pp. 161–171.
[5] Schrenk, E., 1957, *Disc Valves, Flow Patterns, Resistance, and Loading*, BHRA Publications, T547.
[6] Stone, J. A., 1960, "Discharge Coefficients and Steady State Flow Forces for Hydraulic Poppet Valves," Trans. ASME, **144**.
[7] McCloy, D., and McGuigan, R. H., 1964, "Some Static and Dynamic Characteristics of Poppet Valves," Proc. Inst. Mech. Eng., **179**.
[8] Oki, I., and Kawakami, K., 1961, "Characteristics of flat seated valves with broader seat face (experimental research on disc valves, 8th report)," Bull. JSME, **4**, p. 279.
[9] Von Mises, R., 1917, "The Calculation of Flow Coefficient for Nozzle and Orifice," VDA, **61**, pp. 21,22,23.
[10] McCloy, D., and Martin, H. R., 1980, *Control of Fluid Power-Analysis and Design*, Wiley, New York.
[11] Duggins, R. K., 1973, "Further Studies of Flow in a Flapper Valve," Third International Symposium on Fluid Power, Turin, pp. B2–25.
[12] Vaughan, N. D., Johnston, D. N., and Edge, K. A., 1992, "Numerical Simulation of Fluid Flow in Poppet Valves," Proc. Inst. Mech. Eng., **206**, pp. 119–127.
[13] Lee, J. J., and Wellford, L. C., 1997, "Transient Fluid-Structure Interaction in a Control Valve," ASME J. Fluids Eng., **119**, pp. 354–359.
[14] "Control Valve Sizing Equations," ISA-S75.01-1997, Research Triangle Park, North Carolina: Instrument Society of America.
[15] Stiles, G. F., 1964, "Liquid Viscosity Effects on Control Valve Sizing," Proc. Ann. Symp. on Instrumentation for the Process Industries, pp. 52–61.
[16] Driskell, Les, 1983, *Control Valve Selection and Sizing*, Instrument Society of America, Research Triangle Park, N.C., pp. 177–180.
[17] FLUENT, 1995, "User's Guide," Fluent Incorporated, Centerra Resource Park, 10 Cavendish Court, Lebanon, NH 03766.
[18] Davis, J. A., and Stewart, M., 1998, "Geometry Effects when using CFD Analysis as a Design Tool to Predict Control Valve Performance," Nineteenth Southeastern Conference on Theoretical and Applied Mechanics, Deerfield Beach, FL, pp. 38–45.
[19] Davis, J. A., and Stewart, M., 1998, "Effects of Grid Distortion on Predictions of Control Valves and Detection Methods," Proceedings of the Fifth NRC/ASME Symposium on Valve and Pump Testing, Vol. 2, pp. 1C–43.
[20] Davis, J. A., and Stewart, M., 2002, "Predicting Globe Control Valve Performance-Part II: Experimental Validation," ASME J. Fluids Eng., **124**, pp. 778–783.

Predicting Globe Control Valve Performance—Part II: Experimental Verification

James A. Davis
University of Arkansas,
Fayetteville, AR 72701

Mike Stewart
University of North Dakota,
Fargo, ND 58105

An experimental study was undertaken to verify an axisymmetric numerical model of a control valve flow field. The numerical model, which utilized Computational Fluid Dynamics (CFD), was formerly developed to be used as a design tool by manufacturers of control valves. In this work the model was first tested by comparing its results to data taken on an axisymmetric flow field experiment. Then the model's application to actual three-dimensional control valves was tested by studying the pressure and flow field through a three-dimensional control valve. The results showed that the axisymmetric numerical model is accurately modeling an axisymmetric flow field. In addition, the results showed that control valves have a predominantly axisymmetric flow field for most of their plug travel which make them suitable for the model. Finally, the results showed details about the flow field such as where separation and reattachment may occur.
[DOI: 10.1115/1.1490126]

1 Introduction

In Part 1 of this study [1], the authors developed a model that utilized computational fluid dynamics (CFD) as a tool for designing globe style control valves. In the numerical model a globe control valve, which is normally a three-dimensional geometry, was modeled as an axisymmetric geometry. The plug and the seat, being axisymmetric in the actual valve were well represented. However, the three-dimensional inlet and exit of the valve were modeled axisymmetrically as well. The results of this study showed that the control valve flow coefficient C_v and the inherent valve characteristic are well predicted over a large range of percent openings using the simplified geometry model. This implies that the numerical model is accurately predicting an axisymmetric flow field, and that the actual valve flow field is predominantly two-dimensional at some percent openings but not at all percent openings. In an effort to investigate these implications further, experimental testing was undertaken in part two of the paper.

Initially the axisymmetric numerical model was verified by obtaining experimental data from an axisymmetric valve. These data were then compared to computer generated results. Following the axisymmetric study, the features of the valve flow field were studied by constructing two prototype valves. One of the valves was used for studying the pressure field and the other was used for studying the velocity field. The data obtained from the study were then compared to computer generated images for analysis.

2 Literature Review

Different types of valves have been modeled using numerical solutions. Some of these include Huang and Kim [2] who modeled a butterfly valve; Johnston et al. [3] who modeled different types of poppet valves; Lee and Wellford [4] who modeled a spring loaded poppet valve with a globe valve geometry; Ito et al. [5] who modeled a poppet valve; and Ueno et al. [6] who modeled flow in a hydraulic spool valve. Smith [7] points out that the final step with any simulation is to verify the numerical model. One form of model verification with valves is a comparison of an overall valve coefficient. This method was used by Huang and Kim [2] who used their converged pressure and flow fields to calculate an overall loss coefficient which was then compared to other representative values. While the valve flow coefficient is the primary parameter of interest to valve users, other parameters of interest to valve designers include pressure, velocity, and jet behavior. Therefore, complete verification of a valve numerical model would include experimental comparisons of these additional parameters. One method of verifying the pressure field is to take static pressure readings at the boundaries of the flow field. This method was used by Ito et al. [5] and also by Ueno et al. [6]. Computed flow patterns can be verified by using photographically obtained streakline images. Johnston et al. [3] used hydrogen bubbles generated using electrodes upstream of the valve. Another technique was used by Ueno et al. [6] where the streaklines were studied using cavitation bubbles.

In this paper, a control valve model was verified by using experimentally obtained pressure readings and streakline images. The pressure readings were taken at the surface of the flow field and the streakline images were obtained by using milk as a tracer fluid which was injected into water. Goldstein [8] points out that the fat content of milk has been presumed to retard its diffusion which makes the filament more distinct.

3 Apparatus

Three valves were used in this study. These valves were labeled valves D, E, and F. This labeling convention follows the sequencing previously used by the authors in [1] where valves A, B, and C were studied. Valve D was a custom built axisymmetric valve that was used for verifying the axisymmetric numerical model. Both pressure measurements and streakline images were obtained from valve D. Valves E and F were used for verifying the dimensionality of a three dimensional globe valve flow field. The pressure field was studied using data collected from valve E. However, due to its small size, valve E could not be used effectively for flow visualization studies. Therefore, valve F, which was a scaled up version of valve E, was used for this purpose. The plug of all three valves (valves D, E, and F) was geometrically similar.

3.1 Valve D Description. A schematic of valve D is shown in Fig. 1. This valve was constructed of transparent PVC pipe with a 7.62 cm nominal diameter and a 2.13 m overall length. Long radius elbows were used at the inlet and exit to reduce the effects of secondary flow regions. Pressure taps were installed in the plug and seat area as shown in Fig. 2. One tap was located directly upstream of the seat, one tap was located approximately midway through the seat, one tap was located in the seat chamber, and one

Contributed by the Fluids Engineering Division for publication in the JOURNAL OF FLUIDS ENGINEERING. Manuscript received by the Fluids Engineering Division June 1, 2001; revised manuscript received April 3, 2002. Associate Editor: B. Schiavello.

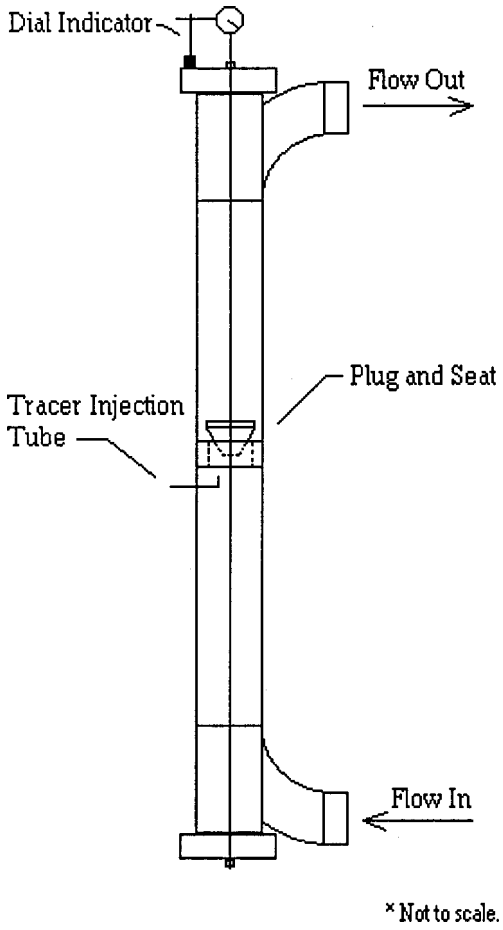

Fig. 1 Schematic of valve D

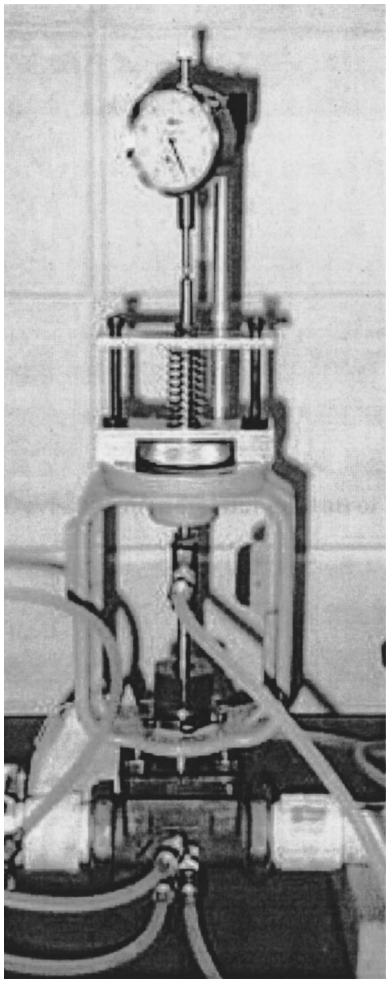

Fig. 3 Photograph of valve E

tap was located directly downstream of the seat. In addition, two pressure taps were located in the plug. Valve D was also equipped with tracer fluid injection capabilities for obtaining streakline images. This was accomplished by using a small tube located on the upstream side of the seat. Milk was used as the tracer fluid, which provided a contrasting image with the dark background.

3.2 Valve E Description. Valve E was a 2.54 cm nominal globe style control valve equipped with several pressure taps in the plug and seat area. This valve is shown pictorially in Fig. 3 and the plug and seat are shown schematically in Fig. 4. As seen in Fig. 4, one tap was located directly upstream of the seat, two taps were located in the seat, and one tap was located directly downstream of the seat. In addition, one tap was located in the plug as shown in Fig. 4. A mechanical actuator equipped with a dial indicator for measuring the percent opening was also installed on the valve.

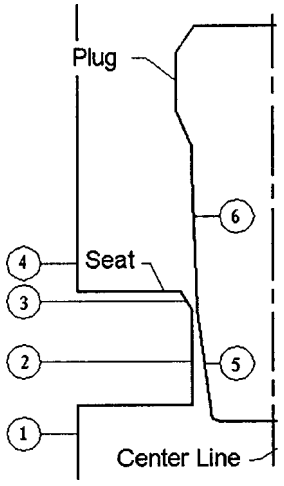

Fig. 2 Pressure tap locations for valve D, 50 percent open

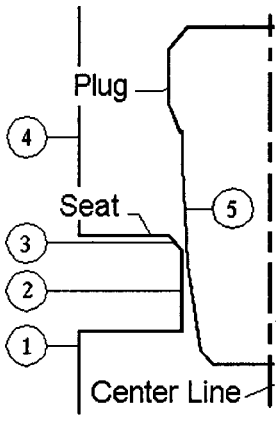

Fig. 4 Pressure tap locations for valve E, 50 percent open

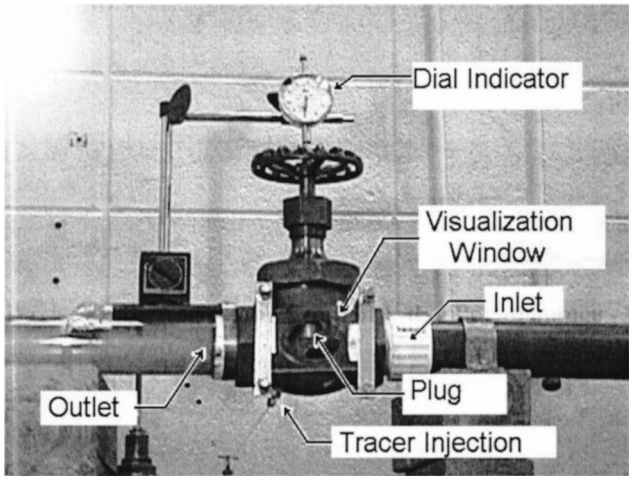

Fig. 5 Photograph of valve F

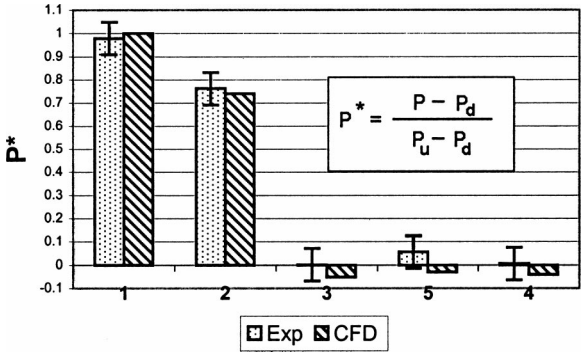

Fig. 7 Dimensionless pressures for valve D, 50 percent open. Pu=upstream pressure, Pd=downstream pressure. Numbers on abscissa correspond to pressure tap locations shown in Fig. 2.

3.3 Valve F Description. Valve F was a 5.08 cm nominal globe valve equipped with a viewing window as shown pictorially in Fig. 5. This valve was used for flow visualization studies by mounting a tracer injection tube on the upstream side of the seat as shown in Fig. 5.

3.4 Flow Loop and Tracer Injection Description. Valves D, E, and F were installed in the test section of a flow loop which is shown in Fig. 6. This flow loop consisted of a tank, pump, flow meter, test section, and a valve located downstream of the test section for controlling the volumetric flow. In addition, a pressure gauge was installed upstream and downstream of the test section. These gauges were used for measuring the overall pressure drop across the control valves.

In addition to the flow loop, a tracer fluid injection system was constructed. This system consisted of a pressure regulator, a tracer fluid holding tank, and a throttling valve. The pressure regulator was set to a pressure slightly higher than the flow loop pressure. The holding tank was filled with milk which was injected in the control valve when the throttling valve was opened.

3.5 Experimental Uncertainty. Experimental uncertainty in this project has several sources. The most obvious and easiest to quantify is the error associated with the instrumentation. This includes the pressure gauges and the flow meters. The pressure gauges had an uncertainty of ± 2.6 kPa. This level of uncertainty in the pressure reading propagates to an uncertainty in the dimensionless pressures of ± 0.07 for valve D (Fig. 7) and ± 0.01 for valve E (Fig. 10). The results for valve D had a larger uncertainty due to the fact that valve D was a larger valve and limited the magnitude of the overall pressure drop across the valve. The flow meter had an error of one percent of the reading. Other sources of error in the study included the plug percent opening (a measure of how far the plug is stroked relative to its maximum stroke length) and the errors caused by plug centering. The plug percent opening error was investigated experimentally using repeated measurements and statistical arguments. The measurements were taken using a dial indicator that gave an error of one percent of the valve percent opening. After the investigation, a conclusion was drawn that the uncertainty associated with plug percent opening error was negligibly small. Centering the plug with equally spaced adjusting screws and pressure taps minimized the uncertainty in the seat pressure reading of valve D. With this method the error was kept to a value of 4 percent of the pressure reading. Experiments also showed that the error in the seat pressure reading of valve E could be significantly affected by plug centering effects. Since the purpose of valve E was to study the pressure field through an actual three dimensional control valve, no effort was made to center the plug in this valve. Therefore, the pressure readings in this valve could be affected significantly by plug centering. This was verified experimentally by rotating the plug while taking measurements in the seat. The results of this study showed that the pressure in the seat could vary by a maximum of 8 percent depending on the plug rotation. This error would affect the pressures taken at locations 2 and 3 in Fig. 4.

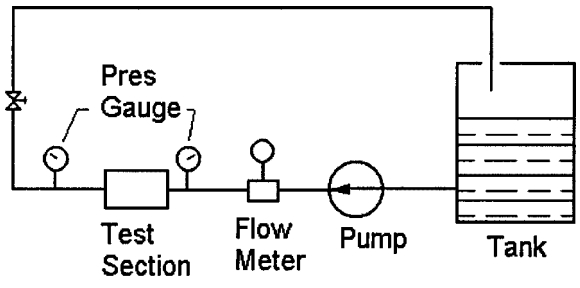

Fig. 6 Schematic of test loop used in the experimental study

4 Procedure

Verification of the axisymmetric model was accomplished using valve D. Initially, this valve was numerically modeled at several different percent openings using the procedure developed by the authors in [1]. The converged pressure field and streamlines were then recorded for later comparison to experimental data. To obtain the experimental data, valve D was installed in the flow loop shown in Fig. 6. The valve percent opening and the volumetric flow rate were set to a value that corresponded to the numerical model. Then the pressures at each tap in the valve were recorded. Following the pressure recording, the experimental streaklines were obtained. This was accomplished by opening the throttling valve on the tracer fluid injection system while simultaneously taking a picture of the plug and seat region of valve D just as the tracer fluid entered the flow field. If a significant delay occurred between the opening of the tracer fluid throttling valve and the time the picture was taken, the tracer fluid dispersed, which in turn clouded the flow field to the point that streaklines were not visible. Obtaining the streakline images usually required several iterations. A comparison between the experiments and the predictions was undertaken to verify the axisymmetric model. This process was repeated for several different percent openings. The results of this comparison are discussed in the next section.

In valve E the pressure field was initially numerically modeled using the model and techniques presented by the authors in [1]. Then the pressure field was experimentally determined. The plug position and flow rate were set and the flow field allowed to sta-

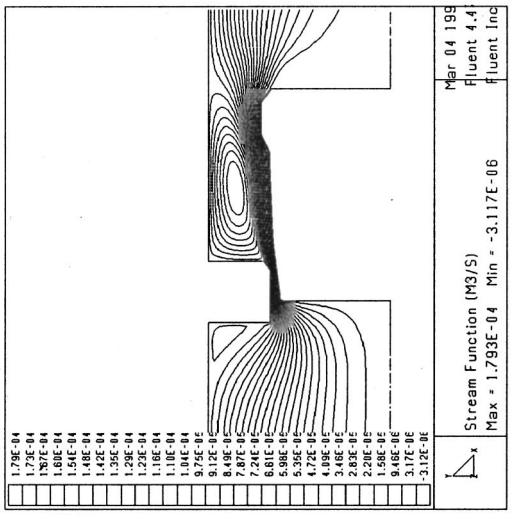

(*a*) CFD

(*b*) Experimental.

Fig. 8 Comparison of CFD and flow visualization for valve D, 70 percent open

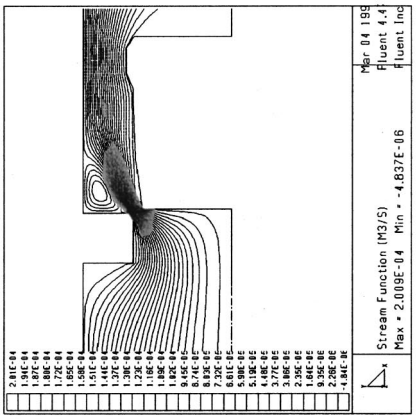

(*a*) CFD.

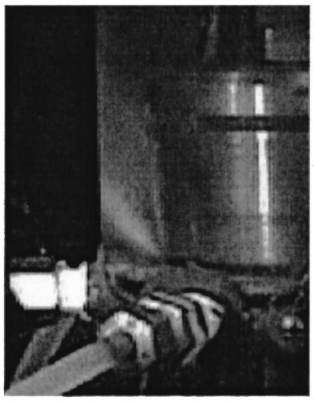

(*b*) Experimental.

Fig. 9 Comparison of CFD and flow visualization for valve D, 100 percent open

bilize. The static pressures were then recorded. This procedure was repeated for several percent openings of the plug.

Valve F was used for the control valve flow visualization study. With this valve the percent opening was initially set. Then the flow was adjusted to give a fully turbulent flow field ($Re_v > 10^4$). Following these settings the tracer fluid was injected into the flow field and captured using a digital camera. Due to the turbulence in the flow field, the tracer fluid was quickly dissipated. Therefore, typically, two pictures were captured. The first picture was taken at the instant the tracer fluid was injected into the flow field. The second picture was taken a few seconds after the tracer fluid was injected. This process was repeated for several different plug percent openings of the valve.

5 Results

The results of the study are discussed in this section. Initially the verification of the axisymmetric numerical model is discussed by comparing results from the numerical model to experimentally obtained data. Then the study of the valve flow features is discussed by comparing a numerically generated pressure field to pressure readings that were obtained experimentally. The valve flow is then discussed further by comparing predictions with experimentally obtained streaklines.

5.1 Verifying the Axisymmetric Numerical Model. Valve D was used to verify the axisymmetric numerical model. This valve was initially modeled for the converged pressure and flow fields, and then experimentally investigated for pressures and streaklines. A comparison of the numerically obtained pressures to the experimentally obtained pressures is shown in Fig. 7. These results are shown for a 50 percent opening case of the valve. In this figure the pressure is nondimensionalized with respect to the total pressure drop across the valve. Over-bars are used to show the experimental uncertainty. This uncertainty is based on the accuracy of the pressure gauge as discussed in Section 3.5. Figure 7 shows that the numerical and experimental results agree with less than 12 percent difference for all locations except Location 3 where the error was 21 percent. One possible explanation for the discrepancy at this point is due to the fact that the chamfer on the valve seat forces an adverse pressure gradient to exist in the flow field. The K-ε model has been shown to introduce significant error in adverse pressure gradients [9]. Tests were also carried out at other percent openings of the valve which yielded similar results.

Figures 8 and 9 show the results of the modeled streamlines and the experimentally obtained streaklines. The numerical and experimental results in these figures are in good agreement. In Fig. 8 the fluid issues from the plug and seat area in the form of a wall jet. The fluid remains attached to the plug as it travels axially downstream. A large recirculation region was also observed downstream of the seat. In addition, the jet separates at the trailing edge

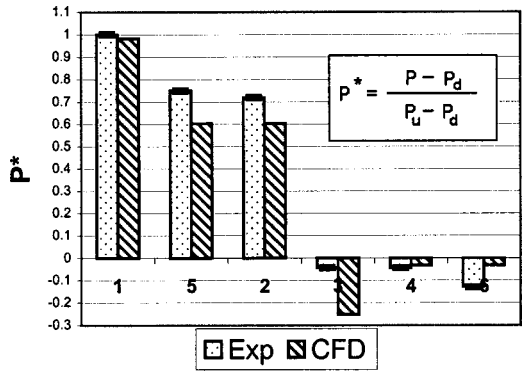

Fig. 10 Dimensionless pressures for valve E, 50 percent open. Pu=upstream pressure, Pd=downstream pressure. Numbers on abscissa correspond to pressure tap locations shown in Fig. 4.

of the plug and expands radially until it attaches to the wall. These phenomena were observed in both the numerical results and the experimental results. Figure 9 shows valve D for the 100 percent open case. In this figure the fluid separates from the plug and travels as a free jet until striking the wall of the valve body. Two large recirculation areas were observed in this case. One was immediately downstream of the seat and the other was between the free jet and the plug. These phenomena were modeled well and were supported by the experimental observations. Similar tests were carried out at other percent openings of the valve which yielded similar results. However, due to limited space, all of the results could not be presented in this paper.

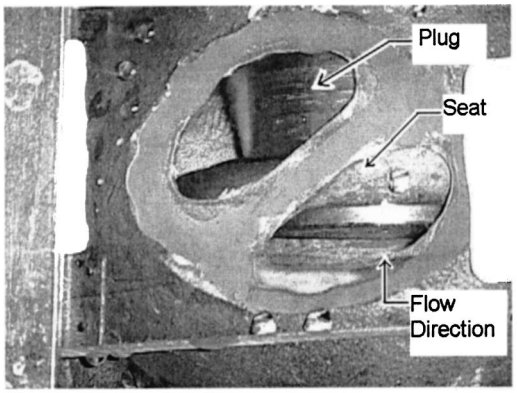

(*a*) Initial jet.

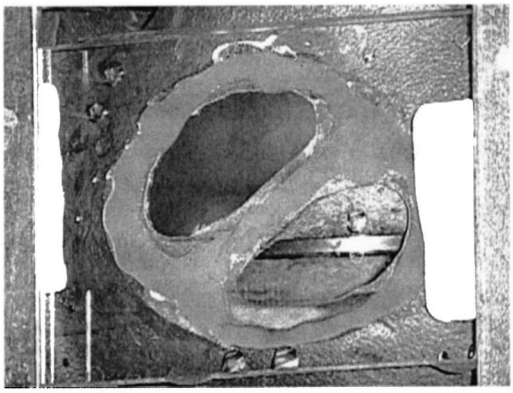

(*b*) Steady jet.

Fig. 11 Flow visualization for valve F, 50 percent open

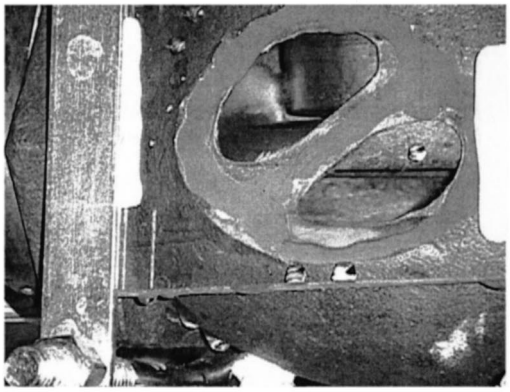

(*a*) Initial jet.

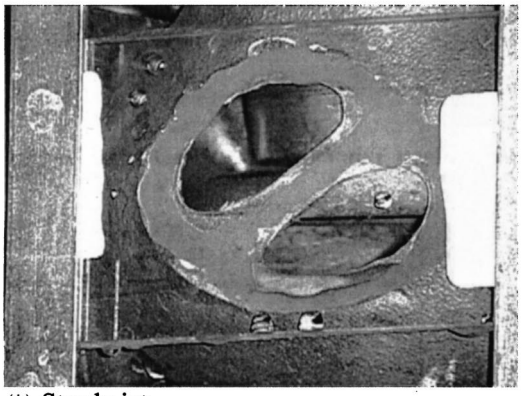

(*b*) Steady jet

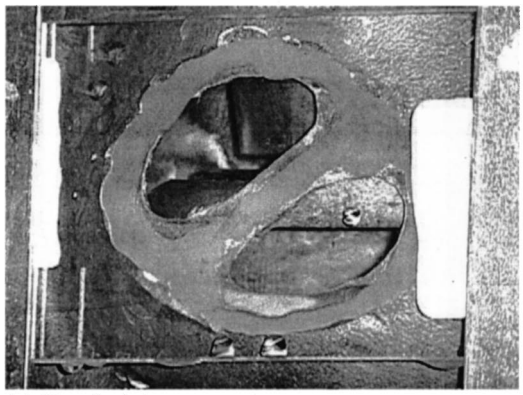

(*c*) Steady jet.

Fig. 12 Flow visualization for valve F, 100 percent open

The results presented here show that the numerical axisymmetric model closely models an axisymmetric flow field.

5.2 Control Valve Flow Field Comparisons to Predictions. The results published previously by the authors in [1] showed that the flow coefficients for globe control valves were well modeled using an axisymmetric numerical model. In particular, better agreement was observed at lower percent openings than at higher percent openings. These results implied that the actual valve flow field is predominantly axisymmetric at some percent openings but not at all percent openings. To investigate these implications, valves E and F were numerically modeled and experimentally investigated as discussed in Section 3 with valve E used for pressure studies and valve F used for streakline studies.

Figure 10 contains a plot of the numerically obtained pressures and the experimentally obtained pressures which were normalized

with respect to the total pressure drop across the valve. The data were obtained with the valve positioned at 50 percent opening. This figure shows that the agreement between the numerical and experimental results was good with less than nine percent difference for all pressure locations. This analysis was also undertaken for valve positions of 30 and 70 percent open and yielded similar results with the maximum differences occurring at the seat chamfer. The largest percent difference occurred at a valve position of 30 percent opening with a value of 26 percent, the experimental value being higher than the numerical one. The results of this analysis show that the pressure field is predominantly two-dimensional in the regions where the plug has not retracted from the seat.

Figure 11 shows the results for valve F positioned at 50 percent opening, and Fig. 12 shows the results for valve F positioned at 100 percent opening. In Fig. 11 two pictures are shown. The first picture, Fig. 11(*a*), shows the tracer fluid as it was initially injected into the flow field and the second picture, Fig. 11(*b*), shows the tracer fluid several seconds after injection. Figure 11(*a*) shows that the wall jet issuing from the plug and seat region initially travels up the side of the plug. Then as seen in Fig. 11(*b*) the fluid rolls over and travels down the side of the valve body. The second effect is verified by observing that the viewing window becomes cloudy shortly after injection of the tracer fluid. This is seen in Fig. 11(*b*). Figure 12 shows valve F at 100 percent open. In this figure the first picture shows the tracer fluid at the instant it was injected into the flow field, and the second and third pictures show the tracer fluid in consecutive time intervals several seconds after its initial injection. These pictures support the assumption that the valve flow field changes to three dimensions as the plug retracts beyond the plane of the seat. This observation was drawn from the fact that the viewing window in Fig. 12(*b*) and 12(*c*) never becomes cloudy which indicates that the fluid does not roll over at the top of the plug, but instead travels down the pipe after issuing from the seat.

The results in this section showed that control valve flow fields in single seat globe style control valves are predominantly two dimensional in regions where the plug has not retracted beyond the plane of the seat. In addition, the flow field becomes predominantly three dimensional as the plug starts to retract from the seat.

6 Conclusions

An axisymmetric numerical model developed for designing control valves was experimentally verified. The numerically obtained pressure and flow fields were compared to experimental data which was obtained from an axisymmetric geometry. In addition, the dimensional dominance of an actual three dimensional control valve was investigated while studying the effectiveness of applying the numerical model to this geometry.

Based on the results presented in Section 5 the authors made several conclusions:

1 The axisymmetric numerical model is accurately predicting an axisymmetric flow field.
2 The important features of the flow field in single seat globe control valves is predominantly axisymmetric before the plug retracts from the plane of the seat, but then the flow field makes a transition to a three-dimensional pattern after the plug retracts from the plane of the seat.
3 The three-dimensional portions of the flow field do not appear to significantly affect the performance except at the extreme large values of valve opening. Single seat globe style control valves are modeled accurately for largest portion of the opening range by using the K-ε model with an axisymmetric geometry.

References

[1] Davis, J. A., and Stewart, M. B., 2002, ''Predicting Globe Control Valve Performance—Part I: CFD Modeling,'' ASME J. Fluids Eng., **124**, pp. 772–777.
[2] Huang, C., and Kim, R. H., 1996, ''Three-Dimensional Analysis of Partially Open Butterfly Valve Flows,'' ASME J. Fluids Eng., **118**, pp. 562–568.
[3] Johnston, D. N., Edge, K. A., and Vaughan, N. D., 1991, ''Experimental Investigation of Flow and Force Characteristics of Hydraulic Poppet and Disc Valves,'' Proc. Inst. Mech. Eng., **205**, pp. 161–171.
[4] Lee, J. J., and Wellford, L. C., 1997, ''Transient Fluid-Structure Interaction in a Control Valve,'' ASME J. Fluids Eng., **119**, pp. 354–359.
[5] Ito, K., Takahashi, K., and Inoue, K., 1993, ''Flow in a Poppet Valve Computation of Pressure Distribution using a Streamline Coordinate System,'' Japan Society of Mechanical Engineers, Series B, **36**, pp. 42–50.
[6] Ueno, H., Okajima, A., Tanaka, H., and Hasegawa, T., 1994, ''Noise Measurement and Numerical Simulation of Oil Flow in Pressure Control Valves,'' Japan Society of Mechanical Engineers, Series B, **37**, No. 2, pp. 336–341.
[7] Smith, J. M., 1997, *Mathematical Modeling and Digital Simulation for Engineers and Scientists*, Wiley, New York.
[8] Goldstein, R. J., 1996, *Fluid Mechanics Measurements, 2nd. ed.*, Taylor and Francis, Washington, D.C., p. 422.
[9] Rodi, W., 1980, ''Turbulence Models and Their Application in Hydraulics-A State of the Art Review,'' University of Karlsruhe.

The Effect of the Operating Point on the Pressure Fluctuations at the Blade Passage Frequency in the Volute of a Centrifugal Pump

Jorge L. Parrondo-Gayo
e-mail: parrondo@correo.uniovi.es

José González-Pérez

Joaquín Fernández-Francos

Universidad de Oviedo,
Área de Mecánica de Fluidos,
Campus de Viesques,
33204 Gijón (Asturias), Spain

An experimental investigation is presented which analyzes the unsteady pressure distribution existing in the volute of a conventional centrifugal pump with a nondimensional specific speed of 0.48, for flow-rates from 0% to 160% of the best-efficiency point. For that purpose, pressure signals were obtained at 36 different locations along the volute casing by means of fast-response pressure transducers. Particular attention was paid to the pressure fluctuations at the blade passage frequency, regarding both amplitude and phase delay relative to the motion of the blades. Also, the experimental data obtained was used to adjust the parameters of a simple acoustic model for the volute of the pump. The results clearly show the leading role played by the tongue in the impeller-volute interaction and the strong increase in the magnitude of dynamic forces and dipole-like sound generation in off-design conditions. [DOI: 10.1115/1.1493814]

Introduction

When operating at off-design conditions, the impellers of centrifugal pumps with volute casings are subjected to some static radial thrust, due to the nonuniform distributions of pressure and moment flux around the impeller [1]. These pumps can also present nonsteady radial forces, which are mostly associated with the frequency of rotation and the blade passage frequency (and with their harmonics). Excitation at the frequency of rotation may be due to small manufacturing imperfections and mechanical unbalance. Excitation at the blade passage frequency is the consequence of the nonuniform distribution of the flow coming out the impeller from both sides of each blade, due to the differences between pressure and suction sides (jet-wake flow pattern). In centrifugal pumps with vaned diffusers significant excitation may also exist at the diffuser vane passage frequency. Other frequencies can be excited too, with mechanical origin (impeller whirling) or purely hydrodynamic origin (rotating stall).

The magnitude of the resulting dynamic forces is affected by the rotor-stator interaction through the flow, and hence it is dependent on the point of operation of the pump. In the case of excitation at the blade passage frequency, the dominant factor is the interaction between the blades of the impeller and the tongue of the volute. Among others, this blade-tongue interaction was studied by Lézé et al. [2], who conducted extensive pressure fluctuation measurements to quantify the unsteady pressure field in both impeller (with front shroud removed) and volute of a fan and relate the pressure field to the noise generation mechanisms.

Chu et al. [3–5] used particle image velocimetry complemented with noise and pressure measurements to measure the velocity distribution and compute the unsteady pressure field in the near-tongue region of the volute of a centrifugal pump. This pump was operating 35% above design flow-rate during tests, and it could be equipped with several different volutes having tongue gaps ranging from 7% to 28% of the impeller radius. They obtained an exhaustive description of the flow, which led them to conclude that primary sources in noise generation are associated with the interaction of the nonuniform outflux from the impeller (jet-wake phenomenon) with the tongue, and that small increments in the gap between impeller and tongue (up to gap values of 20% of the impeller radius) cause significant reduction of noise levels.

Morgenroth and Weaver [6] investigated the transmission to the ducting system of the blade passing frequency pressure fluctuations from a pump, for different rotational speeds and flow-rates, by identifying the acoustic wave modes from the signals of several pressure transducers along the pipeline. They found that when acoustic resonance occurred the magnitude of the pressure was a minimum for the best efficiency flow-rate. They also tested several tongues with different tip radius while keeping a constant gap between impeller and tongue (5.8% of impeller radius), and found that rounding the tongue tip resulted in a reduction of the emitted noise.

Kaupert and Staubli [7] investigated the unsteady pressure field within a high specific speed centrifugal impeller operating in a double spiral volute, by means of 25 piezoresistive pressure transducers mounted along one single channel and a telemetry system to transport the pressure signals. They measured the pressure pulses induced by both tongues (tongue passing frequency), which propagated upstream along each channel. The pulses amplitude was particularly high at the trailing edge of the blades, on their pressure sides, and reached 35% of the pump head at off-design conditions.

This paper presents an experimental study on the unsteady pressure field around the outlet of the impeller of an industrial centrifugal pump with volute casing (nondimensional specific speed $\omega_S = 0.48$). This study is a continuation of previous work [8] on a similar pump with a larger clearance between tongue and impeller (15.8% of impeller radius instead of 10% in the present study). Particular attention has been paid to the dependence of the blade passing frequency excitation on the point of operation of the machine. For this purpose four piezoelectric pressure transducers were placed at 36 locations around the front side of the volute casing. The pressure signals were FFT processed to analyze the amplitude and phase delay of the fluctuations as a function of position and flow-rate. The experimental data obtained were then used to adjust the parameters of a simple acoustic model for the volute by means of a least square error procedure. The results

Contributed by the Fluids Engineering Division for publication in the JOURNAL OF FLUIDS ENGINEERING. Manuscript received by the Fluids Engineering Division June 8, 2001; revised manuscript received March 29, 2002. Associate Editor: B. Schiavello.

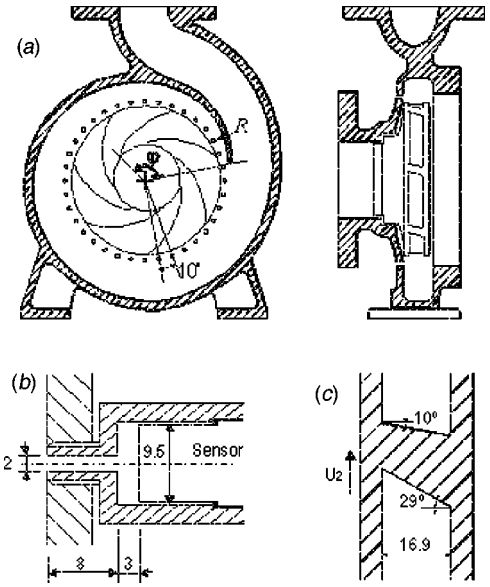

Fig. 1 (*a*) Sketch of the test pump showing location of the pressure taps; (*b*) detail of pressure transducer mounting; (*c*) detail of impeller outlet (all dimensions in mm)

obtained permitted a quantification of the effects of the hydrodynamic blade-tongue interaction on the unsteady pressure field in the volute and the generation of noise.

Experimental Equipment

The pump used for this investigation had single axial suction and spiral volute casing (Fig. 1), and it was equipped with an impeller of 200 mm in outer diameter and 7 backward curved blades with logarithmic profile. Other impeller dimensions were: inlet diameter (tip) = 52 mm, discharge width $b_2 = 16.9$ mm, blade angle at outlet = 29 deg, rake angle (outlet pressure side) = 10 deg, rake angle (outlet suction side) = 29 deg (Fig. 1(*c*)). The cross-section of the volute increased linearly from 2.5 to 40 cm^2, with a minimum gap between tongue and impeller of 10 mm (= 10% of impeller radius).

The pump was tested in a hydraulic set-up designed according to ISO 3555:1977, in which appropriate piping permitted the water to be pumped from and returned to a reservoir with a capacity of 40 m^3 (Fig. 2). Flow-rate could be finely regulated by means of a set of butterfly valves located close to the discharge reservoir. The flow-rate was measured with an Ultraflux UF321 ultrasonic

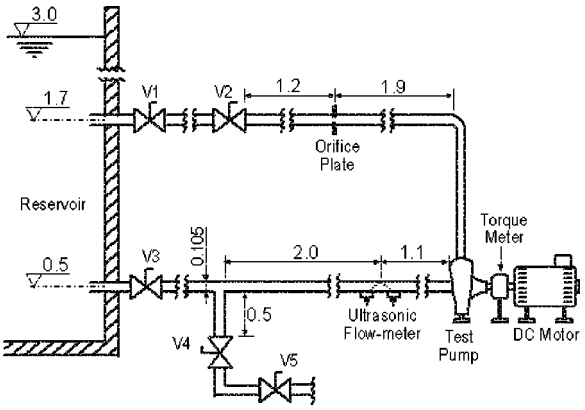

Fig. 2 Experimental test loop (all dimensions in m). Valve V5 was always closed.

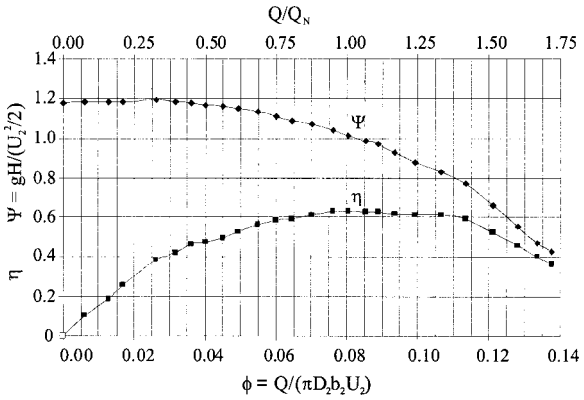

Fig. 3 Performance curves of the pump (head and efficiency)

flow-meter (up to 0.008 m^3/s) and with a calibrated orifice plate connected to an inclined piezo-metric mercury manometer (flow-rates above 0.008 m^3/s). Measurement uncertainty was estimated to be less than $\pm 2.5\%$ for flow-rate values greater than 0.0085 m^3/s, and less than $\pm 4\%$ for the lower flow-rates. The pump was driven by a DC-motor governed by a regulation device that allowed for continuous adjustment of the rotational speed, with a precision of ± 1.0 rpm. Figure 3 shows the head and efficiency performance curves obtained for the pump, which indicate a best efficiency flow coefficient of 0.081 (maximum relative uncertainty was $\pm 1.5\%$ for the head and $\pm 5.0\%$ for the efficiency). This corresponds to a best efficiency flow-rate $Q_N = 0.0145$ m^3/s and a nominal head $H_N = 15.04$ m when the pump is run at 1620 rpm, which is the nominal speed used in the tests. For a special series of tests this speed was varied up to 2520 rpm, but even at this velocity and with the maximum flow-rate achieved (0.036 m^3/s), the NPSH available at the pump inlet was at least twice the NPSH required by the pump, according to the manufacturer's technical data. So, all the tests were carried out with no cavitation in the pump.

Pressure taps with 2 mm diameter were located every 10 deg around the front side of the volute, at 2.5 mm from the outlet of the impeller (Fig. 1). Static pressure at those positions could be obtained with a Kistler 4043A10 piezo-resistive pressure transducer and a current amplifier, which provided absolute pressure values with an uncertainty of less than $\pm 0.5\%$ (according to manufacturer's data). Also, four Kistler 701A miniature fast-response piezo-electric pressure transducers (natural frequency >70 kHz) could be installed on the wall of the volute at any of the 36 tap locations, in order to measure the unsteady pressure. These transducers were mounted inside a special adapter, with an internal cavity previously filled with water (Fig. 1(*b*)). The calculated resonance frequency of the cavity (assumed as a Helmholtz resonator) was 8.8 kHz, more than 20 times above the range of frequencies considered in this study (0–400 Hz).

Calibration checks were conducted by comparing the response of each piezoelectric pressure transducer, with its mounting adapter, to the response of another reference transducer. This reference transducer was piezo-resistive (a Kistler 4043A10). For these tests the two transducers were located at a very close position from each other along the outlet pipe, so that they were exposed to the pressure perturbations emitted from the pump. The reference transducer was installed directly on the wall of the pipe, flush-mounted with respect to the internal surface, whereas the other transducer was installed by means of the connecting adapter indicated above. As expected, the response of both transducers at the frequencies of interest (rotation frequency, blade-passing frequency and harmonics) were the same for each different flow-rate, with differences of less than 1%, i.e., the mounting adapters of the transducers did not introduce any disturbing effect on the measurements.

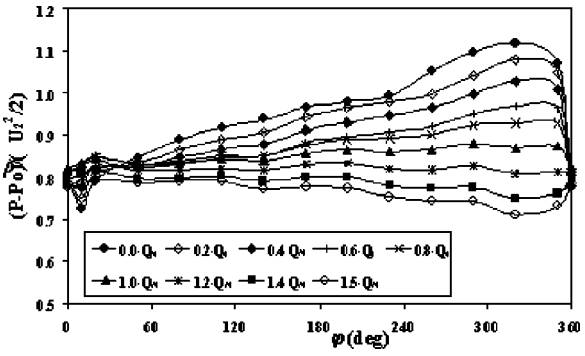

Fig. 4 Steady-static pressure distribution along the volute (front side) as a function of flow-rate

Each of the transducers was connected to a charge amplifier Kistler 5037-A (frequency bandwidth of 30 kHz), which provided pressure measurements with a combined uncertainty of less than $\pm 1.5\%$, according to manufacturer's data. The resulting pressure signals, as well as the signal from an optical tachometer, could be digitized and stored in a personal computer equipped with a multichannel digital-to-analog conversion card. Spectral analysis of the signals was then performed by software.

Static Pressure Distribution

To begin with, a series of tests was conducted to measure the static pressure along the volute, as a function of the flow-rate, by means of the piezo-resistive pressure transducer. Figure 4 shows the peripheral distribution of the static pressure, relative to the total pressure P_0 at the pump inlet, for several values of the flow-rate; angular position φ is zero at the edge of the tongue and it increases with anticlockwise orientation (see Fig. 1). In agreement with the trends indicated in classic texts [1], the static pressure around the volute is quite uniform for flow-rates close to the best efficiency point, but it exhibits either a maximum for low flow-rates or a minimum for high flow-rates in the region $\varphi = 300-330$ deg. Also, a sharp pressure decrease may be observed for the smallest flow-rates close to the volute tongue ($\varphi = 10-20$ deg). These nonuniform pressure distributions are related to the acceleration (high flow-rates) or deceleration (low flow-rates) of the flow along the volute for off-design conditions. The nonuniformity of the pressure in the volute is seen from the flow in the rotating impeller as an unsteady boundary condition, and thus it affects the resulting fluctuations in the pressure field.

Unsteady Pressure Measurements

For the fluctuating pressure measurements, each of the four piezoelectric pressure transducers was mounted at some given position around the volute. During each test the flow-rate was progressively increased from 0 to $1.6 \cdot Q_N$, with steps of $0.1 \cdot Q_N$, where Q_N (best efficiency flow-rate) is equal to $0.0145\ m^3/s$ for the nominal rotational speed of 1620 rpm. For each flow-rate, 50 samples of 1 second long and a digitizing frequency of 1024 Hz were recorded in the computer simultaneously for the four pressure signals and the tachometer signal. Check tests proved that this procedure was sufficient to obtain consistent and repeatable results. After the tests, each recorded sample was FFT processed (a Hanning window was used), and then the frequency averaged power spectrum and cross-power spectrum between signals were finally obtained. The power spectrum provides a direct measure of the amplitude of the fluctuations at each frequency, whereas the phase of the cross-power spectrum provides a measure of the phase delay between the fluctuations of two signals, if acquired simultaneously.

During these series of tests, three of the four piezoelectric pressure transducers were progressively moved around the volute until

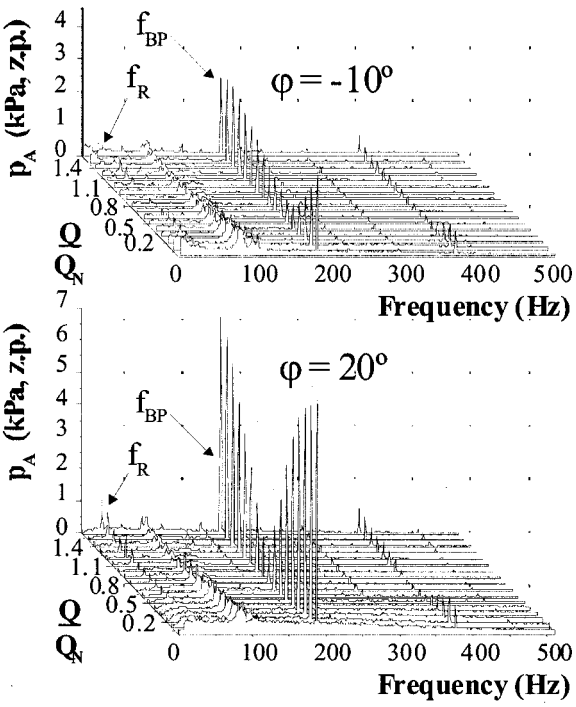

Fig. 5 Pressure pulsations magnitude (zero-to-peak) spectrum as a function of flow-rate for positions $\varphi = -10$ and $\varphi = 20$ deg (position *R* in Fig. 1)

covering the 36 pressure taps. The remaining transducer was located permanently at the tap with $\varphi = 20$ deg, the one labeled as *R* in Fig. 1, so that examination of the corresponding spike amplitude at a given frequency and for a given flow-rate permitted to check the maintenance of the flow conditions between successive tests. After 12 series of measurements of the pressure power spectrum at position *R*, the standard deviation of the zero-to-peak amplitude at the blade passage frequency was found to be less than 0.0006 (non-dimensional value) for each of the 17 flow-rates tested.

Figure 5 shows the evolution with respect to the flow-rate of the power spectrum of the pressure pulsations at the measurement positions $\varphi = -10$ and $\varphi = 20$ deg (the reference position *R*). As expected, the predominant spikes correspond to the frequency of rotation of the impeller (27 Hz) and in particular to the blade passage frequency (189 Hz), together with their respective harmonics. Though both measurement positions are quite close from each other, the trends shown in the spectra are very different, because each position is at one different side of the tongue edge. This is further discussed below for the pressure fluctuations at the blade passage frequency.

Another series of tests was conducted to check the existence or not of acoustic resonance phenomena in the piping [6]. For such purpose the pump was run at several speeds ranging from 1020 to 2520 rpm, while monitoring the pressure fluctuations at the reference position *R* and at the inlet and outlet of the pump. The results obtained for position *R*, at the corresponding blade passage frequency, are shown in Fig. 6 as a function of the relative flow-rate. All the curves are seen to converge in a relatively narrow band, as expected from similarity considerations, except the one associated to 2040 rpm for the low range of flow-rates. This particular behavior was identified to be associated to an acoustic resonance in the suction line (a transducer located at the pump inlet gave pressure amplitudes at f_{BP} that were up to 8 times greater than for normal conditions). Interestingly, after some investigation the phenomenon was found to disappear when slightly opening a butterfly valve located in a branch of the suction pipe (V4 in Fig. 2),

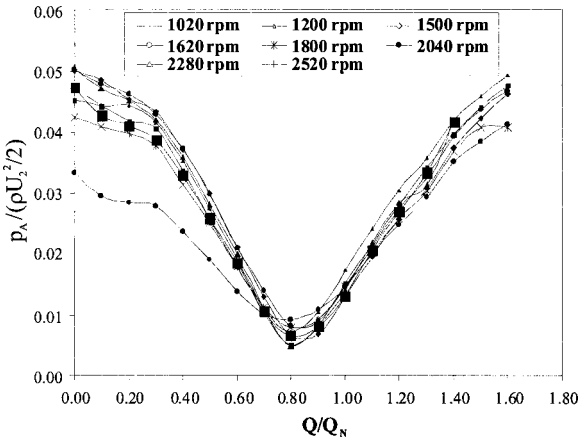

Fig. 6 Normalized amplitude (zero to peak) of pressure fluctuation (blade passage frequency) at position *R* ($\varphi = 20$ deg) as a function of flow rate for different pump rotational speeds

though that branch leaded to a dead end and, hence, in no case there was any flowing water through it (valve V5 in Fig. 2 was always closed). These tests permitted to ensure that no special acoustic phenomena in the piping affects the pressure measurements now reported (obtained with a speed of 1620 rpm.).

Results at the Blade Passage Frequency

For each of the 36 measurement positions the amplitude and the phase of the pressure fluctuations at the blade passage frequency was obtained as a function of the flow-rate, in a fashion similar to the one of Fig. 6 for the reference position *R* ($\varphi = 20$ deg). Figure 6 shows that the pressure amplitude in the tongue region has a minimum in a range of flow-rates around the best efficiency range, and that it increases fast for both lower and higher flow-rates. This is a foreseeable result since only for one capacity (at given speed) there is a good matching between the flow coming out the impeller and the flow in the volute, with nearly no recirculation through the gap between impeller and tongue. This impeller-volute matching capacity is usually around the best efficiency flow-rate, but can be shifted depending on: (a) distribution of various losses (hydraulic, volumetric, disk friction), and (b) volute geometry (mostly spiral shape). At off-design conditions however the absolute velocity at the impeller outlet forms a large incidence angle with respect to the mean flow in the volute (behind the tongue region), which leads to big flow disturbances accompanying each blade passage.

Figure 7 shows the zero-to-peak amplitude of the pressure fluctuations as a function of the flow-rate and the angular position φ around the volute. The map of Fig. 7 has been obtained from the evolutions of the pressure amplitude with respect to flow-rate for each of the 36 measurement points. For each flow-rate, the behavior observed is very different from that of the stationary pressure distribution (Fig. 4). As stated above, in general the pressure fluctuations are comparatively small in the best efficiency region. The maximum amplitudes, which correspond to the region just behind the tongue (measurement positions from $\varphi = 10$ to 50 deg) for very low and high flow-rates, reach a non-dimensional value of 0.05 (about 6% of the static pressure rise through the pump for high flow-rates). These fluctuation values are up to 50% greater than the fluctuations measured by Parrondo et al. [8] for the same volute and a slightly smaller impeller (190 mm), which corresponds to a tongue-impeller gap of 15.8% of impeller radius instead of the present 10%.

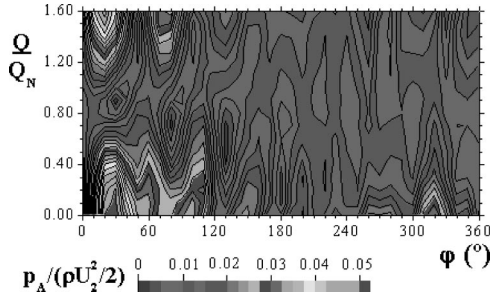

Fig. 7 Normalized amplitude (zero-to-peak) of pressure fluctuation (blade passage frequency) along the volute as a function of flow-rate

Especially for off-design conditions, Fig. 7 presents a modulated pattern along the volute, with node and anti-node positions, somewhat variable with the flow-rate, which is a typical effect of the superposition of correlated waves.

Figure 8 shows the time history of the instantaneous pressure (only the blade passage frequency component) around the volute, during the period between the passage of two consecutive blades in front of the tongue. These results are presented for the flow-rates 20%, 60%, 100%, 130%, and 160% of the best-efficiency flow-rate Q_N. Bold arrows indicate the angular position of the seven blades (pressure side edge on hub shroud) along time. For $Q/Q_N = 100\%$ the pressure fluctuations are observed to behave similarly along the whole volute; they are synchronized with the passage of each blade in front of each measurement position, and so the peak values of the fluctuations occur at different instants for each position. These perturbations result from the nonuniform blade-to-blade distribution of the flow coming out the impeller, and their effects are only local.

For off-design conditions, however, the region of the volute close to the tongue presents a simultaneous evolution of the pressure fluctuations, with big amplitudes in the whole region. Indeed, the pressure pulsations around the impeller outlet and volute inlet are the result of the strong interaction between the blades and the tongue, which produces acoustic pressure waves capable of propagating through the pump towards the inlet and outlet pipelines. Chu et al. [4], who studied a pump operating at 135% of the best efficiency flow-rate, associated the noise production to the impingement on the tongue of the wake behind the passing blades and the associated trains of vortices. Comparing the graphs of Fig. 8 for flow-rates above and below Q_N, the fluctuations in the region close to the tongue are seen to be shifted 180 deg from each other. This is related to the shift of the stagnation point on the tongue and the different characteristics of the recirculation flow through the gap. For low flow-rates the alignment of the blades with the tongue coincides with a positive value of the pressure, whereas it coincides with a negative value for the high flow-rates (in agreement with [4]).

A Simple Acoustic Model

The experimental data obtained suggest that the unsteady pressure field (blade passing frequency) in the volute results from the combination of: (*i*) the hydraulic disturbances (jet-wake pattern) associated to the continuous blade rotation around the volute, and (*ii*) the intermittent interaction of those disturbances and the volute tongue, which is capable of generating acoustic pressure waves. As an attempt to quantify those two components, a simple acoustic model was considered for the volute, which involves a number of system parameters; these parameters were to be estimated for each different flow-rate, so that the predictions of the model on the peripheral distribution of the pressure fluctuation amplitude p_A (at the frequency f_{BP}) could be as close as possible to the experimental data of Fig. 7. In this acoustic model, the interaction between the rotating jet-wake pattern behind the blades and the volute tongue was simulated by means of a number of ideal point sources, each located at some position in the volute. These ideal sources are assumed to radiate plane sound waves (at

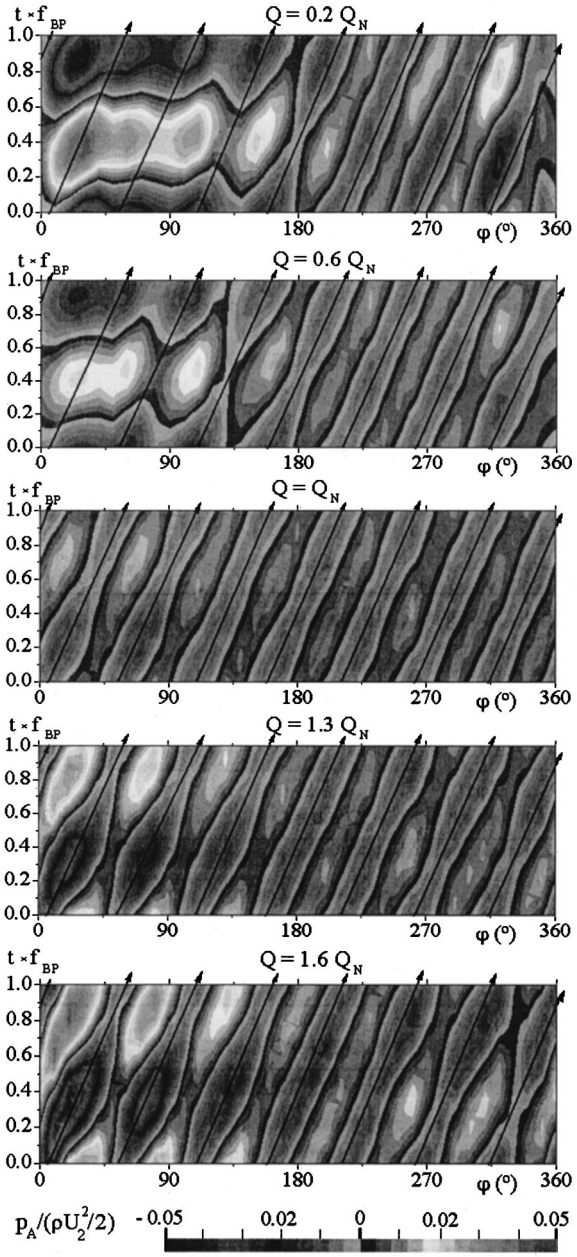

Fig. 8 Time history of the pressure coefficient distribution along the volute (blade passage frequency component) between the passage of two blades, for several flow-rates

f_{BP}) toward the direction of impeller rotation (positive) and also toward the opposite direction (negative). Successive sound circulations along the volute are affected by: (i) divergence (duct with variable section), (ii) sound emission through the impeller channels toward the inlet of the pump, (iii) partial reflection at the tongue edge for waves travelling in the negative direction, due to the abrupt increment in cross-section, and (iv) sound emission through the outlet pipe for waves arriving at the exit of the volute. No incident sound was considered coming from either the inlet or the outlet pipes of the pump.

A calculation algorithm was developed in which the sound reflected or re-circulated from the tongue edge was simulated by means of new, secondary sound sources, so that the resulting pressure field p (at f_{BP}) can be modeled at any angular position φ as:

$$p(\varphi,t)=\sum_{F=1}^{N}\left[P_F\left(\frac{S_\varphi}{S_F}\right)^{\alpha}\cdot e^{-j\cdot(\omega t-k\cdot|\varphi-\varphi_F|-\beta_F)}\right]+P_B\cdot e^{-j\cdot(\omega t-7\varphi)} \quad (1)$$

where $\omega=2\pi f_{BP}$, $\alpha=-(0.5+k_E)$ for $\varphi\geqslant\varphi_F$, $\alpha=0.5-k_E$ for $\varphi<\varphi_F$ and $j=\sqrt{-1}$. In Eq. (1), the term with the P_B pressure amplitude represents the contribution of the continuously rotating jet-wake pattern to the pressure fluctuation field, whereas the term with the summatory represents the contribution of the blade-tongue interaction. Index F accounts for the different sound sources used, either primary or secondary, P_F is the source pressure amplitude, φ_F its angular location and β_F the accumulated time phase delay with respect to the fluctuations associated to the blades motion. In order of keeping a reasonable degree of simplicity for the model, the amplitude of the blade pressure fluctuations, P_B, was always considered uniform along the volute, in spite of the non-uniformity in the static pressure distribution shown in Fig. 4 for off-design conditions. Other parameters used, constant for all flow-rates, were:

(i) k: angular wave number. It is equivalent to the conventional wave number (=number of waves per meter) but relative to angular distances rather than linear distances. For the present case: $k=0.09$ rad^{-1}.

(ii) k_R: sound pressure reflection coefficient at tongue edge. This coefficient, which takes values between -1 and 1, represents the fraction of incident pressure waves that become reflected at some specific position, like at a boundary between two media or at an abrupt change in cross-section. The latter is the case of the tongue gap for waves travelling in the negative direction. Under ideal conditions, if the sections before and after the gap are S_0 and S_1, the pressure reflection coefficient may be shown to be $k_R=(S_0-S_1)/(S_0+S_1)$ (see reference [9] for instance). Hence, when $S_0<S_1$, like in the present case, the sign of k_R is negative, which means a phase delay of 180 deg in the reflected waves with respect to the incident sound. The difference between the incident and the reflected sound waves is transmitted to the other side of the tongue, and so a new circulation is produced along the negative direction. The value $k_R=-0.81$ was adopted for the present case.

(iii) k_E: exponent of sound emission through impeller. If the sound energy propagated along the volute conduit was constant then the pressure along the volute would be proportional to the square root of the volute cross-section, i.e., $\alpha=0.5$ in Eq. (1). However that is not the case because some sound energy is continuously "lost" or emitted through the impeller channels toward the impeller inlet. At this position part of the incident sound waves are reflected back toward the volute (with about 180 deg of phase shift), once again due to the abrupt increment in cross-section. The net proportion of sound energy emitted through the impeller depends on the acoustic impedance of the channels. The effect on the amplitude pressure evolution along the volute is that the exponent α has to be either increased (positive propagation) or decreased (negative propagation) from the value 0.5 in a certain amount k_E. The value finally adopted, $k_E=1.4$, was found to originate reasonably good results when fitting the experimental data for each flow-rate.

The general trends of the experimental results suggested to consider not one but two primary sound sources to reflect the effect of the blade-tongue interaction. The pressure amplitude (P_1, P_2), peripheral position (φ_1, φ_2) and time phase delay (β_1, β_2) for both ideal sources, plus the pressure amplitude P_B, were estimated for each flow-rate by means of a least square error procedure. In this procedure both sources were initially considered totally independent, with no relationship between their locations in the volute, amplitudes or relative phase delay: the only common feature was to radiate harmonic sound at the blade passing fre-

Table 1 Parameters for Eq. (1) and determination coefficient R^2, for each flow-rate tested

Q/Q_N	$\frac{P_B}{\rho U_2^2/2}$	$\frac{P_1}{\rho U_2^2/2}$	φ_1 (deg)	β_1 (deg)	$\frac{P_2}{\rho U_2^2/2}$	φ_2 (deg)	β_2 (deg)	R^2
0.0	0.0162	0.2219	47.5	142.6	0.1913	63.6	-33.7	0.803
0.1	0.0144	0.1799	46.3	143.5	0.1520	65.8	-29.7	0.864
0.2	0.0129	0.1733	46.4	152.6	0.148	65.2	-21.0	0.895
0.3	0.0120	0.1432	46.0	159.8	0.1208	65.5	-11.9	0.914
0.4	0.0112	0.1287	46.7	162.9	0.1097	65.1	-8.9	0.931
0.5	0.0106	0.1207	48.6	165.0	0.1064	63.8	-7.8	0.922
0.6	0.0100	0.0558	50.0	158.1	0.0440	77.5	-6.6	0.854
0.7	0.0103	0.0165	26.9	-161.7	0.0194	72.9	17.3	0.782
0.8	0.0095	0.0059	50.0	-73.3	0.0109	80.0	47.2	0.848
0.9	0.0097	0.0085	14.8	-86.3	0.0138	35.3	56.3	0.775
1.0	0.0100	0.0422	20.0	-43.1	0.0240	49.0	126.4	0.684
1.1	0.0104	0.0634	22.3	-37.2	0.0388	49.2	142.3	0.830
1.2	0.0110	0.0906	24.3	-27.8	0.0622	46.6	156.8	0.915
1.3	0.0116	0.0931	24.4	-22.2	0.0596	52.0	164.3	0.938
1.4	0.0120	0.1048	24.6	-20.5	0.0657	54.3	167.6	0.958
1.5	0.0129	0.1169	25.3	-12.4	0.0731	56.1	174.5	0.969
1.6	0.0139	0.1274	25.7	-4.0	0.0814	55.6	-177.0	0.955

quency. However, as a result of the process for finding the best fitting of the experimental data, the two primary sources were found to be associated in a dipole-like fashion.

Table 1 shows those seven parameters for the seventeen flow-rates tested, whereas Fig. 9 shows the estimated distribution of the pressure amplitude together with the corresponding experimental data for several flow-rates. The last column of Table 1 is the statistical determination coefficient, R^2, defined as:

$$R^2 = 1 - \left(\sum_{i=1}^{36} (P_i - P(\varphi_i))^2 \right) \Big/ \left(\sum_{i=1}^{36} (P_i - \overline{P})^2 \right) \qquad (2)$$

where P_i is the amplitude of the pressure (dimensional) measured at position φ_i, $P(\varphi_i)$ is the amplitude calculated from Eq. (1), and $\overline{P}$ is the arithmetic average of the 36 experimental data. This coefficient takes values between $-\infty$ and 1 and gives a measure of the degree of agreement with the Eq. (1) model for the data fitted, the closer to 1 the better fitting. Bearing in mind that Eq. (1) assumes implicitly notorious simplifications (point sound sources, uniform distribution for P_B, simplified geometry . . .), an R^2 coefficient of about 0.9 or greater may be considered satisfactory.

As expected, the pressure amplitudes of both sound sources (P_1 and P_2 in Table 1) happen to be large at off-design conditions (particularly for very low flow-rates), thus indicating a strong blade-tongue interaction. Their order of magnitude is up to more than 10 times larger than the order of the blade amplitude fluctuation P_B. Also, they are two or three times greater than the maximum pressure amplitude measured for the respective flow-rate. However, P_1 and P_2 are very small for flow-rates between 70% and 100% of Q_N, because in the range of the best efficiency point the on-coming flow from the impeller is expected to distribute regularly around the tongue, producing little disturbance. As a result, the R^2 coefficient obtained for that flow range is poorer than for off-design conditions.

For all flow-rates, the angular positions φ_1 and φ_2 estimated for the two sound sources (Table 1) are located in the first quadrant, close to the tongue edge, with a difference between them of about 20 and 30 deg for small and big flow-rates, respectively. Also, the amplitude P_2 is about 70–80% of P_1, and the phase delays β_1 and β_2 are about 180 deg shifted from each other for both small and big flow-rates. All this suggests that the second sound source actually results from the sound radiation of the former along the adjacent channel of the impeller, followed by a negative reflection at the impeller inlet due to (once again) the abrupt increment in cross-section. Since these two ideal sound sources are close positioned, have the same order of magnitude and radiate sound with a relative phase delay of about 180 deg, they behave very much like a dipole that radiates harmonic sound at the blade passing frequency (no other frequency has been analyzed in this study).

Additionally, when comparing the typical value of the same phase delay, either β_1 or β_2, for both small and big flow-rates,

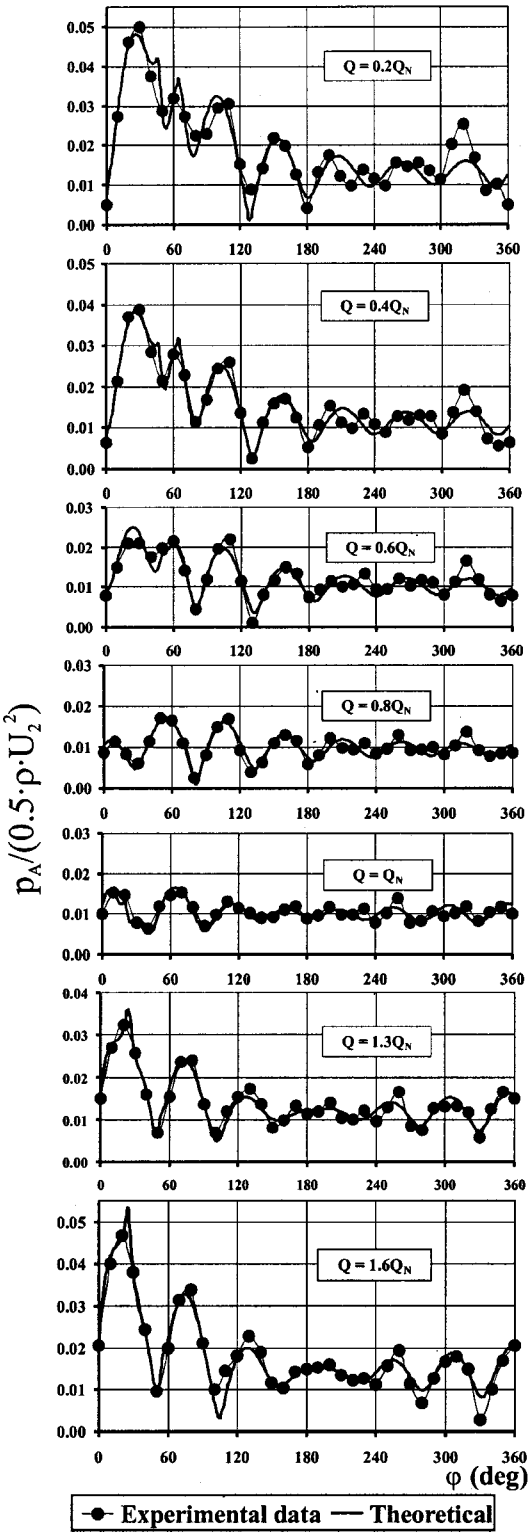

Fig. 9 Comparison of the experimental and theoretical amplitude (zero-to-peak) of the pressure fluctuations coefficient at the blade passage frequency for several flow rates

they happen to be shifted about 180 deg, in agreement with the time positions associated to the maximum pressure values in Fig. 8 for different flow-rates.

In summary, the effect of the blade-tongue interaction on the fluctuating pressure field (at f_{BP}) in the volute of the pump tested can be reasonably simulated by means of two ideal sound sources

that form a dipole, with amplitude that increases fast when diverging from the best-efficiency flow-rate. The positive or negative combination of that sound field with the fluctuations associated to the continuous rotation of the blades leads to the modulated pattern in the pressure amplitude suggested by Figs. 7 and 9 for off-design conditions.

Conclusions

A systematic series of tests have been conducted to measure the dynamic pressure in a number of positions around the single volute of a centrifugal pump with a nondimensional specific speed of 0.48. The analysis focused on the pressure amplitude and phase delay at the blade passage frequency. The pressure fluctuations registered around the volute were found to be very dependent on both angular position and flow-rate; maximum values corresponded to the tongue region for off-design conditions. Comparison of the present data with previous results for a pump with the same volute and a smaller impeller shows that reducing the tongue gap from 15.8% to 10% of the impeller radius leads to an increase in the maximum pressure amplitudes at off design conditions of about 50%.

For a given flow-rate, the data obtained indicate that the pressure fluctuations at any peripheral position along the volute result from the superposition of the perturbations induced by: (*i*) the passage of each blade in front of that point; and (*ii*) the passage of each blade in front of the tongue. In order to quantify the effects of this blade-tongue interaction, a simple acoustic model was considered in which two point sources radiate plane sound waves along the volute. The properties obtained for these two ideal sources after fitting the experimental data by means of a least-square error procedure show that they are coupled forming a dipole. This blade-tongue interaction appears to be dominant in the generation of the dynamic pressure field in the volute (and the generation of noise) for off-design conditions.

Acknowledgments

The authors gratefully acknowledge the financial support of the Ministerio de Ciencia y Tecnología (Spain) under Projects TAP-99-0738-C02-02 and DPI-00-0686.

Nomenclature

D_2 = impeller diameter at outlet (=200 mm)
P_0 = total pressure at pump inlet
P_B, P_F = zero-to-peak pressure amplitude (Eq. (1))
P_1, P_2 = zero-to-peak pressure amplitude of two dipole-like sound primary sources in volute (Table 1)
Q, Q_N = flow-rate, flow-rate at best efficiency point
S_φ = cross-section of volute at position φ
R^2 = determination coefficient (Eq. (2))
U_2 = peripheral velocity at impeller outlet
b_2 = impeller width at outlet (=16.9 mm)
c = speed of sound
f_R, f_{BP} = frequency of rotation, blade passage frequency
k = $\pi f_{BP} D_2/c$: angular wave number (Eq. (1))
k_E = exponent of sound emission through the impeller channels (Eq. (1))
k_R = sound reflection coefficient
p, p_A = pressure, zero-to-peak pressure amplitude
α = net acoustic divergence exponent (Eq. (1))
β_F = time phase delay (Eq. (1))
ϕ = $Q/(\pi D_2 b_2 U_2)$: flow coefficient
φ = angular position around impeller
ρ = fluid density
ω_S = $2\pi f_R Q_N^{1/2}/(gH_N)^{3/4}$: specific speed (=0.48)
ψ = $gH/(U_2^2/2)$: head coefficient

References

[1] Stepanoff, A. J., 1957, *Centrifugal and Axial Flow Pumps* (2nd ed.), J. Wiley, New York.
[2] Lézé, F., Besombes, M., Tourret, J., Pluviose, M., and Bertinier, M., 1992, "Visualization of the Dynamic Pressure Field in a Centrifugal Fan in the Study of Noise Generation Mechanisms," *Proc. of Fan Noise Symposium*, Senlis, France, pp. 213–220.
[3] Chu, S., Dong, R., and Katz, J., 1995, "Relationship Between Unsteady Flow, Pressure Fluctuations, and Noise in a Centrifugal Pump; Part A: Use of PDV Data to Compute the Pressure Field," ASME J. Fluids Eng., **117**, pp. 24–29.
[4] Chu, S., Dong, R., and Katz, J., 1995, "Relationship Between Unsteady Flow, Pressure Fluctuations, and Noise in a Centrifugal Pump; Part B: Effects of Blade-Tongue Interaction," ASME J. Fluids Eng., **117**, pp. 30–35.
[5] Dong, R., Chu, S., and Katz, J., 1997, "Effect of Modification to Tongue and Impeller Geometry on Unsteady Flow, Pressure Fluctuations, and Noise in a Centrifugal Pump," ASME J. Turbomach., **119**, pp. 506–515.
[6] Morgenroth, M., and Weaver, D. S., 1998, "Sound Generation by a Centrifugal Pump at Blade Passing Frequency," ASME J. Turbomach., **120**, pp. 736–743.
[7] Kaupert, K. A., and Staubli, T., 1999, "The Unsteady Pressure Field in a High Specific Speed Centrifugal Pump Impeller. Part I: Influence of the Volute," ASME J. Fluids Eng., **121**, pp. 621–626.
[8] Parrondo, J. L., Fernández, J., Santolaria, C., and González, J., 1996, "Measurements in the Dynamic Pressure Field of the Volute of a Centrifugal Pump," Proc. XVIII IAHR Symposium on Hydraulic Machinery and Cavitation, E. Cabrera et al., eds., Kluwer Academic Publishers, Dordrecht, Netherlands, pp. 401–410.
[9] Turner, J. D., and Pretlove, A. J., 1991, *Acoustics for Engineers*, MacMillan Education Ltd, Houndmills, UK, pp. 142–149.

G. Wuibaut

G. Bois

Laboratoire de Mecanique de Lille,
(URA CNRS 1441),
ENSAM, 8, Bd Louis IV,
59046 Lille, Cedex, France

P. Dupont
Laboratoire de Mecanique de Lille,
(URA CNRS 1441),
Ecole Centrale de Lille,
BP 48, 59651 Villeneuve d'Ascq Cedex, France

G. Caignaert
Laboratoire de Mecanique de Lille,
(URA CNRS 1441),
ENSAM, 8, Bd Louis IV,
59046 Lille, Cedex, France
e-mail: Guy.Caignaert@lille.ensam, fr

M. Stanislas
Laboratoire de Mecanique de Lille,
(URA CNRS 1441),
Ecole Centrale de Lille,
BP 48, 59651 Villeneuve d'Ascq Cedex, France

PIV Measurements in the Impeller and the Vaneless Diffuser of a Radial Flow Pump in Design and Off-Design Operating Conditions

This paper presents and discusses the results of an experimental program that has been made on an air test rig of a radial flow pump. The tested impeller is the so-called SHF impeller. Many experimental data have already been produced (tests in air and in water) on that geometry and these results are still used as databases for the validation of CFD codes. For the present study, an air test rig has been chosen for optical access facilities and measurements were realized with a vaneless diffuser. The 2D Particle Image Velocimetry technique has been used and measurements of flow velocities have been made simultaneously in the outer part of the impeller and in the vaneless diffuser. Measurements have been realized in five planes, in the hub to shroud direction, for various relative flow rates (design and off-design operating conditions). First, the paper focus on the evolutions of the phase averaged velocity charts in the impeller and the diffuser. Limitations of the phase averaging technique clearly appear in the very low partial flow rates and this will be related to previous pressure measurements analysis establishing the occurrence of rotating stall within the impeller for such operating conditions. The paper also proposes an analysis of the rates of fluctuations of the velocity charts and the evolutions in the various measuring planes as the relative flow rate becomes lower.
[DOI: 10.1115/1.1486473]

Introduction

The design of pumps is mainly based on steady flow assumptions in runner, vaneless, and vaned diffusers. This kind of approach is suitable for design operating conditions of classical turbomachinery geometries. However, to understand and take into account wide operating ranges in pump designs, it is necessary to improve the knowledge of unsteady effects and rotor-stator interactions. Experimental data are more and more required in order to calibrate new design techniques including the unsteady character of the flow. For a better optimization of the pump design, numerical simulations of internal flow are now proposed, including a coupling between the different parts of the machines, and it is necessary to validate these methods to define the validity range of the various kinds of approach.

The present paper refers to a first series of results of an experimental program that has been realized on an air test rig of a radial flow pump (optical access facilities). These first results are related to a pump configuration with a vaneless diffuser and no volute. The tested impeller is the so-called SHF impeller for which many experimental and numerical investigations have already been made and described in previous works (references [1–8]).

Up to now, these results mainly refer to static and dynamic pressure measurements and to hot wire (s) anemometers or Laser Doppler Velocimetry. Particle Image Velocimetry appears to be very useful for a better understanding of phenomena associated to rotor-stator interactions [9–12].

In the present paper, PIV has been used for the analysis of flow velocities in the outer part of the impeller and the vaneless diffuser. Results in design and off-design operating conditions are presented and analyzed.

Contributed by the Fluids Engineering Division for publication in the JOURNAL OF FLUIDS ENGINEERING. Manuscript received by the Fluids Engineering Division July 27, 2001; revised manuscript received April 4, 2002. Associate Editor: J. Katz.

1 Experimental Setup

The air test rig has been already described in references [13,14], as well as the PIV measurement device and data acquisition procedure. The impeller main characteristics are the following:

- outlet radius: R2 = 256.6 mm
- tip inlet diameter: 282.2 mm
- outlet width: 38.5 mm
- outlet blade angle: 22.5 deg (measurement from the peripheral direction)
- mean blade thickness: 9 mm
- number of blades: $Z = 7$
- speed of rotation: up to 2500 rpm
- design flow rate: $QN = 0.336\ m^3/s$ (at 1710 rpm)

The outlet part of that impeller is characterized by a 2D design. The vaneless diffuser has been designed with an inlet diameter equal to 515 mm, an outlet diameter equal to 575 mm and a constant width B3 equal to 39 mm. As it can be seen in Fig. 1, PIV measurements have been made in planes perpendicular to the pump axis of rotation. Each plane is defined by its axial position B with a reference to the hub part of the diffuser. Through the transparent shroud parts of the impeller and the diffuser, the PIV camera observes the Poly Ethylene Glycol particles which are injected into the flow with a smoke generator. The PIV System is based on cross correlation technique. An electronic box has been used in order to synchronize the CCD camera and YAG pulsed laser with the impeller rotation. One instantaneous velocity field is measured

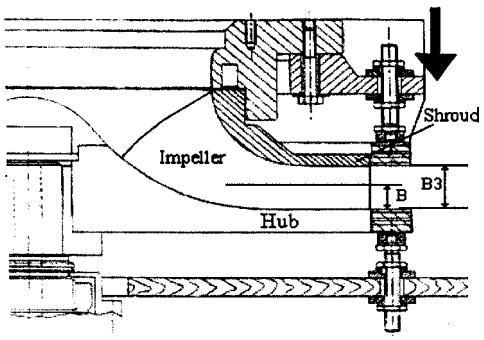

Fig. 1 Definition of a measurement plane

each two complete revolution of the impeller.
The tests have been made with the following conditions:

- energy of each laser pulse: 250 mJ
- pulse duration: 10 ns
- delay between two pulses: 35 μs

The camera is a Kodak camera with 1008×1016 pixels.
The experimental database contains results for the following conditions:

- speed of rotation: 1710 rpm
- relative flow rates Q/QN: 0.26, 0.45, 0.63, 0.91, 1.02, 1.61
- five measurements planes in the hub to shroud direction: B/B3 = 0.12, 0.25, 0.50, 0.74, 0.87
- two different views: view 1 covers the outlet throat of the impeller and view 2 covers one blade trailing edge. The two views are symbolically presented in Fig. 2.

For each operating and measuring conditions, 230 sets of two successive images have been registered. Each set of two successive images is then analyzed in order to get one velocity map, using the image cross correlation technique. In order to improve the quality of the results, a background view has been subtracted on each PIV image. All sets of two consecutive images have then been analyzed with 32×32 or 24×24 pixels elementary cells. For the analysis of operating conditions near design conditions, an advanced digital interrogation technique has been used by using a window offset [15]. Finally, a mask has been used for each view in order to eliminate vectors in non-fluid zones. Such a procedure allows for the determination of two components of absolute fluid velocities (in the measuring plane), defined in the frame of each view. A post-treatment procedure has been developed in order to locate the point of the pump axis of rotation in the view frame so that it becomes possible to define the radial and peripheral directions in each point of a view and then obtain the absolute or relative velocities and their radial and peripheral components or the flow angles α (between the absolute velocity and the peripheral direction) and β (between the relative velocity and the peripheral direction).

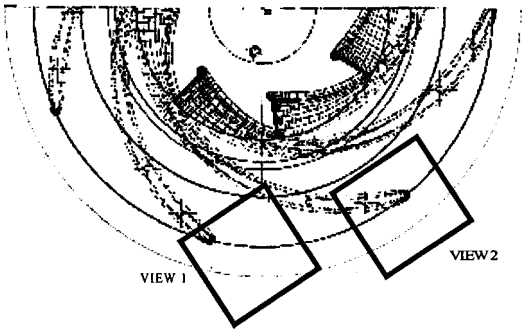

Fig. 2 Definition of the two views

In every measurement plane and for each view, 230 instantaneous velocity maps are available for every operating condition. Measurements have been made for the same position of the impeller and synchronous averages have been calculated for each series of 230 instantaneous velocity fields. According to the various sources of uncertainties during the measurement procedure, the relative uncertainty of the instantaneous flow velocity, in each point of the measurement grid, has been estimated to 2%. In each point of the measurement grid of a view, the instantaneous components of the absolute flow velocity are defined as $u(x,y,t)$ and $v(x,y,t)$. A good estimation of the synchronous averaged velocity in that point can so be obtained with an arithmetical average over the 230 data (Eq. (1)).

$$\overline{u}(x,y)=\frac{1}{230}\sum_{i=0}^{229}u(x,y,t_0+i\Delta t)$$
$$\overline{v}(x,y)=\frac{1}{230}\sum_{i=0}^{229}v(x,y,t_0+i\Delta t) \tag{1}$$

Using the Reynolds decomposition model (Eq. (2)) it becomes possible to obtain a kinetic turbulence energy K from the calculation of the arithmetical average of the square of velocity fluctuations $u'(x,y,t)$ and $v'(x,y,t)$ (Eq. (5)).

$$u(x,y,t)=\overline{u}(x,y)+u'(x,y,t)\quad v(x,y,t)=\overline{v}(x,y)+v'(x,y,t) \tag{2}$$

$$\overline{u'^2}(x,y)=\frac{1}{230}\sum_{i=0}^{229}u'^2(x,y,t_0+i\Delta t) \tag{3}$$

$$\overline{v'^2}(x,y)=\frac{1}{230}\sum_{i=0}^{229}v'^2(x,y,t_0+i\Delta t) \tag{4}$$

$$K(x,y)=\frac{1}{2}(\overline{u'^2}(x,y)+\overline{v'^2}(x,y)) \tag{5}$$

$$Tu(x,y)=\frac{\sqrt{K(x,y)}}{R_2.\Omega} \tag{6}$$

2 Phase Averaged Velocity Components

Blade to blade evolutions of $\overline{C_u}/U_2$, nondimensional mean absolute velocity peripheral components, are shown for a particular radius inside the impeller ($R/R_2=0.91$) in Fig. 3. That particular section has been chosen for further comparisons with LDV measurements and calculations from [15] and [7]. The various parts of Fig. 3 correspond to four measuring planes between hub and shroud. In each figure, the evolutions have been plotted for various operating conditions, from $Q/QN=0.45$ to $Q/QN=1.61$. Each figure contains averaged results issued from the two views with some amount of overlapping. That overlapping in the post-treatment shows a very good coherence between the results in the two views, for the flow rates $Q/Qn=1.61$ to 1.02. In Fig. 3, for the part load conditions $Q/Qn=0$, 45 and 0.63, close to the position angle $\theta/(2\pi/7)$, the gap in the curves can be explained by the fact that the coherence between two view's data is decreasing due to the unsteady character of the flow. In Fig. 3, for the position angle between 0.1 and 0.25, the gap in curves is due to a lack of informations between the two views as shown in Fig. 2.

First of all, it is interesting to make a comparison between integrated values of $R.\overline{\overline{Cu}}$ issued from the PIV measurements with the ones deduced from the available overall performances of the impeller in terms of internal head [1]. No PIV measurements can be obtained at impeller outlet ($R=R2$) because of flare due to

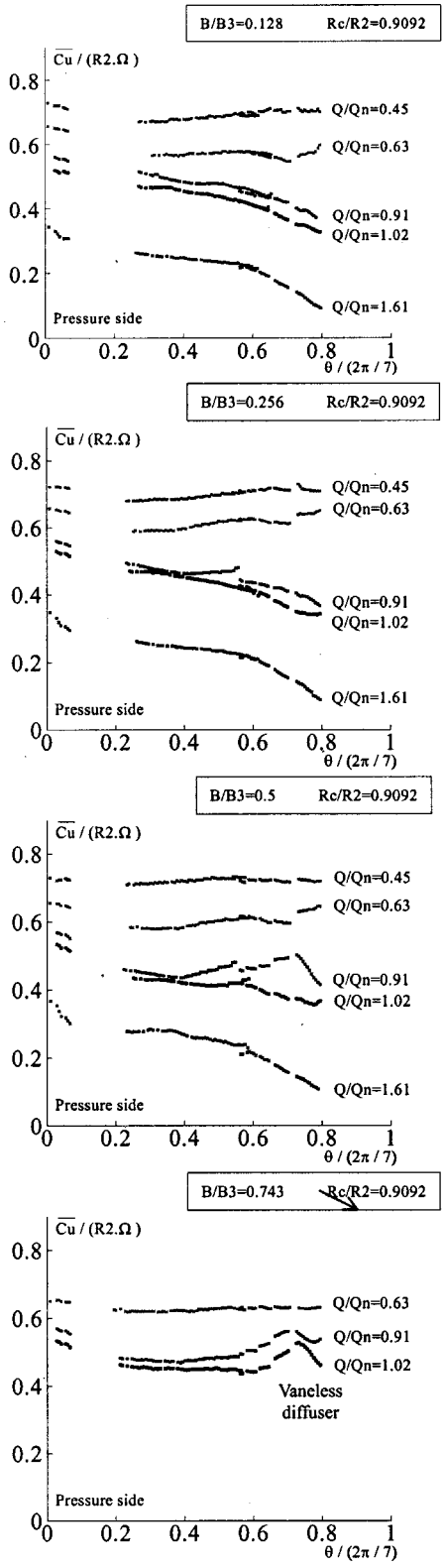

Fig. 3 Evolutions of $\overline{Cu}/U_2$ in the blade to blade direction for various axial positions and a fixed radius

the gap between the rotating and the stationary parts of the pump. In order to obtain the mean value of $R.\ \overline{\overline{Cu}}$ at the impeller outlet, both results inside the impeller and in the vaneless diffuser have been extrapolated to the outlet impeller radius. The integrated local values of $R\ \overline{\overline{Cu}}$ from PIV measurements are based on only five hub to shroud positions.

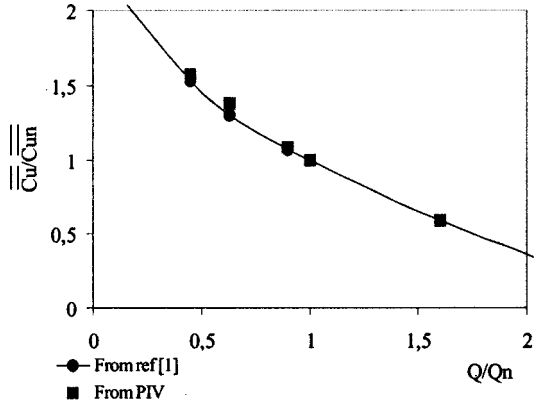

Fig. 4 Overall mean values of the peripheral component of flow velocities at impeller outlet

So, it is evident that the obtained value of $R\ \overline{\overline{Cu}}$ may be wrong. It has been decided to plot the ratio $\overline{\overline{Cu}}/\overline{\overline{Cun}}$ with PIV, making the assumption that the relative error could be of the same order of magnitude for different mass flow conditions.

For design conditions, the total head coefficient obtained by the PIV measurements and the one deduced from torque measurements are quite in agreement within $\pm 0.3\%$.

For the other operating conditions, it can be seen in Fig. 4 that the PIV results closely correspond to the overall curve of reference [1] except for a nondimensional flow rate equal to 0.63.

Looking at the blade-to-blade evolution of C_u/u_2, it can be seen that they are quite similar, for each flow rate, whatever the axial position B/B3 between 0.128 and 0.50. In the shroud region, levels and gradients are modified, especially for operating conditions corresponding to a nondimensional flow rate equal to 0.63. Similar considerations can be extracted from the observation of the radial velocity components. A clear modification can be observed for B/B3 = 0.74, below the design flow rate in the suction side of the impeller blade.

It appears that the impeller suction side shroud corner is dominated by an important relative velocity gradient and an accumulation of low momentum fluid. For the rest of the blade passage section, the relative velocity is mainly uniform along the blade height while it regularly increases from the pressure side to the suction side as can be seen in Fig. 5 for design conditions, corresponding to a classical nonviscous flow pattern. These kinds of flow structures have been already well reported by Eckardt [17] and Ubaldi [18] for machines comparable to the present one.

For the present case and for design flow operating conditions, this particular flow structure seems to start below values of $R/R_2 = 0.80$ inside the impeller. This location is situated after the axial to radial bend of the impeller where important decrease of turbulence due to Coriolis effects occur in the suction side shroud corner as explained by Eckardt.

The so-called wake can be easily detected in the Fig. 5 by the comparison between the isovalues curves of the relative mean velocity in view 2 for axial positions B/B3 = 0.871 and B/B3 = 0.743, starting from the shroud compared with the one obtained at mid-height (B/B3 = 0.5).

When the flow goes toward the blade outlet section, suction blade curvature continues to act on the fluid with higher values of Coriolis effects due to rotation. Wake is so carried toward the mid-height on the suction side. The wake coming from the pressure side can also be seen in the vaneless diffuser channel where its location tends to be transported toward the mid blade to blade passage.

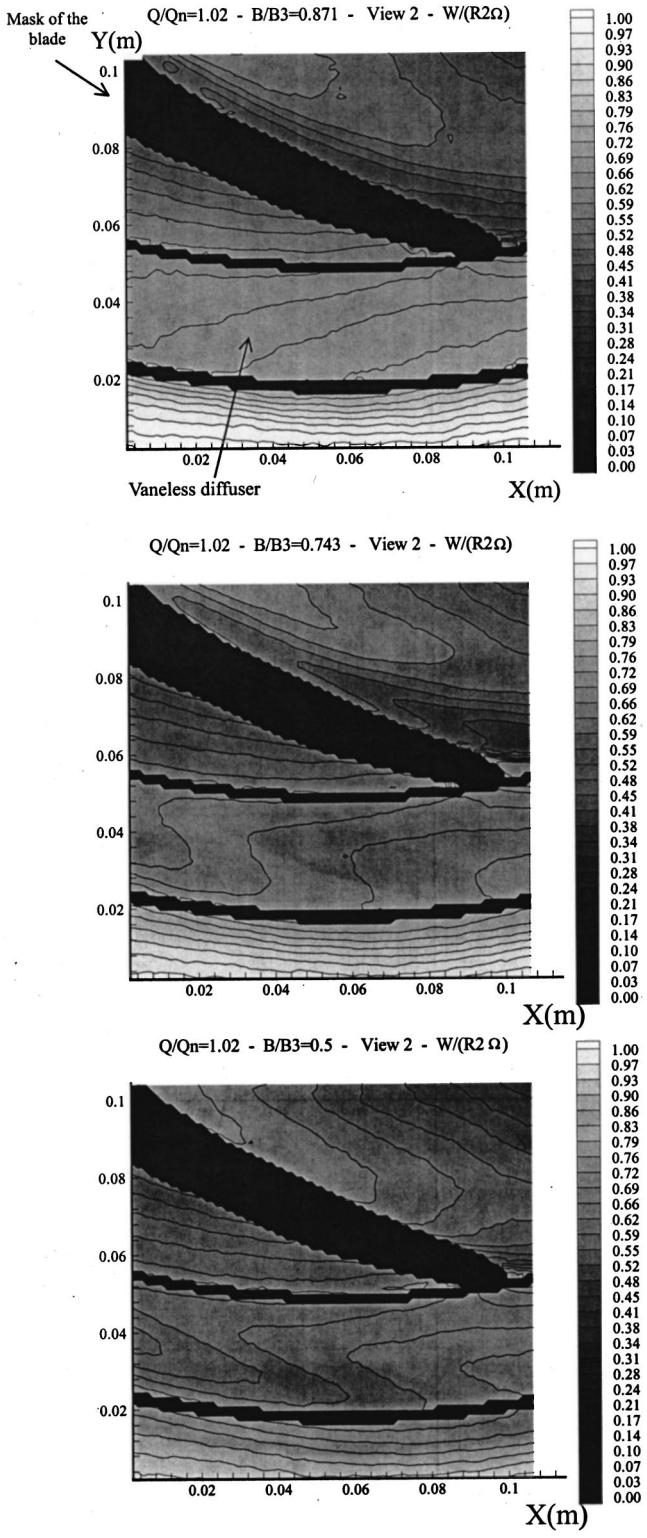

Fig. 5 Isovalues of non-dimensional mean relative velocities

3 Off-Design Conditions

Always for the same radial position $R/R_2=0.91$ and for partial flow operating conditions, the wake structure grows, reaches the blade mid-height for $Q/QN=0.91$ and fill the entire blade suction side for $Q/QN=0.63$. For $Q/QN=0.45$, the wake structure is no longer detected since the effects of the positive incidence at the blade leading edge of the impeller blades lead to dominant effects

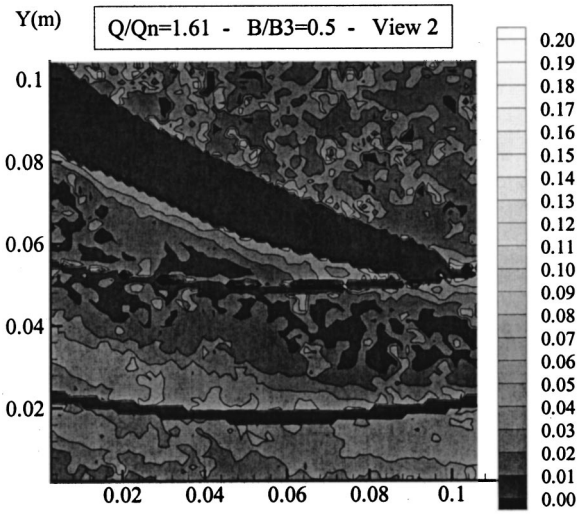

Fig. 6 Rates of velocity fluctuations B/B3=0.5 Q/Qn=1.61 view 2

on the losses over the entire blade suction side. It also has to be noted that, for $Q/QN=0.63$, the potential flow organization outside the wake region does not exist anymore. This aspect may be related to the modification already described in Section 2 concerning the tangential velocity gradient modifications. It must be remembered ([1]) that the impeller inlet recirculation critical flow rate has been experimentally determined for $Q/QN=0.68$.

So, for $Q/QN=0.63$, the inlet impeller recirculation may be more extended; this can also explain the velocity field modifications observed inside the impeller and the vaneless diffuser. The evolutions of nondimensional velocity fluctuation rate $Tu(x,y)$ (Eq. (6)) are presented in Figs. 6–10 for different flow rates.

These figures relate to measurements at mid-height. In design conditions (Fig. 7), the velocity fluctuations are very low within the outer part of the impeller: they present less than 5% of the peripheral velocity based on the outlet impeller radius R_2. In this region, the fluctuations seem to be equivalent in the pressure and suction sides vicinity, with higher values in the suction side outlet region of the impeller.

For $Q/QN=1.61$, fluctuations on the suction side are lower but the level reaches 6% on the pressure side. In the diffuser outlet,

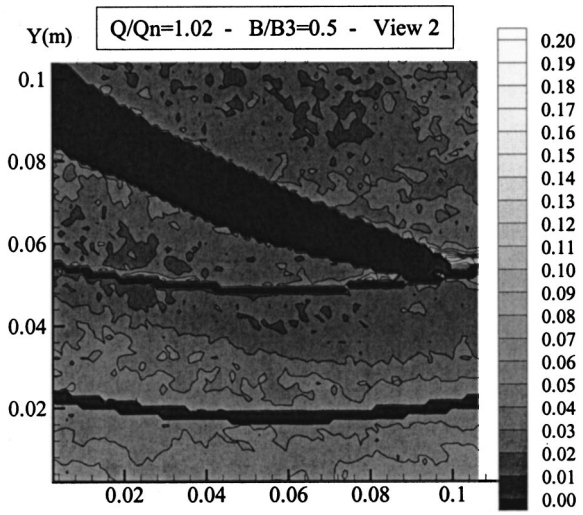

Fig. 7 Rates of velocity fluctuations B/B3=0.5 Q/Qn=1.02 view 2

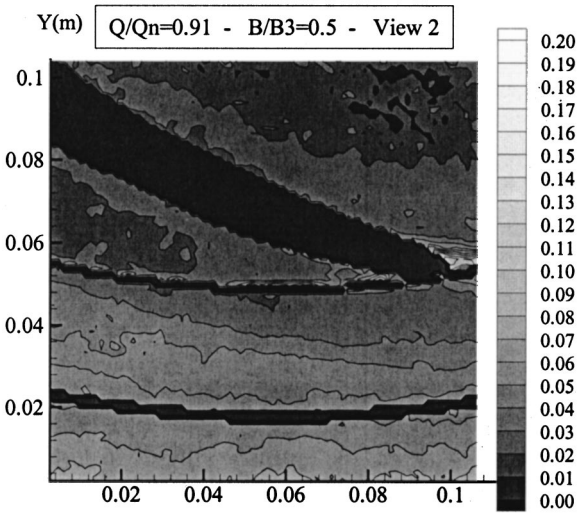

Fig. 8 Rates of velocity fluctuations B/B3=0.5 Q/Qn=0.91 view 2

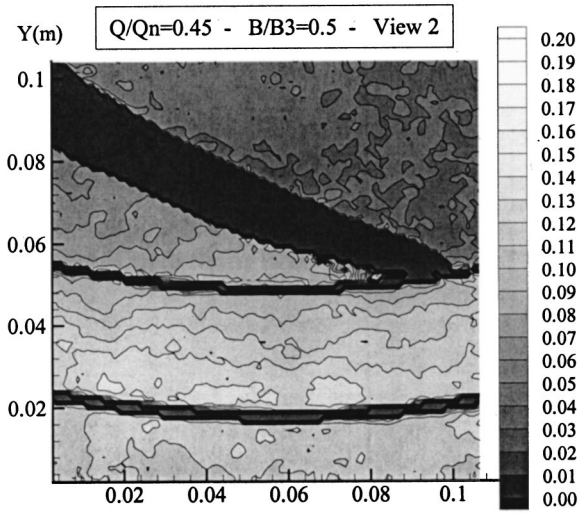

Fig. 10 Rates of fluctuations B/B3=0.5 Q/Qn=0.45 view 2

the fluctuation rates become higher (nearly 6%) as the absolute flow velocities are becoming much smaller: this can also be attributed to the influence of the sudden expansion at the diffuser outlet and to flow stability limits, with higher fluctuations near the shroud as already described in [16] for a vaneless diffuser with a higher outlet radius.

Figure 11(*a*) presents the same type of results, at mid-height also, but for the view 1. As it can be seen on that figure, some problems with light reflection and diffusion by the trailing edge of the blade have been encountered during the tests, and it has been decided to mask a part of the view in order to protect the camera. In that figure, it appears first that the rate of velocity fluctuations within the diffuser is higher (up to 7%) along what can be called the wake of an impeller blade.

As shown in Fig. 11(*b*) the spread of that wake zone appears to be wider near the hub. Second, a large region with very low fluctuation rates can be seen within the impeller blade to blade section near the suction side. This is probably related to the evolution of the low momentum part that develops inside the blade passage near the shroud section side corner as already pointed out in the previous section.

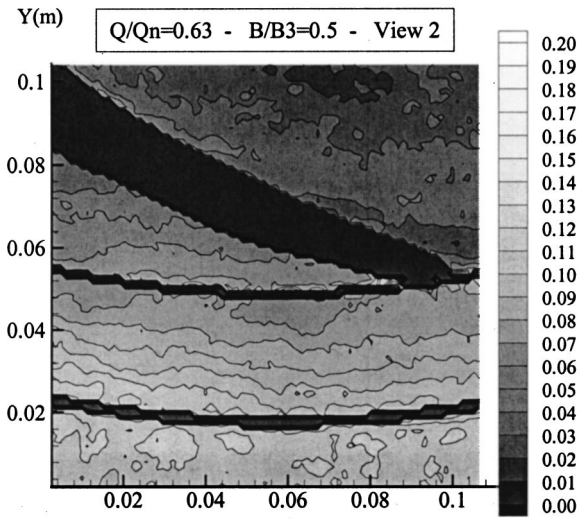

Fig. 9 Rates of velocity fluctuations B/B3=0.5 Q/Qn=0.63 view 2

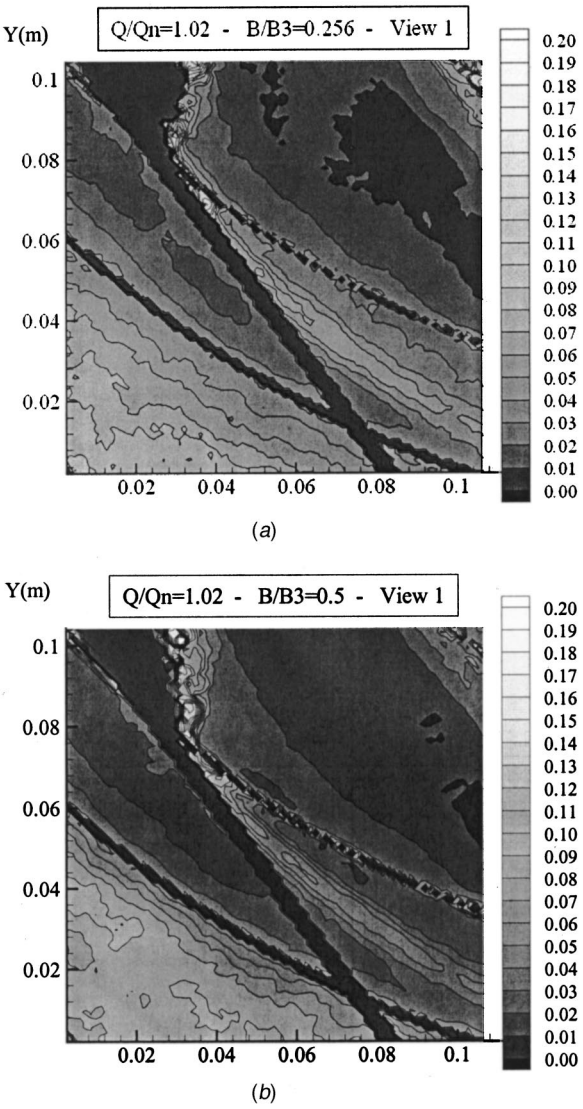

Fig. 11 (*a*) rates of fluctuations B/B3=0.5 Q/Qn=1.02 view 1; (*b*) rates of fluctuations B/B3=0.256 Q/Qn=1.02 view 1

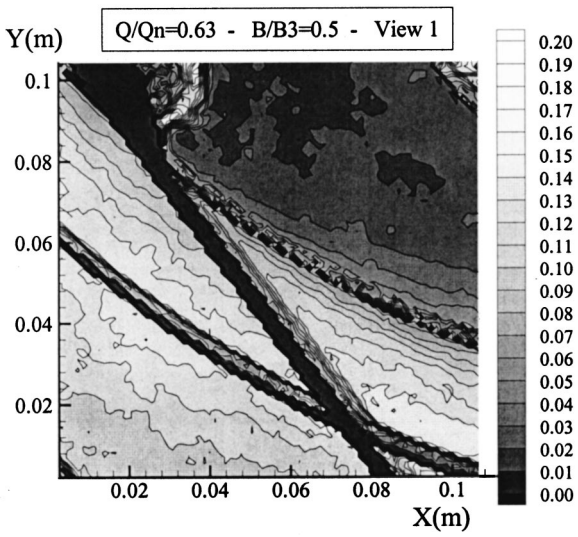

Fig. 12 Rates of fluctuations B/B3=0.5 Q/Qn=0.63 view 1

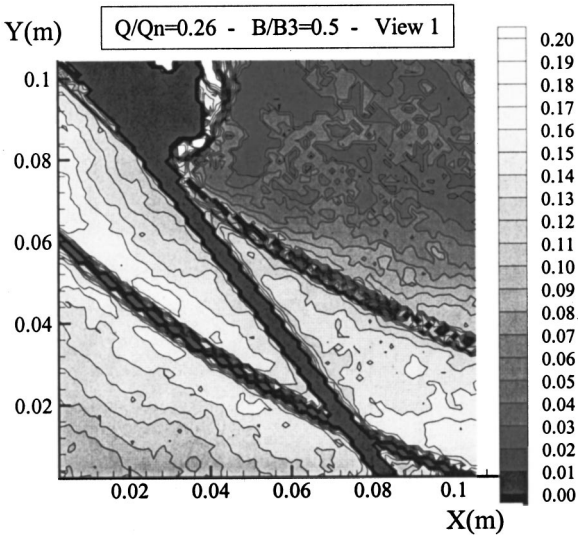

Fig. 13 Rates of fluctuations B/B3=0.5 Q/Qn=0.26 view 1

For lower flow rates, Figs 12 and 13, the rates of fluctuations regularly increase both in the vaneless diffuser (0.08 to 0.14 for $Q/QN=0.63$) and in the pressure side zone inside the impeller (up to 10% for $Q/QN=0.26$ where large instabilities with reverse flows have been observed in relationship with the behavior of the vaneless diffuser in partial flow conditions). In these cases, the instabilities progressively propagate from the outer part of the diffuser to the outer part of the impeller pressure side. However, it has to be kept in mind that it is rather difficult to define correctly a phase averaged velocity chart for relative flow rates lower than 0.45 with only 230 instantaneous velocity charts. On the contrary, the suction side zone is not affected by the vaneless diffuser instabilities since the fluctuation rates remain low (about 3%), except for $Q/QN=0.63$ where the levels reach locally 8% close to the suction side. This corresponds to a zone which has been already described by several authors: a new increase of turbulence may occur near the suction side of the blade, in association with the boundary layer separation that creates the so-called jet and wake configuration.

Conclusion and Perspectives

The PIV technique has been successfully applied to the instantaneous characterization of velocity distributions in a radial flow pump impeller associated with a vaneless diffuser for design and off-design operating conditions. Near design conditions, flow within each blade to blade passage can be considered as steady in the relative frame according to the axisymmetry of the casing (vaneless diffuser without volute). The so-called ''jet and wake'' structure can also be observed inside impeller blade passage as well as in the vaneless diffuser, associated with local velocity fluctuations and/or instabilities coming from the diffuser itself. The pressure side region is affected by diffuser instabilities whereas the suction side is more dependent on inlet conditions and impeller flow developments. At very low flow rates ($Q/QN=0.26$), large instabilities develop in the vaneless diffuser and even propagate in the outer part of the impeller with unsteady flow patterns in the relative frame.

The available database still need the development of post-treatment procedures in order to become more useful especially for the validation of numerical approaches in off-design conditions. These developments and comparisons are still in progress. The technique is now used on the same test rig to study impeller-vaned diffuser interactions.

Nomenclature

R = radius
R_2 = outlet radius of the impeller
Z = number of blades of the impeller
N = speed of rotation
Ω = impeller angular velocity
Q = flow rate
QN = design flow rate
B3 = constant width of the vaneless diffuser
B = distance between the laser sheet and the hub
(x,y) = coordinates of a point in the frame grid
t_0 = time of the first sample
Δt = duration of two turns of the impeller
$u(x,y,t)$ = absolute instantaneous velocity (x component)
$v(x,y,t)$ = absolute instantaneous velocity (y component)
$\overline{u}(x,y)$ = phase averaged velocity (x component) (Eq. (1))
$\overline{v}(x,y)$ = phase averaged velocity (y component) (Eq. (1))
$u'(x,y,t)$ = instantaneous velocity fluctuation (x component) (Eq. (2))
$v'(x,y,t)$ = instantaneous velocity fluctuation (y component) (Eq. (2))
$K(x,y)$ = turbulent kinetic energy at location (x,y) (Eq. (5))
$\overline{C_u}$ = peripheral component of phase averaged absolute velocity for a constant B
$\overline{\overline{C_u}}$ = mass averaged peripheral velocity
$\overline{\overline{C_{un}}}$ = mass averaged peripheral velocity at nominal flow rate
$\overline{C_r}$ = radial component of phase averaged absolute velocity
U_2 = $U_2=\Omega R_2$
W = phase averaged relative velocity (Fig. 5)
θ = angle

References

[1] Barrand, J. P., Caignaert, G., Canavelis, R., and Guiton, P., 1984, ''Experimental Determination of the Reverse Flow Onset in a Centrifugal Impeller,'' Proceedings of the First International Pump Symposium. Texas A&M University.
[2] Barrand, J. P., Caignaert, G., Graeser, J. E., and Rieutord, E., 1985, ''Synthèse de Résultats an Air et en eau en vue de la Détection des Débits Critiques de Recirculation à l'entrée et à la Sortie de la roue d'une Pompe Centrifuge,'' La Houille Blanche No. 5, pp. 405–420.
[3] Caignaert, G., Desmet, B., Maroufi, S., and Barrand, J. P., 1985, ''Velocities and Pressure Measurements and Analysis at the Outlet of a Centrifugal Pump,'' ASME Paper 85-WA/FE-6.
[4] Caignaert, G., Barrand, J. P, and Desmet, B., 1988, ''Recirculation at Impeller

Inlet and Outlet of a Centrifugal Pump,'' Proceedings of the Institution of Mechanical Engineers, ImechE 1988-5, paper C337-88, pp. 61–68.
[5] Caignaert, G., and Morel, P., 1995, ''Mean Pressure Measurements Within a Centrifugal Pump Impeller at Partial Flow Rates,'' VDI Berichte, 1186, pp. 405–419.
[6] Caignaert, G., and Patricio, O., 1998, ''Pressure Fluctuations Within the Impeller and the Inlet Duct of a Centrifugal Pump,'' *Hydraulic Machinery and Cavitation*, World Scientific, ed, pp. 703–710.
[7] Combes, J. F., and Rieutord, E., 1992, ''Numerical and Experimental Analysis of the Flow in a Centrifugal Pump at Nominal and Partial Flow Rate,'' ASME paper 92 GT 248, 12 pages.
[8] El Hajem, M., Morel, M., Spettel, F., and Bois, G., 1998, ''Etude de l'Ecoulement Moyen en Sortie de roue d'une Pompe Centrifuge (roue SHF),'' La Houille Blanche, No. 7, pp. 24–31.
[9] Stanislas, M., Kompenhans, J., and Westerweel, J., 2000, *Particle image velocimetry: towards industrial applications*, Kluwer Academic Press, Amsterdam.
[10] Sinha, M., and Katz, J., 2000, ''Quantitative Visualization of the Flow in a Centrifugal Pump With Diffuser Vanes. I: on Flow Structures and Turbulence,'' ASME J. Fluids Eng., **122**, pp. 97–107.
[11] Sinha, M., Katz, J., and Meneveau, Ch., 2000, ''Quantitative Visualization of the Flow in a Centrifugal Pump With Diffuser Vanes. II: Addressing Passage-Averaged and Large-Eddy Simulation Modeling Issues in Turbomachinery Flows,'' ASME J. Fluids Eng., **122**, pp. 108–116.
[12] Myers, K. J., Ward, R. W., and Bakker, A., 1997, ''A Digital Particle Image Velocimetry Investigation of Flow Field Instabilities of Axial-Flow Impellers,'' ASME J. Fluids Eng., **119**, pp. 623–632.
[13] Wuibaut, G., Dupont, P., Caignaert, G., and Stanislas, M., 2000, ''Experimental Analysis of Velocities in the Outlet Part of a Radial Flow Pump Impeller and the Vaneless Diffuser Using Particle Image Velocimetry,'' XX IAHR Symposium, Charlotte, 6–9 Aug. 2000, paper GU03.
[14] Wuibaut, G., Dupont, P., Bois, G., Caignaert, G., and Stanislas, M., 2001, ''Analysis of Flow Velocities Within the Impeller and the Vaneless Diffuser of a Radial Flow Pump,'' 4th European Conference on Turbomachinery, Fluid Dynamics and Thermodynamics, 20–23 March, 2001, Firenze, Italy, paper ATI-CST-047/01.
[15] Raffel M., Willert C., and Kompenhans, J., 1998, *Particle Image Velocimetry*, Springer-Verlag, Berlin Heidelberg, p. 127.
[16] Johnston, J. P., and Eide, S. A., 1976, ''Turbulent Boundary Layers on Centrifugal Compressors Blades: Prediction of the Effects of Surface Curvature and Rotation,'' ASME J. Fluids Eng., **98**, pp. 374–381.
[17] El Hajem, M., Akhras, A., Morel, R., and Champagne, J. Y., 2001, ''Rotor Stator Interactions in a Centrifugal Pump Equipped with a Vaned Diffuser,'' 4th European Conference on Turbomachinery, Fluid Dynamics and Thermodynamics, 20–23 Mar. Firenze, Italy.
[18] Ubaldi, M., Zunino, P., and Cattanei, A., 1993, ''A. Relative Flow and Turbulence Measurements Downstream of a Backward Centrifugal Impeller,'' ASME J. Turbomach., **115**, pp. 543–551.

CFD Calculation of a Mixed Flow Pump Characteristic From Shutoff to Maximum Flow

Felix A. Muggli

Peter Holbein[1]

Sulzer Innotec,
Sulzer Markets & Technology Ltd.,
Winterthur,
Switzerland

Philippe Dupont

Sulzer Pumps Ltd.,
Winterthur,
Switzerland

The behavior of the flow in a vertical semi-axial mixed flow pump has been analyzed by numerical flow simulations of the entire stage, and the results have been compared to test data. As the flow is expected to be unsteady at part load in such a pump, the steady-state simulations were complemented with unsteady flow simulations of the entire machine at one part load operating point. Pressure measurements at different locations in the casing of the pump provided valuable data for the validation of the calculated pressure head. This paper shows that the pump characteristic can be quite accurately predicted from full load to part load by modern numerical tools. Simulations of the unsteady flow, which use much more computer resources, are also feasible in an industrial environment and yield detailed information about the flow patterns and pressure fluctuations in the pump.
[DOI: 10.1115/1.1478061]

Introduction

Vertical semi-axial flow pumps are widely used for water transportation or as cooling water pumps in thermal power stations. Their operating range spans from full load down to close to the shutoff head. In order to develop a reliable machine for this demanding operation, the behavior of the flow in the entire pump has to be predicted by a reliable computational method.

For pumps, important questions are to what extent can the current 3D Navier-Stokes design tools be used to identify the onset of instabilities in the flow, and how accurately can the pump characteristic be predicted.

It is well known that a reduction of flow increases the head and causes a rise of power for pumps with specific speeds higher than 120. Therefore the maximum power required by the pump motor is determined by the power required by the pump running at the shut off operating point. This means that the whole characteristic of a semi-axial flow pump has to be accurately predicted, including part load operating points. Therefore it is necessary to generate a detailed model of the pump for the numerical simulation of the flow. Furthermore, the limitations of the code for a particular application have to be well known.

Steady-state simulations using CFX-TASCflow (AEA Technology [1]) are routinely used for the prediction of the flow in single stages and entire machines in the design process. However, due to unsteady effects it can still be difficult to predict the pump characteristic correctly. Unsteady effects in turbomachinery include the interaction of the rotor and stator, the surge and stall limits in compressors, and the instabilities in pumps. The latter effect was the motivation to carry out an unsteady flow simulation of the same semi-axial pump with the code STAR-CD (Computational Dynamics [2]). Furthermore the limits of unsteady flow simulation within an industrial environment could be explored.

The comparison of the experimental data and the results of the steady and unsteady flow simulations show the capability of modern CFD codes. Depending on the information required for the design of a pump impeller it is not necessary to carry out an unsteady flow simulation of the entire pump. Steady calculations were performed for different relative positions between the stator and the rotor in a frozen position. The steady results have been compared to the fully unsteady solution. The possibility of using this frozen rotor approach in order to predict unsteady behavior of the pump is discussed.

Steady State Numerical Flow Simulations

The computational domain consists of the inlet pipe, the semi-axial flow impeller with four blades, and the diffuser with seven vanes. The corresponding CAD model is shown in Fig. 1.

Two sets of steady-state simulations were carried out. For the first set of simulations the rib in the inlet pipe upstream of the impeller was neglected. For the second set of simulations this strut was included in the computational grid. The flow in the impeller is computed in the rotating frame of reference, while the flow in the inlet pipe and vaned diffuser is calculated in the stationary frame of reference. A quasi-steady approximation with a mixing plane interface is used, where the core spanwise profile is preserved across the span, and the interface passes the data from one component to the other.

The grids, numerical schemes, and convergence criteria satisfy stringent quality guidelines for CFD applications (unpublished internal guidelines within Quality System ISO 9000 and ERCOFTAC Best Practice Guidelines [3]).

CFD Code. For these studies a commercial software package, CFX-TASCflow from AEA Technology [1], was used. The three-dimensional Reynolds-averaged Navier-Stokes equations are solved by this code in strong conservation form. The pressure and Cartesian velocity components are solved either in the stationary or rotating frame of reference. The transport equations are discretized using a conservative finite volume method. These simulations were run with a second order accurate skew upwind differencing scheme and physical advection correction. The system of equations is solved by a coupled algebraic multigrid method (coupled solution of mass and momentum). In these calculations the turbulence effects were modeled by the k-ε turbulence model. Logarithmic wall functions are used to model the viscous sublayer. Multi-block boundary fitted meshes with many to one grid interfaces and local grid refinement can be used. Both incompressible and compressible flows can be analyzed by CFX-TASCflow.

For these calculations, where stationary and rotating components are analyzed simultaneously, the frozen rotor and stage interfaces were employed.

At the frozen rotor interface there is a frame change, but no change in relative position. The flow can freely recirculate across the interface. Local flow features are transported across the inter-

[1]Current address: Fachhochschule Landshut, Landshut, Germany.

Contributed by the Fluids Engineering Division for publication in the JOURNAL OF FLUIDS ENGINEERING. Manuscript received by the Fluids Engineering Division July 27, 2001; revised manuscript received October 17, 2001. Associate Editor: J. Katz.

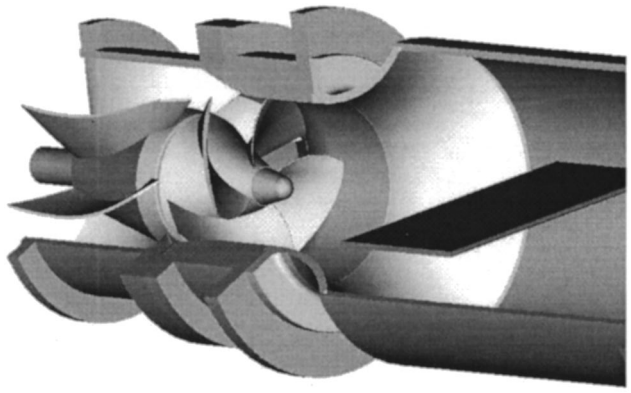

Fig. 1 Solid model assembly of the semi axial pump

face without being averaged. The frozen rotor interface can even be applied when there is a non-integer pitch change. In this case, the profiles at the interface are artificially compressed or expanded by the pitch ratio. The error at the interface increases with the pitch ratio. The error introduced at the interface reduces as the machine speed becomes small relative to the meridional flow speed.

At the stage interface the flow is averaged in the circumferential direction. Therefore single passages can be analyzed independent of the pitch change between the stationary and rotating component. This averaging removes the circumferential influence of one component on the other one. Variations, like flow recirculation, in the meridional plane are maintained. Errors induced by the stage interface are small, when the circumferential flow variations during a revolution are small at the interface.

Details regarding the theoretical basis and handling of the boundary conditions of the code are reported in full by AEA Technology [1]. Many successful applications of this code to turbomachinery problems within the authors' company have been reported in the technical literature. For example, it has been used for pump impellers by Schachenmann et al. [4], for unsteady flow in pump diffusers by Muggli et al. [5,6], for a transonic compressor rotor by Dalbert and Wiss [7], for a turbine draft tube by Drtina et al. [8], and for a complete Francis Turbine (Keck et al. [9]).

Despite the success of the code for turbomachinery flow calculations involving impeller blade rows and inlet and outlet ducts, a comparison of the calculated and measured static pressure for this specific application was considered prudent.

Geometry and Grid. The geometry of a semi-axial flow pump with a specific speed of $n_q = 155$ was discretized by structured computational meshes. An automatic elliptic grid generator developed at Sulzer Pumps provides fast grid generation for the impeller and diffuser. One grid was generated for the impeller and inlet pipe and a second one was generated for the vaned diffuser. For the case where the rib in the inlet is included, a separate grid had been generated for the inlet pipe with the rib. These meshes were then put together in the CFX-TASCflow preprocessor. In order to check the influence of the grid on the results, meshes with different numbers of nodes were tested. The final mesh consists of about 250,000 nodes.

Boundary Conditions and Operating Point. The simulations were carried out over a wide range of operating points, from the best efficiency point (100%) down to 25% of the nominal mass flow rate. Due to severe convergence problems it was not possible to compute part load operating points lower than 25%. It was assumed, that the flow phenomena are the same in all the blade passages of the impeller and diffuser. Therefore it was only necessary to discretize one passage of the impeller and diffuser and to simulate the adjacent passage with the help of periodic boundary conditions. Walls were modeled using the logarithmic law of the wall. Mass flow and axial direction was specified at the inlet while the average static pressure field was defined at the outlet boundary. The inlet and outlet boundary conditions were placed far away from the bladed components in order to minimize the influence of the boundary conditions on the flow field.

The flow in the impeller is computed in the rotating frame of reference, while the flow in the inlet pipe with the rib and in the vaned diffuser is calculated in the stationary frame of reference. A mixing plane, referred to as a stage interface, where circumferential variations are mixed out in circumferential direction, passes the data from one grid to the other. At these mixing planes the frozen rotor option was selected in order to get much better convergence compared to simulations using the stage interface. Tests showed only minor differences in the predicted head rise between simulations using a stage interface and the ones using the frozen rotor interface. As the pitch change at the frozen rotor interface is rather small (four impeller passages connected to seven diffuser passages) only small errors are generated. This explains the small differences in the head rise predictions mentioned before. To check the influence of the relative position of the components on the results, the frozen rotor simulations for two operating points were carried out at four different relative angle settings.

These interfaces between the components of the pump model the flow in an idealized form and could therefore have a impact on the results and lead to slight deviations from the measured data. For example the circumferential variations of the flow are not taken into account which could mean that the incidence in the component downstream of the interface might be in error.

Unsteady Numerical Flow Simulations

Due to the high computer resources required for unsteady flow simulations it was considered useful to carry out a simple feasibility test before working with the complex geometry of the entire pump. A two-dimensional test case, representing a simple rotor stator interaction, was computed with two different codes. Based on the experience gained from this preliminary work, it was decided to use STAR-CD (Computational Dynamics [2]) for the further unsteady computations.

CFD Code. In the software package STAR-CD different discretization schemes are available to solve the Navier-Stokes equations. The differential equations governing the conservation of mass, momentum and energy within the fluid are discretized by the finite volume method. Simulations were run with three different schemes to assess the effect of these. The first one used the upwind differencing (UD) scheme. This first order scheme which selects the nearest upwind neighbor value can lead to numerical diffusion. The second scheme used for these simulations was the monotone advection and reconstruction scheme (MARS). This second order accurate differencing scheme operates in two separate steps, reconstruction and advection. As this scheme does not rely on any problem dependent parameters to work properly, it has the least sensitivity of solution accuracy to grid structure and skewness. The third order scheme used was the quadratic upstream interpolation of convective kinematics (QUICK). It fits a parabola through two points upstream and one point downstream to get an interpolated value.

All the results presented in this paper were computed with the second order accurate MARS scheme. As CFX-TASCflow uses a second order scheme for solving the Reynolds averaged Navier-Stokes equations, too, it is feasible to compare the results of the simulations of two different codes.

The standard k-ε turbulence model with logarithmic wall functions was used to take the turbulent effects into account. The connections between the rotating impeller and the stationary inlet pipe and diffuser were modeled by a sliding mesh method with an arbitrary interface. This means that the nodes on each side of the interface do not have to match while the meshes are moved. A full implicit coupling between the stationary and rotating parts is retained.

Geometry and Grid. As the unsteady flow in the pump is not periodic in the circumferential direction it was necessary to model the entire 360 degrees of the inlet pipe with the strut, the impeller with four blades and the diffuser with seven vanes. In order to gain experience with unsteady simulations of the three-dimensional pump geometry a very coarse grid consisting of 12,300 nodes was generated first. For the final simulations a grid with a more realistic node density of about 506,000 nodes was prepared.

Computational Effort. Two sets of unsteady simulations were carried out: first, a run with the very coarse grid and then a run with the finer grid. Both computations were run at the same part load point of 35% of the nominal mass flow rate. All simulations were run on an SGI Power Challenge with R10,000 processors. The computational time required for the simulation with the coarse mesh was about ten hours on one processor for 29 revolutions of the impeller. The simulation with the fine mesh was run on five processors and about 15 hours were needed for five revolutions of the pump impeller.

As this is a transient simulation it was necessary to store the data for every time step that resulted in an output file of about 6 Gbytes.

This computational effort is close to the upper limit possible in an industrial environment. With the introduction of new processors for workstations a speed up of a factor of five can be expected and unsteady simulations could become routine.

Discussion of Results

For the steady-state simulations with and without ribs, various operating points were calculated and the computed characteristic was compared with the one derived from the measurements. Static pressure measurements at four axial locations along the casing of the pump provided the data for the verification of the results. The unsteady simulations were carried out at one part load operating point for which experimental data and results of the steady simulations are available.

Within this project results from simulations using two different codes were compared against experimental data. To minimize any errors due the use of two different simulation programs, all computations used a second order accurate discretization scheme and the standard k-ε turbulence model. The geometry used to generate the meshes for both codes were derived from the same CAD data base. The same, or where necessary similar, postprocessing was used to generate the plots for the experimental and numerical data. As already described in the previous sections interfaces were used in the simulations between the rotating and stationary parts of the pump. As these interfaces are idealized models they could influence the flow field downstream and lead to some discrepancies in the comparison to the experimental data described in the following sections.

Static Pressure Rise. The semi-axial model pump with a typical diameter of 300 mm has been tested in a closed loop with an axial inlet. A rib has been placed in front of the pump flare. Flow rate, torque on the shaft, electric motor power consumption and pump head were measured. The pump head was measured between pump suction (Ps), upstream of the rib, and discharge at the diffuser outlet (P4).

Static pressure probes were located at four positions on the casing of the pump, see Fig. 2. The first probe (P0) is upstream of the impeller at the inlet pipe. P2 is located at the wall of the casing at the impeller outlet, i.e., the mixing plane between the impeller and diffuser. The pressure taps P3 and P4 are in the vaned diffuser, close to the leading edge and downstream of the trailing edge of the vane, respectively. As Fig. 2 shows these probes are positioned at different angles in the circumferential direction.

All the pressures are measured by taps drilled through the pump casing at shroud or through the pipe walls. The static pressure difference in the impeller is based on P2-Ps and the static pressure difference in the diffuser is based on P4-P2. The pressure tap in front of the impeller P0 is only used to determine the onset of recirculation. The pressure losses between Ps and P0 are estimated by the static pressure difference obtained for the largest flow rate at which no recirculation is expected.

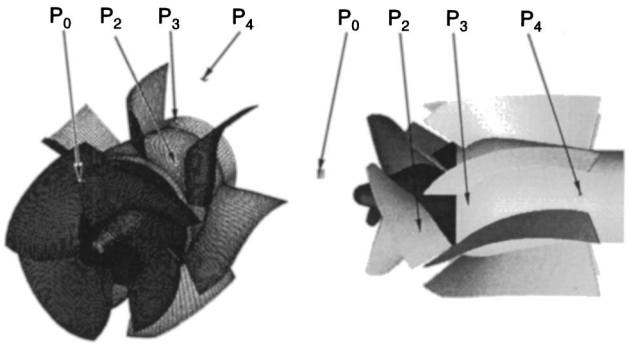

Fig. 2 Location of the pressure sensors on the casing of the pump

Figure 3 shows the head rise (total pressure difference between pressure sensor P4 and P0) for the entire stage. The static pressure difference in the impeller and the diffuser is shown in Figs. 4 and 5. The pressure data from the steady-state simulations were processed in two ways: First the pressure was taken from the cell at the wall where the pressure sensor is located (label ''local'' in Figs. 4 and 5). The label ''circ'' in Figs. 4 and 5 indicates that the static pressure at the casing was averaged in circumferential direction. As the pressure in just one cell is very sensitive to local distortions, there are differences between the two pressure curves. These differences correspond to some extent with the amplitudes of the unsteady pressure data.

Figure 3 with the head curve for the entire stage clearly shows that the simulation, in which the rib in the inlet pipe is included, corresponds very well with the curve obtained from the measurements. The simulation without the strut shows a drop in pressure rise towards the shut off head, especially at the shroud, which does not correspond with the real semi-axial flow pump. The reason for the quite large discrepancies at part load is the elimination of the prerotation of the flow upstream of the impeller by the strut located in the inlet pipe. This prerotation negatively affects the static pressure rise in the impeller. The time average of the unsteady pressure computed by the unsteady flow simulation corresponds well with the value of the steady state simulation at this part load operating point. The vertical bar in Figs. 4 and 5 indi-

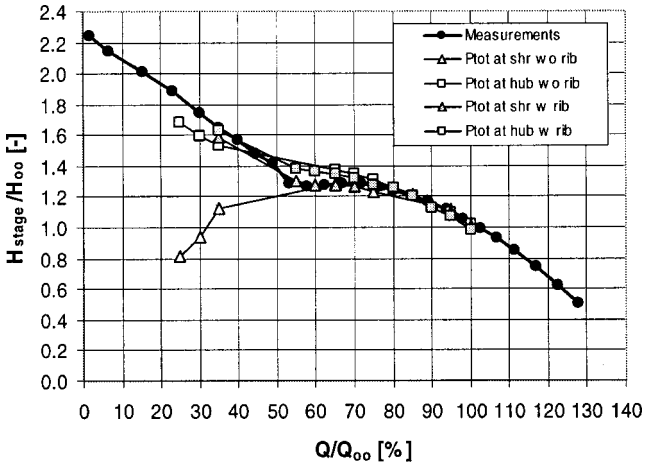

Fig. 3 Measured and calculated stage head (total pressure) curve without and with inlet rib

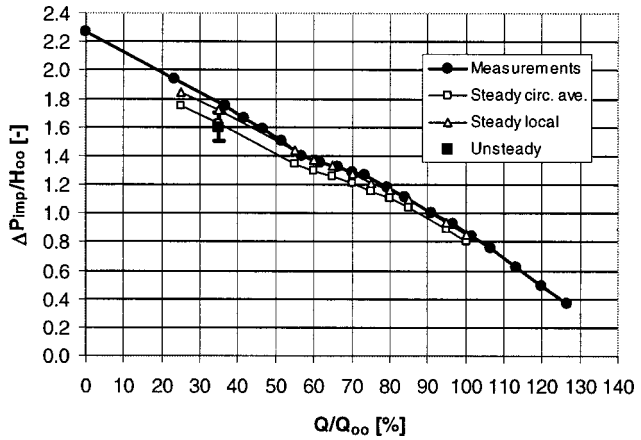

Fig. 4 Measured and calculated static pressure difference in the impeller

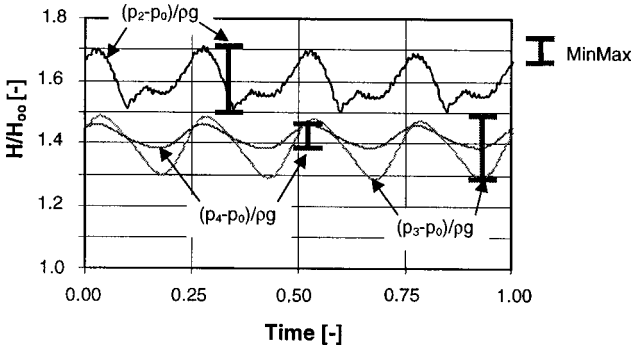

Fig. 6 Unsteady pressure calculation at different locations for $Q/Q_0=35\%$

cates the amplitude. This demonstrates the value of the mixing plane approach for predicting the steady state characteristics of pumps.

The static pressure curves for the impeller are shown in Fig. 4. The steady-state simulations slightly under predict the pressure rise, and the mean value of the unsteady simulation is equal to the steady result. In the diffuser (Fig. 5) the static pressure is under predicted by all simulations. At part load operating points below $Q/Q_0=68\%$ there is a pressure loss in the diffuser of the pump. The CFD simulations use an interface upstream of the diffuser, where in each case some flow features are idealized or neglected. This could lead to a flow incidence at the diffuser vane which does not quite agree with the real flow. This could explain why the difference between the measured and calculated pressures is greatest at in the diffuser. In summary it can be seen that all simulations slightly underpredict the static pressure rise of the entire stage and of its components.

The pressure oscillations of the unsteady simulations for one revolution of the impeller are shown in Fig. 6. The passing of the four impeller blades is clearly visible in the pressure rise in the impeller (P2-P0 and P3-P0) and in the entire stage (P4-P0). Since the diffuser has a negative pressure recovery at this part load operating point, the pressure for the entire stage is lower than in the impeller alone.

These results show, that for the prediction of global values, like the pump characteristic, it is not necessary to carry out an unsteady simulation of the entire pump. Although rather simple grids were used for these computations, it was still possible to get a very accurate prediction of the static head rise for all operating points.

Comparison Between Unsteady and Frozen Rotor Approach. For a simulation using the frozen rotor interface, the circumferential angle between the components is fixed. To investigate the influence of the relative circumferential position of the components, the steady simulations, including the rib, were carried out with four different angle settings at two operating points ($Q/Q_0=100\%$ and 35%). That means that the diffuser and the inlet pipe are positioned at four different locations relative to the impeller. These four positions were chosen to be within one partition of the vaned diffuser, i.e., within $\Theta=360/7$ degrees. The results (Fig. 7) show that this angle has a slight influence on the computed head rise.

It is interesting to note that the head variation caused by different angular positions in the frozen rotor simulations correspond very well with the amplitude of the head of the unsteady flow simulation, but this is probably purely fortuitous.

Total Pressure Rise. Figure 8 shows the circumferentially averaged total pressure in a meridional plane for two selected operating points ($Q/Q_0=100\%$, 35%) of the pump. The supporting strut at the inlet prevents a prerotation upstream of the impeller, which occurs at part load. This prerotation causes flow recirculation in the impeller. The absence of the prerotation also reduces the losses, which are shown here as total pressure. Note that the simulation has been carried out with a specified backpressure at the outlet plane, so that lower losses are visible as

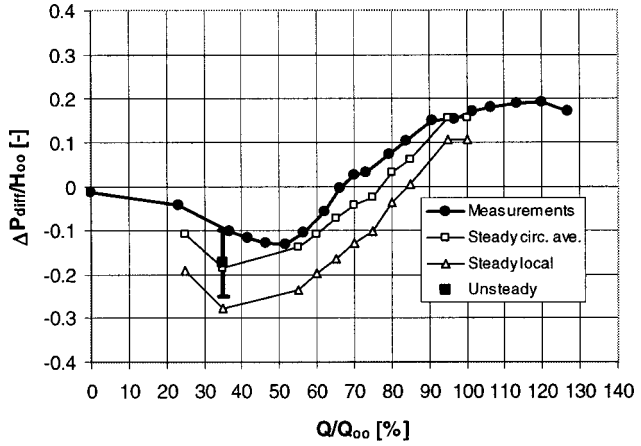

Fig. 5 Measured and calculated static pressure difference in the diffuser

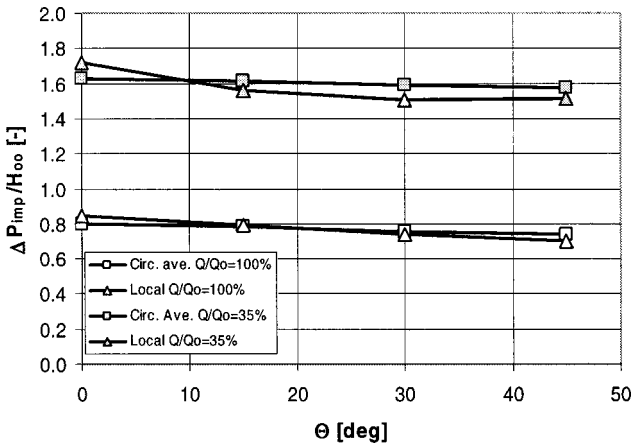

Fig. 7 Local and circumferential-averaged static pressure at impeller outlet for different relative rotor-stator positions ($Q/Q_0=35\%$ and 100%)

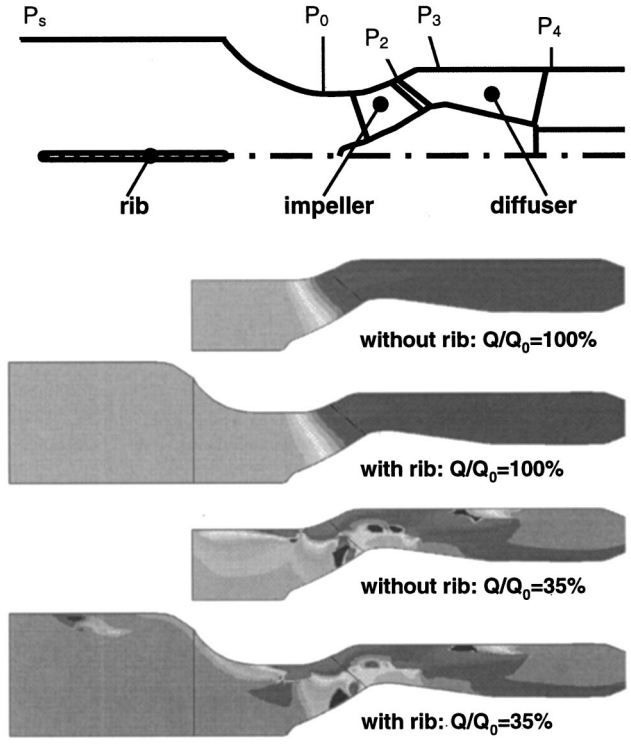

Fig. 8 Circumferentially averaged total pressure in the meridional plane ($Q/Q_0=35\%$ and 100%)

higher total pressure in upstream planes. The supporting strut at the inlet of the pump does not affect the flow in the diffuser. The distortions of the flow caused by the prerotation are mixed out within the impeller and the flow patterns in the diffuser are almost identical for both simulations.

At the part load operating point ($Q/Q_0=35\%$) areas of high losses are visible in the impeller and in the diffuser. A detailed analysis revealed, that these spots of high losses correspond quite well with the locations of the vortex cores, which could be visualized from the data of the unsteady simulations (see Fig. 9).

Vortex Structures. In order to get a good insight into the unsteady flow phenomena in the mixed flow pump a video was created from the results of the unsteady flow simulations. A snapshot from this video in Fig. 9 shows the vortex structures for this part load operating point. At this low flow rate a strong vortex can be observed just upstream of the impeller leading edge at the casing and a vortex rotating in the opposite direction is located at the exit of the impeller. This second vortex extends from the hub to the casing.

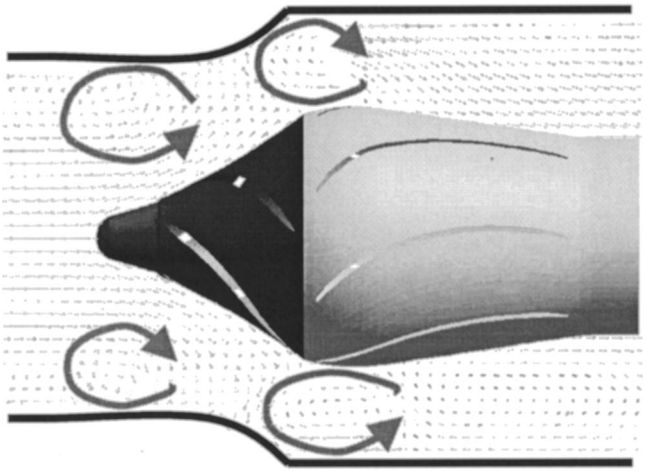

Fig. 9 Vortex structures at $Q/Q_0=35\%$

Summary

To correctly predict the static pressure rise of a semi-axial flow pump at part load it is absolutely necessary to model the correct geometry of the entire pump including the inlet. A prerotation upstream of the impeller exists if the rib in the inlet pipe is neglected, which causes a drop in static pressure rise at part load operating points. By means of stage simulations it is possible to compute the flow in the rotating and stationary parts of the pump simultaneously without large computational effort. The computed pump characteristic corresponds quite well the one derived from the pressure measurements. The range of head variation caused by different angular positions between the stator and the rotor in the frozen rotor simulations has the same amplitude as the head fluctuation in the unsteady flow simulation. The unsteady flow simulations, which use much more computer resources, give a detailed insight into the unsteady flow structures, which are quite strong at part load operating points. Both methods, steady and unsteady flow simulations, are useful for the prediction of the flow and both help significantly to understand the flow and to improve the design of future semi-axial flow pumps.

Acknowledgments

The authors wish to thank the management of Sulzer Innotec and Sulzer Pumps for financial support of this work and for permission to publish this paper.

Nomenclature

g = gravity
H = head
H_0 = nominal head
n = rotational speed
n_q = $n\sqrt{Q_0}/H_0^{0.75}$ specific speed
p = static pressure
Q = discharge
Q_0 = nominal discharge
Θ = circumferential angle
ρ = Density

References

[1] AEA Technology, 1999: *CFX-TASCflow Documentation Version 2.9*. Advanced Scientific Computing Ltd., Waterloo, Canada.
[2] Computational Dynamics, 1999, *STAR-CD User Guide Version 3.10*, Computational Dynamics Ltd., London.
[3] Casey, M. V., and Wintergerste, T. (editors), 2000, "ERCOFTAC Special Interest Group on Quality and Trust in Industrial CFD Best Practice Guidelines," Version 1.0, January 2000, ERCOFTAC.
[4] Schachenmann, A., Muggli, F., and Gülich, J., 1993, "Comparison of three Navier-Stokes Codes with LDA-Measurements on an Industrial Radial Pump Impeller," *Proc. of the ASME Fluids Engineering Conference*, Washington D.C.
[5] Muggli, F. A., Wiss, D., Eisele, K., Zhang, Z., Casey, M. V., and Galpin, P., 1996, "Unsteady Flow in the Vaned Diffuser of a Medium Specific Speed Pump," *Proc. of the 1996 Int. Gas Turbine and Aeroengine Congress & Exhibition*, 10–13 June 1996, ASME-Paper 96-GT-157, New York.
[6] Muggli, F. A., Eisele, K., Casey, M. V. et al., 1997, "Flow Analysis in a Pump Diffuser-Part 2: Validation and Limitations of CFD for Diffuser Flows," ASME J. Fluids Eng., **119**, Dec.
[7] Dalbert, P., and Wiss, D., 1995, "Numerical Transonic Flow Field Predictions for NASA Compressor Rotor 37," *Proc. Of the ASME Gas Turbine Conference*, Houston.
[8] Drtina, P., Göde, E., and Schachenmann, A., 1992, "Three-dimensional turbulent flow simulation for two different hydraulic turbine draft tubes," *Proc. of the First European CFD conference*, Brussels, September 7–11.
[9] Keck, H., Drtina, P., and Sick, M., 1996, "Numerical Hill Chart Prediction by means of CFD Stage Simulation for a Complete Francis Turbine," *Proc. of the XVIII IAHR Symposium*, Valencia, Spain.

Journal of Fluids Engineering

Technical Briefs

Application of Fractional Calculus to Fluid Mechanics

Vladimir V. Kulish
Assoc. Mem., ASME, Assistant Professor
School of Mechanical and Production Engineering,
Nanyang Technological University,
Singapore 639798

José L. Lage
Mem. ASME, Professor
Mechanical Engineering Department,
Southern Methodist University,
Dallas, TX 75275-0337
e-mail: JLL@ENGR.SMU.EDU

In this note we present the application of fractional calculus, or the calculus of arbitrary (noninteger) differentiation, to the solution of time-dependent, viscous-diffusion fluid mechanics problems. Together with the Laplace transform method, the application of fractional calculus to the classical transient viscous-diffusion equation in a semi-infinite space is shown to yield explicit analytical (fractional) solutions for the shear-stress and fluid speed anywhere in the domain. Comparing the fractional results for boundary shear-stress and fluid speed to the existing analytical results for the first and second Stokes problems, the fractional methodology is validated and shown to be much simpler and more powerful than existing techniques.

1 Introduction

Fractional calculus is a mathematical concept of differentiation and integration to arbitrary (noninteger) order, such as $\partial^{-2/3} f/\partial x^{-2/3}$. Some useful definitions and properties of fractional derivatives are presented in the Appendix. Interest in fractional calculus became evident almost as soon as the ideas of classical calculus were known. In fact, Leibnitz [1] mentioned it in a letter to L'Hospital back in 1695.

Systematic studies of fractional calculus were undertaken during the first half of the 19th century [2–4]. Euler [5], Lagrange [6], and Fourier [7] mentioned the concept of derivatives of arbitrary order earlier in their studies without contemplating any specific application.

Notable contributions have been made to both the theory and application of fractional calculus during the 20th century when some rather special, but natural, properties of differintegrals (i.e., derivatives of arbitrary order) were examined with respect to arbitrary functions [8–11]. Applications include those to problems in rheology [12,13] to electrochemistry [14–16], and to chemical physics [17].

The lack of applications of fractional calculus to solving problems in engineering, and more particularly in fluid dynamics, is notorious. This note fulfills our objective to bring forth the concept of fractional calculus to the fluid mechanics community.

We consider the problem of time-dependent momentum diffusion with a semi-infinite Newtonian fluid exposed to a time-dependent excitation at the solid-fluid interface to show how fractional calculus, together with the Laplace transform method, can be utilized to reduce the order of the differential equation ruling the phenomenon. We also show how to obtain closed-form general analytical solutions of boundary shear-stress (when the boundary velocity is known) or boundary velocity (when the boundary shear-stress is known) to this problem. Finally, we validate the analysis by considering the classical 1st and 2nd Stokes problems, and comparing the solutions obtained with the fractional approach to the solutions obtained by different methods.

2 The Extraordinary Viscous-Diffusion Equation

To contemplate how fractional calculus can be useful in fluid dynamics, we consider a one-dimensional time-dependent viscous-diffusion problem of a semiinfinite fluid bounded by a flat plate. The momentum equation, assuming constant and uniform viscosity and neglecting convective inertia (advection) effects, is:

$$\frac{\partial F(y,t)}{\partial t} - v\,\frac{\partial^2 F(y,t)}{\partial y^2} = 0 \tag{1}$$

where $F(y,t)$ is the fluid vorticity, or the fluid velocity in the case of negligible pressure effect, t is the time, v is the fluid kinematic viscosity, and y is the spatial coordinate normal to, and with origin at, the plate.

Assume the fluid to be (or, is) initially at equilibrium, so that $F(y,t<0)=F_0$, with F_0 being a constant value. Also, the condition far from the plate remains $F(\infty,t)=F_0$. The boundary of the fluid interfacing the plate is exposed to a time-dependent excitation $F(0,t>0)=F^+(t)$ caused by the plate movement. Changing the variables to $\xi = y v^{-1/2}$ and $G(\xi,t)=F(y,t)-F_0$, Eq. (1) becomes

$$\frac{\partial G(\xi,t)}{\partial t} - \frac{\partial^2 G(\xi,t)}{\partial \xi^2} = 0. \tag{2}$$

The initial and boundary conditions are now written as $G(\xi,0)=0$, $G(\infty,t)=0$, and $G(0,t)=F^+(t)-F_0=G^+(t)$, respectively. The Laplace transform of Eq. (2) is

$$\frac{d^2 G^*(\xi,s)}{d\xi^2} - sG^*(\xi,s) = 0 \tag{3}$$

where $G^*(\xi,s)$ is the Laplace transform of $G(\xi,t)$. Also, since $G(\infty,t)=0$ we then have $G^*(\infty,s)=0$. The solution of Eq. (3) is

$$G^*(\xi,s) = C_1(s)e^{[\xi(s^{1/2})]} + C_2(s)e^{[-\xi(s^{-1/2})]} \tag{4}$$

Contributed by the Fluids Engineering Division of THE AMERICAN SOCIETY OF MECHANICAL ENGINEERS. Manuscript received by the Fluids Engineering Division October 13, 1999; revised manuscript received February 18, 2002. Associate Editor: U. Ghia.

where C_1 and C_2 are arbitrary functions of s. The boundary condition $G^*(\infty,s)=0$ requires that $C_1(s)=0$, and Eq. (5) simplifies to:

$$G^*(\xi,s)=C(s)e^{[-\xi(s^{1/2})]} \tag{5}$$

where $C(s)$ remains unspecified. Now, $C(s)$ can be eliminated by using Eq. (5) and the expression

$$\frac{\partial G^*(\xi,s)}{\partial \xi}=-s^{1/2}C(s)e^{[-\xi(s^{1/2})]} \tag{6}$$

which results upon differentiating Eq. (5). Combining Eqs. (5) and (6), the resulting equation in transform space is

$$\frac{\partial G^*(\xi,s)}{\partial \xi}=-s^{1/2}G^*(\xi,s). \tag{7}$$

Equation (7) can be inverted by recognizing that $L^{-1}[\partial G^*(\xi,s)/\partial\xi]=\partial\{L^{-1}[G^*(\xi,s)]\}/\partial\xi=\partial G(\xi,t)/\partial\xi$, and using the Laplace transform property $L[\partial^f G(\xi,t)/\partial t^f]=s^f L[G(\xi,t)]=s^f G^*(\xi,s)$, valid for a function $G(\xi,t)$ that satisfies $G(\xi,0)=0$, where $\partial^f()/\partial t^f$ is a differential operator of order f. Thus, Eq. (7) becomes:

$$\frac{\partial G(\xi,t)}{\partial \xi}=-\frac{\partial^{1/2}G(\xi,t)}{\partial t^{1/2}} \tag{8}$$

and, on restoring the original variables,

$$v^{1/2}\frac{\partial F(y,t)}{\partial y}=-\frac{\partial^{1/2}[F(y,t)-F_0]}{\partial t^{1/2}}. \tag{9}$$

Using the properties of fractional calculus (*A*2) and (*A*7), listed in the Appendix, Eq. (9) can be rewritten as

$$\frac{\partial F(y,t)}{\partial y}=-v^{-1/2}\frac{\partial^{1/2}F(y,t)}{\partial t^{1/2}}+(\pi v t)^{-1/2}F_0. \tag{10}$$

Thereby, the viscous-diffusion Eq. (1), which is an ordinary PDE of first order in time and second order in space, is transformed into an extraordinary PDE of half-th order in time and first order in space, Eq. (10). Observe that this transformation is valid anywhere in the domain, including at the fluid-plate interface.

Now, recalling the diffusion constitutive law for the flux $J(t)$ at the fluid-plate interface, namely,

$$J(t)=-\mu\frac{dF(0,t)}{dy} \tag{11}$$

where μ is the fluid dynamic viscosity, and using Eq. (10) to find an expression for $dF(0,t)dy$, the surface flux $J(t)$ can be directly computed from the surface excitation $F(0,t)$ using

$$J(t)=\frac{\mu}{v^{1/2}}\left[\frac{d^{1/2}F(0,t)}{dt^{1/2}}-\frac{1}{(\pi t)^{1/2}}F_0\right]. \tag{12}$$

Therefore, the flux at the fluid boundary can be obtained by simply semi-differentiating the intensive scalar quantity $F(0,t)$. Note that for a given flux excitation $J(t)$ at the boundary, the fluid response $F(0,t)$ can be obtained by taking $\partial^{-1/2}$ [Eq. (12)] $/\partial t^{-1/2}$ resulting in:

$$F(0,t)=\frac{v^{1/2}}{\mu}\frac{d^{-1/2}J(t)}{dt^{-1/2}}+F_0. \tag{13}$$

It is important to emphasize that the transformation of the diffusion Eq. (1) into the extraordinary PDE Eq. (10) is general and not restricted by any additional assumption on the physics of the process in question.

3 Validation

To validate the previous results, consider, for instance, the first Stokes problem, i.e., the case of a flat plate that is suddenly jerked in an infinite fluid domain and whose velocity for $t>0$ is constant and equal to U. The equation of motion for this simple case is

$$\frac{\partial u(y,t)}{\partial t}-v\frac{\partial^2 u(y,t)}{\partial y^2}=0 \tag{14}$$

where u is the local fluid velocity. The initial and boundary conditions for this problem are $u(y,0)=0$, $u(0,t)=U$, and $u(\infty,t)=0$.

Upon identification of u with F, Eq. (14) becomes identical to Eq. (1), with the same kind of initial and boundary conditions (with $F_0=0$). One can, therefore, use Eq. (12) with $J(t)$ replaced by the shear-stress at the surface $\tau_w(t)$, and write

$$\tau_w(t)=\mu v^{-1/2}\frac{d^{1/2}U}{dt^{1/2}} \tag{15}$$

or, using property (*A*7), obtain

$$\tau_w(t)=\mu(\pi v t)^{-1/2}U \tag{16}$$

which is exactly the same as the result obtained by solving Eq. (14) analytically for the velocity with the entire domain, using the similarity variable, and then obtaining an expression for the wall shear-stress via the constitutive relationship for a Newtonian fluid [18]. Observe that, with the fractional approach, the same result is obtained in one simple operation, i.e., finding the semi-derivative of the uniform fluid speed U (observe that the semi-derivative of a constant is nonzero—see Eq. (*A*7) in the Appendix).

From Eq. (16), one can observe that the displacement thickness, δ^*, for the case of a suddenly jerked flat plate, is proportional to $(\pi v t)^{1/2}$. By substituting t with x/U, one can find

$$\delta^*=(\pi v x/U)^{1/2} \tag{17}$$

or, after dividing Eq. (17) by x,

$$\frac{\delta^*}{x}=\pi^{1/2}\mathrm{Re}^{-1/2} \tag{18}$$

where $\mathrm{Re}=xU/v$. By noticing that $\pi^{1/2}\approx 1.77$, one can conclude that the result obtained by means of the fractional calculus approach is much closer to the precise value 1.721 than the value 1.83 which one can get after applying the more laborious integral method [19].

Consider now a more complicated problem (the so-called second Stokes problem) in which the plate velocity is time-dependent and varies as $U(t)=U\sin(\omega t)$. The wall shear-stress at the steady periodic regime can be obtained analytically in this case as well. The procedure to obtain this solution involves first modifying the viscous-diffusion equation to a complex velocity model, then solving the differential equation for the complex velocity, extracting the velocity solution from the complex velocity and finally using the constitutive relationship for a Newtonian fluid to obtain the corresponding shear-stress ([18], pp. 138–141). The result is

$$\tau_w(t)=U\mu\left(\frac{\omega}{2v}\right)^{1/2}[\sin(\omega t)+\cos(\omega t)]. \tag{19}$$

Using the fractional calculus approach, Eq. (12) gives for the shear-stress

$$\tau_w=\mu v^{-1/2}\frac{d^{1/2}[U\sin(\omega t)]}{dt^{1/2}}. \tag{20}$$

Now, using (*A*3), (*A*4), and (*A*8) with Eq. (20), one has

$$\tau_w(t)=\mu v^{-1/2}U\omega^{1/2}\left\{\sin\left(\omega t+\frac{\pi}{4}\right)-2^{1/2}\Lambda\left[\left(\frac{2\omega t}{\pi}\right)^{1/2}\right]\right\} \tag{21}$$

where Λ is the auxiliary Fresnel function (see Appendix). Observe that Eq. (21) is not identical to Eq. (19). This is because Eq. (21) is the general solution for the shear-stress, which includes the initial transient regime, see Fig. 1. On the other hand, Eq. (19) is the solution only of the steady-periodic regime, i.e., when time

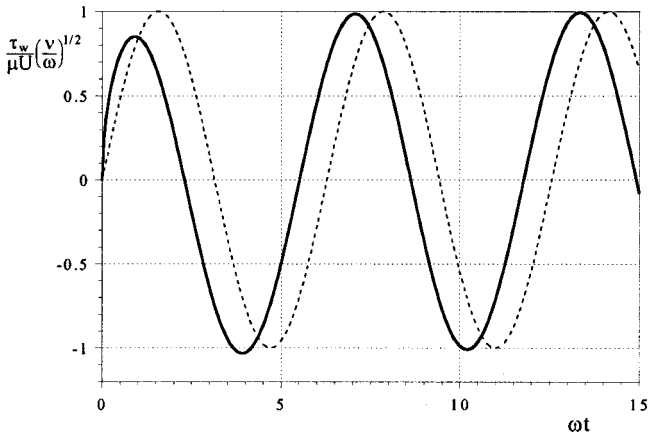

Fig. 1 Time evolution of surface shear stress, Eq. (21), and the imposed boundary condition (dashed line): $U(t)/U=\sin(\omega t)$.

is long enough for the flow process to become periodic. Notice that the term proportional to the auxiliary Fresnel function Λ of Eq. (21) governs the initial unsteady regime. When time is long enough, the contribution of the auxiliary Fresnel function to Eq. (21) becomes negligible because $\Lambda(z)$ approaches zero as z increases (for instance, at $t\sim 10\pi/\omega$, $|\max\{\Lambda[2\omega t/\pi)^{1/2}]\}| < 0.001$). In this case, and upon expanding the sine function, one recovers from Eq. (21) exactly the solution for the steady-periodic regime presented in Eq. (19).

4 Summary and Conclusions

A brief historical overview of fractional calculus was presented. considering the viscous-diffusion problem of a semi-infinite fluid bounded by a moving solid surface, the simplified transport PDE, of first order in time and second order in space, was converted, via Laplace transform, into an extraordinary differential equation of half order in time and first order in space.

Closed-form analytical solutions for the flux and for the scalar response (fluid vorticity or velocity) at the fluid-solid interface were found. The results were validated considering the known solutions for the 1st and 2nd Stokes problems. The simplicity and accuracy involved in obtaining the local system response to a transient excitation within a semi-infinite viscous-diffusion system using the fractional approach was then established. Moreover, specifically regarding the 2nd Stokes problems, the fractional approach leads to an analytical solution for the entire regime, Eq. (21), including the nonperiodic initial regime. Observe that the nonperiodic initial regime is not covered by the analytical solution, Eq. (19).

The fractional approach presented here has the potential for becoming a powerful tool in solving other differential equations in fluid mechanics (such as time-diffusion vorticity equations with sources or sinks, linearized compressible aerodynamics equations, linearized viscous sublayer equations, and acoustic wave equations).

The application of fractional calculus need not be restricted to linear equations. Moreover, the factorization of time-diffusive operators (i.e., $\partial/\partial t-\nabla^2$), common in fluid dynamics equations, can be proposed as a more direct and general method (because it is not restricted to one-dimension) for obtaining the fractional equivalent to the original PDE's. Being of reduced order, the resulting fractional equation should require less computational effort to be solved. Finally, we point out that by using an extension to Taylor's series applied to fractional derivatives [20], the discretization of fractional equations does not require the use of transform definitions.

Appendix

In this Appendix, some useful definitions and properties of fractional derivatives are presented. From the several equivalent definitions of fractional derivatives, the most elegant is the Riemann-Liouville definition [21], namely:

$$\frac{d^f[g(t)]}{dt^f}=\frac{1}{\Gamma(-f)}\int_0^t\frac{g(\tau)}{(t-\tau)^{1+f}}d\tau \tag{A1}$$

where f is any negative number and Γ is the Gamma function. Some of the useful properties derived from Eq. (A1) are:

$$\frac{d^f[u(t)+v(t)]}{dt^f}=\frac{d^f[u(t)]}{dt^f}+\frac{d^f[v(t)]}{dt^f} \tag{A2}$$

$$\frac{d^f[Cg(t)]}{dt^f}=C\frac{d^fg(t)}{dt^f}\quad \frac{d^f[tg(t)]}{dt^f}=t\frac{d^fg(t)}{dt^f}+f\frac{d^{f-1}g(t)}{dt^{f-1}} \tag{A3}$$

$$\frac{d^h}{dt^h}\left(\frac{d^fg(t)}{dt^f}\right)=\frac{d^{h+f}g(t)}{dt^{h+f}}\quad \frac{d^f[g(Ct)]}{dt^f}=C^f\frac{d^fg(Ct)}{d(Ct)^f} \tag{A4}$$

$$\frac{d^f\delta(t-\tau)}{dt^f}=\frac{1}{\Gamma(-f)}(t-\tau)^{-f-1},\quad f<0 \tag{A5}$$

$$\frac{d^f[t^n]}{dt^f}=\frac{\Gamma(n+1)}{\Gamma(n+1-f)}t^{n-f}\quad \frac{d^f[C]}{dt^f}=\frac{Ct^{-f}}{\Gamma(1-f)} \tag{A6}$$

where $\delta(t-\tau)$ is the Dirac delta function, defined as $\delta(t-\tau)=\infty$, if $t=\tau$, otherwise, $\delta(t-\tau)=0$. In the previous formulas, C is a nonzero constant. Observe that the first expression in (A4) is not general (see [20] for limitations).

The semi-derivatives (case of f being $\pm 1/2$) of some common functions are:

$$\frac{\partial^{1/2}[C]}{\partial t^{1/2}}=C(\pi t)^{-1/2} \tag{A7}$$

$$\frac{d^{1/2}[\sin(t)]}{dt^{1/2}}=\sin\left(t+\frac{\pi}{4}\right)-2^{1/2}\Lambda\left[\left(\frac{2t}{\pi}\right)^{1/2}\right] \tag{A8}$$

$$\frac{d^{1/2}[\cos(t)]}{dt^{1/2}}=\frac{1}{(\pi t)^{1/2}}+\cos\left(t+\frac{\pi}{4}\right)-2^{1/2}\Omega\left[\left(\frac{2t}{\pi}\right)^{1/2}\right] \tag{A9}$$

$$\frac{d^{-1/2}[C]}{dt^{-1/2}}=2C\left(\frac{t}{\pi}\right)^{1/2} \tag{A10}$$

$$\frac{d^{-1/2}[\sin(t)]}{dt^{-1/2}}=\sin\left(t-\frac{\pi}{4}\right)+2^{1/2}\Omega\left[\left(\frac{2t}{\pi}\right)^{1/2}\right] \tag{A11}$$

$$\frac{d^{-1/2}[\cos(t)]}{dt^{-1/2}}=\cos\left(t-\frac{\pi}{4}\right)+2^{1/2}\Lambda\left[\left(\frac{2t}{\pi}\right)^{1/2}\right] \tag{A12}$$

In Eqs. (A8), (A9), (A11), and (A12), Ω and Λ are the auxiliary Fresnel integrals (function f and g, respectively, in [22], p. 300).

References

[1] Leibnitz, G. W., Letter from Hanover, Germany, September 30, 1695, to G. A. L'Hospital, Leibnizen Mathematische Schriften, **2**, pp. 301–302. Olms Verlag, Hildesheim, Germany, 1962, First published in 1849.

[2] Liouville, J., 1932, "Mémoie: Sur le calcul des différentielles à indices quelconques," Journal Ecole Polytechniuqe, **13**, p. 71.

[3] Riemann, B., 1953, "Versuch einer allgemeinen Auffasung der Integration und Differentiation," *The Collected Works of Bernhard Riemann*, H. Weber, ed., 2nd ed., Dover, New York.

[4] Holmgren, H. J., 1864, "Om differentialkalkylen med indices of hvad nature sam helst," Kgl. Sv. Vetenskapsakademia Handl, **11**, p. 1.

[5] Euler, L., 1730, *Mémoire dans le tome V des Comment*, Saint Petersberg Années, **55**.

[6] Lagrange, J. L., 1772, "Sur une nouvelle espèce de calcul relatif à la differentiation et à l'integration des quantités variables," Ouvres de Lagrange, **3**, Gauthier-Villars, Paris, p. 441.

[7] Fourier, J. B. J., 1822, ''Théorie analytique de la chaleur,'' Oeuvres de Fourier, **1**, Didot, Paris, p. 508
[8] Weyl, H., 1917, ''Bemerkungen zum Begriff des Differentialquotienten gebrochener Ordnung,'' Vierteljschr. Naturforsch. Gesellsch., Zürich, **62**, p. 296.
[9] Hardy, G. H., and Littlewood, J. E., 1928, ''Some properties of fractional integrals, I,'' Math. Z., **27**, p. 565.
[10] Kober, H., 1940, ''On fractional integrals and derivatives,'' Quarterly Journal of Mathematics Oxford Series, **11**, p. 193.
[11] Kuttner, B., 1953, ''Some theorems on fractional derivatives,'' Proc. London Math. Soc., **3**, p. 480.
[12] Scott Blair, G. W., Veinoglou, B. C., and Caffyn, J. E., 1947, ''Limitations of the Newtonian time scale in relation to non-equilibrium rheological states and a theory of quasiproperties,'' Proc. R. Soc. London, Ser. A, **187**, pp. 69–85.
[13] Graham, A., Scott Blair, G. W., and Withers, R. F. J., 1961, ''A methodological problem in rheology,'' British Journal Philosophical Science, **11**, pp. 265–278.
[14] Belavin, V. A., Nigmatullin, R. Sh., Miroshnikov, A. I., and Lutskaya, N. K., 1964, ''Fractional differentiation of oscillographic polarograms by means of an electrochemical two-terminal network (in Russian),'' Trudy Kazan Aviatsion Institutel, **5**, pp. 144–152.
[15] Oldham, K. B., 1972, ''Signal-independent electroanalytical method,'' Anal. Chem., **44**, pp. 196–208.
[16] Grenness, M., and Oldham, K. B., 1972, ''Semiintegral electroanalysis: theory and verification,'' Anal. Chem., **44**, pp. 1121–1139.
[17] Somorjai, R. L.,and Bishop, D. M., 1970, ''Integral-transformation trial functions of the fractional-integral class,'' Phys. Rev. A, **1**, pp. 1013–1026.
[18] White, F. M., 1991, *Viscous Fluid Flow*, McGraw-Hill, New York.
[19] Schlichting, H., 1978, *Boundary Layer Theory* (translated by J. Kestin), McGraw-Hill, New York.
[20] Oldham, K. B., and Spanier, J., 1974, *The Fractional Calculus*, Academic Press, New York.
[21] Riesz, M., 1949, ''L'intégral de Riemann-Liouville et le problème de Cauchy,'' Acta Math., **81**, p. 1.
[22] Abramowitz, M., and Stegun, I. A., 1964, *Handbook of Mathematical Functions*, Dover, New York.

Constant Pressure Laminar, Transitional and Turbulent Flows—An Approximate Unified Treatment

J. Dey
Department of Aerospace Engineering,
Indian Institute of Science,
Bangalore 560012, India

A nondimensional number that is constant in two-dimensional, incompressible and constant pressure laminar and fully turbulent boundary layer flows has been proposed. An extension of this to constant pressure transitional flow is discussed.
[DOI: 10.1115/1.1486221]

1 Introduction

For the two-dimensional (2-D), constant pressure and incompressible laminar flow and fully turbulent flow over a semi-infinite flat plate, a nondimensional number that is independent of the nature of these flows has been proposed here. This nondimensional number is based on the boundary layer momentum thickness, the shape factor, the skin-friction coefficient, and the streamwise distance.

Since the proposed nondimensional number is constant for the constant pressure laminar and turbulent flows, it is assumed to have the same value in constant pressure transitional boundary layer flows. This is utilized to propose an implicit solution of the momentum integral equation for the laminar, transition and turbulent regions.

Contributed by the Fluids Engineering Division of THE AMERICAN SOCIETY OF MECHANICAL ENGINEERS. Manuscript received by the Fluids Engineering Division November 14, 2000; revised manuscript received January 31, 2002. Associate Editor: E. Graf.

2 Analysis

We consider the 2-D constant pressure, and incompressible boundary layer flow over a semi-infinite plate. Let u and v denote the boundary layer velocity components in the x and y directions, respectively; x is the streamwise direction. The free-stream velocity is denoted by U. The constant pressure momentum integral equation considered here is [1],

$$d\theta/dx = C_f/2. \tag{1}$$

Here, θ and C_f denote the local momentum thickness, and the skin-friction coefficient, respectively:

$$\theta = \int_0^\infty \frac{u}{U}\left(1-\frac{u}{U}\right)dy, \quad C_f = 2\nu U^{-2}(\partial u/\partial y)_{y=0},$$

where ν is the kinematic viscosity. Although the momentum integral equation (1) is valid for the laminar, turbulent and transitional flows, only the laminar and turbulent cases have been solved (see Ref. [1]), separately. Usually, one requires a correlation for C_f to obtain θ.

We propose the nondimensional quantity,

$$L = \theta/(xC_fH^{0.7}). \tag{2}$$

Here $H(=\delta^*/\theta)$ is the shape parameter, and δ^* is the local displacement thickness:

$$\delta^* = \int_0^\infty \left(1-\frac{u}{U}\right)dy.$$

For the laminar flow, the Blasius solution [1] ($C_f=\theta/x$, $H=2.6$) gives the value of this nondimensional quantity as $L \simeq 0.51$. Similarly, the 1/7th power-law for fully turbulent flow [1] ($\theta/x \simeq 0.036R_x^{-0.2}$, $C_f \simeq 0.0592R_x^{-0.2}$, $H=1.27$, where R_x $(=Ux/\nu)$ is the Reynolds number) gives $L \cong 0.51$. The 1/7th law being a popular one and in view of the availability of reliable experimental data, the 1/5th or 1/10th power-law has not been considered here. The experimental data for fully turbulent flows show that both H and C_f decrease slowly with x (see, for example, Proc. AFOSR-IFP-Stanford Confc. [2]). As shown in Fig. 1, the measured constant pressure data (number 1400 and 3000) of AFOSR-IFP-Stanford Confc. [2] also show that $L \simeq 0.5$ at high Reynolds number; in this figure R_θ denotes the Reynolds number based on the momentum thickness. (It may be noted that the AFOSR-IFP-Stanford Confc. Data are those carefully selected for the data bank value.) It can be seen in this figure that, except at $R_\theta \simeq 600$, the experimental data show an excellent collapse over a large Reynolds number range; the maximum deviation of 12% is attributed to the scatter usually associated with the experimental data. The behavior at $R_\theta \simeq 600$ is attributed to the low Reynolds number effect; for example, it is known [3] that the Cole's wake function agrees with the experimental data for fully turbulent flows at $R_\theta \simeq 1000$. The momentum equation (1) does not contain H, which is associated with the boundary layer velocity profile shapes. An inspection of the momentum integral equation (1) suggests that the quantity $\theta/(xC_f)$ can be of the order of unity. This

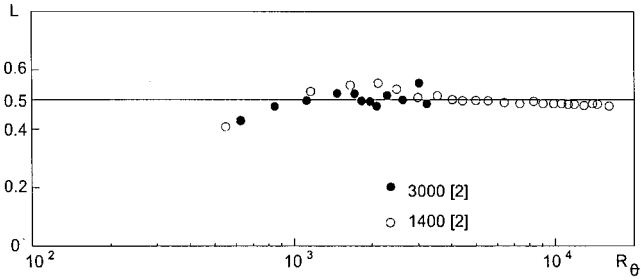

Fig. 1 Fully turbulent data showing a constant value of *L*

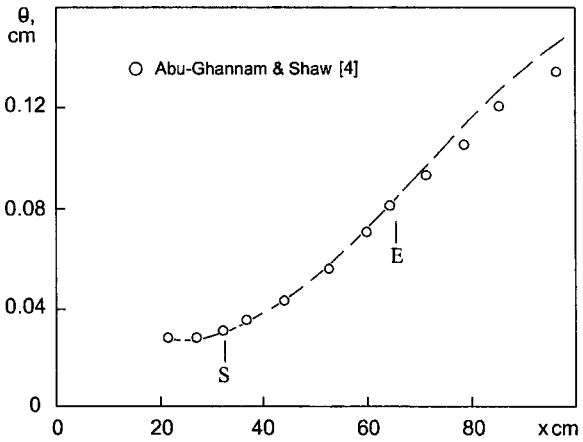

Fig. 2 Streamwise variation of the momentum thickness from laminar to turbulent state; S and E: start and end of transition; line: fits to the data

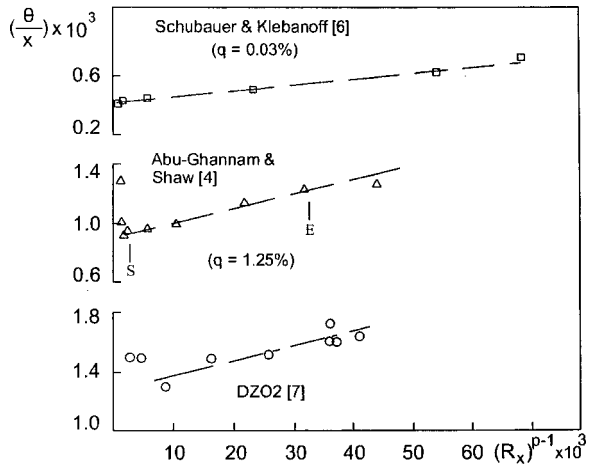

Fig. 3 Linear variation of θ/x with $(R_x)^{p-1}$ during transition; S and E: start and end of transition for the data of [4]; line: fit to the data

is expected since θ is a direct measure of the drag force for flow over a flat plate [1]. However, the numerical values of the quantity $\theta/(xC_f)$ will be different for the Blasius and fully turbulent flows. The introduction of the factor $H^{0.7}$ in (2) provides a numerically constant value of L in these two flows; this value of the exponent is found to yield $L \simeq 0.5$. We therefore conclude that the *proposed nondimensional number does not distinguish between a constant pressure laminar or turbulent boundary layer flow. A layman number*?

For the constant pressure transitional flow, one expects L to be about 0.5, as well. During transition, both C_f and θ increase from the laminar value to the fully turbulent value in the streamwise direction; a typical variation of θ is shown in Fig. 2, where the data of Abu-Ghannam and Shaw [4] have been used; S and E marked in this figure denote the start and end of transition, respectively, as reported by these authors. The shape parameter, however, decreases from the laminar value to the turbulent value in the transition region. It is important to note here that, unlike the Blasius boundary layer and the turbulent boundary layer originating at $x=0$, the transitional boundary layer *does not originate at* $x=0$. Although the intermittency distribution [5] or correlation is used to infer the onset of transition, we consider the following. We assume that the boundary layer parameters change, in reference to the appropriate origin of the transitional boundary layer, in such a way that the value of L is still about 0.5. For $L \simeq 0.5$, we have, $\theta/(xH^{0.7}) \simeq C_f/2$. The momentum integral equation (1) now becomes,

$$\theta^{-1} d\theta/dx = x^{-1} H^{-0.7}. \tag{3}$$

We consider a solution of this with locally prescribed value of H. The value of $H^{-0.7}$ varies from about 0.5, for the laminar flow, to about 0.8, for the turbulent flow, in the transition region. We therefore make a weak assumption that $H^{-0.7}$ is *locally independent of* x, i.e., locally constant. Under this assumption, the solution of (3) is,

$$\theta = Ex^p, \quad p \equiv H^{-0.7}, \tag{4}$$

where E is a constant. The growth rate of θ for the Blasius flow or the 1/7th power-law turbulent flow can easily be recovered from this expression for θ. As suggested by a referee, we recast (4) as: $\theta/x = E'(R_x)^{p-1}$; E' is a constant. As shown in Fig. 3, the measured transitional data of Schubauer and Klebanoff [6], Abu-Ghannam and Shaw [4], and DZO2 of Dey and Narasimha [7] show a linear variation of θ/x with $(R_x)^{p-1}$. We note here that the value of p has been prescribed locally from the measured data. In this figure, the first data point of Schubauer and Klebanoff and the second data point of DZO2 correspond to the intermittency, γ, based onset of transition; as is known, $\gamma \rightarrow 1$, asymptotically to the fully turbulent state; the freestream turbulence level, $q\%$, for the data of Schubauer and Klebanoff and Abu-Ghannam and Shaw are also indicated in this figure. Figure 3 indicates some dependence of the slope of θ/x versus $(R_x)^{p-1}$ line on q. This is not discussed here and requires a separate investigation. It can be seen (in Fig. 3) that the proposed linear variation of θ/x with $(R_x)^{p-1}$ in the transition region is very satisfactory. A complete agreement cannot be expected as the flow Reynolds number at the end of transition usually remains lower (for most of the data) than the Reynolds number range for which the 1/7th law or any fully turbulent relation is valid. The present analysis also relies on a correlation for C_f. But being an outcome of constant L, this correlation is flow independent. One weakness of the present proposal is that the exponent of x in (4) is $H^{-0.7}$, when H itself depends on θ. This is attributed to the nonlinear feature associated with the governing

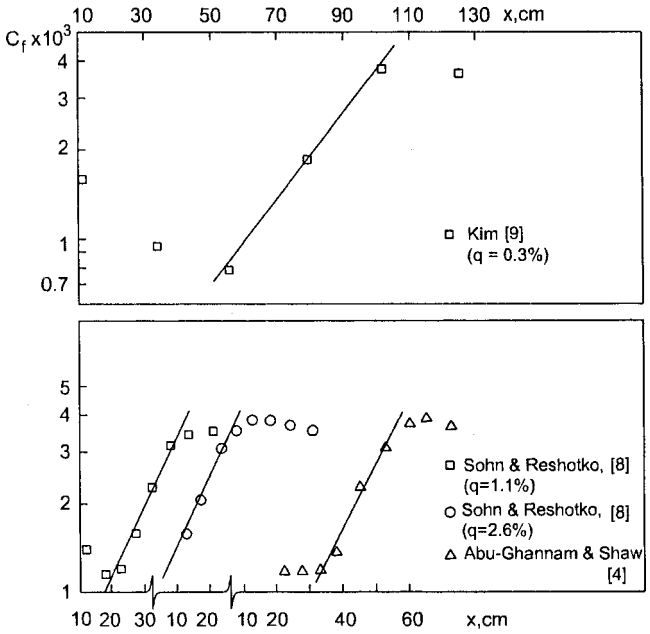

Fig. 4 Exponential growth of the skin-friction during transition; line: fit to data

equation. Thus, like many approximate but useful solutions of the momentum integral equation (1), the present proposal seems quite meaningful.

Another aspect of the transition region worth mentioning here is the observed exponential growth rate of C_f, i.e., $C_f \propto \exp(x)$, as shown in Fig. 4; the experimental data of Sohn and Reshotko [8] and Kim [9] shown in this figure are taken from the data complied by Volino and Simon [10]. Consequently, the growth rate of θ in the transition zone is also exponential. It is not difficult to arrive at this result by assuming the quantity $xH^{0.7}$ to be constant in the transition region as another possible solution of (3). This and the earlier assumption of locally constant $H^{0.7}$ need not be viewed as conflicting ones, since (3) can have different solutions, depending on the assumption made for the boundary layer parameters, and yet maintaining a value of $L \simeq 0.5$. On the whole, although more justifying analyses are needed for the transition region, this new observation may be useful in predicting transition.

3 Conclusion

For 2-D constant pressure and incompressible boundary layer flows, a new nondimensional number L has been defined in (2). It is found that $L \simeq 0.5$ for both the laminar and high Reynolds number turbulent flows. For $L \simeq 0.5$ and locally constant value of the shape parameter, the momentum integral equation is solved to obtain an implicit solution for the integral parameters in constant pressure laminar, transitional and turbulent flows.

References

[1] White, F. M., 1974, *Viscous Fluid Flow*, McGraw-Hill, New York.

[2] Coles, D. E., and Hirst, E. A., 1968, *Proc. Computation of Turbulent Boundary Layers-1968*, AFOSR-IFP-Stanford Confc., Vol. II.

[3] Purtell, L. P., and Klebanoff, P. S., 1981, "Turbulent Boundary Layer at Low Reynolds Number," Phys. Fluids, **24**(5), pp. 802–811.

[4] Abu-Ghannam, B. J., and Shaw, R., 1980, "Natural Transition of Boundary Layers—The Effects of Turbulence, Pressure Gradient and Flow History," J. Mech. Eng. Sci., **22**(5), pp. 213–228.

[5] Narasimha, R., 1957, "On the Distribution of Intermittency in the Transition Region of a Boundary Layer," J. Aeronaut. Sci., **14**, pp. 711–712.

[6] Schubauer, G. B., and Klebanoff, P. S., 1955, "Contributions on the Mechanics of Boundary Layer Transition," NACA TN 3489.

[7] Dey, J., and Narasimha, R., 1990, "Integral Method for the Calculation of Incompressible Two-Dimensional Transitional Boundary Layers," J. Aircr., **27**(10), pp. 859–865.

[8] Sohn, K. H., and Reshotko, E., 1989, "Some Characteristics of Bypass Transition in a Heated Boundary Layer," NASA TM-102126.

[9] Kim, J., 1990, "Free-stream Turbulence and Concave Curvature Effects on Heated Transitional Boundary Layers," Ph.D. thesis, Dept. Mechanical Eng., University of Minnesota.

[10] Volino, R. J., and Simon, T. W., 1991, "Bypass Transition in Boundary Layers Including Curvature and Favorable Pressure Gradient Effects," NASA CR 187187.

Journal of Fluids Engineering

Discussion

Discussion: "Comprehensive Approach to Verification and Validation of CFD Simulations—Part 1: Methodology and Procedures" (Stern, F., Wilson, R. V., Coleman, H. W., and Paterson, E. G., 2001, ASME J. Fluids Eng., 123, pp. 793–802)

William L. Oberkampf
Distinguished Member Technical Staff,
Validation and Uncertainty Estimation Dept., MS 0828,
Sandia National Laboratories, Albuquerque,
New Mexico 87185

The paper by Stern et al. proposes a comprehensive approach to verification and validation of computational fluid dynamics simulations. Although the authors present a new perspective for quantifying verification and validation, I believe there is a conceptual flaw in the proposed approach to validation. Three criticisms follow.

1 The authors define verification as " . . . a process for assessing simulation numerical uncertainty . . . " I agree with the authors when they say that their definition of verification is not contradictory with the broader definitions developed by Roache [1] and the AIAA Guide [2]. However, as pointed out clearly by Roache and others, there are two other important facets of verification: code verification and software quality assurance. Code verification deals with assessing the correctness of the computer program in implementing the discrete form of the partial differential equations, as well as the numerical algorithms needed to solve the discrete equations. Software quality assurance deals with topics such as code robustness, version control, static and dynamic testing, and documentation. In this paper, the authors only address the issue of solution verification, neglecting to mention these two other topics of equal importance. For a paper claiming to present a comprehensive approach, this is misleading.

2 The authors state that their definition of verification is implemented in Eq. (10), which is

$$S_C = T + \delta_{SM} + \varepsilon_{SN}$$

where S_C is the result from the corrected simulation, T is the "truth," δ_{SM} is the simulation modeling error, and ε_{SN} is the estimated numerical error from the simulation. Although the authors do not clearly state what the "truth" is in this expression, the only interpretation that makes sense, based on their discussion starting with Eq. (1), is that T is the true value resulting from experimental measurement. Discussing verification in terms of experimental measurements and simulation modeling error causes a great deal of confusion when people are trying to understand the fundamental differences between verification and validation. As Roache [1] lucidly puts it, "Verification deals with mathematics, validation deals with physics."

When substituting the definition of δ_{SM} into Eq. (10), one obtains

$$S_C = M + \varepsilon_{SN}$$

where M is defined as the exact, or analytical, solution to the continuum partial differential equations. This equation appears to be consistent with accepted definitions of verification. However, in order to get to Eq. (10), the authors had to define the error in the corrected solution, δ_{S_C}, as

$$\delta_{S_C} = S_C - T$$

That is, the authors had to introduce the true value from experiment in order to get to their equation for verification. This is a confusing and circuitous route to verification.

3 The authors define validation as " . . . a process for assessing simulation modeling uncertainty . . . " which is consistent with broader definitions of validation developed by Roache [1] and the AIAA Guide [2]. The authors claim to implement this definition using their Eq. (17) and the narrative that follows. Their result is

$$|E| < \sqrt{U_D^2 + U_{SPD}^2 + U_{SN}^2}$$

where E is the comparison error, U_D is the uncertainty in an individual experimental measurement, U_{SPD} is the uncertainty in the simulation model due to use of previous data, and U_{SN} is the uncertainty in the numerical error estimate. E is defined as $D - S$, where D is the result obtained from an individual experimental measurement, and S is the result from a numerical simulation.

The authors' implementation of validation does not embody their definition of validation because of the way they define the comparison error E. First, they define the comparison error using an individual experimental measurement D. This is in contrast to using the true experimental value T. As the number of experimental measurement samples increases, the statistical mean converges to the true value, ignoring systematic (bias) error. That is, as more experimental realizations are obtained, the key issue becomes: how does the simulation compare to the mean as opposed to any individual measurement?

Second, they define the comparison error using an individual numerical simulation result S. Since S can have an arbitrary magnitude of numerical error, it is not a reflection of the true value from the model, which is M. Validation should measure how well the true value from the model compares with the experiment, not how well a simulation value polluted by numerical error compares with the experiment.

Because of the way in which they define the comparison error E, the authors' implementation of validation is forced into the following situation. The simulation can be declared validated by increasing the right side of their validation equation. The right side can be increased by: (a) increasing the experimental uncertainty; (b) increasing the uncertainty in data used from previous analyses; or (c) increasing the numerical uncertainty in a given simulation. As pointed out by Roache [3] and Oberkampf and Trucano [4], this makes no sense.

The authors responded to Roache's criticism in a previous Author's Closure [3], as well as in the subject paper, by saying that what is really important is the magnitude of the validation measure required by the application of the code. In my opinion, this is sidestepping the criticism because the criticism is directed at the way the validation measure *itself* is defined, not how it might be used. Resorting to the use of application requirements in defining the validation measure is contrary to the fundamental meaning of validation. This misunderstanding, widespread in the community, presumes that validation means assessing whether the simulation has ''passed'' or ''failed'' an application requirement.

Validation, as defined by the AIAA Guide [2], and earlier by the Defense Modeling and Simulation Office of the Department of Defense [5], is: ''The process of determining the degree to which a model is an accurate representation of the real world from the perspective of the intended uses of the model.'' Stated differently, validation is *only* a measure of the agreement between simulation and experiment. The magnitude of the measure is not an issue as far as validation is concerned. This may seem contradictory to people who are new to the terminology of verification and validation. Validation is defined in this way for two reasons. First, the required magnitude of the validation measure varies from one application to another. For example, the magnitude of a validation measure that is satisfactory for one application may be a factor of ten or more larger than what is needed for another application. Second, in multi-physics simulations one does not know before hand what level of validation is needed for each component of physics. There is actually an interaction of validation measure requirements, and trade-off between requirements, in order to achieve the accuracy required for the particular system response quantity of interest. That is why application requirements cannot be used to defend a particular implementation of a validation measure.

Acknowledgment

Sandia is a multiprogram laboratory operated by Sandia Corporation, a Lockheed Martin Company, for the United States Department of Energy under Contract DE-AC04-94AL85000.

References

[1] Roache, P. J., 1998, *Verification and Validation in Computational Science and Engineering*, Hermosa Publishers, Albuquerque, NM.

[2] AIAA, 1998, ''Guide for the Verification and Validation of Computational Fluid Dynamics Simulations,'' American Institute of Aeronautics and Astronautics, AIAA-G-077-1998, Reston, VA.

[3] Roache, P. J., 1998, ''Discussion: Uncertainties and CFD Code Validation,'' ASME J. Fluids Eng., **120**, pp. 635–636.

[4] Oberkampf, W. L., and Trucano, T. G., 2000, ''Validation Methodology in Computational Fluid Dynamics,'' American Institute of Aeronautics and Astronautics, AIAA 2000-2549, Fluids 2000 Conference, Denver, CO.

[5] DoD, 1996, ''DoD Instruction 5000.61: Modeling and Simulation (M&S) Verification, Validation, and Accreditation (VV&A),'' Defense Modeling and Simulation Office, Office of the Director of Defense Research and Engr.

Closure to ''Discussion of 'Comprehensive Approach to Verification and Validation of CFD Simulations—Part 1: Methodology and Procedures''' (2002, ASME J. Fluids Eng., 124, p. 809)

Hugh W. Coleman
Eminent Scholar in Propulsion, Professor,
Propulsion Research Center, Department of Mechanical and Aerospace Engineering, University of Alabama in Huntsville, Huntsville, AL 35899

(1): I do not understand how the word ''simulation'' in the title can be misinterpreted as ''code'' or ''software.''

(2) and (3): I believe the confusion arises from his use of the definition of uncertainty as ''A potential deficiency in any phase of the modeling process that is due to lack of knowledge'' (which does not quantify a range within which truth lies with a specified degree of confidence) as opposed to the concepts and definitions used in current experimental uncertainty analysis [1] (which do quantify such a range).

The ranges $D \pm U_D$ and $S \pm U_S$ both contain (with 95% confidence) the truth T, which is independent of experiment or simulation. The assumption (also made in Oberkampf and Trucano, 2000) that D is ''an individual experimental measurement'' is inaccurate. The experimental result is D, and U_D *is the uncertainty considering any averaging, any correlated systematic uncertainties, and any correlated random uncertainties* [1].

M is the simulation result with the continuous equations solved exactly ($U_{SN}=0$) with no uncertainty in the inputs ($U_{\mathrm{SPD}}=0$), *but includes the errors due to modeling assumptions*. Thus, the assumption ''the true value from the model, which is M'' is inaccurate. Again, the true value T is independent of experiment or simulation.

After enlightening discussions over the last two years (particularly with Patrick Roache), my view has evolved to consider ''a validated simulation'' to mean that a simulation has undergone the validation process and that a level of validation (the larger of $|E|$ and $|U_V|$) has been established. I agree with Oberkampf that ''the magnitude of the measure''—in my words, the level of validation—''is not an issue as far as validation is concerned.'' However, it follows logically that the qualification ''from the perspective of the intended uses of the model'' should not be part of a definition of validation since the level of validation of a simulation variable is independent of the intended use of the model.

Reference

[1] Coleman, H. W., and Steele, W. G., 1999, *Experimentation and Uncertainty Analysis for Engineers*, 2nd Edition, Wiley, New York.

Closure to ''Discussion of 'Comprehensive Approach to Verification and Validation of CFD Simulations—Part 1: Methodology and Procedures'''' (2002, ASME J. Fluids Eng., 124, p. 809)

Fred Stern

Robert Wilson

In the discussion, the definitions of truth T, experimental result D, modeled solution M, and simulation solution S seem to differ from ours. These key variables were defined using a sequence of initial boundary value problems (IBVP) summarized in the paper and derived in [13].

The IBVP for T by definition contains no modeling or numerical errors. Approximate solutions for T are provided by experimental, analytical, and simulation methods. Experimental methods use measurement systems and data acquisition and reduction procedures to provide D with error $\delta_D = D - T$. Analytical and simulation methods reformulate the IBVP for T using approximate models for the partial differential equation operators, initial and/or boundary conditions. Analytical methods solve the IBVP for M and δ_{SM} exactly, and thus are limited to simple fluid mechanics

problems. The continuous IBVP for M is reduced to a discreet IBVP for S, which is solved by the CFD computer code, introducing additional numerical errors. The $\delta_{SN}=S-M$ is defined by transforming the discreet IBVP back to a continuous IBVP. As this shows, we believe that D, M, and S inherently have errors, which are estimated using experimental uncertainty analysis and verification and validation (V&V) methodologies and procedures, respectively.

Response to criticism (1)

The focus of our paper is on V&V methodology and procedures for CFD simulations with an already developed CFD code. It is implicitly assumed that code verification and software quality assurance issues have already been addressed during code development.

Response to criticism (2)

T in Eq. (10) has been clearly defined as the truth, which differs from the simulation result S by simulation error δ_S and from the experimental result D by experimental error δ_D. Therefore, we in no way have introduced experimental measurements or simulation modeling error in discussing verification and deriving Eq. (10).

Response to criticism (3)

The experimental result D in Eqs. (13), (14), and (18) has been clearly defined as the experimental result with error δ_D and associated uncertainty U_D. D is not an individual measurement, but based on appropriate averaging. S is the simulation result with simulation error δ_S and associated uncertainty U_S, comprised of the addition and root-sum-square of numerical and modeling errors and uncertainties, as defined by Eqs. (1) and (2), respectively. S is based on iterative and input parameter convergence studies using multiple solutions and systematic parameter refinement. The value used is usually the finest value of input parameter. The numerical and modeling error and uncertainty estimates are not arbitrary. The V&V procedures described in our paper provide quantitative estimates for levels of numerical and modeling errors and uncertainties. We have not used application requirements in defining validation, but rather used our validation definition to assess application requirements. The level of validation is important in that it determines one's ability to discriminate among modeling assumptions/approaches, and to judge if a particular application requirement has been met. We have already addressed issues related to fact that validation uncertainty excludes modeling assumption uncertainty and ''noisy'' data and solutions are easier to validate in our paper and have no further comment.